Counterion Effects in Reductive Catalysis: Synthesis and Reactivity of Low-Valent Cobaltate Salts and Applications in Alkene Hydrogenation

Dissertation

zur Erlangung des Doktorgrades der Naturwissenschaften

Dr. rer. nat.

am Institut für Anorganische Chemie

an der Fakultät für Chemie und Pharmazie

der Universität Regensburg

vorgelegt von:

Martin Gawron

aus Waldkraiburg

Regensburg, Mai 2025

Der experimentelle Teil der vorliegenden Arbeit wurde in der Zeit zwischen Juni 2021 und April 2025 unter Anleitung von Prof. Dr. Robert Wolf am Institut für Anorganische Chemie der Universität Regensburg angefertigt.

Die Arbeit wurde angeleitet von:		Prof. Dr. Robert Wolf
Promotionsgesuch eingereicht am:		21. Mai 2025
Datum der mündlichen Prüfung:		31. Juli 2025
Promotionsausschuss:	Vorsitz	Prof. Dr. Patrick Nürnberger
	Erstgutachter	Prof. Dr. Robert Wolf
	Zweitgutachter	Prof. Dr. Axel Jacobi von Wangelin
	Drittprüferin	Prof. Dr. Ruth M. Gschwind

Thesis Overview

This thesis primarily reports on low-valent cobaltate complexes and their applications in hydrogenation catalysis. Chapter 1 reviews the reactivity of selected s-block and d-block bimetallic compounds in small molecule activation and catalysis, focusing on counterion effects. Chapter 2 describes the hydrogenation of alkenes using a series of anionic cobaltate pre-catalysts with different countercations. A significant change in reactivity is observed, which is documented in comparative analyses and supported by computational studies. Chapter 3 reports the synthesis and characterization of an unsupported magnesium cobaltate complex. Its bonding situation is analyzed by experimental and computational methods, and its catalytic activity in alkene hydrogenation is described. Chapter 4 reports the synthesis and characterization of phosphine-stabilized cobalt hydride complexes. The hydrogenation of magnesium cobaltates in the presence of a diphosphine affords β-diketiminate magnesium salts of anionic tetrahydrido cobaltates, which are characterized spectroscopically and computationally, and subjected to reactivity studies. Chapter 5 presents a thematically different project on the photocatalytic functionalization of white phosphorus (P_4) with aryl bromides and chlorides. Triarylphosphines and tetraarylphosphonium salts are directly accessed using an acridinium-based photocatalyst and near-UV light irradiation. Lastly, chapter 6 summarizes the results described in this thesis and provides a short outlook.

Aufbau der Arbeit

Diese Dissertation befasst sich mit niedervalenten Kobaltatkomplexen und deren Anwendung in der Hydrierkatalyse. Kapitel 1 gibt einen Überblick über die Reaktivität bimetallischer s-Block- und d-Block-Verbindungen in der Katalyse und Aktivierung kleiner Moleküle, mit einem besonderen Fokus auf Gegenioneneffekte. Kapitel 2 beschreibt die Hydrierung von Alkenen mit einer Reihe von anionischen Kobaltat-Präkatalysatoren mit unterschiedlichen Gegenionen. Es wird eine signifikante Änderung der Reaktivität in Abhängigkeit von den Kationen beobachtet, die in vergleichenden Analysen dokumentiert und durch quantenchemische Berechnungen gestützt wird. Kapitel 3 beschreibt die Synthese und Charakterisierung eines nackten Magnesium-Kobaltat-Komplexes. Die Bindungssituation wird experimentell und mit quantenchemischen Methoden analysiert und der Komplex in der Alkenhydrierung eingesetzt. Kapitel 4 behandelt die Synthese von Phosphan-stabilisierten Kobalthydridkomplexen. Die Hydrierung von Magnesium-kobaltaten in Gegenwart eines Diphosphans führt zu β-Diketiminatomagnesium-Salzen anionischer Tetrahydridokobalt-Komplexe, die spektroskopisch und quantenchemisch charakterisiert und hinsichtlich ihrer Reaktivität untersucht werden. Kapitel 5 umfasst ein thematisch unterschiedliches Projekt zur photokatalytischen Funktionalisierung von weißem Phosphor (P_4) mit Arylbromiden und -chloriden. Triarylphosphine und Tetraaryl-phosphoniumsalze werden mittels eines Acridinium-basierten Photokatalysators unter Bestrahlung mit nahem UV-Licht zugänglich gemacht. Abschließend werden in Kapitel 6 die Ergebnisse dieser Arbeit zusammengefasst und ein kurzer Ausblick gegeben.

Table of Contents

1 Synergistic Effects in Bimetallic s-Block and d-Block Metal Compounds: Small Molecule Activation and Catalysis 1

1.1 Tunable Features, General Reactivity and Ion Pairing in Heterobimetallic Complexes Based on s-Block and d-Block Metals 3

1.2 Cation Effects and Heterobimetallic Reactivity 5

1.2.1 Hydrogenation Reactions 5

1.2.2 C–H, C–C, C–O, C–X, and N–H Bond Activation 9

1.2.3 Isomerization Reactions 15

1.2.4 Polymerization Reactions 19

1.2.5 Miscellaneous Small Molecule Activation Reactions 23

1.3 Summary and Outlook 25

1.4 References 26

2 Counterion Effect in Cobaltate-Catalyzed Alkene Hydrogenation 31

2.1 Introduction 33

2.2 Results and Discussion 35

2.2.1 Pre-Catalyst Synthesis and Initial Evaluation of Counterion Influence 35

2.2.2 Catalyst Properties of [(^{Dep}nacnac)Mg][Co(η^4-cod)$_2$] (4) 36

2.2.3 Catalyst Topicity 37

2.2.4 Modeling Alkene Coordination 39

2.2.5 Counterion Influence on Hydrogen Uptake 40

2.2.6 Computational Studies 42

2.3 Conclusion 46

2.4 Supporting Information 48

2.4.1 General Information 48

2.4.2 Synthesis of Compounds 49

2.4.3 Synthesis of Starting Materials 53

2.4.4 Hydrogenation Reactions 55

2.4.5 Kinetic Studies and Mechanistic Experiments 58

2.4.6 NMR Spectroscopic Data 75

2.4.7 Single-Crystal X-ray Diffraction Data 81

2.4.8 Computational Studies 84
2.5 References 109
3 A Highly Reduced Magnesium Dicobalt Complex for the Hydrogenation of Tri- and Tetra-Substituted Alkenes 115
3.1 Introduction 117
3.2 Results and Discussion 118
3.3 Conclusion 122
3.4 Supporting Information 123
3.4.1 General Information 123
3.4.2 Synthesis and Characterization of $Mg[Co(\eta^4\text{-}cod)_2]_2$ (1) 123
3.4.3 Hydrogenation Study 125
3.4.4 Mercury Poisoning Experiments 126
3.4.5 Additional Experiments 128
3.4.6 Reaction of $Mg[Co(\eta^4\text{-}cod)_2]_2$ (1) with THF and DMAP 134
3.4.7 Reaction of $Mg[Co(\eta^4\text{-}cod)_2]_2$ (1) with Styrene and Dibenzo[*a*,*e*]cyclooctene . 137
3.4.8 NMR Monitoring of the Hydrogenation of α-Methylstyrene 139
3.4.9 NMR Spectra of $Mg[Co(\eta^4\text{-}cod)_2]_2$ (1) 141
3.4.10 Single Crystal X-ray Diffraction Data 144
3.4.11 Quantum Chemical Calculations 145
3.5 References 151
4 Synthesis, Characterization and Reactivity of Phosphine-Stabilized Cobalt Hydrides 155
4.1 Introduction 157
4.2 Results and Discussion 160
4.2.1 Synthesis and Characterization of $[(^{Ar}nacnac)Mg][CoH_4(dcpe)]$ (Ar = Dep, 1; Ar = Mes, 2) 160
4.2.2 Hydrogenation Reactions with $[(^{Dep}nacnac)Mg][CoH_4(dcpe)]$ (1) 163
4.2.3 Synthesis and Characterization of $[(^{Ar}nacnac)Mg][(\mu,\eta^4\text{:}\eta^4\text{-}P_4)Co(dcpe)]$ (Ar = Dep, 5; Ar = Mes, 6) 167
4.3 Conclusion 170
4.4 Supporting Information 171
4.4.1 General Information 171

4.4.2 Synthesis of Compounds 172
4.4.3 Synthesis and Attempted Isolation of [((−)-(*S*)-Naphnacnac)Mg][CoH_4(dcpe)] (3) 176
4.4.4 Hydrogenation Reactions with [(Depnacnac)Mg][CoH_4(dcpe)] (1)..... 177
4.4.5 Supporting Studies on the Reactivity of [(Depnacnac)Mg][CoH_4(dcpe)] (1)..... 179
4.4.6 DOSY NMR Analysis of [(Depnacnac)Mg][CoH_4(dcpe)] (1)..... 186
4.4.7 Reactivity Study of [(Depnacnac)Mg][(μ,η^4:η^4-P_4)Co(dcpe)] (5)..... 190
4.4.8 NMR Spectroscopic Data..... 195
4.4.9 IR Spectroscopic Data..... 204
4.4.10 Single Crystal X-ray Diffraction Data 206
4.4.11 Computational Studies 210
4.5 References..... 216
5 Photocatalytic Functionalization of White Phosphorus with Aryl Bromides and Chlorides 221
5.1 Introduction..... 223
5.2 Results and Discussion 224
5.3 Conclusion..... 228
5.4 Supporting Information..... 229
5.4.1 General Information..... 229
5.4.2 General Protocol for Photocatalytic Functionalization of P_4 (0.04 mmol Scale) 230
5.4.3 Optimization of Reaction Conditions 231
5.4.4 Characterization of Photocatalytic Arylation Reactions at 0.04 mmol Scale 237
5.4.5 Synthesis of [Ph_4P]Br and (*o*-tol)$_3$P on a Preparative Scale 266
5.4.6 NMR Spectroscopic Investigations..... 273
5.4.7 Photocatalytic Phenylation of $PhPH_2$, Ph_2PH, Ph_4P_2 and Ph_3P and Stability Study with [Ph_4P]Br..... 279
5.4.8 Photocatalytic Arylation of $NaPH_2$ 281
5.5 References..... 285
6 Summary and Conclusion..... 289
7 Acknowledgements 295
8 Curriculum Vitae..... 297
9 List of Publications..... 299

Chapter 1 Synergistic Effects in Bimetallic s-Block and d-Block Metal Compounds: Small Molecule Activation and Catalysis[a]

Abstract: Transition metal catalysts enable a vast array of important chemical transformations. In most cases, mononuclear transition metal complexes are employed that have been carefully optimized by stereoelectronic modification of their ligand framework. However, numerous recent studies have shown that combining two metals in a heterobimetallic complex can unlock reactivities surpassing those of the single-metal systems. This introduction explores reactions of heterobimetallic complexes comprised of s-block metal and d-block metal atoms. We describe the key interactions that determine the reactivity of such systems. The participation of two metal atoms enables the exploitation of complementary electronic effects, structural preorganization and multisite substrate activation. Electrostatic interactions are another important parameter in the hetero-bimetallic ion pairs that can significantly influence their reactivity. A defining feature of these systems is their ability to adopt cation-sensitive mechanisms, which is examined for its potential to complement and diversify catalyst design. We anticipate that heterobimetallic systems will become increasingly useful in the development of more efficient catalytic transformations.

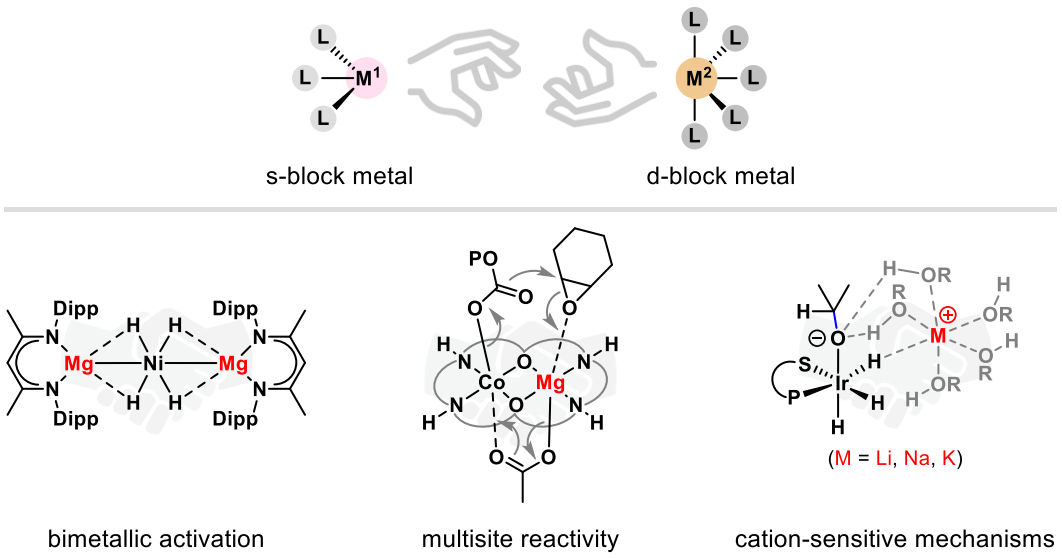

[a] Martin Gawron wrote the manuscript.

1.1 Tunable Features, General Reactivity and Ion Pairing in Heterobimetallic Complexes Based on s-Block and d-Block Metals

Transition metal complexes are an integral part of modern synthetic chemistry and have been instrumental in the development of many established catalytic procedures. Although the majority of transition metal complexes used in homogenous catalysis are monometallic, there is a growing interest in bimetallic systems.[1] Numerous homo- and heterobimetallic transition metal complexes are known,[2] which are often inspired by natural metalloenzymes, many of which function via bimetallic synergism.[3]

A third rapidly growing class is the combination of a main group metal (MGM) with a transition metal (TM) to furnish a heterobimetallic MGM/TM complex (Figure 1). Frequently used MGMs are alkali and alkaline earth metals (described herein), as well as selected group 13 elements, including Al, Ga and In,[4] which are paired with late transition metals such as Fe, Co, Ni but also Ir and Pd. Such bimetallic systems have several distinct features that are inaccessible for mononuclear species. These include complementary effects based on the different stereoelectronic properties of the metal centers M^1 and M^2 (such as internal polarization), as well as structural preorganization and the ability to activate bonds at multiple sites (Figure 1a).[5] According to Campos and co-workers, bond activation occurs via distinct pathways involving two different metal atoms (Figure 1b): (i) the simultaneous binding of a single substrate to both metal centers, (ii) the binding of one substrate to one metal center with assistance from the second metal center, and (iii) the binding of two distinct substrates to separate metal centers.[2c],[5]

In a heterobimetallic complex comprising an s-block metal atom and a d-block metal atom, the bond activation predominantly occurs at the transition metal center (M^2, Figure 1b). The s-block metal (M^1, Figure 1b) serves as a secondary activator, facilitating the overall activation (multisite (i)-(iii), Figure 1b) through stereoelectronic modulation.

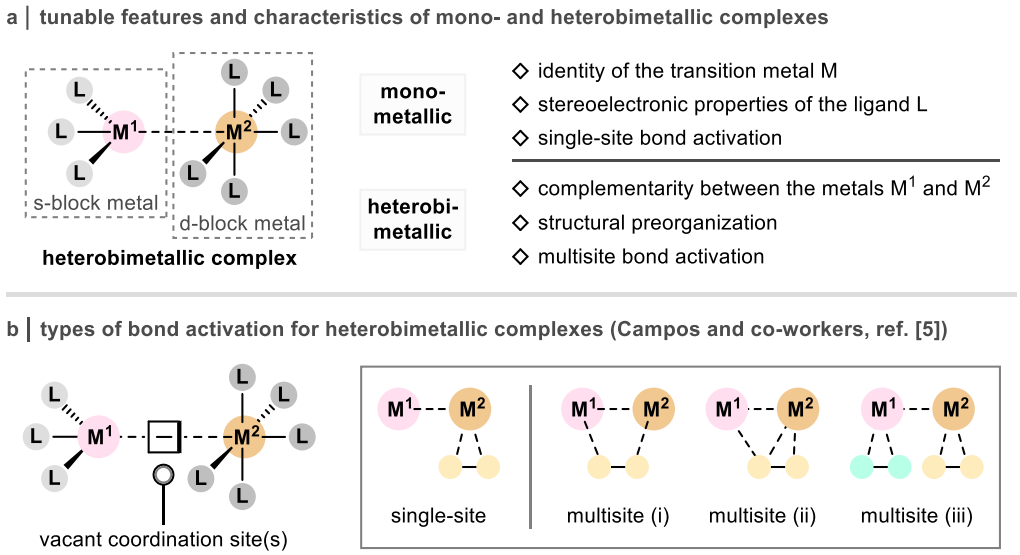

Figure 1. (a) Tunable features of monometallic and heterobimetallic complexes. (b) Types of bond activation at one and two metal sites for heterobimetallic complexes (Campos and co-workers, ref. [5]).

However, both metals are essential to the success of the chemical transformation. This situation is due to the different characteristics of the s- and d-block metal centers in the heterobimetallic complexes, which are not only reflected in their bonding behavior but also set them apart from purely transition metal-based complexes. While the d-block metal atoms typically display covalent bonding,[1a],[6] the interactions in s-block/d-block bimetallics are predominantly electrostatic with very low covalent character (Figure 2).[7] Consequently, ion pairing effects must be taken into account to accurately understand the reactivity of such systems.[8] These include the charge density of the ionic fragments, the relative orientations of the ions within the heterobimetallic ion pairs, and their coordination by solvent molecules.

The solvation behavior can be summarized in a simplified picture, which classifies three types of ion pairs (Figure 2).[8] In solvents with a low dielectric constant, contact ion pairs with a common solvent shell and no solvent molecule interposing are energetically favored. In higher dielectric solvents, the ions are separated by a shared solvent shell or exhibit each a separate solvent shell and are termed solvent-shared and solvent-separated ion pairs, respectively. In order to exert cooperative reactivity (i.e., an ion pairing effect), the ionic fragments need to be in close proximity, which is possible in contact and solvent-shared ion pairs. Given that such an arrangement is provided, the heterobimetallic systems can further adopt cation-sensitive mechanisms, which offers an alternative strategy to alter reaction rates and selectivities.

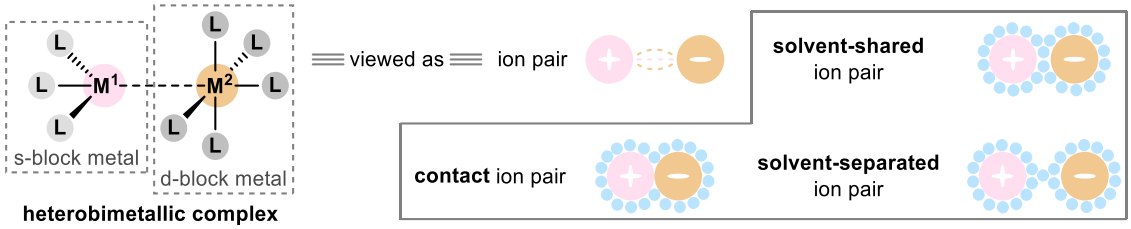

Figure 2. Ion pairing aspects for heterobimetallic complexes of s-block and d-block metals with ionic character.

In this work, we review the literature of heterobimetallic systems composed of an s-block metal atom and a d-block metal atom. In considering examples from fundamental chemical reactions (e.g., hydrogenation), we analyze the cooperative mechanisms at play and, where applicable, discuss reactivity changes induced by alteration of the s-block metal cation. Ion pairing significantly influences the reactivity of many systems described in this review. Finally, we present an outlook on future challenges and opportunities, hopefully motivating other researchers to explore heterobimetallic synergies in chemical transformations and utilize cation-sensitive mechanisms.

1.2 Cation Effects and Heterobimetallic Reactivity

1.2.1 Hydrogenation Reactions

1.2.1.1 Anionic Hydrogenation Catalysis with Alkoxide Bases

Catalytic hydrogenation using H_2 gas is usually the domain of late transition metal complexes. A convenient way to generate the active catalyst is by treating a transition metal halide precursor with a strong base (e.g., KO^{t}Bu).[9] If the pre-catalyst contains a Brønsted acidic site, the active complex can be formed through a salt elimination and deprotonation sequence[9a,c,e] or base-assisted hydrogenolysis.[9d] Although this typically produces a neutral hydride complex, the activation with excess strong base can also generate anionic active species. Among these are TM/XH (X = N, O) bifunctional catalysts in which an *X*–*H* motif in the coordinating ligand is deprotonated by the external base.[10]

Kempe and co-workers reported the use of heterobimetallic Mn and Fe pre-catalysts bearing a deprotonatable *N*–*H* motif in hydrogenation catalysis (Figure 3a-c).[11] Starting from the precursor complexes [MnH]H_2 and [FeBr]H_2 (Figure 3c), the double deprotonation with an alkali metal alkoxide (in the presence of H_2) generates the dianionic complexes [MnH]M_2 and [FeH]M_2 (M = Li, Na, K; see Figure 3d for M = K). The potassium salts efficiently hydrogenate imines and ketones with high functional group tolerance, while analogous Li^+ and Na^+ salts were less active. Kinetic studies for the manganese system revealed that altering the co-catalytic alkoxide base MO^{t}Bu (M = Li, Na, K) accelerates the reaction in the order $Li^+ < Na^+ < K^+$ (Figure 3a).[11a] Similarly, the substitution of potassium (K^+) by sodium (Na^+) or lithium (Li^+) in the iron system significantly decreased the catalytic activity (Figure 3b).[11c]

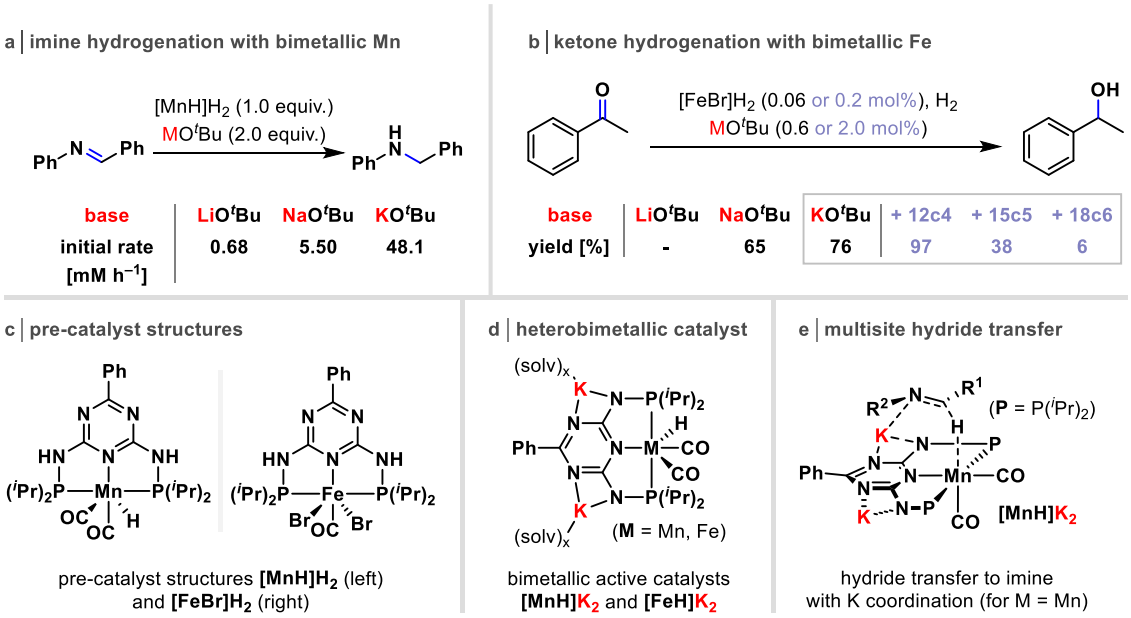

Figure 3. (a) + (b) Imine and ketone hydrogenation with Mn and Fe catalysts showing alkali cation influence on the reactivity. (c) Pre-catalyst structures. (d) + (e) Bimetallic K–M (M = Mn, Fe) active catalyst and graphical representation of the proposed rate-determining hydride transfer step (for the imine hydrogenation). 12c4 = 12-crown-4. 15c5 = 15-crown-5. 18c6 = 18-crown-6. solv = thf or 12c4.

Inhibition experiments employing crown ethers as sequestering agents showed that the conversion in the hydrogenation reaction is reduced considerably in the order: 18-crown-6 > 15-crown-5 > 12-crown-4, consistent with their decreasing binding affinity for K^+. These findings suggest that direct proximity of the alkali metal cation to the transition metal anion is required for high activity. The authors propose that the rate-determining hydride transfer follows an outer-sphere mechanism, where the transition metal and alkali metal play an active role (see Figure 3e for TM = Mn and M = K).[12] The potassium cation, which is positioned in a ligand cavity, coordinates to the nitrogen atom of the incipient amide during hydride transfer. The short-lived potassium amide then rapidly reacts with HO^{t}Bu to yield the amine, KO^{t}Bu, and a monopotassium salt, which is subsequently converted back into the dianionic catalyst [MnH]K_2 by reacting with KO^{t}Bu and H_2.

When using ligands that lack a protic motif such as *P*,*S*-disubstituted ferrocenes,[13] the Poli group demonstrated that the hydrogenation of ketones with an iridium chloride pre-catalyst and alkoxide base proceeds via an anionic tetrahydride complex (Figure 4).[14] A pronounced cation effect was observed, when different alkali metal bases (MOR; M = Li, Na, K; R = ^{i}Pr or ^{t}Bu) were used in the (asymmetric) hydrogenation of acetophenone (Figure 4a).[14c] The product formation significantly increased following the trend: $Li^+ < Na^+ < K^+$, while the addition of 18-crown-6 to the most active potassium system resulted in a drastic reduction of the catalytic activity.

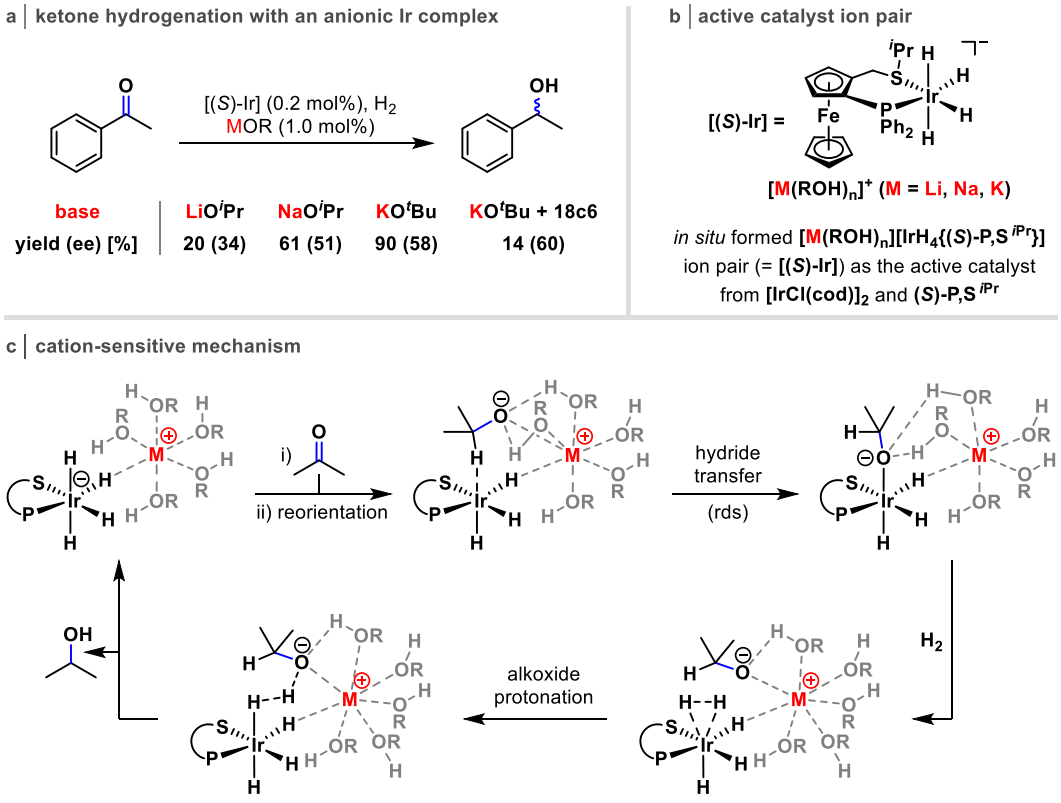

Figure 4. (a) Influence of the alkali metal cation in the iridium-catalyzed hydrogenation of acetophenone. (b) Proposed structure of the *in situ* formed alkali metal iridium tetrahydride ion pair catalyst. (c) Simplified mechanism of the hydrogenation of acetone showing ion pairing interactions. R = Me, ^{i}Pr.

Moreover, no reaction was observed when an ammonium base ([NMe_4OH]) was used instead of an alkali metal base, indicating that the presence of an alkali metal cation is essential for effective reactivity. Detailed DFT calculations on the active catalyst ion pairs (Figure 4b) showed that the explicit solvation of the alkali metal cation by five alcohol ligands (forming $[M(ROH)_5]^+$) is crucial to reproduce the experimental results. The hydrogenation follows a hydride transfer/protonation sequence, in which both metals cooperatively activate and coordinate the substrate (Figure 4c). The rate-determining hydride transfer is accompanied by a rearrangement of the solvation sphere, followed by the displacement of one or more solvent molecules as the newly formed alkoxide anion binds to the alkali metal cation. The authors propose that the observed cation effect does not stem from direct interactions between the alkali metal and the substrate or the anionic iridium fragment. Instead, they are inherently linked to cation-dependent coordination sphere rearrangements.

1.2.1.2 H_2 Activation with a β-Diketiminate Magnesium Nickelate

The activation of H_2 by a single-site transition metal complex often involves the oxidative addition of H_2 to the metal center. Conceptually different from mononuclear activation, the activation of H_2 can also proceed by bimetallic cooperation.[15] Established systems include complexes that incorporate either two transition metal atoms or a combination of transition metal and main group elements, the latter usually being a group 13 element such as B, Al, Ga, and In.[2a,d],[16] In contrast, very few systems describe the H_2 activation using a hetero-bimetallic system that includes an s-block metal alongside a transition metal atom.[16] The activation of H_2 using a molecular s- and d-block bimetallic complex was reported by Xu and co-workers in their study of an ethylene nickel complex that is supported by a Mg-based metalloligand (Figure 5).[7d],[18]

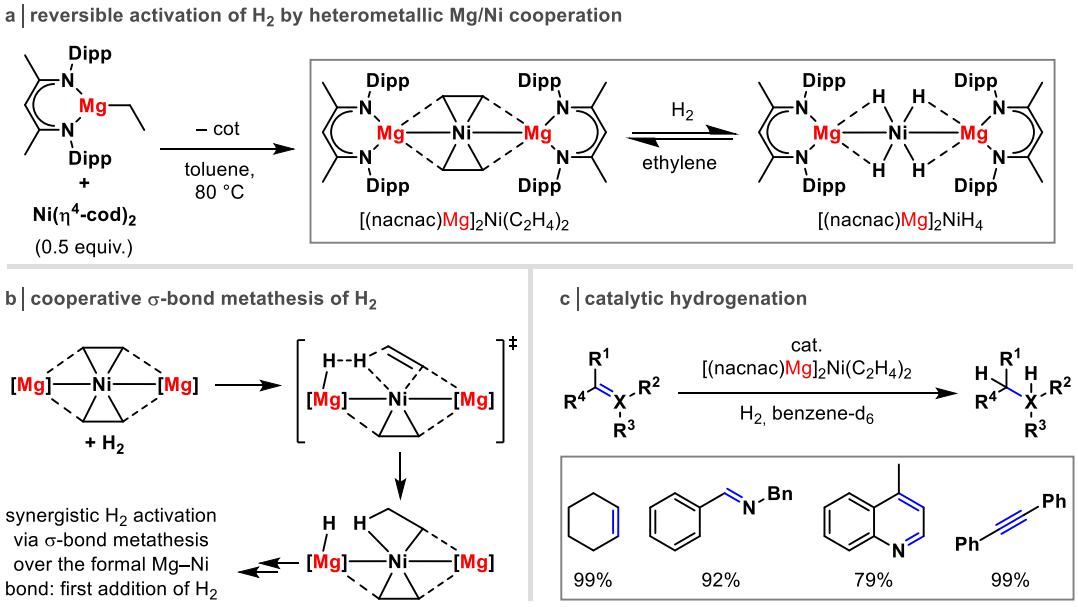

Figure 5. (a) Synthesis of heterotrimetallic complex $[(nacnac)Mg]_2Ni(C_2H_4)_2$ and reversible H_2 activation. (b) Computed σ-bond metathesis of H_2 over the formal Mg–Ni bond to $[(nacnac)Mg]_2NiH_4$. (c) Catalytic hydrogenation of different substrates using $[(nacnac)Mg]_2Ni(C_2H_4)_2$. cot = cyclooctene.

The complex $[(nacnac)Mg]_2Ni(C_2H_4)_2$ (nacnac = β-diketiminate) exhibits a linear Mg–Ni–Mg interaction and a planar nickelaspiropentane moiety. Exposure to H_2 (1 bar) led to the formation of the tetrahydride complex $[(nacnac)Mg]_2NiH_4$, featuring four covalent Ni–H bonds with additional weak Mg–H interactions (Figure 5a). DFT calculations of the reaction of $[(nacnac)Mg]_2Ni(C_2H_4)_2$ with H_2 revealed a bimetallic pathway, which is initiated by the σ-bond metathesis of H_2 with the formal Mg–Ni bond, resulting in an unstable intermediate containing terminal Mg–H and Ni–H bonds (Figure 5b). The cooperation between Mg and Ni allows for the stepwise addition of H_2 without oxidation at the Ni center, showcasing the mechanistic versatility that arises from the second metal fragment. Given the facile activation of H_2 with $[(nacnac)Mg]_2Ni(C_2H_4)_2$, the magnesium nickelate served as an efficient pre-catalyst for the hydrogenation of various unsaturated substrates, such as alkenes, imines, quinolines, and alkynes (Figure 5c).

In a separate study, the Xu group employed the same complex in alkene hydrosilylation.[19] Reaction of the complex with phenylsilane allowed for the isolation of silyl hydride complexes featuring a Ni-Si-H-Mg interaction, closely resembling the structural motif observed in the σ-bond metathesis of H_2 (see above). The use of this silyl hydride, along with other bimetallic silyl-nickel complexes as pre-catalysts, demonstrated that the hydrosilylation reaction proceeds via an analogous bimetallic pathway.

1.2.1.3 Hydrogenation with a Homogenous/Heterogenous Alkaline Earth Metal/Iron System

The study of bimetallic cooperativity mostly focuses on well-defined molecular complexes or ion pairs, where the steric and electronic interactions between the metals, alongside with solvation effects, dictate the observed synergistic behavior (see the previous examples). An alternative yet equally effective strategy involves pairing a molecular metal species with a heterogenous metal to induce bimetallic reactivity at the interface of the metal surface and the dissolved metal species.[20]

In this vein, Harder and co-workers showed that the addition of metallic iron to metallic barium or molecular s-block metal compounds drastically improved the hydrogenation activities compared to the monometallic systems, enabling the hydrogenation of unactivated alkenes, imines and arenes (Figure 6).[16] For example, the hydrogenation of benzene with Fe^0 or Ba^0 formed by metal vapor synthesis did not or only very slowly (>6 d) produce cyclohexane, while the heterobimetallic BaFe mixture reduced benzene quantitatively within 0.5 h (Figure 6a). The authors reason that the marked enhancement in reactivity arises from several key factors: (1) the dissociative adsorption of H_2 on the Fe^0 surface produces reactive hydrogen radicals that convert Ba^0 into soluble (and highly reactive) BaH_2; (2) unsaturated substrates are activated through adsorption as π-complexes on the Fe^0 surface, thereby facilitating the hydride attack; and (3) highly reactive $H^{\bullet}$ radicals formed on the Fe^0 surface directly react with alkylbarium intermediates to yield the saturated hydrocarbon products

(Figure 6b). Additionally, a direct interaction between Ba^0 and Fe^0 is proposed, in which the electropositive Ba^0 improves the substrate activation of Fe^0 by increasing the electron density on Fe. The quantitative hydrogenation of benzene using well-defined $[(nacnac)MgH]_2/Fe^0$ supports the hypothesis that the main group metal in the Ba^0/Fe^0 system forms a soluble metal hydride species. A tentative reaction sequence outlines the formation of cyclohexane by the cooperative interaction of monomeric (nacnac)MgH and Fe^0 with benzene (Figure 6c).

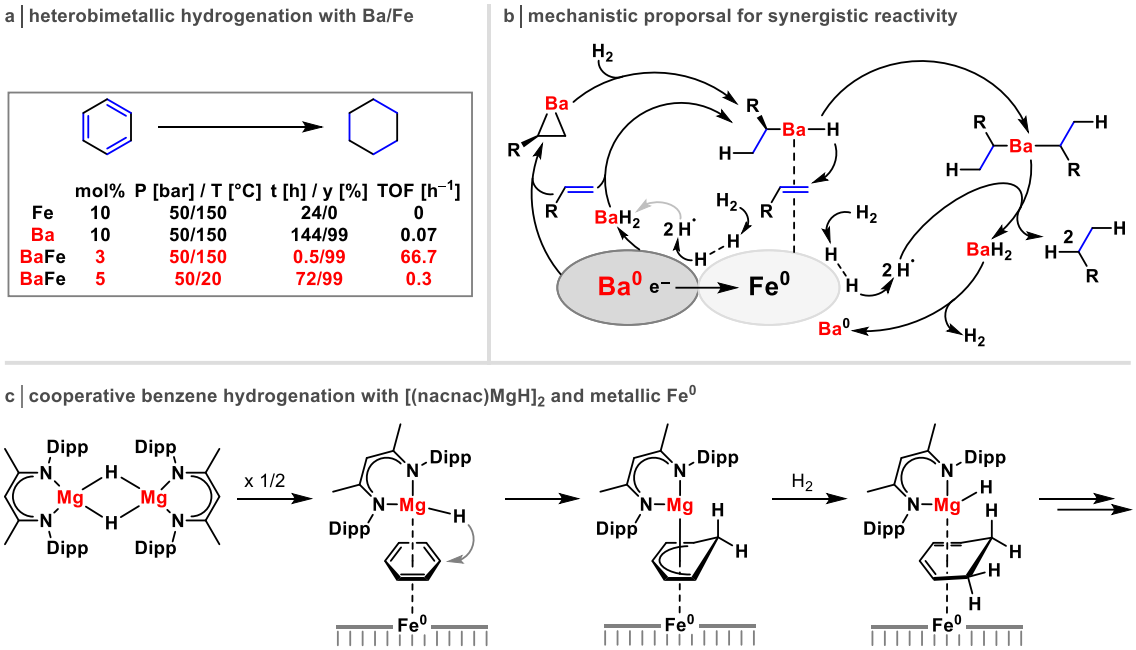

Figure 6. (a) Hydrogenation of benzene with Fe^0, Ba^0 and Ba^0/Fe^0. (b) Mechanistic proposal for the synergistic hydrogenation with Ba^0 and Fe^0. (c) Cooperative benzene hydrogenation with soluble $[(nacnac)MgH]_2$ and Fe^0. Ba^0/Fe^0 describes the metal powder activated by metal vapor synthesis.

1.2.2 C–H, C–C, C–O, C–X, and N–H Bond Activation

1.2.2.1 C–H and C–X (X = F, I) Bond Activation by Alkali Metal Metalates (M = Mn, Fe, Co)

The activation of carbon-halogen and carbon-hydrogen bonds forms the basis of numerous catalytic processes that are of much importance for organic synthesis.[21] Traditionally mediated by a monometallic reagent, these reactions involve the formation of an organometallic intermediate featuring a direct metal-carbon bond. However, recent studies increasingly recognize bimetallic interactions as a common motif in the organometallic intermediates during C–X and C–H activation.[22]

In this context, Hevia and co-workers showed that alkali metal manganates $M_2Mn^{II}(CH_2SiMe_3)_4$ (M = Li, Na, K) promote the homocoupling of aryl iodides and terminal alkynes in the presence of an oxidizing agent (Figure 7).[23] The bimetallic complexes can be generated either *in situ* by treating MCH_2SiMe_3 with $MnCl_2$ or isolated as Lewis donor-stabilized solids (Figure 7a,b). The homocoupling of 4-iodoanisole using $Li_2Mn(CH_2SiMe_3)_4$ gave 94% of the biphenyl product. In contrast, the monometallic $Mn(CH_2SiMe_3)_2$ failed completely, while $Li(CH_2SiMe_3)$ gave a smaller yield (62%) (Figure

7a).[23a] Further evidence of the cooperative reactivity of Li and Mn emerged during the assessment of the homocoupling reaction in the presence of Lewis donors. While bidentate TMEDA (*N*,*N*,*N*′,*N*′-tetramethylethane-1,2-diamine) showed no effect, the lithium-specific sequestering agent 12-crown-4 completely inhibited the reaction. This indicates that the close proximity of the lithium cation to the manganate anion is a key requirement for cooperative reactivity. Mechanistic investigations further confirmed that the formation of intimate Li/Mn ion pairs is essential for promoting both Mn–I exchange and C(sp^2)–C(sp^2) bond formation. By isolating a tetra-arylated lithium manganate complex, the authors showed that such species successfully form bi(aryl) products when exposed to O_2 (Figure 7c).

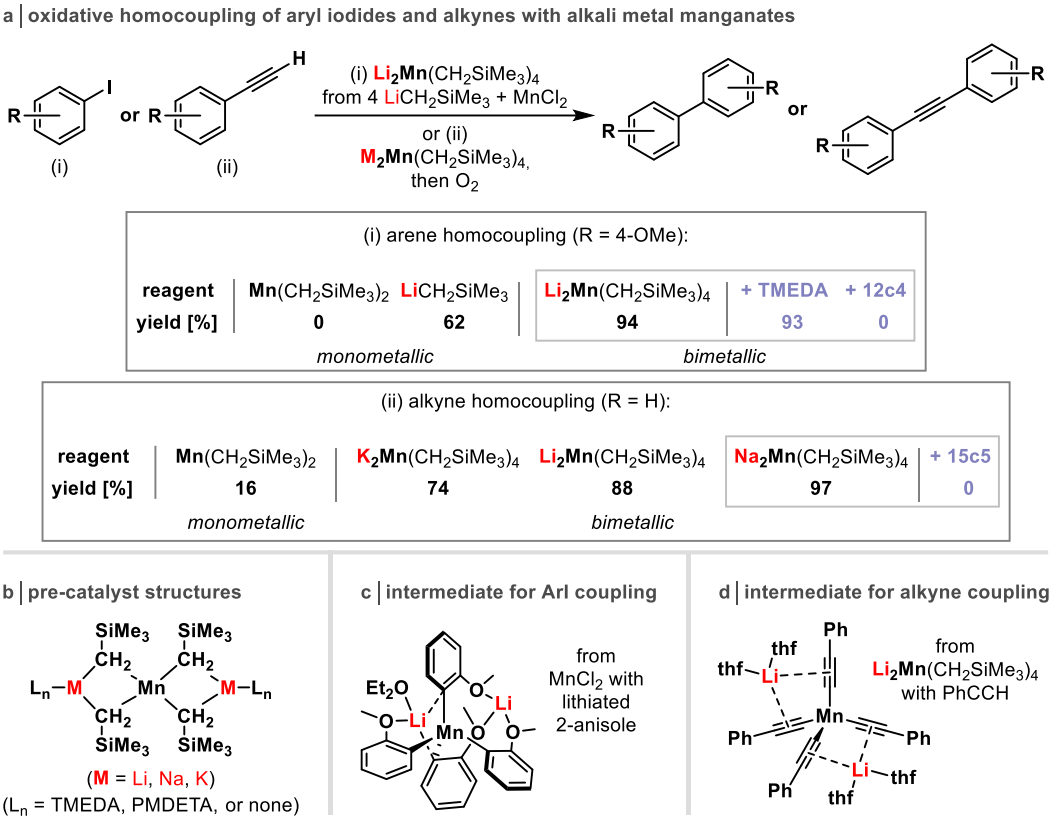

Figure 7. (a) Oxidative homocoupling of arenes and alkynes mediated by bimetallic alkali metal manganates. (b) Structure of the alkali metal manganates $M_2Mn(CH_2SiMe_3)_4$ (M = Li, Na, K). (c) + (d) Bimetallic arene and alkyne manganates which undergo homocoupling when exposed to an oxidant. PMDETA = *N*,*N*,*N*′,*N*″,*N*″-pentamethyldiethylenetriamine.

Expanding the scope to terminal alkynes, a series of analogous alkali metal manganates was equally effective in the oxidative homocoupling to give 1,3-diynes (Figure 7a).[23b] The nature of the alkali metal cation directly influenced the product formation following the trend: $K^+ < Li^+ < Na^+$, while the addition of 15-crown-5 to the Na/Mn system completely shuts down the reaction. Structural studies suggest the involvement of intimate alkali metal/Mn ion pairs, which can be independently synthesized by treating the terminal alkynes with $M_2Mn(CH_2SiMe_3)_4$ under inert conditions. The Li/Mn alkynyl complex is an organometallic intermediate in the homocoupling of phenylacetylene, that generates the corresponding

1,3-diyne when exposed to dry air (Figure 7d).

Developing this theme further, the Hevia group investigated the C–H and C–F bond activation utilizing Na/Fe and Na/Co complexes in various fluoroaromatic substrates (Figure 8).[24] The heterobimetallic bases were obtained by pairing $M(HMDS)_2$ (M = Fe, Co; HMDS = $N(SiMe_3)_2$) with Na(HMDS) to form tris(amide) metalates, $Na[M(HMDS)_3]$, which effectively metalate fluoroarenes at the C–H position adjacent to a fluorine group (Figure 8a).[25] The regioselective functionalization proceeds only in the presence of the bimetallic ate complexes, whereas neither the monometallic Na(HMDS) or $M(HMDS)_2$ (M = Fe, Co) alone activate the C–H bond. Experimental and computational studies using C_6F_5H as the substrate have shown that the metalation is based on a stepwise cooperative sequence involving both metal centers in $Na[M(HMDS)_3]$ (Figure 8b).[24b,d]

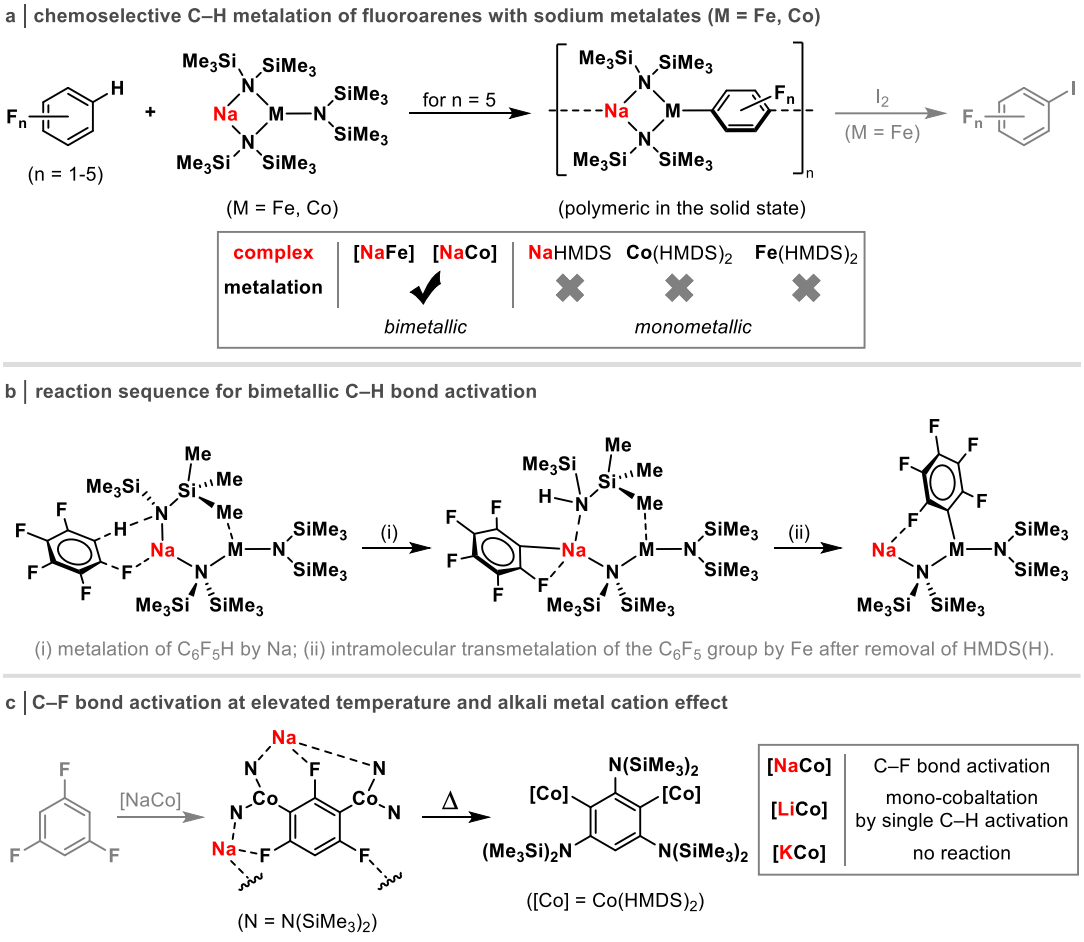

Figure 8. (a) Chemoselective C–H metalation of fluoroarenes with sodium metalates (M = Fe, Co). (b) Reaction sequence for the bimetallic C–H bond activation by means of DFT calculations. (c) C–F bond activation at elevated temperature and alkali metal cation effect.

The mechanism involves the coordination and metalation of C_6F_5H by sodium, followed by an intramolecular transmetalation of the fluoroaryl group to iron or cobalt. The resulting bimetallic intermediate featuring a covalent C–Fe bond and a dative Na···F bond could be isolated for M = Fe in the presence of 1,4-dioxane. Building on the understanding of the role of the sodium amide in the metalation process, the substitution of Na(HMDS) by the more

basic and sterically hindered NaTMP (TMP = 2,2,6,6-tetramethylpiperidinide) was attempted. In the iron-based system, this modification enabled the C–H activation of more inert substrates such as toluene and benzene, which the authors attribute to a similar bimetallic mechanism involving $Na[Fe(TMP)(HMDS)_2]$.[24b]

When testing the limits of the metalation protocols, an unexpected substitution of fluoride by amide was observed at elevated temperature (Figure 8c). This reaction is proposed to follow a cascade process, which involves alternating eliminations of NaF and $M(HMDS)_2$, followed by subsequent $M(HMDS)_2$ additions to benzyne intermediates. For M = Co, the authors observed an alkali metal cation effect ($Li^+ < Na^+ > K^+$), which manifested in no reaction of $K[Co(HMDS)_3]$ with 1,3,5-trifluorobenzene, while $Li[Co(HMDS)_3]$ was only able to form $Li[Co(HMDS)_2(C_6F_3H_2)]$ via mono-cobaltation, regardless of stoichiometry or conditions employed (Δ).[24f]

1.2.2.2 C–O and C–C Bond Activation by Alkali Metal Nickelates

Research into the reactivity of alkali metal nickelates dates back to the 1970s and 1980s, when anionic nickelates were extensively studied in the context of alkene polymerization[26] and the activation of small molecules such as dinitrogen.[27] The discovery of nickel-catalyzed cross-coupling reactions further established the importance of nickel in the formation of a range of C–C and C–heteroatom bonds.[28] The direct coupling of Grignard reagents in the Kumada-Corriu type coupling is conventionally described through a cycle of oxidative addition, transmetalation, and reductive elimination steps, involving neutral Ni^0 and Ni^{II} complexes.[29] However, recent experimental and computational studies indicate that this simplified mechanism does not fully account for substrate classes such as aryl ethers, for which the direct oxidation of C–O bonds is unfavored.[30] Instead, an alternative mechanism involving heterobimetallic nickelate intermediates has been proposed.[31] Such species have been independently synthesized via the reaction of nickel(0) alkene complexes with organometallic nucleophiles,[27a],[32] and have been suggested as intermediates in other Ni-mediated functionalization reactions.[33]

Building on these observations, Hevia and co-workers demonstrated that the Ni-catalyzed cross-coupling of aryl ethers with PhLi proceeds via heterobimetallic nickelates (Figure 9).[34] A dramatic solvent and additive effect was observed for the cross-coupling of 2-methoxynaphthalene with different lithium organyls catalyzed by $Ni(\eta^4\text{-cod})_2$ (cod = 1,5-cyclooctadiene, Figure 9a). In C_6D_6, the cross-coupling product was formed using donor-free PhLi, whereas in THF-d_8, only *ortho*-lithiation of 2-methoxynaphthalene was observed. In addition, stoichiometric coordination of PhLi with THF only marginally reduced the cross-coupling, while bidentate TMEDA led exclusively to *ortho*-lithiation. These findings suggest that lithium and nickel must be in close proximity, with lithium coordinated by a labile ligand (e.g., THF) that can be easily replaced. Direct reactions of $Ni(\eta^4\text{-cod})_2$ with PhLi led to well-defined lithium nickelates, which show contact ion pair structures in the solid

state where the Li^+ cations interact with the phenyl and cod ligands at Ni (see Figure 9b for $Li_2(thf)_4[Ph_2Ni(\eta^2\text{-cod})]$).

The catalytic use of these nickelates in place of $Ni(\eta^4\text{-cod})_2$ in the cross-coupling reaction resulted in near-identical activity, which the authors explored further through detailed structural, kinetic and computational studies (Figure 9c). The mechanism starts from the 2:1-complex $Li_2(thf)_2[Ph_2Ni(\eta^2\text{-cod})]$, formed by the reaction of $Ni(\eta^4\text{-cod})_2$ with PhLi(thf), which binds 2-methoxynaphthalene at the Lewis acidic Li^+ via Li···O interaction (step i). π-Coordination of the substrate to Ni induces the release of the cod ligand (step ii), followed by the rate-determining oxidative addition of the C–O bond at Ni with transfer of the methoxy group to Li (step iii). LiOMe-PhLi exchange then produces the tetra-arylated lithium nickelate (step iv), which reductively eliminates the cross-coupling product and regenerates $Li_2(thf)_2[Ph_2Ni(\eta^2\text{-cod})]$ (step v). The isolation of the η^2-arene and the tetra-arylated lithium nickelates as donor complexes supports the mechanistic proposal.

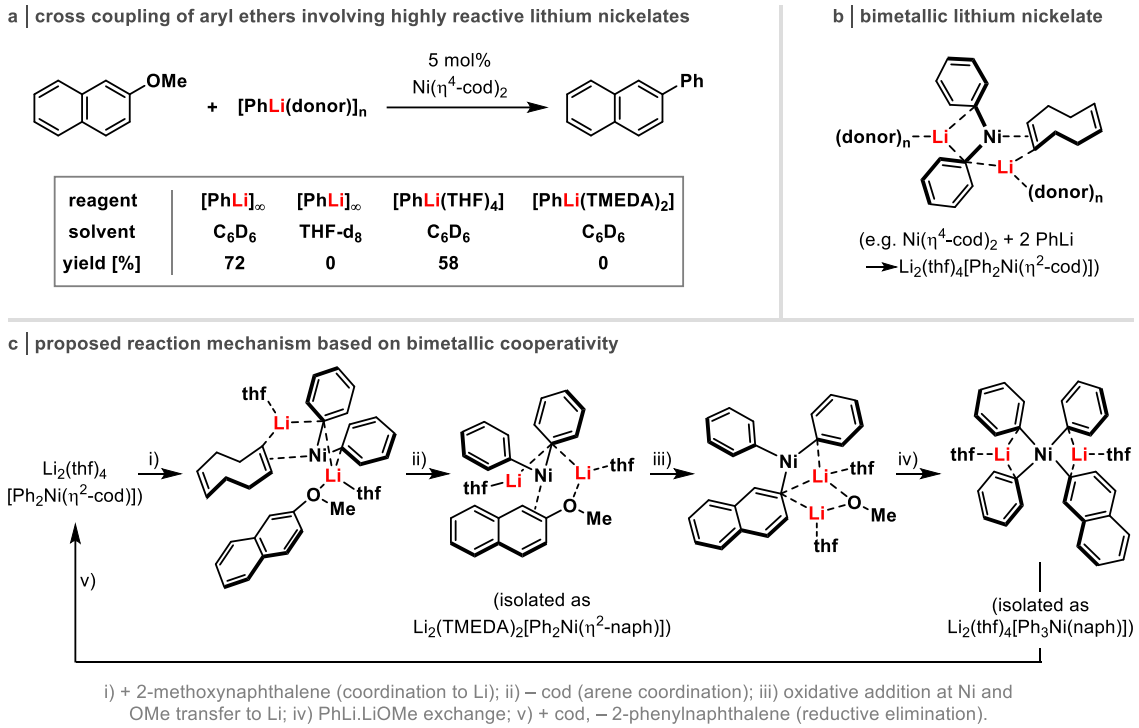

Figure 9. (a) Nickel-catalyzed cross-coupling of aryl ethers involving highly reactive lithium nickelates. (b) Co-complexation affords a heterobimetallic lithium nickelate. (c) Proposed reaction mechanism based on bimetallic cooperativity.

After demonstrating that heterobimetallic nickelates serve as key intermediates in the catalytic cross-coupling of C–O bonds, the Hevia group investigated the reactivity of related nickelates toward the activation of C–C bonds (Figure 10).[35] Using a series of alkali metal nickelate complexes (M = Li, Na, K) that η^4-coordinate biphenylene, the C–C bond cleavage to form the ring-opened analogs was found to strongly depend on the alkali metal cation and its coordination environment (Figure 10a,b). The Li^+ complex underwent oxidative addition to Ni in just 15 minutes upon warming from –30 °C to ambient temperature, whereas the Na

and K analogs required 3 and 12 hours, respectively.

DFT studies modeling the C–C cleavage as a single concerted step reflected this trend (Li^+ << Na^+ < K^+), yet the lowest computed barrier (33.4 kcal/mol for Li) was too high relative to the experimentally observed rates. Further analysis of the ion pair constitution showed that the position of the alkali metal cation and its solvation is decisive for the C–C cleavage barrier (Figure 10c). In the case of Na, the relocation of one sodium cation to the opposite side of the biphenylene plane along with the reorientation of solvent resulted in a reduced C–C cleavage barrier consistent with the experimentally determined activation barrier for the sodium nickelate. Further analysis of the solvation dynamics of the biphenylene alkali metal nickelates by ab initio molecular dynamics (AIMD) simulations revealed that the diffusion behavior was strongly dependent on the identity of the alkali metal cation (Figure 10d). While the Li^+ cations rotate around the Ni center in a 10.3 ps simulation, the K^+ cations oscillate in near-unchanged positions above the phenylene rings. The virtually unhindered movement of Li^+ might have a beneficial effect on the cation relocation prior to C–C bond cleavage.

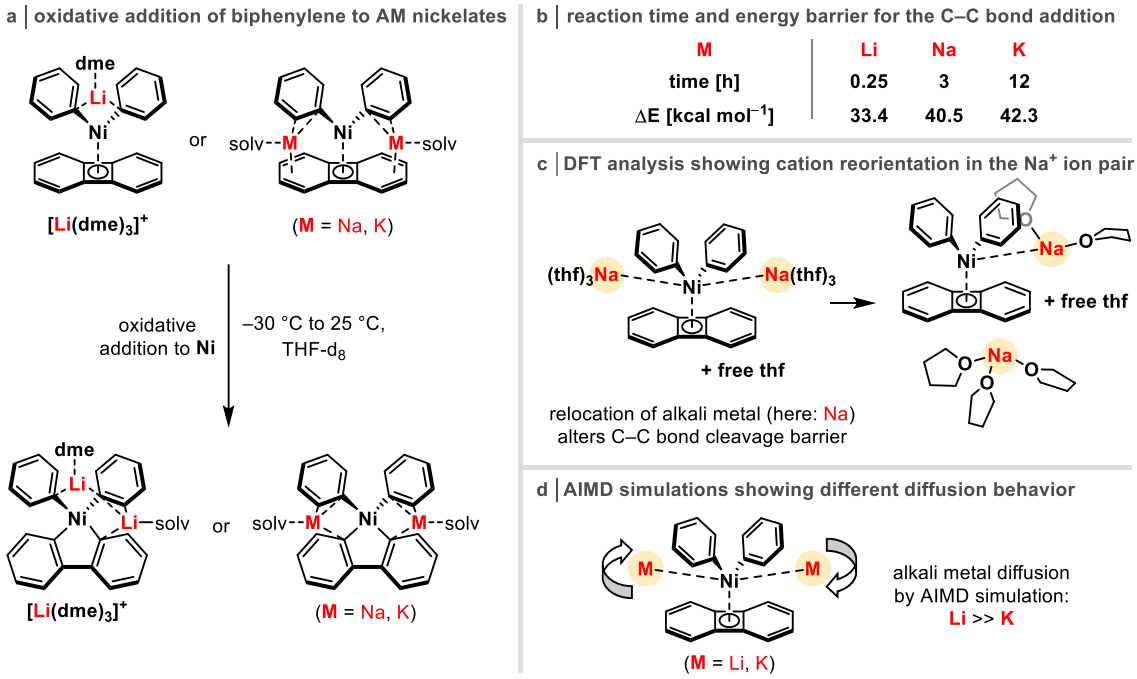

Figure 10. (a) Oxidative addition of η^4-coordinated biphenylene to alkali metal nickelates (M = Li, Na, K). (b) Reaction time and energy barrier for the C–C bond addition dependent on the alkali metal cation. (c) + (d) Mechanistic analyses by DFT calculations and AIMD simulations showing cation reorientation and different diffusion behavior of the ion pairs.

1.2.2.3 N–H Bond Activation by Alkali Metal Ferrates

The Hevia group also reported the hydroamination of alkenes using a series of heterobimetallic alkali metal ferrates (Figure 11).[36] The addition of an N–H unit across a C–C unsaturated bond typically requires a single-site metal catalyst, which promotes the reaction either through π-coordination of the hydrocarbon reactant (typical for late transition metals)[37] or via deprotonation of the amine to give a nucleophilic metal amide

species (typical for s-block metals).[38] Building on their previous work employing sodium ferrates in stoichiometric C–H metalation reactions (section 1.2.2.1),[24a-c] Hevia and co-workers investigated the catalytic potential of novel alkali metal trialkyl ferrate complexes (M = Li, Na, K) in the intermolecular hydroamination of styrene with piperidine (Figure 11a,b). The bimetallic ate complexes were anticipated to readily deprotonate the amine substrate due to an increased basicity while also activating the alkene by the Lewis acidic alkali metal site. Indeed, the hydroamination reaction was efficiently catalyzed by these complexes, exhibiting a pronounced alkali metal cation effect ($K^+ << Li^+ < Na^+$) and significantly higher catalytic activity than the monometallic counterparts $(TMEDA)Fe(CH_2SiMe_3)_2$ and $Na(CH_2SiMe_3)$ (Figure 11a). The reaction of the sodium ferrate with piperidine yielded a tetranuclear complex containing six piperidide fragments, which proved to be an equally effective catalyst for the hydroamination of piperidine (Figure 11c). Consequently, alkali metal amido ferrate complexes are proposed to be catalytically active intermediates. Alkenes insert into the iron-amide bond to form an alkyl iron intermediate, which is protonated by amine to complete the catalytic cycle (Figure 11c for M = Na).

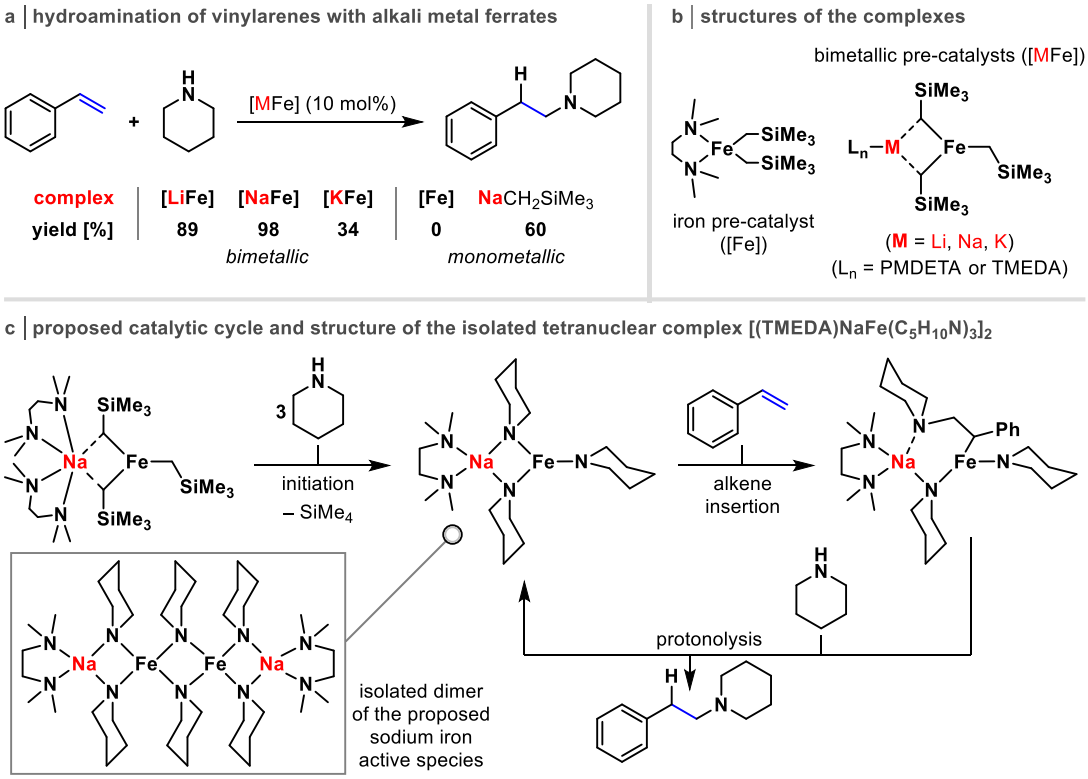

Figure 11. (a) Hydroamination of styrene catalyzed by different alkali metal ferrates (M = Li, Na, K). (b) Structures of the monometallic and bimetallic complexes. (c) Proposed catalytic cycle and structure of the isolated tetranuclear complex $[(TMEDA)NaFe(C_5H_{10}N)_3]_2$ as a catalytically active intermediate.

1.2.3 Isomerization Reactions

1.2.3.1 H/D Exchange Reaction with an Iridium Crown Ether Complex and $MBAr^F_4$

Most of the previous examples have employed transition metalates comprised of d-block metal anions forming tight ion pairs with s-block metal cations. An alternative approach

incorporates s-block metal cations into a mononuclear transition metal complex using supramolecular ligand frameworks such as crown ethers. The second metal atom can influence the reactivity and selectivity of the bimetallic complex through steric and electronic tuning, such as modulation of the ligand's binding properties.[39] Examples of such cation-responsive systems have been reported in hydroformylation,[40] hydrogenation,[41] and polymerization catalysis (section 1.2.4).[42]

The Miller group investigated the use of pincer-crown ether complexes as catalysts in different small molecule activation reactions.[43] The complexes contain a macrocyclic hemilabile ligand that can reversibly bind the transition metal center in response to a substrate interaction (Figure 12a). This process can be controlled by the addition of an alkali metal cation, which interacts with the crown ether in a manner dependent on the identity and stoichiometry of the cation.

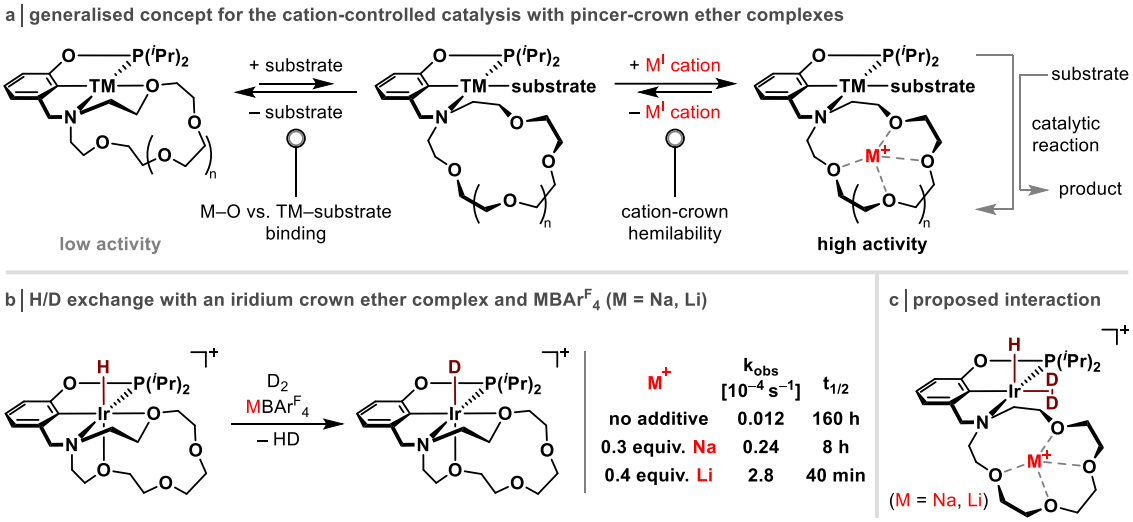

Figure 12. (a) Generalized concept for cation-controlled catalysis with pincer-crown ether complexes with and without an alkali metal cation additive. (b) H/D exchange with an iridium crown ether complex and $MBAr^F_4$ (M = Na, Li; Ar^F = 3,5-bis(trifluoromethyl)phenyl). (c) Proposed alkali metal cation interaction.

As will be shown in the following examples, this results in switchable catalysis with reversible on/off control over reactivity,[44] as well as tunable catalysis with continuous reactivity.[45] The hydrogen-deuterium exchange using an aza-15-crown-5 iridium hydride complex under D_2 atmosphere was found to proceed slowly in the absence of an alkali metal cation, suggesting that the weakly coordinating D_2 substrate does not bind effectively to the metal center (Figure 12b).[45a] When the reaction was repeated in the presence of substoichiometric $MBAr^F_4$ (M = Na, Li; Ar^F = 3,5-bis(trifluoromethyl)phenyl), a 20-fold rate enhancement for Na^+ and an approximately 250-fold rate enhancement for Li^+ was observed. The cation concentration was identified as another critical parameter: the exchange reaction is accelerated significantly when increasing the amount of the alkali metal cation from sub- to superstoichiometric quantities (0.3 equiv. Na^+: $t_{1/2}$ = 8 h vs. 1.2 equiv. Na^+: $t_{1/2}$ = 2 h). The authors propose that the alkali metal cation promotes D_2 coordination by binding to the

macrocycle and displacing the crown ether oxygen cis to the hydride ligand (Figure 12c). The best improvement was observed for Li^+, which likely binds more selectively to the tetrameric crown ether motif than Na^+.

1.2.3.2 Alkene Isomerization Catalysis with Crown Ether Complexes and $MBAr^F_4$

Having demonstrated a cation-controlled transformation using the iridium pincer-crown ether complex (see above), Miller and co-workers focused on developing a catalytic reaction that operates under ion-responsive conditions. The isomerization of alkenes was identified as a suitable candidate, given that it involves the direct coordination of a single substrate to the transition metal center, thereby limiting the potential for other side reactions (Figure 13).[44b],[45b],[46] In the reaction of allylbenzene with the same iridium hydride complex, slow conversion to β-methylstyrene was observed over 141 h, with an initial turnover frequency (TOF) of 1.8 h^{-1} (Figure 13a, (i) and b).[45b] The modest activity of the iridium complex is attributed to the hemilabile crown ether ligand *cis* to the hydride ligand, which can be displaced by the alkene substrate, albeit with an equilibrium that disfavors alkene binding (Figure 13b, mid). The addition of $MBAr^F_4$ (M = Li, Na, K) to the iridium catalyst significantly increased the rate of isomerization to β-methylstyrene, with up to a 1000-fold increase observed for M = Li (TOF = 2000 h^{-1}). Supported by kinetic analyses, the marked rate enhancement is linked to a change in the reaction mechanism involving a second catalytic cycle mediated by the alkene-bound Li^+ iridium complex. The hemilabile crown ether ligand is now fully dissociated from the transition metal center through coordination to Li^+, which promotes the alkene binding and renders the reaction zero-order in allylbenzene (Figure 13b, right).

Building upon this methodology, Miller and co-workers designed a cation-controlled pincer-crown ether iridium catalyst that converts terminal alkenes to two internal isomers (Figure 13a, (ii) and c).[46] The new complex features an extended aza-18-crown-6 ether, which binds alkali metal cations through pentadentate coordination. The isomerization of 1-butenes bearing different functional groups revealed that the 18-crown-6-based catalyst promoted multipositional isomerizations, with regioselectivity and stereoselectivity dependent on the presence of an alkali metal cation. In the absence of a salt additive, the isomerization of 4-phenyl-1-butene selectively produced the 2-alkene (93%, E:Z = 14:1) (Figure 13a). Under otherwise identical conditions, addition of $NaBAr^F_4$ shifted the selectivity to the 3-alkene (94%, E:Z = 50:1).

The mechanism for the positional isomerization is proposed to depend on noncovalent interactions, which direct the catalyst toward either kinetic or thermodynamic control (Figure 13c). In the absence of $NaBAr^F_4$, the 2-alkene is formed as the kinetic product via isomerization from a catalyst adopting a tetradentate binding mode at Ir, with one ether oxygen coordinated to Ir during turnover (Figure 13c, left). Steric constraints likely permit the conversion to the internal 2-alkene but prevent further isomerization to the 3-alkene due

to kinetic hindrance. With $NaBAr^F_4$ present, the 3-alkene regioisomer is selectively formed under thermodynamic control (when the 3-alkene is more stable than the other isomers). This isomerization proceeds through a catalyst structure featuring a tridentate binding mode at Ir due to strong Na^+-crown interactions, which break the coordination of the ether oxygens to the iridium center (Figure 13c, right). This sterically less crowded geometry likely lowers the isomerization barriers, promoting the formation of the most stable regioisomer under thermodynamic control (typically the 3-alkene).

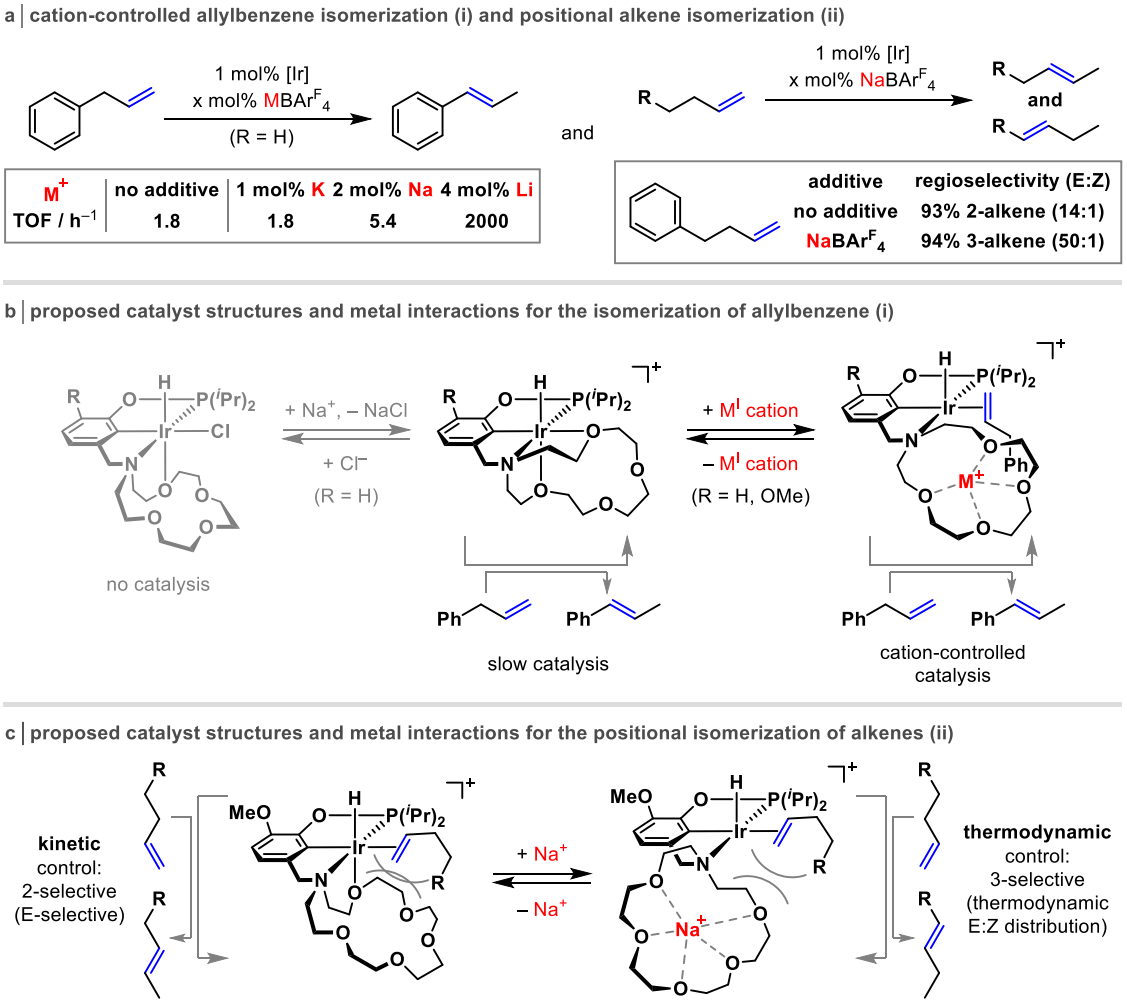

Figure 13. (a) Cation-controlled isomerization of allylbenzene (i) and positional isomerization of alkenes (ii). (b) + (c) Proposed catalyst structures and metal interactions for the isomerization reactions (i) and (ii).

In further work, the authors extended the switchable alkene isomerization reactivity to a palladium pincer-crown ether complex bearing a tetradentate aza-15-crown-5 motif.[44b] In contrast to the iridium-based systems,[45a,b],[46] the palladium catalyst displayed on/off switchable behavior in the isomerization of 1-hexene, with no reactivity in the absence of Li^+ salts and maximum reactivity when Li^+ was present. This switchable behavior was attributed to an enhanced crown ether binding due to palladium's greater electrophilicity, thereby preventing substrate coordination when Li^+ is absent. The proposed mechanism proceeds through either a carbocation or an η^3-allyl intermediate, depending on the alkene substrate,

and represents a mechanistically distinct pathway from the insertion–elimination route suggested for the iridium hydrido complexes.

1.2.4 Polymerization Reactions

1.2.4.1 Ring-Opening Copolymerization Catalysis

The combination of an s-block element with a transition metal has been recognized as a promising strategy to improve catalyst activity in polymerization reactions.[42],[47] Recent years have seen a marked surge in the development of heterobimetallic systems that leverage the synergistic reactivity of two distinct metal centers. A growing subset of these systems includes bimetallic catalysts applied in ring-opening copolymerization (ROCOP) catalysis.[47] The reactions benefit from heterometallic cooperativity, which provides multiple active sites for substrate binding and activation, with each metal center contributing a distinct function in the catalytic process.

Williams and co-workers developed a heterodinuclear Co(II)Mg(II) complex for the copolymerization of CO_2 with epoxides (Figure 14a,b).[47a,c] The catalyst features a macrocyclic tetraaza-bis(olate) ligand, which accommodates both metals in a planar coordination environment (Figure 14b). When employed in the reaction of cyclohexene oxide (CHO) under 1 bar of CO_2 pressure, the Co(II)Mg(II) catalyst exhibited catalytic performance far superior to its homodinuclear Co(II)Co(II) and Mg(II)Mg(II) counterparts (Figure 14a). The polymerization is proposed to follow a chain shuttling mechanism, which is based on the alternate binding of the polymer chain to both metal centers.

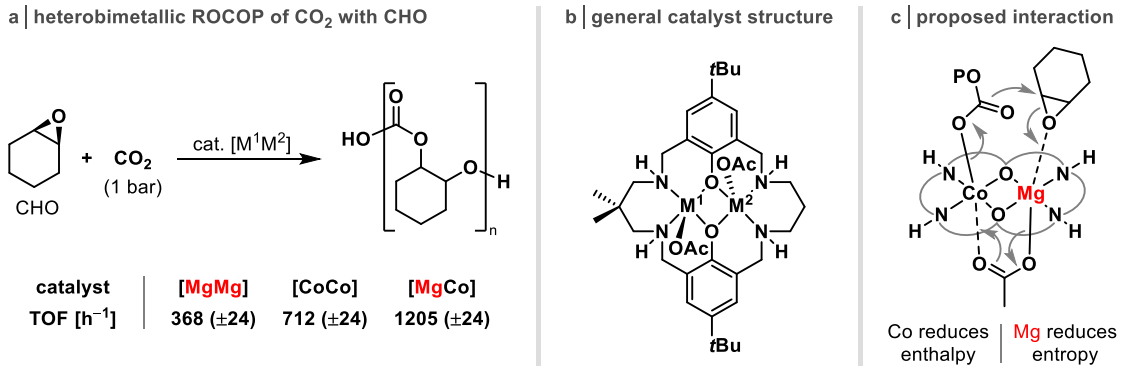

Figure 14. (a) Ring-opening copolymerization (ROCOP) of cyclohexene oxide (CHO) and CO_2 catalyzed by a heterodinuclear Co(II)Mg(II) catalyst. (b) General catalyst structure ($M^{1/2}$ = Co, Mg). (c) Proposed interaction in the rate-determining step involving Co and Mg.

The rate-determining step involves coordination of the epoxide at Mg(II), which is attacked by the carbonate ligated to Co(II) (Figure 14c). Polymerization kinetic analyses of the homodinuclear and heterodinuclear catalysts indicate that each metal independently contributes to reducing the overall kinetic barrier. Co(II) decreases the transition state enthalpy by increasing the nucleophilicity of the metal carbonate, while Mg(II) reduces the reaction entropy associated with epoxide coordination due to its low bond directionality and higher oxophilicity. When exploring other transition metals in Mg(II)TM(II) catalysts, the

authors demonstrated that the synergistic reactivity is preserved across a series of heterobimetallic combinations, including Mg(II)Mn(II), Mg(II)Fe(II), and Mg(II)Ni(II), all of which exhibited superior ROCOP activity compared to Mg(II)Mg(II).[47d]

Following the successful application of heterodinuclear Mg(II)TM(II) catalysts, the Williams group explored the pairing of group 1 metals (M = K, Na, Rb, Cs) with a salen-based Co(III) complex for ROCOP catalysis (Figure 15a,b).[47b,e-h] The dinuclear complexes consist of a Co(III) atom positioned within the Schiff base cavity, adjacent to a macrocyclic crown ether moiety that binds the group 1 metal (Figure 15b).[47b] Evaluation of the Co(III)M(I) complexes in the ROCOP of propylene oxide (PO) and CO_2 (20 bar) revealed that the Co(III)K(I) catalyst was the most active, with a general trend for the turnover frequency of K(I) >> Na(I) >> Rb(I) > Cs(I) (Figure 15a). While the initial assessment attributed the alkali metal effect to a size mismatch between the alkali metal and the crown ether pocket, subsequent investigations on the same catalyst system with M = Na(I), K(I), Ca(II), Sr(II), and Ba(II) established a direct correlation between s-block metal Lewis acidity and catalytic performance.[47f,h] The most active and selective catalysts feature the least acidic s-block metals, Na(I) and K(I).

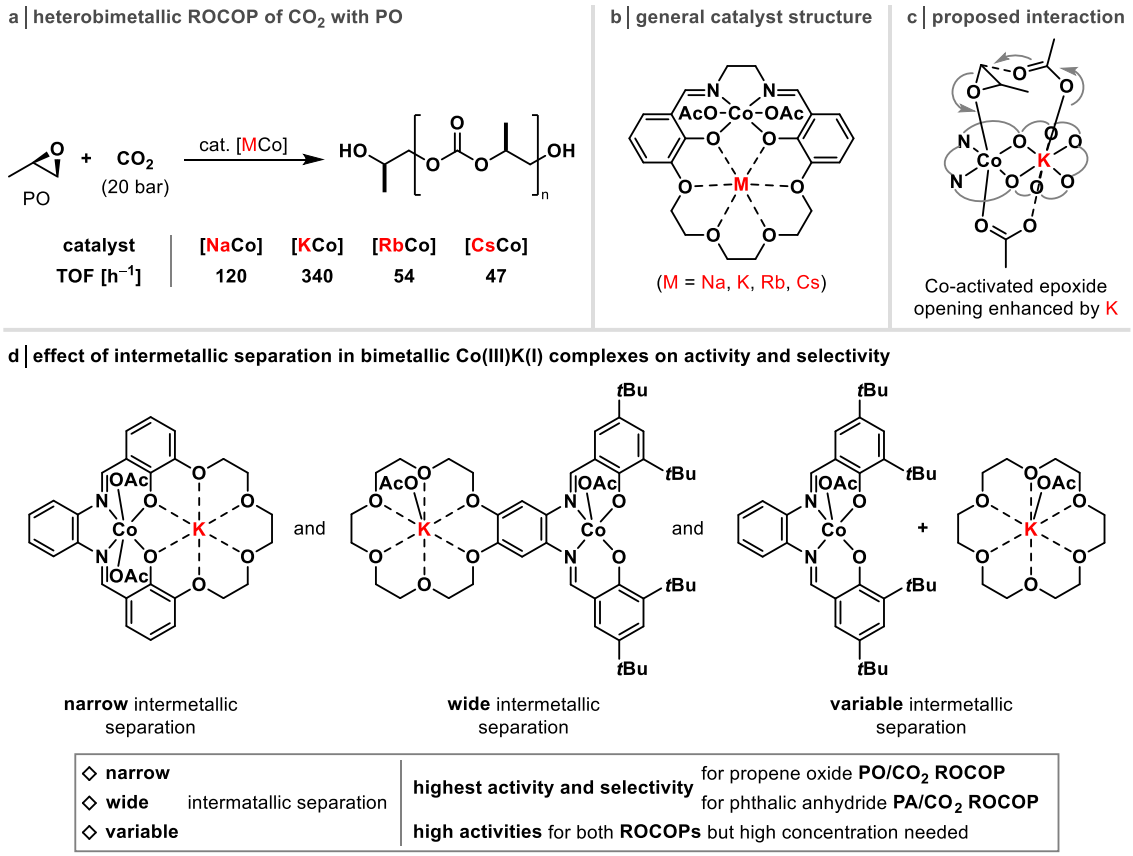

Figure 15. (a) Ring opening copolymerization (ROCOP) of propene oxide (PO) and CO_2 catalyzed by heterobimetallic Co(III)M(I) catalysts (M = Na, K, Rb, Cs). (b) General catalyst structure. (c) Proposed rate-determining step involving Co(III) and K(I) based on DFT calculations. (d) Effect of intermetallic separation in bimetallic Co(III)K(I) complexes on activity and selectivity in PO/CO_2 and phthalic anhydride (PA)/CO_2 ROCOP.

Computational and kinetic studies of the polymerization catalyzed by Co(III)K(I) support a dinuclear metalate mechanism involving Co(III)-coordinated propylene oxide and K(I)-bound carbonate (Figure 15c).[47e] The ring-opening of propylene oxide by the carbonate nucleophile is identified as the rate-determining step. The authors suggest that a reduction in metal Lewis acidity can destabilize such metal-carbonate intermediates (ground state destabilization) and may also lower activation barriers for epoxide ring-opening.

Three Co(III)K(I) heterobimetallic catalysts with different intermetallic separation were tested for the ring-opening copolymerization of propylene oxide with CO_2 or phthalic anhydride (Figure 15d).[47g] Offering either a fixed narrow, fixed wide or variable separation of the Co(III) and K(I) metal sites, the modified catalysts exhibited distinct reactivity in the polymerization reactions. For epoxide/CO_2 ROCOP, catalysts with closely spaced metals (3-4 Å) were most effective, while epoxide/anhydride ROCOP benefited from wider metal separations (8-9 Å). The flexible bicomponent system using a Co(III) complex and potassium salt was active in both reactions but required high catalyst loadings to achieve concentrations sufficient for effective association of the two metal components. These findings emphasize that not only the identity of the metal sites but also their distance and structural preorganization influence the reactivity. This can ultimately result in different mechanisms, by which the individual catalysts operate.

1.2.4.2 Alkene Polymerization Catalysis

Heterobimetallic complexes containing an s- and d-block metal are increasingly being explored in alkene polymerization due to the possibility of site-specific catalytic roles. The transition metal center carries out the polymerization reaction, while the s-block metal atom can modulate reactivity through stereoelectronic tuning of the alkene coordination and insertion steps. This ensures that the metal centers do not compete for substrate binding and prevents steric congestion from two polymer chains growing in the same catalyst structure. Such heterobimetallic complexes are commonly prepared by coordinating the s-block metal to a polyethylene glycol (PEG) side chain, which is integrated into the ligand bound to the transition metal. Comparable strategies for constructing heterobimetallic catalysts have been employed in isomerization catalysis using pincer-crown ether complexes (section 1.2.3)[43] and ROCOP catalysis with *O*,*N*-macrocyclic multidentate complexes (section 1.2.4.1).[47]

The Do group investigated the polymerization of ethylene using a series of nickel complexes that are supported by dinucleating phenoxyimine ligands bearing a pendant PEG side chain (Figure 16).[42a,b,f] Upon addition of $MBAr^F_4$ salts (M = Li, Na, K, Cs), heterobimetallic complexes were formed with both 1:1 and 1:2 alkali metal-to-nickel ratios, likely dependent on the length of the glycol chain (see Figure 16b for the 1st generation catalysts).[42a] Introducing a methylene spacer at the beginning of the PEG chain favored the formation of alkali metal-nickel complexes in a 1:1 ratio, which was expected to improve polymerization activity (see Figure 16b for the 2nd generation catalysts).[42f] When employing both catalysts

in the polymerization of ethylene (200 psi), two key observations emerged (Figure 16a): (1) alkali metal–nickel catalysts with matching PEG side chains showed improved performance over their monometallic counterparts, and (2) the 2nd generation catalysts exhibited a clear trend in polymerization activity ($Li^+ > Na^+ > K^+ > Cs^+$) that appeared to correlate with the Lewis acidity of the alkali metal cation. While the precise mechanisms behind the observed reactivity remain unclear, the authors attributed the overall beneficial effect to a greater effective charge on nickel and modifications to its coordination environment induced by the spatial arrangement of the alkali metal PEG moiety.[42d,f]

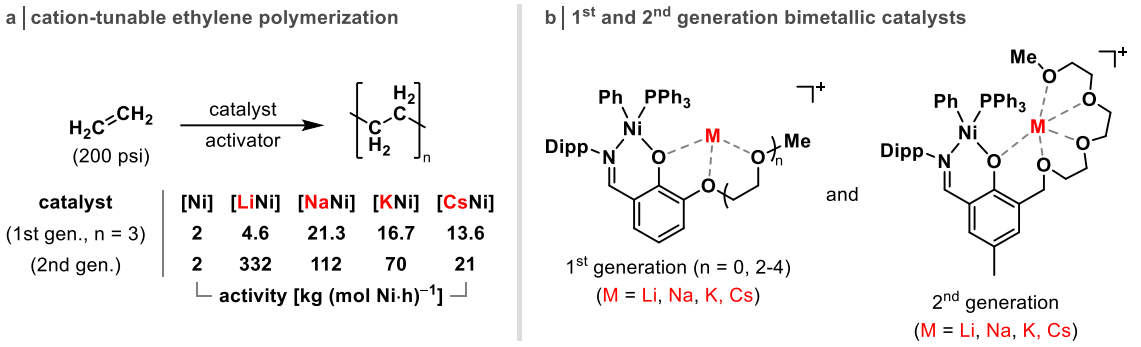

Figure 16. (a) Polymerization of ethylene with cation-tunable (M = Li, Na, K, Cs) nickel phenoxyimine catalysts. (b) Molecular structures of the first- and second-generation bimetallic complexes.

Polymerization studies on related heterobimetallic nickel complexes containing a phenoxyphosphine ligand reproduced the alkali metal cation effect (Figure 17a,b).[42d] Similar to the phenoxyimine system, the polymerization of ethylene followed the activity trend: $Li^+ > Na^+ > K^+ > Cs^+$. Cyclic voltammetry of the mono- and heterobimetallic complexes revealed a positive shift in the oxidation peak following the trend: $Li^+ > Na^+ > K^+ > Cs^+$, relative to the monometallic analog. This suggests that the alkali metal cations reduce the electron density at the nickel center.

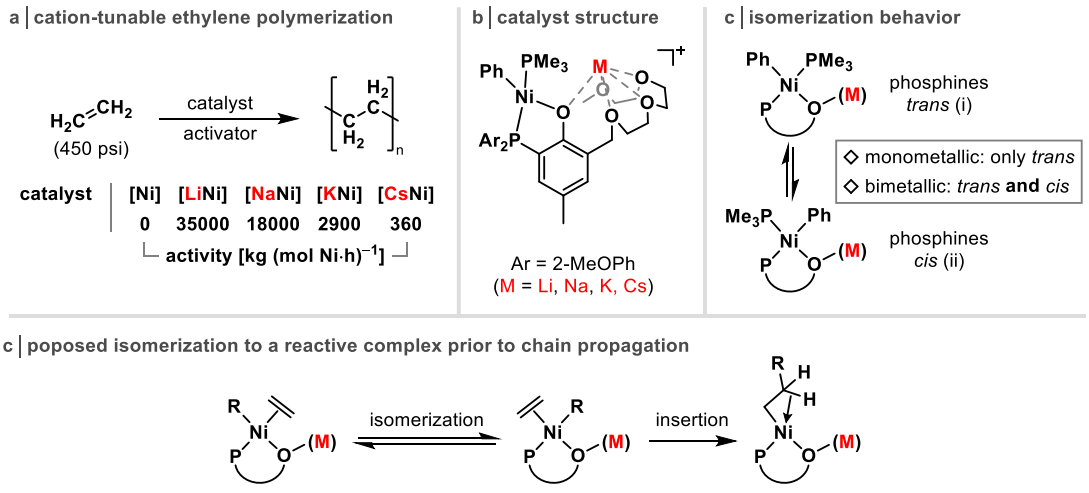

Figure 17. Polymerization of ethylene with cation-tunable (M = Li, Na, K, Cs) nickel phenoxyphosphine catalysts. (b) Molecular structures of the bimetallic complexes. (c) Isomerization behavior of the mono- and heterobimetallic complexes. (d) Proposed isomerization pathway to a reactive complex prior to chain propagation.

Buried volume analyses of the heterobimetallic catalysts further showed that the alkali ions can impart substantial steric shielding in the heterobimetallic catalysts, as compared to a conventional monometallic reference. Finally, the presence of an alkali metal cation favors the formation of the cis isomer (to varying extents), which was not observed for the monometallic catalysts (Figure 17c). DFT analyses of the cis isomer show a cation-π interaction with the phenyl group, leading the authors to hypothesize that similar interactions might also occur during the polymerization process (Figure 17d). DFT studies suggest that the alkali metal cation is directly involved in the cis/trans isomerization prior to the first ethylene insertion, with an activation barrier reducing effect ($Li^+ < Na^+ < K^+ < Cs^+$) complementary to the experimental rates.[48]

1.2.5 Miscellaneous Small Molecule Activation Reactions

This final section reviews three examples of small molecule activation in heterometallic complexes, relevant for the understanding of cooperative reactivity (Figure 18).[7c],[49],[50]
Among these is the C–F bond activation of fluorinated aromatic substrates using a heterobimetallic nucleophile (Figure 18a).[49] The Crimmin group reported that the contact ion pair [(^{Dipp}nacnac)Mg][CpFe(CO)$_2$] reacts with 0.5 equivalents of 2-(pentafluoro-phenyl)pyridine to form the ferration product in 4-position and a trinuclear magnesium fluoride by-product. DFT computational analyses indicate a stepwise S_NAr mechanism, which involves the formation of a Meisenheimer intermediate featuring separate Fe and Mg interactions (Figure 18a, right). The two metal fragments in the Meisenheimer complex are charge-separated, facilitated by the inherently ionic Mg–Fe bond in the heterobimetallic complex. This high bond polarity is essential for the proposed mechanism and the observed regioselectivity, as demonstrated by the comparison with the homodinuclear [(nacnac)Mg]$_2$ reagent, which contains an apolar Mg–Mg bond and activates the same substrate in the 2-position.[51] The authors suggest that the level of bond polarity alters the mechanism, with highly polar bimetallic complexes favoring a stepwise S_NAr pathway and less polar ones a concerted S_NAr pathway. This highlights how metal identity and metal-metal bond polarity in bimetallic complexes can fundamentally influence reaction pathways and selectivity.
Xu and co-workers showed that heterobimetallic complexes can coordinate and activate small molecules at one or both of the metal centers, allowing each site to serve a distinct function (Figure 18b).[50] Reactions of the heterometallic hydride-bridged dimagnesium nickel complex with isocyanides resulted in the formation of nickel-bound isocyanide complexes (Figure 18b, left). In contrast, treatment with carbodiimides led to magnesium amidinate species, formed via hydromagnesiation accompanied by Mg–Ni bond cleavage (Figure 18b, right). Lastly, an acetylide-bridged Mg-Ni complex was generated by treatment of the starting material with phenylacetylene, accompanied by the release of H_2. The coordination study illustrates how each metal center in a heterobimetallic complex can engage selectively with different substrates.

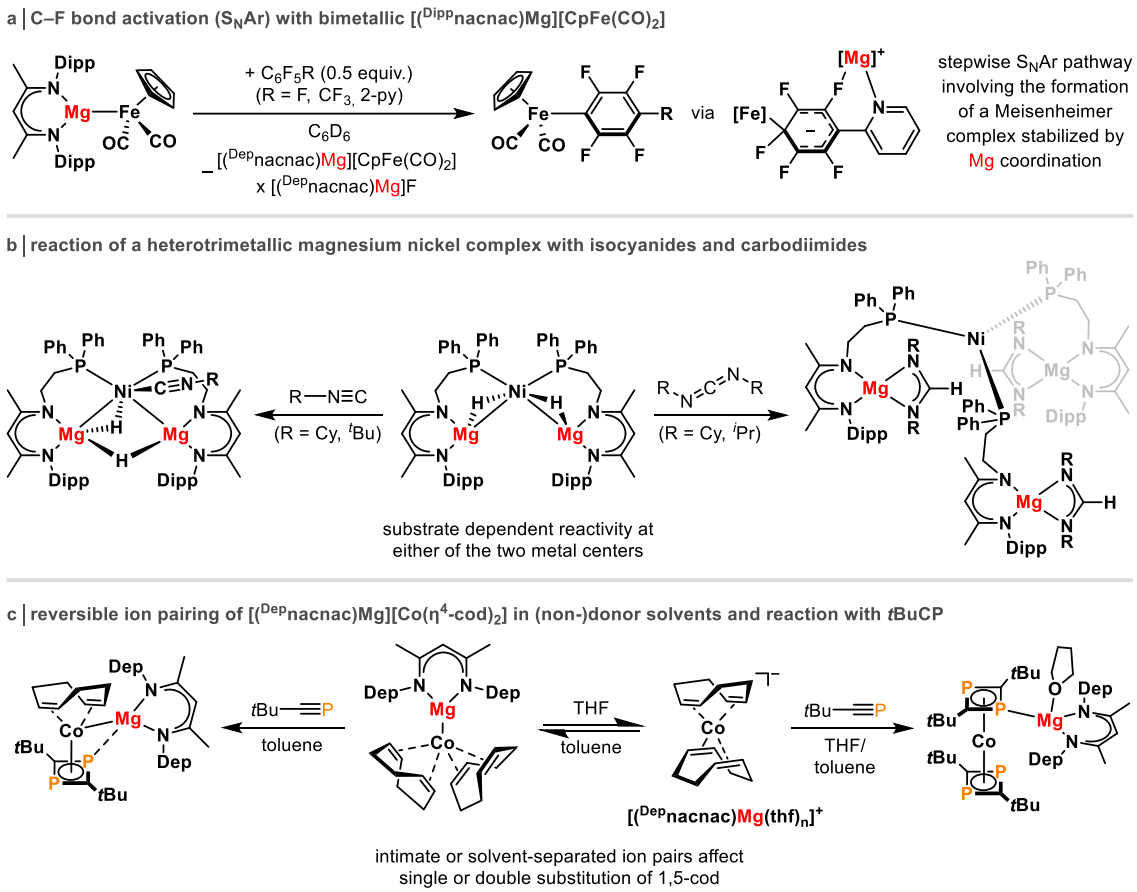

Figure 18. (a) C–F Bond activation (S_NAr) with bimetallic [(Dippnacnac)Mg][CpFe(CO)$_2$] and proposed Meisenheimer intermediate of the stepwise S_NAr pathway. (b) Reaction of a heterotrimetallic dimagnesium nickel complex with isocyanides and carbodiimides. (c) Reversible ion pairing of [(Depnacnac)Mg][Co(η^4-cod)$_2$] in (non-)donor solvents and reaction with *tert*-butylphosphaalkyne resulting in single or double substitution of 1,5-cod.

This enables tailored reactivity when appropriate metal and substrate combinations are used.

Structural and reactivity studies of a β-diketiminate magnesium cobaltate complex by the Wolf group demonstrated that solvation and ion pairing play a crucial role in small molecule activation (Figure 18c).[7c] The heterobimetallic Mg-Co complex features a non-covalent magnesium-cobalt interaction, and reversibly adopts either a contact or solvent-separated ion pair structure depending on the donor strength of the solvent. Upon reaction with *tert*-butylphosphaalkyne, the heteroleptic sandwich complex is formed in toluene by substitution of one 1,5-cyclooctadiene ligand (Figure 18c, left), whereas only the homoleptic complex resulting from the substitution of both 1,5-cyclooctadiene ligands can be isolated when the reaction is conducted in THF (Figure 18c, right). The proximity and solvation of cation and anion prove critical in determining the reaction outcome. Solvent separation of the ion pair results in reactivity resembling that of the naked cobaltate anion, whereas close contact leads to a cooperative mechanism involving both ions.

1.3 Summary and Outlook

In this introduction, we have surveyed fundamental chemical reactions that employ heterobimetallic complexes composed of s-block metal and d-block metal atoms. Such complexes introduce new opportunities for reactivity through the cooperative effects of two distinct metal centers. In many cases, the transition metal serves as the primary catalytic site, while the s-block metal modulates reactivity via electrostatic interactions, structural preorganization, or electronic stabilization. This is complemented by selected systems in which both metal atoms engage in the reaction, each having a site-specific role.

Anionic hydrogenation catalysts show cation-sensitive reactivity that is highly dependent on the identity and solvation of the s-block metal cation. Synergistic modes of dihydrogen activation have been identified in heterobimetallic ate complexes, representing reactivity patterns that are inaccessible to mononuclear analogs.[11],[14],[16],[7d] The use of alkali metal ate complexes in a broad range of C–H, C–C, C–O, C–X, and N–H bond activation reactions illustrates a wide spectrum of bimetallic cooperativity, as supported by detailed structural and mechanistic investigations. The necessity of both metals is underscored by comparative studies, in which monometallic complexes typically fail or show diminished efficiency in driving the same transformations.[23],[24],[34]-[36] Isomerization reactions can be significantly accelerated by transition metal catalysts whose activity is modulated by the binding of alkali metal cations. The pairing of the transition metal with the alkali metal induces bimetallic reactivity that enhances isomerization rates and even enables cation-dependent regioselectivity.[43]-[46] Polymerization catalysis likewise benefits from the incorporation of an s-block metal cation into a transition metal complex, as evidenced in ring-opening copolymerization and alkene polymerization reactions. Heterobimetallic complexes of macrocyclic ligands are employed that exhibit enhanced activities owing to favorable electronic and steric interactions of the transition metal and s-block metal cation.[42],[47],[48]

The examples given in this chapter demonstrate distinct substrate activation modes, including the simultaneous binding of a substrate to both metals (section 1.2.1.2), cooperative activation by one metal with assistance from the other (section 1.2.2.2), and the activation of two substrates at separate sites (section 1.2.4.1). This is further extended by cation-sensitive reactivity, in which the characteristics of a reaction are altered by varying the identity of the s-block metal cation (section 1.2.3.2).

Importantly, ion pairing effects significantly influence the reactivity of the heterobimetallic complexes. The formation of contact ion pairs enables strong interactions between the metal centers, which are essential for synergistic bond activation.

Heterobimetallic systems combining s- and d-block metals hold promise in expanding the reactivity landscape of organometallic chemistry. With a growing body of studies highlighting *and* evaluating cooperative behavior, metal-metal cooperativity and ion pairing will play an increasing role in reaction design. We hope this introduction inspires new approaches that leverage the interplay between s- and d-block metals in heterobimetallic chemistry.

1.4 References

[1] a) S. T. Liddle, *Molecular Metal-Metal Bonds: Compounds, Synthesis, Properties*, Wiley, Weinheim **2015**; b) P. Kalck, Homo- and Heterobimetallic Complexes in Catalysis: Cooperative Catalysis, Springer, Cham **2016**.

[2] a) R. C. Cammarota, L. J. Clouston, C. C. Lu, *Coord. Chem. Rev.* **2017**, *334*, 100; b) N. P. Mankad, *Chem. Commun.* **2018**, *54*, 1291; c) B. Chatterjee, W.-C. Chang, S. Jena, C. Werlé, *ACS Catal.* **2020**, *10*, 14024; d) P. C. Abhyankar, C. M. Thomas, *Angew. Chem. Int. Ed.* **2024**, *63*, e202416100.

[3] a) P. A. Lindahl, *J. Inorg. Biochem.* **2012**, *106*, 172; b) W. Lubitz, H. Ogata, O. Rüdiger, E. Reijerse, *Chem. Rev.* **2014**, *114*, 4081; c) K. Tanifuji, Y. Ohki, *Chem. Rev.* **2020**, *120*, 5194; d) R. M. Bullock, J. G. Chen, L. Gagliardi, P. J. Chirik, O. K. Farha, C. H. Hendon, C. W. Jones, J. A. Keith, J. Klosin, S. D. Minteer, R. H. Morris, A. T. Radosevich, T. B. Rauchfuss, N. A. Strotman, A. Vojvodic, T. R. Ward, J. Y. Yang, Y. Surendranath, *Science* **2020**, *369*, eabc3183; e) A. C. Ghosh, C. Duboc, M. Gennari, *Coord. Chem. Rev.* **2021**, *428*, 213606.

[4] a) R. C. Cammarota, C. C. Lu, *J. Am. Chem. Soc.* **2015**, *137*, 12486; b) M. V. Vollmer, J. Ye, J. C. Linehan, B. J. Graziano, A. Preston, E. S. Wiedner, C. C. Lu, *ACS Catal.* **2020**, *10*, 2459; c) B. J. Graziano, M. V. Vollmer, C. C. Lu, *Angew. Chem. Int. Ed.* **2021**, *60*, 15087; d) N. Gorgas, A. J. P. White, M. R. Crimmin, *J. Am. Chem. Soc.* **2022**, *144*, 8770; e) J. T. Moore, M. J. Dorantes, Z. Pengmei, T. M. Schwartz, J. Schaffner, S. L. Apps, C. A. Gaggioli, U. Das, L. Gagliardi, D. A. Blank, C. C. Lu, *Angew. Chem. Int. Ed.* **2022**, *61*, e202205575; f) S. Sinhababu, M. R. Radzhabov, J. Telser, N. P. Mankad, *J. Am. Chem. Soc.* **2022**, *144*, 3210; g) S. Fernández, S. Fernando, O. Planas, *Dalton Trans.* **2023**, *52*, 14259; h) R. P. Singh, S. Sinhababu, N. P. Mankad, *ACS Catal.* **2023**, *13*, 12519; i) N. Gorgas, B. Stadler, A. J. P. White, M. R. Crimmin, *J. Am. Chem. Soc.* **2024**, *146*, 4252; j) B. Stadler, N. Gorgas, S. J. Elliott, M. R. Crimmin, *Angew. Chem. Int. Ed.* **2024**, e202408257.

[5] a) J. Campos, *Nat. Rev. Chem.* **2020**, *4*, 696; b) M. Navarro, J. J. Moreno, M. Pérez-Jiménez, J. Campos, *Chem. Commun.* **2022**, *58*, 11220.

[6] a) L. H. Gade, *Angew. Chem. Int. Ed.* **2000**, *39*, 2658; b) J. P. Krogman, C. M. Thomas, *Chem. Commun.* **2014**, *50*, 5115; c) J. F. Berry, C. C. Lu, *Inorg. Chem.* **2017**, *56*, 7577.

[7] For selected examples that analyze the bonding in s-block and d-block heterobimetallic complexes: a) M. P. Blake, N. Kaltsoyannis, P. Mountford, *Chem. Commun.* **2013**, *49*, 3315; b) C. Birchall, G. J. Moxey, J. McMaster, A. J. Blake, W. Lewis, D. L. Kays, *Inorg. Chim. Acta* **2017**, *458*, 97; c) J. A. Kelly, J. Gramüller, R. M. Gschwind, R. Wolf, *Dalton Trans.* **2021**, *50*, 13985; d) Y. Cai, S. Jiang, T. Rajeshkumar, L. Maron, X. Xu, *J. Am. Chem. Soc.* **2022**, *144*, 16647.

[8] a) A. Macchioni, *Chem. Rev.* **2005**, *105*, 2039; b) Y. Marcus, G. Hefter, *Chem. Rev.* **2006**, *106*, 4585.

[9] Selected examples for base-activated hydrogenation catalysts: a) R. Langer, G. Leitus, Y. Ben-David, D. Milstein, *Angew. Chem. Int. Ed.* **2011**, *50*, 2120; b) J. E. Perea-Buceta, I. Fernández, S. Heikkinen, K. Axenov, A. W. T. King, T. Niemi, M. Nieger, M. Leskelä, T. Repo, *Angew. Chem. Int. Ed.* **2015**, *54*, 14321; c) B. Butschke, M. Feller, Y. Diskin-Posner, D. Milstein, *Catal. Sci. Technol.* **2016**, *6*, 4428; d) R. van Putten, E. A. Uslamin, M. Garbe, C. Liu, A. Gonzalez-de-Castro, M. Lutz, K. Junge, E. J. M. Hensen, M. Beller, L. Lefort, E. A. Pidko, *Angew. Chem. Int. Ed.* **2017**, *56*, 7531; e) S. Thiyagarajan, C. Gunanathan, *Org. Lett.* **2019**, *21*, 9774.

[10] a) M. Nielsen, E. Alberico, W. Baumann, H.-J. Drexler, H. Junge, S. Gladiali, M. Beller, *Nature* **2013**, *495*, 85; b) P. A. Dub, N. J. Henson, R. L. Martin, J. C. Gordon, *J. Am. Chem. Soc.* **2014**, *136*, 3505; c) E. Alberico, A. J. J. Lennox, L. K. Vogt, H. Jiao, W. Baumann, H.-J. Drexler, M. Nielsen, A. Spannenberg, M. P. Checinski, H. Junge, M. Beller, *J. Am. Chem. Soc.* **2016**, *138*, 14890; d) Z. Liang, T. Yang, G. Gu, L. Dang, X. Zhang, *Chin. J. Chem.* **2018**, *36*, 851; e) C. Liu, R. Van Putten, P. O. Kulyaev, G. A. Filonenko, E. A. Pidko, *J. Catal.* **2018**, *363*, 136; f) C. Yin, Y.-F. Jiang, F. Huang, C.-Q. Xu, Y. Pan, S. Gao, G.-Q. Chen, X. Ding, S.-T. Bai, Q. Lang, J. Li, X. Zhang, *Nat. Commun.* **2023**, *14*, 3718.

[11] a) F. Freitag, T. Irrgang, R. Kempe, *J. Am. Chem. Soc.* **2019**, *141*, 11677; b) G. Zhang, T. Irrgang, M. Schlagbauer, R. Kempe, *Chem Catal.* **2021**, *1*, 681; c) N. Sila, A. Dürrmann, B. Weber, F. W. Heinemann, T. Irrgang, R. Kempe, *J. Am. Chem. Soc.* **2024**, *146*, 26877.

[12] P. A. Dub, J. C. Gordon, *Nat. Rev. Chem.* **2018**, *2*, 396.

[13] Examples for base-activated (transfer) hydrogenation catalysts with non-deprotonatable sites: a) N. Debono, M. Besson, C. Pinel, L. Djakovitch, *Tetrahedron Lett.* **2004**, *45*, 2235; b) R. J. Lundgren, M. Stradiotto, *Chem. Eur. J.* **2008**, *14*, 10388; c) A. Binobaid, M. Iglesias, D. Beetstra, A. Dervisi, I. Fallis, K. J. Cavell, *Eur. J. Inorg. Chem.* **2010**, *2010*, 5426; d) M. V. Jiménez, J. Fernández-Tornos, J. J. Pérez-Torrente, F. J. Modrego, S. Winterle, C. Cunchillos, F. J. Lahoz, L. A. Oro, *Organometallics* **2011**, *30*, 5493.

[14] a) J. M. Hayes, E. Deydier, G. Ujaque, A. Lledós, R. Malacea-Kabbara, E. Manoury, S. Vincendeau, R. Poli, *ACS Catal.* **2015**, *5*, 4368; b) P. Kisten, E. Manoury, A. Lledós, A. C. Whitwood, J. M. Lynam, J. M. Slattery, S. B. Duckett, R. Poli, *Dalton Trans.* **2023**, *52*, 2495; c) P. Kisten, S. Vincendeau, E. Manoury, J. M. Lynam, J. M. Slattery, S. B. Duckett, A. Lledós, R. Poli, *Chem. Sci.* **2024**, *15*, 20478.

[15] See for H_2 activation by two metalloradicals or over an intact M–M bond: a) X.-X. Zhang, B. B. Wayland, *J. Am. Chem. Soc.* **1994**, *116*, 7897; b) M. K. Karunananda, N. P. Mankad, *J. Am. Chem. Soc.* **2015**, *137*, 14598.

[16] J. Takaya, *Chem. Sci.* **2021**, *12*, 1964.

[17] C. Färber, P. Stegner, U. Zenneck, C. Knüpfer, G. Bendt, S. Schulz, S. Harder, *Nat. Commun.* **2022**, *13*, 3210.

[18] See for the reversible activation of H_2 by a heterobimetallic Pd-Mg hydride complex: a) M. Garçon, C. Bakewell, G. A. Sackman, A. J. P. White, R. I. Cooper, A. J. Edwards, M. R. Crimmin, *Nature* **2019**, *574*, 390; b) M. Garçon, A. Phanopoulos, A. J. P. White, M. R. Crimmin, *Angew. Chem. Int. Ed.* **2023**, *62*, e202213001.

[19] Y. Cai, S. Jiang, X. Xu, *Chin. J. Chem.* **2024**, *42*, 2133.

[20] a) P. Stegner, C. Färber, U. Zenneck, C. Knüpfer, J. Eyselein, M. Wiesinger, S. Harder, *Angew. Chem. Int. Ed.* **2021**, *60*, 4252; b) C. Knüpfer, C. Färber, J. Langer, S. Harder, *Angew. Chem. Int. Ed.* **2023**, *62*, e202219016.

[21] Selected reviews on C–H and C–X activation of arenes and alkynes: a) P. Siemsen, R. C. Livingston, F. Diederich, *Angew. Chem. Int. Ed.* **2000**, *39*, 2632; b) R. Chinchilla, C. Nájera, *Chem. Rev.* **2007**, *107*, 874; c) D. Alberico, M. E. Scott, M. Lautens, *Chem. Rev.* **2007**, *107*, 174; d) K. S. Sindhu, G. Anilkumar, *RSC Adv.* **2014**, *4*, 27867; e) P. Gandeepan, T. Müller, D. Zell, G. Cera, S. Warratz, L. Ackermann, *Chem. Rev.* **2019**, *119*, 2192.

[22] a) N. Yoshikai, H. Matsuda, E. Nakamura, *J. Am. Chem. Soc.* **2009**, *131*, 9590; b) S. Pal, C. Uyeda, *J. Am. Chem. Soc.* **2015**, *137*, 8042; c) C. Wu, S. P. McCollom, Z. Zheng, J. Zhang, S.-C. Sha, M. Li, P. J. Walsh, N. C. Tomson, *ACS Catal.* **2020**, *10*, 7934; d) S. Deolka, O. Rivada-Wheelaghan, S. L. Aristizábal, R. R. Fayzullin, S. Pal, K. Nozaki, E. Khaskin, J. R. Khusnutdinova, *Chem. Sci.* **2020**, *11*, 5494.

[23] a) M. Uzelac, P. Mastropierro, M. De Tullio, I. Borilovic, M. Tarrés, A. R. Kennedy, G. Aromí, E. Hevia, *Angew. Chem. Int. Ed.* **2021**, *60*, 3247; b) P. Mastropierro, A. W. J. Platten, A. R. Kennedy, E. Hevia, M. Uzelac, *Chem. Eur. J.* **2023**, *29*, e202300593.

[24] a) L. C. H. Maddock, T. Nixon, A. R. Kennedy, M. R. Probert, W. Clegg, E. Hevia, *Angew. Chem. Int. Ed.* **2018**, *57*, 187; b) L. C. H. Maddock, M. Mu, A. R. Kennedy, M. García-Melchor, E. Hevia, *Angew. Chem. Int. Ed.* **2021**, *60*, 15296; c) L. C. H. Maddock, A. R. Kennedy, E. Hevia, *Helv. Chim. Acta* **2021**, *104*, e2100206; d) A. Logallo, M. Mu, M. García-Melchor, E. Hevia, *Angew. Chem. Int. Ed.* **2022**, *61*, e202213246; e) A. Logallo, E. Hevia, *Chem. Commun.* **2023**, *59*, 5383; f) A. Logallo, E. Hevia, *Chimia* **2024**, *78*, 238.

[25] A single example for C–H ferration has been reported using a related Na-Fe complex: P. Alborés, L. M. Carrella, W. Clegg, P. García-Álvarez, A. R. Kennedy, J. Klett, R. E. Mulvey, E. Rentschler, L. Russo, *Angew. Chem. Int. Ed.* **2009**, *48*, 3317.

[26] a) G. Wilke, B. Bogdanovič, P. Borner, H. Breil, P. Hardt, P. Heimbach, G. Herrmann, H.-J. Kaminsky, W. Keim, M. Kröner, H. Müller, E. W. Müller, W. Oberkirch, J. Schneider, J. Stedefeder, K. Tanaka, K. Weyer, G. Wilke, *Angew. Chem. Int. Ed. Engl.* **1963**, *2*, 105; b) B. Bogdanović, M. Kröner, G. Wilke, *Liebigs Ann. Chem.* **1966**, *699*,

1; c) K. Fischer, K. Jonas, P. Misbach, R. Stabba, G. Wilke, *Angew. Chem. Int. Ed. Engl.* **1973**, *12*, 943.

[27] a) K. Jonas, *Angew. Chem. Int. Ed. Engl.* **1973**, *12*, 997; b) K. Jonas, *Angew. Chem. Int. Ed. Engl.* **1976**, *15*, 47; c) K. Jonas, D. J. Brauer, C. Krueger, P. J. Roberts, Y. H. Tsay, *J. Am. Chem. Soc.* **1976**, *98*, 74.

[28] a) R. J. P. Corriu, J. P. Masse, *J. Chem. Soc., Chem. Commun.* **1972**, 144a; b) K. Tamao, K. Sumitani, M. Kumada, *J. Am. Chem. Soc.* **1972**, *94*, 4374.

[29] J. B. Diccianni, T. Diao, *Trends Chem.* **2019**, *1*, 830.

[30] a) K. W. Quasdorf, A. Antoft-Finch, P. Liu, A. L. Silberstein, A. Komaromi, T. Blackburn, S. D. Ramgren, K. N. Houk, V. Snieckus, N. K. Garg, *J. Am. Chem. Soc.* **2011**, *133*, 6352; b) J. Cornella, E. Gómez-Bengoa, R. Martin, *J. Am. Chem. Soc.* **2013**, *135*, 1997; c) M. C. Schwarzer, R. Konno, T. Hojo, A. Ohtsuki, K. Nakamura, A. Yasutome, H. Takahashi, T. Shimasaki, M. Tobisu, N. Chatani, S. Mori, *J. Am. Chem. Soc.* **2017**, *139*, 10347; d) A. M. Borys, E. Hevia, *Synthesis* **2022**, *54*, 2976.

[31] a) H. Ogawa, H. Minami, T. Ozaki, S. Komagawa, C. Wang, M. Uchiyama, *Chem. Eur. J.* **2015**, *21*, 13904; b) K. Kojima, Z.-K. Yang, C. Wang, M. Uchiyama, *Chem. Pharm. Bull.* **2017**, *65*, 862.

[32] a) D. J. Brauer, C. Krüger, P. J. Roberts, Y. Tsay, *Angew. Chem. Int. Ed. Engl.* **1976**, *15*, 48; b) K. Jonas, K. R. Pörschke, C. Krüger, Y. Tsay, *Angew. Chem. Int. Ed. Engl.* **1976**, *15*, 621; c) K. Jonas, C. Krüger, *Angew. Chem. Int. Ed. Engl.* **1980**, *19*, 520; d) K. Pörschke, K. Jonas, G. Wilke, R. Benn, R. Mynott, R. Goddard, C. Krüger, *Chem. Ber.* **1985**, *118*, 275; e) K. Pörschke, K. Jonas, G. Wilke, *Chem. Ber.* **1988**, *121*, 1913.

[33] a) C. Zarate, M. Nakajima, R. Martin, *J. Am. Chem. Soc.* **2017**, *139*, 1191; b) L. Nattmann, S. Lutz, P. Ortsack, R. Goddard, J. Cornella, *J. Am. Chem. Soc.* **2018**, *140*, 13628; c) S. Lutz, L. Nattmann, N. Nöthling, J. Cornella, *Organometallics* **2021**, *40*, 2220; d) V. K. Rawat, K. Higashida, M. Sawamura, *Synthesis* **2021**, *53*, 3397; e) A. M. Borys, E. Hevia, *Dalton Trans.* **2023**, *52*, 2098; f) A. M. Borys, L. Vedani, E. Hevia, *J. Am. Chem. Soc.* **2024**, *146*, 10199; g) A. M. Borys, L. Vedani, E. Hevia, *Organometallics* **2024**, *43*, 3171.

[34] a) A. M. Borys, E. Hevia, *Angew. Chem. Int. Ed.* **2021**, *60*, 24659; b) H. Liang, A. M. Borys, E. Hevia, M.-E. L. Perrin, P.-A. Payard, *J. Am. Chem. Soc.* **2023**, *145*, 19989.

[35] E. Hevia, A. M. Borys, A. E. F. Denjean, L. Vedani, D. Balcells, *Angew. Chem. Int. Ed.* **2025**, e202501995.

[36] A. Tortajada, E. Hevia, *ACS Org. Inorg. Au* **2024**, *5*, 62.

[37] a) L. Huang, M. Arndt, K. Gooßen, H. Heydt, L. J. Gooßen, *Chem. Rev.* **2015**, *115*, 2596; b) A. Trowbridge, S. M. Walton, M. J. Gaunt, *Chem. Rev.* **2020**, *120*, 2613.

[38] J. Escorihuela, A. Lledós, G. Ujaque, *Chem. Rev.* **2023**, *123*, 9139.

[39] C. Yoo, H. M. Dodge, A. J. M. Miller, *Chem. Commun.* **2019**, *55*, 5047.

[40] a) S. B. Owens, G. M. Gray, *Organometallics* **2008**, *27*, 4282–4287; b) A. Vidal-Ferran, I. Mon, A. Bauzá, A. Frontera, L. Rovira, *Chem. Eur. J.* **2015**, *21*, 11417; c) J. R. Martin, E. C. Cagle, A. L. Lucius, G. M. Gray, *Organometallics* **2016**, *35*, 2609.

[41] a) G. Ouyang, Y. He, Y. Li, J. Xiang, Q. Fan, *Angew. Chem. Int. Ed.* **2015**, *54*, 4334; b) H. Fernández-Pérez, I. Mon, A. Frontera, A. Vidal-Ferran, *Tetrahedron* **2015**, *71*, 4490.

[42] a) Z. Cai, D. Xiao, L. H. Do, *J. Am. Chem. Soc.* **2015**, *137*, 15501; b) Z. Cai, L. H. Do, *Organometallics* **2017**, *36*, 4691; c) Z. Cai, L. H. Do, *Organometallics* **2018**, *37*, 3874; d) T. V. Tran, L. J. Karas, J. I. Wu, L. H. Do, *ACS Catal.* **2020**, *10*, 10760; e) T. V. Tran, E. Lee, Y. H. Nguyen, H. D. Nguyen, L. H. Do, *J. Am. Chem. Soc.* **2022**, *144*, 17129; f) L. C. Ruiz De Castilla, T. Ganguly, B. Tahmouresilerd, C. J. Laconsay, J. I. Wu, L. H. Do, *Organometallics* **2024**, *43*, 2643.

[43] a) A. J. M. Miller, *Dalton Trans.* **2017**, *46*, 11987; b) S. Acosta-Calle, A. J. M. Miller, *Acc. Chem. Res.* **2023**, *56*, 971.

[44] a) J. B. Smith, S. H. Kerr, P. S. White, A. J. M. Miller, *Organometallics* **2017**, *36*, 3094; b) A. H. Farquhar, K. E. Gardner, S. Acosta-Calle, A. M. Camp, C.-H. Chen, A. J. M. Miller, *Organometallics* **2022**, *41*, 3366.

[45] a) M. R. Kita, A. J. M. Miller, *J. Am. Chem. Soc.* **2014**, *136*, 14519; b) M. R. Kita, A. J. M. Miller, *Angew. Chem. Int. Ed.* **2017**, *56*, 5498; c) H. M. Dodge, M. R. Kita, C.-H. Chen, A. J. M. Miller, *ACS Catal.* **2020**, *10*, 13019.

[46] A. M. Camp, M. R. Kita, P. T. Blackburn, H. M. Dodge, C.-H. Chen, A. J. M. Miller, *J. Am. Chem. Soc.* **2021**, *143*, 2792.

[47] a) A. C. Deacy, A. F. R. Kilpatrick, A. Regoutz, C. K. Williams, *Nat. Chem.* **2020**, *12*, 372; b) A. C. Deacy, E. Moreby, A. Phanopoulos, C. K. Williams, *J. Am. Chem. Soc.* **2020**, *142*, 19150; c) W. T. Diment, W. Lindeboom, F. Fiorentini, A. C. Deacy, C. K. Williams, *Acc. Chem. Res.* **2022**, *55*, 1997; d) N. V. Reis, A. C. Deacy, G. Rosetto, C. B. Durr, C. K. Williams, *Chem. Eur. J.* **2022**, *28*, e202104198; e) A. C. Deacy, A. Phanopoulos, W. Lindeboom, A. Buchard, C. K. Williams, *J. Am. Chem. Soc.* **2022**, *144*, 17929; f) F. Fiorentini, W. T. Diment, A. C. Deacy, R. W. F. Kerr, S. Faulkner, C. K. Williams, *Nat. Commun.* **2023**, *14*, 4783; g) F. Fiorentini, K. H. S. Eisenhardt, A. C. Deacy, C. K. Williams, *J. Am. Chem. Soc.* **2024**, *146*, 23517; h) F. Butler, F. Fiorentini, K. H. S. Eisenhardt, C. K. Williams, *Angew. Chem. Int. Ed.* **2025**, e202422497.

[48] P. Apilardmongkol, M. Ratanasak, J. Hasegawa, V. Parasuk, *ChemCatChem* **2022**, *14*, e202200028.

[49] M. Garçon, C. Bakewell, A. J. P. White, M. R. Crimmin, *Chem. Commun.* **2019**, *55*, 1805.

[50] J. Huang, X. Zheng, I. Del Rosal, B. Zhao, L. Maron, X. Xu, *Inorg. Chem.* **2020**, *59*, 13473.

[51] C. Bakewell, A. J. P. White, M. R. Crimmin, *J. Am. Chem. Soc.* **2016**, *138*, 12763.

Chapter 2 Counterion Effect in Cobaltate-Catalyzed Alkene Hydrogenation[a,b]

Abstract: We show that countercations exert a remarkable influence on the ability of anionic cobaltate salts to catalyze challenging alkene hydrogenations. An evaluation of the catalytic properties of [Cat][Co(η^4-cod)$_2$] (Cat = K (**1**), Na (**2**), Li (**3**), (^{Dep}nacnac)Mg (**4**), and N(^{n}Bu)$_4$ (**5**); cod = 1,5-cyclooctadiene, ^{Dep}nacnac = {2,6-Et$_2$C$_6$H$_3$NC(CH$_3$)}$_2$CH) demonstrated that the lithium salt **3** and magnesium salt **4** drastically outperform the other catalysts. Complex **4** was the most active catalyst, which readily promotes the hydrogenation of highly congested alkenes under mild conditions. A plausible catalytic mechanism is proposed based on density functional theory (DFT) investigations. Furthermore, combined molecular dynamics (MD) simulation and DFT studies were used to examine the turnover-limiting migratory insertion step. The results of these studies suggest an active co-catalytic role of the counterion in the hydrogenation reaction through the coordination to cobalt hydride intermediates.

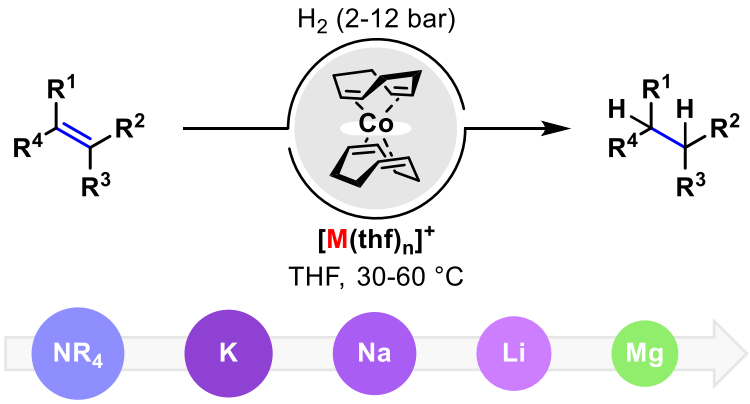

[a] Reproduced with changes from M. Gawron, F. Gilch, D. Schmidhuber, J. A. Kelly, T. M. Horsley Downie, A. Jacobi Von Wangelin, J. Rehbein, R. Wolf, *Angew. Chem. Int. Ed.* **2024**, *63*, e202315381 with permission from Wiley.

[b] Martin Gawron performed all experiments except those mentioned below and wrote the manuscript draft. Franziska Gilch synthesized and characterized complexes **5** and **7** and performed and analyzed the poisoning studies with PMe$_3$ and P(OMe)$_3$, conducted the arene hydrogenation experiments and performed the high pressure NMR tube hydrogenation reactions and the Hg poisoning experiments at elevated temperature and pressure. John A. Kelly contributed to the project through the synthesis and characterization of complexes **4** and **7**. Daniel Schmidhuber carried out all MD simulations and DFT calculations under the supervision of Julia Rehbein. Axel Jacobi von Wangelin and Robert Wolf guided and supervised the project. All authors edited the manuscript.

2.1 Introduction

The hydrogenation of alkenes is among the most widely utilized reactions for the synthesis of petrochemical intermediates, fine chemicals, drugs, agrochemicals, and nutrients.[1],[2] Noble metals such as rhodium, palladium and iridium are routinely used as catalysts owing to their high reactivity, high selectivity, mild reaction conditions, and ease of operation.[3] However, growing environmental and economic awareness has emphasized more sustainable technologies including the use of first row transition metals due to their higher abundance in the Earth's crust.[4] As a result, the development of effective hydrogenation protocols with Mn, Fe, Co, and Ni has gained traction over the last decade.[5] Among them, anionic pre-catalysts, such as(ene)metalate salts (M = Fe, Co, Ni) and heteroleptic diimine cobaltates, have been shown to exhibit high catalytic activity for unbiased and bulky alkenes (Figure 1A).[6]-[9]

While the modular nature of such metalate pre-catalysts has enabled large variations of the ligands and metal ions, the potential of adopting counterion-sensitive mechanisms has so far not been investigated. Despite the availability of numerous anionic organometallic reagents and coordination complexes,[10] detailed studies of countercation effects on molecular reactivity have remained scarce and have only recently gained greater recognition.[11],[12] For example, Miller and co-workers demonstrated the cooperative effect of alkali metal cation binding in the Ir-catalyzed isomerization of allylbenzene (Figure 1B).[13] Addition of 1–4 mol% $MBArF_4$ (M = Li, Na, K; Ar^F = 3,5-bis(trifluoromethyl)phenyl) to the iridium catalyst drastically increased the rate of isomerization to β-methylstyrene with turnover frequencies ranging from 1.8 h^{-1} (M = K) to 2000 h^{-1} (M = Li). Kempe and co-workers observed a remarkable influence of the alkali metal cation on the manganese catalyzed imine hydrogenation (Figure 1C).[14] Alteration of the co-catalytic alkoxide base MO^tBu (M = K, Na, Li) accelerates the reaction following the trend: $K^+ > Na^+ > Li^+$. An outer-sphere mechanism was proposed, in which a potassium cation actively participates in the rate-determining hydride transfer step. Similar observations have been made for Ru-catalyzed (asymmetric) Noyori-type hydrogenations.[15]

Previous studies from our group documented a strong counterion effect in the hydrogenation of 1,5-cyclooctadiene (cod) with bis(imino)acenaphthene (BIAN) cobaltates $[M(thf)_n][(^{Dipp}BIAN)Co(\eta^4\text{-cod})]$ (M = Li, n = 3.5; M = K, n = 1) used as catalysts.[7] Using the lithium cobaltate generated 61% cyclooctene, while the potassium analog gave only 1%. We reasoned that such behavior could be more general and provide an additional parameter for catalyst optimization. Herein, we report a strong countercation effect on the catalytic hydrogenation of bulky alkenes with homoleptic $[Co(\eta^4\text{-cod})_2]^-$ pre-catalysts, with the best-performing pre-catalyst bearing a magnesium counterion (Figure 1D). The topicity of the catalytic system and the reaction-time profile is investigated by H_2 uptake studies. Combined molecular dynamics (MD) and density functional theory (DFT) studies indicate

an active role of the counterion in the turnover-limiting migratory insertion step via a M-μ_2-H–Co moiety.

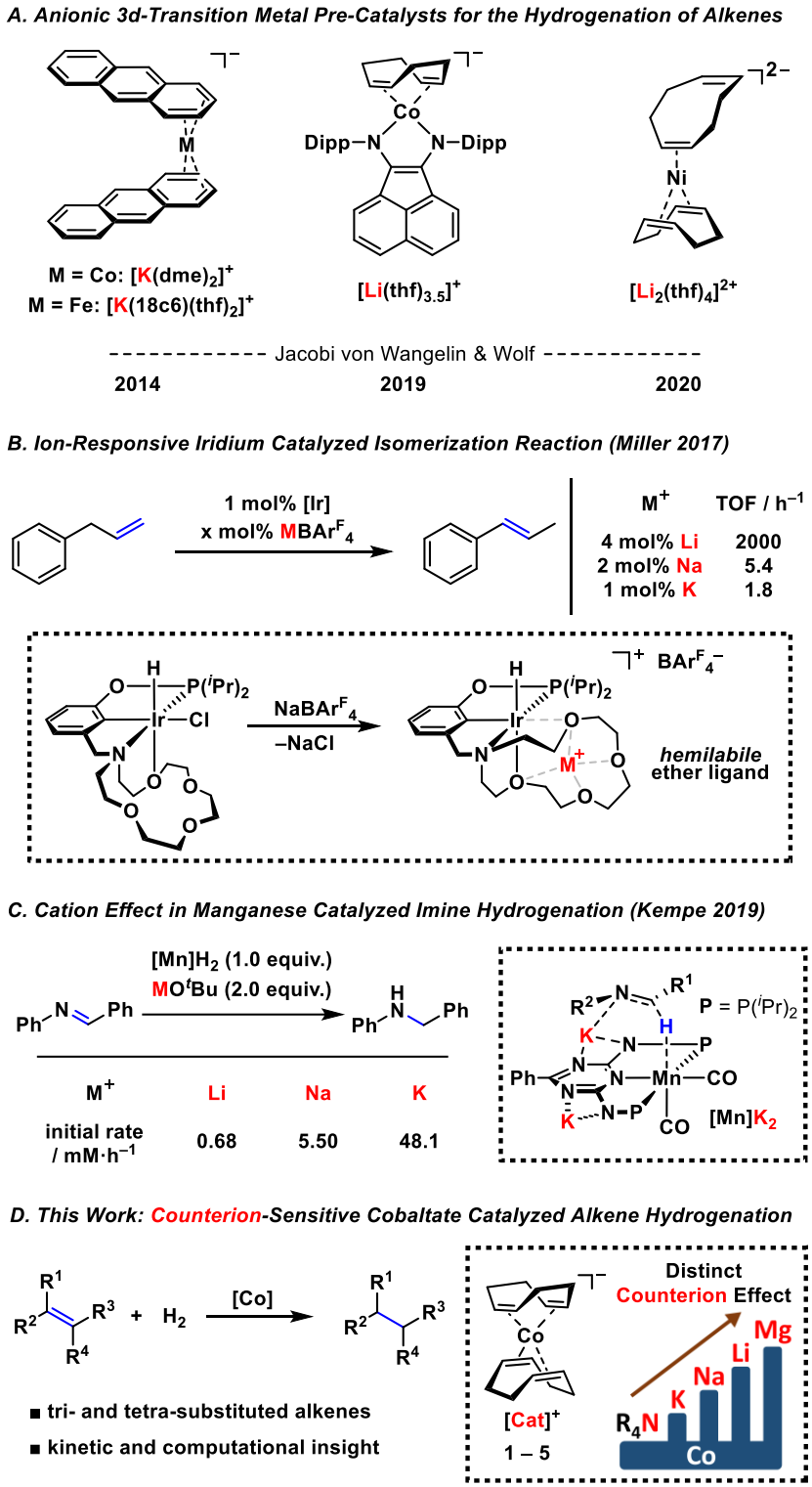

Figure 1. A: Anionic 3d-transition metalates used for alkene hydrogenation (18c6 = 18-crown-6; Dipp = 2,6-diisopropylphenyl). B: Ion-responsive iridium catalyzed isomerization reaction. C: Counterion effect in manganese catalyzed imine hydrogenation and graphical representation of the proposed rate-determining hydride transfer step. The pre-catalyst **[Mn]H$_2$** carries two protons in place of the two K$^+$ ions in **[Mn]K$_2$**. D: This work: Counterion-sensitive cobaltate catalyzed alkene hydrogenation.

2.2 Results and Discussion

2.2.1 Pre-Catalyst Synthesis and Initial Evaluation of Counterion Influence

In order to systematically examine the influence of different countercations on the catalytic potential, we synthesized a series of bis(η^4-cod)cobaltate salts [Cat][Co(η^4-cod)$_2$] (Cat=K(thf)$_{0.2}$ (**1**), Na(thf)$_{1.5}$ (**2**), Li(thf)$_2$ (**3**), (^{Dep}nacnac)Mg (**4**), and N(^{n}Bu)$_4$ (**5**); Scheme 1, top). While complexes **1**, **3** and **4** were readily obtained via known procedures,[16],[17] the sodium salt **2** was prepared from **3** by a cation exchange reaction with NaO^{t}Bu in 34% yield (Scheme 1a). Single crystal X-ray diffraction (SC-XRD) analysis on crystals grown from THF/*n*-hexane revealed the formation of a solvent-separated ion pair [Na(thf)$_6$][(Co(η^4-cod)$_2$] (Na1–Co1 8.220(7) Å; Figure S31). Substitution of the metal-based cation by reaction of **1** with equimolar N(^{n}Bu)$_4$Cl afforded [N(^{n}Bu)$_4$][Co(η^4-cod)$_2$] (**5**) in 28% yield (Scheme 1b). SC-XRD analysis revealed that complex **5** shows an ion-separated structure (N1–Co1 6.207(1) Å) similar to **2** in the solid state (Figure S32). A comparative study of the catalytic activities of the cobaltates **1**–**5** in alkene hydrogenations (2–12 bar H_2, 30–60 °C, Table 1) revealed a clear trend of increasing activity from potassium cobaltate **1** to magnesium cobaltate **4**.

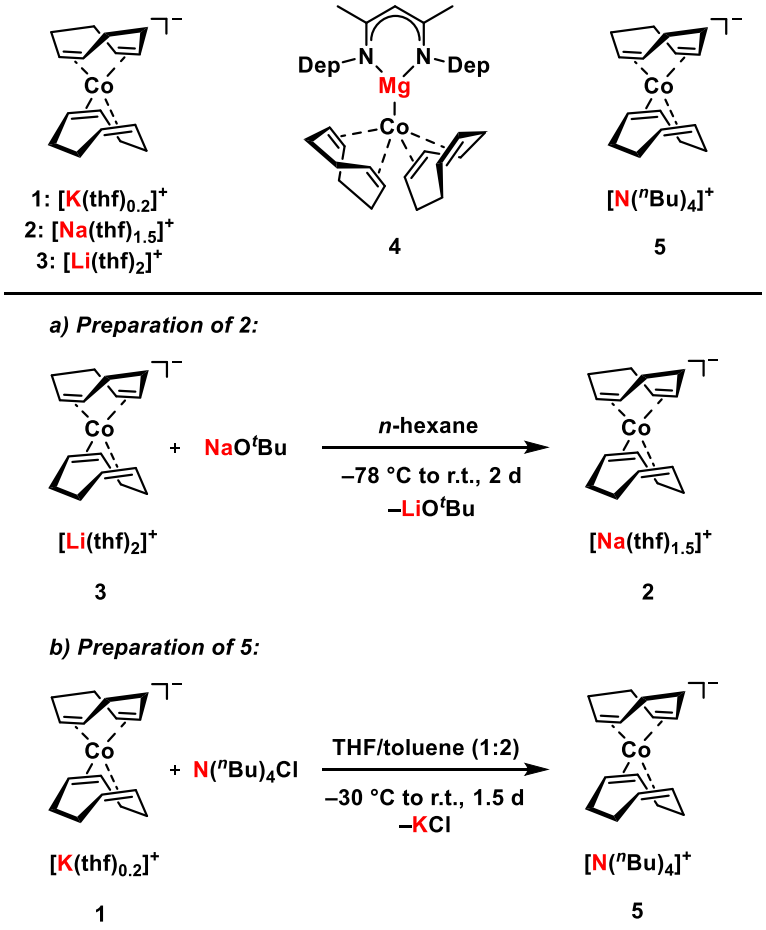

Scheme 1. Top: Olefin cobaltates **1**–**5** tested in the hydrogenation reaction of unsaturated substrates; Dep = 2,6-diethylphenyl. Bottom: a) Preparation of [Na(thf)$_{1.5}$][Co(η^4-cod)$_2$] (**2**). b) Preparation of [N(^{n}Bu)$_4$][Co(η^4-cod)$_2$] (**5**).

1-Octene was hydrogenated quantitatively by the Li^+, Na^+ and (^{Dep}nacnac)Mg^+ salts **2**–**4** but to a much lower degree with the K^+ salt **1** (Table 1, entry 1). The (^{Dep}nacnac)Mg cobaltate **4** gave the highest conversions in the hydrogenation of tri- and tetra-substituted alkenes (Table 1, entries 3–6), whereas the tetrabutylammonium derivative **5** showed negligible activity (Table 1, entries 1–3). To gain further insight into the reaction course, the hydrogenation of α-methylstyrene was monitored by ^{1}H NMR spectroscopy using $[K(thf)_{0.2}][Co(\eta^4\text{-cod})_2]$ (**1**) and [(^{Dep}nacnac)Mg][Co(η⁴-cod)₂] (**4**) as pre-catalysts (10 mol%, 2 bar H_2, ambient temperature, Figure S12 and Figure S13). These experiments confirmed that **4** is the more expedient pre-catalyst, enabling the complete hydrogenation of α-methylstyrene in <266 min. In contrast, pre-catalyst **1** gave 24% of cumene after 263 min. It is also important to note that well-resolved NMR spectra with sharp signals are observed until the hydrogenation reaction has ceased. This strongly indicates the absence of (paramagnetic) cobalt particles in the reaction mixtures.

Table 1. Hydrogenation of alkenes with olefin cobaltates **1** – **5**.[a]

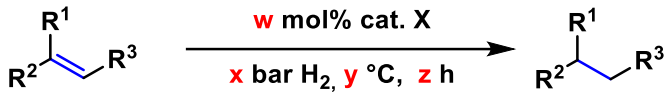

Entry	Olefin	Yield (Conv.) [%] Cat. **1**	Cat. **2**	Cat. **3**	Cat. **4**	Cat. **5**
1[b]	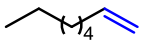	63[e]	98	>99	>99	1 (23)
2[b]	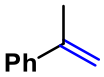	8 (15)	76 (82)	>99	>99	1 (7)
3[b]	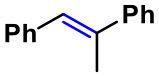	1 (<5)	5 (8)	93	>99	0 (2)
4[c]	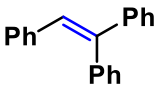	9 (11)	20 (20)	>99	>99	/
5[c]	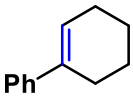	4 (6)	5 (11)	72 (77)	94	/
6[d]	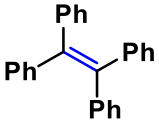	15 (18)	2 (11)	29 (37)	81 (85)	/

[a] Standard conditions: 0.2 mmol substrate (0.4 mol/L THF). Yields and conversions were determined by quantitative GC-FID analysis vs. internal *n*-pentadecane. Conversions are given in parentheses if <90%. [b] 3 mol% cat., 2 bar H_2, 30 °C, 3 h. [c] 5 mol% cat., 8 bar H_2, 40 °C, 22 h. [d] 5 mol% cat., 12 bar H_2, 60 °C, 22 h. [e] Isomerization to internal double bonds.

2.2.2 Catalyst Properties of [(^{Dep}nacnac)Mg][Co(η⁴-cod)₂] (4)

These promising findings prompted us to investigate the substrate scope for complex **4**. Following initial screening and control experiments (see section 2.4.4.2 for details), the

hydrogenation of different alkenes was tested using **4**. A low catalyst loading and mild H_2 pressure (3 mol% **4**, 2 bar H_2, 30 °C for 3 h; Figure 2, Protocol A) sufficed for the hydrogenation of linear α-olefins (e.g., 1-octene, styrene) to tri-substituted olefins (e.g., trans-α-methylstilbene). In terms of functional group tolerance, α-methylstyrene substituted with 4-OMe- or 4-F groups did not impede hydrogenation, but 4-Cl and 4-Br substituents did. Using a slightly modified protocol (5 mol% **4**, 12 bar H_2, 40 °C, 22 h; Figure 2, Protocol B), more challenging tri- and tetra-substituted olefins were successfully hydrogenated. The quantitative hydrogenation of naphthalene to 1,2,3,4-tetrahydronaphthalene and the hydrogenation of the C–C σ-bond in cyclopropylbenzene highlighted the high activity of pre-catalyst **4**. In addition, α,β-unsaturated esters underwent facile hydrogenation with high chemoselectivity for the C=C double bond showcasing an extension to functionalized alkene substrates. Finally, tetra-substituted olefins such as 2,3-dimethyl-1*H*-indene, 2-methyl-3-phenyl-1*H*-indene, 1,1,2,2-tetramethylethylene, 1-phenyl-1,2,2-trimethylethylene and even the very sterically hindered 1,1,2,2-tetraphenylethylene were hydrogenated in good to excellent yields (61–94%).

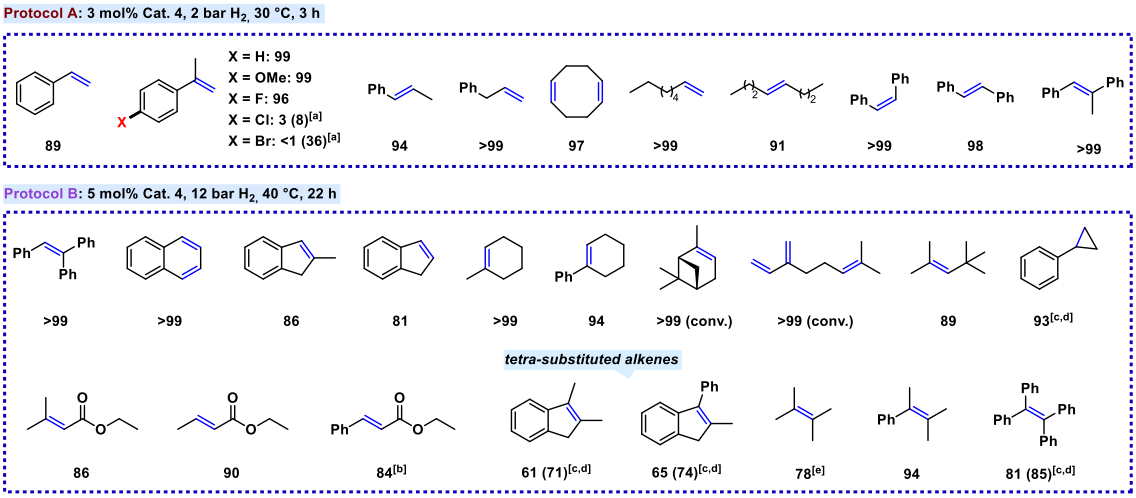

Figure 2. Hydrogenation of alkenes using **4**. Standard conditions: 0.2 mmol substrate (0.4 mol/L in THF). Protocol A: 3 mol% **4**, 2 bar H_2, 30 °C, 3 h. Protocol B: 5 mol% **4**, 12 bar H_2, 40 °C, 22 h. Yields and conversions were determined by quantitative GC-FID analysis vs. internal n-pentadecane. Conversions are given in parentheses if <90%. [a] 8 bar H_2, 6 h. [b] Solvent = toluene. [c] V = 1.0 mL. [d] T = 60 °C. [e] Only product calibrated due to solvent overlap of starting material in GC-FID.

2.2.3 Catalyst Topicity

Further studies focused on reaction progress analyses and kinetic poisoning experiments to distinguish between a homotopic (single molecular) vs. a heterotopic (multiple aggregated) active site.[18] The investigations focused on complex **4**, for which reaction progress analysis of the hydrogenation of α-methylstyrene (3 mol%, 2 bar H_2, 25 °C) showed a short induction period between 30 to 90 s (Figure 3, black curve; see section 2.4.5.2 for further information). Initial ligand exchange with the respective alkene substrate parallel to its hydrogenation can account for the delay in reaction onset.[19],[20] This is followed by steady conversion giving >90% hydrogenation product after 10 min. The attempted amalgamation

with excess mercury (1690 mol%, 563.3 equiv. with respect to **4**) at 0 min had only a minor effect on the reaction rate and full conversion was still reached after 20 min (Figure 3, blue curve).[21] Use of trimethylphosphine (PMe_3, 12 mol%, 4.0 equiv. with respect to **4**) resulted in catalyst inhibition pointing to a homotopic active species (Figure 3, green curve).[7],[22] A four-fold excess of PMe_3 is necessary to occupy all the vacant coordination sites at the Co center.[23] Poisoning with dibenzo[*a*,*e*]cyclooctene (dct, 60 mol%, 20.0 equiv. with respect to **4**) resulted in catalyst inhibition (Figure 3, red curve). An excess of dct (10.0 equiv. per coordination site) is needed to suppress the hydrogenation of α-methylstyrene which can be attributed to the concomitant partial hydrogenation of dct.[7] This is supported by the observation that the homoleptic dct complex [(^{Dep}nacnac)Mg][Co(η^4-dct)$_2$](thf)$_{1.7}$ (**6**) is also active in the hydrogenation of α-methylstyrene but with varying induction periods ranging from 0 to 10 min, while the addition of 60 mol% dct to **6** suppresses the hydrogenation activity (see Figure S6 for details).[24]

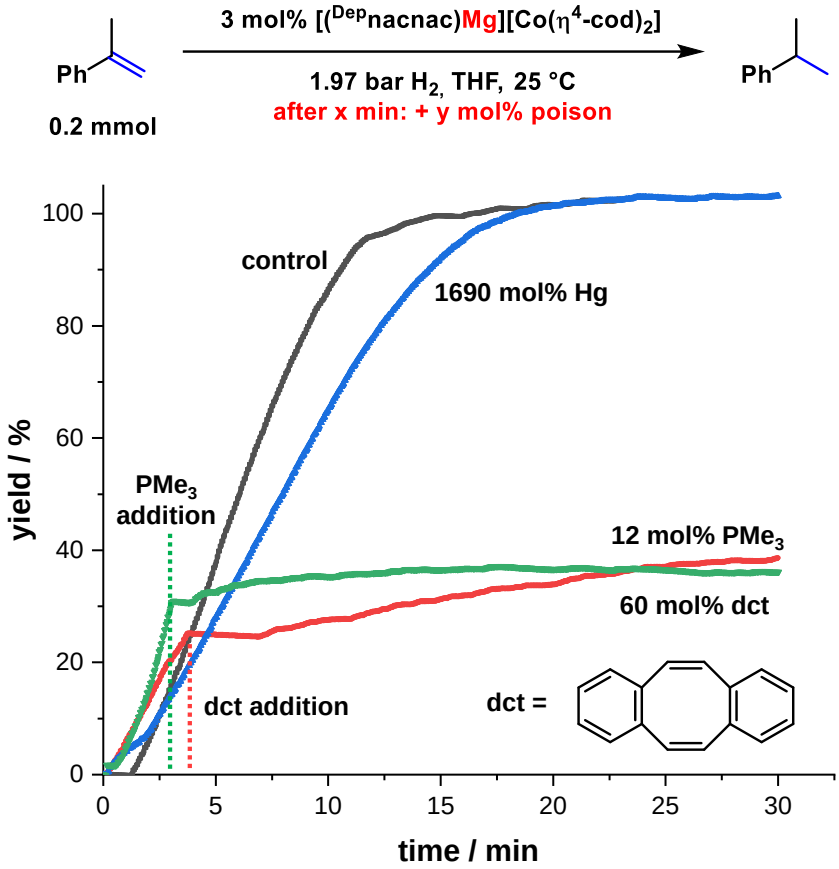

Figure 3. Kinetic poisoning studies with PMe_3, dct and Hg using pre-catalyst **4**.

Further investigation was conducted using protocol B (12 bar H_2 and 40 °C) to examine the potential formation of Co nanoparticles under these conditions. The presence of excess Hg had no impact on the hydrogenation of α,ß-unsaturated esters, but varying outcomes were recorded for 1,1,2-triphenylethylene (yielding 55-94% of 1,1,2-triphenylethane; see Table S4). In this context, it is worth mentioning that an excess of Hg caused complete poisoning of an *in situ* generated Co nanoparticle catalyst under the same conditions (Table S4).[25] In

conclusion, a homotopic hydrogenation mechanism is consistent with these poisoning experiments for **4**. However, assessing catalyst topicity is intricate for anionic metalates, and the partial inhibition of the 1,1,2-triphenylethylene hydrogenation using protocol B suggests that cobalt particles may contribute to some extent at elevated temperature and pressure.

2.2.4 Modeling Alkene Coordination

To model substrate coordination to the cobalt center, the bis(η^2-styrene)cobaltate salt [(^{Dep}nacnac)Mg][Co(η^4-cod) (η^2-styrene)$_2$](thf)$_{3.5}$ (**7**) was prepared in 43% yield by reaction of **4** with 4.0 equiv. of styrene in THF (Scheme 2, top). SC-XRD analysis of crystals obtained from THF/*n*-hexane revealed a solvent-separated ion pair (Mg1–Co1 7.509(2) Å), in which the [(^{Dep}nacnac)Mg]$^+$ cation is coordinatively saturated with three THF molecules. The [(Co(η^4-cod)(η^2-styrene)$_2$]$^-$ anion is bound in a distorted tetrahedral fashion to one η^4-1,5-cyclooctadiene and two η^2-styrene ligands (Scheme 2, bottom).

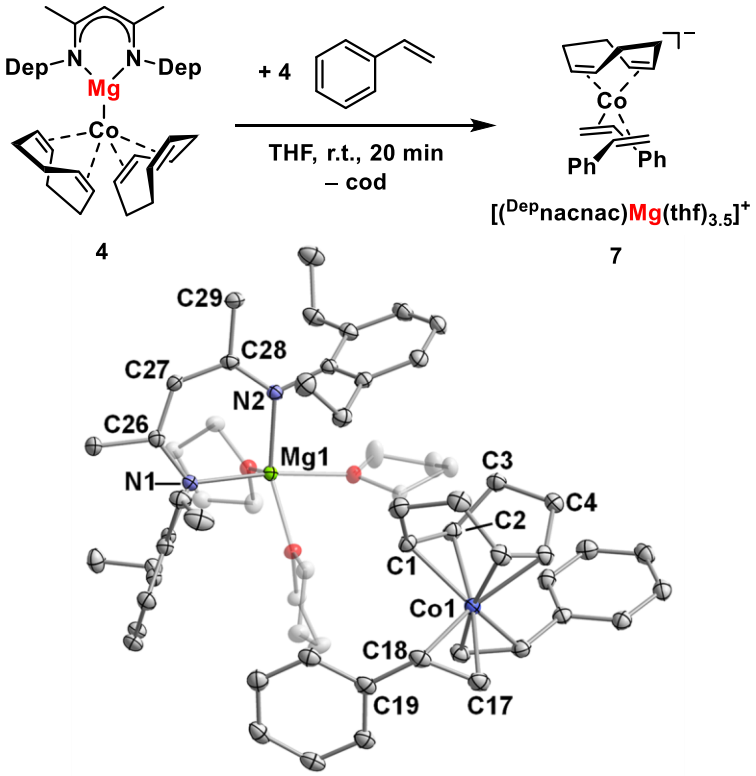

Scheme 2. Top: Synthesis of [(^{Dep}nacnac)Mg][Co(η^4-cod)(η^2-styrene)$_2$](thf)$_{3.5}$ (**7**). Bottom: Solid state molecular structure of **7**. Thermal ellipsoids are drawn at 40% probability level. H atoms and non-coordinated solvent molecules are omitted for clarity.

Catalytic tests on the hydrogenation of selected alkenes using **7** (Table 2, toluene solvent) demonstrated comparable activity with respect to pre-catalyst **4** for α-methylstyrene (Table 2, Entry 1) and naphthalene (Table 2, Entry 4), while complex **7** was superior for 1,1,2,2-tetramethylethylene (Table 2, Entry 5; **4**: 78% vs. **7**: 98% yield). Thus, complex **7** presumably represents a substrate stabilized form of the active catalytic species.

Table 2. Hydrogenation of alkenes with olefin cobaltates **4** and **7**.[a]

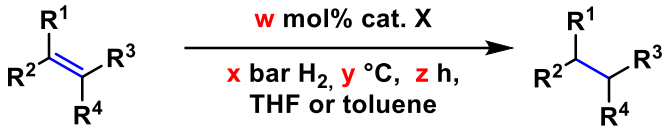

Entry	Alkene	Conditions	Yield [%] Cat. **4**	Cat. **7**
1	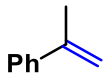	3 mol% cat., 2 bar H_2, 30 °C, 3 h	>99	>99
2	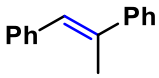		>99	>99
3	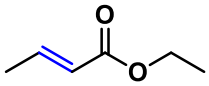		90	93
4	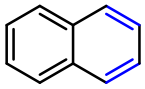	5 mol% cat., 12 bar H_2, 40 °C, 22 h	>99	>99
5[b]	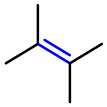		78	98

[a] Standard conditions: 0.2 mmol substrate (0.4 mol/L). Solvent = THF for pre-catalyst **4** and solvent = toluene for pre-catalyst **7**. Yields and conversions were determined by quantitative GC-FID analysis vs. internal *n*-pentadecane. [b] Only product calibrated due to solvent overlap of starting material in GC-FID.

2.2.5 Counterion Influence on Hydrogen Uptake

To gain further insight on the influence of the countercation on the reaction rate, we monitored the H_2 uptake for the α-methylstyrene hydrogenation reaction catalyzed by complexes **1** – **4** (3 mol% pre-catalyst, 2 bar H_2, 25 °C; Figure 4). The results show that the (^{Dep}nacnac)Mg^+ salt **4** enabled the quantitative hydrogenation of the alkene after 15 min (Figure 4a), while the Li^+ salt **3** gave ≈90% after 30 min (Figure 4b). In contrast, the hydrogenation with K^+ salt **1** and Na^+ salt **2** gave only 16% and 32% yield, respectively, over a significantly longer time period (2 h) (Figure 4c,d). These observations are consistent with the reactivity trend observed for various other substrates (Table 1, see above). Furthermore, significant catalyst deactivation occurred for **1** – **3** between 10 and 20 min after the reaction onset, while the initial rate of hydrogenation also appeared to be lower with **1** and **2** than with **3** and **4**. These results illustrate the notable influence of the countercation on the catalytic activity. Since the hydrogenation of the cod ligand in the complexes might be a crucial factor contributing to their catalytic activity, the H_2 uptake of the complexes themselves was also monitored (2 bar H_2, 25 °C, 1 h; Table 3 and the Supporting Information for further details) by quantifying the formation of cyclooctene and cyclooctane (which emerge from the uptake of one and two equiv. of H_2, respectively) by GC-FID. The results show increasing H_2 incorporation by the cobaltate salts in the order **1** < **2** < **3** ≈ **4** (**1**: 12%, **2**: 24%, **3**: 45% **4**: 38%; Table 3, entries 1-4).

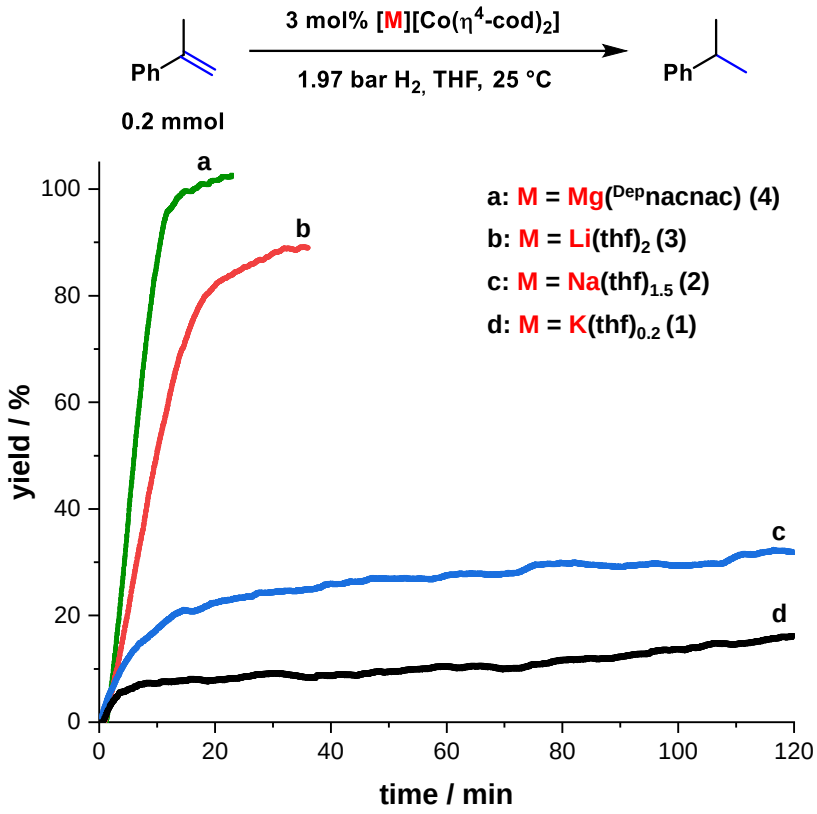

Figure 4. Reaction profile analysis of the hydrogenation of α-methylstyrene with pre-catalysts **1** – **4**.

In contrast, the hydrogenation of tetrabutylammonium cobaltate **5** gave only 1% H_2 incorporation (Table 3, entry 5), which indicates the need of an alkali metal or alkaline earth metal counterion for substantial hydrogenation activity.

Table 3. Hydrogenation of olefin cobaltates **1** – **5**.[a]

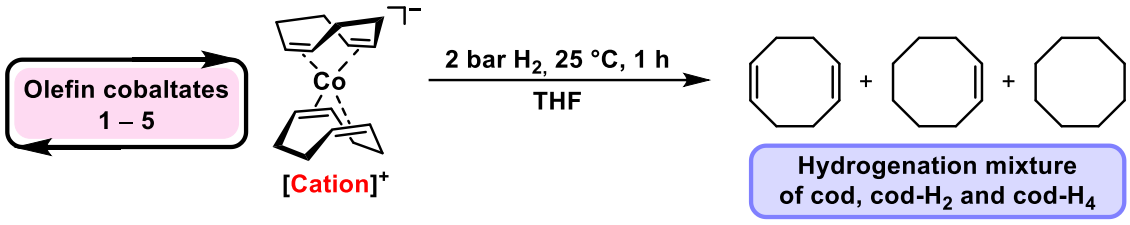

Pre-Catalyst ([Cation][Co(η⁴-cod)₂])		cod	cod-H_2	cod-H_4	H_2 Incorp.
$[K(thf)_{0.2}]^+$	(**1**)	59	5	10	**12**
$[Na(thf)_{1.5}]^+$	(**2**)	58	8	21	**24**
$[Li(thf)_2]^+$	(**3**)	33	10	41	**45**
$[(^{Dep}nacnac)Mg]^+$	(**4**)	32	13	31	**38**
$[N(^nBu)_4]^+$	(**5**)	88	1	0	**1**

[a] Standard conditions: 0.025 mmol pre-catalyst (0.05 mol/L THF). Substance ratios [%] and H_2 incorporation [%] were determined by quantitative GC-FID analysis vs. internal *n*-pentadecane as share of the overall hydrogenation mixture quantity. cod = 1,5-cyclooctadiene. cod-H_2 = cyclooctene. cod-H_4 = cyclooctane.

Remarkably, the heteroleptic complex **7** was fully hydrogenated when placed under an atmosphere of H_2 (Figure S4), which is in line with its superior catalytic activity (see above) and suggests that the monodentate styrene ligand enables pre-catalyst hydrogenation under very mild conditions.

2.2.6 Computational Studies

To further understand the effect of the counterion, we performed a combined MM (molecular mechanics) MD simulation and DFT investigation to model the reaction mechanism and the interaction between the catalytically active anion and the cations. To begin, the whole reaction profile for the hydrogenation of styrene starting from anionic $[Co(\eta^4\text{-cod})(\eta^2\text{-styrene})_2]^-$ ($\mathbf{7_A}$) was calculated at DFT level (r^{2}SCAN-3c, CPCM[THF]) on the singlet surface and in the absence of any counterion (Scheme 3). Dissociation of one styrene molecule forms the 16 valence electron complex $[Co(\eta^4\text{-cod})(\eta^2\text{-styrene})]^-$ ($\mathbf{8_A}$), which adds H_2 via oxidative addition ($\mathbf{9_A} \rightarrow [\mathbf{10_A}]^{\ddagger} \rightarrow \mathbf{11_A}$). Subsequent migratory insertion of the styrene double bond into the Co–H bond of dihydride complex $[Co(\eta^4\text{-cod})(\eta^2\text{-styrene})H_2]^-$ ($\mathbf{11_A} \rightarrow [\mathbf{12_A}]^{\ddagger} \rightarrow \mathbf{13_A}$) is found to be the turnover-limiting step (TLS) with an activation barrier of 19.0 kcal/mol and a total energy barrier of 31.2 kcal/mol. The corresponding transition state structure is highly asynchronous with Pauling bond orders[26] BO = 0.95 for the Co–C_2 bond and BO = 0.54 for the C_1–H^a bond (see the structure of $[\mathbf{12_A}]^{\ddagger}$ in Scheme 3). Coordination of another styrene molecule precedes the reductive elimination of ethylbenzene from $[Co(\eta^4\text{-cod})(\eta^2\text{-styrene})(H)(CH_2CH_2Ph)]^-$ ($\mathbf{14_A} \rightarrow [\mathbf{15_A}]^{\ddagger} \rightarrow \mathbf{8_A}$), which drives the reaction downhill in energy ($\Delta G = -9.9$ kcal/mol).

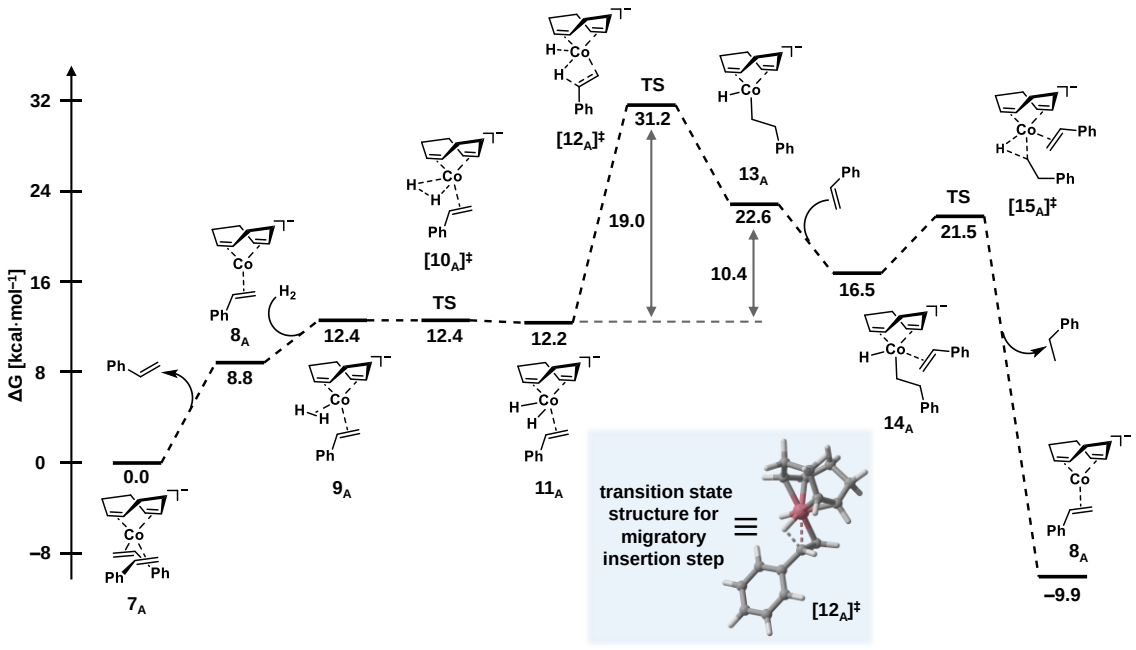

Scheme 3. Calculated reaction profile for the hydrogenation of styrene by anionic complex $[Co(\eta^4\text{-cod})(\eta^2\text{-styrene})_2]^-$ ($\mathbf{7_A}$, level of theory: r^{2}SCAN-3c, CPCM[THF]).

While this initial analysis established the elementary steps of the hydrogenation reaction, the anion-only model was not able to provide a reasonable total energy barrier (31.2 kcal/mol) for the hydrogenation of styrene at the experimental temperature of 298 K.[26] Thus, we decided to investigate the influence of a metal-based counterion (M^+ = K^+, Na^+, Li^+ or [^{Dep}nacnac]Mg^+) on structures $\mathbf{11_A}$ – $\mathbf{13_A}$ in the turnover-limiting migratory insertion step. To adequately model the dynamic behavior of the solvated ion pairs $[M(thf)_n][Co(\eta^4\text{-cod})(\eta^2\text{-styrene})H_2]$ (denoted as: $\mathbf{11_K}$, $\mathbf{11_{Na}}$, $\mathbf{11_{Li}}$ and $\mathbf{11_{Mg}}$), force field based MD simulations were performed (see section 2.4.8.1). After initial force field parametrization, the time-dependent structural behavior of the system in a bulk of THF molecules ($n_{THF} \geq 500$) was studied and the most-populated ion pair structures were identified. According to the MD simulations, complexes $\mathbf{11_K}$ to $\mathbf{11_{Mg}}$ exhibit short distances between the metal cation and the cobalt anion indicating tight ion pairing.

To further characterize the counterion interactions in the migratory insertion step, the obtained geometries were then re-optimized at DFT level (r^{2}SCAN-3c) with explicit solvation in the first coordination sphere of the metal cation to capture solvent screening effects on the ion pair structures and energies. Intimate ion pairs were observed for complexes $\mathbf{11_{K\text{-}Mg}}$, transition state structures $[\mathbf{12_{K\text{-}Mg}}]^‡$ and insertion products $\mathbf{13_{K\text{-}Mg}}$.

Figure 5 displays the transition state geometries for the migratory insertion step for the pure anion $[\mathbf{12_A}]^‡$ and the two potassium and magnesium cobaltate salts $[K(thf)_5][Co(\eta^4\text{-cod})(\eta^2\text{-styrene})H_2]$ ($[\mathbf{12_K}]^‡$) and [(^{Dep}nacnac)Mg(thf)]-$[Co(\eta^4\text{-cod})(\eta^2\text{-styrene})H_2]$ ($[\mathbf{12_{Mg}}]^‡$). The ion pairs $[\mathbf{12_K}]^‡$ and $[\mathbf{12_{Mg}}]^‡$ represent the two reactivity extremes for the alkali and alkaline earth metal cobaltate salts used in the hydrogenation reaction (see above). Direct cation hydride interactions are present in both transition states $[\mathbf{12_K}]^‡$ and $[\mathbf{12_{Mg}}]^‡$ (and also in $[\mathbf{12_{Na/Li}}]^‡$), while no cation styrene interaction can be observed (see Figure S36 for the other ion pair structures). An analysis of the NPA charges for the pure anion $[\mathbf{12_A}]^‡$ reveals a weak polarization of the two Co–H bonds with H^a exhibiting a slightly protic character whereas H^b is weakly hydridic (Figure 5, A and B; and Table 4, Entry A.5).

This polarization difference of the Co–H^a/Co–H^b bond quantified by Δδ is already present in the intermediate structure $\mathbf{11_A}$ (Table 4, Entry A.4: 0.07) and is only slightly increased (to 0.14) in $[\mathbf{12_A}]^‡$. In contrast, a stark increase Δδ is observed when a counterion is introduced in $[\mathbf{12_{K\text{-}Mg}}]^‡$ (e.g., for Mg: Table 4,Entry E.4: 0.16 vs. E.5: 0.64). This can also be seen in the transition state geometries of $[\mathbf{12_K}]^‡$ and $[\mathbf{12_{Mg}}]^‡$, where H^b is directly oriented toward the metal cation thereby inducing a pronounced negative polarization in the Co–H^b bond (Figure 5, C and D). The polarization difference Δδ in the transition state structures $[\mathbf{12_{K\text{-}Mg}}]^‡$ was most pronounced for the magnesium salt $[\mathbf{12_{Mg}}]^‡$ (Table 4, Entry A.5-E.5). This polarization may facilitate the migratory insertion of the alkene molecule. In addition, a distinct coordination geometry for $[\mathbf{12_{Mg}}]^‡$ in comparison to $[\mathbf{12_{K\text{-}Li}}]^‡$ was observed.

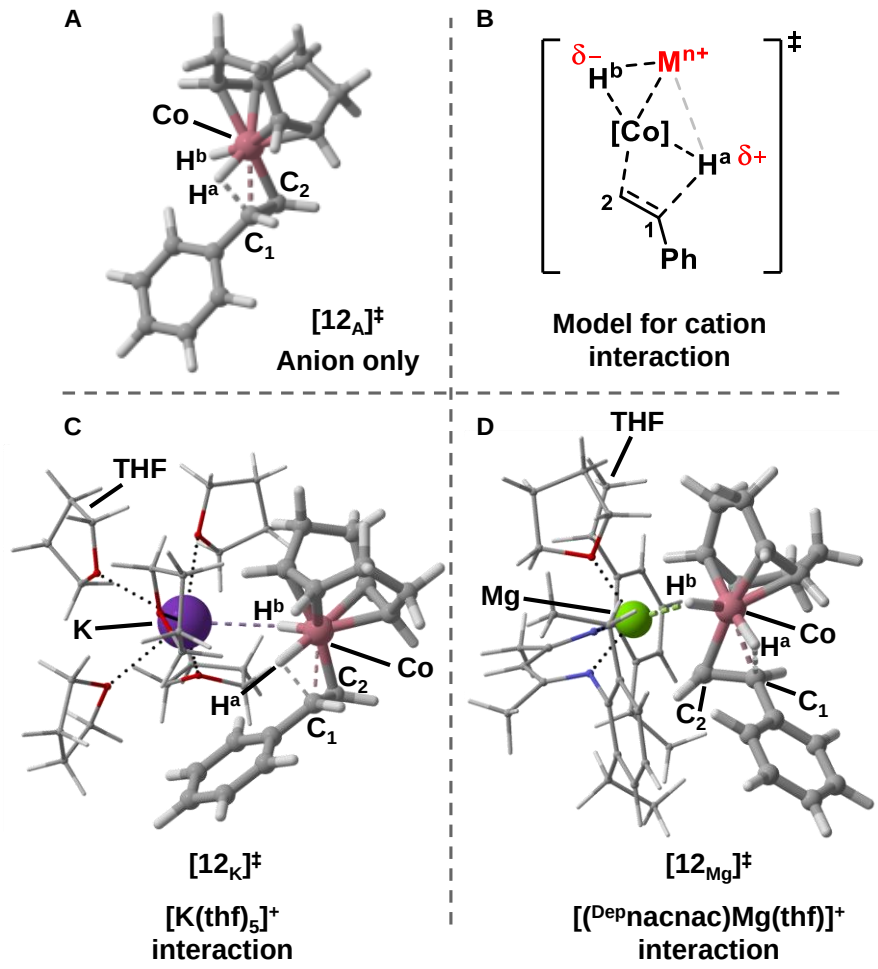

Figure 5. Transition state geometries of the turnover-limiting migratory insertion step. A: Anion only structure [**12**$_A$]‡ B: Model for cation interaction. C: [K(thf)$_5$][Co(η^4-cod)(η^2-styrene)H$_2$] structure ([**12**$_K$]‡). D: [(^{Dep}nacnac)Mg(thf)][Co(η^4-cod)(η^2-styrene)H$_2$] structure ([**12**$_{Mg}$]‡).

While the alkali metal cobaltate salts exhibit a more central positioning of the cation between the two Co–H bonds (Figure 5C for [**12**$_K$]‡), in [**12**$_{Mg}$]‡ only the more hydridic H^b is in direct proximity to the magnesium cation (Figure 5D). Moreover, the benzyl unit of the styrene molecule is rotated outwards away from magnesium, while the benzyl group is oriented toward the alkali metal cation (Figure 5, C vs. D). Furthermore, a stepwise decrease in transition state energy (and thus total energy barrier) for the migratory insertion step corroborated the beneficial effect of the counterion (Table 4, A.1-E.1). A sequential decrease of the transition state energy in the order [**12**$_A$]‡ > [**12**$_K$]‡ = [**12**$_{Na}$]‡ > [**12**$_{Li}$]‡ = [**12**$_{Mg}$]‡ is observed, which is in qualitative agreement with the observed reactivity trend of complexes **1** – **4**.

In order to further examine the [Co–H^b]···M$^+$ interaction, we conducted non-covalent interaction (NCI) analyses on the transition state structures [**12**$_{K\text{-}Mg}$]‡ (Figure 6). The calculations were performed on the fully optimized geometries (r^{2}SCAN-3c) and the electron densities calculated at ωB97M-V/def2-QZVP level of theory (see section 2.4.8.2 for all NCI analyses). In all four transition state structures, an attractive interaction between Co–H^b and the cation is observed.

Table 4. Key parameters for the reactivity differences for the migratory insertion step based on ground state structures $\mathbf{11_A}$ / $\mathbf{11_{K\text{-}Mg}}$ and transition state structures [$\mathbf{12_A}$]‡ / [$\mathbf{12_{K\text{-}Mg}}$]‡.

Entry		A	B	C	D	E
	$\mathbf{M^{n+}}$	**none**	$\mathbf{K^+}$	$\mathbf{Na^+}$	$\mathbf{Li^+}$	$\mathbf{Mg^{2+}}$
1	**$\Delta G^‡$ ([12]‡) [kcal/mol]**	19.0[a]	17.0	17.0	15.5	15.5
2	**BO ($Co–C_2$)[b]**	0.95	0.95	0.95	0.97	0.90
3	**BO ($C_1–H^a$)[b]**	0.54	0.60	0.61	0.61	0.55
4	**$\Delta\delta$ (11)[c]**	0.07	0.14	0.13	0.16	0.16
5	**$\Delta\delta$ ([12]‡)[c]**	0.14	0.58	0.55	0.55	0.64
6	**r ($M^{n+}–H^b$; [12]‡) [Å]**	/	2.58	2.15	1.81	1.96

[a] Gibbs free energy derived from anion-only reaction profile calculation (Scheme 3). [b] Pauling bond orders using c = 0.6 for TS structures.[26] [c] Polarization difference of $Co–H^a$/$Co–H^b$ bonds expressed by the differences of the natural population analysis (NPA) charges at H^a and H^b.

For [$\mathbf{12_K}$]‡, this interaction is indicated by the green isosurface between H^b and the potassium cation (Figure 6a) and by the green region in the two-dimensional NCI plot ($\text{sign}(\lambda_2)\rho < 0$; Figure 6b). Along the series of alkali metal cations, the attractive metal-hydride interaction becomes stronger following the trend: $K^+ < Na^+ < Li^+$ (Figure 6c for [$\mathbf{12_{Na}}$]‡, and Figure 6d for [$\mathbf{12_{Li}}$]‡). For lithium, a fairly strong interaction can be observed which is indicated by the additional blue color in the NCI isosurface and NCI plot cutout ($\text{sign}(\lambda_2)\rho \approx -0.3$; Figure 6d). The most pronounced attractive interaction was found between $Co–H^b$ and the magnesium cation in [$\mathbf{12_{Mg}}$]‡ reaching into the range of strong non-covalent interactions ($\text{sign}(\lambda_2)\rho \approx -0.5$; Figure 6e), thereby surpassing the hydride interaction with the alkali metal cations of [$\mathbf{12_{K\text{-}Li}}$]‡.

Overall, NCI analysis established an increasing attractive cation-hydride interaction following the trend: $K^+ < Na^+ < Li^+ < Mg^{2+}$. This trend is in agreement with the stronger bond polarization ($Co–H^a$ vs. $Co–H^b$) found for the magnesium cobaltate salt, its reduced transition state energy for the turnover-limiting migratory insertion step and its distinct coordination geometry.

For completeness, the reductive elimination of styrene (**14** → [**15**]‡) was analyzed in the same manner for the Na^+ and (^{Dep}nacnac)Mg^+ salts (see Figure S37 for details). This is the second elementary step to finalize the reduction of the styrene double bond. Even though this step is not turnover-limiting a distinct counterion effect on the transition state energy was observed for the more Lewis-acidic Mg^{2+}, while the sodium salt exhibited a near-identical reaction barrier ([$\mathbf{15_{Na}}$]‡) to the anion-only model.

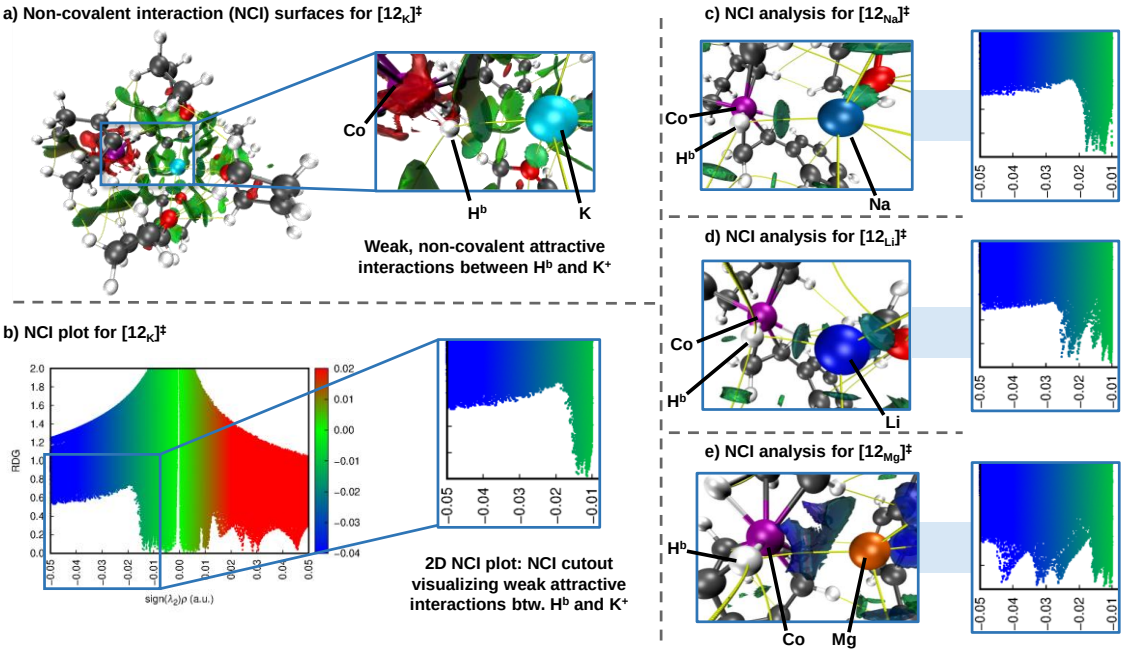

Figure 6. NCI plots (2D) and surface visualization (3D) of [$\mathbf{12_{K\text{-}Mg}}$]‡. Diagrams show plots of RDG := reduced density gradient over sign(λ_2)ρ := density with sign of the second derivative Hessian matrix. The sign(λ_2)ρ > 0 (red) are read as strong repulsive interactions, sign(λ_2)ρ ≈ 0 (green) as weak interactions and sign(λ_2)ρ < 0 (blue) as strong attractive interactions.

NCI analysis of [$\mathbf{15_{Mg}}$]‡ identified an interaction between the magnesium cation and the η^2-bound styrene molecule, which likely accounts for the reduction in transition state energy. The accumulated computational data corroborates the heightened activity for magnesium cobaltate **4** (and $\mathbf{11_{Mg}}$) in the hydrogenation reactions which we observe experimentally.

2.3 Conclusion

This work shows that countercations have a remarkable effect on alkene hydrogenation reactions catalyzed by anionic cobalt complexes. The investigation of the series of [Cat][Co(η^4-cod)$_2$] complexes (Cat = K (**1**), Na (**2**), Li (**3**), (^{Dep}nacnac)Mg (**4**), N(^{n}Bu)$_4$ (**5**)) revealed that the lithium and magnesium salts are much more powerful catalysts for the hydrogenation of challenging, highly-substituted alkene substrates than the potassium and sodium salts. The presence of the non-coordinating tetrabutylammonium cation results in a sharp decrease in hydrogenation activity. [(^{Dep}nacnac)Mg][Co(η^4-cod)$_2$] (**4**) showed the highest activity and to our knowledge is among the most active first-row transition metal catalysts for the hydrogenation of tri- and tetra-substituted alkenes.[5b,f,h,i],[7] In line with these catalytic investigations, reaction progress analyses and pre-catalyst hydrogenation experiments revealed differing reaction rates for the cobaltate salts **1** to **5**. The homotopic nature of the reaction mechanism was supported by poisoning studies.

A combined MD and DFT study suggests the coordination of the countercation to the hydride in the turnover limiting migratory insertion step and demonstrates a beneficial, energy-lowering effect in comparison with the anion-only model system. The lowest energy

barriers were calculated for M = Li (**3**) and M = (^{Dep}nacnac)Mg (**4**). The NCI analyses of the migratory insertion transition state for complexes **1** to **4** illustrate the increasingly attractive interactions of the metal cations with one of the hydrido ligands following the trend: K^+ (**1**) < Na^+ (**2**) < Li^+ (**3**) < (^{Dep}nacnac)Mg^+ (**4**), resulting in stronger Co–H bond polarization.

The results of this study show that counterion coordination can strongly modulate reactivity in hydrogenation reactions and probably other catalytic reactions involving hydride intermediates. Furthermore, the nacnac ligand in **4** should enable the design of new structural motifs, such as asymmetric modifications. Investigations in these directions are ongoing.

2.4 Supporting Information

2.4.1 General Information

All reactions and product manipulations were carried out in flame-dried glassware under an inert atmosphere of argon/nitrogen using standard Schlenk-line or glovebox techniques (maintained at <0.1 ppm H_2O and <0.1 ppm O_2). $[K(thf)_{0.2}][Co(\eta^4\text{-cod})_2]$ (**1**),[16a] $[Li(thf)_2][Co(\eta^4\text{-cod})_2]$ (**3**),[16b] (^{Dep}nacnac)MgI·OEt_2[28] and [(^{Dep}nacnac)Mg][$Co(\eta^4\text{-cod})_2$] (**4**)[17] were prepared according to procedures previously reported in the chemical literature.

Solvents were dried and degassed with an *MBraun SPS800* solvent purification system. All dry solvents were stored under argon over activated 3 Å molecular sieves in gas-tight ampules. Commercially available olefins were purified by distillation (Kugelrohr) and in case of liquids degassed and dried over molecular sieves (3 Å).

NMR spectra were recorded on Bruker Avance 300 or 400 spectrometers at 298 K unless otherwise noted and internally referenced to residual solvent resonances (^{1}H NMR: THF-d_8: 1.72 ppm, C_6D_6: 7.16 ppm $CDCl_3$: 7.26 ppm, $^{13}C\{^1H\}$ NMR: THF-d_8: 25.3 ppm, C_6D_6: 128.0 ppm, $CDCl_3$: 77.2 ppm). Chemical shifts δ are given in ppm referring to external standards of tetramethylsilane (^{1}H, $^{13}C\{^1H\}$ spectra), 85% phosphorus acid (^{31}P and $^{31}P\{^1H\}$ spectra) and 1.0 M LiCl in D_2O ($^7Li\{^1H\}$ spectra). ^{1}H and ^{13}C NMR signals were assigned based on 2D NMR spectra (^{1}H, ^{1}H-COSY, ^{1}H,^{13}C-HSQC, ^{1}H,^{13}C-HMQC).

Thin layer chromatography (TLC) was performed using aluminium plates with silica gel and fluorescent indicator (*Macherey-Nagel*, 60, UV254). TLC plates were visualized by exposure to UV light (366 or 254 nm). Flash column chromatography was conducted with silica gel 60 from Sigma Aldrich (63 – 200 μm).

Hydrogenation reactions were carried out in a 300 mL high pressure reactor (*Parr*™) in 4 mL glass vials or in a *Man on the Moon* X204 gas uptake system.[29] The reaction vessels were loaded under argon, purged with hydrogen, sealed and the internal pressure was adjusted. Hydrogen (99.9992%) was purchased from *Linde*.

Yields of the catalytic and kinetic studies were determined using gas chromatography with FID detector (GC-FID) by *Shimadzu GC2025*. H_2 was used as carrier gas. A *Restek Rxi*® (30 m x 0.25 mm x 0.25 μm) column was used. The standard heating procedure was: 50 °C (2 min), 25 °C/min → 280 °C (5min). Calibration with internal standard *n*-pentadecane and analytically pure samples. Non-commercial calibration samples were prepared by hydrogenation with Pd/C (10% Pd basis). Gas chromatography with mass-selective detector (GC-MS) was conducted with an *Agilent 7820A GC* system with *mass detector 5977B*. H_2 as carrier gas and a *HP-5MS* (30 m x 0.25 mm x 0.25 μm) column were used. The standard heating procedure was: 50 °C → 300 °C.

2.4.2 Synthesis of Compounds

[Na(thf)$_{1.5}$][Co(η^4-cod)$_2$] (2):

[Li(thf)$_{1.5}$][Co(η^4-cod)$_2$] (**3**) (0.85 g, 2.0 mmol, 1.0 equiv.) and NaO^{t}Bu (0.19 g, 2.0 mmol, 1.0 equiv.) were suspended in *n*-hexane at −78 °C. Upon warming to ambient temperature, the suspension was left to stir for 3 days at this temperature. The brown supernatant was filtered off and the residual yellow greenish solid was washed with *n*-hexane (1 x 20 mL, 2 x 10 mL) and dried under reduced pressure. The resulting pale-yellowish solid was dissolved in a minimal amount of THF (6.0 mL), filtered and layered with *n*-hexane (12.0 mL). Storage at −30 °C for 3 days afforded [Na(thf)$_{1.5}$][Co(η^4-cod)$_2$] (**2**) as a pale-yellow powder after washing with *n*-hexane (3 x 2.0 mL) and drying under reduced pressure. The resulting powder was once more crystallized from THF/*n*-hexane (1:2) at −30 °C to obtain **2** in analytical purity. The THF content was determined by ^{1}H NMR analysis.

Crystals suitable for X-ray crystallography were grown from a THF/*n*-hexane (1:2) solution at −30 °C overnight.

[Na(thf)$_{1.5}$]$^+$

$C_{16}H_{24}CoNa\cdot(C_4H_8O)_{1.5}$, MW = 406.50 g/mol

Yield: 274 mg, 34%

^{1}H NMR (400.13 MHz, 298 K, THF-d$_8$) δ = 3.66-3.59 (m, 6H, $(CH_2)_2(CH_2)_2O$–THF), 2.26-2.07 (m, 16H, C_8H_{12}–COD), 1.92-1.81 (m, 8H, C_8H_{12}–COD), 1.81-1.75 (m, 6H, $(CH_2)_2(CH_2)_2O$–THF) ppm.

^{13}C{^{1}H} NMR (100.61 MHz, 298 K, THF-d$_8$) δ = 69.6 (s, C_8H_{12}–COD), 68.2 (s, $(CH_2)_2(CH_2)_2O$–THF), 34.7 (s, C_8H_{12}–COD), 26.4 (s, $(CH_2)_2(CH_2)_2O$–THF) ppm.

^{7}Li{^{1}H} NMR (155.46 MHz, 298 K, THF-d$_8$): no resonance was observed in the range from −20 to +20 ppm.

Elemental Analysis calcd. C 65.00, H 8.94; found C 65.28, H 8.83

[N(^{n}Bu)$_4$][Co(η^4-cod)$_2$] (5):

A solution of [K(thf)$_{0.4}$][Co(η^4-cod)$_2$] (**1**) (0.55 g, 1.6 mmol, 1.0 equiv.) in THF (5.0 mL) was added to a suspension of N(^{n}Bu)$_4$Cl (0.45 g, 1.6 mmol, 1.0 equiv.) in toluene (10.0 mL) at −30 °C. The reaction mixture was stirred for 1.5 d while slowly reaching ambient temperature. THF was removed from the resulting yellowish-brown suspension under

reduced pressure, the remaining toluene suspension was filtered, and the clear yellowish-brown filtrate evaporated to dryness. The brownish residue was recrystallized from THF/Et_2O (2.0/4.0 mL) at −30 °C to obtain $[N(^nBu)_4][Co(\eta^4\text{-cod})_2]$ (**5**) as yellow needles. The supernatant was decanted, the crystalline solid was washed with Et_2O and dried under reduced pressure.

Crystals suitable for X-ray crystallography were grown from a THF/*n*-hexane solution (1:1) at ambient temperature after two days.

$[N(^nBu)_4]^+$

$C_{32}H_{60}CoN$, MW = 517.77 g/mol

Yield: 234 mg, 0.45 mmol, 28%

^{1}H NMR (400.13 MHz, 298 K, thf-d_8) δ = 3.27 (m, 8H, $N(CH_2CH_2CH_2CH_3)_4$), 2.31-2.07 (m, 16H, C_8H_{12}–COD), 1.96-1.81 (m, 8H, C_8H_{12}–COD), 1.77-1.62 (m, 8H, $N(CH_2CH_2CH_2CH_3)_4$) overlay with residual signal of non-deuterated thf, 1.43 (sext, 8H, $^3J_{HH}$ = 7.2 Hz, $N(CH_2CH_2CH_2CH_3)_4$), 1.02 (t, 12H, $^3J_{HH}$ = 7.2 Hz, $N(CH_2CH_2CH_2CH_3)_4$).

^{13}C{^{1}H} NMR (100.61 MHz, 298 K, thf-d_8) δ = 69.9 (bs, olefinic-C_8H_{12}–COD), 59.5 (s, $N(CH_2CH_2CH_2CH_3)_4$), 34.9 (s, aliphatic-C_8H_{12}–COD), 24.8 (s, $N(CH_2CH_2CH_2CH_3)_4$), 20.8 (s, $N(CH_2CH_2CH_2CH_3)_4$), 14.2 (s, $N(CH_2CH_2CH_2CH_3)_4$).

Elemental Analysis calcd. C 74.23, H 11.68, N 2.71; found C 73.94, H 11.85, N 2.85.

$[(^{Dep}nacnac)Mg][Co(\eta^4\text{-dct})_2](thf)_{1.7}$ (6):

To a stirred solution of $[(^{Dep}nacnac)Mg][Co(\eta^4\text{-cod})_2]$ (**4**) (263 mg, 0.4 mmol, 1.0 equiv.) in THF (2.0 mL) was added a solution of dibenzo[*a*,*e*]cyclooctene (162 mg, 0.8 mmol, 2.0 equiv.) in THF (1.0 mL) over 2 minutes at −30 °C. A color change from yellow-brown to orange-brown was observed. The mixture was allowed to reach ambient temperature and stirred overnight. The solvent was removed under reduced pressure, the residue washed with *n*-hexane (2 x 1.0 mL), dried and dissolved in THF (2.5 mL). The THF solution was filtered, concentrated to approx. 2.0 mL and layered with *n*-hexane (6.0 mL). Storage at ambient temperature overnight afforded $[(^{Dep}nacnac)Mg][Co(\eta^4\text{-dct})_2](thf)_{1.7}$ (**6**) as an orange solid after washing with *n*-hexane (1 x 2.0 mL) and drying under reduced pressure. The resulting solid was again crystallized from THF/*n*-hexane (1:2) at ambient temperature to obtain **6** in analytical purity. The THF content was determined by ^{1}H NMR analysis.

Crystals suitable for X-ray crystallography were grown from a THF/*n*-hexane solution (1:2) at ambient temperature overnight.

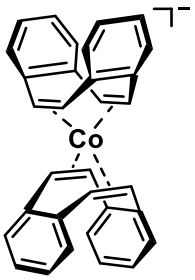

[(^{Dep}nacnac)Mg(thf)$_{1.7}$]$^+$

$C_{57}H_{57}CoMgN_2 \cdot (C_4H_8O)_{1.7}$, MW = 976.00 g/mol

Yield: 254 mg, 65%

^{1}H NMR (400.13 MHz, 298 K, THF-d_8) δ = 7.23-7.12 (m, 6H, C*H*$_{aromatic}$-Dep), 6.55-6.48 (m, 8H, C*H*$_{aromatic}$-dct), 6.45-6.38 (m, 8H, C*H*$_{aromatic}$-dct), 5.11 (s, 1H, $CH_3C(N)CH$=), 3.65-3.59 (m, 6.8H, $(CH_2)_2(CH_2)_2$O-THF), 3.39 (s, 8H, C*H*$_{olefinic}$-dct), 2.25 (m, 8H, CH_2CH_3-Dep), 1.80-1.75 (m, 6.8H, $(CH_2)_2(CH_2)_2$O-THF), 1.66 (s, 6H, $CH_3C(N)$), 1.29 (t, 12H, $^3J_{HH}$ = 7.6 Hz, CH_2CH_3-Dep) ppm.
^{13}C{^{1}H} NMR (100.61 MHz, 298 K, THF-d_8) δ = 170.4 (s, $CH_3C(N)$), 152.9 (s, *C*$_{aromatic}$-dct), 149.3 (s, *C*$_{aromatic}$-Dep), 137.8 (s, *C*$_{aromatic}$-Dep), 126.6 (s, *C*$_{aromatic}$-Dep), 125.9 (s, *C*$_{aromatic}$-Dep), 124.9 (s, *C*$_{aromatic}$-dct), 122.8 (s, *C*$_{aromatic}$-dct), 96.9 (s, $CH_3C(N)CH$=), 81.7 (s, *C*H$_{olefinic}$-dct), 86.3 (s, $(CH_2)_2(CH_2)_2$O–THF), 26.4 (s, $(CH_2)_2(CH_2)_2$O–THF), 25.0 (s, CH_2CH_3-Dep), 24.5 (s, $CH_3C(N)$), 14.1 (s, CH_2CH_3-Dep) ppm.

Elemental Analysis calcd. C 78.51, H 7.31, N 2.87; found C 77.96, H 6.95, N 2.76.

[(^{Dep}nacnac)Mg][Co(η^4-cod)(η^2-styrene)$_2$](thf)$_{3.5}$ (7)

At ambient temperature, styrene (0.73 mL, 6.4 mmol, 4.0 equiv.) was added dropwise over 2 minutes to a stirring solution of [(^{Dep}nacnac)Mg][Co(η^4-cod)$_2$] (**4**) (1.05 g, 1.6 mmol, 1.0 equiv.) in THF (50 mL). Upon addition, the yellow brownish solution turned reddish orange. The mixture was left to stir for 15 minutes, after which the solution was concentrated to ½ of its initial volume, filtered and layered with *n*-hexane (50 mL). The mixture was stored at −30 °C overnight, the brownish supernatant decanted, and the product was dried *in vacuo* to afford [(^{Dep}nacnac)Mg][Co(η^4-cod)(η^2-styrene)$_2$](thf)$_{3.5}$ (**7**) as dark red needles. A second crop was obtained from the motherliquor stored at −30 °C overnight. The THF content was determined by ^{1}H NMR analysis.
Crystals suitable for X-ray crystallography were grown from a THF/*n*-hexane solution (1:2) at −30 °C after two days.

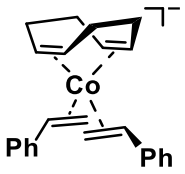

[(^{Dep}nacnac)Mg(thf)$_{3.5}$]$^+$

$C_{49}H_{61}CoMgN_2{\cdot}(C_4H_8O)_{3.5}$, MW = 1013.66 g/mol

Yield: 671 mg, 41%

^{1}H NMR (400.13 MHz, 298 K, C_6D_6) δ = 7.27-7.20 (d, 2H, $^2J_{HH}$ = 7.1 Hz, Ar*H*), 7.16-6.99 (m, 10H, Ar*H*), 6.70-6.44 (m, 3H, Ar*H* and Ph–C*H*-styrene, **styrene 1**), 5.62 (d, 1H, $^3J_{HH}$ = 17.6 Hz, *trans-H*-CH_2-styrene, **styrene 1**), 5.08 (d, 1H, $^3J_{HH}$ = 10.9 Hz, *cis-H*-CH_2-styrene, **styrene 1**) 5.04 (s, 1H, $CH_3C(N)CH$=), 3.57 (bs, 14H, $(CH_2)_2(CH_2)_2$O-THF), 3.45 (t, 1H, $^3J_{HH}$ = 7.2 Hz, Ph–*C*H-styrene, **styrene 2**), 2.94-2.78 (m, 4H, CH_2CH_3-Dep), 2.77-2.58 (m, 4H, CH_2CH_3-Dep), 2.40-2.15 (m, 3H, C_8H_{12}–COD), 1.72 (s, 6H, $CH_3C(N)$), 1.90-1.57 (m, C_8H_{12}–COD, overlapping signal), 1.42 (bs, 14H, $CH_2)_2(CH_2)_2$O-THF), 1.23 (t, 6H, $^3J_{HH}$ = 7.4 Hz, CH_2CH_3-Dep, 6H), 1.19-1.05 (m, 6H, CH_2CH_3-Dep), 0.94-0.90 (overlapping d and t, 2H, $^3J_{HH}$ = 7.4 Hz, CH_2-styrene, **styrene 2** and residual *n*-hexane), 0.80-0.30 (m, 3H, C_8H_{12}–COD), −1.92 (d, 1H, $^3J_{HH}$ = 6.2 Hz, CH_2-styrene, **styrene 2**) ppm; Overall H-atom signals account to 53 H-atoms (61 expected). Signals of C_8H_{12}-COD are in part not visible in the ^{1}H NMR spectrum due to line broadening. Signals of the aromatic H-atoms are not observed due to overlap with proton signals from partially deuterated benzene.
^{13}C{^{1}H} NMR (100.61 MHz, 298 K, C_6D_6) δ = 169.8 (s, $CH_3C(N)$), 147.0 (s, $C_{aromatic}$-Dep), 138.0 (s, Ph–*C*H-styrene, **styrene 1**), 137.6 (s, $C_{aromatic}$), 137.4 (s, $C_{aromatic}$), 128.8 (s, $C_{aromatic}$), 126.6 (s, $C_{aromatic}$), 126.4 (s, $C_{aromatic}$), 126.2 (s, $C_{aromatic}$), 125.4 (s, $C_{aromatic}$), 124.3 (s, $C_{aromatic}$), 113.7 (CH_2-styrene**, styrene 1**), 110.7 (s, $C_{aromatic}$), 95.4 (s, $CH_3C(N)$), 67.9 (s, Ph–*C*H-styrene, **styrene 2**), 67.8 (s, $(CH_2)_2(CH_2)_2$O-THF), 25.8 (s, $(CH_2)_2(CH_2)_2$O-THF), 24.9 (s, CH_2CH_3-Dep), 24.4 (s, CH_2CH_3-Dep), 14.6 (s, CH_2CH_3-Dep), 14.0 (s, CH_2CH_3-Dep), 6.7 (CH_2-styrene, **isomer 2**) ppm; Signals of C_8H_{12}-COD are not visible in the ^{13}C{^{1}H} NMR spectrum due to line broadening.

Elemental Analysis calcd. C 74.63, H 8.87, N 2.76; found C 74.71, H 8.57, N 2.86.

K(^{Dep}nacnac):

^{Dep}nacnacH (1.74 g, 4.8 mmol, 1.0 equiv.) and KHMDS (1.03 g, 5.2 mmol, 1.1 equiv.) were combined in a Schlenk flask, cooled to 0 °C and dissolved in Et_2O (20 mL; cooled to 0 °C) to give a clear yellow solution. The reaction mixture was stirred overnight while reaching ambient temperature. The yellow-brown solution was dried under reduced pressure and the residual off-white powder was washed with *n*-hexane (2 x 20 mL). After repeated drying *in vacuo*, the off-white powder was dissolved in a minimal amount of Et_2O (5 mL; pale yellow solution), filtered, *n*-hexane (15 mL) was added and the mixture placed at −30 °C for 7 d.

The supernatant was decanted from the microcrystalline precipitate, the residue washed with *n*-hexane (2 x 2 mL) and dried under reduced pressure to obtain K(^{Dep}nacnac) as a white solid.

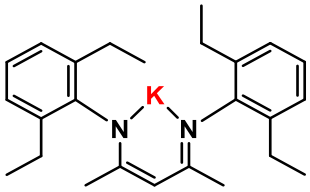

$C_{25}H_{33}KN_2$, MW = 400.65 g/mol

Yield: 830 mg, 43%

^{1}H NMR (400.13 MHz, 298 K, THF-d_8) δ = 6.90 (d, 4H, $^2J_{HH}$ = 7.4 Hz, *o*-C*H*$_{aromatic}$-Dep), 6.67 (t, 2H, $^2J_{HH}$ = 7.3 Hz, *p*-C*H*$_{aromatic}$-Dep), 4.42 (s, 1H, $CH_3C(N)CH$=), 2.53 (q, 8H, $^3J_{HH}$ = 7.4 Hz, C*H*$_2$CH$_3$-Dep), 1.47 (s, 6H, C*H*$_3$C(N)) 1.16 (t, 12H, $^3J_{HH}$ = 7.5 Hz, CH$_2$C*H*$_3$-Dep) ppm.
^{13}C{^{1}H} NMR (100.61 MHz, 298 K, THF-d_8) δ = 159.8 (s, CH$_3$*C*(N)), 154.5 (s, q-*C*$_{aromatic}$-Dep), 135.6 (s, q-*C*$_{aromatic}$-Dep), 125.5 (s, *o*-*C*H$_{aromatic}$-Dep), 120.0 (s, *p*-*C*H$_{aromatic}$-Dep), 90.2 (s, CH$_3$C(N)*C*H=), 24.9 (s, *C*H$_2$CH$_3$-Dep), 23.7 (s, *C*H$_3$C(N)), 14.7 (s, CH$_2$*C*H$_3$-Dep) ppm.

Elemental Analysis calcd. C 74.95, H 8.30, N 6.99 found C 75.10, H 8.15, N 6.69.

2.4.3 Synthesis of Starting Materials

4-Methoxy-α-methylstyrene:

The synthesis was performed according to a literature procedure.[29]

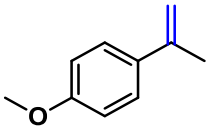

$C_{10}H_{12}O$, MW = 148.21 g/mol

Yield: 1.32 g, 38%

^{1}H NMR (300.13 MHz, 298 K, $CDCl_3$) δ = 7.46-7.38 (m, 2H, C*H*$_{aromatic}$), 6.91-6.83 (m, 2H, C*H*$_{aromatic}$), 5.29 (q, 1H, $^4J_{HH}$ = 0.7 Hz, C*H*$_{olefinic}$), 4.99 (qt, 1H, $^2J_{HH}$ & $^4J_{HH}$ = 1.5 Hz, C*H*$_{olefinic}$), 3.82 (s, 3H, C*H*$_3$-Methoxy), 2.14 (q, 3H, $^4J_{HH}$ = 0.7 Hz, C*H*$_3$-Methyl) ppm.
^{13}C{^{1}H} NMR (75.47 MHz, 298 K, $CDCl_3$) δ = 159.2 (s), 142.7 (s) 133.9 (s),126.7 (s), 113.7 (s), 110.8 (s), 55.4 (s), 22.1 (s) ppm.

Analytical data were in full agreement with the literature.[29]

(3-Methylbut-2-en-2-yl)benzene:

The synthesis was performed according to a literature procedure.[30]

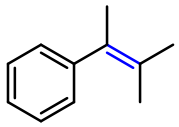

$C_{11}H_{14}$, MW = 146.23 g/mol

Yield: 2.32 g, 22%

^{1}H NMR (300.13 MHz, 298 K, $CDCl_3$) δ = 7.37-7.27 (m, 2H, C*H*$_{aromatic}$), 7.24-7.10 (m, 3H, C*H*$_{aromatic}$), 1.97 (s, 3H, C*H*$_3$-Methyl), 1.82 (s, 3H, C*H*$_3$-Methyl), 1.62 (s, 3H, C*H*$_3$-Methyl) ppm.
^{13}C{^{1}H} NMR (75.47 MHz, 298 K, $CDCl_3$) δ = 145.5 (s), 130.1 (s), 128.6 (s), 128.1 (s), 127.3 (s), 125.8 (s), 22.2 (s), 20.9 (s), 20.7 (s) ppm.

Analytical data were in full agreement with the literature.[30]

(1-Cyclopropylvinyl)benzene:

The synthesis was performed according to a literature procedure.[29]

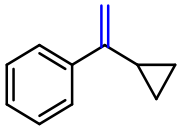

$C_{11}H_{12}$, MW = 144.22 g/mol

Yield: 1.17 g, 79%

^{1}H NMR (300.13 MHz, 298 K, $CDCl_3$) δ = 7.65-7.56 (m, 2H, C*H*$_{aromatic}$), 7.40-7.27 (m, 2H, C*H*$_{aromatic}$), 5.29 (s, 1H, C*H*$_{olefinic}$), 4.94 (s, 1H, C*H*$_{olefinic}$), 1.73-1.60 (m, 1H, C*H*$_{cyclopropyl}$), 0.89-0.80 (m, 1H, C*H*$_{cyclopropyl}$), 0.65-0.56 (m, 1H, C*H*$_{cyclopropyl}$) ppm.
^{13}C{^{1}H} NMR (75.47 MHz, 298 K, $CDCl_3$) δ = 149.5 (s), 141.8 (s), 128.3 (s), 127.6 (s), 126.3 (s), 109.2 (s), 15.8 (s), 6.8 (s) ppm.

Analytical data were in full agreement with the literature.[29]

2,3-Dimethyl-1*H*-indene:

The synthesis was performed according to a literature procedure.[31]

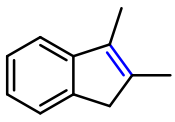

$C_{11}H_{12}$, MW = 144.22 g/mol

Yield: 590 mg, 17%

^{1}H NMR (300.13 MHz, 298 K, $CDCl_3$) δ = 7.41-7.34 (m, 1H, C*H*$_{aromatic}$), 7.31-7.19 (m, 2H, C*H*$_{aromatic}$), 7.17-7.08 (m, 1H, C*H*$_{aromatic}$), 3.27 (s, 2H, C*H*$_2$-Methylene), 2.09-2.06 (m, 3H, C*H*$_3$-Methyl), 2.06-2.02 (m, 3H, C*H*$_3$-Methyl) ppm.
^{13}C{^{1}H} NMR (75.47 MHz, 298 K, $CDCl_3$) δ = 147.7 (s), 142.5 (s), 138.2 (s), 132.6 (s), 126.2 (s), 123.7 (s), 123.1 (s), 118.1 (s), 42.6 (s), 14.1 (s), 10.3 (s) ppm.

Analytical data were in full agreement with the literature.[31]

2-Methyl-3-phenyl-1*H*-indene:

The synthesis was performed according to a literature procedure.[31]

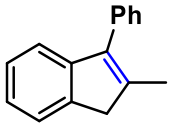

$C_{16}H_{14}$, MW = 206.29 g/mol

Yield: 3.426 g, 80%

^{1}H NMR (400.13 MHz, 298 K, $CDCl_3$) δ = 7.52-7.33 (m, 6H, C*H*$_{aromatic}$), 7.27-7.22 (m, 2H, C*H*$_{aromatic}$), 7.22-7.13 (m, 1H, C*H*$_{aromatic}$), 3.47 (s, 2H, C*H*$_2$-Methylene), 2.16 (s, 3H, C*H*$_3$-Methyl) ppm.
^{13}C{^{1}H} NMR (100.61 MHz, 298 K, $CDCl_3$) δ = 146.5 (s), 142.5 (s), 140.8 (s), 138.7 (s), 129.3 (s), 128.5 (s), 127.1 (s), 126.3 (s), 124.1 (s), 123.5 (s), 119.4 (s), 43.2 (s), 15.0 (s) ppm.

Analytical data were in full agreement with the literature.[31]

2.4.4 Hydrogenation Reactions

2.4.4.1 General Procedure

In a glovebox, an oven-dried (160 °C) 4 mL reaction vial was charged with *n*-pentadecane (20 µL, 72.4 µmol) as the internal standard for GC-FID quantification. The substrate (0.2 mmol) was added followed by the pre-catalyst as a stock solution in THF (0.5 mL), if not stated otherwise. The reaction vial was transferred to a high-pressure reactor which was sealed and removed from the glovebox. The reactor was purged with H_2 (3 × 3.0 bar to 0.5 bar overpressure for hydrogenations at 8 and 12 bar H_2 and 3 × 0.8 bar to 0.3 bar overpressure for hydrogenations at 2.0 bar H_2) and the reaction pressure and temperature were set. After the indicated reaction time, the reaction vessel was depressurized, the vials were retrieved and treated with a saturated aqueous solution of NH_4Cl (1.0 mL) and diluted with ethyl acetate. An aliquot of the organic phase was filtered over a short pad of silica and washed with ethyl acetate (1 x 2.0 mL). The solution was analyzed by GC-FID (and GC-MS for selected experiments).

Hydrogenation Protocol **A**: 3 mol% [(^{Dep}nacnac)Mg][Co(η^4-cod)$_2$] (**4**), 2 bar H_2, 30 °C, 3 h. Hydrogenation Protocol **B**: 5 mol% [(^{Dep}nacnac)Mg][Co(η^4-cod)$_2$] (**4**), 12 bar H_2, 40 °C, 22 h.

2.4.4.2 Optimization of Reaction Conditions

Initial optimization and control experiments were performed to identify the influence of the (^{Dep}nacnac)Mg$^+$ cation on the greater hydrogenation activity observed for **4** (Table S1**,** Entries 5-9). The hydrogenation reaction of α-methylstyrene with potassium salt **1** was not improved by addition of (^{Dep}nacnac)K, (^{Dep}nacnac)H, or MgI_2 prior to reaction. This suggests that the significantly higher activity of **4** compared to **1** is caused by the magnesium counterion and not merely due to the presence of the anionic ^{Dep}nacnac motif.[33] A solvent screening for the hydrogenation of trans-α-methylstilbene using **4** showed quantitative conversion in the polar solvents THF and DME, while no hydrogenation was observed in the non-polar solvents toluene and *n*-hexane (Table S1, Entries 10-13).

Table S1. Optimization of reaction conditions and control experiments.

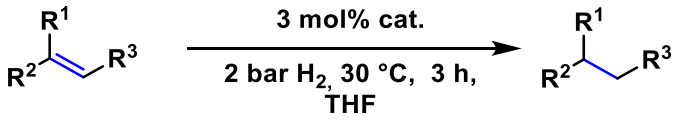

Entry	Olefin	Catalyst	Manipulation	Yield (conv.) [%]
1		no catalyst	/	<1 (5)
2		(^{Dep}nacnac)MgI·OEt$_2$	/	<1 (6)
3		(^{Dep}nacnac)K	/	<1 (6)
4		[(^{Dep}nacnac)Mg][Co(η^4-cod)$_2$] (**4**)	none	>99
5		[K(thf)$_{0.2}$][Co(η^4-cod)$_2$] (**1**)	none	8 (15)
6		[K(thf)$_{0.2}$][Co(η^4-cod)$_2$] (**1**)	3 mol% (^{Dep}nacnac)K	5 (14)[a]
7		[K(thf)$_{0.2}$][Co(η^4-cod)$_2$] (**1**)	3 mol% MgI_2	11 (18)[b]
8		[K(thf)$_{0.2}$][Co(η^4-cod)$_2$] (**1**)	3 mol% (^{Dep}nacnac)H	9 (23)
9		[(^{Dep}nacnac)Mg][Co(η^4-cod)$_2$] (**4**)	3 mol% (^{Dep}nacnac)H	97
10	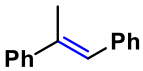	[(^{Dep}nacnac)Mg][Co(η^4-cod)$_2$] (**4**)	none	>99
11		[(^{Dep}nacnac)Mg][Co(η^4-cod)$_2$] (**4**)	solvent = DME	>99
12		[(^{Dep}nacnac)Mg][Co(η^4-cod)$_2$] (**4**)	solvent = toluene	1 (3)
13		[(^{Dep}nacnac)Mg][Co(η^4-cod)$_2$] (**4**)	solvent = *n*-hexane	<1 (<1)

[a] Stirring of [K(thf)$_{0.2}$][Co(η^4-cod)$_2$] (**1**) and (^{Dep}nacnac)K in THF for 10 min prior to addition of α-methylstyrene and IS and subsequent hydrogenation reaction. [b] Stirring of [K(thf)$_{0.2}$]-[Co(η^4-cod)$_2$] (**1**) and MgI_2 in THF for 2 h prior to addition of α-methylstyrene and IS and subsequent hydrogenation reaction.

2.4.4.3 GC-FID Data for Non-Calibrated Substrates

For the substrates myrcene and (+)-(*R*)-α-pinene the peak area of the substrate and the corresponding products in the chromatogram (GC-FID) were compared to estimate the yield and conversion. Peaks at 5.8 min correspond to the internal standard *n*-pentadecane.

Myrcene:

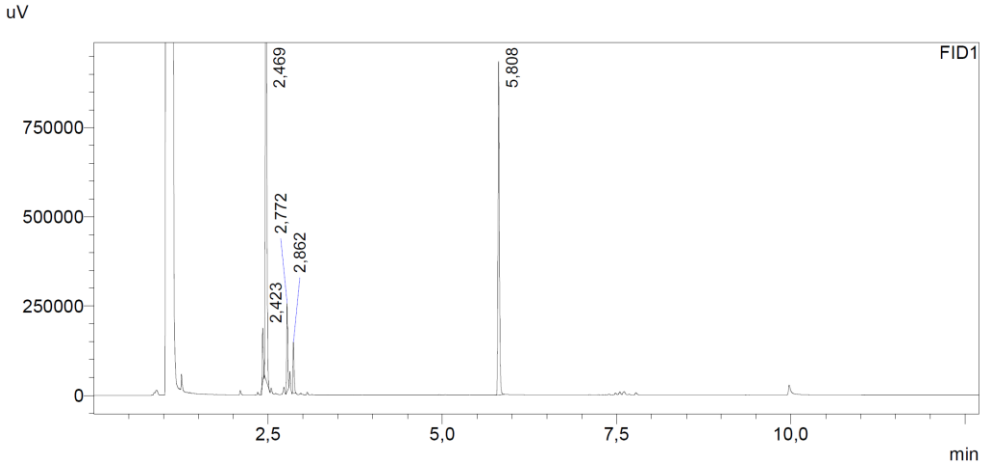

Figure S1. GC-FID chromatogram for the hydrogenation of myrcene.

Table S2. Analysis of the GC-FID chromatogram for the hydrogenation of myrcene.

Retention time [min]	Assignment	Peak area	Relative peak area [%]
2.469	2,5-dimethyloctane	2182772	>99 ()
2.772	α-pinane	261288	()
2.862	α-pinane	157074	()

(+)-(*R*)-α-Pinene:

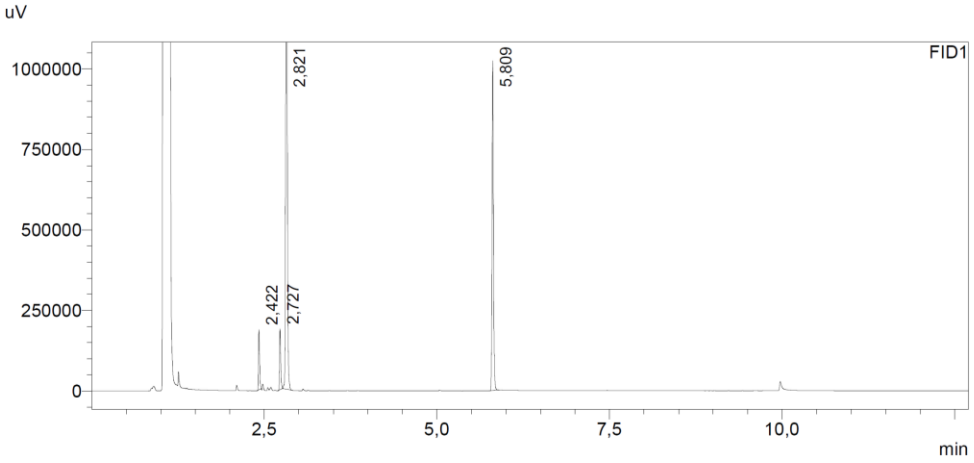

Figure S2. GC-FID chromatogram for the hydrogenation of (+)-(*R*)-α-Pinene.

Table S3. Analysis of the GC-FID chromatogram for the hydrogenation of (+)-(*R*)-α-pinene.

Retention time [min]	Assignment	Peak area	Relative peak area [%]
2.727	α-pinane	221040	>99
2.832	α-pinane	2970723	

2.4.5 Kinetic Studies and Mechanistic Experiments

2.4.5.1 Reaction Progress Analysis

General Procedure for Reaction Progress Analysis

An oven-dried (160 °C) 10 mL two-necked flask was connected to a Man on the Moon X204 gas uptake system[29] with a reservoir pressure of 10 bar H_2 and a constant reaction pressure of 1.97 bar H_2 (see Figure S3 for the reaction set-up).

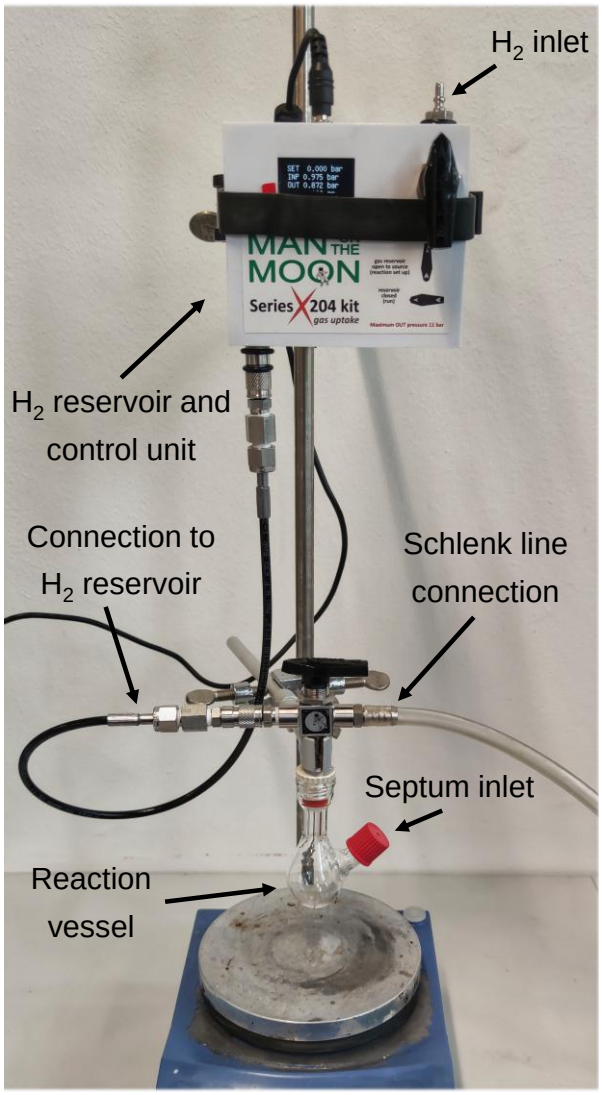

Figure S3. Picture of the experimental set-up used for reaction progress analyses and poisoning studies.

After three vacuum/argon cycles, followed by flushing with H_2 (3 x), a freshly prepared substrate solution (in 0.3 mL THF, 0.2 mmol; 20 µL internal standard *n*-pentadecane) was added via syringe. The recording of the H_2 uptake was started immediately after addition of the pre-catalyst solution (in 0.2 mL THF, 0.006 mmol, 3 mol%). After the reaction, the mixture was treated with a saturated aqueous solution of NH_4Cl (1.0 mL), purged with H_2 (1x), and a background curve of the H_2 loss was recorded. The reaction mixture was extracted with ethyl acetate (2 × 1.0 mL), filtered over silica, and analyzed by GC-FID (and GC-MS for selected experiments).

- *Reaction monitoring with [(^{Dep}nacnac)Mg][Co(η⁴-cod)(η²-styrene)₂](thf)₃.₅ (**7**):*

The reaction progress analysis was conducted following the general procedure described above, albeit with toluene as the reaction solvent. No induction period was observed and α-methylstyrene was fully hydrogenated after 10 min with a turnover frequency (TOF) = 187 h^{-1} (Figure S4a). In a separate experiment, subjection of **7** (25.3 mg, 0.025 mmol, dissolved in 0.5 mL toluene) to 2 bar H_2 at 25 °C resulted in quantitative hydrogenation of the coordinating 1,5-cyclooctadiene and styrene after approximately 15 to 20 min as indicated by subsequent GC-FID analysis (Figure S4b, depicted as a pressure vs. time curve).

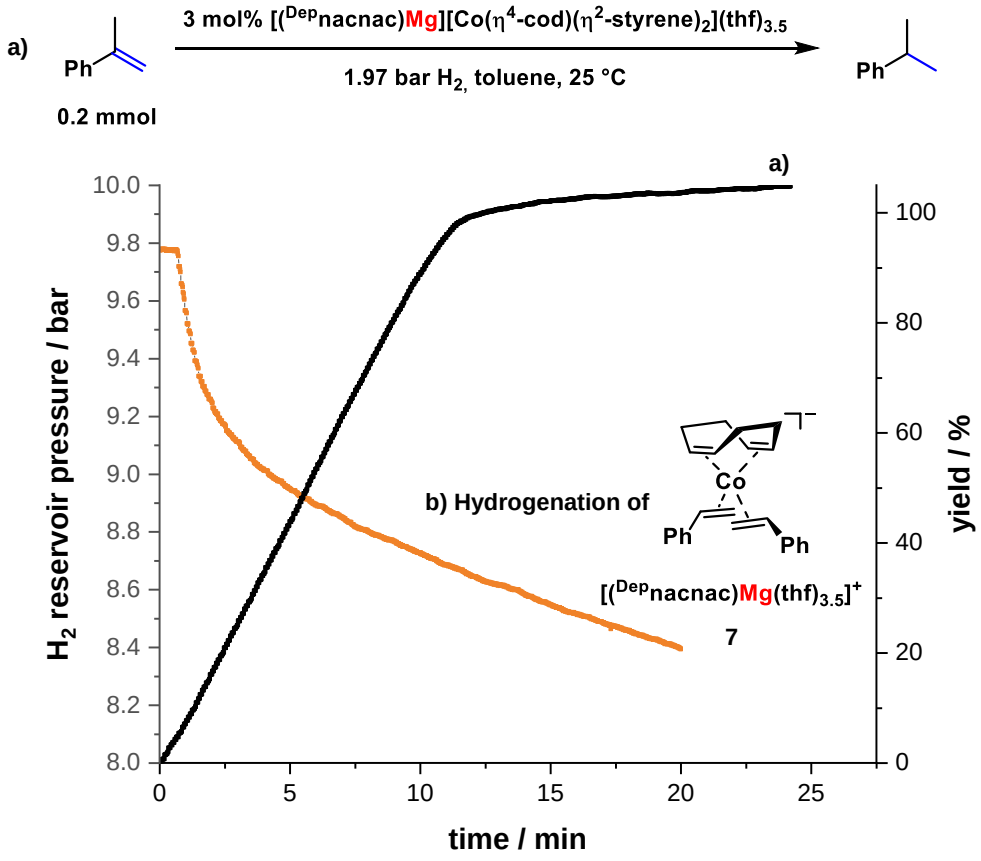

Figure S4. a) Hydrogenation of α-methylstyrene with 3 mol% [(^{Dep}nacnac)Mg][Co(η⁴-cod)-(η²-styrene)₂](thf)₃.₅ (**7**). Yields were determined by quantitative GC-FID analysis vs. *n*-pentadecane. b) Direct hydrogenation of **7** in toluene.

Note: The TOF was determined from reaction progress analyses by analyzing the slope of a selected part of the reaction time profile showing a linear ascent. The linear part for the reaction time profile was chosen between 20% and 60% hydrogenation yield.

2.4.5.2 Poisoning Experiments

The general procedure was applied. All experiments were performed in THF. The poisoning reagents (PMe_3 and $P(OMe)_3$ as THF solutions) were added after a reservoir pressure loss of approx. 1.5 bar H_2 or prior to addition of the substrate.

- *Dibenzo[a,e]cyclooctene (dct) poisoning:*

Addition of dct to the reaction mixture containing α-methylstyrene and 3 mol% **4** resulted in reduced hydrogenation of α-methylstyrene (Figure S5). Excess of dct with respect to the catalyst loading (60 mol%, 20.0 equiv. in total, 10.0 equiv. assuming a 2:1-dct:Co stoichiometry) was needed to inhibit the hydrogenation of α-methylstyrene (Figure S5, green curve, 35% yield). When 30 mol% (10.0 equiv. in total, 5.0 equiv. assuming a 2:1-dct:Co stoichiometry) and 12 mol% (4.0 equiv. in total, 2.0 equiv. assuming a 2:1-dct:Co stoichiometry) of dct were added, the hydrogenation of α-methylstyrene was only partially inhibited giving cumene in 58% and 88% yield, respectively (Figure S5, blue and red curve).

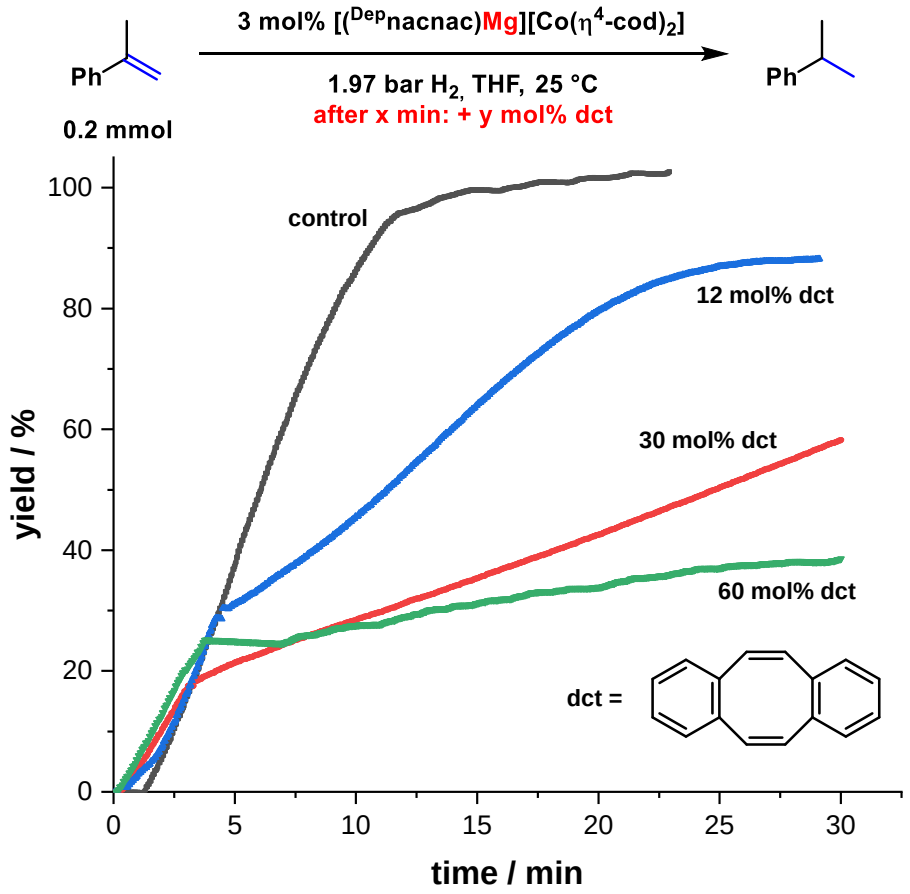

Figure S5. Hydrogenation of α-methylstyrene with 3 mol% [(Depnacnac)Mg][Co(η4-cod)2] (**4**) and varying amounts of dct. Yields were determined by quantitative GC-FID analysis vs. *n*-pentadecane.

In all three experiments, partial hydrogenation of dct to dct-H_2 and dct-H_4 was observed. The defined dct-complex [(^{Dep}nacnac)Mg][Co(η^4-dct)$_2$](thf)$_{1.7}$ (**6**) was further tested in the hydrogenation of α-methylstyrene to evaluate its catalytic activity (Figure S6). When using 3 mol% of **6**, α-methylstyrene was quantitatively hydrogenated in 10 min to 40 min. Different induction periods were observed ranging from 0 min to 10 min while dct was consistently hydrogenated to dct-H_4 between 40% and 60% in all three experiments (Figure S6, green, blue and red curve; determined by relative ratios by GC-FID analysis). This suggests that the initial hydrogenation of dct does not occur uniformly resulting in varying starting points for the hydrogenation of α-methylstyrene. Addition of excess dct with respect to **6** (60 mol%, 20.0 equiv. in total, 10.0 equiv. assuming a 2:1-dct:Co stoichiometry) resulted in significant inhibition of the hydrogenation of α-methylstyrene as observed for **4** (black curve, 35% yield). This indicates that dct acts as a competing substrate and poison at the same time. If dct is (partially) hydrogenated, the rigid binding to the molecular catalyst is no longer active and α-methylstyrene occupies the vacant coordination sites followed by hydrogenation. The dct hydrogenation occurs regardless of whether the dct-complex is formed *in situ* or used as an isolated species. A 10-fold excess is necessary to ensure the complete (chelating) coordination with intact dct through the course of the reaction and significantly inhibit the hydrogenation of α-methylstyrene.

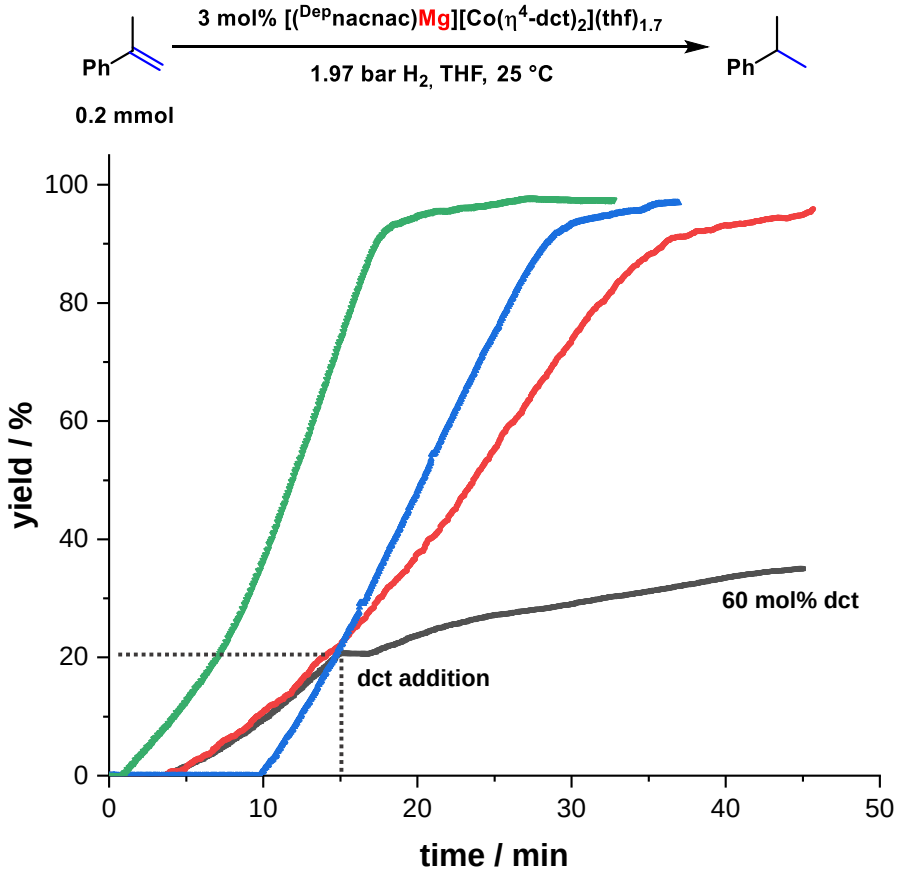

Figure S6. Hydrogenation of α-methylstyrene with 3 mol% [(^{Dep}nacnac)Mg][Co(η^4-dct)$_2$](thf)$_{1.7}$ (**6**) and poisoning with 60 mol% dct. Yields were determined by quantitative GC-FID analysis vs. *n*-pentadecane.

In contrast, a heterotopic catalyst species poorly binds dct to its surface.[18] Thus, the inhibiting effect observed here likely supports the homotopic nature of the active catalyst.

- *PMe_3 poisoning:*

Addition of PMe_3 to the reaction mixture containing α-methylstyrene and 3 mol% **4** resulted in partial hydrogenation of the phenyl ring of α-methylstyrene as ascertained by reaction progress analysis (Figure S7). Highest H_2-incorporation into the aromatic ring (formation of isopropylcyclohexane) was observed when 1.0 equiv. of PMe_3 (3 mol%) with respect to the catalyst was used (as quantified by GC-FID analysis vs. internal *n*-pentadecane). While the reactivity of the catalytic system was altered, no inhibition with substoichiometric amounts of PMe_3 with respect to the catalyst was observed (Figure S7, 0.1 equiv. to 1.0 equiv.). Superstoichiometric amounts of PMe_3 (2.0 equiv. to 4.0 equiv.) inhibited the hydrogenation reaction. This indicates the presence of a (altered) homotopic catalyst, which is inhibited by coordination of PMe_3 to up to four coordination sites of the active molecular species.[34]

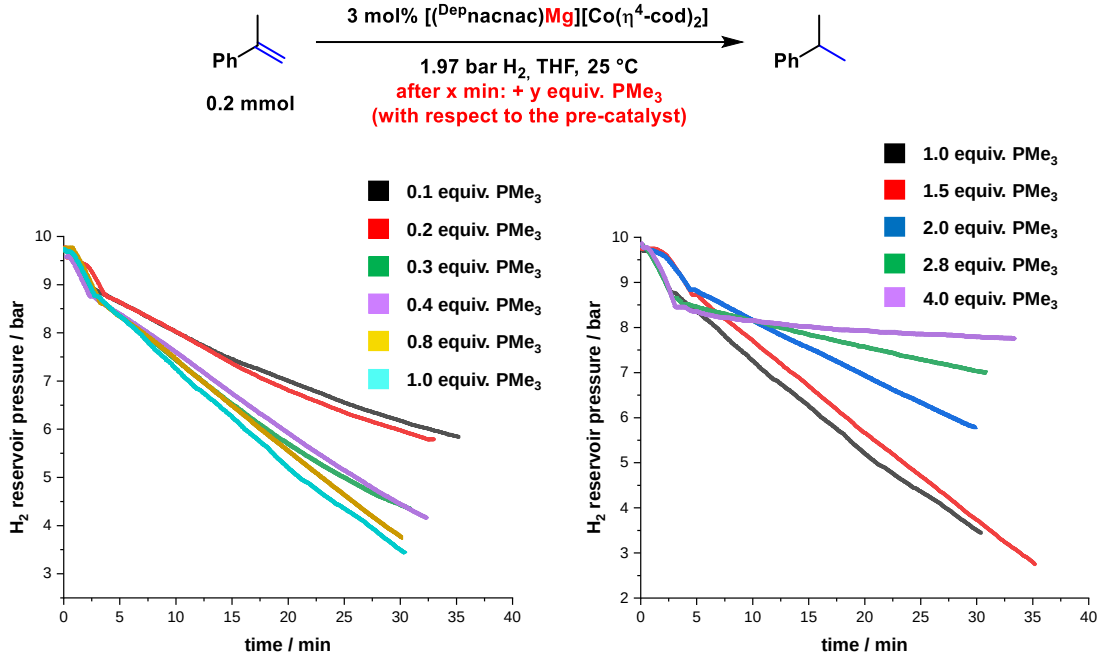

Figure S7. Hydrogenation of α-methylstyrene with 3 mol% [(Depnacnac)Mg][Co(η4-cod)2] (**4**) and varying amounts of PMe_3 (0.1 to 4.0 equiv., in respect to **4**).

Arene hydrogenation with the addition of 1.0 equiv. of PMe_3 was conducted using benzene, toluene and α-methylstyrene as model substrates (Scheme S1). Hydrogenation in presence of PMe_3 resulted in low to moderate formation of the respective reduction products. Benzene was hydrogenated in 14% yield to give cyclohexane; toluene was hydrogenated to 28% yield giving methylcyclohexane and α-methylstyrene was hydrogenated in 42% yield providing isopropylcyclohexane.

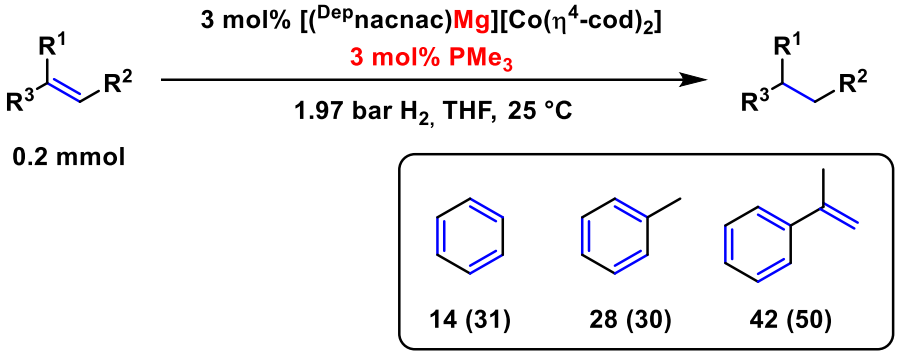

Scheme S1. Arene hydrogenation with 3 mol% [(Depnacnac)Mg][Co(η4-cod)2] (**4**) and 3 mol% PMe_3. Yields were determined by ^1H NMR spectroscopy using 1,3,5-trimethoxybenzene.

Reaction progress analysis of the hydrogenation of benzene and toluene with 3 mol% [(Depnacnac)Mg][Co(η4-cod)2] (**4**) and 3 mol% PMe_3 shows early decline of the hydrogenation rate between 10 min and 15 min pointing to fast catalyst deactivation at low product yields (Figure S8).

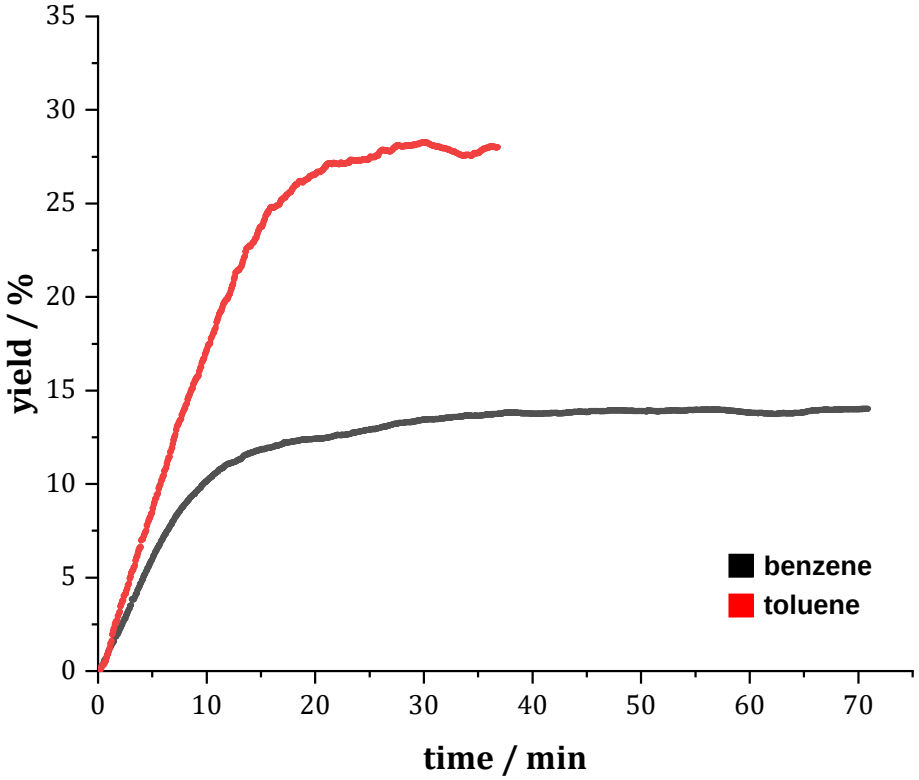

Figure S8. Reaction progress analysis of the hydrogenation of benzene and toluene with 3 mol% [(Depnacnac)Mg][Co(η4-cod)2] (**4**) and 3 mol% PMe_3. Yields were determined by ^1H NMR spectroscopy using 1,3,5-trimethoxybenzene.

- *$P(OMe)_3$ poisoning:*

$P(OMe)_3$ was used as an alternative poisoning reagent to further evaluate the topicity indications of the preceding poisoning experiments with dct and PMe_3. NMR scale reaction of pre-catalyst **4** with 0.3 equiv. of $P(OMe)_3$ in THF-d_8 resulted in the decomposition of the complex as indicated by the vanishing of the characteristic signals of **4** (e.g.,

C*H*=C(N)-^{Dep}nacnac at 5.11 ppm, signal ○) and the formation of a new molecular species (Figure S9). The $^{31}P\{^{1}H\}$ NMR spectrum was silent. It is noteworthy, that this decomposition takes place in the absence of H_2 and thus of a catalytically active species.

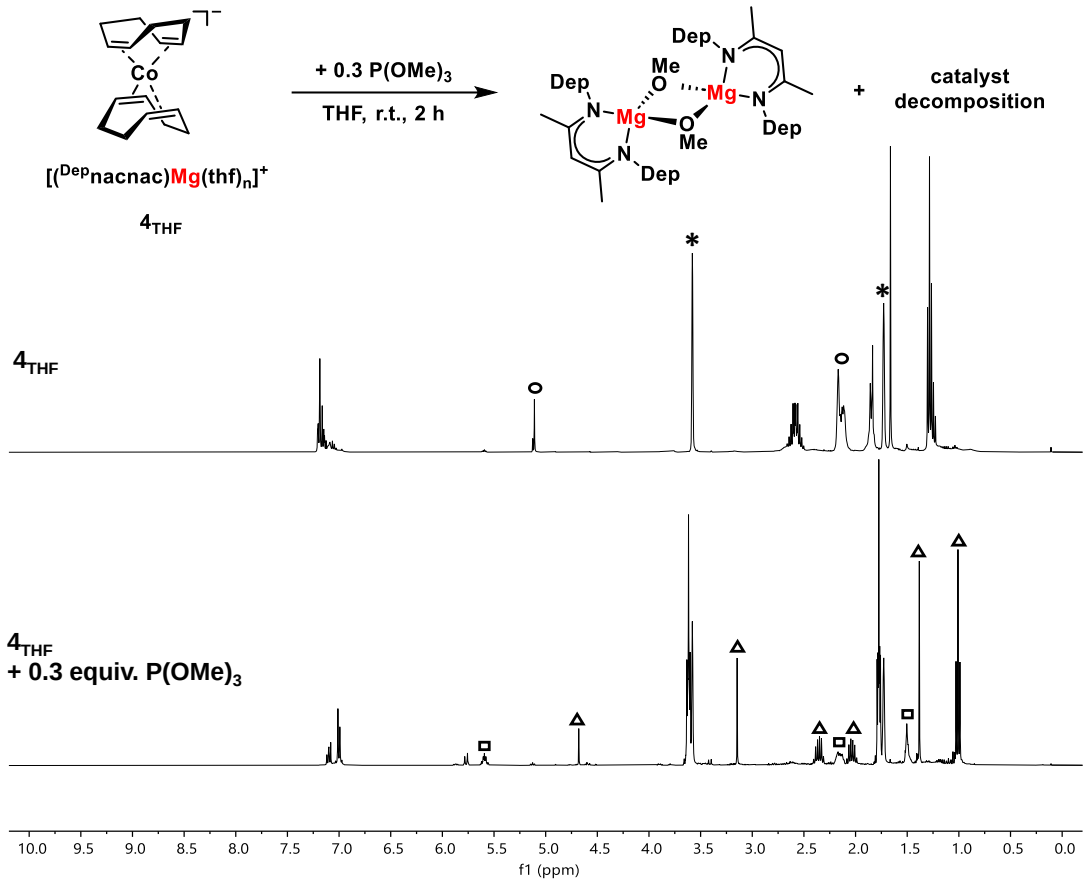

Figure S9. Reaction of [(^{Dep}nacnac)Mg][Co(η^4-cod)$_2$] (**4**) with 0.3 equiv. of P(OMe)$_3$ in THF-d$_8$. *: THF-d$_8$. ○: selected characteristic signals of complex **4**. □: free cyclooctene. Δ: characteristic signals of [(^{Dep}nacnac)Mg(OMe)]$_2$.

In a separate experiment, 0.3 equiv. of P(OMe)$_3$ in THF was added to a solution of [(^{Dep}nacnac)Mg][Co(η^4-cod)$_2$] (**4**) in THF and the black-to-brown mixture was stirred for 2 h at ambient temperature. The reaction mixture was filtered, the filtrate dried under reduced pressure and the residue dissolved in toluene. X-ray quality single-crystals were obtained from toluene/*n*-hexane by vapor diffusion at ambient temperature to give bright yellow blocks of the methoxy-bridged dimer [(^{Dep}nacnac)Mg(OMe)]$_2$ (Figure S10).

In contrast, no cobalt-containing species could be isolated nor detected by NMR analysis (^{1}H and $^{31}P\{^{1}H\}$). This indicates a P–O bond cleavage reaction which leads to the selective formation of the dimeric magnesium complex (as indicated by ^{1}H NMR) and presumably to insoluble cobalt phosphorus by-products (indicated by a turbid reaction mixture after P(OMe)$_3$ addition). The substoichiometric use of P(OMe)$_3$ in the hydrogenation reaction of α-methylstyrene with 3 mol% [(^{Dep}nacnac)Mg][Co(η^4-cod)$_2$] (**4**) resulted in immediate reaction inhibition. As observed for pre-catalyst **4**, the inhibition is likely caused by an analogous P–O bond cleavage reaction of the active species. Yet, it cannot be clearly stated

whether this inhibition occurs due to decomposition of the active species or inhibition by irreversible binding to a structurally intact active species. Hence, $P(OMe)_3$ proved to be not suitable as a poisoning reagent for pre-catalyst **4**.

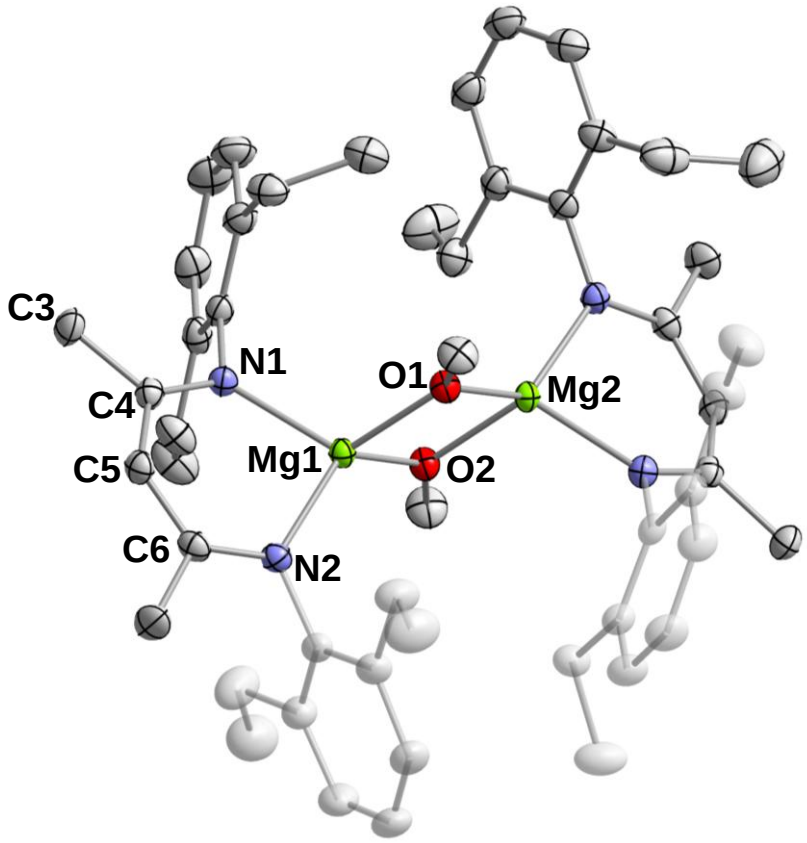

Figure S10. Solid state molecular structure of **[(Depnacnac)Mg(OMe)]2** isolated from the reaction of [(Depnacnac)Mg][Co(η4-cod)2] (**4**) with 0.3 equiv. of $P(OMe)_3$. Thermal ellipsoids are drawn at the 40% probability level. H atoms are omitted for clarity. Selected bond lengths [Å] and angles [°]: Mg1–Mg2: 2.8962(6), Mg1–O1: 1.9569(10), Mg1–O2: 1.9409(10), Mg1–N1: 2.0413(12), Mg1–N2: 2.0507(12), N1–C4: 1.3276(18), N2–C6: 1.3297(18), C4–C5: 1.405(2), C5–C6: 1.405(2), O1–Mg1–O2: 83.89(4), O1–Mg2–O2: 84.00(4), Mg1–O1–Mg2: 96.07(4), N1–Mg1–N2: 92.95(5), N1–C4–C5: 123.82(13).

- *Hg poisoning:*

Addition of mercury (1690 mol% based on catalyst loading) at 0 min to the hydrogenation reaction of α-methylstyrene with pre-catalyst **4** (3 mol%) gave full hydrogenation within 15 min while a decrease in TOF (from 225 h^{-1} to 148 h^{-1}) was observed (Figure S11, curve **a** and **b**). To test whether a slow amalgamation reaction is taking place,[18] pre-catalyst **4** (in THF) was stirred for 30 min and 90 min, respectively, with Hg prior to the addition of α-methylstyrene (in THF). When Hg was added 30 min in advance, the hydrogenation of α-methylstyrene was varying. The substrate was either fully hydrogenated within <10 min exceeding the TOF of the standard reaction (331 h^{-1} vs. 225 h^{-1}; Figure S11, curve **d**), almost completely hydrogenated (86%) within 1 h (Figure S11, curve **e**) or hydrogenated to 53% within 1 h (Figure S11, curve **f**). The control reaction of α-methylstyrene with a 30 min pre-hydrogenated catalyst solution resulted in the rapid and full hydrogenation of the

alkene exhibiting a remarkably higher TOF (552 h^{-1} vs. 225 h^{-1}) than the standard reaction (Figure S11, curve **c**).

This irregular hydrogenation behavior is linked to an unsteady pre-hydrogenation of the pre-catalyst **4** (hydrogenation of the stabilizing COD ligand) when subjected to H_2 in the presence of Hg. This likely results in the partial formation of less active cobalt particles which then can react with Hg by amalgamation or adsorption. If the majority of the pre-catalyst is hydrogenated in 30 min, slow hydrogenation will take place through the remaining particles while a fast reaction occurs if less pre-catalyst is hydrogenated, and a molecular species is majorly present. To test this hypothesis, pre-catalyst **4** was stirred for 90 min with Hg prior to the addition of α-methylstyrene. Analogously, α-methylstyrene was reacted with a 90 min pre-hydrogenated catalyst solution in the control experiment.

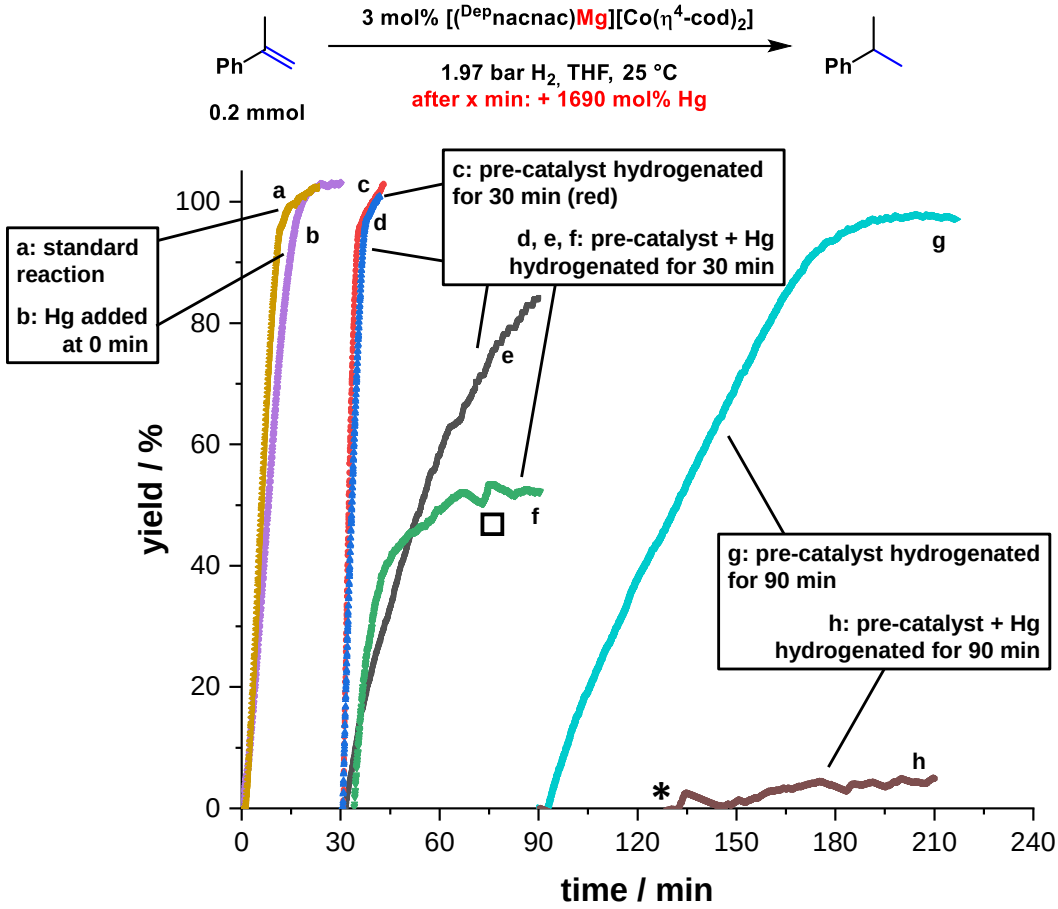

Figure S11. Hydrogenation of α-methylstyrene with 3 mol% [(Depnacnac)Mg][Co(η4-cod)2] (**4**) and Hg (1690 mol%). Addition of Hg at 0 min, –30 min and –90 min. Pre-hydrogenation of sole catalyst solution for 30 min and 90 min prior to substrate addition. □ : Alternation due to external pressure change. *: Slow hydrogenation results in "negative" yield due to background hydrogen loss. Yields were determined by quantitative GC-FID analysis vs. *n*-pentadecane.

While slow but full hydrogenation was observed with the 90 min pre-hydrogenated catalyst solution in the absence of Hg (Figure S11, curve **g**), the hydrogenation of α-methylstyrene with the 90 min pre-hydrogenated catalyst solution in the presence of Hg resulted in negligible product formation (Figure S11, curve **h**). This finding supports the hypothesis

that the more active, major species is homotopic in nature but can be converted into a less active heterotopic species by (destructive) hydrogenation of the pre-catalyst.

Note: The turnover frequencies (TOFs) were determined from reaction progress analyses by analyzing the slope of a selected part of the reaction time profile showing a linear ascent. The linear part for reaction time profiles a, b, c, and d (Figure S11) was chosen between 20% and 60% hydrogenation yield.

Additional mercury poisoning experiments were performed to investigate the catalyst topicity at elevated pressure and temperature (see protocol B, Figure 2, main text). Following the general procedure, the hydrogenation of 1,1,2-triphenylethylene and the α,β-unsaturated esters ethyl cinnamate, ethyl crotonate and ethyl 3,3-dimethylacrylate was performed using pre-catalyst **4** in the absence and presence of excess Hg (see Table S4). In the absence of Hg, near-quantitative hydrogenation was observed for all investigated substrates. In the presence of Hg (1690 mol%; addition at t = 0 min), no inhibition was observed for the α,β-unsaturated esters and the hydrogenation reached a comparable level of completeness (Table S4, entries 7-8). The demanding substrate 1,1,2-triphenylethylene was hydrogenated between 55% and 94% in four single reaction runs (Table S4, entry 2).

Table S4. Hg poisoning experiments at elevated temperature and pressure (protocol B).[a]

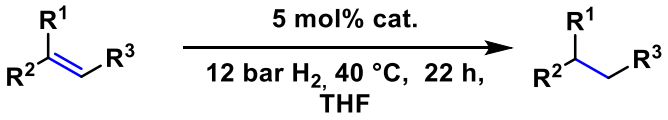

Entry	Olefin	Catalyst	Manipulation	Yield (conv.) [%]
1	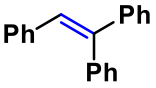	[(Dep nacnac)Mg] [Co(η⁴-cod)₂] (**4**)	none	>99
2			Hg (1690 mol%)	55 (50), 66 (69), 91 (97), 94 (93)[c]
3		*in situ* Co-nanoparticles[b]	none	56 (59)
4			Hg (1690 mol%)	0 (6)
5	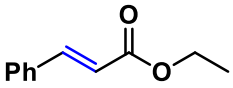	[(Dep nacnac)Mg] [Co(η⁴-cod)₂] (**4**)	None	98
6			Hg (1690 mol%)	90
7	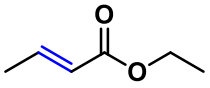		none	90
8			Hg (1690 mol%)	91
9	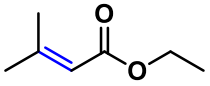		none	91
10			Hg (1690 mol%)	92

[a] Standard conditions: 0.2 mmol substrate (0.4 mol/L in THF). Protocol B: 5 mol% cat., 12 bar H_2, 40 °C, 22 h. [b] The *in situ* Co nanoparticle catalyst was prepared according to the literature.[25] Lithium (7.2 mg, 1.04 mmol, 2.0 equiv.), naphthalene (156.0 mg, 1.22 mmol, 2.35 equiv.) and $CoCl_2$ (67.4 mg, 0.52 mmol, 1.0 equiv.) were suspended in THF (2.5 mL) and stirred for 24 h. For the catalytic hydrogenation reaction, 48 µL (0.01 mmol in Co, 5 mol%) of the *in situ* Co-nanoparticle suspension were added to the reaction mixture containing 1,1,2-triphenylethylene and *n*-pentadecane in THF. [c] Yields and conversions observed over four single reaction runs.

This variation in yield possibly hints at the formation of catalytically active cobalt nanoparticles that are inhibited by the heterotopic catalyst poison mercury. In addition, the hydrogenation of 1,1,2-triphenylethylene was conducted with Co nanoparticles, prepared *in situ* following a previously reported procedure by Feldmann, Jacobi von Wangelin, Wolf and co-workers.[25] While hydrogenation with the Co nanoparticles following protocol B afforded 56% (59%) of 1,1,2-triphenylethane, addition of Hg (1690 mol%) to the reaction mixture at t = 0 min resulted in the complete inhibition of the hydrogenation reaction and no product formation was observed (Table S4, entries 3-4). The acquired data indicates that the catalyst system based on pre-catalyst **4** remains predominantly homotopic at elevated temperature (40 °C) and pressure (12 bar H_2). This is supported by the selective poisoning of intentionally prepared Co nanoparticles with Hg, while the hydrogenation with pre-catalyst **4** is only partially (if at all) inhibited under identical conditions.

2.4.5.3 Catalytic Experiments

- *NMR tube hydrogenation with [K(thf)$_{0.2}$][Co(η^4-cod)$_2$] (**1**) and [(^{Dep}nacnac)Mg]-[Co(η^4-cod)$_2$] (**4**):*

Reaction monitoring by ^{1}H NMR spectroscopy was carried out in a Norell® intermediate pressure valved NMR tube (S-5-600-MW-IPV-7). The pre-catalyst [K(thf)$_{0.2}$][Co(η^4-cod)$_2$] (**1**) or [(^{Dep}nacnac)Mg][Co(η^4-cod)$_2$] (**4**) (in each case 10 µmol, 10 mol%) was dissolved in THF-d8 (0.5 mL), α-methylstyrene (13.0 µL, 0.1 mmol, 1.0 equiv.) was added and the solution was transferred to the NMR tube. The first ^{1}H NMR spectrum was recorded (Figure S12 and Figure S13). Subsequently, the atmosphere was exchanged with H_2 by three consecutive freeze pump thaw cycles and set to 2 atm of H_2 pressure. Subsequent spectra were recorded after irregular intervals until the substrate was fully consumed or until no further consumption was observed. The reaction was quenched with 1.0 mL of saturated NH4Cl solution and 20 µL *n*-pentadecane (72.4 µmol) were added as the internal standard for GC-FID quantification. The reaction mixture was extracted with 1.5 mL ethyl acetate, filtered over a pad of silica, washed with ethyl acetate, and analyzed by quantitative GC-FID. When potassium cobaltate **1** was used, partial hydrogenation of α-methylstyrene (14% according to ^{1}H NMR spectroscopy, by relative peak integrals) was observed after 131 min, which was indicated by the observation of two new signals at ~2.9 ppm and ~1.2 ppm (Figure S12). After 194 min, 21% cumene has formed and after 263 min 24% cumene was observed. The well-resolved NMR spectra strongly suggest the absence of nanoparticulate cobalt in the reaction mixture at this point. In the following time period (+1 day), significant line broadening was observed in the ^{1}H NMR spectrum, indicating the formation of Co nanoparticles (catalyst deactivation). GC-FID analysis of the hydrogenation mixture after one day (25 h 6 min) indicated the formation of 33% (29%) cumene (overlap of cumene and cyclooctane in GC-FID), which shows that no significant hydrogenation occurred after catalyst deactivation.

When magnesium cobaltate **4** was used, hydrogenation of α-methylstyrene to 15% (according to ^{1}H NMR spectroscopy, by relative peak integrals) was observed after only 26 min, as indicated by the appearance of two new signals at ~2.9 ppm and ~1.2 ppm (Figure S13). After 130 min, 46% of cumene has formed and after 190 min near-quantitative hydrogenation of α-methylstyrene (84%) was observed. After 266 min, α-methylstyrene was fully consumed. Significant line broadening was observed, which indicates catalyst decomposition (and Co nanoparticle formation), consistent with the observations for cobaltate salt **1**. GC-FID analysis of the hydrogenation mixture showed quantitative formation of cumene (>99% conversion).

The hydrogenation of α-methylstyrene illustrates the strongly differing reaction rates for cobaltate salts **1** and **4**. Using **1**, only 21% cumene is observed after 194 min (14% after 131 min, see Figure S12), while use of **4** gives 84% of cumene after 190 min (46% after 130 min, see Figure S13).

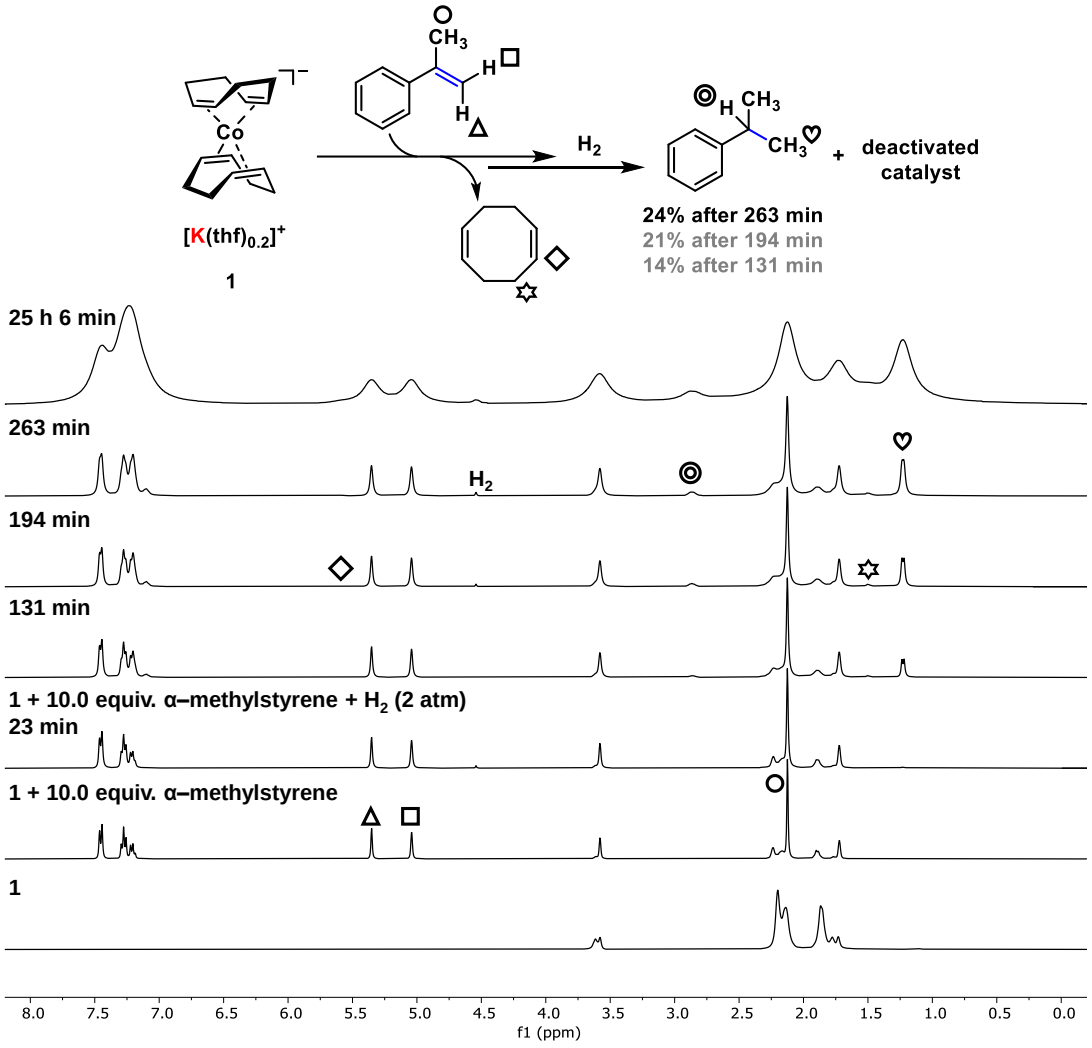

Figure S12. ^{1}H NMR spectroscopic monitoring (THF-d_8) of the hydrogenation of α-methylstyrene with 10 mol% [K(thf)$_{0.2}$][Co(η^4-cod)$_2$] (**1**). Bottom: Isolated sample of cobaltate **1**. In ascending order: After addition of α-methylstyrene (10.0 equiv.) at ambient temperature and after pressurizing with 2 atm H_2. ◊ and ☆: free (isomerized) 1,3-cod or hydrogenation products thereof. ◯, ☐ and Δ: α-methylstyrene. ◎ and ♡: cumene.

The well-resolved NMR spectra over the course of the hydrogenation reactions are a strong indication for the absence of cobalt nanoparticles. These NMR studies corroborate a pronounced counterion effect on a catalyst that is likely to be homotopic. However, catalyst decomposition to cobalt nanoparticles seemingly occurs toward the end of the catalytic reaction. This is indicated by line-broadening in the ^{1}H NMR spectra as observed for potassium cobaltate **1** after 263 min and for magnesium cobaltate **4** after 190 min.

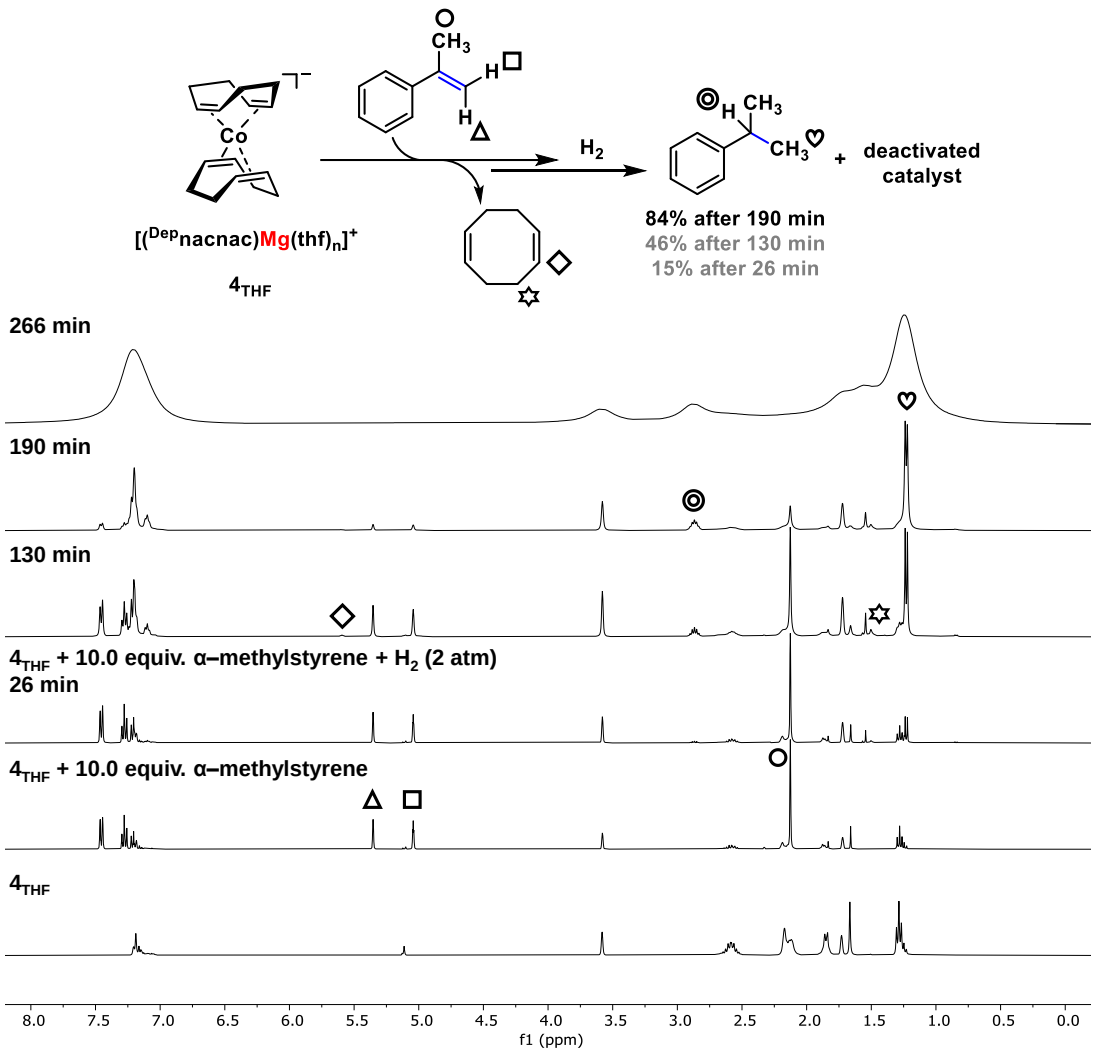

Figure S13. ^{1}H NMR spectroscopic monitoring (THF-d$_8$) of the hydrogenation of α-methylstyrene with 10 mol% [(^{Dep}nacnac)Mg][Co(η^4-cod)$_2$] (**4**). Bottom: Isolated sample of cobaltate **4**. In ascending order: After addition of α-methylstyrene (10.0 equiv.) at ambient temperature and after pressurizing with 2 atm H$_2$. ◊ and ☆: free (isomerized) 1,3-cod or hydrogenation products thereof. ◯, ☐ and Δ: α-methylstyrene. ◎ and ♡: cumene.

- *Ligand exchange reaction with [(^{Dep}nacnac)Mg][Co(η^4-dct)$_2$](thf)$_{1.7}$ (**6**):*

Reaction monitoring by ^{1}H NMR spectroscopy was carried out in a J. Young NMR tube. A solution of [(^{Dep}nacnac)Mg][Co(η^4-dct)$_2$](thf)$_{1.7}$ (**6**) (11.2 mg, 11.5 µmol, 1.0 equiv.) in THF-d$_8$ (0.6 mL) was transferred to an NMR tube. Then, styrene (13.2 µL, 115 µmol, 10.0 equiv.) was added to the solution. After rotating the sample for 24 h, the ^{1}H NMR

spectrum was recorded (Figure S14, top). No ligand exchange reaction was observed as seen by the absence of any resonance for non-coordinated dct.

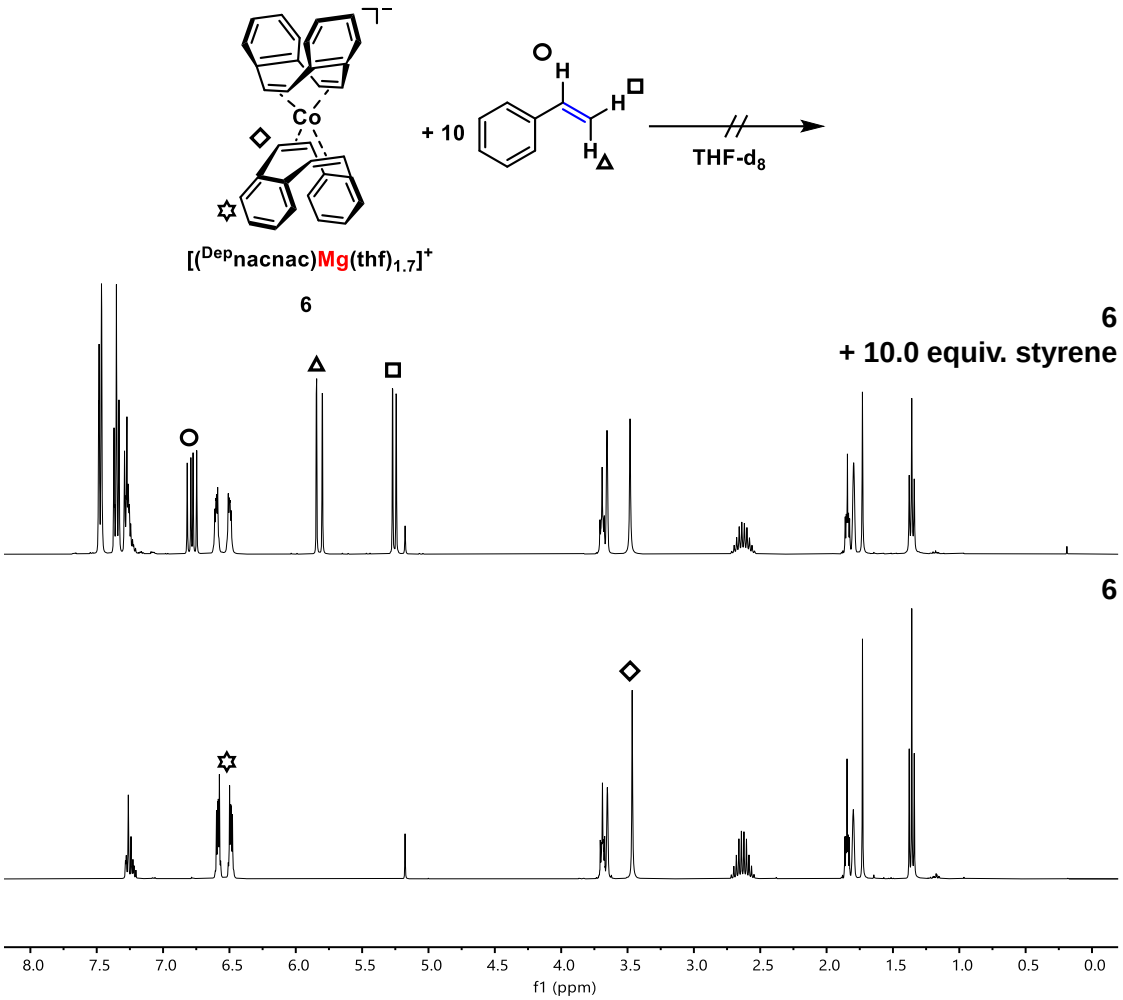

Figure S14. ^{1}H NMR spectroscopic monitoring (THF-d_8) of the reaction of [(^{Dep}nacnac)Mg][Co(η^4-dct)$_2$](thf)$_{1.7}$ (**6**) with 10.0 equiv. of styrene. Bottom: Pure sample of cobaltate **6** before addition. Top: After addition of styrene (10.0 equiv.) after +24 h at ambient temperature. ◊ and ☆: characteristic signals for coordinated dct. ◯, ☐ and Δ: styrene.

- *Radical probe experiment:*

(1-Cyclopropylvinyl)benzene (0.2 mmol in 0.5 mL THF) was submitted to the hydrogenation protocol A (3 mol% **4**, 2 bar H_2, 30 °C, 3 h). The reaction mixture was quenched with sat. NH_4Cl (1.0 mL), EtOAc (3.0 mL) was added, the phases separated, and the organic phase filtered over silica. The solution was dried over $MgSO_4$, again filtered and the solvent removed under reduced pressure. The colorless liquid residue was dissolved in $CDCl_3$ and submitted to ^{1}H NMR spectroscopic analysis (Figure S15).

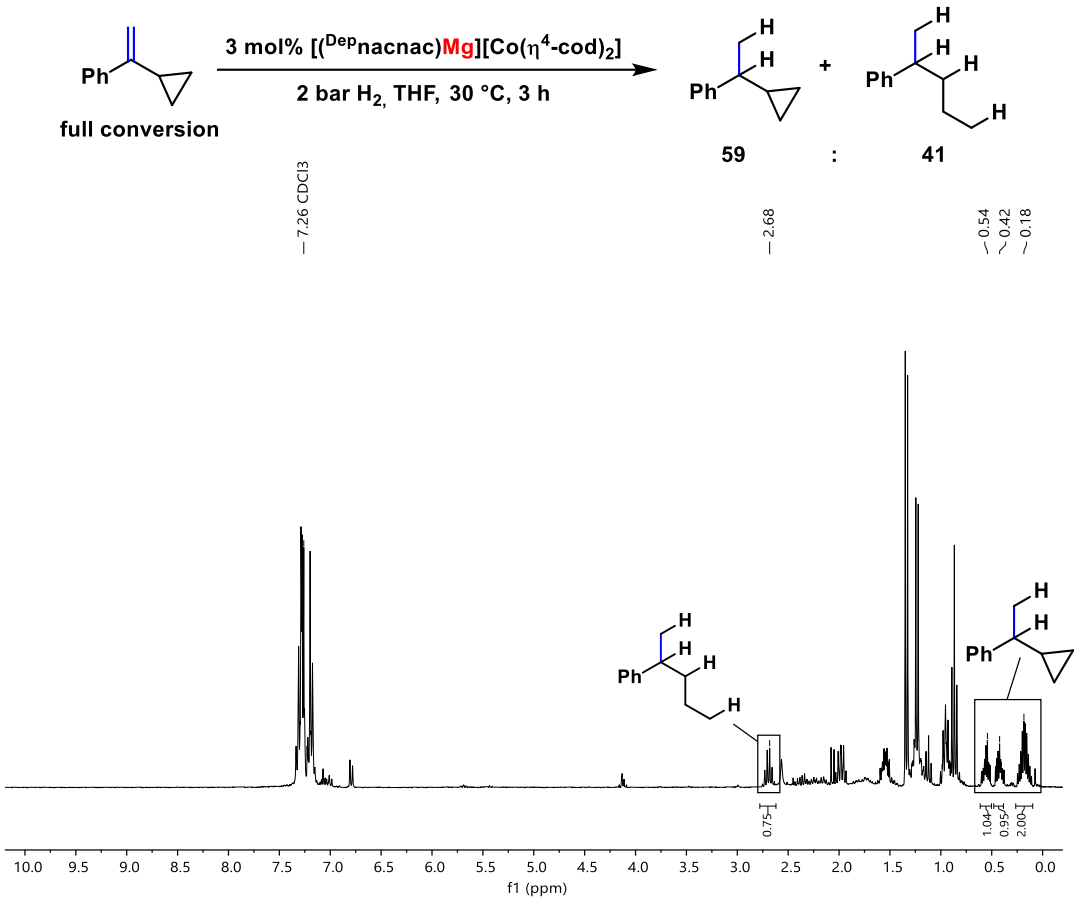

Figure S15. ^{1}H NMR spectrum (300.13 MHz, 298 K, $CDCl_3$) of the hydrogenation reaction of (1-cyclopropylvinyl)benzene with 3 mol% [(^{Dep}nacnac)Mg][Co(η^4-cod)$_2$] (**4**). Relative product ratios were determined by ^{1}H NMR analysis.

- *Isomerization reactions:*

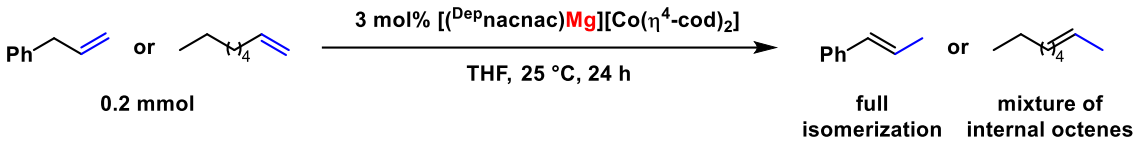

Figure S16. Isomerization reaction of allylbenzene or 1-octene with 3 mol% [(^{Dep}nacnac)Mg][Co(η^4-cod)$_2$] (**4**) in the absence of dihydrogen.

Allylbenzene or 1-octene (0.2 mmol in 0.5 mL THF) were stirred for 24 h at ambient temperature with 3 mol% [(^{Dep}nacnac)Mg][Co(η^4-cod)$_2$] (**4**) (Figure S16). The reaction mixture was quenched, filtered and directly subjected to GC-FID and GC-MS analysis. The chromatograms (GC-FID) for the isomerization experiments with allylbenzene (Figure S17) and 1-octene (Figure S18) are shown below. Peaks at 17.6 min and 24.7 min correspond to the internal standard *n*-pentadecane. The reaction products were verified by GC-MS analysis.

Allylbenzene:

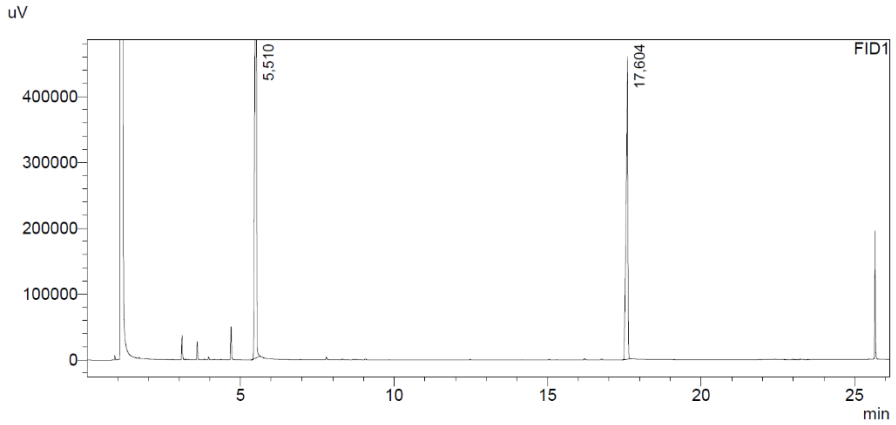

Figure S17. GC-FID chromatogram for the isomerization of allylbenzene.

Table S5. Analysis of the GC-FID chromatogram for the isomerization of allylbenzene.

Retention time [min]	Assignment	Peak area	Relative peak area [%]
5.510	α- or β-methylstyrene	3411671	>99

1-octene:

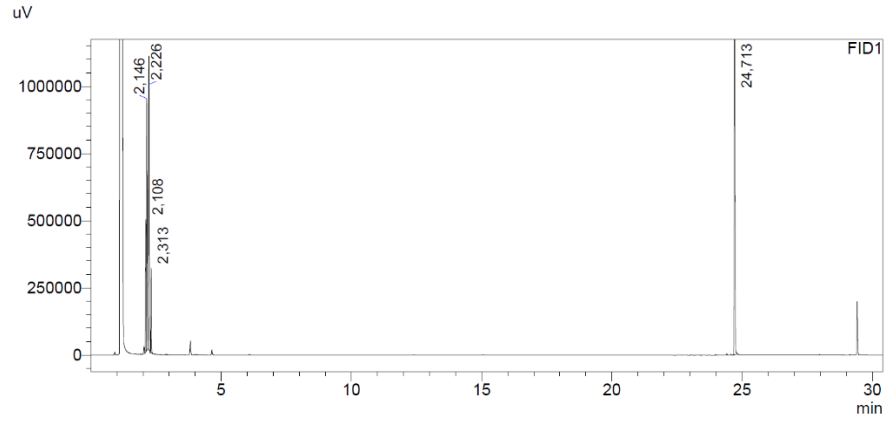

Figure S18. GC-FID chromatogram for the isomerization of 1-octene.

Table S6. Analysis of the GC-FID chromatogram for the isomerization of 1-octene.

Retention time [min]	Assignment	Peak area	Relative peak area [%]
2.108	Internal 3-octene	708312	16
2.146	Internal 3-octene	1728965	38
2.226	Internal 2-octene	1636262	36
2.313	Internal 2-octene	425150	3

- *Pre-catalyst hydrogenation experiments:*

The respective pre-catalyst **1** – **5** (0.025 mmol, dissolved in 0.5 mL THF) was subjected to 2 bar H_2 at 25 °C for 1 h in a high pressure reactor (Table S7). The reaction mixture was quenched, filtered and directly subjected to GC-FID and GC-MS analysis to determine the ligand hydrogenation (mixtures of cod, cod-H_2 and cod-H_4). Next to the targeted ligand hydrogenation (cod at 2.482 min, cod-H_2 at 2.288 min and cod-H_4 at 2.421 min), formation

of bicyclo[X.Y.Z]octane at 2.099 min was observed as indicated by GC-FID and GC-MS analysis as well as the formation of an additional unidentified species at 3.718 min, which could not be identified by additional GC-MS analysis (see Figure S19 for the direct hydrogenation of $[K(thf)_{0.2}][Co(\eta^4\text{-cod})_2]$ (**1**)). The exact structure of the formed bicycle could not be determined. The formation of bicyclo[X.Y.Z]octane and the unidentified species accounts for the sub-quantitative amount of the ligand hydrogenation mixture (between 74-89%).

Table S7. Hydrogenation of olefin cobaltates **1 – 5**.

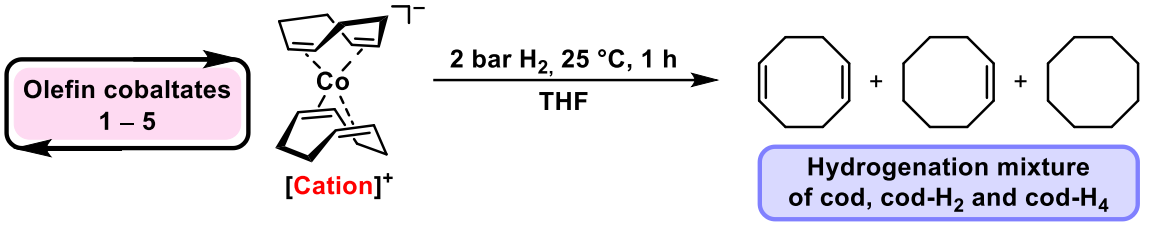

Entry	Pre-Cat.	[K(thf)$_{0.2}$]$^+$	[Na(thf)$_{1.5}$]$^+$	[Li(thf)$_2$]$^+$	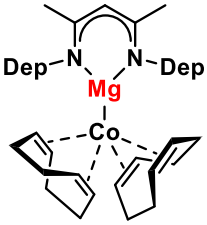	[N(^{n}Bu)$_4$]$^+$
		1	**2**	**3**	**4**	**5**
1	cod	59	58	33	32	88
2	cod-H$_2$	5	8	10	13	1
3	cod-H$_4$	10	21	41	31	0
4	H$_2$ Incorp.	12	24	45	38	1

[a] Standard conditions: 0.025 mmol pre-catalyst (0.05 mol/L THF). Substance ratios [%] and H$_2$ incorporation [%] were determined by quantitative GC-FID analysis vs. internal *n*-pentadecane as share of the overall hydrogenation mixture quantity. cod = 1,5-cyclooctadiene. cod-H$_2$ = cyclooctene. cod-H$_4$ = cyclooctane. Total hydrogenation mixture does not account to 100% as further (in part unidentified) by-products are formed.

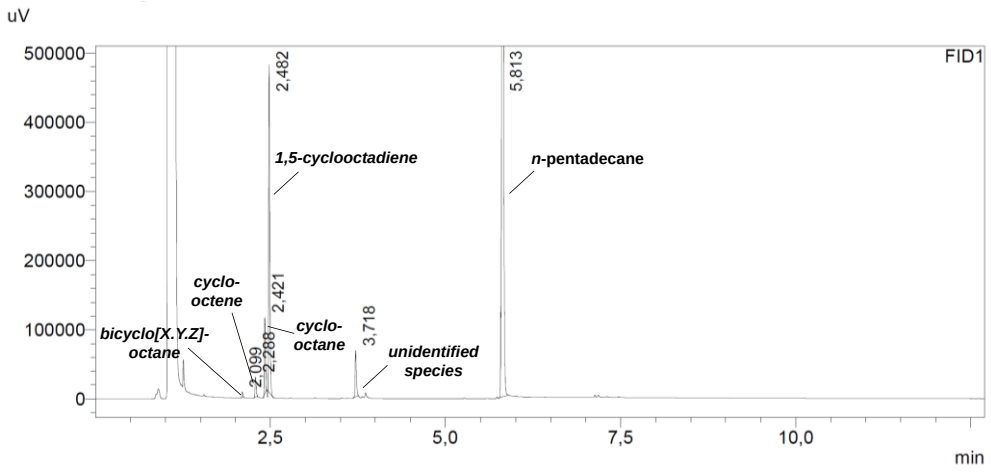

Figure S19. GC-FID chromatogram for the direct hydrogenation of $[K(thf)_{0.2}][Co(\eta^4\text{-cod})_2]$ (**1**).

2.4.6 NMR Spectroscopic Data

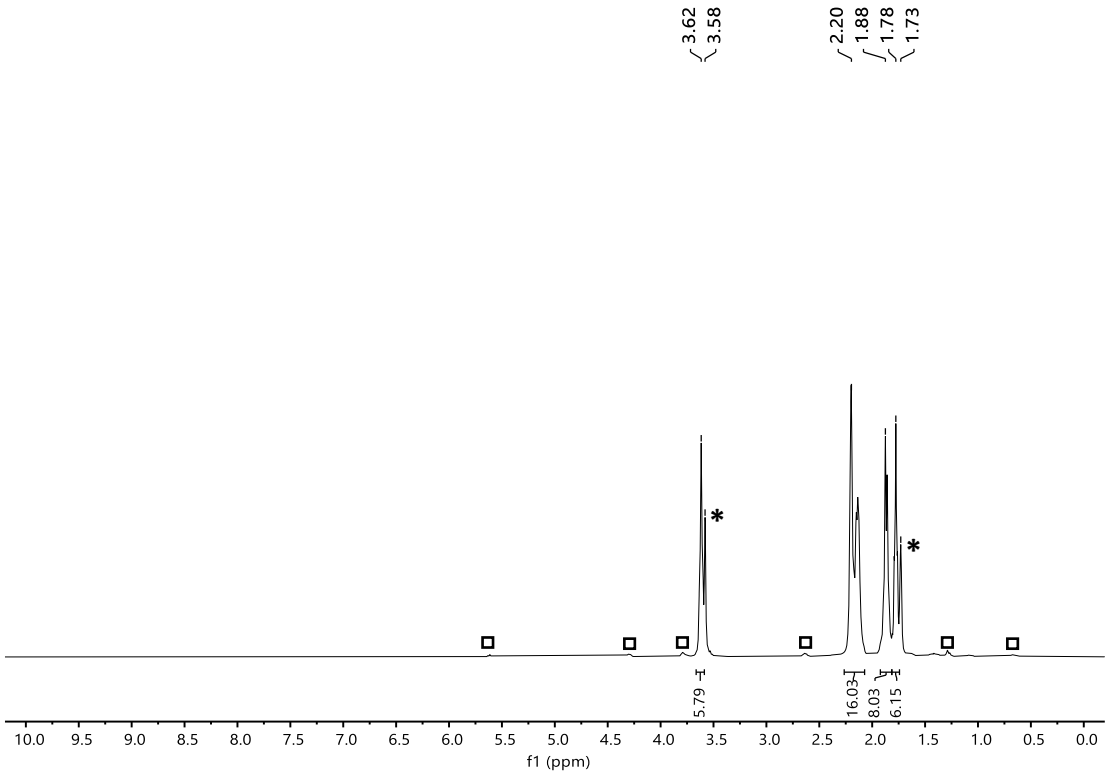

Figure S20. ^{1}H NMR spectrum (400.13 MHz, 298 K, THF-d_8) of **2**. *: THF-d_8. □: unidentified impurities.

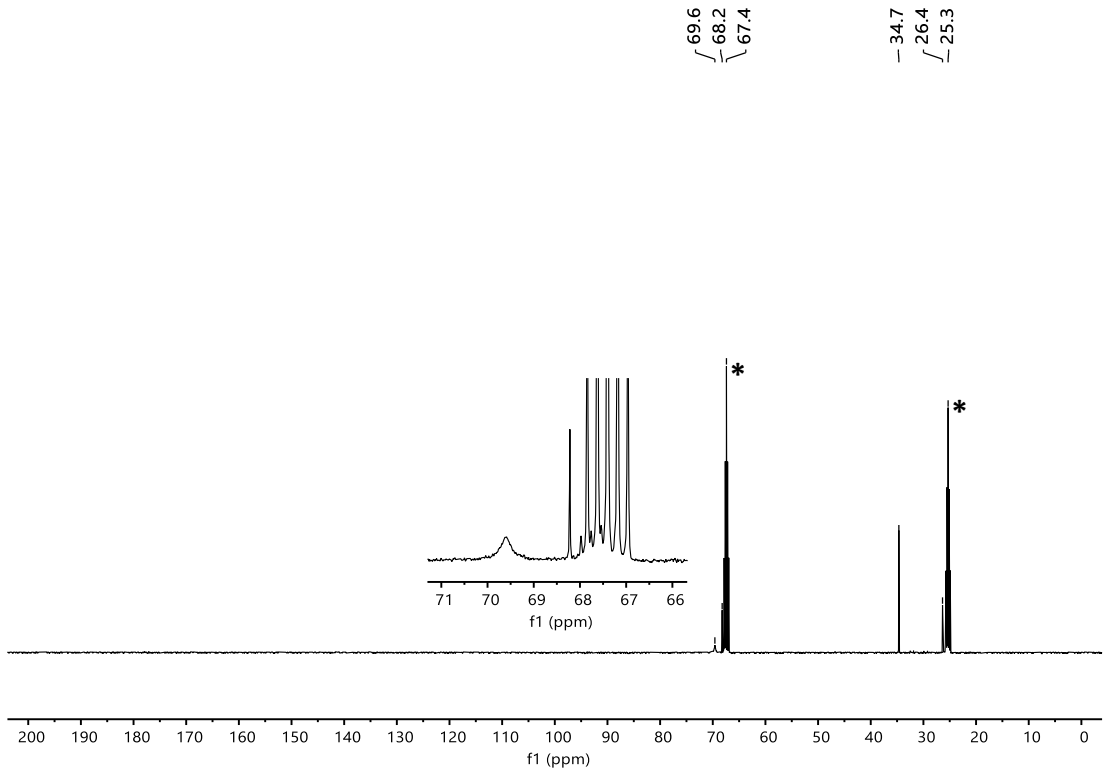

Figure S21. ^{13}C{^{1}H} NMR spectrum (100.61 MHz, 298 K, THF-d_8) of **2**. *: THF-d_8.

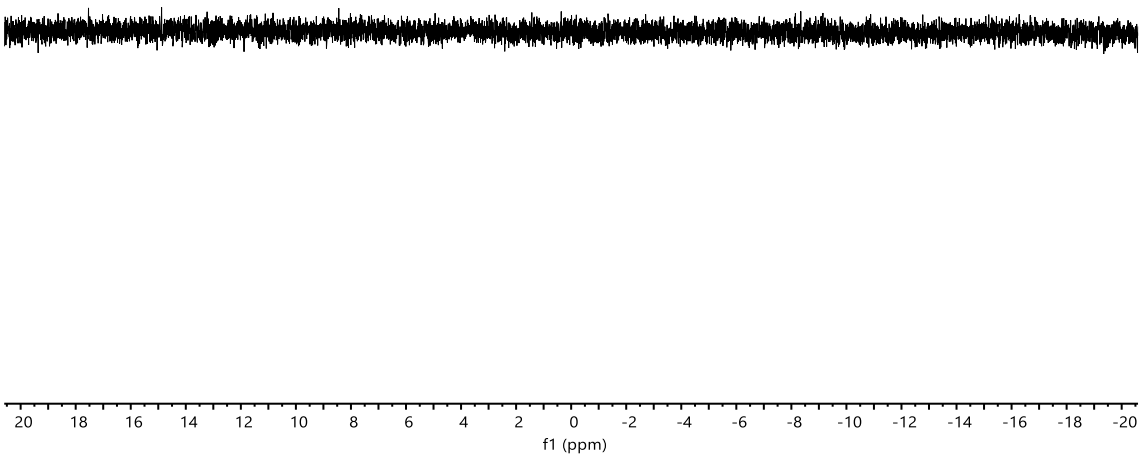

Figure S22. $^{7}Li\{^{1}H\}$ NMR spectrum (155.46 MHz, 298 K, THF-d_8) of **2**.

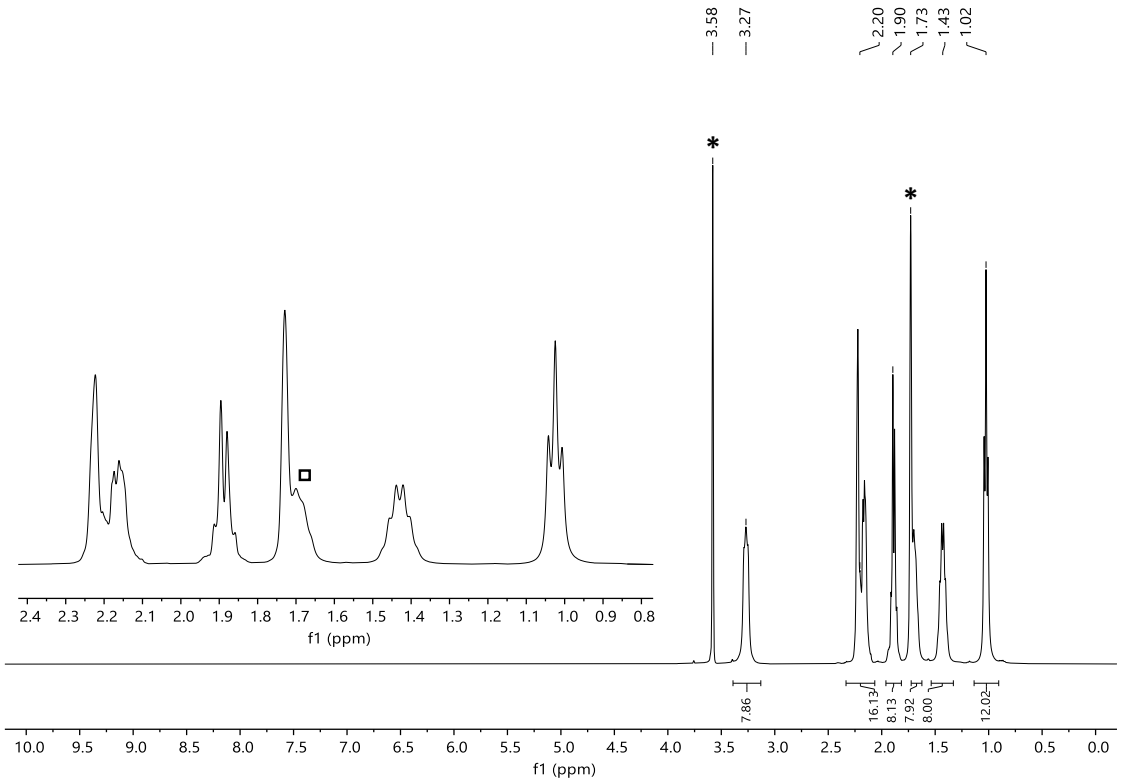

Figure S23. ^{1}H NMR spectrum (400.13 MHz, 298 K, THF-d_8) of **5**. *: THF-d_8. □ : signal overlap with residual protonated THF.

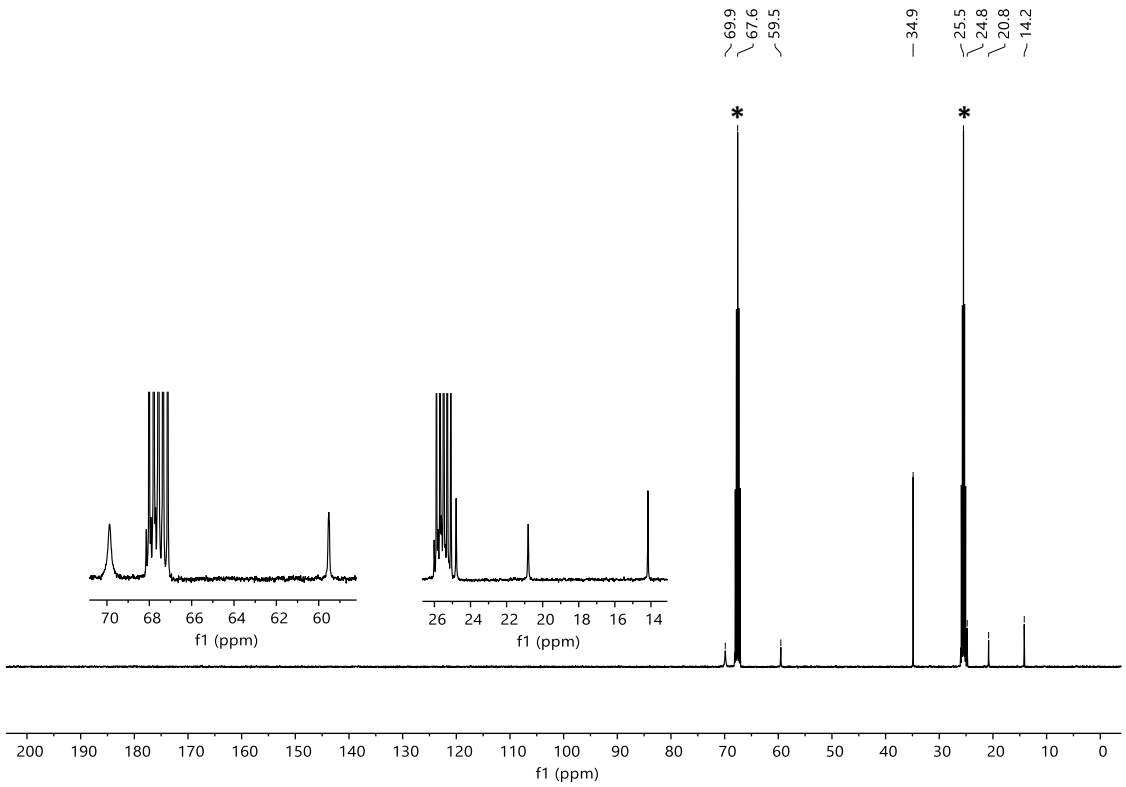

Figure S24. $^{13}C\{^{1}H\}$ NMR spectrum (100.61 MHz, 298 K, THF-d_8) of **5**. *: THF-d_8.

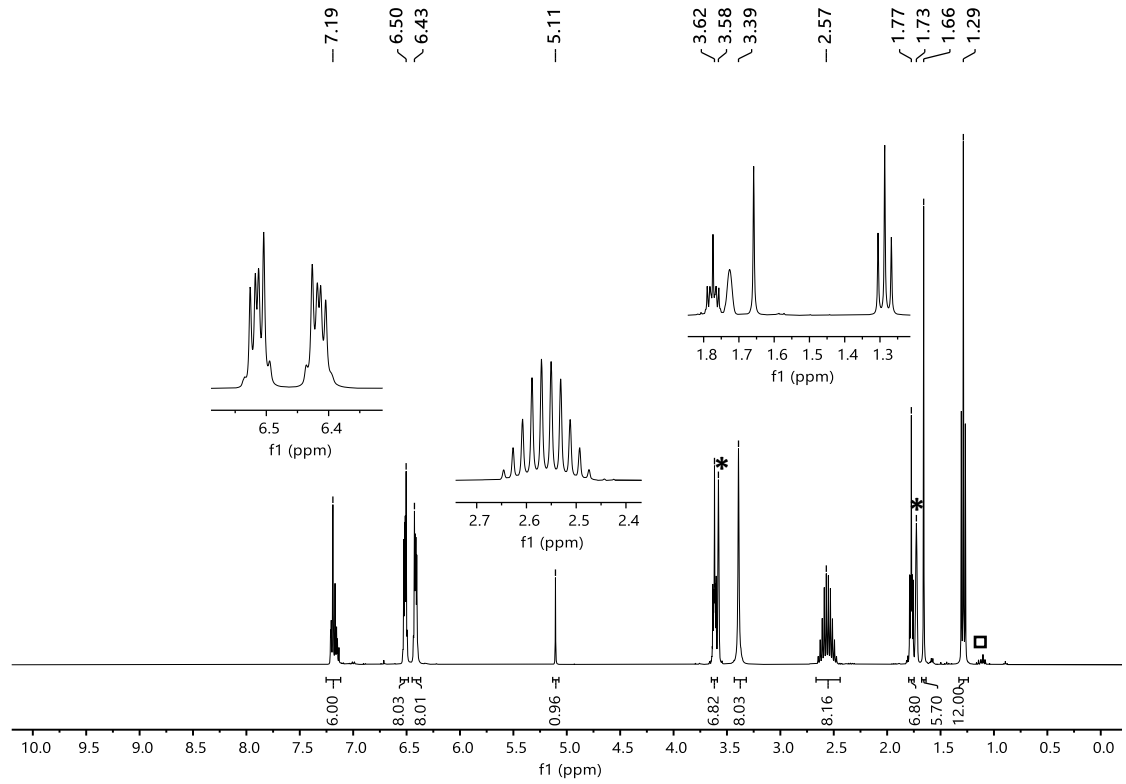

Figure S25. ^{1}H NMR spectrum (400.13 MHz, 298 K, THF-d_8) of **6**. *: THF-d_8. □: unidentified impurity.

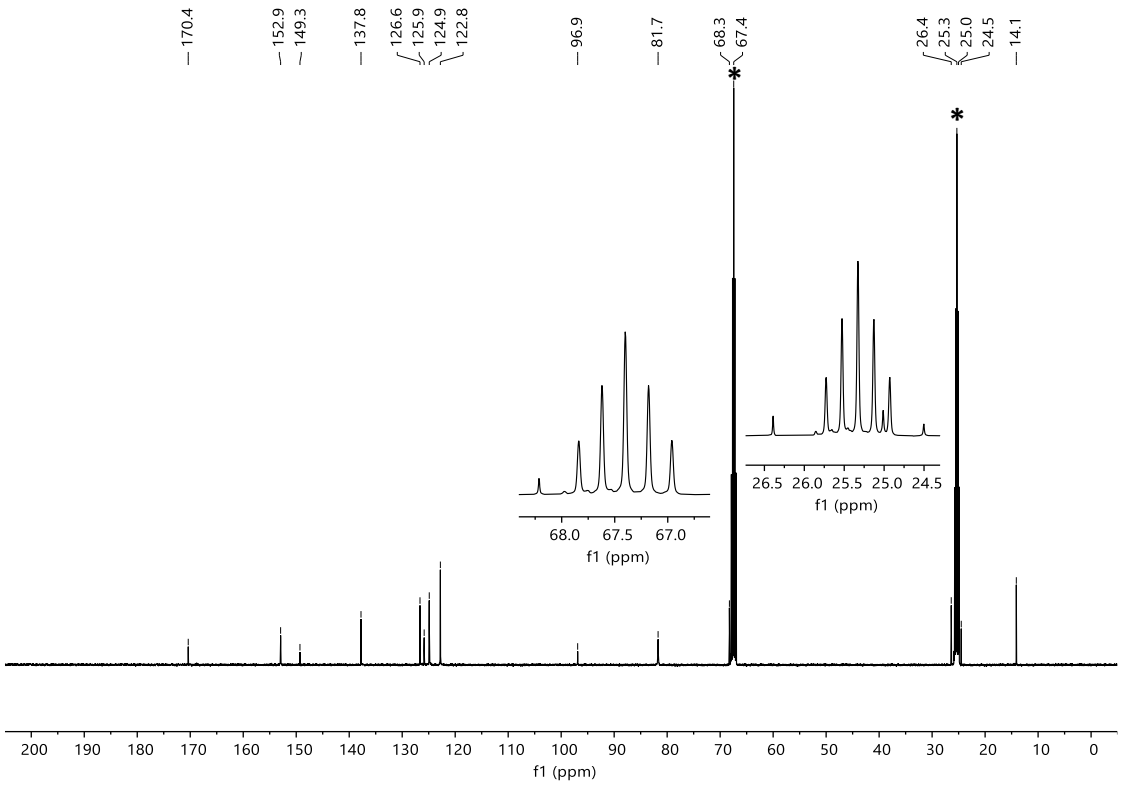

Figure S26. $^{13}C\{^{1}H\}$ NMR spectrum (100.61 MHz, 298 K, THF-d_8) of **6**. *: THF-d_8.

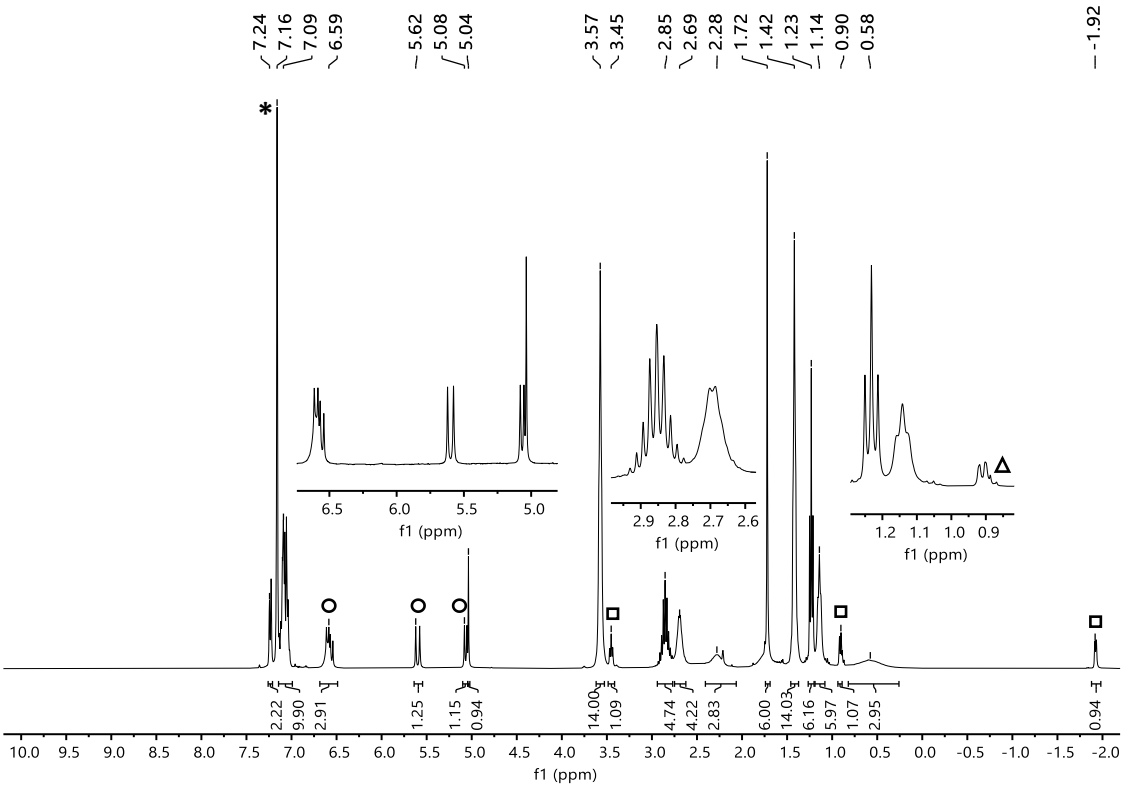

Figure S27. ^{1}H NMR spectrum (400.13 MHz, 298 K, C_6D_6) of **7**. *: C_6D_6. ◯: olefinic signals of styrene 1. □ : olefinic signals of styrene 2. Δ: residual *n*-hexane.

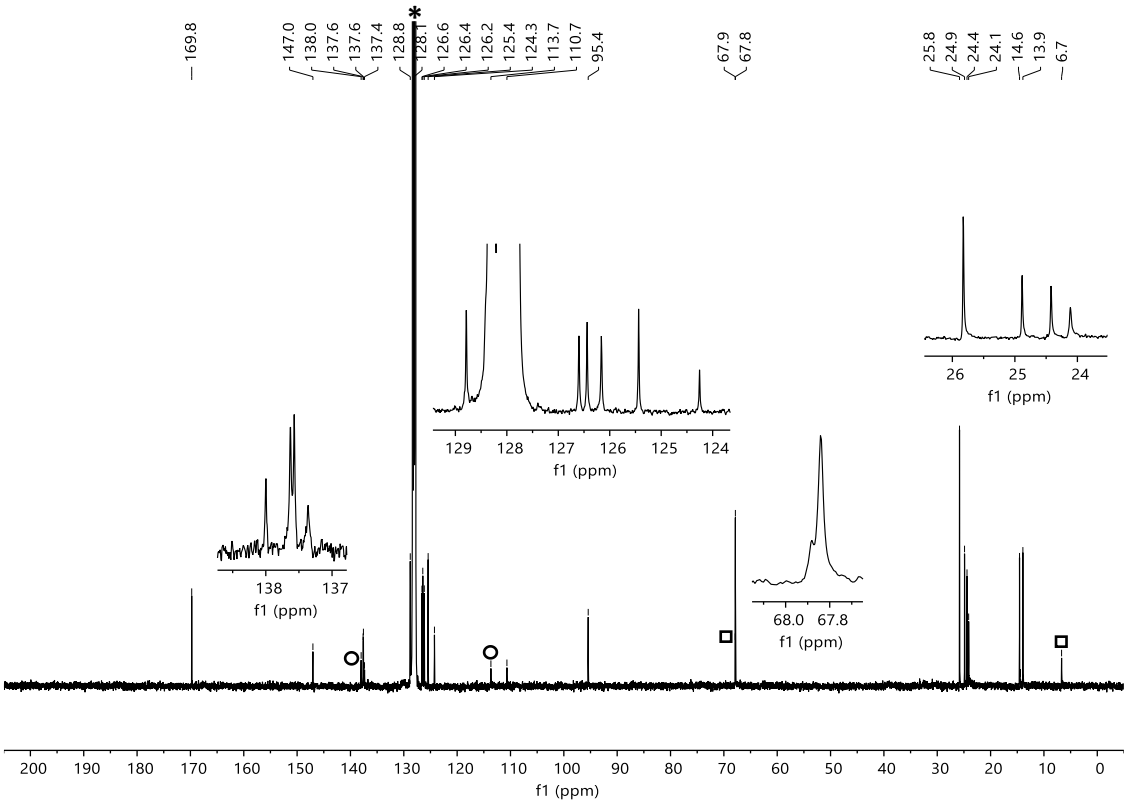

Figure S28. $^{13}C\{^{1}H\}$ NMR spectrum (100.61 MHz, 298 K, C_6D_6) of **7**. *: C_6D_6. ◯: olefinic signals of styrene 1. ☐ : olefinic signals of styrene 2.

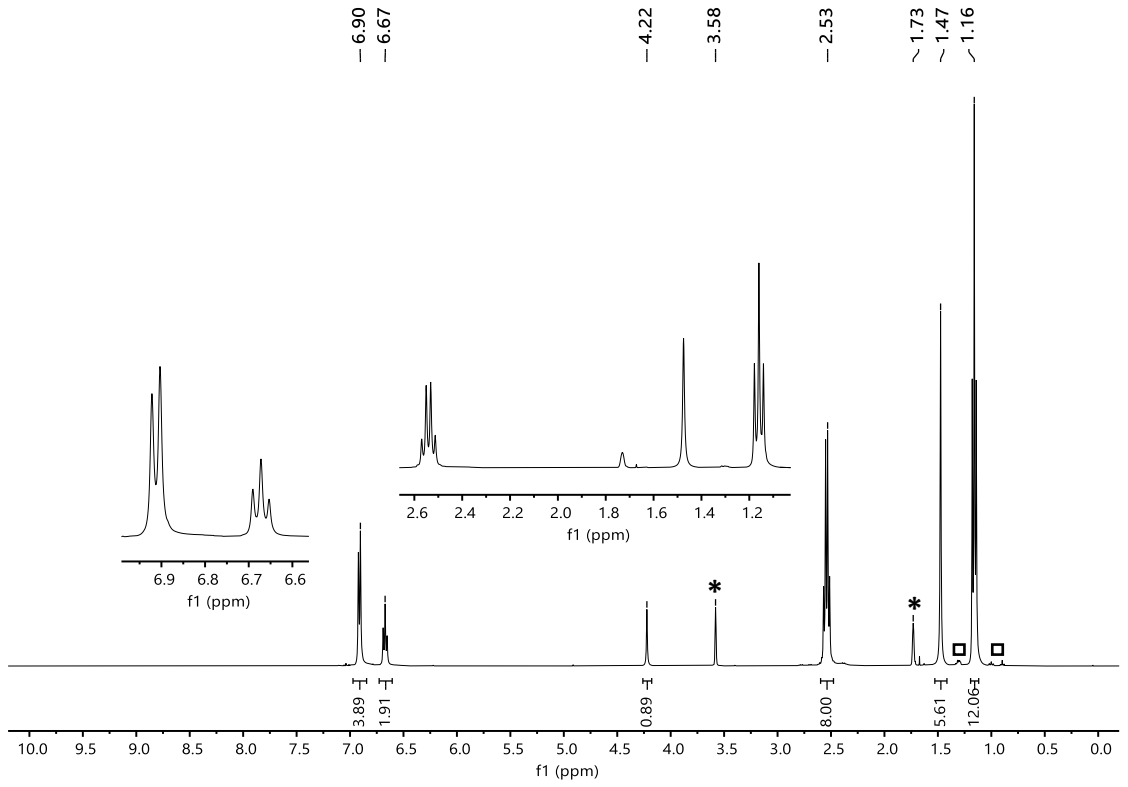

Figure S29. ^{1}H NMR spectrum (400.13 MHz, 298 K, THF-d_8) of K(^{Dep}nacnac). *: THF-d_8. ☐ : residual *n*-hexane and unidentified impurity.

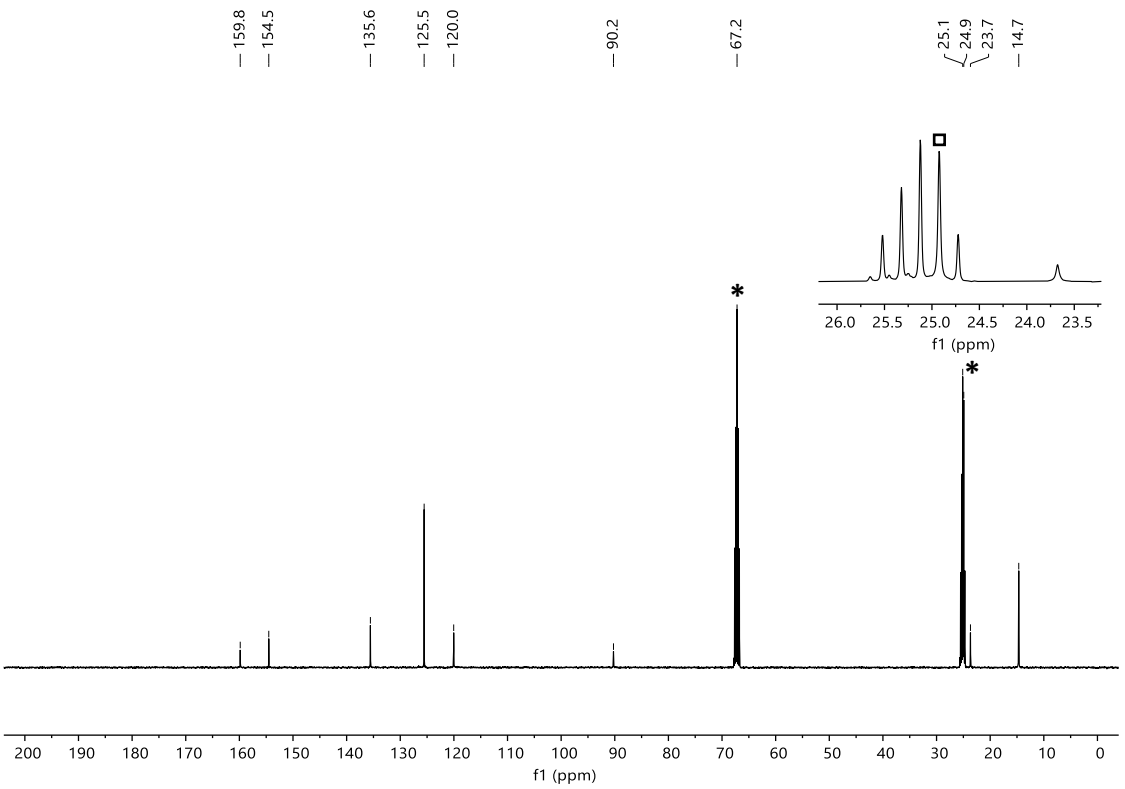

Figure S30. $^{13}C\{^{1}H\}$ NMR spectrum (100.61 MHz, 298 K, THF-d_8) of K(^{Dep}nacnac). *: THF-d_8. □ : signal of K(^{Dep}nacnac) overlapping with residual THF peak.

2.4.7 Single-Crystal X-ray Diffraction Data

The single-crystal X-ray diffraction data were recorded on Rigaku Synergy DW or GV1000 Titan^{S2} diffractometers with Cu-K_α radiation (λ= 1.54184 Å). Crystals were selected under mineral oil, mounted on micromount loops and quench-cooled using an Oxford Cryosystems open flow N_2 cooling device. Either semi-empirical multi-scan absorption correction[35] or analytical ones[36] were applied to the data. The structures were solved with SHELXT[37] solution program using dual methods and by using Olex2 as the graphical interface.[38] The models were refined with ShelXL[37] using full matrix least squares minimization on F^2.[39] The hydrogen atoms were located in idealized positions and refined isotropically with a riding model. The disorder in **6** and **7** was treated with soft displacement parameter and geometrical restraints.

Table S8. Crystallographic data and structure refinement for compounds **2**, **5**, **6**, **7** and **[(Depnacnac)Mg(OMe)]2**.

Compound	**2**	**5**	**6**	**7**	**[(Depnacnac)Mg(OMe)]2**
CCDC	2294851	2294850	2294853	2294808	2294852
Formula	$C_{80}H_{144}Co_2Na_2O_{12}$	$C_{32}H_{60}CoN$	$C_{65}H_{73}CoMgN_2O_2$	$C_{69}H_{101}CoMgN_2O_5$	$C_{52}H_{72}Mg_2N_4O_2$
$D_{calc.}$/ g cm^{-3}	1.232	1.153	1.164	1.227	1.137
ρ/mm^{-1}	3.859	4.625	2.800	2.061	0.759
Formula Weight	1461.78	517.74	997.49	1121.75	833.75
Color	dull yellowish brown	clear light yellow	clear orange	clear reddish orange	clear light yellow
Shape	block	block	block	block	block
Size/mm^3	0.489 x 0.456 x 0.343	0.205 x 0.156 x 0.136	0.133 x 0.11 x 0.098	0.628 x 0.429 x 0.246	0.859 x 0.569 x 0.339
T/K	100(1)	123(1)	123(1)	123(1)	123(1)
Crystal System	monoclinic	monoclinic	tetragonal	triclinic	monoclinic
Space Group	$P2_1/c$	$I2/a$	$P4_2/n$	P-1	$P2_1/c$
a/Å	16.7184(2)	19.82900(10)	13.6368(1)	12.4880(2)	17.8168(2)
b/Å	27.8917(3)	11.51220(10)	13.6368(1)	13.3974(3)	20.1947(2)
c/Å	17.8808(2)	26.4822(2)	30.6119(3)	19.0437(3)	14.7818(2)
α/°	90	90	90	97.616(2)	90
β/°	109.0730(10)	99.3020(10)	90	95.5500(10)	113.6650(10)
γ/°	90	90	90	104.078(2)	90
V/Å^3	7880.17(16)	5965.74(8)	5692.66(10)	3035.50(10)	4871.31(10)
Z	4	8	4	2	4
Z'	1	1	0.5	1	1
Wavelength/Å	1.54184	1.54184	1.54184	1.39222	1.54184
Radiation type	Cu Kα	Cu Kα	Cu Kα	Cu Kβ	Cu Kα
2θ range for data collection	5.594 to 146.53	6.764 to 150.512	5.774 to 146.13	4.266 to 120.022	5.416 to 151.76
Index ranges	-20 ≤ h ≤ 16, -34 ≤ k ≤ 33, -22 ≤ l ≤ 21	-22 ≤ h ≤ 24, -14 ≤ k ≤ 14, -33 ≤ l ≤ 32	-11 ≤ h ≤ 16, -15 ≤ k ≤ 16, -37 ≤ l ≤ 37	-15 ≤ h ≤ 15, 15 ≤ k ≤ 16, -23 ≤ l ≤ 23	-19 ≤ h ≤ 22, -25 ≤ k ≤ 25, -18 ≤ l ≤ 18
Reflections collected	72986	43368	5580	45639	10022
Independent Reflections	15118 [R_{int} = 0.0386, R_{sigma} = 0.0286]	6112 [R_{int} = 0.0315, R_{sigma} = 0.0183]	5580 [R_{int} = 0.0409, R_{sigma} = 0.0211]	11975 [R_{int} = 0.0380, R_{sigma} = 0.0297]	10022 [R_{int} = 0.0580, R_{sigma} = 0.0202]
R_{int}	0.0386	0.0315	0.0409	0.0380	0.0580
Parameters	934	311	407	755	555
Restraints	36	0	204	102	0
Largest Peak	0.41	0.213	0.31	0.97	0.76
Deepest Hole	-0.36	-0.298	-0.35	-0.49	-0.38
GooF	1.059	1.074	1.074	1.043	1.014
wR_2 (all data)	0.1277	0.0833	0.1561	0.1108	0.1327
wR_2	0.01230	0.0824	0.1497	0.1081	0.1306
R_1 (all data)	0.0545	0.0327	0.0617	0.0446	0.0504
R_1	0.0453	0.0311	0.0534	0.0413	0.0475

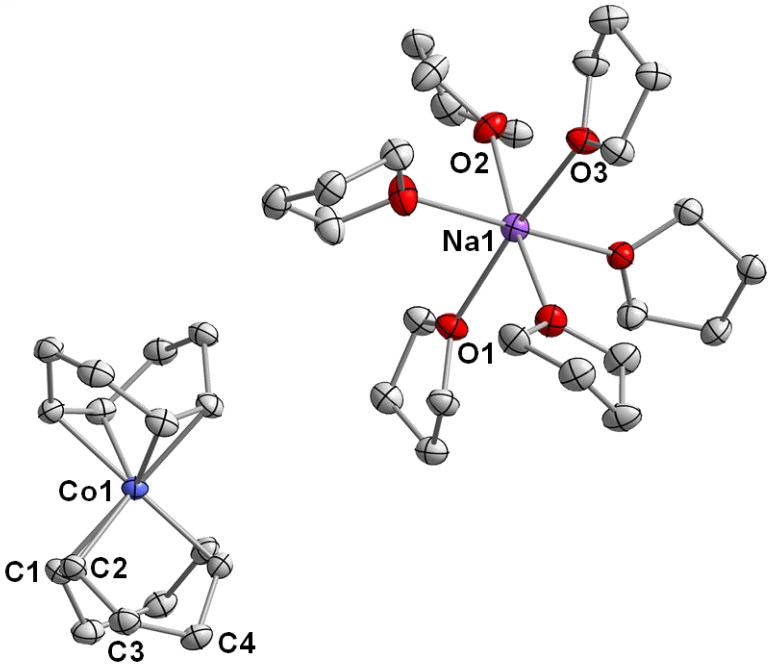

Figure S31. Molecular structure of **2** in the solid state. Ellipsoids are set at the 40% probability level. Hydrogen atoms were omitted for clarity. Selected bond lengths [Å] and angles [°]: Na1–O1: 2.4440(15), Na1–Co1: 8.2197(7), Co1–C1: 2.034(2), Co1–C2: 2.0401(19), C1–C2: 1.419(3), C2–C3: 1.511(3), C3–C4: 1.535(3), O2–Na1–O1: 95.77(6), O1–Na1–O3: 172.85(6), C1–Co1–C2: 40.76(8), C1–C2–C3: 123.90(18).

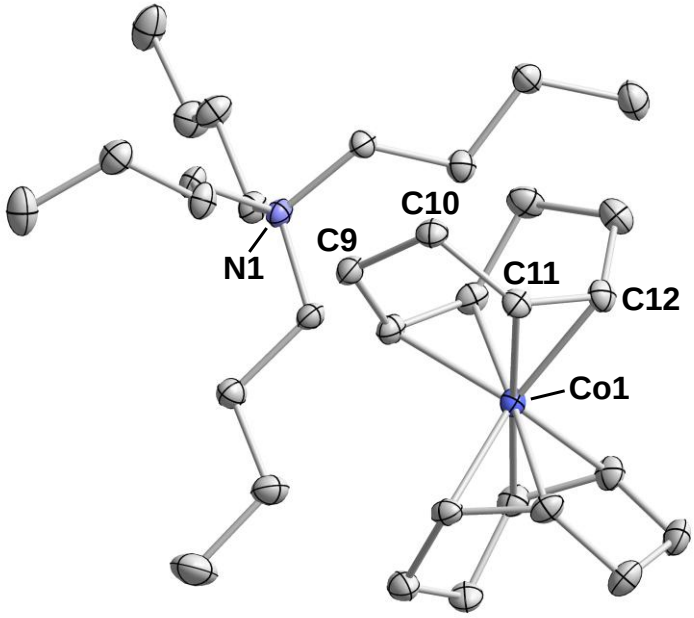

Figure S32. Molecular structure of **5** in the solid state. Ellipsoids are set at the 40% probability level. Hydrogen atoms were omitted for clarity. Selected bond lengths [Å] and angles [°]: N1–Co1: 6.2068(11), Co1–C11: 2.0443(13), Co1–C12: 2.0474(13), C11–C12: 1.4152(19), C10–C11: 1.5194(19), C9–C10: 1.5371(19), C11–Co1–C12: 40.47(5), C10–C11–C12: 125.66(12).

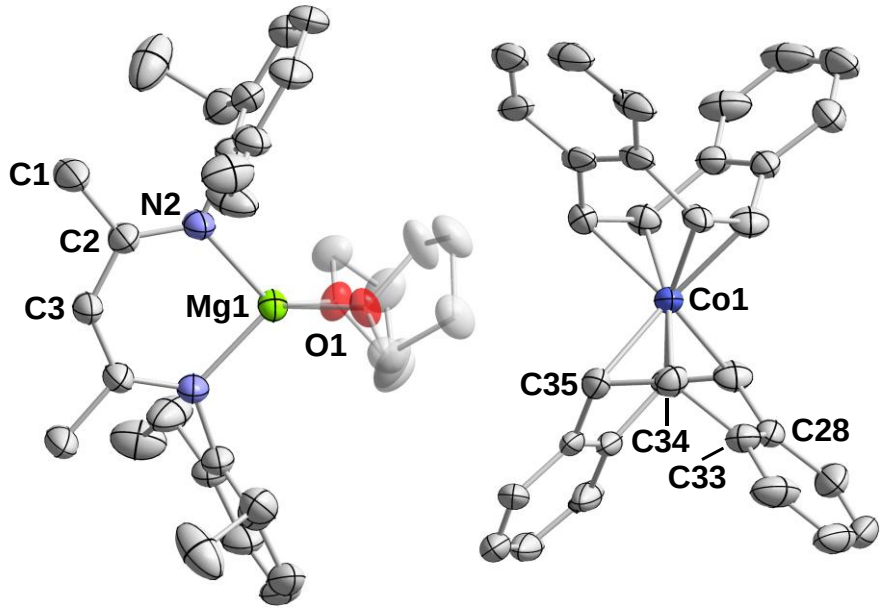

Figure S33. Molecular structure of **6** in the solid state (part 0 and 2 depicted). Ellipsoids are set at the 40% probability level. Hydrogen atoms were omitted for clarity. Selected bond lengths [Å] and angles [°]: Mg1–O1: 1.9924(16), Mg1–N2: 2.0088(19), C2–N2: 1.337(3), C1–C2: 1.502(3), C2–C3: 1.397(3), Co1–C35: 2.074(8), Co1–C34: 1.906(11), C34–C35: 1.406(11), C33–C34: 1.611(11), C28–C33: 1.375(3), N2–Mg1–N2^{1}: 95.22(11), O1–Mg1–O1^{1}: 92.86(9), N2–Mg1–O1: 109.75(8), C34–Co1–C35: 41.1(3), C33–C34–C35: 130.4(8).

2.4.8 Computational Studies

2.4.8.1 Molecular Dynamics (MD) Simulations

All MD simulations were performed with the software GROMACS 2021.5[40],[41] after equilibration by use of the Leapfrog algorithm with 10^8 time steps, each 2 fs. The force field generation and parametrization details can be found on https://onlinelibrary.wiley.com/doi/full/10.1002/anie.202315381 (Supporting Information). The V-rescale thermostat was used to keep the temperature constant at 298 K, the Berendsen barostat was used to keep the pressure constant at 1.0 bar. A set of 20 anionic complex molecules [Co(η^4-cod)(η^2-styrene)H_2]$^-$ (**11$_A$**) and 20 cations [M(thf)$_n$]$^+$ (M = K, Na, Li, (^{Dep}nacnac)Mg) were simulated in minimum 500 THF molecules. Each simulation run was checked for total energy conservation, constant temperature, and constant pressure with the GROMACS integrated "energy" tool.

Radial distribution functions were calculated using the GROMACS integrated "rdf" tool (Figure S34). The radial distribution function (M–Co distance) for ion pair structures [M(thf)$_n$][Co(η^4-cod)(η^2-styrene)H_2] (**11$_{K\text{-}Mg}$**) (M = K, Na, Li, (^{Dep}nacnac)Mg) shows three decreasing, narrow peaks for the alkali metal cobaltates following the trend: K (3.43 Å) > Na (3.02 Å) > Li (2.80 Å). The magnesium cobaltate is located between the lithium and sodium cobaltate at 2.93 Å. Following the approach described above, a set of 20 anionic complex molecules [Co(η^4-cod)(η^2-styrene)(H)(CH_2CH_2Ph)]$^-$ (**14$_A$**) and 20 cations [M(thf)$_n$]$^+$ [M = K, Na, Li, (^{Dep}nacnac)Mg] were simulated in minimum 500 THF molecules.

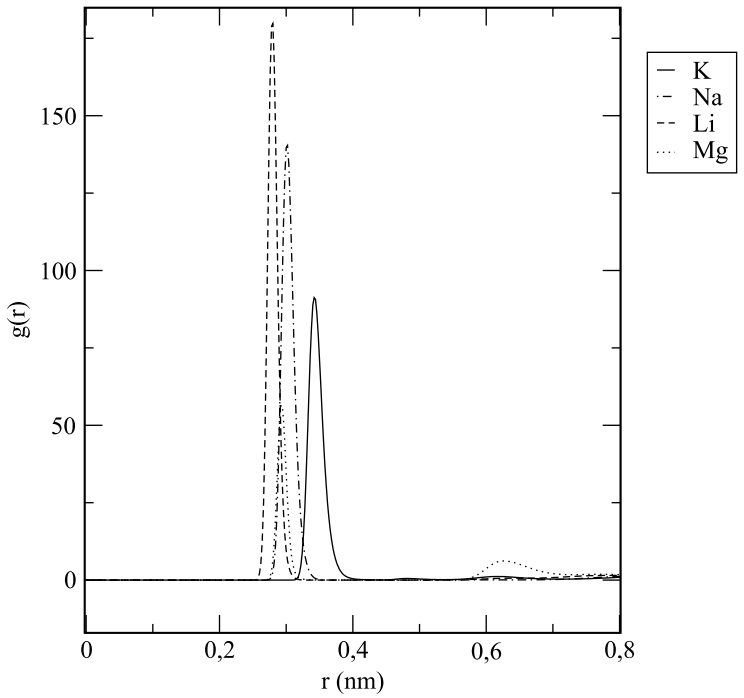

Figure S34. Radial distribution function (M–Co distance) for ion pair structures $[M(thf)_n][Co(\eta^4\text{-cod})(\eta^2\text{-styrene})H_2]$ (**$11_{K\text{-}Mg}$**) (M = K, Na, Li, (^{Dep}nacnac)Mg).

Radial distribution functions were calculated using the GROMACS integrated "rdf" tool (Figure S35). The radial distribution function (M–Co distance) for ion pair structures $[M(thf)_n][Co(\eta^4\text{-cod})(\eta^2\text{-styrene})(H)(CH_2CH_2Ph)]$ (**$14_{K\text{-}Mg}$**) (M = K, Na, Li, (^{Dep}nacnac)Mg) shows a widened distribution of ion pair arrangements with M–Co distances ranging between ca. 3.0 Å and 12.0 Å. Relevant ion pair structures are intimate ion pairs and fully solvated ion pairs. The observed structures are discussed in further detail in section 2.4.8.2.

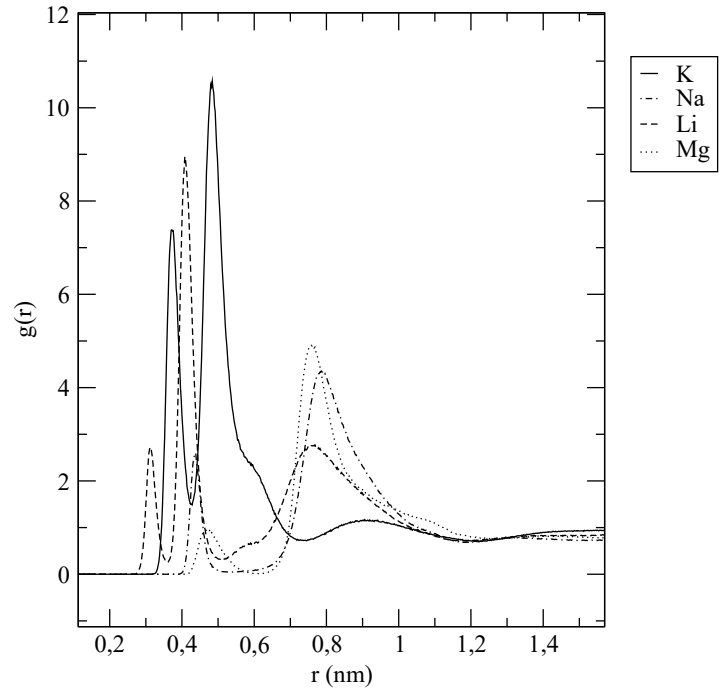

Figure S35. Radial distribution function (M–Co distance) for ion pair structures $[M(thf)_n][Co(\eta^4\text{-cod})(\eta^2\text{-styrene})(H)(CH_2CH_2Ph)]$ (**$14_{K\text{-}Mg}$**) (M = K, Na, Li, (^{Dep}nacnac)Mg).

2.4.8.2 Density Functional Theory (DFT) Calculations

- *General Considerations*

All calculations were performed with the Orca 5.0.3[42] quantum chemistry program package at the r²SCAN-3c[43] level of theory. Stationary points were confirmed as local minima (no imaginary frequencies) or transition states (only one imaginary frequency) by frequency analysis. The anion-only reaction profile for the hydrogenation of styrene with anionic complex [Co(η⁴-cod)(η²-styrene)₂]⁻ (**7**$_{\mathbf{A}}$) was calculated with implicit solvation (r²SCAN-3c, CPCM[THF]; see Scheme 3, main part). The migratory insertion step was calculated with direct participation of the counterion and explicit THF solvent coordination (r²SCAN-3c; explicit THF coordination derived from initial MD simulations, see above). Further molecular properties were analyzed using natural bond orbital (NBO 7.0) analyses[44] and NCI analyses (multiwfn 3.8[45]) for non-covalent interactions. Shown iso-surfaces were plotted with VMD 1.9.3.[46] Rendered transition state structures [**12**$_{\mathbf{K\text{-}Mg}}$]‡ were plotted with CYLview.[47]

- *Coordination Geometries for the Migratory Insertion Step with Participation of the Counterion*

In extension to Figure 5 (main part), all transition state geometries for the migratory insertion step including the counterion are displayed in Figure S36 (additional structural data in Table S9).

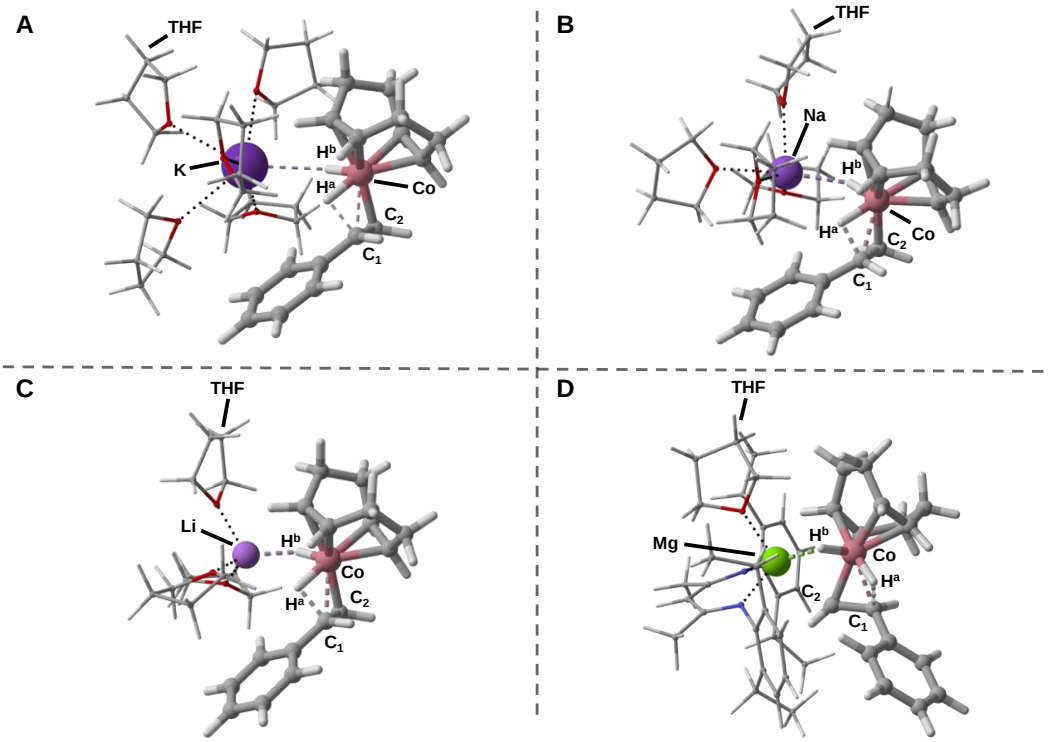

Figure S36. Transition state structures for the migratory insertion step with cation participation. A: [K(thf)₅][Co(η⁴-cod)(η²-styrene)H₂] ([**12**$_{\mathbf{K}}$]‡). B: [Na(thf)₄][Co(η⁴-cod)(η²-styrene)H₂] ([**12**$_{\mathbf{Na}}$]‡). C: [Li(thf)₃][Co(η⁴-cod)(η²-styrene)H₂] ([**12**$_{\mathbf{Li}}$]‡). D: [($^{\mathrm{Dep}}$nacnac)Mg(thf)][Co(η⁴-cod)(η²-styrene)H₂] ([**12**$_{\mathbf{Mg}}$]‡).

Table S9. Key parameters for the reactivity differences for the migratory insertion step based on ground state structures $\mathbf{11_A}$ and $\mathbf{11_{K\text{-}Mg}}$ and transition state structures $[\mathbf{12_A}]^{‡}$ and $[\mathbf{12_{K\text{-}Mg}}]^{‡}$.

Entry		A	B	C	D	E
	$\mathbf{M^{n+}}$	**none**	$\mathbf{K^+}$	$\mathbf{Na^+}$	$\mathbf{Li^+}$	$\mathbf{Mg^{2+}}$
1	**$\Delta G^{≠}$ ([12]‡) [kcal/mol]**	19.0[a]	17.0	17.0	15.5	15.5
2	**$\Delta_R G$ (11→13) [kcal/mol]**	11.2[a]	8.4	11.2	8.2	7.2
2	**BO ($Co–C_2$)[b]**	0.95	0.95	0.95	0.97	0.90
3	**BO ($C_1–H^a$)[b]**	0.54	0.60	0.61	0.61	0.55
4	**Δδ (11)[c]**	0.07	0.14	0.13	0.16	0.16
5	**Δδ ([12]‡)[b]**	0.14	0.58	0.55	0.55	0.64
6	**r ($M^{n+}–H^b$; [12]‡) [Å]**	/	2.58	2.15	1.81	1.96

[a] Gibbs free energy derived from the anion-only reaction profile calculations (see the main part in Scheme 3). [b] Pauling bond orders using c = 0.6 for TS structures. [c] Polarization of C–H bonds expressed by the differences of the natural population analysis (NPA) charges at H^a and H^b.

- *Analysis of the Counterion Influence on the Reductive Elimination Step*

To determine whether coordination of the substrate to the cation can affect other elementary steps in the catalytic cycle, the reductive elimination ($\mathbf{14_A} \rightarrow [\mathbf{15_A}]^{‡}$) was analyzed following the MD/DFT approach (see above). In contrast to the MD simulations for $\mathbf{11_{K\text{-}Mg}}$ (see Figure S34 for the RDFs), the RDF for ion pair structures $[M(thf)_n][Co(\eta^4\text{-cod})(\eta^2\text{-styrene})(H)(CH_2CH_2Ph)]$ (M = K, Na, Li, (^{Dep}nacnac)Mg; $\mathbf{14_{K\text{-}Mg}}$) shows a widened distribution of ion pairing with M–Co distances ranging between ca. 3.0 Å and 12.0 Å. For the Mg and the Li salts of **14**, the RDF provided two main assemblies; one that can be described as a contact ion pair, featuring a cation-π interaction with the η^2-bound styrene molecule (Figure S37A) and another that shows solvent-separated ions.
In contrast, the sodium salt $\mathbf{14_{Na}}$ only appears as a solvent-separated ion pair with a fully solvated sodium counterion $[Na(thf)_6]^+$ (Figure S37B; the ion pair structure was assessed both by RDF analysis and manually checking the MD simulation). The potassium salt $\mathbf{14_K}$ exhibits a distinct ion pair arrangement, showing close ion pairing involving one cobalt complex and one potassium cation, but also some ion triples consisting of one potassium cation and two cobalt complexes.
The two ion pair structures [(^{Dep}nacnac)Mg][Co(η^4-cod)(η^2-styrene)(H)(CH_2CH_2Ph)] ($\mathbf{14_{Mg}}$) and $[Na(thf)_6][Co(\eta^4\text{-cod})(\eta^2\text{-styrene})(H)(CH_2CH_2Ph)]$ ($\mathbf{14_{Na}}$) representing the two reactivity regimes (Mg: higher vs. Na: lower) were re-optimized at DFT level to further analyze the influence of the counterion on the reductive elimination step

($\mathbf{14}_{\mathbf{Mg/Na}}$ → $[\mathbf{15}_{\mathbf{Mg/Na}}]^{‡}$). For transition state $[\mathbf{15}_{\mathbf{Mg}}]^{‡}$, the activation barrier for the reductive elimination is reduced to 1.5 kcal/mol, rendering the process effectively barrierless. In contrast, the activation barrier for transition state $[\mathbf{15}_{\mathbf{Na}}]^{‡}$ does not significantly change compared to the anion-only model (4.5 kcal/mol for $[\mathbf{15}_{\mathbf{Na}}]^{‡}$ vs. 5.0 kcal/mol for $[\mathbf{15}_{\mathbf{A}}]^{‡}$). While a stabilizing interaction of the magnesium cation and the styrene molecule likely accounts for the reduction in transition state energy, the fully solvated sodium cation was not able to beneficially affect the reductive elimination step by interaction with the anion. NCI analyses of the transition states $[\mathbf{15}_{\mathbf{Mg}}]^{‡}$ and $[\mathbf{15}_{\mathbf{Na}}]^{‡}$ support the attractive interaction between $[(^{Dep}\text{nacnac})\text{Mg}]^{+}$ and styrene, while no attractive interaction was identified between $[\text{Na(thf)}_6]^{+}$ and the complex anion (Figure S42 and Figure S43).

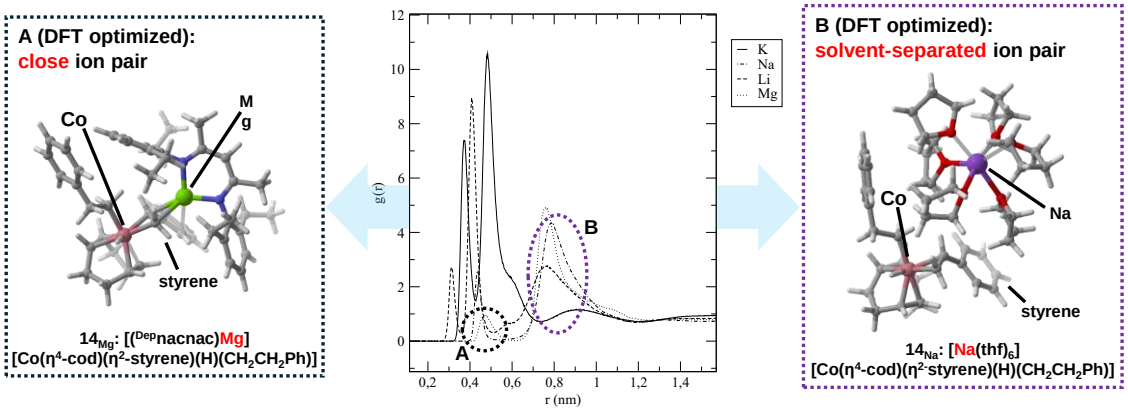

Figure S37. Radial distribution function (M–Co distance) for ion pairs $[\text{M(thf)}_n][\text{Co}(\eta^4\text{-cod})(\eta^2\text{-styrene})(\text{H})(\text{CH}_2\text{CH}_2\text{Ph})]$ ($\mathbf{14}_{\mathbf{K\text{-}Mg}}$) (M = K, Na, Li, $(^{Dep}\text{nacnac})\text{Mg}$) and relevant ion pair structures of $\mathbf{14}_{\mathbf{Mg}}$ (A) and $\mathbf{14}_{\mathbf{Na}}$ (B) after re-optimization at DFT level. In ion pair $[(^{Dep}\text{nacnac})\text{Mg}][\text{Co}(\eta^4\text{-cod})(\eta^2\text{-styrene})(\text{H})(\text{CH}_2\text{CH}_2\text{Ph})]$ ($\mathbf{14}_{\mathbf{Mg}}$), styrene is essentially sandwiched between the magnesium cation and the cobalt anion. In ion pair $[\text{Na(thf)}_6][\text{Co}(\eta^4\text{-cod})(\eta^2\text{-styrene})(\text{H})(\text{CH}_2\text{CH}_2\text{Ph})]$ ($\mathbf{14}_{\mathbf{Na}}$), solvent separation of the ions is observed and no cation styrene interaction found.

- *Non-Covalent Interaction (NCI) Plots*

Non-Covalent Interaction (NCI) analyses based on electron densities from single point calculations on ωB97M-V/def2-QZVP[48] level of theory were performed for the transition state structures $[\text{M(L}_n)][\text{Co}(\eta^4\text{-cod})(\eta^2\text{-styrene})\text{H}_2]$ ($[\mathbf{12}_{\mathbf{K\text{-}Mg}}]^{‡}$; M = K(thf)_5, Na(thf)_4, Li(thf)_3, $(^{Dep}\text{nacnac})\text{Mg(thf)}$) and for the transition state structures $[\text{M(L}_n)][\text{Co}(\eta^4\text{-cod})(\eta^2\text{-styrene})\text{-(H)}(\text{CH}_2\text{CH}_2\text{Ph})]$ ($[\mathbf{15}_{\mathbf{Mg/Na}}]^{‡}$; M = Na(thf)_6 or $(^{Dep}\text{nacnac})\text{Mg}$). The fine integration grid of the software multiwfn[45] was used for all NCI plot calculations. Full representations of rendered structures with and without NCI surfaces (3D), as well as the full NCI plots (2D) are available below.

*NCI analysis for transition state structure [K(thf)$_5$][Co(η^4-cod)(η^2-styrene)H$_2$] ([**12$_K$**]‡)*

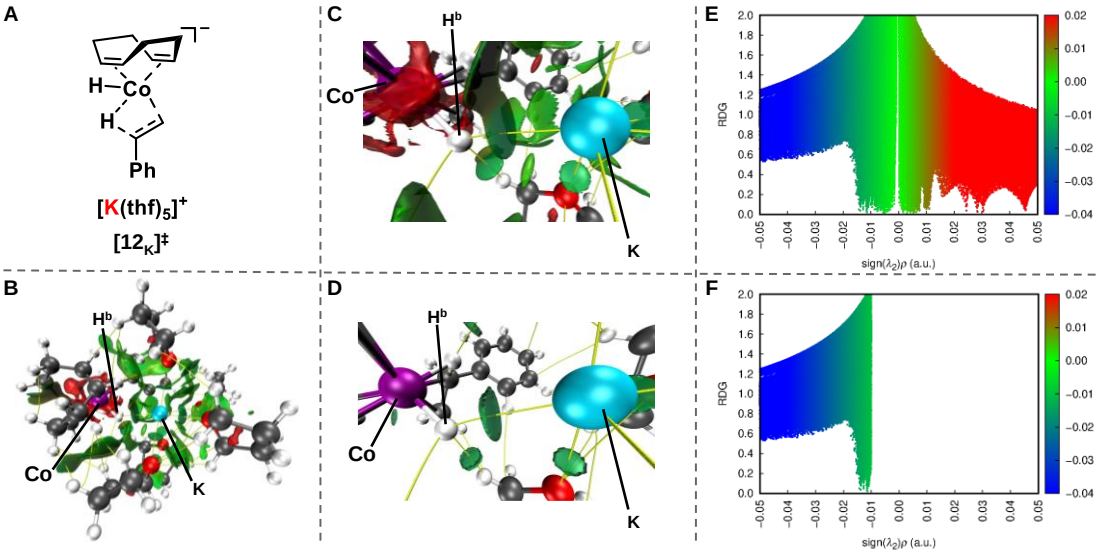

Figure S38. A: Structure of [K(thf)$_5$][Co(η^4-cod)(η^2-styrene)H$_2$] ([**12$_K$**]‡). B: NCI Surface visualization (3D) of [**12$_K$**]‡. C: Cutout of the NCI surface visualization (3D) of [**12$_K$**]‡ showing the [Co–H$_b$]···K$^+$ interaction. D: As C with cutoff at sign(λ2)ρ < –0.01. E: NCI plot (2D) of [**12$_K$**]‡. F: As E with cutoff at sign(λ2)ρ < –0.01; diagrams show plots of RDG := reduced density gradient over sign(λ2)ρ := density with sign of the second derivative Hessian matrix. The sign(λ2)ρ > 0 (red) are read as strong repulsive interactions, sign(λ2)ρ ≈ 0 (green) as weak interactions and sign(λ2)ρ < 0 (blue) as strong attractive interactions.

*NCI analysis for transition state structure [Na(thf)$_4$][Co(η^4-cod)(η^2-styrene)H$_2$] ([**12$_{Na}$**]‡)*

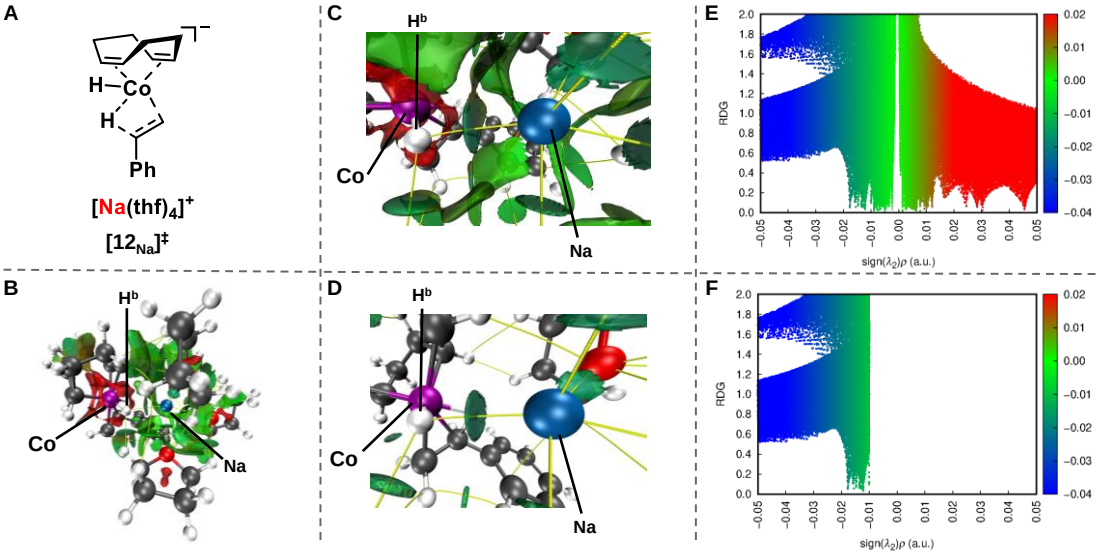

Figure S39. A: Structure of [Na(thf)$_4$][Co(η^4-cod)(η^2-styrene)H$_2$] ([**12$_{Na}$**]‡). B: NCI Surface visualization (3D) of [**12$_{Na}$**]‡. C: Cutout of the NCI surface visualization (3D) of [**12$_{Na}$**]‡ showing the [Co–H$_b$]···Na$^+$ interaction. D: As C with cutoff at sign(λ2)ρ < –0.01. E: NCI plot (2D) of [**12$_{Na}$**]‡. F: As E with cutoff at sign(λ2)ρ < –0.01; diagrams show plots of RDG := reduced density gradient over sign(λ2)ρ := density with sign of the second derivative Hessian matrix. The sign(λ2)ρ > 0 (red) are read as strong repulsive interactions, sign(λ2)ρ ≈ 0 (green) as weak interactions and sign(λ2)ρ < 0 (blue) as strong attractive interactions.

*NCI analysis for transition state structure [Li(thf)$_3$][Co(η^4-cod)(η^2-styrene)H$_2$] ([**12$_{Li}$**]‡)*

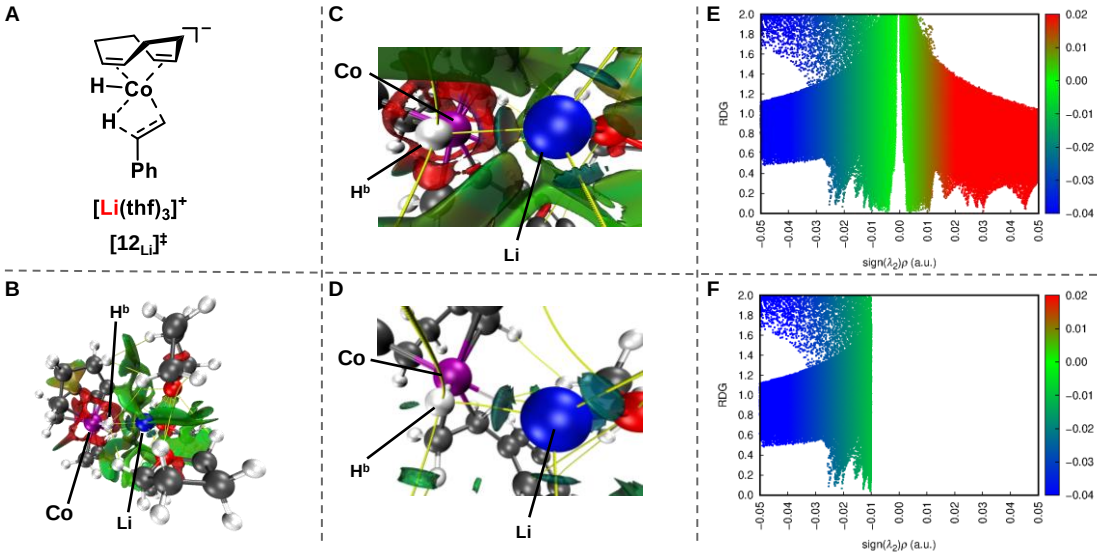

Figure S40. A: Structure of [Li(thf)$_3$][Co(η^4-cod)(η^2-styrene)H$_2$] ([**12$_{Li}$**]‡). B: NCI Surface visualization (3D) of [**12$_{Li}$**]‡. C: Cutout of the NCI surface visualization (3D) of [**12$_{Li}$**]‡ showing the [Co–H$_b$]···Li$^+$ interaction. D: As C with cutoff at sign(λ2)ρ < –0.01. E: NCI plot (2D) of [**12$_{Li}$**]‡. F: As E with cutoff at sign(λ2)ρ < –0.01; diagrams show plots of RDG := reduced density gradient over sign(λ2)ρ := density with sign of the second derivative Hessian matrix. The sign(λ2)ρ > 0 (red) are read as strong repulsive interactions, sign(λ2)ρ ≈ 0 (green) as weak interactions and sign(λ2)ρ < 0 (blue) as strong attractive interactions.

*NCI analysis for transition state structure [(^{Dep}nacnac)Mg(thf)][Co(η^4-cod)-(η^2-styrene)H$_2$] ([**12$_{Mg}$**]‡)*

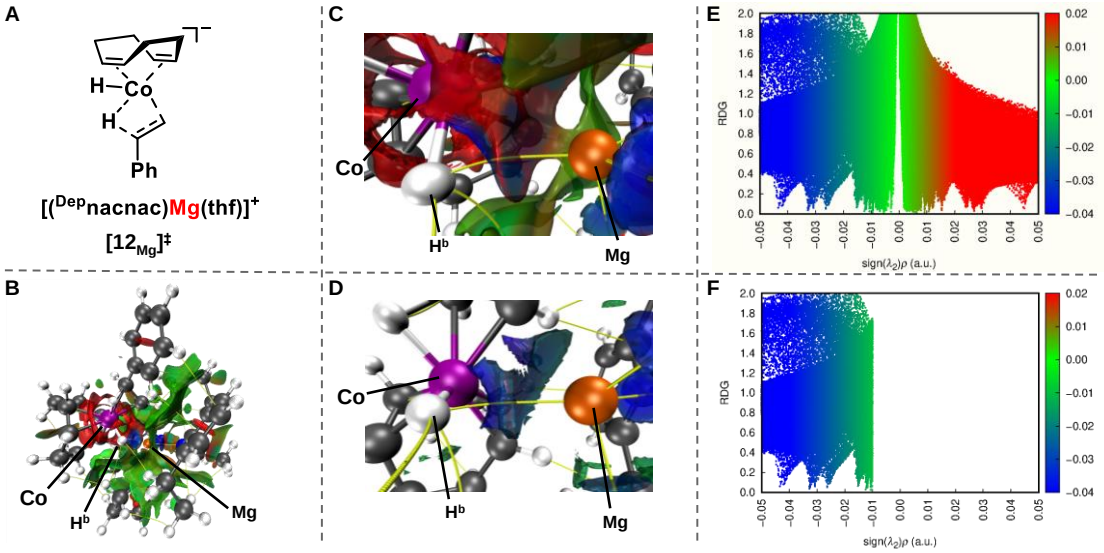

Figure S41. A: Structure of [(^{Dep}nacnac)Mg(thf)][Co(η^4-cod)(η^2-styrene)H$_2$] ([**12$_{Mg}$**]‡). B: NCI Surface visualization (3D) of [**12$_{Mg}$**]‡. C: Cutout of the NCI surface visualization (3D) of [**12$_{Mg}$**]‡ showing the [Co–H$_b$]···Mg(^{Dep}nacnac)$^+$ interaction. D: As C with cutoff at sign(λ2)ρ < –0.01. E: NCI plot (2D) of [**12$_{Mg}$**]‡. F: As E with cutoff at sign(λ2)ρ < –0.01; diagrams show plots of RDG := reduced density gradient over sign(λ2)ρ := density with sign of the second derivative Hessian matrix. The sign(λ2)ρ > 0 (red) are read as strong repulsive interactions, sign(λ2)ρ ≈ 0 (green) as weak interactions and sign(λ2)ρ < 0 (blue) as strong attractive interactions.

*NCI analysis for transition state structure [(Depnacnac)Mg]-[Co(η⁴-cod)(η²-styrene)(H)(CH₂CH₂Ph)] ([**15**Mg]‡)*

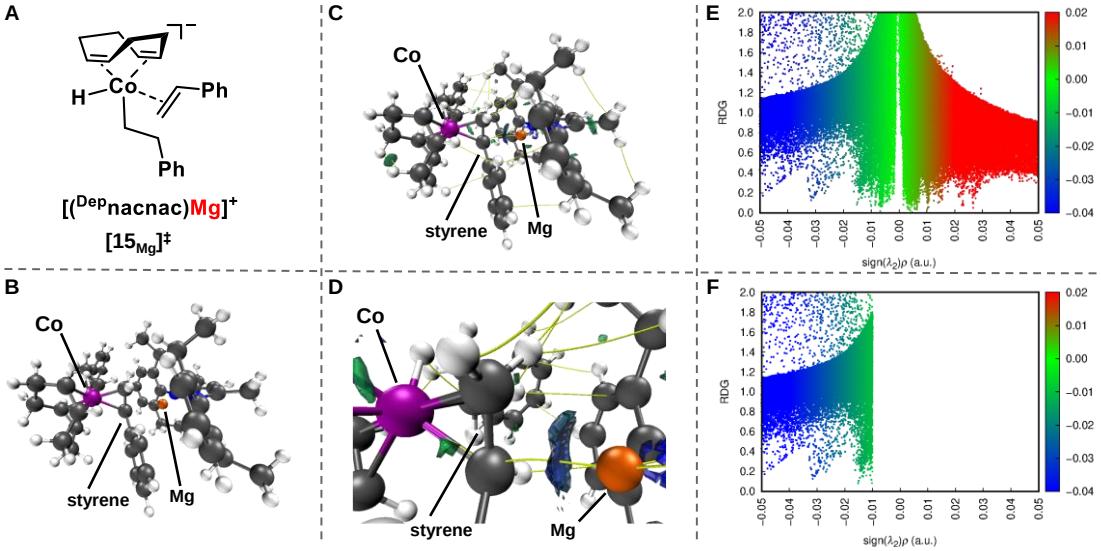

Figure S42. A: Structure of [(Depnacnac)Mg][Co(η⁴-cod)(η²-styrene)(H)(CH₂CH₂Ph)] ([**15**Mg]‡). B: Rendered transition state structure of [**15**Mg]‡. C: NCI Surface visualization (3D) of [**15**Mg]‡ with cutoff at sign(λ2)ρ < –0.01. D: Cutout of the NCI surface visualization (3D) of [**15**Mg]‡ showing the styrene···Mg(Depnacnac)+ interaction with cutoff at sign(λ2)ρ < –0.01. E: NCI plot (2D) of [**15**Mg]‡. F: As E with cutoff at sign(λ2)ρ < –0.01; diagrams show plots of RDG := reduced density gradient over sign(λ2)ρ := density with sign of the second derivative Hessian matrix. The sign(λ2)ρ > 0 (red) are read as strong repulsive interactions, sign(λ2)ρ ≈ 0 (green) as weak interactions and sign(λ2)ρ < 0 (blue) as strong attractive interactions.

*NCI analysis for transition state structure [Na(thf)₆][Co(η⁴-cod)(η²-styrene)(H)-(CH₂CH₂Ph)] ([**15**Na]‡)*

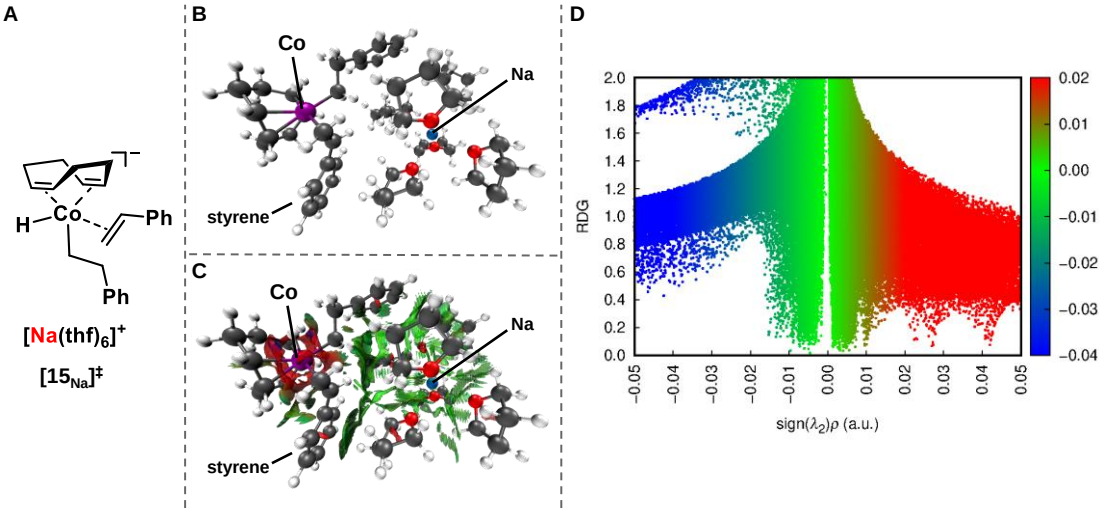

Figure S43. A: Structure of [Na(thf)₆][Co(η⁴-cod)(η²-styrene)(H)(CH₂CH₂Ph)] ([**15**Na]‡). B: Rendered transition state structure of [**15**Na]‡. C: NCI Surface visualization (3D) of [**15**Na]‡. D: NCI plot (2D) of [**15**Na]‡; diagrams show plots of RDG := reduced density gradient over sign(λ2)ρ := density with sign of the second derivative Hessian matrix. The sign(λ2)ρ > 0 (red) are read as strong repulsive interactions, sign(λ2)ρ ≈ 0 (green) as weak interactions and sign(λ2)ρ < 0 (blue) as strong attractive interactions.

2.4.8.3 Cartesian Coordinates and Thermochemistry Output of the Optimized Structures

- *Anion-Only Hydrogenation of Styrene with Anionic [Co(η⁴-cod)(η²-styrene)₂]⁻ (**7**ₐ)*

[Co(η⁴-cod)(η²-styrene)₂]⁻ (**7**ₐ)
H = -2313.57741318 Eh
G = -2313.64780625 Eh
Co 0.394412 -0.000139 -0.001014
C -0.924239 -0.780947 -1.386983
H -0.341302 -1.216007 -2.202191
C -1.931047 -1.715439 -0.747924
H -1.516656 -2.728034 -0.761814
H -2.863279 -1.751835 -1.340114
C -2.23559 -1.323864 0.712504
H -3.131652 -0.692952 0.767112
H -2.467715 -2.230392 1.286078
C -1.05714 -0.614228 1.357521
H -0.566121 -1.177215 2.146295
C -0.918292 0.78136 1.390238
H -0.331826 1.216004 2.203134
C -1.926982 1.716492 0.755135
H -1.511984 2.728859 0.767641
H -2.856907 1.753401 1.350925
C -2.237408 1.325348 -0.704181
H -3.134285 0.69531 -0.755504
H -2.470854 2.232187 -1.276728
C 1.818813 0.817832 -1.170094
H 2.760062 0.267987 -1.112992
H 1.52362 1.040474 -2.196774
C 1.547573 1.768256 -0.141766
C 1.822844 -0.819173 1.16244
H 2.764206 -0.269914 1.101729
H 1.531516 -1.04186 2.190213
C 1.547002 -1.769302 0.135068
H 2.176921 1.733115 0.746458
H 2.172783 -1.734481 -0.755682
C -1.062096 0.614744 -1.353856
H -0.573931 1.177299 -2.144711
C 0.89835 -3.063266 0.293574
C 0.771511 -3.908857 -0.832367
C 0.413975 -3.568915 1.518973
C 0.150741 -5.147646 -0.754483
H 1.159084 -3.560789 -1.788376
C -0.215614 -4.806527 1.594729
H 0.54104 -2.986981 2.426582
C -0.36581 -5.606138 0.460425
H 0.065426 -5.762892 -1.647579
H -0.58256 -5.158893 2.556536
H -0.855295 -6.573812 0.525554
C 0.899095 3.062591 -0.29791
C 0.777099 3.908425 0.828378
C 0.410321 3.568333 -1.521527
C 0.15677 5.147568 0.752677
H 1.168213 3.560287 1.78292
C -0.218842 4.8063 -1.59506
H 0.53358 2.98619 -2.42953
C -0.364214 5.606162 -0.460296
H 0.075308 5.763036 1.645983
H -0.589277 5.15874 -2.555501
H -0.853369 6.574117 -0.523681

[Co(η⁴-cod)(η²-styrene)]⁻ (**8**ₐ)
H = -2004.11174998 Eh
G = -2004.16916218 Eh
Co 1.041492 1.278301 6.677926
C 2.651989 1.147921 7.934257
H 3.556378 0.649848 7.581659
H 2.863691 2.087552 8.455108
C 2.227251 1.775923 5.160872
H 3.205862 2.116436 5.504903
C 1.577383 0.313159 8.367779
H 1.643592 -0.774549 8.395888
C 0.177498 2.363202 8.575135
H 1.041693 3.017956 8.583624
C -1.100854 2.935426 8.67942
H -1.198363 4.015741 8.579347
C 0.307473 -0.175062 5.500075
H 0.265727 -1.126082 6.039047
C 1.157025 2.701263 5.235387
H 1.378815 3.674359 5.681783
C 0.324208 0.929473 8.684054
C -0.70707 0.775853 5.78015
H -1.443345 0.512495 6.541588
C -2.227688 2.169703 8.938098
H -3.207475 2.632539 9.01786
C 2.302722 0.63021 4.168491
H 3.14002 -0.010291 4.477184
H 2.550442 0.986856 3.151032
C -1.181313 1.841097 4.809773
H -1.857866 2.505543 5.364001
H -1.780784 1.420195 3.980569
C -0.839094 0.181667 9.063079
H -0.735417 -0.889223 9.231423
C 1.013482 -0.218418 4.149298
H 0.335699 0.136061 3.361637
H 1.264536 -1.254382 3.885745
C -0.010223 2.677903 4.256461
H 0.323934 2.276033 3.290585
H -0.350426 3.702024 4.052456
C -2.071402 0.781351 9.167028
H -2.938851 0.181814 9.437699

[Co(η⁴-cod)(η²-styrene)(H₂)]⁻ (**9**ₐ)
H = -2005.27657999 Eh
G = -2005.33430758 Eh
Co -0.638696 -0.458318 -0.48509
C 0.122995 1.401655 -0.84145
H -0.488183 1.919632 -1.584946
C 0.283692 2.137111 0.474688
H -0.6674 2.640401 0.693655
H 1.043912 2.936918 0.405965
C 0.613917 1.172853 1.633551
H 1.69905 1.084229 1.765334
H 0.236162 1.594746 2.574641
C -0.015305 -0.196309 1.397714
H -0.824211 -0.437373 2.092057
C 0.665822 -1.302784 0.813837
H 0.375951 -2.300912 1.152721
C 2.097218 -1.211599 0.313119
H 2.303713 -2.110026 -0.283355
H 2.829863 -1.219005 1.142349
C 2.313127 0.033406 -0.575201
H 2.683722 0.874213 0.02247
H 3.098949 -0.176041 -1.313204
C -2.399489 -1.203165 0.095935
H -2.842963 -1.937286 -0.578492
H -2.437675 -1.517052 1.140966
C -2.567742 0.192149 -0.193019
H -2.53063 0.890386 0.645335
C 1.031437 0.425764 -1.296862

H 1.036362 0.233756 -2.37077
H -0.982842 -0.910126 -1.949691
H -0.51302 -1.593574 -1.546732
C -3.196968 0.745058 -1.380606
C -3.685439 -0.037222 -2.45528
C -3.354024 2.146512 -1.504819
C -4.262322 0.545089 -3.575166
H -3.598197 -1.11948 -2.407499
C -3.929225 2.725948 -2.629128
H -3.001516 2.78062 -0.692974
C -4.38886 1.934373 -3.6839
H -4.625031 -0.093645 -4.378317
H -4.023133 3.808861 -2.682649
H -4.84112 2.384835 -4.562788

$[Co(\eta^4\text{-cod})(\eta^2\text{-styrene})(H_2)]^-$ (**[10$_A$]$^-$**)

H = -2005.27714764 Eh
G = -2005.33435325 Eh
Co -0.719798 -0.478566 -0.384032
C 0.278683 1.124376 -1.156553
H -0.294373 1.555641 -1.980837
C 0.631034 2.104476 -0.054543
H -0.218741 2.788223 0.068276
H 1.494506 2.73707 -0.331834
C 0.891342 1.394569 1.29056
H 1.958429 1.173194 1.41095
H 0.634899 2.073151 2.114737
C 0.065582 0.121078 1.409484
H -0.745368 0.172941 2.138115
C 0.535222 -1.167317 1.077757
H 0.100438 -2.013061 1.613524
C 1.92224 -1.423606 0.517773
H 1.949886 -2.455701 0.146257
H 2.696448 -1.357799 1.304555
C 2.259941 -0.467133 -0.646072
H 2.78447 0.420621 -0.274109
H 2.960539 -0.962442 -1.33117
C -2.520694 -0.812753 0.418021
H -3.140236 -1.537471 -0.109791
H -2.494162 -0.98262 1.496271
C -2.479075 0.54028 -0.050316
H -2.260799 1.322144 0.678632
C 1.008781 -0.054871 -1.409843
H 0.931331 -0.469068 -2.414861
H -1.24591 -1.023918 -1.670914
H -0.70356 -1.851299 -0.973866
C -3.133355 1.047132 -1.249716
C -3.083779 2.429038 -1.540375
C -3.841747 0.236777 -2.165906
C -3.680644 2.963982 -2.676393
H -2.555884 3.085975 -0.85128
C -4.442083 0.7737 -3.296771
H -3.910755 -0.832699 -1.987011
C -4.367515 2.14284 -3.571728
H -3.612578 4.033847 -2.862944
H -4.980483 0.115922 -3.976249
H -4.838034 2.557649 -4.4587

$[Co(\eta^4\text{-cod})(\eta^2\text{-styrene})H_2]^-$ (**11$_A$**)

H = -2005.27719664 Eh
G = -2005.33468952 Eh
Co -0.706127 -0.495828 -0.432938
C 0.338548 1.071383 -1.198758
H -0.193875 1.488983 -2.056319
C 0.674967 2.086443 -0.12478
H -0.171055 2.78085 -0.048574
H 1.551406 2.701001 -0.402837
C 0.895281 1.426094 1.250452
H 1.956424 1.198684 1.404496
H 0.624381 2.134967 2.043461
C 0.061626 0.164131 1.405494
H -0.781885 0.248928 2.090521
C 0.521063 -1.127089 1.137464
H 0.041853 -1.950144 1.666842
C 1.906457 -1.431156 0.604353
H 1.917568 -2.476849 0.274787
H 2.663367 -1.348161 1.404853
C 2.281631 -0.52804 -0.588626
H 2.809949 0.367192 -0.239978
H 2.991918 -1.06128 -1.23371
C -2.517746 -0.826334 0.343288
H -3.164466 -1.489448 -0.228647
H -2.477317 -1.079869 1.404538
C -2.437296 0.556792 -0.019509
H -2.217238 1.277501 0.768027
C 1.057891 -0.127888 -1.402101
H 1.012597 -0.561318 -2.39983
H -1.284517 -0.750506 -1.762067
H -0.539144 -1.956142 -0.707446
C -3.107155 1.170156 -1.164178
C -3.086822 2.572778 -1.312697
C -3.797989 0.439627 -2.1548
C -3.701136 3.207257 -2.387329
H -2.571722 3.168895 -0.561614
C -4.417598 1.074148 -3.223516
H -3.840181 -0.643461 -2.085125
C -4.374061 2.464687 -3.357562
H -3.657411 4.291534 -2.465567
H -4.94345 0.476829 -3.965571
H -4.858139 2.956155 -4.196896

$[Co(\eta^4\text{-cod})(\eta^2\text{-styrene})H_2]^-$ ([**12$_A$**]$^-$)

H = -2005.24708970 Eh
G = -2005.30435354 Eh
Co 0.709303 -0.288831 -0.379384
C 0.046849 0.901923 1.178863
H 0.884334 1.187083 1.818188
C -0.7358 2.070579 0.615245
H -0.017177 2.872389 0.400973
H -1.443402 2.482123 1.359373
C -1.460506 1.699426 -0.690861
H -2.487447 1.368815 -0.484419
H -1.559269 2.595649 -1.317701
C -0.694463 0.61611 -1.448238
H -0.352911 0.925622 -2.438113
C -0.990864 -0.789352 -1.290985
H -0.861839 -1.408125 -2.182582
C -2.076389 -1.315178 -0.369544
H -1.980885 -2.408261 -0.331604
H -3.092258 -1.110958 -0.760904
C -1.918762 -0.754357 1.053277
H -2.553361 0.129402 1.192336
H -2.266091 -1.491341 1.789439
C 2.547182 0.521006 -0.125964
H 3.223386 0.610611 -0.976551
H 2.624414 1.365657 0.559503
C 2.494841 -0.816715 0.505785
H 2.397163 -0.794913 1.596399
C -0.469439 -0.39191 1.343383
H 0.03175 -1.028128 2.074012
H 1.343223 -1.602832 0.130981
H 1.302534 -0.674334 -1.68063
C 3.517755 -1.83243 0.106229
C 3.856402 -2.063549 -1.234867

C 4.182047 -2.579801 1.087312

C 4.830755 -2.994814 -1.577049

H 3.336252 -1.507593 -2.010301

C 5.156007 -3.517028 0.746785

H 3.932015 -2.419895 2.134491

C 5.487757 -3.730059 -0.589061

H 5.076214 -3.154362 -2.624425

H 5.655473 -4.083009 1.529451

H 6.245907 -4.46022 -0.859041

[Co(η⁴-cod)(H)(CH_2CH_2Ph)]⁻ (**13**$_A$)

H = -2005.25798762 Eh

G = -2005.31806398 Eh

Co 0.604603 -0.3941 -0.368521

C -1.221694 -1.003567 -1.006817

H -1.059328 -1.796355 -1.739754

C -2.093232 -1.405517 0.162227

H -1.897956 -2.465425 0.371748

H -3.169672 -1.334447 -0.079072

C -1.76938 -0.582897 1.430825

H -2.417641 0.29942 1.490964

H -1.995272 -1.18554 2.320133

C -0.3098 -0.169724 1.445032

H 0.315826 -0.683655 2.177049

C 0.149706 1.063991 0.94578

H 1.090073 1.452875 1.345099

C -0.735508 2.118963 0.318684

H -0.080592 2.862492 -0.154848

H -1.32652 2.667356 1.074657

C -1.664223 1.518268 -0.760457

H -2.628283 1.233607 -0.32271

H -1.889128 2.285024 -1.513236

C -1.008386 0.321099 -1.421837

H -0.662754 0.481712 -2.444023

H 1.25125 -1.000447 -1.653548

C 2.431224 -0.587834 0.417925

H 2.42792 -0.355842 1.499913

H 2.7821 -1.630774 0.328647

C 3.487283 0.320059 -0.247559

H 3.150902 1.36613 -0.217163

H 3.58813 0.049785 -1.30616

C 4.833208 0.22417 0.424044

C 5.75093 -0.767576 0.05449

C 5.177905 1.074213 1.482251

C 6.967207 -0.907693 0.717611

H 5.501831 -1.438269 -0.765971

C 6.392533 0.938057 2.150589

H 4.479026 1.852622 1.783769

C 7.294744 -0.054851 1.771431

H 7.665454 -1.682152 0.40902

H 6.63849 1.612049 2.967818

H 8.244223 -0.161028 2.28927

[Co(η⁴-cod)(η²-styrene)(H)(CH_2 CH_2Ph)]⁻ (**14**$_A$)

H = -2314.72039916 Eh

G = -2314.79336941 Eh

Co 0.350268 0.257717 -0.394573

C -0.271222 -1.09123 1.033759

H 0.586369 -1.466471 1.589354

C -1.375944 -0.554972 1.919895

H -0.905079 -0.037222 2.763123

H -1.977545 -1.374372 2.355131

C -2.27216 0.445129 1.174906

H -3.150325 -0.055348 0.74858

H -2.663082 1.187056 1.883477

C -1.502339 1.166685 0.083206

H -1.293206 2.212459 0.285715

C -1.501005 0.773588 -1.254202

H -1.344974 1.545454 -2.006795

C -2.204163 -0.469876 -1.756281

H -1.883003 -0.644933 -2.789731

H -3.296033 -0.309266 -1.789058

C -1.862368 -1.710998 -0.906479

H -2.625078 -1.868541 -0.13315

H -1.896379 -2.603363 -1.544428

C 1.227155 2.060493 -0.549009

H 2.082081 2.060893 -1.222674

H 0.528878 2.876403 -0.745808

C 1.41639 1.618372 0.79627

H 2.344544 1.093026 1.016985

C -0.483883 -1.604015 -0.265515

H 0.2435 -2.325017 -0.637311

H 0.422841 0.115762 -1.872568

C 2.169098 -0.652898 -0.722703

H 2.891672 0.144177 -0.955513

H 2.132438 -1.29479 -1.615406

C 2.77413 -1.511726 0.405842

H 2.152606 -2.399292 0.57918

H 2.805975 -0.945872 1.346788

C 4.166865 -1.964122 0.057379

C 5.278968 -1.170893 0.366775

C 4.385068 -3.154852 -0.646844

C 6.563325 -1.55292 -0.010758

H 5.128243 -0.240846 0.912544

C 5.667355 -3.541007 -1.028852

H 3.533059 -3.785124 -0.89598

C 6.764539 -2.741109 -0.712643

H 7.412069 -0.923619 0.246001

H 5.812348 -4.472214 -1.571294

H 7.766354 -3.042299 -1.006554

C 0.830451 2.207914 1.9955

C 1.090474 1.616904 3.252528

C 0.044406 3.380441 2.004441

C 0.565484 2.129459 4.429579

H 1.710332 0.722013 3.284205

C -0.492517 3.887545 3.183664

H -0.130208 3.914365 1.074408

C -0.247457 3.266639 4.408155

H 0.786644 1.637846 5.374615

H -1.097481 4.791301 3.147254

H -0.663783 3.668865 5.327471

[Co(η⁴-cod)(η²-styrene)(H)(CH_2 CH_2Ph)]⁻ ([**15**$_A$]⁻)

H = -2314.71272928 Eh

G = -2314.78540704 Eh

Co 0.332651 0.204338 -0.369581

C -0.459908 -0.609633 1.353229

H 0.330932 -0.800512 2.081412

C -1.597022 0.25297 1.862692

H -1.160792 1.036936 2.492706

H -2.285736 -0.321948 2.50907

C -2.363097 0.926088 0.708699

H -3.221978 0.319917 0.395591

H -2.782167 1.877608 1.061609

C -1.435079 1.195727 -0.469017

H -1.25344 2.253882 -0.645918

C -1.294058 0.345065 -1.594312

H -1.049139 0.820502 -2.54677

C -2.026521 -0.975893 -1.728122

H -1.572005 -1.535648 -2.555963

H -3.088176 -0.82878 -1.999683

C -1.908374 -1.809249 -0.436813

H -2.760917 -1.620894 0.225156

H -1.951949 -2.878179 -0.684214
C 1.303882 1.848331 -0.962776
H 2.152445 1.647005 -1.61809
H 0.669068 2.653112 -1.338326
C 1.517489 1.71515 0.448245
H 2.445154 1.234466 0.760153
C -0.600874 -1.514884 0.284256
H 0.121608 -2.327891 0.226589
H 0.882653 -0.597366 -1.471678
C 2.127407 -0.961816 -0.647235
H 2.880743 -0.266114 -1.040859
H 2.173641 -1.848513 -1.302151
C 2.613655 -1.463924 0.737878
H 1.929142 -2.226616 1.125335
H 2.623664 -0.638949 1.456407
C 3.994592 -2.052264 0.629432
C 5.12884 -1.245432 0.785777
C 4.184471 -3.399888 0.297689
C 6.409398 -1.76626 0.622765
H 4.99875 -0.19486 1.040879
C 5.463426 -3.924946 0.130619
H 3.31464 -4.04281 0.174319
C 6.583326 -3.110238 0.292613
H 7.275795 -1.123103 0.756602
H 5.587882 -4.975318 -0.121198
H 7.582065 -3.519166 0.166066
C 0.926625 2.517988 1.504213
C 1.255014 2.239035 2.853436
C 0.039585 3.597795 1.288441
C 0.698766 2.946799 3.908585
H 1.951999 1.427721 3.059114
C -0.523955 4.29983 2.347809
H -0.204983 3.892228 0.272544
C -0.212312 3.981286 3.671036
H 0.974052 2.690602 4.929754
H -1.208432 5.119338 2.13691
H -0.652745 4.535273 4.495174

H_2

H = -1.15611935 Eh
G = -1.17091002 Eh
H 0 0 0.371076
H 0 0 -0.371076

1,5-Cyclooctadiene (1,5-cod)

H = -311.75080429 Eh
G = -311.78987505 Eh
C 1.202112 -1.221302 -0.50765
H 1.794328 -1.812754 -1.208231
C 1.918946 -0.002231 0.00048
H 2.453725 0.443637 -0.850631
H 2.70958 -0.321829 0.697516
C 1.074255 1.094451 0.673844
H 0.63806 0.71999 1.601533
H 1.759558 1.898691 0.966845
C 0.025334 1.678079 -0.238994
H 0.327881 2.586438 -0.761833
C -1.202111 1.221309 -0.507636
H -1.794326 1.812767 -1.208214
C -1.918946 0.002234 0.000482
H -2.45373 -0.443623 -0.850632
H -2.709576 0.321825 0.697526
C -1.074256 -1.09446 0.673829
H -0.638063 -0.720014 1.601526
H -1.759561 -1.898703 0.966816
C -0.025333 -1.678076 -0.239013
H -0.327877 -2.586431 -0.761861

Styrene

H = -309.42665903 Eh
G = -309.46561167 Eh
C -1.028183 -0.319787 -0.05756
C -0.973654 -1.706921 -0.052784
C 0.256136 -2.367208 -0.021459
C 1.432618 -1.623744 0.00556
C 1.378683 -0.233217 0.000836
C 0.150485 0.444121 -0.031403
C 0.15539 1.911563 -0.036073
C -0.90671 2.723216 -0.078022
H -1.996234 0.172333 -0.081158
H -1.896331 -2.280628 -0.073286
H 0.293281 -3.452915 -0.017666
H 2.395564 -2.126396 0.030718
H 2.300623 0.34357 0.022298
H 1.147908 2.361892 -0.001752
H -0.775166 3.800665 -0.076796
H -1.928072 2.354288 -0.115114

Ethylbenzene

H = -310.62662206 Eh
G = -310.66635800 Eh
C -1.488007 -0.483788 -0.000053
C -1.540767 -1.872704 0.000008
C -0.361309 -2.618173 0.000076
C 0.861882 -1.956541 0.000085
C 0.910726 -0.561352 0.000023
C -0.262403 0.19624 -0.000048
C -0.264561 1.709817 -0.00013
C 1.104075 2.381839 0.000071
H -2.412743 0.090664 -0.000104
H -2.503725 -2.376754 0.000004
H -0.398599 -3.704069 0.000126
H 1.788138 -2.525318 0.000141
H 1.878167 -0.068433 0.000033
H -0.83669 2.050534 -0.874072
H -0.836997 2.050628 0.873573
H 0.988077 3.469938 0.000042
H 1.687231 2.108792 0.886317
H 1.687502 2.108779 -0.885992

- *Migratory Insertion Step with Participation of the Counterion*

$[K(thf)_5][Co(\eta^4\text{-cod})(\eta^2\text{-styrene})H_2]$ (**11**$_K$)

H = -3766.50856342 Eh
G = -3766.64128464 Eh
H 6.305353 8.031082 7.682549
H 6.697412 8.856720 9.825332
C 5.814327 7.435073 8.463247
H 7.311160 7.219527 10.043639
C 6.393582 7.802493 9.841900
H 6.042481 6.389803 8.222585
H 3.969244 8.439164 7.726300
C 4.310522 7.645505 8.386278
C 5.379621 7.651868 10.955771
H 5.617557 8.247668 11.838663
H 5.788334 5.154966 9.968976
Co 3.480780 7.975529 10.313760
C 3.403902 6.636305 8.687084
C 4.598869 6.494526 11.174693
C 4.752442 5.242319 10.322132
H 2.410900 6.720851 8.245676
H 4.166306 4.645842 8.295229

C 3.771432 5.239351 9.138260
H 4.224606 6.327976 12.185657
H 4.577984 4.353980 10.941822
H 2.846900 4.739122 9.450613
H 3.336658 8.702146 11.580200
H 3.844037 9.376931 9.881885
C 1.538711 8.437569 10.054805
C 1.618205 7.248331 10.836724
H 1.200602 8.364985 9.020880
H 1.241366 9.366241 10.535316
C 1.393256 7.184074 12.283309
H 1.458029 6.292482 10.341361
C 0.920452 8.271175 13.042612
C 1.647334 5.986411 12.978847
C 0.748028 8.174653 14.417290
H 0.669799 9.198828 12.535918
C 1.032726 6.987514 15.091757
H 0.367786 9.031422 14.971318
C 1.475495 5.889988 14.353763
H 1.996785 5.123892 12.414780
H 1.683706 4.947598 14.855304
H 0.891389 6.912206 16.166090
H 7.933803 9.840458 8.103294
H 5.590900 10.324488 8.259531
C 7.703396 10.900651 8.237736
C 6.207606 11.197986 8.018754
H 8.321849 11.469731 7.536524
H 8.287561 10.564744 10.354617
C 7.962559 11.370472 9.688158
H 8.711962 12.176324 9.717853
C 5.945882 12.284616 9.050820
O 6.707671 11.866800 10.194371
H 4.900799 12.367865 9.363944
H 7.175007 9.069207 15.360419
H 6.299661 13.271087 8.700820
H 4.610360 11.517078 15.314543
C 6.704699 8.652055 14.455311
H 3.636902 9.055526 15.148910
H 7.059793 6.650085 15.268993
H 7.375724 8.817844 13.602448
C 3.822522 12.277489 15.267622
O 5.466965 9.346620 14.205304
C 6.334444 7.184824 14.648471
C 4.348001 8.478831 14.547103
K 4.703208 10.859771 11.978112
H 5.039027 7.514514 16.363988
C 2.614627 11.942964 16.156298
H 2.412131 10.982951 9.302645
H 2.583178 10.869056 16.372696
C 4.948997 7.294435 15.293107
O 3.324153 12.358943 13.907169
H 3.846652 8.163624 13.621642
C 2.037152 11.983703 9.538912
H 6.261242 6.681839 13.677610
O 2.803848 12.474504 10.655681
C 2.571549 13.885096 10.675637
C 2.228055 13.032332 8.432580
C 1.420345 12.327742 15.275503
H 4.340640 6.394613 15.171200
C 1.943473 11.950492 13.898592
H 0.978040 11.912001 9.834830
H 0.501221 11.797715 15.542366
H 1.452663 12.460037 13.064506
H 1.873135 10.861828 13.740874
H 3.621896 14.650633 8.930949
C 2.614625 14.321292 9.203566
H 3.027634 12.732794 7.748152
H 1.929397 15.151281 9.008776
H 1.317249 13.157249 7.840460
H 5.985206 11.516066 6.995726
H 3.338983 14.343351 11.306088
H 1.581706 14.092747 11.117041
H 4.261429 13.252921 15.515550
H 2.638585 12.479125 17.109250
H 1.230118 13.406575 15.323619
H 5.091205 14.204504 13.127393
H 6.352885 14.075810 11.856873
C 6.147082 13.990459 12.937970
C 7.122727 14.846238 13.755655
H 6.651758 15.172390 14.687352
H 7.440544 15.738230 13.208213
C 8.294971 13.874986 14.048627
H 8.465343 13.786554 15.124876
H 9.231570 14.201017 13.587483
O 6.391795 12.646141 13.364141
C 7.815369 12.538214 13.454038
H 8.041709 11.666764 14.075354
H 8.234295 12.383074 12.446619

$[K(thf)_5][Co(\eta^4\text{-cod})(\eta^2\text{-styrene})H_2]$ ($[\mathbf{12_K}]^{\ddagger}$)

H = -3766.48244121 Eh
G = -3766.61425464 Eh

H 6.214327 8.395824 7.484263
H 6.563648 9.129518 9.663490
C 5.922319 7.645235 8.231450
H 7.537727 7.657835 9.714843
C 6.503619 8.036336 9.607736
H 6.365151 6.703030 7.884135
H 3.866998 8.231897 7.635947
C 4.404441 7.522677 8.264391
C 5.617827 7.592926 10.752423
H 5.782147 8.142476 11.682682
H 6.486880 5.358507 9.498454
Co 3.679546 7.564948 10.144889
C 3.742635 6.298505 8.549511
C 5.095602 6.280393 10.868359
C 5.499250 5.151881 9.928201
H 2.764330 6.169289 8.084218
H 4.876472 4.541975 7.914378
C 4.443667 4.983298 8.831547
H 4.804614 5.956526 11.870961
H 5.613112 4.218935 10.495218
H 3.683396 4.272189 9.180039
H 3.223958 7.647700 11.577031
H 3.732709 9.113083 10.161507
C 1.699431 7.748581 9.935602
C 1.945271 7.082773 11.208999
H 1.289951 7.133901 9.137445
H 1.228441 8.729000 9.984590
C 1.375200 7.601092 12.486370
H 1.925815 5.991006 11.188852
C 1.159878 8.970576 12.704668
C 1.088649 6.718548 13.535421
C 0.645894 9.425716 13.913080
H 1.396218 9.680229 11.915474
C 0.359865 8.536190 14.947074
H 0.463934 10.488040 14.050234
C 0.590437 7.175980 14.751039
H 1.257018 5.653901 13.386795
H 0.372292 6.466589 15.545223
H -0.045855 8.896695 15.888437
H 7.724671 10.185805 7.898923
H 5.387258 10.557808 8.178785

C 7.473627 11.220311 8.146745
C 5.957915 11.482604 8.034950
H 8.037154 11.874544 7.474234
H 8.226518 10.710794 10.173131
C 7.797563 11.553377 9.621926
H 8.483336 12.412159 9.694391
C 5.706268 12.411607 9.214513
O 6.547145 11.889554 10.253801
H 4.677164 12.400497 9.585303
H 7.113980 8.920468 15.370579
H 5.997844 13.451652 8.979756
H 4.575772 11.110946 15.360525
C 6.689454 8.498309 14.446500
H 3.525993 8.475956 14.961078
H 7.245117 6.510736 15.183187
H 7.334513 8.776443 13.602991
C 3.864623 11.939906 15.396862
O 5.379786 9.069797 14.239165
C 6.483978 6.989086 14.559951
C 4.371495 8.039563 14.417413
K 4.596354 10.637655 12.057579
H 5.090279 7.093511 16.230027
C 2.619827 11.682236 16.233889
H 2.305454 10.580760 9.579908
H 2.288066 10.649047 16.084851
C 5.071981 6.905164 15.149598
O 3.352444 12.124854 14.067473
H 4.019935 7.711383 13.429190
C 1.852103 11.568181 9.726646
H 6.504676 6.530615 13.564702
O 2.587735 12.219162 10.783371
C 2.262515 13.607956 10.671980
C 1.973400 12.509937 8.523838
C 1.610542 12.669167 15.621467
H 4.587303 5.941080 14.971618
C 2.124984 12.865430 14.176761
H 0.800089 11.455240 10.036793
H 0.586504 12.286159 15.649060
H 2.314605 13.929686 13.964901
H 1.446618 12.477916 13.409785
H 3.140769 14.344664 8.813037
C 2.202562 13.903716 9.162688
H 2.825893 12.221557 7.901300
H 1.399013 14.607990 8.928961
H 1.078746 12.477627 7.896147
H 5.675734 11.924917 7.074708
H 3.030442 14.175574 11.208111
H 1.285713 13.799089 11.146985
H 4.390544 12.852399 15.729965
H 2.780930 11.849355 17.303108
H 1.623139 13.620430 16.163338
H 5.068224 13.880869 13.333456
H 6.304330 13.844567 12.032851
C 6.123165 13.696864 13.110789
C 7.104552 14.518794 13.954852
H 6.655260 14.775413 14.918616
H 7.389614 15.450272 13.457246
C 8.302421 13.554789 14.151620
H 8.510980 13.406589 15.214523
H 9.217178 13.925201 13.680104
O 6.398159 12.333482 13.453784
C 7.825738 12.246325 13.493959
H 8.087556 11.345425 14.056290
H 8.215765 12.157945 12.467232

$[K(thf)_5][Co(\eta^4\text{-cod})(H)(CH_2CH_2Ph)]$ (**13κ**)

H = -3766.49886785 Eh
G = -3766.63049983 Eh

H 4.177979 8.710811 7.427152
H 5.438781 9.471228 9.240867
C 4.225911 7.986959 8.250965
H 6.327209 7.995255 8.856639
C 5.353542 8.373878 9.221655
H 4.442353 7.020507 7.781119
H 2.159519 8.678492 8.681326
C 2.888995 7.921891 8.971874
C 5.064869 7.916793 10.637445
H 5.646838 8.453363 11.39192
H 5.264263 5.633876 9.145404
Co 3.088152 7.871196 11.002665
C 2.386653 6.707061 9.475011
C 4.672197 6.60082 10.983458
C 4.548023 5.479033 9.962513
H 1.301369 6.623849 9.565987
H 3.107333 4.951309 8.395936
C 3.109058 5.377924 9.414878
H 4.895798 6.278747 12.004357
H 4.830613 4.525207 10.424959
H 2.546738 4.671592 10.03913
H 2.230743 6.635793 12.133888
H 3.434102 8.752748 12.208256
C 1.28322 8.519157 11.432549
C 1.254764 7.214451 12.242685
H 0.553506 8.526842 10.612588
H 1.130648 9.391184 12.07146
C 1.02868 7.369993 13.720852
H 0.510976 6.520868 11.82743
C -0.165406 7.922444 14.196728
C 1.98607 6.965709 14.653953
C -0.396007 8.061737 15.560645
H -0.917248 8.243088 13.478293
C 0.569449 7.656031 16.480982
H -1.333813 8.486761 15.9098
C 1.762356 7.106652 16.021196
H 2.91831 6.536452 14.292548
H 2.520459 6.781933 16.729672
H 0.389583 7.764383 17.54703
H 7.487787 10.026472 7.861882
H 6.037133 11.804048 8.461144
C 7.977634 10.796622 8.462642
C 7.094023 12.053765 8.608532
H 8.93328 11.03848 7.987732
H 7.876836 9.302949 10.105537
C 8.198977 10.331772 9.920814
H 9.255188 10.435579 10.213416
C 7.320649 12.444693 10.063801
O 7.391907 11.188668 10.75095
H 6.515901 13.027051 10.520661
H 8.306289 9.24473 14.524368
H 8.270009 12.995525 10.185624
H 4.271467 11.229979 14.896021
C 7.636359 8.969756 13.691747
H 5.090676 8.786186 15.474546
H 8.40266 6.920844 13.804918
H 8.010903 9.432711 12.771385
C 3.271395 11.681615 14.871199
O 6.317009 9.48848 13.939298
C 7.471549 7.458279 13.601876
C 5.489132 8.436363 14.513272
K 4.845293 10.897537 11.953178
H 6.838548 7.170008 15.658441
C 2.130621 10.680215 14.959457
H 2.657838 10.512036 9.897495
H 2.367015 9.774982 14.387306

C 6.389963 7.208444 14.658695
O 3.109298 12.336119 13.593921
H 4.652744 8.26129 13.82114
C 2.55824 11.516216 9.458673
H 7.108067 7.173053 12.608559
O 3.601752 12.35327 9.997431
C 3.630768 13.515678 9.160446
C 2.782778 11.583363 7.95226
C 1.001927 11.455672 14.274905
H 5.841035 6.276648 14.493869
C 1.744089 12.153729 13.137827
H 1.574894 11.936032 9.732361
H 0.203862 10.802242 13.912981
H 1.328443 13.135939 12.881687
H 1.762002 11.529026 12.23417
H 4.161334 13.053172 7.077445
C 3.287213 13.029758 7.734465
H 3.549986 10.857711 7.665218
H 2.518238 13.664721 7.28467
H 1.875921 11.35787 7.38442
H 7.364774 12.848305 7.906383
H 4.625576 13.964841 9.246822
H 2.885113 14.242724 9.519264
H 3.208474 12.432005 15.676784
H 1.893064 10.385593 15.985019
H 0.56781 12.190613 14.964102
H 4.630167 14.313482 13.438299
H 6.182413 15.126528 13.029761
C 5.711502 14.301697 13.593918
C 6.135118 14.32937 15.058958
H 5.413601 13.763766 15.65631
H 6.194968 15.344037 15.463325
C 7.501974 13.611228 15.033432
H 7.608446 12.920536 15.874058
H 8.328134 14.327089 15.083294
O 6.196188 13.042462 13.114563
C 7.506479 12.867572 13.678145
H 7.67686 11.79222 13.767685
H 8.259424 13.290109 12.994639

$[Na(thf)_4][Co(\eta^4\text{-cod})(\eta^2\text{-styrene})H_2]$ (**11**$_{Na}$)

H = -3096.61175751 Eh

G = -3096.72854975 Eh

H 5.378649 8.128058 7.212389
H 6.087652 8.690151 9.342038
C 4.883351 7.529279 7.987064
H 6.466399 6.972000 9.389794
C 5.631933 7.693100 9.323115
H 4.942437 6.489070 7.644217
H 3.130870 8.821876 7.524647
C 3.422355 7.934041 8.079249
C 4.718112 7.593071 10.524855
H 5.097603 8.106267 11.408970
H 4.694401 5.151226 9.351701
Co 2.819651 8.206434 10.112426
C 2.424636 7.026543 8.403383
C 3.811059 6.535773 10.751789
C 3.714160 5.346178 9.806367
H 1.413851 7.271523 8.077799
H 2.892741 5.000030 7.803400
C 2.646598 5.563214 8.720373
H 3.513075 6.347984 11.784359
H 3.471995 4.442199 10.378710
H 1.694220 5.151924 9.075418
H 2.865044 8.763962 11.469484
H 3.374928 9.567221 9.722012
C 0.941312 8.931962 10.079791
C 0.921702 7.660299 10.724138
H 0.517133 9.023363 9.079452
H 0.813046 9.830007 10.680250
C 0.774901 7.456510 12.169547
H 0.603682 6.795877 10.145160
C 0.422877 8.483373 13.064433
C 0.979542 6.176210 12.718998
C 0.317131 8.249101 14.430564
H 0.212074 9.474829 12.673179
C 0.552589 6.980701 14.957504
H 0.024209 9.060955 15.093896
C 0.875563 5.942374 14.083518
H 1.234893 5.358292 12.048423
H 1.043297 4.939958 14.470569
H 0.463782 6.798793 16.024640
H 8.181262 10.160434 9.265783
H 5.958082 10.774314 8.425851
C 7.743906 11.091449 9.637240
C 6.589377 11.602958 8.767555
H 8.537779 11.844998 9.690392
H 6.773830 9.869328 11.176131
C 7.082058 10.908585 11.008640
H 7.728078 11.223414 11.837940
C 5.819162 12.454127 9.762943
O 5.884781 11.726340 11.005667
H 4.761518 12.578389 9.517093
H 6.712150 9.040624 14.796746
H 6.285571 13.445301 9.890027
H 4.913668 11.550036 14.750427
C 6.222776 8.578614 13.922371
H 3.405692 9.376148 14.901792
H 6.478683 6.608755 14.844505
H 6.907125 8.634524 13.069005
C 4.129272 12.302255 14.612999
O 5.028589 9.308588 13.590864
C 5.757642 7.164305 14.237174
C 3.889069 8.657464 14.228622
Na 3.916934 10.604996 11.663323
H 4.625549 7.665398 16.020017
C 3.227219 12.480384 15.833599
H 1.914407 11.249384 9.055182
H 3.149989 11.540532 16.392897
C 4.436845 7.433626 14.965060
O 3.264390 11.863196 13.540040
H 3.178156 8.379980 13.440898
C 1.726435 12.237957 9.481830
H 5.580650 6.613216 13.306724
O 2.558638 12.354731 10.648496
C 2.597649 13.751084 10.965060
C 2.134117 13.418078 8.598043
C 1.878412 12.818851 15.189795
H 3.735361 6.596977 14.914647
C 1.889456 11.898249 13.977547
H 0.667548 12.311602 9.780261
H 1.025470 12.634810 15.849084
H 1.279822 12.246235 13.137149
H 1.568666 10.881123 14.245900
H 3.584644 14.877000 9.364298
C 2.590520 14.494986 9.613586
H 2.960386 13.128538 7.940724
H 1.907549 15.348827 9.641834
H 1.309833 13.758139 7.964885
H 6.929994 12.170816 7.896778
H 3.490489 13.925957 11.572267
H 1.709303 14.019371 11.560524
H 4.592823 13.253434 14.312645
H 3.592263 13.255344 16.513454

H 1.855967 13.868890 14.873505

[Na(thf)$_4$][Co(η^4-cod)(η^2-styrene)H$_2$] ([**12$_{Na}$**]‡)

H = -3096.58711418 Eh

G = -3096.70142028 Eh

H 5.050523 8.588434 6.965763

H 5.657533 9.316827 9.070645

C 4.852289 7.832806 7.736558

H 6.644398 7.850558 8.999920

C 5.602956 8.222829 9.028287

H 5.242411 6.889594 7.333535

H 2.741964 8.434597 7.419229

C 3.352678 7.716641 7.965334

C 4.878683 7.771677 10.279661

H 5.154716 8.325547 11.180520

H 5.560972 5.544630 8.914005

Co 2.876667 7.769280 9.929681

C 2.725925 6.498674 8.334339

C 4.367342 6.465144 10.458798

C 4.637821 5.339646 9.468815

H 1.691396 6.375099 8.010099

H 3.753714 4.738059 7.553362

C 3.447692 5.178631 8.520141

H 4.205597 6.136194 11.486100

H 4.821138 4.404835 10.013883

H 2.735383 4.471222 8.964096

H 2.511548 7.775211 11.406925

H 3.022243 9.300203 9.954905

C 0.918941 8.099789 9.841649

C 1.165591 7.324095 11.051367

H 0.430784 7.584768 9.017626

H 0.535068 9.108299 9.980815

C 0.638668 7.777079 12.370359

H 1.075507 6.240320 10.950764

C 0.411718 9.132019 12.662561

C 0.356251 6.837273 13.370833

C -0.108654 9.517912 13.894611

H 0.627145 9.888130 11.910662

C -0.386666 8.571556 14.878123

H -0.305282 10.570205 14.086225

C -0.144951 7.225114 14.608328

H 0.527219 5.782992 13.163470

H -0.359181 6.472257 15.362483

H -0.796730 8.876467 15.836486

H 7.767881 10.683100 8.880732

H 5.654414 11.717817 8.566152

C 7.526889 11.421997 9.649057

C 6.297191 12.267607 9.261681

H 8.407509 12.054243 9.798231

H 7.114835 9.656804 10.924307

C 7.110942 10.749264 10.976491

H 7.755532 11.074553 11.807783

C 5.577455 12.430268 10.592952

O 5.755290 11.161276 11.240696

H 4.501955 12.605989 10.506304

H 6.018929 9.069790 14.982464

H 6.030971 13.231555 11.202058

H 5.615907 11.613123 13.809046

C 5.629604 8.681728 14.025171

H 3.553249 8.628222 15.684552

H 6.175044 6.714596 14.803303

H 6.255605 9.058997 13.211479

C 4.861145 12.319367 14.167950

O 4.298544 9.178541 13.821958

C 5.501101 7.150608 14.060178

C 3.461474 8.325954 14.626977

Na 3.595796 10.274672 11.779788

H 3.869029 6.284541 15.285895

C 4.466947 12.101059 15.625240

H 1.847401 10.751376 9.128533

H 4.536428 11.036835 15.876867

C 4.008082 6.915968 14.403920

O 3.654973 12.130745 13.391257

H 2.427523 8.458847 14.302573

C 1.514313 11.744338 9.444954

H 5.744823 6.722332 13.084371

O 2.055906 11.973812 10.762053

C 1.888998 13.382065 10.993256

C 2.060700 12.902929 8.615550

C 3.001776 12.546956 15.628571

H 3.485765 6.446986 13.565490

C 2.524471 12.014861 14.283972

H 0.412953 11.775432 9.496571

H 2.426588 12.139697 16.465033

H 1.690376 12.579905 13.852276

H 2.228661 10.959088 14.361937

H 3.099931 14.570621 9.598652

C 2.127962 14.068835 9.631009

H 3.060605 12.650297 8.246648

H 1.361650 14.824957 9.436502

H 1.429802 13.127656 7.751001

H 6.566487 13.224576 8.805017

H 2.598279 13.671449 11.773146

H 0.863196 13.571349 11.349021

H 5.223680 13.344832 13.999478

H 5.095268 12.667826 16.318337

H 2.932071 13.641003 15.657711

[Na(thf)$_4$][Co(η^4-cod)(H)(CH$_2$CH$_2$Ph)] (**13$_{Na}$**)

H = -3096.59477379 Eh

G = -3096.71062728 Eh

H 4.187722 8.964261 7.022076

H 5.014478 9.642156 9.087180

C 4.163948 8.156237 7.764650

H 6.093130 8.277088 8.795295

C 5.035072 8.547324 8.975045

H 4.583575 7.276681 7.260944

H 1.985156 8.559818 7.758065

C 2.725633 7.879671 8.183717

C 4.517715 7.951817 10.269043

H 4.865729 8.472861 11.164678

H 5.244338 5.861874 8.706469

Co 2.509263 7.719735 10.172916

C 2.271031 6.577962 8.514733

C 4.193211 6.588488 10.441665

C 4.414701 5.549147 9.352638

H 1.210443 6.376472 8.345961

H 3.378313 4.983071 7.507089

C 3.134448 5.334328 8.525961

H 4.225976 6.207043 11.465435

H 4.731195 4.600462 9.804044

H 2.547844 4.531032 8.990660

H 1.641440 6.483567 11.187936

H 2.474595 8.738538 11.321693

C 0.593817 8.151881 10.227249

C 0.602311 6.994917 11.201177

H 0.039521 7.940182 9.306252

H 0.261232 9.100317 10.643138

C 0.335091 7.247350 12.666855

H -0.028365 6.163455 10.854519

C -0.032012 8.493795 13.177533

C 0.496068 6.192300 13.575278

C -0.235248 8.677279 14.544574

H -0.166218 9.331411 12.501187
C -0.070125 7.621064 15.434001
H -0.535041 9.655411 14.914259
C 0.297502 6.370152 14.938527
H 0.791371 5.214532 13.197501
H 0.426738 5.531318 15.617553
H -0.231999 7.765100 16.498599
H 7.460985 10.557196 8.862054
H 5.812287 12.217673 8.864951
C 7.551675 11.220242 9.725550
C 6.586659 12.422804 9.610643
H 8.594059 11.544101 9.795575
H 6.933846 9.441772 10.905357
C 7.111903 10.513679 11.024474
H 7.848931 10.671540 11.827460
C 5.956039 12.491390 10.998077
O 5.863181 11.119920 11.410911
H 4.947764 12.912378 11.021340
H 5.833222 9.239577 15.202995
H 6.595575 13.049102 11.703303
H 5.211394 11.787870 14.146769
C 5.678041 8.910987 14.159905
H 2.739428 8.196102 14.749854
H 6.712431 7.030688 14.608931
H 6.327458 9.501970 13.506228
C 4.301475 12.339022 14.408977
O 4.319034 9.155260 13.766297
C 5.861936 7.406117 14.031832
C 3.528736 7.951931 14.028958
Na 3.640454 10.372443 11.795617
H 4.510783 6.866841 15.642287
C 3.615458 11.818838 15.666688
H 2.101904 10.213658 9.264988
H 3.745080 10.733892 15.738799
C 4.510012 6.897930 14.546399
O 3.348257 12.170400 13.335726
H 3.061814 7.669476 13.078807
C 1.868126 11.285650 9.247469
H 6.000644 7.134847 12.978501
O 2.285833 11.833888 10.515886
C 2.237895 13.252810 10.332596
C 2.624125 12.123330 8.217131
C 2.147584 12.153969 15.383266
H 4.260259 5.899087 14.177953
C 2.045111 11.857953 13.891678
H 0.778212 11.415079 9.144471
H 1.448919 11.552368 15.971513
H 1.297578 12.462492 13.367014
H 1.822432 10.793647 13.718317
H 3.826317 13.818737 8.932548
C 2.778442 13.502507 8.910401
H 3.603686 11.674719 8.018625
H 2.208684 14.287755 8.404943
H 2.088475 12.185176 7.265685
H 7.092739 13.351910 9.333365
H 2.819559 13.715638 11.135279
H 1.192193 13.592241 10.415176
H 4.544559 13.409239 14.497283
H 3.998067 12.287995 16.577783
H 1.948182 13.213794 15.581629

$[Li(thf)_3][Co(\eta^4\text{-cod})(\eta^2\text{-styrene})H_2]$ ($\mathbf{11}_{Li}$)

H = -2709.59886654 Eh
G = -2709.69915099 Eh
H 4.785120 7.997323 6.649748
H 5.888884 9.290165 8.220140
C 4.653688 7.616344 7.670024
H 6.638218 7.738226 8.579492
C 5.678744 8.285946 8.604061
H 4.838976 6.537041 7.612933
H 2.610671 8.480567 7.474186
C 3.219735 7.846431 8.112378
C 5.170018 8.445600 10.021010
H 5.683592 9.237297 10.573650
H 5.337443 5.786698 9.566876
Co 3.145243 8.669771 10.086992
C 2.559118 6.972296 8.961902
C 4.598091 7.405502 10.786332
C 4.504947 5.981504 10.255133
H 1.470265 6.978451 8.924276
H 3.246343 4.926523 8.802215
C 3.157234 5.719793 9.564427
H 4.650933 7.497223 11.871425
H 4.633913 5.273503 11.082705
H 2.448879 5.340804 10.310630
H 3.416780 9.599936 11.183950
H 3.276823 9.910060 9.209438
C 1.212291 9.110023 10.430282
C 1.625095 8.133241 11.381100
H 0.548701 8.808114 9.620203
H 1.036074 10.128080 10.767266
C 1.897310 8.410869 12.796480
H 1.353750 7.094475 11.204483
C 1.662291 9.659806 13.402165
C 2.409183 7.389690 13.617051
C 1.924683 9.868732 14.749870
H 1.252468 10.473049 12.810163
C 2.442562 8.845959 15.544190
H 1.708335 10.839719 15.190998
C 2.682702 7.602214 14.962467
H 2.599638 6.414613 13.173165
H 3.078232 6.788293 15.565051
H 2.641451 9.010769 16.599356
H 7.886761 10.351979 8.962206
H 7.083872 10.955987 6.798336
C 7.874300 11.432719 8.790609
C 7.070128 11.775556 7.521600
H 8.906935 11.790453 8.745573
H 7.171503 11.668406 10.879212
C 7.064391 12.111236 9.885440
H 7.290498 13.190403 9.940933
C 5.644392 12.057581 8.044399
O 5.700675 11.921985 9.480700
H 4.892722 11.344133 7.690866
H 5.316647 13.077114 7.791448
Li 4.176259 11.094102 10.485651
H 1.663451 11.447967 9.098949
C 1.716478 12.499212 9.392143
O 2.914465 12.649465 10.183198
C 3.305460 14.038068 10.142962
C 1.912356 13.476185 8.244900
H 0.836492 12.764427 10.000257
H 3.237382 15.235487 8.296391
C 2.562564 14.676534 8.950707
H 2.591615 13.039736 7.504032
H 1.793894 15.369960 9.306771
H 0.975289 13.735357 7.744012
H 7.479411 12.663513 7.029952
H 4.394914 14.061029 10.030672
H 3.036352 14.520198 11.093095
H 3.937079 12.871770 13.229034
H 5.377796 13.379107 12.297977
C 4.978793 12.617258 12.977475
C 5.813819 12.405916 14.231179

H 5.589180 13.134985 15.015198

H 6.881364 12.472858 13.988006

C 5.426930 10.972567 14.610191

H 4.471421 10.962443 15.143658

H 6.172827 10.476102 15.236687

O 5.015794 11.354383 12.290306

C 5.267357 10.285123 13.253961

H 4.428209 9.583266 13.225138

H 6.183327 9.770472 12.936283

$[Li(thf)_3][Co(\eta^4\text{-cod})(\eta^2\text{-styrene})H_2]$ ($[\mathbf{12_{Li}}]^{\ddagger}$)

H = -2709.57546378 Eh

G = -2709.67444261 Eh

H 4.345867 8.094953 6.354169

H 5.589778 9.434606 7.762189

C 4.473380 7.635973 7.342319

H 6.570913 7.975857 7.877339

C 5.576351 8.396644 8.112963

H 4.786259 6.601769 7.150825

H 2.329384 8.155939 7.572041

C 3.142959 7.641211 8.080513

C 5.329167 8.425626 9.607796

H 5.851181 9.231904 10.131535

H 5.716691 5.852966 8.884839

Co 3.319077 8.362459 9.966680

C 2.776995 6.635121 9.006773

C 5.015375 7.268841 10.355840

C 5.046251 5.871145 9.752263

H 1.707827 6.442263 9.107273

H 3.642045 4.684227 8.556539

C 3.630970 5.435970 9.366712

H 5.232573 7.304910 11.424431

H 5.478463 5.167559 10.474972

H 3.165189 4.943454 10.230174

H 3.427073 8.805413 11.422477

H 3.300724 9.803624 9.405295

C 1.419459 8.657243 10.483996

C 2.134890 8.233379 11.685414

H 0.726425 7.944465 10.043192

H 1.015701 9.668210 10.498769

C 1.999872 8.978262 12.975944

H 2.137369 7.157149 11.871019

C 1.798630 10.364948 13.028416

C 2.052829 8.280837 14.189566

C 1.618375 11.016353 14.243610

H 1.782624 10.938435 12.106359

C 1.652407 10.306134 15.442359

H 1.438963 12.089236 14.255707

C 1.880154 8.932323 15.407046

H 2.212430 7.204845 14.171428

H 1.913795 8.362115 16.331779

H 1.501081 10.815409 16.389767

H 7.689228 10.292677 8.628181

H 6.816866 11.328705 6.649802

C 7.760045 11.384644 8.632726

C 6.894088 11.992099 7.515084

H 8.813309 11.668451 8.552324

H 7.249641 11.329714 10.786344

C 7.097052 11.932738 9.887108

H 7.413603 12.970658 10.087834

C 5.524371 12.220761 8.187624

O 5.693023 11.902179 9.587591

H 4.733399 11.565429 7.807751

H 5.196486 13.266602 8.092851

Li 4.240138 10.864599 10.531782

H 1.734018 11.310933 9.170106

C 1.729423 12.317155 9.598189

O 2.930172 12.432819 10.392048

C 3.249639 13.834598 10.525625

C 1.848365 13.447769 8.590063

H 0.844106 12.448029 10.242211

H 3.060421 15.267254 8.865149

C 2.438736 14.579699 9.445364

H 2.539071 13.156689 7.791366

H 1.636168 15.164347 9.906617

H 0.889015 13.714268 8.137653

H 7.315808 12.943181 7.174472

H 4.332875 13.927368 10.392503

H 2.986425 14.174629 11.536962

H 3.938204 12.377606 13.253403

H 5.477175 12.969854 12.553396

C 5.003022 12.150827 13.107248

C 5.686012 11.827521 14.430213

H 5.291505 12.427898 15.254955

H 6.766600 12.000940 14.357998

C 5.386756 10.332619 14.577217

H 4.360292 10.180038 14.926820

H 6.071244 9.820548 15.259343

O 5.108615 10.949776 12.307839

C 5.522716 9.837351 13.144924

H 4.876692 8.984567 12.920433

H 6.561928 9.581722 12.890290

$[Li(thf)_3][Co(\eta^4\text{-cod})(H)(CH_2CH_2Ph)]$ ($\mathbf{13_{Li}}$)

H = -2709.58542706 Eh

G = -2709.68612025 Eh

H 4.926959 8.728006 6.819846

H 6.453299 9.200156 8.522862

C 4.844093 8.037951 7.671054

H 6.906585 7.527241 8.207129

C 6.084918 8.169856 8.571344

H 4.792204 7.035736 7.228702

H 3.002434 9.194105 8.123018

C 3.566496 8.318403 8.451764

C 5.771487 7.885349 10.023150

H 6.459917 8.364608 10.717838

H 5.357628 5.565314 8.676049

Co 3.833541 8.329905 10.461102

C 2.821068 7.277345 9.050714

C 5.101702 6.731039 10.472643

C 4.670767 5.616738 9.530377

H 1.747497 7.445794 9.166165

H 3.067604 5.346274 8.061078

C 3.219771 5.816583 9.048950

H 5.281570 6.433015 11.507537

H 4.758356 4.649280 10.039535

H 2.545786 5.292718 9.739158

H 4.530184 9.179966 11.531962

C 2.228220 9.371293 10.919934

C 2.048419 8.187433 11.880983

H 1.440306 9.406093 10.157091

H 2.212483 10.319295 11.471275

C 2.007260 8.573642 13.333545

H 1.153621 7.606984 11.620924

C 3.051463 8.263581 14.205956

C 0.913052 9.288865 13.834061

C 3.006249 8.654125 15.542684

H 3.909953 7.718884 13.819815

C 1.914765 9.367637 16.028335

H 3.828147 8.399252 16.207360

C 0.864880 9.682459 15.166365

H 0.096424 9.541205 13.160705

H 0.004282 10.233170 15.537158

H 1.876742 9.670442 17.071130
H 8.298261 10.891886 8.406932
H 6.757221 10.699318 6.668123
C 7.766165 11.834142 8.247773
C 6.654260 11.656162 7.186775
H 8.500037 12.595906 7.969714
H 7.458874 11.868131 10.435965
C 6.994436 12.216863 9.511111
H 6.844503 13.308815 9.573971
C 5.348147 11.713479 8.000395
O 5.728907 11.560888 9.378920
H 4.640926 10.911963 7.771794
H 4.842762 12.683287 7.872553
Li 4.183917 10.834879 10.616175
H 1.676556 11.185895 8.691246
C 1.723042 12.184006 9.131875
O 2.959351 12.281550 9.851532
C 3.190985 13.680335 10.076445
C 1.788836 13.322804 8.116304
H 0.876775 12.307296 9.827334
H 3.381785 14.829165 8.214644
C 2.598230 14.414578 8.854815
H 2.320353 12.989141 7.219788
H 1.960954 15.243990 9.174517
H 0.795578 13.664369 7.812409
H 6.676119 12.449226 6.433822
H 4.268537 13.810848 10.206665
H 2.685963 13.986697 11.005105
H 3.057060 11.130210 13.349341
H 3.198758 12.912373 13.256495
C 3.753449 11.977324 13.391164
C 4.580625 11.929308 14.667937
H 3.994294 11.562026 15.514489
H 4.981909 12.920454 14.912775
C 5.706105 10.974866 14.261097
H 5.340944 9.942909 14.276139
H 6.594435 11.051640 14.894701
O 4.708292 11.864802 12.299963
C 5.978091 11.401336 12.825478
H 6.324205 10.573742 12.195333
H 6.696772 12.233792 12.780312
H 2.891095 7.424373 11.770589

[(^{Dep}nacnac)Mg(thf)][Co(η^4-cod)(η^2-styrene)H_2] (**11$_{Mg}$**)

H = -3518.87234826 Eh
G = -3519.00222260 Eh
Mg 3.517736 8.493403 9.181243
N 4.055449 9.071580 7.239273
N 3.831149 10.482317 9.865210
C 4.785343 10.147914 6.965282
C 3.139386 10.978486 11.013929
C 5.116437 11.136808 7.908987
H 5.753644 11.932027 7.539532
C 4.572491 11.358868 9.189700
C 3.605486 8.274825 6.146820
C 1.978858 11.765783 10.849394
C 4.320453 7.117299 5.782213
C 1.433633 12.104989 9.479343
H 1.945493 11.498781 8.725855
H 1.683122 13.149814 9.241778
C 4.837871 12.736648 9.764598
H 4.053439 13.432508 9.444887
H 5.789372 13.125292 9.393337
H 4.844535 12.739619 10.856502
C 3.594168 10.650126 12.305886
C 1.328198 12.245302 11.987744
H 0.435497 12.853140 11.872496
C 1.795148 11.959530 13.262327
H 1.271935 12.342010 14.133751
C 2.413189 8.626728 5.484773
C 2.918155 11.159058 13.414193
H 3.281056 10.910953 14.409751
C 5.288914 10.369662 5.554371
H 5.752759 9.463408 5.151317
H 6.009666 11.188269 5.519672
H 4.458992 10.615053 4.882388
C 3.834153 6.328291 4.740708
H 4.372065 5.434794 4.440924
C 4.814136 9.793458 12.525697
H 4.896153 9.060461 11.719176
H 4.680418 9.233709 13.459476
C 1.679844 9.890159 5.872881
H 2.189837 10.754259 5.420505
H 1.790758 10.037891 6.952015
C 6.111921 10.608074 12.608228
H 6.318536 11.117914 11.661991
H 6.966689 9.962251 12.840253
H 6.042764 11.370888 13.391297
C 5.575828 6.759069 6.539421

H 6.260984 7.618753 6.517575
H 5.306511 6.638396 7.597426
C 1.950156 7.798238 4.460359
H 1.024794 8.041561 3.947898
C 2.654185 6.661795 4.086480
H 2.279212 6.029538 3.287006
C -0.081327 11.914399 9.343907
H -0.389672 12.074560 8.305358
H -0.642860 12.620031 9.962958
H -0.376798 10.901717 9.636262
C 0.200001 9.934394 5.501444
H 0.044025 9.960137 4.418389
H -0.265528 10.832316 5.919059
H -0.333685 9.063500 5.898207
C 6.311843 5.512953 6.059742
H 6.622791 5.601348 5.013270
H 5.689827 4.616053 6.153734
H 7.215021 5.351042 6.657607
C 6.978927 6.039775 9.964339
C 7.705098 7.279195 9.386087
C 6.697664 8.428778 9.551128
O 5.426347 7.790015 9.816011
C 5.720187 6.617985 10.604432
H 7.587212 5.495695 10.691804
H 6.707092 5.343343 9.165404
H 7.958682 7.125761 8.334139
H 8.631380 7.499255 9.923802
H 6.566507 9.056289 8.667093
H 6.951999 9.067991 10.407054
H 4.840818 5.975612 10.557413
H 5.898548 6.925578 11.646524
H 3.007800 3.927764 6.951996
H 4.086663 4.208442 8.990074
C 2.308384 4.119180 7.774774
H 3.032466 2.861750 9.407317
C 3.033564 3.927120 9.121308
H 1.504381 3.381610 7.669034
H 2.206410 6.145598 6.871420
C 1.725586 5.506897 7.602317
C 2.466166 4.783129 10.230705
H 3.157939 4.970932 11.050850
H 0.418210 3.153551 9.530276
Co 1.785143 6.589779 9.502287
C 0.441332 5.833744 7.976068
C 1.108579 4.920914 10.537208

C 0.021776 4.134613 9.820269
H 0.009166 6.720212 7.511757
H -0.886518 4.148650 7.830904
C -0.545338 4.869253 8.591640
H 0.861957 5.259492 11.541430
H -0.790764 3.929310 10.526310
H -1.437225 5.430605 8.889371
H 2.493979 7.154985 10.689196
H 3.153733 6.627263 8.833821
C 1.019995 8.471001 9.313345
C 0.128680 7.654899 10.091054
H 0.686655 8.735310 8.308711
H 1.443303 9.330550 9.843472
C -0.113794 7.766338 11.535676
H -0.751540 7.286104 9.571454
C 0.678487 8.521470 12.412358
C -1.197507 7.062405 12.088485
C 0.402254 8.563246 13.771995
H 1.523857 9.083588 12.029872
C -0.670943 7.851087 14.304979
H 1.031919 9.166618 14.420265
C -1.472165 7.099686 13.449988
H -1.832223 6.473635 11.428594
H -2.317655 6.541762 13.844167
H -0.881271 7.885686 15.370007

[(^{Dep}nacnac)Mg(thf)][Co(η^4-cod)(η^2-styrene)H_2] ([**12**$_{Mg}$]$^+$)

H = -3518.84858251 Eh
G = -3518.97748539 Eh
Mg 3.637325 8.292068 9.250342
N 3.834111 9.040968 7.273357
N 3.854587 10.244746 10.015590
C 4.491711 10.168042 7.017729
C 3.254746 10.642550 11.245030
C 4.946947 11.059905 8.006059
H 5.552890 11.881946 7.640761
C 4.553297 11.165892 9.354525
C 3.202782 8.366311 6.186966
C 2.186558 11.566408 11.247967
C 3.823612 7.244936 5.600799
C 1.590342 12.140755 9.980864
H 2.125849 11.766936 9.103480
H 1.734568 13.230868 9.989874
C 4.943852 12.464108 10.034415
H 4.177428 13.230083 9.869727
H 5.878420 12.842174 9.611819
H 5.055868 12.343751 11.114568
C 3.714483 10.094689 12.461106
C 1.658102 11.979458 12.472467
H 0.852533 12.709997 12.477809
C 2.128574 11.471168 13.672855
H 1.705635 11.807615 14.615334
C 1.931202 8.796640 5.750774
C 3.137980 10.517125 13.658057
H 3.504996 10.099793 14.593146
C 4.773783 10.570027 5.584373
H 4.938031 9.701154 4.941851
H 5.643105 11.229610 5.534808
H 3.921551 11.118587 5.166911
C 3.130681 6.527010 4.626744
H 3.584899 5.650482 4.176385
C 4.864688 9.122478 12.511672
H 4.732524 8.348959 11.748868
H 4.835865 8.605113 13.478013
C 1.313975 10.062331 6.305910
H 1.723115 10.923062 5.755700
H 1.651422 10.199350 7.337869
C 6.229843 9.796406 12.336497
H 6.310750 10.258002 11.348330
H 7.044572 9.070480 12.442371
H 6.377130 10.578864 13.088855
C 5.238536 6.879598 5.991682
H 5.925872 7.614939 5.543585
H 5.352896 7.016331 7.071977
C 1.273588 8.046567 4.774443
H 0.286063 8.348982 4.440769
C 1.859081 6.914134 4.225165
H 1.327091 6.336323 3.474964
C 0.092584 11.845609 9.821089
H -0.296211 12.341928 8.925663
H -0.486012 12.200157 10.679247
H -0.094717 10.771740 9.727758
C -0.211556 10.129181 6.255773
H -0.593197 10.166428 5.230719
H -0.562146 11.030205 6.767124
H -0.661699 9.265269 6.756720
C 5.689286 5.472599 5.611769
H 5.729930 5.329160 4.527537
H 5.013274 4.718236 6.030055
H 6.695278 5.280265 6.000221
C 7.240872 6.021808 9.246716
C 7.883918 7.260430 8.585907
C 6.863068 8.392376 8.814928
O 5.699952 7.761980 9.412433
C 6.188043 6.628604 10.160161
H 7.962261 5.408552 9.793466
H 6.756906 5.391907 8.493868
H 8.065597 7.093998 7.520570
H 8.840807 7.509356 9.053488
H 6.526781 8.889191 7.905103
H 7.240549 9.151605 9.510569
H 5.325778 5.996652 10.369493
H 6.626556 6.981762 11.106006
H 4.829741 4.200386 8.812843
H 4.514407 4.368115 11.112195
C 3.764417 4.181983 9.073695
H 3.523744 2.951010 10.866499
C 3.610737 4.017973 10.601715
H 3.357652 3.304874 8.553801
H 3.750767 6.064379 7.932082
C 3.087717 5.440039 8.532348
C 2.431915 4.789955 11.147888
H 2.536160 5.143473 12.171227
H 1.539881 2.793745 9.567915
Co 1.946311 6.398096 9.936604
C 1.725688 5.469028 8.135946
C 1.137341 4.619008 10.639243
C 0.807427 3.609034 9.552931
H 1.488756 6.183211 7.345375
H 0.982754 3.578901 7.366935
C 0.775702 4.292883 8.183477
H 0.308344 4.888887 11.292637
H -0.162078 3.144786 9.768435
H -0.236601 4.674225 7.997035
H 1.104945 6.929029 11.034240
H 3.103667 7.116591 10.723309
C 1.196678 8.123455 9.150452
C 0.188351 7.443215 9.954271
H 1.050040 8.103796 8.073914
H 1.461252 9.119171 9.526471
C -0.618593 8.173724 10.988197
H -0.461361 6.771129 9.389966
C -0.041448 8.879649 12.048462
C -2.012457 8.168042 10.871976

C -0.839141 9.565465 12.956804

H 1.040373 8.886153 12.167711

C -2.225707 9.560744 12.827128

H -0.368283 10.104891 13.772668

C -2.810770 8.858302 11.778323

H -2.473247 7.618123 10.054316

H -3.891592 8.840919 11.667380

H -2.844816 10.094612 13.542508

[(^{Dep}nacnac)Mg(thf)][Co(η^4-cod)(H)(CH_2CH_2Ph)] (**13$_{Mg}$**)

H = -3518.86121547 Eh

G = -3518.99071017 Eh

Mg 3.335773 8.154684 9.351726

N 3.763516 8.919980 7.415359

N 3.564712 10.119197 10.142215

C 4.421284 10.059011 7.204504

C 2.872207 10.531779 11.321437

C 4.781616 10.962951 8.216367

H 5.391604 11.799685 7.895195

C 4.293000 11.053752 9.534618

C 3.275970 8.235312 6.263671

C 1.774213 11.413653 11.220906

C 4.004797 7.153214 5.732965

C 1.270595 11.942981 9.894145

H 1.850715 11.514595 9.071815

H 1.450961 13.027537 9.863794

C 4.604202 12.364451 10.233008

H 3.851899 13.119956 9.979158

H 5.572504 12.744530 9.896432

H 4.609589 12.264987 11.320440

C 3.291104 10.068204 12.583154

C 1.164154 11.859780 12.394589

H 0.326930 12.549916 12.325322

C 1.609474 11.451214 13.641758

H 1.123251 11.816289 14.541616

C 2.037946 8.617497 5.712402

C 2.660211 10.548997 13.728297

H 3.003380 10.203816 14.701804

C 4.815280 10.445345 5.793518

H 5.245054 9.598962 5.248778

H 5.529753 11.270351 5.801763

H 3.935583 10.763553 5.223036

C 3.473689 6.455655 4.649361

H 4.017115 5.616919 4.226032

C 4.460521 9.130230 12.732073

H 4.472041 8.422749 11.899027

H 4.319547 8.540323 13.646203

C 1.287638 9.800080 6.282958

H 1.742262 10.730997 5.911396

H 1.449917 9.825532 7.365705

C 5.805910 9.863344 12.807390

H 6.004491 10.415510 11.883857

H 6.633328 9.162663 12.970948

H 5.806300 10.583920 13.632372

C 5.325069 6.775510 6.361344

H 5.983483 7.656033 6.354204

H 5.153150 6.566870 7.426636

C 1.535382 7.882436 4.637329

H 0.573236 8.144785 4.209209

C 2.243366 6.810925 4.109809

H 1.834460 6.248268 3.275682

C -0.219676 11.688805 9.639700

H -0.525803 12.156425 8.697515

H -0.847902 12.097528 10.436845

H -0.428446 10.617133 9.576327

C -0.210763 9.827441 5.991910

H -0.425586 9.981771 4.929661

H -0.684142 10.643903 6.545291

H -0.688424 8.890818 6.300858

C 6.062264 5.602067 5.725637

H 6.305319 5.796463 4.675571

H 5.474987 4.678835 5.771251

H 7.003538 5.417625 6.254143

C 7.204394 6.063439 9.901883

C 7.705537 7.326339 9.163260

C 6.546345 8.327806 9.299103

O 5.405218 7.545201 9.740340

C 5.965157 6.559425 10.635147

H 7.946626 5.647016 10.588232

H 6.925186 5.283113 9.186801

H 7.920781 7.108656 8.113712

H 8.616192 7.729007 9.615311

H 6.263233 8.825449 8.373818

H 6.752493 9.090204 10.061444

H 5.205169 5.802670 10.818043

H 6.230509 7.047425 11.585285

H 3.450479 4.517788 6.932716

H 4.555286 4.759162 8.959191

C 2.787193 4.371618 7.792654

H 3.920756 3.139390 9.209131

C 3.621616 4.193101 9.071041

H 2.212692 3.463143 7.575454

H 2.027943 6.359299 7.191393

C 1.844070 5.558198 7.900970

C 2.905153 4.711861 10.296403

H 3.549555 4.989894 11.126534

H 1.385625 2.667522 9.368216

Co 1.650388 6.279678 9.815432

C 0.515812 5.421559 8.341950

C 1.588950 4.386787 10.643409

C 0.738204 3.409029 9.851014

H -0.194397 6.154700 7.952773

H -0.365580 3.471165 7.962224

C -0.128607 4.136830 8.809622

H 1.325134 4.501534 11.695829

H 0.096515 2.846179 10.538651

H -1.091333 4.394896 9.269732

H 0.199484 6.403744 10.818091

H 2.580187 7.011619 10.824449

C 0.827283 8.040672 9.442694

C -0.192713 7.398315 10.380881

H 0.431334 8.197671 8.435284

H 1.173028 8.996705 9.854614

C -0.609914 8.189179 11.592955

H -1.081702 7.089353 9.822434

C 0.128978 8.151509 12.775033

C -1.785174 8.944114 11.558798

C -0.309171 8.834477 13.903998

H 1.050490 7.573441 12.799825

C -1.484158 9.578252 13.864829

H 0.273899 8.788286 14.819290

C -2.217212 9.639132 12.683285

H -2.371291 8.978248 10.642615

H -3.136876 10.216715 12.640601

H -1.826942 10.108362 14.749068

- *Reductive Elimination Step with Participation of the Counterion: [Na(thf)$_6$][Co(η^4-cod)(η^2-styrene)(H)(CH$_2$CH$_2$Ph)] and [(^{Dep}nacnac)Mg][Co(η^4-cod)-(η^2-styrene)(H)(CH$_2$CH$_2$Ph)]*

[Na(thf)$_6$][Co(η^4-cod)(η^2-styrene)(H)(CH$_2$CH$_2$Ph)] (**14$_{Na}$**)

H = -3870.60836432 Eh

G = -3870.76527859 Eh

Co -1.910978 -0.836100 1.731379
C -1.712699 0.138065 -0.085036
H -1.587216 1.208053 0.097709
C -0.648740 -0.474782 -0.969446
H 0.304118 0.017602 -0.751072
H -0.861203 -0.277017 -2.035398
C -0.488015 -1.983928 -0.715451
H -1.073622 -2.570751 -1.433782
H 0.559080 -2.267819 -0.877557
C -0.876243 -2.361738 0.703875
H -0.044157 -2.668796 1.331283
C -2.141211 -2.813163 1.081195
H -2.201315 -3.470443 1.947185
C -3.314385 -2.908682 0.129505
H -4.218655 -3.067312 0.727856
H -3.208035 -3.789828 -0.526661
C -3.487275 -1.624706 -0.705469
H -2.953320 -1.709839 -1.659496
H -4.546282 -1.502863 -0.965298
C -0.853037 -1.181269 3.386954
H -1.395182 -0.911614 4.291273
H -0.407297 -2.175537 3.446794
C -0.170123 -0.154526 2.654209
H -0.425809 0.879422 2.883700
C -3.008906 -0.391619 0.047011
H -3.796804 0.306187 0.320105
H -3.105252 -1.449705 2.342490
C -2.821309 0.739973 2.625763
H -2.573165 1.616488 2.001916
H -2.325946 0.904553 3.594397
C -4.337653 0.774230 2.899909
H -4.598465 0.006576 3.639016
H -4.896406 0.529657 1.987801
C -4.764042 2.132152 3.398715
C -4.728948 3.241953 2.541286
C -5.128378 2.356621 4.730895
C -5.007658 4.522566 3.002516
H -4.473783 3.085618 1.494902
C -5.408121 3.639047 5.201096
H -5.203246 1.507312 5.406768
C -5.336664 4.732224 4.342920
H -4.982625 5.363316 2.313173
H -5.701457 3.779804 6.239516
H -5.568844 5.731279 4.702728
C 1.131373 -0.250554 2.012442
C 1.620065 0.852761 1.276033
C 1.987534 -1.368337 2.108986
C 2.859361 0.833598 0.655920
H 0.979119 1.728257 1.177874
C 3.226560 -1.390319 1.479382
H 1.681014 -2.221290 2.707517
C 3.678395 -0.294929 0.744904
H 3.190289 1.700535 0.088360
H 3.855601 -2.272525 1.574702
H 4.647258 -0.317242 0.255167
H 1.751261 -0.142303 4.941012
H 3.384111 0.739575 3.337381
C 2.699613 0.214221 5.363507
C 3.395418 1.132516 4.356014
H 3.305748 -0.646809 5.658441
H 1.632216 0.903678 7.179569
C 2.447000 1.183939 6.505362
H 3.364570 1.338367 7.097276
C 2.571597 2.406693 4.489227
O 2.080236 2.431015 5.865230
H 1.706862 2.385252 3.811529
H 3.536405 4.959691 9.248835
H 3.147500 3.322200 4.312786
H -0.745001 6.482487 9.182866
C 2.936138 4.100094 8.919015
H 1.168791 4.628460 10.952352
H 3.629407 3.210296 10.787908
H 3.211761 3.846379 7.890074
C -1.381054 6.432964 8.292093
O 1.537230 4.476392 8.899974
C 3.059955 2.913796 9.901259
C 0.943097 3.961753 10.102264
Na 0.377341 3.919052 6.728026
H 1.501885 2.203227 11.293813
C -2.793448 6.960375 8.503525
H -0.692303 2.693123 3.893983
H -3.153892 6.689086 9.502893
C 1.602249 2.602687 10.280442
O -1.540308 5.045579 7.934946
H -0.138630 3.933690 9.942679
C -1.283936 3.604860 3.789503
H 3.565163 2.055440 9.451661
O -0.786763 4.565936 4.746805
C -1.324478 5.819354 4.306625
C -1.133830 4.291690 2.431054
C -3.565554 6.194188 7.424201
H 1.158893 1.891968 9.574095
C -2.894237 4.822637 7.457267
H -2.337212 3.377376 4.007493
H -4.639604 6.134081 7.618996
H -2.849496 4.331036 6.479326
H -3.400541 4.152806 8.166452
H -0.282871 6.315174 2.451311
C -1.193804 5.802359 2.776081
H -0.174157 4.032385 1.974061
H -2.044889 6.301218 2.304125
H -1.927159 3.982879 1.746909
H 4.435210 1.311699 4.657631
H -0.765217 6.616440 4.807645
H -2.386757 5.879989 4.593375
H -0.877106 6.966000 7.468653
H -2.859846 8.046531 8.393950
H -3.424118 6.671368 6.448356
H 1.536358 5.612945 4.091311
H 3.213964 5.872542 4.651708
C 2.167919 6.198891 4.764379
C 2.049055 7.725496 4.588148
H 1.163800 7.992158 4.003977
H 2.921474 8.128302 4.066270
C 1.940992 8.257251 6.039595
H 0.929511 8.623938 6.241586
H 2.641036 9.071475 6.246728
O 1.731155 5.926506 6.105954
C 2.227547 7.017817 6.889502

H 1.718766 6.993185 7.856116
H 3.311726 6.892613 7.052589
H -2.848684 1.421044 5.720219
H -0.475876 0.997939 5.575508
H -2.840016 -0.301395 6.098592
C -2.487089 0.676893 6.434620
C -0.970408 0.751920 6.519603
H -0.538933 -0.184137 6.911349
C -2.941125 1.030000 7.867503
O -0.728104 1.827556 7.455239
H -3.767884 1.746338 7.850244
H -3.276510 0.146738 8.418652
C -1.677606 1.631276 8.518279
H -1.250330 0.939261 9.261481
H -1.840198 2.602954 8.993067

$[Na(thf)_6][Co(\eta^4\text{-cod})(\eta^2\text{-styrene})(H)(CH_2CH_2Ph)]$ ($[\mathbf{15}_{Na}]^{\ddagger}$)

H = -3870.60245690 Eh
G = -3870.75800458 Eh
Co -1.860200 -0.818951 1.722004
C -1.466595 -0.033098 -0.155247
H -1.191666 1.020179 -0.051363
C -0.450841 -0.889190 -0.881967
H 0.548783 -0.519931 -0.630039
H -0.554966 -0.776539 -1.975735
C -0.550399 -2.371683 -0.473346
H -1.189706 -2.930885 -1.167728
H 0.443740 -2.829452 -0.546737
C -1.061266 -2.520906 0.953691
H -0.328178 -2.937628 1.642907
C -2.418067 -2.726476 1.298381
H -2.616479 -3.299216 2.205558
C -3.540226 -2.765273 0.280049
H -4.490307 -2.698399 0.825402
H -3.559228 -3.727801 -0.262207
C -3.453327 -1.587720 -0.711995
H -2.884872 -1.873288 -1.604148
H -4.460063 -1.333358 -1.068329
C -0.853964 -1.054827 3.423196
H -1.435251 -0.783902 4.305339
H -0.332281 -2.004476 3.549899
C -0.220856 0.000271 2.681999
H -0.524392 1.025372 2.901845
C -2.824582 -0.365576 -0.063260
H -3.514717 0.455563 0.123850
H -3.150758 -0.831291 2.421253
C -3.015959 0.729687 2.597550
H -2.594011 1.539380 1.980566
H -2.636241 0.871656 3.617846
C -4.545923 0.922658 2.641418
H -5.002462 0.177490 3.306817
H -4.972638 0.759207 1.643665
C -4.884589 2.307668 3.123522
C -4.787339 3.407786 2.261445
C -5.219439 2.552877 4.459766
C -4.992610 4.703623 2.720967
H -4.546101 3.234088 1.214429
C -5.421269 3.849568 4.927720
H -5.325931 1.709525 5.138830
C -5.301014 4.933802 4.062353
H -4.927693 5.539047 2.028158
H -5.691489 4.012108 5.968927
H -5.476073 5.945223 4.420052
C 1.046457 -0.055764 1.983434
C 1.503068 1.086075 1.282011
C 1.893267 -1.186359 1.957503
C 2.706154 1.095895 0.594075
H 0.865612 1.969227 1.265303
C 3.095037 -1.175420 1.262674
H 1.597662 -2.082097 2.494742
C 3.521283 -0.038399 0.574200
H 3.010826 1.992103 0.057939
H 3.715918 -2.068695 1.262847
H 4.461559 -0.037726 0.031432
H 1.830350 -0.260163 4.878357
H 3.368722 0.813771 3.301029
C 2.722949 0.205000 5.315868
C 3.331416 1.197856 4.322916
H 3.418450 -0.581916 5.621345
H 1.530563 0.762572 7.095061
C 2.345676 1.128288 6.463505
H 3.220480 1.340413 7.100007
C 2.378027 2.376055 4.455311
O 1.909930 2.362497 5.839760
H 1.513602 2.247142 3.790521
H 3.562013 4.912207 9.068130
H 2.846186 3.347966 4.263570
H -0.709638 6.414372 9.293354
C 2.948796 4.037395 8.812049
H 1.223970 4.504112 10.938199
H 3.704931 3.236755 10.694740
H 3.156418 3.747133 7.776271
C -1.373903 6.412731 8.422079
O 1.546386 4.403993 8.874048
C 3.148039 2.886292 9.819496
C 1.002635 3.844675 10.081573
Na 0.295173 3.899254 6.752295
H 1.651000 2.089242 11.229184
C -2.761145 6.978820 8.692661
H -0.860755 2.705933 3.937137
H -3.098936 6.694436 9.696315
C 1.713863 2.508283 10.220787
O -1.587939 5.042297 8.028790
H -0.081103 3.778989 9.949116
C -1.435077 3.627310 3.824519
H 3.699002 2.047484 9.386648
O -0.995201 4.548050 4.846604
C -1.501470 5.824953 4.431992
C -1.175918 4.364165 2.514400
C -3.592372 6.264423 7.621475
H 1.283414 1.792950 9.510722
C -2.964960 4.871945 7.602248
H -2.504008 3.405943 3.955182
H -4.660979 6.233682 7.851329
H -2.972056 4.399237 6.613808
H -3.465494 4.204627 8.318519
H -0.519286 6.459083 2.574209
C -1.370976 5.852346 2.896979
H -0.151385 4.180175 2.175281
H -2.271947 6.273649 2.442627
H -1.858586 4.033599 1.728221
H 4.343793 1.482447 4.637051
H -0.922956 6.594719 4.954028
H -2.560905 5.904188 4.721519
H -0.877984 6.954097 7.599446
H -2.795506 8.068843 8.611254
H -3.466731 6.760274 6.652523
H 1.325545 5.638142 4.076834
H 3.027550 5.877204 4.565938
C 1.989781 6.206220 4.733497
C 1.871663 7.736231 4.596893
H 0.953676 8.020121 4.074608
H 2.713046 8.145348 4.030980
C 1.854654 8.237038 6.063440

H 0.863864 8.619677 6.328486
H 2.582059 9.032269 6.248720
O 1.613258 5.907064 6.087619
C 2.162715 6.973971 6.870430
H 1.700807 6.934511 7.859759
H 3.251226 6.829519 6.978104
H -2.930884 1.741925 5.901321
H -0.593406 1.074611 5.639273
H -3.065539 -0.017972 6.036894
C -2.627028 0.872854 6.494144
C -1.110969 0.813218 6.566296
H -0.762683 -0.180543 6.892959
C -3.020784 1.053188 7.972262
O -0.781228 1.804926 7.565362
H -3.888764 1.709290 8.085270
H -3.269680 0.091842 8.431624
C -1.750825 1.650133 8.620975
H -1.343500 0.978110 9.391724
H -1.907298 2.638606 9.062687

[(^{Dep}nacnac)Mg][Co(η^4-cod)(η^2-styrene)(H)(CH_2CH_2Ph)] (**14**$_{Mg}$)

H = -3595.98836771 Eh
G = -3596.12205540 Eh
Co -1.874944 -2.316930 0.333967
C -2.377343 -3.271443 -1.438973
H -2.651104 -2.495547 -2.154824
C -1.289595 -4.210095 -1.908775
H -0.590511 -3.641644 -2.530774
H -1.713968 -4.990932 -2.562754
C -0.510369 -4.841733 -0.740533
H -0.925441 -5.820653 -0.474503
H 0.522416 -5.028871 -1.057996
C -0.486292 -3.941863 0.480377
H 0.483963 -3.513350 0.712394
C -1.396015 -4.003182 1.527378
H -1.065635 -3.640060 2.499500
C -2.578590 -4.944075 1.567722
H -3.238571 -4.623199 2.381010
H -2.242133 -5.964159 1.815777
C -3.370947 -4.939843 0.246665
H -3.002787 -5.720352 -0.428683
H -4.417621 -5.190895 0.453907
C -0.565696 -1.023689 1.053611
H -1.064382 -0.182122 1.542536
H 0.199287 -1.507849 1.668135
C -0.444681 -1.040494 -0.420137
H -1.057192 -0.323443 -0.971239
C -3.313462 -3.590675 -0.449987
H -4.251916 -3.044457 -0.469076
H -2.662365 -2.321764 1.563039
C -3.226881 -0.816744 0.063364
H -3.510085 -0.871529 -0.998868
H -2.722527 0.153150 0.190387
C -4.502130 -0.782114 0.919973
H -4.236861 -0.582055 1.965888
H -4.985493 -1.768318 0.916709
C -5.509452 0.246790 0.461908
C -6.067366 0.178821 -0.820008
C -5.911831 1.293407 1.293811
C -6.982225 1.128912 -1.257571
H -5.779342 -0.635300 -1.481559
C -6.824201 2.252876 0.860841
H -5.500565 1.353184 2.299337
C -7.360441 2.177897 -0.420617
H -7.405938 1.051844 -2.255631
H -7.121120 3.058025 1.528418
H -8.074728 2.922037 -0.761600
C 0.737698 -1.489516 -1.165387
C 0.729138 -1.417345 -2.580241
C 1.918018 -1.982905 -0.560866
C 1.800062 -1.856968 -3.334744
H -0.163013 -1.035740 -3.070996
C 2.984722 -2.442667 -1.332059
H 2.000396 -2.062959 0.521241
C 2.937572 -2.388863 -2.717777
H 1.748706 -1.799343 -4.418773
H 3.855298 -2.850733 -0.825919
H 3.769694 -2.750263 -3.313722
Mg 1.016052 0.523299 0.330366
N 0.455935 2.435933 0.017479
N 2.704666 1.021291 1.329267
C 1.207620 3.487037 0.341354
C 3.408634 -0.073007 1.909642
C 2.481957 3.394590 0.928859
H 2.982470 4.342129 1.094225
C 3.155649 2.271617 1.435058
C -0.904496 2.641817 -0.363117
C 2.856158 -0.673984 3.060024
C -1.277187 2.428590 -1.703654
C 1.701705 -0.045143 3.803030
H 1.205599 -0.819123 4.400152
H 0.946858 0.337392 3.105055
C 4.466569 2.547548 2.136391
H 5.277858 2.598509 1.400824
H 4.719792 1.762639 2.852560
H 4.430201 3.510173 2.651396
C 4.537338 -0.630098 1.277264
C 3.427900 -1.848932 3.546560
H 2.999201 -2.319510 4.428262
C 4.527641 -2.420862 2.919053
H 4.955133 -3.343690 3.299642
C -1.868671 2.970280 0.609779
C 5.077223 -1.806819 1.802008
H 5.938141 -2.257762 1.314334
C 0.679892 4.886233 0.120933
H 0.129669 5.223482 1.007247
H -0.009991 4.933010 -0.724736
H 1.505344 5.583545 -0.039661
C -2.617203 2.575757 -2.059206
H -2.911691 2.401967 -3.091844
C 5.152040 -0.017548 0.039561
H 4.626288 0.904590 -0.221341
H 4.992826 -0.696526 -0.808925
C -1.515963 3.127053 2.073194
H -1.600157 4.186748 2.354911
H -0.468299 2.853778 2.235611
C 6.653951 0.262404 0.178369
H 7.031756 0.777064 -0.710976
H 7.228800 -0.661227 0.293436
H 6.862938 0.887818 1.052122
C -0.255391 2.088428 -2.759110
H 0.463211 1.348426 -2.382405
H -0.773008 1.610467 -3.599603
C -3.192767 3.134725 0.201162
H -3.951146 3.393557 0.933623
C -3.572332 2.936457 -1.117611
H -4.616710 3.033060 -1.398819
C 2.140071 1.104811 4.718561
H 1.289830 1.483647 5.295262
H 2.547689 1.936877 4.136711
H 2.910900 0.770514 5.420712
C -2.403721 2.297219 3.008569
H -2.405388 1.241392 2.717760
H -3.441828 2.640274 2.991885

H -2.045750 2.369896 4.040928

C 0.523140 3.305515 -3.273467

H -0.161987 4.078082 -3.638093

H 1.187501 3.019403 -4.095725

H 1.140036 3.742459 -2.482735

[(^{Dep}nacnac)Mg][Co(η^4-cod)(η^2-styrene)(H)(CH_2CH_2Ph)] ([**15**$_{Mg}$]‡)

H = -3595.98609991 Eh

G = -3596.11964407 Eh

Co -1.894587 -2.317259 0.443438

C -2.158075 -3.399990 -1.311272

H -2.331036 -2.679596 -2.113969

C -0.997589 -4.344951 -1.534366

H -0.217019 -3.807597 -2.083357

H -1.305152 -5.181821 -2.184434

C -0.409453 -4.861598 -0.209396

H -0.867160 -5.813913 0.082338

H 0.657288 -5.072763 -0.349435

C -0.570634 -3.836067 0.901592

H 0.368337 -3.422922 1.267715

C -1.640753 -3.814096 1.815952

H -1.441269 -3.388687 2.800139

C -2.801060 -4.785588 1.779848

H -3.585154 -4.396448 2.440094

H -2.505067 -5.766722 2.188429

C -3.377574 -4.941061 0.359172

H -2.900279 -5.774694 -0.167247

H -4.442025 -5.196322 0.423451

C -0.656565 -0.940238 1.132622

H -1.167402 -0.123268 1.649488

H 0.168309 -1.377927 1.704162

C -0.614975 -0.927395 -0.343203

H -1.263240 -0.207304 -0.847802

C -3.221743 -3.663594 -0.446461

H -4.146203 -3.124855 -0.635267

H -2.926185 -1.990553 1.414438

C -3.430880 -0.890828 0.233688

H -3.512577 -0.916262 -0.862823

H -3.008293 0.086596 0.498449

C -4.849606 -0.964240 0.827454

H -4.806130 -0.845346 1.918316

H -5.283305 -1.956760 0.644422

C -5.765343 0.086967 0.251915

C -6.183122 0.012497 -1.081384

C -6.196831 1.172470 1.016201

C -7.000257 0.991866 -1.632973

H -5.863848 -0.830403 -1.691196

C -7.012530 2.160122 0.468694

H -5.887362 1.241421 2.057315

C -7.416047 2.075035 -0.860080

H -7.318716 0.910062 -2.668888

H -7.339086 2.995101 1.083406

H -8.056391 2.840691 -1.288880

C 0.513384 -1.377751 -1.161733

C 0.445802 -1.234266 -2.571052

C 1.694581 -1.953966 -0.634484

C 1.461626 -1.683940 -3.392912

H -0.446789 -0.786305 -3.001002

C 2.706151 -2.413800 -1.475001

H 1.806955 -2.106861 0.436110

C 2.601908 -2.289892 -2.854154

H 1.365393 -1.572333 -4.469718

H 3.580673 -2.881067 -1.030123

H 3.391425 -2.654476 -3.503551

Mg 0.948302 0.551575 0.330889

N 0.393410 2.475582 0.087852

N 2.659153 1.013379 1.300732

C 1.126561 3.515649 0.476701

C 3.384380 -0.110178 1.794449

C 2.407282 3.404143 1.049163

H 2.900592 4.345948 1.261617

C 3.108557 2.258371 1.459205

C -0.957314 2.663465 -0.330465

C 2.901098 -0.748827 2.955929

C -1.268518 2.531372 -1.696852

C 1.805534 -0.139752 3.797632

H 1.317424 -0.938549 4.368221

H 1.031045 0.309202 3.164103

C 4.455402 2.494010 2.102886

H 5.233470 2.513629 1.330573

H 4.715422 1.699410 2.806355

H 4.476677 3.457095 2.617381

C 4.454910 -0.659862 1.064236

C 3.483781 -1.950958 3.355683

H 3.105710 -2.450935 4.244329

C 4.527207 -2.514353 2.631822

H 4.962167 -3.458764 2.945100

C -1.973549 2.855007 0.626912

C 5.008610 -1.864826 1.503805

H 5.824009 -2.309050 0.938060

C 0.579402 4.917729 0.336668

H 0.051710 5.207119 1.252896

H -0.131504 4.996414 -0.488820

H 1.392571 5.632044 0.187690

C -2.602234 2.624855 -2.093535

H -2.848952 2.514666 -3.147246

C 4.993938 -0.011486 -0.189962

H 4.463078 0.924134 -0.386504

H 4.773765 -0.663071 -1.046658

C -1.659445 2.921277 2.106199

H -1.546546 3.972607 2.409758

H -0.680876 2.461446 2.288005

C 6.504387 0.252142 -0.137444

H 6.833347 0.784137 -1.035919

H 7.075139 -0.679144 -0.077328

H 6.771595 0.855091 0.736435

C -0.191825 2.314906 -2.730977

H 0.535326 1.569797 -2.381283

H -0.657023 1.888403 -3.627735

C -3.291384 2.960305 0.180474

H -4.094271 3.098755 0.896397

C -3.610689 2.843503 -1.164555

H -4.649576 2.892665 -1.477223

C 2.323351 0.933643 4.763690

H 1.516522 1.288595 5.413301

H 2.717679 1.796353 4.218594

H 3.123841 0.535137 5.395681

C -2.702765 2.258682 3.010298

H -2.901440 1.228127 2.695859

H -3.655061 2.796935 3.004055

H -2.346732 2.237952 4.045243

C 0.561382 3.594139 -3.116441

H -0.138210 4.374778 -3.433302

H 1.254627 3.398588 -3.941218

H 1.144260 3.979775 -2.275221

2.5 References

[1] a) S. Nishimura, *Handbook of Heterogeneous Catalytic Hydrogenation for Organic Synthesis*, Wiley, New York **2001**; b) *The Handbook of Homogeneous Hydrogenation* (Eds.: J. G. de Vries, C. J. Elsevier), Wiley-VCH, Weinheim **2007**.

[2] a) M. D. Garba, A. Galadima, *J. Phys. Sci.* **2018**, *29*, 153; b) T. Ohta, H. Takaya, M. Kitamura, K. Nagai, R. Noyori, *J. Org. Chem.* **1987**, *52*, 3174; c) M. K. Gupta, *Practical guide to vegetable oil processing*, Academic Press; AOCS Press, Amsterdam, Urbana, IL **2017**, pp. 171–215.

[3] a) J. A. Osborn, F. H. Jardine, J. F. Young, G. Wilkinson, *J. Chem. Soc., A* **1966**, 1711; b) R. H. Crabtree, J. M. Mihelcic, J. M. Quirk, *J. Am. Chem. Soc.* **1979**, *101*, 7738; c) H. Doucet, T. Ohkuma, K. Murata, T. Yokozawa, M. Kozawa, E. Katayama, A. F. England, T. Ikariya, R. Noyori, *Angew. Chem.* **1998**, *110*, 1792; *Angew. Chem. Int. Ed.* **1998**, *37*, 1703; d) T. Naota, H. Takaya, S.-I. Murahashi, *Chem. Rev.* **1998**, *98*, 2599.

[4] a) P. J. Chirik, *Acc. Chem. Res.* **2015**, *48*, 1687; b) J. Loup, U. Dhawa, F. Pesciaioli, J. Wencel-Delord, L. Ackermann, *Angew. Chem.* **2019**, *131*, 12934; *Angew. Chem. Int. Ed.* **2019**, *58*, 12803; c) L. Alig, M. Fritz, S. Schneider, *Chem. Rev.* **2019**, *119*, 2681; d) P. Gandeepan, T. Müller, D. Zell, G. Cera, S. Warratz, L. Ackermann, *Chem. Rev.* **2019**, *119*, 2192.

[5] a) Q. Knijnenburg, A. D. Horton, H. van der Heijden, T. M. Kooistra, D. G.H. Hetterscheid, J. M.M. Smits, B. de Bruin, P. H.M. Budzelaar, A. W. Gal, *J. Mol. Catal. A. Chem.* **2005**, *232*, 151; b) R. P. Yu, J. M. Darmon, J. M. Hoyt, G. W. Margulieux, Z. R. Turner, P. J. Chirik, *ACS Catal.* **2012**, *2*, 1760; c) S. Monfette, Z. R. Turner, S. P. Semproni, P. J. Chirik, *J. Am. Chem. Soc.* **2012**, *134*, 4561; d) M. R. Friedfeld, M. Shevlin, J. M. Hoyt, S. W. Krska, M. T. Tudge, P. J. Chirik, *Science* **2013**, *342*, 1076; e) T. N. Gieshoff, U. Chakraborty, M. Villa, A. Jacobi von Wangelin, *Angew. Chem.* **2017**, *129*, 3639; *Angew. Chem. Int. Ed.* **2017**, *56*, 3585; f) N. G. Léonard, P. J. Chirik, *ACS Catal.* **2018**, *8*, 342; g) W. Ai, R. Zhong, X. Liu, Q. Liu, *Chem. Rev.* **2019**, *119*, 2876; h) Z. Wei, Y. Wang, Y. Li, R. Ferraccioli, Q. Liu, *Organometallics* **2020**, *39*, 3082; i) Y. Kobayashi, Y. Sunada, *ACS Sustainable Chem. Eng.* **2022**, *10*, 1078.

[6] D. Gärtner, A. Welther, B. R. Rad, R. Wolf, A. Jacobi von Wangelin, *Angew. Chem.* **2014**, *126*, 3796; *Angew. Chem. Int. Ed.* **2014**, *53,* 3722.

[7] S. Sandl, T. M. Maier, N. P. van Leest, S. Kröncke, U. Chakraborty, S. Demeshko, K. Koszinowski, B. de Bruin, F. Meyer, M. Bodensteiner, C. Herrmann, R. Wolf, A. Jacobi von Wangelin, *ACS Catal.* **2019**, *9*, 7596.

[8] T. M. Maier, S. Sandl, P. Melzl, J. Zweck, A. Jacobi von Wangelin, R. Wolf, *Chem. Eur. J.* **2020**, *26*, 6113.

[9] P. Büschelberger, D. Gärtner, E. Reyes-Rodriguez, F. Kreyenschmidt, K. Koszinowski, A. Jacobi von Wangelin, R. Wolf, *Chem. Eur. J.* **2017**, *23*, 3139.

[10] a) J. E. Ellis, *Inorg. Chem.* **2006**, *45*, 3167; b) W. W. Brennessel, J. E. Ellis, *Inorg. Chem.* **2012**, *51*, 9076; c) E. T. Ouellette, J. S. Magdalenski, R. G. Bergman, J. Arnold, *Acc. Chem. Res.* **2022**, *55*, 783.

[11] On cation effects in catalytic studies: a) C. R. Kennedy, S. Lin, E. N. Jacobsen, *Angew. Chem.* **2016**, *128*, 12784; *Angew. Chem. Int. Ed.* **2016**, *55*, 12596; b) A. J. Neel, M. J. Hilton, M. S. Sigman, F. D. Toste, *Nature* **2017**, *543*, 637; c) A. Paparo, J. S. Silvia, T. P. Spaniol, J. Okuda, C. C. Cummins, *Chem. Eur. J.* **2018**, *24*, 17072; d) T. V. Tran, L. J. Karas, J. I. Wu, L. H. Do, *ACS Catal.* **2020**, *10*, 10760; e) T. X. Gentner, A. R. Kennedy, E. Hevia, R. E. Mulvey, *ChemCatChem* **2021**, *13*, 2371; f) A. H. Farquhar, K. E. Gardner, S. Acosta-Calle, A. M. Camp, C.-H. Chen, A. J. M. Miller, *Organometallics* **2022**, *41*, 3366; g) A. M. Borys, E. Hevia, *Dalton Trans.* **2023**, *52*, 2098; h) S. Acosta-Calle, A. J. M. Miller, *Acc. Chem. Res.* **2023**, *56*, 971; i) P. A. Macdonald, S. Banerjee, A. R. Kennedy, A. van Teijlingen, S. D. Robertson, T. Tuttle, R. E. Mulvey, *Angew. Chem. Int. Ed.* **2023**, e202304966.

[12] On cation effects in synthetic studies: a) J. Andrez, V. Guidal, R. Scopelliti, J. Pécaut, S. Gambarelli, M. Mazzanti, *J. Am. Chem. Soc.* **2017**, *139*, 8628; b) D. L. J. Broere, B. Q. Mercado, E. Bill, K. M. Lancaster, S. Sproules, P. L. Holland, *Inorg. Chem.* **2018**, *57*, 9580; c) S. M. Bhutto, P. L. Holland, Eur. J. *Inorg. Chem.* **2019**, *2019*, 1861; d) A. Najafian, T. R. Cundari, *Inorg. Chem.* **2019**, *58*, 12254; e) G. M. Ballmann, M. J. Evans, T. X. Gentner, A. R. Kennedy, J. R. Fulton, M. P. Coles, R. E. Mulvey, *Inorg. Chem.* **2022**, *61*, 19838; f) A. Rae, K. M. Byrne, S. A. Brown, A. R. Kennedy, T. Krämer, R. E. Mulvey, S. D. Robertson, *Chem. Eur. J.* **2022**, *28*, e202104260; g) S. Banerjee, P. A. Macdonald, S. A. Orr, A. R. Kennedy, A. van Teijlingen, S. D. Robertson, T. Tuttle, R. E. Mulvey, *Chem. Eur. J.* **2022**, *28*, e202201085; h) A. Logallo, E. Hevia, *Chem. Commun.* **2023**, *59*, 5383; i) M. J. Evans, C. Jones, *Inorg. Chem.* **2023**, *62*, 14393–14401; j) H.-Y. Liu, M. S. Hill, M. F. Mahon, C. L. McMullin, R. J. Schwamm, *Organometallics* **2023**, *42*, 2881.

[13] M. R. Kita, A. J. M. Miller, *Angew. Chem.* **2017**, *129*, 5590; *Angew. Chem. Int. Ed.* **2017**, *56*, 5498.

[14] a) F. Freitag, T. Irrgang, R. Kempe, *J. Am. Chem. Soc.* **2019**, *141*, 11677; b) G. Zhang, T. Irrgang, M. Schlagbauer, R. Kempe, *Chem Catal.* **2021**, *1*, 681.

[15] P. A. Dub, J. C. Gordon, *Nat. Rev. Chem.* **2018**, *2*, 396.

[16] a) K. Jonas (Studiengesellschaft Kohle mbH), US4169845 A, **1977**; b) K. Jonas, R. Mynott, C. Krüger, J. C. Sekutowski, Y.-H. Tsay, *Angew. Chem.* **1976**, *88*, 808.

[17] J. A. Kelly, J. Gramüller, R. M. Gschwind, R. Wolf, *Dalton Trans.* **2021**, *50*, 13985.

[18] a) J. A. Widegren, R. G. Finke, *J. Mol. Catal. A: Chem.* **2003**, *198*, 317; b) C. A. Jaska, I. Manners, *J. Am. Chem. Soc.* **2004**, *126*, 9776; c) R. H. Crabtree, *Chem. Rev.* **2011**, *112*, 1536; d) D. Gärtner, S. Sandl, A. Jacobi von Wangelin, *Catal. Sci. Technol.* **2020**, *10*, 3502.

[19] An almost immediate reaction onset was observed for the hydrogenation of α-methylstyrene with **7** (Figure S4). Here, the cobaltate motif is coordinated by one η^4-1,5-cyclooctadiene and two η^2-styrene ligands. Ligand exchange and pre-catalyst hydrogenation is significantly facilitated due to the (monodentate) styrene ligands which reduces the induction period to a minimum.

[20] Note that an initial induction period can be in part due to the experimental set up (pressure increase when the last solution is added to the reaction vessel and thus initial consumption of this over-pressure at the start of the measurement).

[21] a) P. J. Dyson, *Dalton Trans.* **2003**, 2964; b) V. Artero, M. Fontecave, *Chem. Soc. Rev.* **2013**, *42*, 2338; On amalgamation with metals: a) C. Gumiński, *J. Mater. Sci.* **1989**, *24*, 3285; b) H. R. Kirchmayr, *Monaths. Chem.* **1964**, *95*, 1479.

[22] On quantitative phosphine and phosphite poisoning of iron group metals: a) K.-N. T. Tseng, J. W. Kampf, N. K. Szymczak, *ACS Catal.* **2015**, *5*, 411; b) S. Sandl, F. Schwarzhuber, S. Pöllath, J. Zweck, A. Jacobi von Wangelin, *Chem. Eur. J.* **2018**, *24*, 3403.

[23] Note that the hydrogenation of α-methylstyrene with 3 mol% **4** and 3 mol% PMe_3 led to additional hydrogenation of the phenyl moiety, giving fully reduced isopropylcyclohexane in 42% yield (see Scheme S1 for further details). This is in accordance with previous reports on arene hydrogenation by transition metal phosphine and phosphite complexes: a) E. L. Muetterties, F. J. Hirsekorn, *J. Am. Chem. Soc.* **1974**, *96*, 4063; b) M. C. Rakowski, F. J. Hirsekorn, L. S. Stuhl, E. L. Muetterties, *Inorg. Chem.* **1976**, *15*, 2379; c) L. S. Stuhl, M. Rakowski DuBois, F. J. Hirsekorn, J. R. Bleeke, A. E. Stevens, E. L. Muetterties, *J. Am. Chem. Soc.* **1978**, *100*, 2405; d) E. L. Muetterties, J. R. Bleeke, *Acc. Chem. Res.* **1979**, *12*, 324; e) K. Jonas, *Angew. Chem. Int. Ed.* **1985**, *24*, 295; f) M. D. Fryzuk, J. B. Ng, S. J. Rettig, J. C. Huffman, K. Jonas, *Inorg. Chem.* **1991**, *30*, 2437.

[24] Contrasting the reactivity of **6**, the known potassium salt $[K(thf)_2][Co(\eta^4\text{-dct})_2]$ was not able to hydrogenate related alkenes (e.g., styrene) under 2 bar H_2 at ambient temperature overnight.[9] This observation once more underscores the substantial impact of the (^{Dep}nacnac)Mg^+ cation on the hydrogenation activity. Furthermore, it seems noteworthy that both **6** and $[K(thf)_2][Co(\eta^4\text{-dct})_2]$ do not undergo ligand exchange with styrene in the absence of H_2 (see Figure S14 for details). These observations suggest that ligand hydrogenation in the pre-catalysts initiates the formation of the catalytically active species.

[25] P. Büschelberger, E. Reyes-Rodriguez, C. Schöttle, J. Treptow, C. Feldmann, A. Jacobi von Wangelin, R. Wolf, *Catal. Sci. Technol.* **2018**, *8*, 2648.

[26] L. Pauling, *J. Am. Chem. Soc.* **1947**, *69*, 542.

[27] a) H. Ryu, J. Park, H. K. Kim, J. Y. Park, S.-T. Kim, M.-H. Baik, *Organometallics* **2018**, *37*, 3228; b) L. N. Mendelsohn, L. Pavlovic, H. Zhong, M. R. Friedfeld, M. Shevlin, K. H. Hopmann, P. J. Chirik, *J. Am. Chem. Soc.* **2022**, *144*, 15764.

[28] R. Lalrempuia, C. E. Kefalidis, S. J. Bonyhady, B. Schwarze, L. Maron, A. Stasch, C. Jones, *J. Am. Chem. Soc.* **2015**, *137*, 8944.

[29] Kinetic kit "X204" gas uptake under: https://www.manonthemoontech.com.

[30] M. Lux, M. Klussmann, *Org. Lett.* **2020**, *22*, 3697.

[31] W. Adam, M. A. Arnold, M. Grüne, W. M. Nau, U. Pischel, C. R. Saha-Möller, *Org. Lett.* **2002**, *4*, 537.

[32] N. G. Léonard, P. J. Chirik, *ACS Catal.* **2018**, *8*, 342.

[33] On recent hydrogenation catalysis with magnesium pincer complexes: a) Y. Liang, U. K. Das, J. Luo, Y. Diskin-Posner, L. Avram, D. Milstein, *J. Am. Chem. Soc.* **2022**, *144*, 19115; b) Y. Liang, J. Luo, Y. Diskin-Posner, D. Milstein, *J. Am. Chem. Soc.* **2023**, *145*, 9164.

[34] On the synthesis of $[M(L_n)][Co(PMe_3)_4]$: R. Hammer, H.-F. Klein, *Z. Naturforsch. B* **1977**, *32*, 138.

[35] a) Sheldrick, G. M. SADABS, Bruker AXS, Madison, USA **2007**; b) CrysAlisPro, Scale3 Abspack, Rigaku Oxford Diffraction **2019**.

[36] R. C. Clark, J. S. Reid, *Acta Crystallogr. A* **1995**, *51*, 887.

[37] G. M. Sheldrick, *Acta Crystallogr. C* **2015**, *71*, 3.

[38] O. V. Dolomanov, L. J. Bourhis, R. J. Gildea, J. A. K. Howard, H. Puschmann, *J. Appl. Crystallogr.* **2009**, *42*, 339.

[39] G. M. Sheldrick, *Acta Crystallogr. A* **2008**, *64*, 112.

[40] a) H. J. C. Berendsen, D. van der Spoel, R. van Drunen, *Comput. Phys. Commun.* **1995**, *91*, 43; b) E. Lindahl, B. Hess, D. van der Spoel, *J. Mol. Model.* **2001**, *7*, 306; c) D. Van Der Spoel, E. Lindahl, B. Hess, G. Groenhof, A. E. Mark, H. J. C. Berendsen, *J. Comput. Chem.* **2005**, *26*, 1701; d) B. Hess, C. Kutzner, D. van der Spoel, E. Lindahl, *J. Chem. Theory Comput.* **2008**, *4*, 435; e) S. Pronk, S. Páll, R. Schulz, P. Larsson, P. Bjelkmar, R. Apostolov, M. R. Shirts, J. C. Smith, P. M. Kasson, D. van der Spoel, B. Hess, E. Lindahl, *Bioinformatics* **2013**, *29*, 845; f) M. J. Abraham, T. Murtola, R. Schulz, S. Páll, J. C. Smith, B. Hess, E. Lindahl, *SoftwareX* **2015**, 1–2, 19; g) S. Páll, M. J. Abraham, C. Kutzner, B. Hess, E. Lindahl, Lecture Notes in Computer Science **2015**, 3–27.

[41] a) Lindahl, Abraham, Hess, Van Der Spoel, GROMACS 2021.5 Documentation, **2022**; b) Lindahl, Abraham, Hess, Van Der Spoel, GROMACS 2021.5 Source Code, Zenodo, **2022**.

[42] a) Neese, F., The ORCA program system. *WIREs Comput. Mol. Sci.* **2012**, 2: 73, https://doi.org/10.1002/wcms.81; b) F. Neese, *WIREs Comput. Mol. Sci.* **2017**, 8:e1327. https://doi.org/10.1002/wcms.1327; c) Neese, F. Software update: The

ORCA program system—Version 5.0. *WIREs Comput. Mol. Sci.* **2022**; 12:e1606. https://doi.org/10.1002/wcms.1606.

[43] a) H. Kruse, S. Grimme, *J. Chem. Phys.* **2012**, *136*, 154101; b) E. Caldeweyher, C. Bannwarth, S. Grimme, *J. Chem. Phys.* **2017**, *147*, 034112; c) E. Caldeweyher, S. Ehlert, A. Hansen, H. Neugebauer, S. Spicher, C. Bannwarth, S. Grimme, *J. Chem. Phys.* **2019**, *150*, 154122; d) J. W. Furness, A. D. Kaplan, J. Ning, J. P. Perdew, J. Sun, *J. Phys. Chem. Lett.* **2020**, *11*, 8208; e) S. Grimme, A. Hansen, S. Ehlert, J.-M. Mewes, *J. Chem. Phys.* **2021**, *154*, 064103.

[44] NBO 7.0. E. D. Glendening, J. K. Badenhoop, A. E. Reed, J. E. Carpenter, J. A. Bohmann, C. M. Morales, P. Karafiloglou, C. R. Landis, and F. Weinhold, Theoretical Chemistry Institute, University of Wisconsin, Madison, WI (**2018**).

[45] Multiwfn: T. Lu, F. Chen, J. *Comput. Chem.* **2011**, *33*, 580. Selected references for NCI analyses: a) E. R. Johnson, S. Keinan, P. Mori-Sánchez, J. Contreras-García, A. J. Cohen, W. Yang, *J. Am. Chem. Soc.* **2010**, *132*, 6498; b) J. Contreras-García, E. R. Johnson, S. Keinan, R. Chaudret, J.-P. Piquemal, D. N. Beratan, W. Yang, *J. Chem. Theory Comput.* **2011**, *7*, 625; c) R. A. Boto, F. Peccati, R. Laplaza, C. Quan, A. Carbone, J.-P. Piquemal, Y. Maday, J. Contreras-García, *J. Chem. Theory Comput.* **2020**, *16*, 4150.

[46] W. Humphrey, A. Dalke, K. Schulten, *J. Mol. Graph.* **1996**, *14*, 33.

[47] CYLview20; Legault, C. Y., Université de Sherbrooke, **2020** (http://www.cylview.org).

[48] a) O. A. Vydrov, T. Van Voorhis, *J. Chem. Phys.* **2010**, *133*, 244103; b) W. Hujo, S. Grimme, *J. Chem. Theory Comput.* **2011**, *7*, 3866; c) N. Mardirossian, M. Head-Gordon, *J. Chem. Phys.* **2016**, *144*, 214110.

Chapter 3 A Highly Reduced Magnesium Dicobalt Complex for the Hydrogenation of Tri- and Tetra-Substituted Alkenes[a]

Abstract: We describe the synthesis and structural characterization of the trinuclear magnesium dicobalt complex $Mg[Co(\eta^4\text{-cod})_2]_2$ (**1**; cod = 1,5-cyclooctadiene), showing an unsupported Co–Mg–Co structural motif. Complex **1** forms a tight ion pair in the solid state and in toluene solution due to electrostatic interactions between the Mg^{2+} cation and the $[Co(\eta^4\text{-cod})_2]^-$ anion. The complex is a successful pre-catalyst for the hydrogenation of sterically challenging tri- and tetra-substituted alkenes, surpassing the catalytic capabilities of related alkali metal and β-diketiminate magnesium complexes.

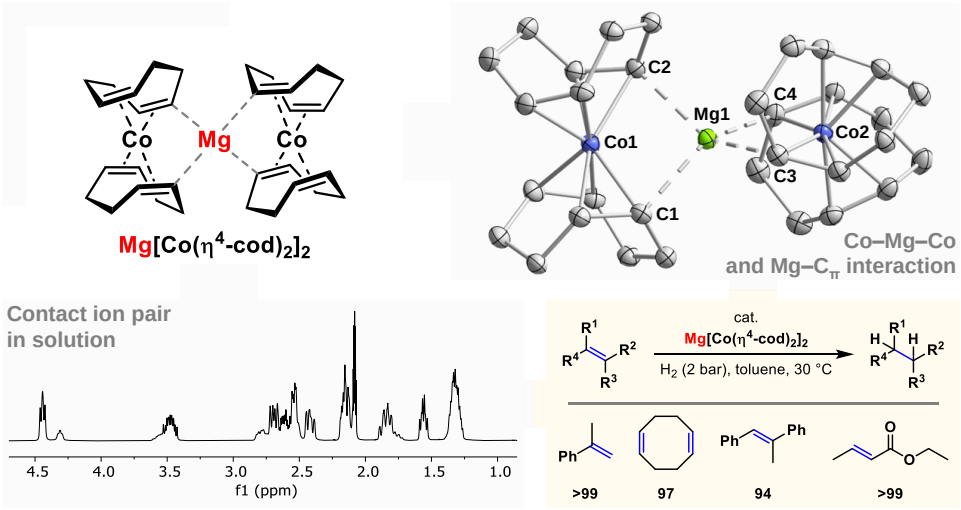

[a] Martin Gawron performed all reactions and characterizations. Johannes Eder conducted and interpreted the DOSY NMR experiments under the supervision of Ruth M. Gschwind. Xaver Weichselgartner assisted in the hydrogenation studies. Robert Wolf supervised and directed the project. Martin Gawron prepared the manuscript with input from Robert Wolf.

3.1 Introduction

Low-oxidation state alkali metal cobaltate salts, such as $[M(thf)_n][Co(\eta^2\text{-}C_2H_4)]$ (M = Li, donor = TMEDA, **A**; M = K, donor = thf, **B**; C_2H_4 = ethylene), $[M(thf)_n][Co(\eta^4\text{-cod})_2]$ (**C**: M = Li; **D**: M = Na; **E**: M = K; cod = 1,5-cyclooctadiene), and $[K([2.2.2]crypt.)][Co(\eta^4\text{-}C_{14}H_{10})_2]$ (**F**; $C_{14}H_{10}$ = anthracene, crypt. = cryptand), are versatile synthetic equivalents for the "Co^-" anion in organometallic chemistry (Figure 1, top).[1] These complexes also display promising reactivities in processes such as small molecule activation,[2] alkene hydrogenation,[1e],[3] and other catalytic reactions.[4] The reactivity and catalytic properties of the cobaltate anions can be manipulated by heteroatomic ligands (e.g., phosphines, bipyridines, or α-diimines).[1c],[6],[7] However, the effect of the counterions on their reactivity has not been thoroughly understood. Only a few alkaline earth metal cobaltates are known, including the "inorganic Grignard reagent" $[MgBr(thf)_2][CpCo(\eta^3\text{-}C_3H_5)]$ (**G**) reported by Jonas, and the carbonyl complexes $[AE(thf)_n][Co(CO)_x(PCy_3)]_2$ reported by Mountford (where x = 1-3 and AE = Mg-Ba; see, for example, complex **H** in Figure 1, bottom).[8] Furthermore, there are few structurally-related cobaltate compounds with counterions beyond group 2, with $Hg[Co(CO)_4]$ and $Zn[Co(\eta^4\text{-}C_4H_6)_2]$ (C_4H_6 = 1,3-butadiene) being scarce examples.[1c],[9]

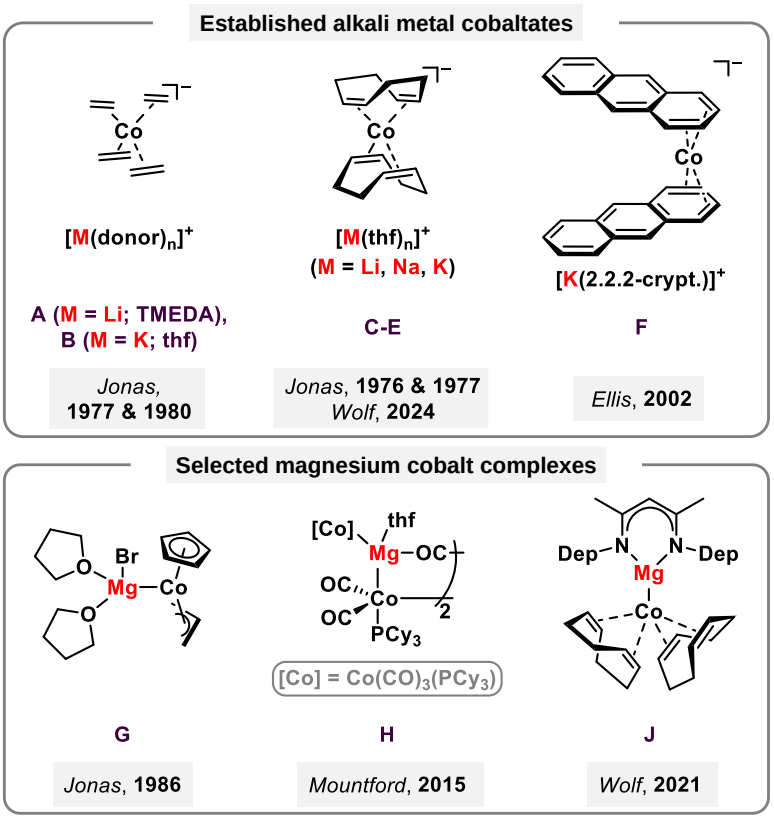

Figure 1. Established alkali metal cobaltates used as synthetic precursors, pre-catalysts or in the activation of small molecules (top) and selected examples of magnesium cobalt complexes (bottom). Dep = 2,6-diethylphenyl. crypt. = cryptand.

Recently, we discovered that countercations have a significant impact on the catalytic properties of anionic cobaltates **C**-**E** and $[(^{Dep}nacnac)Mg][Co(\eta^4\text{-cod})_2]$ (**J**; Dep

=2,6-diethylphenyl) during alkene hydrogenations.[1e] Our studies suggest that the counterion plays an active co-catalytic role in the hydrogenation reaction by coordinating to cobalt hydride intermediates. To investigate the enhanced reactivity of magnesium cobaltates compared to their alkali metal salts, we have now prepared the Mg^{2+} complex, $Mg[Co(\eta^4\text{-cod})_2]_2$ (**1**, Figure 2), which lacks any additional ligands on the magnesium cation. In this report, we describe the synthesis and molecular structure of **1**, which features a linear Co-Mg-Co arrangement. We analyze the bonding situation in **1** and demonstrate that this complex catalyzes the hydrogenation of tri- and tetra-substituted alkenes with a remarkable efficiency.[1e]

3.2 Results and Discussion

Complex **1** was prepared by treating anhydrous $MgCl_2$ with $[K(thf)_{0.33}][Co(\eta^4\text{-cod})_2]$ (**E**) in THF/toluene. The compound was isolated as an orange-yellow powder in 63% yield. Crystals grown from a saturated toluene solution were analyzed by single crystal X-ray diffraction. In the solid state, **1** forms an ion triple with a Mg^{2+} cation sandwiched by two $[Co(\eta^4\text{-cod})_2]^-$ units (Figure 2, bottom; Co1–Mg1–Co2 179.36(4)°).[10] The two $[Co(\eta^4\text{-cod})_2]^-$ anions are rotated toward each other at 50.42(6)° along the Co–Mg–Co axis (plane[C1-Co1-C2]-to-plane[C3-Co2-C4]). The Co–Mg distances (2.631(6) and 2.615(6) Å) are similar to those in complex **J**.[2d] Close contacts of the Mg^{2+} cation with four carbon atoms of the cod ligands (C1, C2, C3 and C4; Mg–C 2.362(8)-2.415(8) Å) presumably arise from an interaction with the π-bonds of the cod ligand.

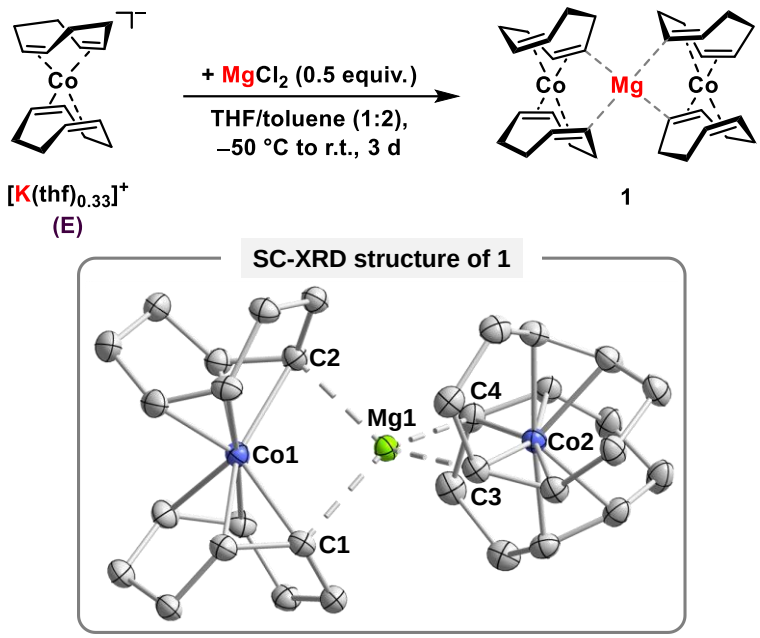

Figure 2. Top: Synthesis of $Mg[Co(\eta^4\text{-cod})_2]_2$ (**1**). Bottom: Solid state molecular structure of **1**. Thermal ellipsoids are drawn at 40% probability level. H atoms are omitted for clarity. Selected bond lengths [Å] and angles [°]: Co1–Mg1 2.631(6), Co2–Mg1 2.615(6), Mg1–C1 2.411(2), Mg1–C2 2.362(2), Mg1–C3 2.363(2), Mg1–C4 2.415(2), Co1–Mg1–Co2 179.36(4).

A quantum chemical analysis using intrinsic bond orbitals (IBOs), second order perturbation theory (SOPT) analysis and quantum theory of atoms in molecules (QTAIM) analysis indicates that these interactions are weakly covalent (see section 3.4.11 for details). The ^{1}H and $^{13}C\{^{1}H\}$ NMR spectra of **1** show the presence of two species in a ratio of approximately 1.0:0.25, which is explained by the presence of rotamers with similar NMR spectra (Figure 3). ^{1}H NMR resonances at 1.2-4.5 ppm are assigned to the (chemically) inequivalent H atoms of the cod ligands (Figure S12). The cod ligands give rise to eight $^{13}C\{^{1}H\}$ NMR resonances between 27.0 and 83.0 ppm (Figure S13). This is in agreement with the contact ion structure observed in the solid state, for which chemically inequivalent carbon atoms are expected.[2d] Broadening of the resonances is observed at elevated temperature (60 °C), which possibly indicates chemical exchange between the rotamers (Figure S17).

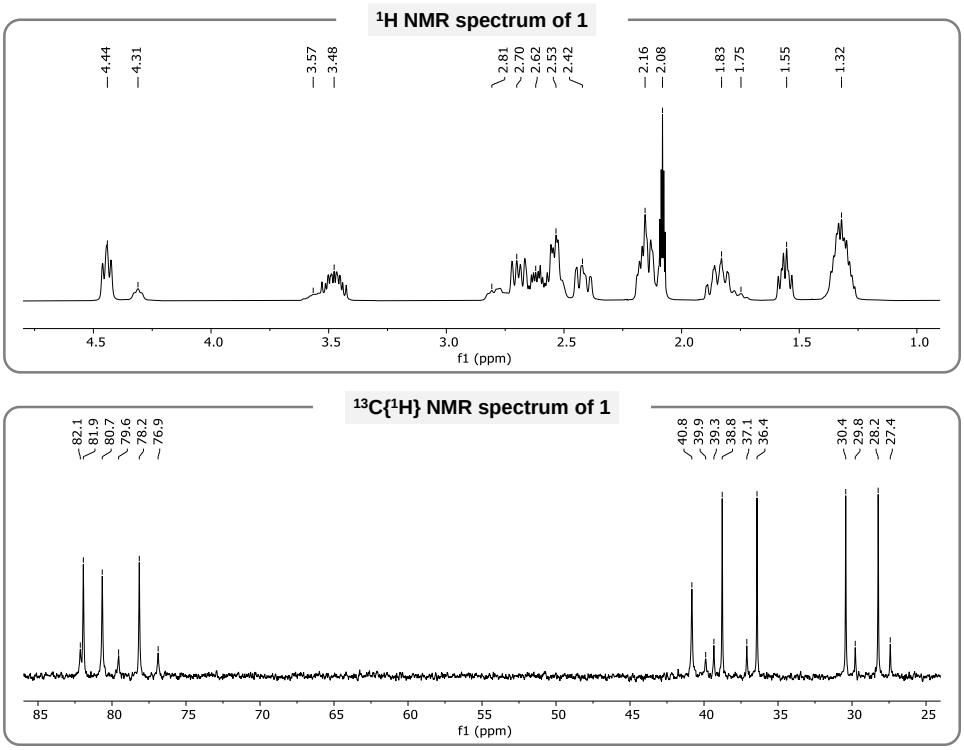

Figure 3. Cutouts of the ^{1}H and $^{13}C\{^{1}H\}$ NMR spectra (400.13/100.61 MHz, 298 K) of **1** in toluene-d_8.

Further confirmation of the intimate ion pair character in solution was provided by DOSY NMR studies of **1** and the lithium salt $[Li(thf)_{1.92}][Co(\eta^4\text{-cod})_2]$ (**C**) (section 3.4.5.1). For **1**, similar diffusion coefficients ($D \approx 9.1 \times 10^{-10}$ m^2 s^{-1}) were obtained for all suitable cod ligand signals, which correspond to a hydrodynamic volume $V_H \approx 754$ Å^3; for comparison, the diffusion coefficients for the 1,5-cod ligand signals ($D \approx 1.0 \times 10^{-9}$ m^2 s^{-1}) and the Li^+ cation ($D \approx 9.9 \times 10^{-10}$ m^2 s^{-1}; ^{7}Li NMR) of **C** give volumes $V_H \approx 566$ Å^3 and $V_H \approx 448$ Å^3, respectively. The larger hydrodynamic volume V_H of **1** strongly supports the presence of the magnesium salt as a contact ion pair in solution.

NMR spectroscopic evidence of this $C_\pi\cdots Mg$ interaction can be found in the $^{13}C\{^{1}H\}$ NMR spectrum of **1**, which features one of four olefinic signals at an unusual chemical shift of

40.8 ppm, significantly upfield shifted compared to the other resonances at ≈ 80.0 ppm (Figure S13 and Figure S14). The $^{13}C\{^1H\}$ NMR chemical shifts calculated at the PBE0/def2-TZVPP level of theory show that this resonance can be assigned to the four inward-facing C_π atoms (δ_{calc} = 44.9 ppm for C1/2/3/4; Table S7). The ^1H NMR spectrum of **1** does not change significantly upon the addition of THF (Figure S6). However, much simpler ^1H and $^{13}C\{1H\}$ NMR spectra are observed with 4-(dimethylamino)pyridine (DMAP), which indicate the formation of the ion-separated complex $[Mg(DMAP)_6][Co(\eta^4\text{-cod})_2]_2$ (**2**, see section 3.4.6.2 for details). In contrast to complex **J**, **1** does not react with styrene and dibenzo[*a*,*e*]cyclooctene even at elevated temperatures (section 3.4.7).[1e] This indicates that the tight ion-pairing in **1** significantly slows down ligand exchange.

Quantum chemical calculations confirm that the bonding in the Co–Mg–Co core of **1** is highly ionic, while weak donor-acceptor interactions between the Mg^{2+} center and four alkene C atoms provide partial covalent stabilization (see above). Natural bond order (NBO) and SOPT analyses show that any donor-acceptor interactions between the cobalt and magnesium atoms are negligible (<1 kcal mol^{-1}; Table S8). The Wiberg bond index for the Co–Mg bond is 0.029 (0.030), and the QTAIM analysis displays no bond critical point (BCP) along the Co–Mg–Co motif (Figure 4a,c). The charges from the natural population analysis (NPA) are positive for the Mg^{2+} cation (+1.74) and overall negative for the $[Co(\eta^4\text{-cod})_2]^-$ anions (–0.87), while the formal Co(–I) center itself has a positive charge (+0.25/+0.26). The C=C double bonds interacting with the Mg^{2+} are polarized (e.g., NPA charge (C4) of –0.54 vs. NPA charge (C8) of –0.20).

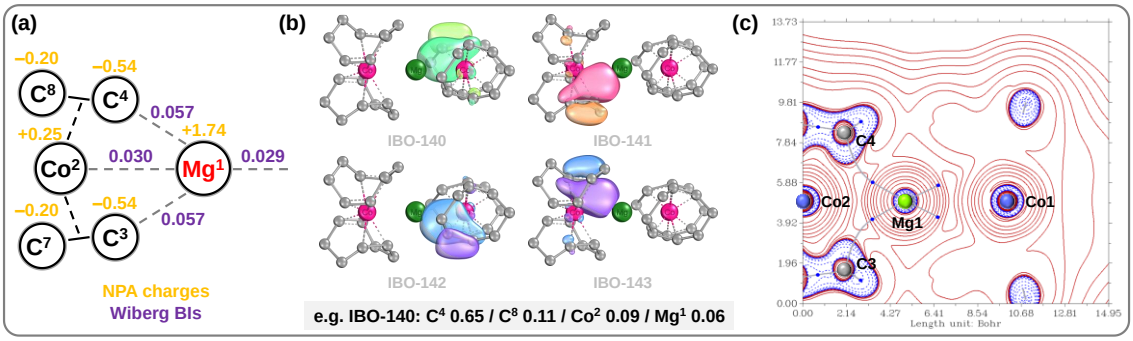

Figure 4. (a) NBO analysis including NPA charges and Wiberg bond indices of **1**. (b) Selected IBOs of **1**. The interaction type and percentage of the electron density on C, Co and Mg are given exemplarily for IBO-140. (c) Plot of the Laplacian of the electron density on the C–Co–Mg plane of **1** fully displaying two of the four bond critical points between C_π and Mg (blue dots: bond critical points; gray lines: bond paths).

To assess the influence of the Mg^{2+} cation, we compared the properties of **1** with **J** in alkene hydrogenation reactions (Figure 5).[1e] Various mono- to tetra-substituted alkenes were hydrogenated quantitatively using **1** under mild H_2 pressure (1.5 mol%, 2-12 bar H_2, 30-60 °C). Catalyst **1** surpasses **J** in terms of yield and reaction rate for most of these substrates (Figure 5, top and Table S1). The sterically most hindered substrate 1,1,2,2-tetraphenylethylene was converted to the corresponding alkane with **1** in 88% yield,

while a modest conversion of only 8% was achieved with **J**. This shows that the β-diketiminate motif is not an essential counterion component for the effective hydrogenation of alkenes. To gain initial information on the topicity of the catalyst, we conducted NMR spectroscopic reaction monitoring and mercury poisoning experiments.[11] The hydrogenation of α-methylstyrene was not inhibited by the addition of Hg, while varying product formation was recorded for 1,1,2-triphenylethylene (52-89% yield), and significant inhibition was found for 1,1,2,2-tetraphenylethylene (35% vs. 88% yield; Table S2).

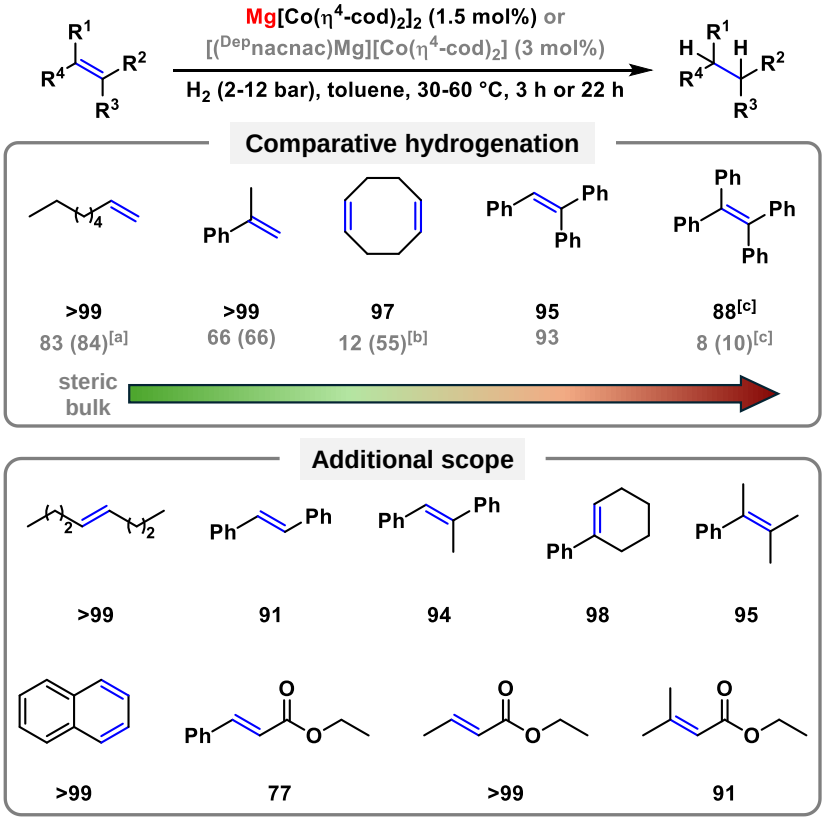

Figure 5. Hydrogenation of alkenes using Mg[Co(η⁴-cod)₂]₂ (**1**) and [(Depnacnac)Mg][Co(η⁴-cod)₂] (**J**). Standard conditions: 0.2 mmol substrate (0.4 mol/L in toluene). 2-12 bar H_2, 30-60 °C, 3 h or 22 h (see section 3.4.3.1 for the individual reaction conditions). Yields and conversions in [%] were determined by quantitative GC-FID analysis vs. internal *n*-pentadecane. Conversions are given in parentheses if <90%. [a] Isomerization to internal double bonds. [b] Formation of *cis*-cyclooctene as the major product. [c] c = 0.1 mol/L; V = 2.0 mL.

These data suggest a homotopic catalyst predominantly operates at mild temperature and H_2 pressure, while heterotopic catalyst species are likely to contribute at higher temperatures and pressure required for challenging substrates such as 1,1,2,2-tetraphenylethylene. The ^1H NMR spectroscopic monitoring of the hydrogenation of α-methylstyrene with **1** (2 mol%, 2 bar H_2, ambient temperature; Figure S11) revealed the complete formation of cumene in <71 min (Figure S11). Moderate line broadening may indicate the formation of a minor amount of cobalt particles (after H_2 addition). While previous monitoring studies with **J** and **E** indicated that the spectroscopic line broadening is accompanied by termination of the hydrogenation reaction,[1e] the hydrogenation reaction with **1** did not cease when spectral

broadening appeared. Thus, we presume that the formed particles are inactive in the hydrogenation and are present alongside a molecular species, which facilitates the hydrogenation.

3.3 Conclusion

The complex $Mg[Co(\eta^4\text{-cod})_2]_2$ (**1**) features an unsupported linear Co–Mg–Co unit and can be synthesized through a simple salt metathesis reaction. Single crystal X-ray diffraction, DOSY NMR spectroscopy, and quantum chemical studies indicate that complex **1** exists as an intact ion triple in the solid state, characterized by an ionic magnesium-cobalt interaction and weak dative bonds between the 1,5-cyclooctadiene ligands and Mg^{2+}. This molecular structure is preserved in toluene solution. Complex **1** effectively catalyzes the hydrogenation of sterically demanding alkenes, surpassing the performance of related alkali metal salts **C**-**E** and the magnesium β-diketiminate salt **J**. These findings highlight a significant counterion effect on catalytic activity that is intrinsic to the Mg^{2+} cation.

3.4 Supporting Information

3.4.1 General Information

All reactions and product manipulations were carried out in flame-dried glassware under an inert atmosphere of argon/nitrogen using standard Schlenk-line or glovebox techniques (maintained at <0.1 ppm H_2O and <0.1 ppm O_2). $[Li(thf)_2][Co(\eta^4\text{-cod})_2]$ (**C**)[1a] and $[K(thf)_{0.2}][Co(\eta^4\text{-cod})_2]$ (**E**)[1b] were prepared according to procedures previously reported in the chemical literature.

Solvents were dried and degassed with an *MBraun SPS800* solvent purification system. All dry solvents were stored under argon over activated 3 Å molecular sieves in gas-tight ampules. Commercially available alkenes were purified by distillation (Kugelrohr) and in case of liquids degassed and dried over molecular sieves (3 Å).

NMR spectra were recorded on Bruker Avance 400 spectrometer at 298 K unless otherwise noted and internally referenced to residual solvent resonances (^{1}H NMR: toluene-d_8: 7.09 ppm, DMF-d_7: 8.03 ppm; ^{13}C{^{1}H} NMR: toluene-d_8: 137.9 ppm, DMF-d_7: 163.2 ppm). Chemical shifts δ are given in ppm referring to the external standard tetramethylsilane (^{1}H, ^{13}C{^{1}H} spectra). ^{1}H and ^{13}C NMR signals were assigned based on 2D NMR spectra (^{1}H/^{1}H-COSY, ^{1}H/^{13}C-HSQC, ^{1}H/^{13}C-HMQC).

Hydrogenation reactions were carried out in a 300 mL high pressure reactor (*Parr*™) in 4 mL glass vials or in NORELL® valved NMR tubes. The reaction vessels were loaded under nitrogen, purged with hydrogen, sealed and the internal pressure was adjusted. Hydrogen (99.9992%) was purchased from *Linde*.

Yields of the catalytic and kinetic studies were determined using gas chromatography with FID detector (GC-FID) by *Shimadzu GC2025*. H_2 was used as carrier gas. A *Restek Rxi*® (30 m x 0.25 mm x 0.25 µm) column was used. The standard heating procedure was: 50 °C (2 min), 25 °C/min → 280 °C (5 min). Calibration with internal standard *n*-pentadecane and analytically pure samples. Non-commercial calibration samples were prepared by hydrogenation with Pd/C (10% Pd basis).
Gas chromatography with mass-selective detector (GC-MS) was conducted with an *Agilent 7820A GC* system with *mass detector 5977B*. H_2 as carrier gas and a *HP-5MS* (30 m x 0.25 mm x 0.25 µm) column were used. The standard heating procedure was: 50 °C → 300 °C.

3.4.2 Synthesis and Characterization of $Mg[Co(\eta^4\text{-cod})_2]_2$ (1)

$[K(thf)_{0.33}][Co(\eta^4\text{-cod})_2]$ (**E**) (501.2 mg, 1.48 mmol, 2.0 equiv.) and $MgCl_2$ (70.6 mg, 0.74 mmol, 1.0 equiv.) were suspended in toluene (20 mL) and cooled to −50 °C. Subsequently, THF (10 mL) was added while stirring. The cooling bath was removed after 30 min, and the mixture was stirred for 3 days. During this time, the formation of a fine,

pale-yellow precipitate was observed, and the reaction mixture turned deep yellow-brown. The solvent was evaporated to ca. ½ of its initial volume under reduced pressure and toluene (20 mL) was added to the residual suspension. The mixture was stirred for 30 min until the pale-yellow solids dissolved and a fine gray powder remained. The mixture was filtered through a PTFE tube equipped with a Whatman filter paper (GF/A, 1.6 µm pore size, 24 mm), and the deep yellow-brown filtrate concentrated to ca. ½ of its initial volume. Storage at −30 °C for 3 days afforded $Mg[Co(\eta^4\text{-cod})_2]_2$ (**1**) as a yellow-to-orange solid, which was washed with *n*-hexane (2 x 2.0 mL) and dried under reduced pressure. Concentrating the mother liquor to ca. ½ of its initial volume and storage at −35 °C gave a second crop of **1**. Crystals suitable for X-ray crystallography were grown from a saturated toluene solution at −35 °C over 3 d.

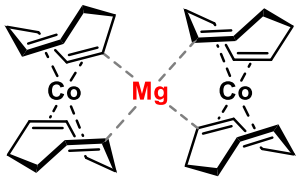

$C_{32}H_{48}Co_2Mg$, MW = 574.91 g/mol

Yield: 269.7 mg, 63% (1st and 2nd crop)

^{1}H NMR (400.13 MHz, 298 K, toluene-d_8; filtered sample) δ = 4.44 (t, 4H, $^3J_{HH}$ = 7.2 Hz, C_8H_{12}–olefinic, isomer **A**), 4.31 (t, 1H, $^3J_{HH}$ = 6.9 Hz, C_8H_{12}–olefinic, isomer **B**), 3.62-3.37 (m, 5H, C_8H_{12}–aliphatic, isomer **A**+**B**), 2.86-2.73 (m, 2H, C_8H_{12}–aliphatic, isomer **B**), 2.73-2.65 (m, 5H, C_8H_{12}–aliphatic, isomer **A**), (2.65-2.58, m, 3H, C_8H_{12}–aliphatic, isomer **A**+**B**), 2.58-2.48 (m, 7H, C_8H_{12}–olefinic, isomer **A**+**B**), 2.48-2.35 (m, 4H, C_8H_{12}–aliphatic, isomer **A**), 2.21-2.10 (m, 8H, C_8H_{12}–aliphatic and C_8H_{12}–olefinic, isomer **A**+**B**), 1.92-1.69 (m, 6H, C_8H_{12}–aliphatic and C_8H_{12}–olefinic, isomer **A**+**B**), 1.61-1.51 (m, 4H, C_8H_{12}–olefinic, isomer **A**), 1.40-1.24 (m, 11H, C_8H_{12}–aliphatic and C_8H_{12}–olefinic, isomer **A**+**B**) ppm.
^{13}C{^{1}H} NMR (100.61 MHz, 298 K, toluene-d_8; filtered sample) δ = 82.1 (s, C_8H_{12}–olefinic, isomer **B**), 81.9 (s, C_8H_{12}–olefinic, isomer **A**), 80.7 (s, C_8H_{12}–olefinic, isomer **A**), 79.6 (s, C_8H_{12}–olefinic, isomer **B**), 78.2 (s, C_8H_{12}–olefinic, isomer **A**), 76.9 (s, C_8H_{12}–olefinic, isomer **B**), 40.8 (s, C_8H_{12}–olefinic, isomer **A**), 39.9 (s, C_8H_{12}–olefinic, isomer **B**), 39.3 (s, C_8H_{12}–olefinic, isomer **B**), 38.8 (s, C_8H_{12}–olefinic, isomer **A**), 37.1 (s, C_8H_{12}–aliphatic, isomer **B**), 36.4 (s, C_8H_{12}–aliphatic, isomer **A**), 30.4 (s, C_8H_{12}–aliphatic, isomer **A**), 29.8 (s, C_8H_{12}–aliphatic, isomer **B**), 28.2 (s, C_8H_{12}–aliphatic, isomer **A**), 27.4 (s, C_8H_{12}–aliphatic, isomer **B**) ppm.

Elemental Analysis calcd. C 66.85, H 8.42; found C 66.54, H 8.53.

3.4.3 Hydrogenation Study

3.4.3.1 General Procedure and Substrate Scope

In a glovebox, an oven-dried (160 °C) 4 mL reaction vial was charged with *n*-pentadecane (20 µL, 72.4 µmol) as the internal standard for GC-FID quantification. The liquid substrate (0.2 mmol) was added followed by the pre-catalyst $Mg[Co(\eta^4\text{-cod})_2]_2$ (**1**; 1.5 mol%; filtered through a 0.2 µm PTFE filter[12] to remove minor insolubilities) or pre-catalyst $[(^{Dep}nacnac)Mg][Co(\eta^4\text{-cod})_2]$ (**J**; 3 mol%) as a stock solution in toluene (0.5 mL). In the case of solid substrates, the solid was first weighed into the vial followed by the addition of the liquids. The reaction vial was transferred to a high-pressure reactor, which was sealed and removed from the glovebox. The reactor was purged with a continuous flow of H_2 (0.5-0.8 bar overpressure for 30 s) and the reaction pressure and temperature were set. After the indicated reaction time, the reaction vessel was depressurized, the vials were retrieved and treated with a saturated aqueous solution of NH_4Cl (1.0 mL) and diluted with ethyl acetate. An aliquot of the organic phase was filtered over a short pad of silica and washed with ethyl acetate (1 x 2.0 mL). The solution was analyzed by GC-FID (and GC-MS for selected experiments).

Hydrogenation Protocol **I**: 2 bar H_2, 30 °C, 3 h; **II**: 2 bar H_2, 30 °C, 22 h; **III**: 8 bar H_2, 30 °C, 22 h; **IV**: 12 bar H_2, 60 °C, 22 h.

Table S1. Substrate scope for the hydrogenation with $Mg[Co(\eta^4\text{-cod})_2]_2$ (**1**) or $[(^{Dep}nacnac)Mg][Co(\eta^4\text{-cod})_2]$ (**J**).

		Cat. $Mg[Co(\eta^4\text{-cod})_2]_2$ (**1**)		Cat. $[(^{Dep}nacnac)Mg][Co(\eta^4\text{-cod})_2]_2$ (**J**)	
Entry	**Substrate**	**Yield [%]**	**Conditions**	**Yield (Conv.) [%]**	**Conditions**
1	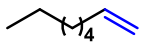	>99	2 bar H_2, 30 °C, 3 h	83 (84)[b]	2 bar H_2, 30 °C, 3 h
2	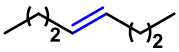	>99	2 bar H_2, 30 °C, 3 h	/	/
3	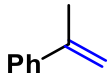	>99	2 bar H_2, 30 °C, 3 h	66 (66)	2 bar H_2, 30 °C, 3 h
4	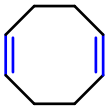	97	2 bar H_2, 30 °C, 3 h	6[23] (38), 12[43] (55), 25[57] (84)[c,d]	2 bar H_2, 30 °C, 3 h
5	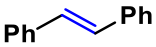	91	2 bar H_2, 30 °C, 3 h	/	/
6	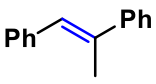	94	2 bar H_2, 30 °C, 3 h	97	2 bar H_2, 30 °C, 22 h
7	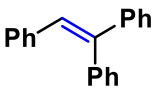	95	2 bar H_2, 30 °C, 22 h	93	2 bar H_2, 30 °C, 22 h

		Cat. $Mg[Co(\eta^4\text{-cod})_2]_2$ (1)		Cat. [(^{Dep}nacnac)Mg]-$[Co(\eta^4\text{-cod})_2]_2$ (J)	
Entry	**Substrate**	**Yield (Conv.) [%]**	**Conditions**	**Yield (Conv.) [%]**	**Conditions**
8	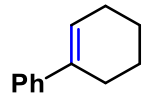	98	2 bar H_2, 30 °C, 22 h	95	2 bar H_2, 30 °C, 22 h
9	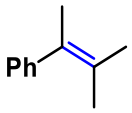	95	8 bar H_2, 30 °C, 22 h	/	/
10	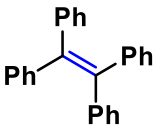	88[e]	12 bar H_2, 60 °C, 22 h	8 (10)[e]	12 bar H_2, 60 °C, 22 h
11	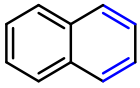	>99[f]	8 bar H_2, 30 °C, 22 h	0 (0)	8 bar H_2, 30 °C, 22 h
12	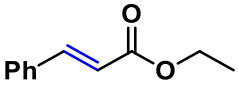	77	2 bar H_2, 30 °C, 3 h	/	/
13	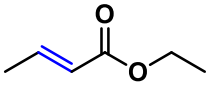	>99	2 bar H_2, 30 °C, 3 h	95	2 bar H_2, 30 °C, 3 h
14	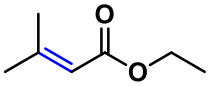	91	2 bar H_2, 30 °C, 3 h	/	/

[a] Standard conditions: 0.2 mmol substrate (0.4 mol/L in toluene). 2-12 bar H_2, 30-60 °C, 3 h or 22 h. 1.5 mol% $Mg[Co(\eta^4\text{-cod})_2]_2$ (**1**) or 3 mol% [(^{Dep}nacnac)Mg][$Co(\eta^4\text{-cod})_2$] (**J**). Yields and conversions were determined by quantitative GC-FID analysis vs. internal *n*-pentadecane. Conversions are given in parentheses if <90%. [b] Isomerization to internal double bonds. [c] Formation of cyclooctene given in [brackets]. [d] Yields and conversions observed over three single reaction runs. [e] c = 0.1 mol/L; V = 2.0 mL. [f] Traces of the fully hydrogenated decalin were observed.

3.4.4 Mercury Poisoning Experiments

Mercury poisoning experiments were performed to investigate the catalyst topicity at different reaction conditions (see protocol **I**/**II**/**IV**). Following the general procedure, the hydrogenation of α-methylstyrene, 1,1,2-triphenylethylene and 1,1,2,2-tetraphenylethylene was performed using pre-catalyst $Mg[Co(\eta^4\text{-cod})_2]_2$ (**1**) in the absence and presence of excess Hg. In the absence of Hg, (near-)quantitative hydrogenation was observed for all investigated substrates. In the presence of Hg (1690 mol%; addition at t = 0 min), no inhibition was observed for α-methylstyrene using protocol **I** (2 bar H_2, 30 °C, 3 h) and the hydrogenation reached the same level of completeness (Table S2, entries 1-2). The more demanding substrate 1,1,2-triphenylethylene was hydrogenated between 52% and 89% in four single reaction runs when using protocol **II** and poisoned with Hg (2 bar H_2, 30 °C, 22 h; Table S2, entries 3-4). Applying protocol **IV** (12 bar H_2, 60 °C, 22 h), the hydrogenation of 1,1,2,2-tetraphenylethylene was significantly reduced to 35%, while the standard reaction yielded 88% of 1,1,2,2-tetraphenylethane (Table S2, entries 5-6).

The (varying) reduction in the yield of 1,1,2-triphenylethane (protocol **II**) points to the formation of catalytically active cobalt nanoparticles that are inhibited by the heterotopic poison mercury. Yet, the inhibition only results in a 11-48% loss of product yield over four individual reaction runs, which suggests that only a fraction of the (active) catalyst is inhibited, while the residual part remains functional. In our previous study,[1e] we could show that deliberately prepared Co(0) nanoparticles[5] were effectively inhibited by Hg when used in the hydrogenation of 1,1,2-triphenylethylene (0% vs. 56% product yield) under similar reaction conditions (12 bar H_2, 40 °C, 22 h, THF).

This indicates that the catalyst system based on pre-catalyst **1** remains mainly homotopic in the hydrogenation of 1,1,2-triphenylethylene (2 bar H_2, 30 °C, 22 h), in agreement with our preceding poisoning experiments with Co(0) nanoparticles.[1e] At higher pressure and temperature (12 bar H_2, 60 °C, 22 h), as required for the hydrogenation of 1,1,2,2-tetraphenylethylene, the poisoning effect of Hg is more pronounced (35% vs. 88% product yield), which shows that the formation of heterotopic particles is likely also affected by the reaction conditions (see the opposing effect for α-methylstyrene, see above).

Overall, the data suggests that the reaction renders predominantly homotopic at (milder) protocols **I** and **II**, while the fraction of heterotopic cobalt particles increases at harsher conditions (protocol **IV**). Finally, it is important to note that the topicity of such cobaltate systems is difficult to unambiguously assign as the catalyst decomposition leading to particle formation can be inconsistent (including not occurring; see Table S2, entry 4 and the previous literature).[1e]

Table S2. Hg poisoning experiments with $Mg[Co(\eta^4\text{-cod})_2]_2$ (**1**) at different reaction conditions.[a]

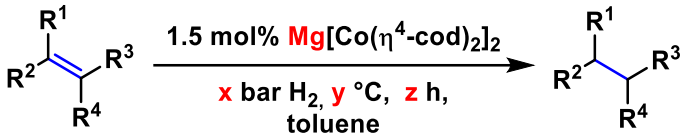

Entry	Substrate	Conditions	Manipulation	Yield (Conv.) [%]
1	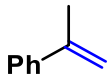	2 bar H_2, 30 °C, 3 h (Protocol **I**)	none	>99
2			Hg (1690 mol%)	>99
3	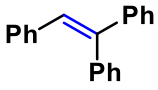	2 bar H_2, 30 °C, 22 h (Protocol **II**)	none	95
4			Hg (1690 mol%)	52 (53), 89 (89), 67 (75), 72 (75)[b]
5	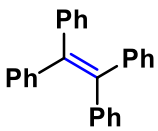	12 bar H_2, 60 °C, 22 h (Protocol **IV**)[c]	none	88
6			Hg (1690 mol%)	35 (37)

[a] Standard conditions: 0.2 mmol substrate (0.4 mol/L in toluene). Hg (1690 mol%; 50 µL) was added at t = 0 min. [b] Yields and conversions observed over four single reaction runs. [c] c = 0.1 mol/L; V = 2.0 mL toluene.

3.4.5 Additional Experiments

3.4.5.1 DOSY NMR Analysis of $Mg[Co(\eta^4\text{-cod})_2]_2$ (1) and $[Li(thf)_{1.92}][Co(\eta^4\text{-cod})_2]$ (C)

General Information

Diffusion-ordered NMR spectroscopy (DOSY) experiments were conducted on a Bruker Avance III HD 600 MHz spectrometer, equipped with a TBI 5 mm $^1H/^{19}F$-BB probe. All measurements were performed at 298 K, with the temperature validated using internal NMR calibration standards from Bruker.

The DOSY measurements were performed with convection compensating double stimulated echo (DSTE) pulse sequence developed by Jerschow and Müller.[13] The diffusion time delay was set to 40 ms. Smoothed square (SMSQ10.100) gradient shapes and a linear gradient ramp (32 increments, 5% to 95% of the maximum gradient strength) were used.

The NMR data were processed, analyzed, and plotted using TopSpin 3.2 software. Data evaluation was carried out using a Python script developed by Christian Scholtes, in which the DOSY data were fitted to the Stejskal-Tanner equation.[14]

$$I = I_0 \cdot \exp\left[-\gamma^2 G^2 \delta^2 \left(\Delta - \frac{\delta}{3}\right) D\right]$$

where I is the signal with the gradient, I_0 is the signal intensity without diffusion weighting, γ is the gyromagnetic ratio, G is the strength of the gradient pulse, δ is the duration of the pulse, Δ is the time interval between the two pulses and D the diffusion coefficient.

The calculated diffusion coefficient for TMS (D_{ref}) was applied to the Stokes-Einstein equation,[15]

$$D_i = \frac{k_B T}{F c \pi \eta r_H}$$

to obtain viscosity correction for each individual sample. Here, k_B is the Boltzmann constant, T the temperature, F is the shape factor (set to 1 for a spherical shape), η the viscosity of the sample, r_H the hydrodynamic radius of the analytes, and c a correction factor which was determined by using a semi-empirical modification by Chen.[16]

$$c_{Chen} = \frac{6F}{1 + 0.695 \left(\frac{r_{solv}}{r_{ref}}\right)^{2.234}}$$

The hydrodynamic radii values for TMS (r_{ref} = 2.96 Å) and toluene (r_{solv} = 2.88 Å) were calculated using hard-sphere increments.[17]

By inserting the Chen correction factor to the Stokes-Einstein equation,

$$\eta\ [kg/ms] = \frac{k_B T \left(1 + 0.695 \left(\frac{r_{solv}}{r_{ref}}\right)^{2.234}\right)}{6\pi D_{ref}\ r_{ref}}$$

the correction factor for the viscosity of each respective sample (η) is determined. Finally, by incorporating all correction equations, the hydrodynamic radii can be iteratively calculated by

$$D = \frac{kT\ (1 + 0.695\ \left(\frac{r_{solv}}{r_H}\right)^{2.234})}{6\pi\eta r_H}$$

Using the hydrodynamic radii, the respective Volumes (V_H) were calculated with the assumption of a spherical shape.

Sample Preparation

A 10 mM solution of either Mg[Co(η⁴-cod)₂]₂ (**1**) or [Li(thf)$_{1.92}$][Co(η⁴-cod)₂] (**C**) was prepared by dissolving the respective sample in toluene-d₈. The solution was then filtered from minor insolubles, and an aliquot (0.5 mL) was transferred into a J. Young NMR tube. Tetramethylsilane (TMS) was used as a reference and was added by withdrawing 500 µL from the headspace of a degassed TMS sample, just above the surface of the liquid and injected into the NMR tube, which was then sealed immediately afterwards.

Experimental Data for Mg[Co(η⁴-cod)₂]₂ (1)

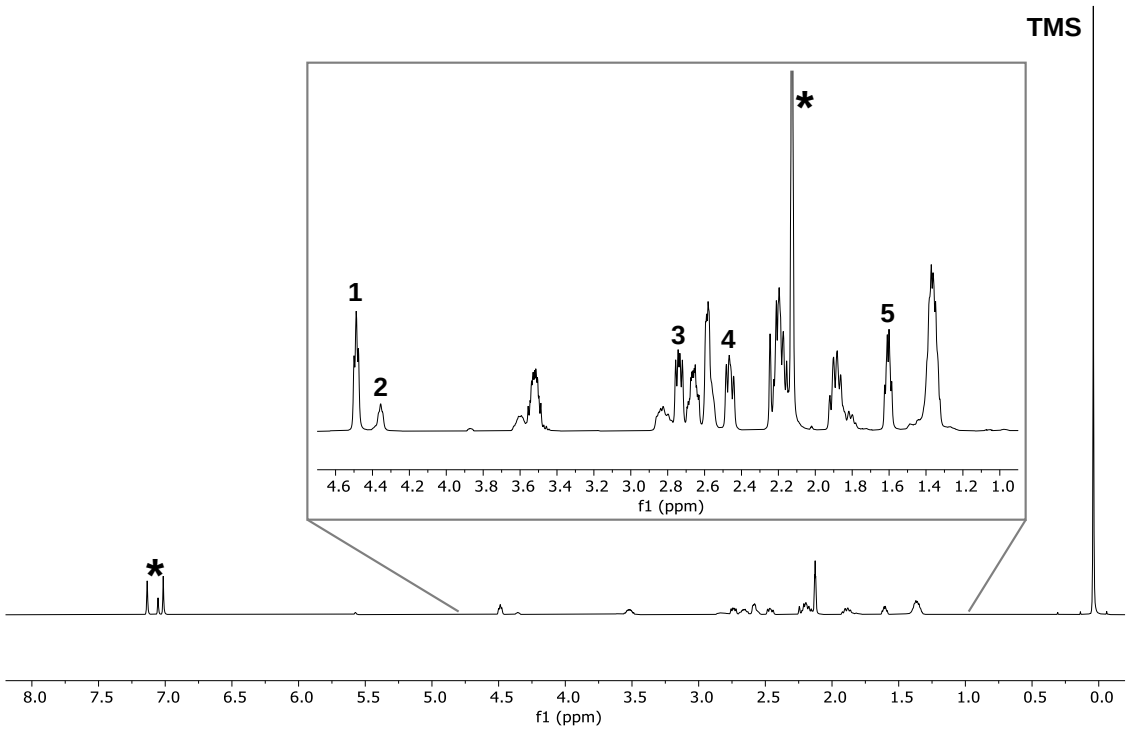

Figure S1. ¹H NMR spectrum of Mg[Co(η⁴-cod)₂]₂ (**1**) and TMS (600.13 MHz, 298 K, toluene-d₈), showing the signals **1**-**5** used for the DOSY analysis. *: toluene-d₈.

Table S3. Self-diffusion coefficients of signals **1**-**5** of Mg[Co(η⁴-cod)₂]₂ (**1**) in toluene-d₈. All signals correspond to the aliphatic and olefinic H atoms of the 1,5-cyclooctadiene ligand.

Signal	**Chemical shift [ppm]**	**Diffusion coefficient D_i [m²·s⁻¹]**
/	TMS	2.48e-09 ± 1.14e-10
1	4.50-4.61	9.1464e-10 ± 1.54e-12
2	4.39-4.48	9.4051e-10 ± 4.26e-12
3	2.77-2.84	9.0042e-10 ± 1.32e-12
4	2.47-2.58	9.0448e-10 ± 1.98e-12
5	1.61-1.71	8.8644e-10 ± 1.96e-12
Mean diffusion coefficient D (**1**-**5**) [m²·s⁻¹]		9.09e-10 ± 1.96e-12
Average radius r_H [Å]		5.646 ± 0.09643
Average volume V_H[a] [Å³]		753.8 ± 38.63

[a] The average volume V_H was calculated assuming a spherical shape.

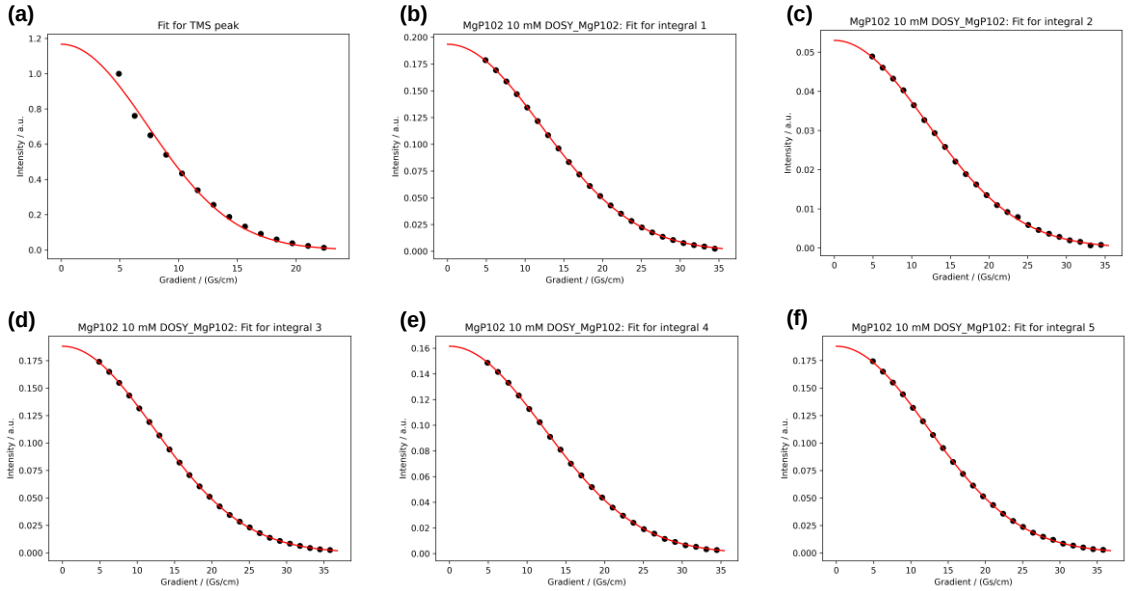

Figure S2. DOSY plots (signal intensity against gradient strength) of TMS and the signals **1**-**5** of Mg[Co(η⁴-cod)₂]₂ (**1**) in toluene-d₈.

Experimental Data for $[Li(thf)_{1.92}][Co(\eta^4\text{-cod})_2]$ (C)

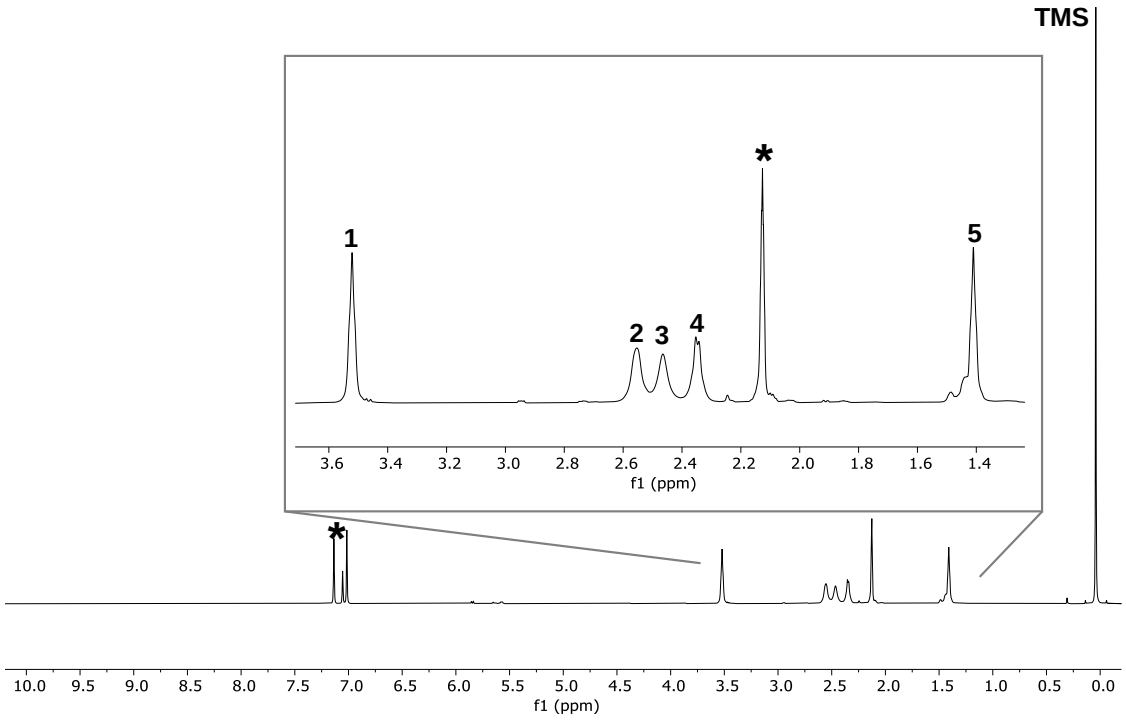

Figure S3. ^{1}H NMR spectrum of $[Li(thf)_{1.92}][Co(\eta^4\text{-cod})_2]$ (**C**) and TMS (600.13 MHz, 298 K, toluene-d_8), showing the signals **1**-**5** used for the DOSY analysis. *: toluene-d_8.

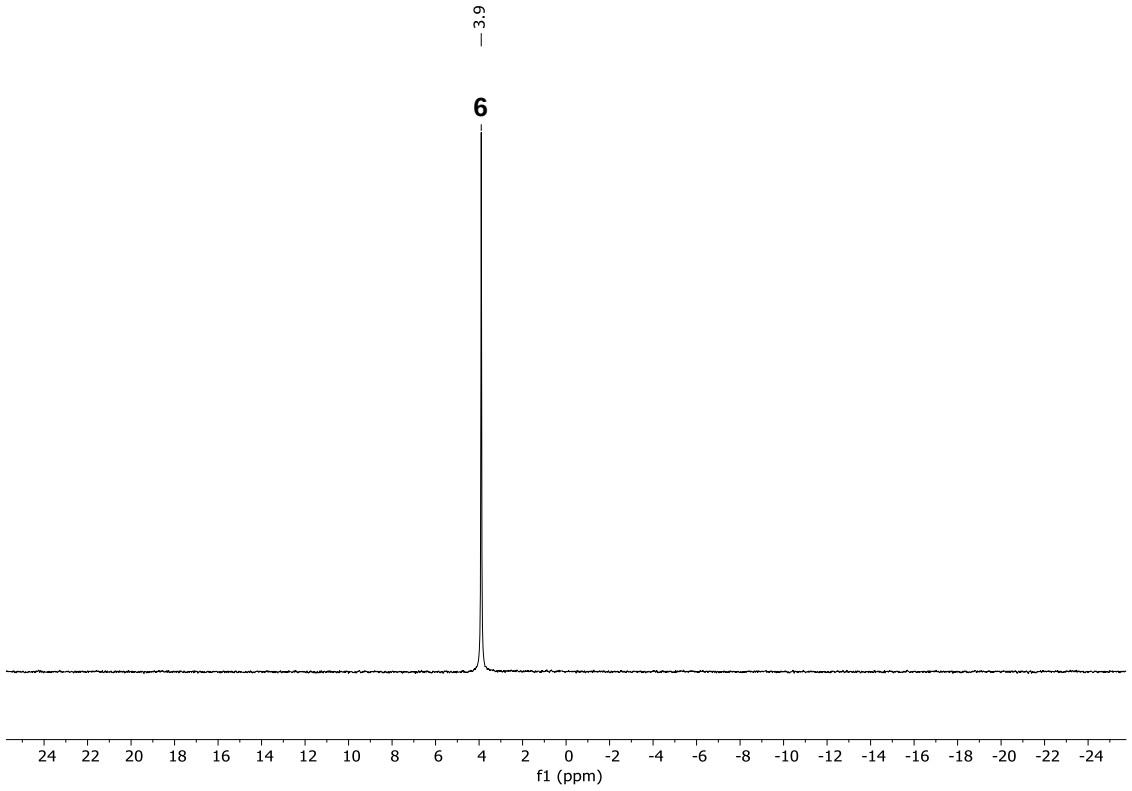

Figure S4. ^{7}Li NMR spectrum of $[Li(thf)_{1.92}][Co(\eta^4\text{-cod})_2]$ (**C**) and TMS (600.13 MHz, 298 K, toluene-d_8), showing the signal 6 used for the DOSY analysis.

Table S4. Self-diffusion coefficients of signals **1**-**6** of $[Li(thf)_{1.92}][Co(\eta^4\text{-cod})_2]$ (**C**) in toluene-d_8.

Signal	Chemical shift [ppm]	Diffusion coefficient D_i [$m^2 \cdot s^{-1}$]
	^{1}H NMR	
/	TMS	2.43e-09 ± 6.24e-11
1 (THF)	3.51-3.61	1.6395e-09 ± 2.42e-11
2 (1,5-cod)	2.57-2.67	1.0371e-09 ± 4.93e-12
3 (1,5-cod)	2.49-2.57	1.0026e-09 ± 3.94e-12
4 (1,5-cod)	2.35-2.47	1.014e-09 ± 5.08e-12
5 (THF)	1.41-1.48	1.6258e-09 ± 1.23e-11
	^{7}Li NMR	
6	3.90	9.92e-10 ± 9.19e-12
Mean diffusion coefficient D (**2**-**4**) [$m^2 \cdot s^{-1}$]		1.02e-09 ± 5.08e-12
Average radius r_H [Å]		5.132 ± 0.0656
Average volume V_H[a] [Å^3]		566.0 ± 21.71
Mean diffusion coefficient D (**1**&**5**) [$m^2 \cdot s^{-1}$]		1.63e-09 ± 1.23e-11
Average radius r_H [Å]		3.723 ± 0.01368
Average volume V_H[a] [Å^3]		216.2 ± 2.384
Mean diffusion coefficient D (**6**) [$m^2 \cdot s^{-1}$]		9.92e-10 ± 9.19e-12
Average radius r_H [Å]		4.746 ± 0.03109
Average volume V_H[a] [Å^3]		447.9 ± 8.802

[a] The average volume V_H was calculated assuming a spherical shape.

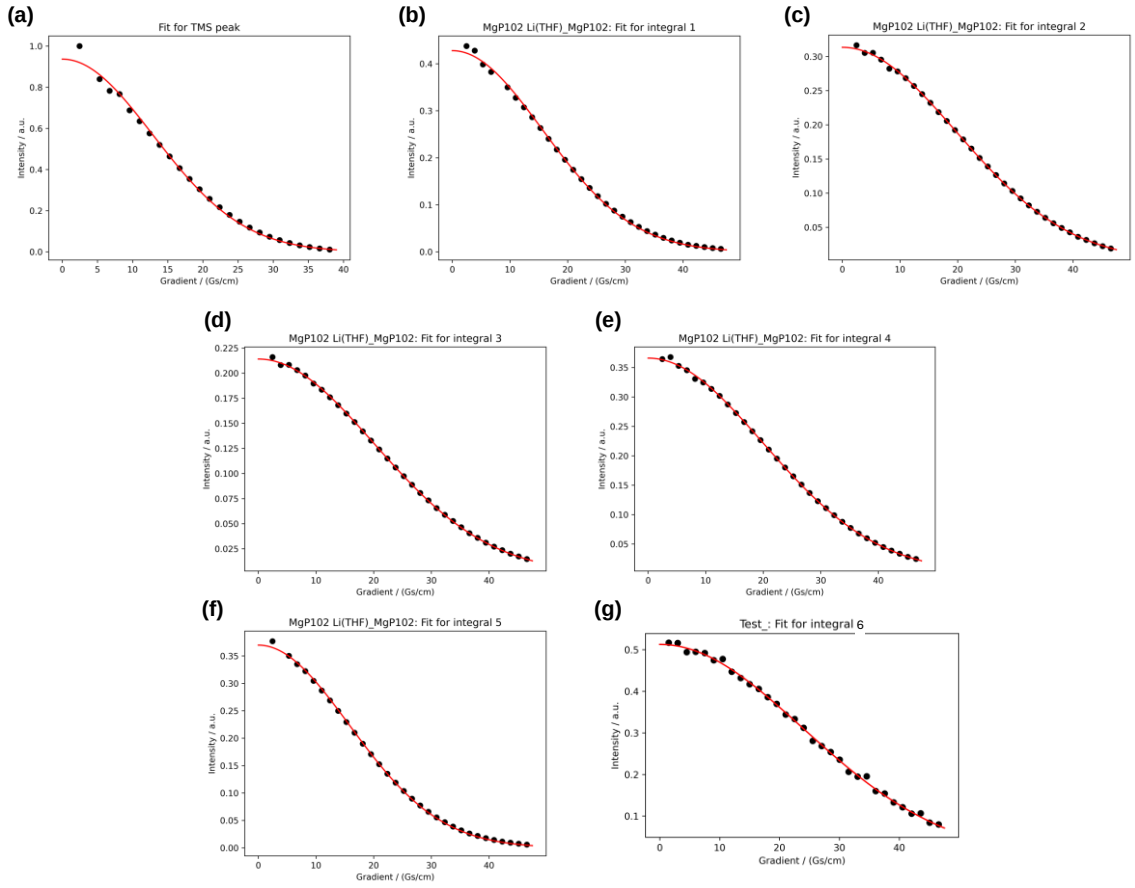

Figure S5. DOSY plots (signal intensity against gradient strength) of TMS and the signals **1**-**6** of $[Li(thf)_{1.92}][Co(\eta^4\text{-cod})_2]$ (**C**) in toluene-d_8.

Discussion

The DOSY NMR analysis of $Mg[Co(\eta^4\text{-cod})_2]_2$ (**1**) gives similar diffusion coefficients for all five cod ligand signals in the ^{1}H NMR spectrum, which results in a mean diffusion coefficient D = 9.09e-10 ± 1.96e-12 m^2 s^{-1} and a respective hydrodynamic volume V_H = 753.8 ± 38.63 Å^3 for the molecular entity (Figure S1 and Table S3). The trinuclear complex **1** was then referenced to the mononuclear lithium cobaltate, $[Li(thf)_{1.92}][Co(\eta^4\text{-cod})_2]$ (**C**), which is the only toluene-soluble alkali metal cobaltate of the series. The diffusion coefficients for the cod ligand signals in the ^{1}H NMR spectrum are matching and give a mean diffusion coefficient D = 1.02 10e-09 ± 5.08e-12 m^2 s^{-1} and a respective hydrodynamic volume V_H = 566.0 ± 21.71 Å^3 for the molecular entity (Figure S3 and Table S4). In agreement with this, the diffusion coefficient for the Li$^+$ cation in the ^{7}Li NMR spectrum was calculated at D = 9.92e-10 ± 9.19e-12 m^2 s^{-1}, resulting in a hydrodynamic volume V_H = 447.9 ± 8.802 Å^3 for the molecular unit (Figure S4 and Table S4). Interestingly, the THF ligands coordinated to the Li$^+$ cation of **C** exhibit a higher (mean) diffusion coefficient (D = 1.63e-09 ± 1.23e-11 m^2 s^{-1}) compared to that of the cod ligands (D = 1.02e-09 ± 5.08e-12 m^2 s^{-1}), which indicates that they are separate entities in solution. This suggests that a $Li[Co(\eta^4\text{-cod})_2]$ unit with close contact between the Li$^+$ cation and the $[Co(\eta^4\text{-cod})_2]^-$ anion is present in solution, which is solvated by THF molecules coordinating in an interchangeable mode (see reference

[1a] for a comparison of ion pair **C** in the solid state). The hydrodynamic volume V_H of **1** (753.8 ± 38.63 Å^3) is found to be approximately 33% and 68% larger, respectively, than the hydrodynamic volume V_H of **C** (^{1}H: 566.0 ± 21.71 Å^3 and ^{7}Li: 447.9 ± 8.802 Å^3, respectively; considered unit: Li[Co(η^4-cod)$_2$]), indicating that **1** is present as a contact ion pair in solution.

3.4.6 Reaction of Mg[Co(η^4-cod)$_2$]$_2$ (1) with THF and DMAP

3.4.6.1 Addition of THF (6.0 equiv.)

To a pale-yellow, filtered solution of Mg[Co(η^4-cod)$_2$]$_2$ (**1**; 10.7 mg, 18.6 µmol, 1.0 equiv.) in toluene-d$_8$ (0.5 mL; J. Young NMR tube) was added THF (9.06 µL, 0.11 mmol, 6.0 equiv.). The mixture was visually unchanged after the addition. The reaction solution was analyzed by ^{1}H NMR spectroscopy after 1 d at ambient temperature (Figure S6), which showed that the intimate ion pair structure of **1** was still intact and no solvent-separated ion pair was formed. This shows that **1** forms a stable contact ion pair in the presence of THF, contrasting the behavior of the alkali metal cobaltate salts [M^I(thf)$_n$][Co(η^4-cod)$_2$] (M^I = Li, Na, K; **C**-**E**).[1a,b,e]

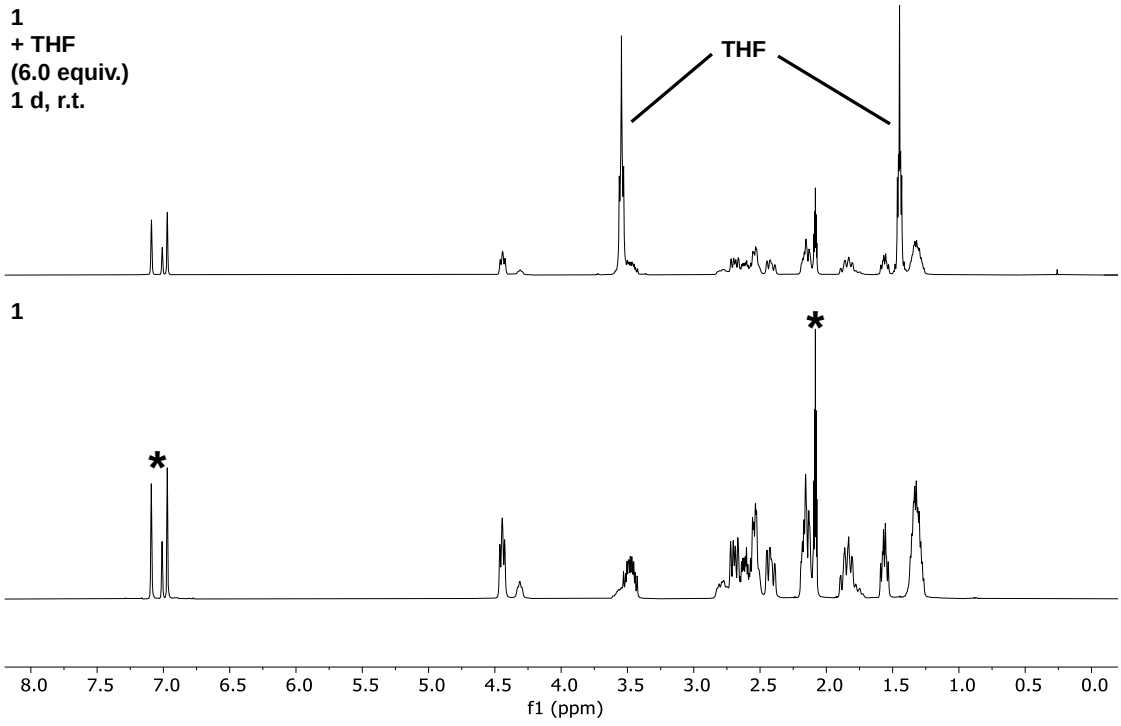

Figure S6. Addition of THF (6.0 equiv.) to Mg[Co(η^4-cod)$_2$]$_2$ (**1**) after 1 day at ambient temperature (400.13 MHz, 298 K, toluene-d$_8$). *: toluene-d$_8$.

3.4.6.2 Reaction with DMAP (6.0 equiv.)

Following the addition of THF, the reaction of Mg[Co(η^4-cod)$_2$]$_2$ (**1**) with the strong Lewis base 4-(dimethylamino)pyridine (DMAP) was investigated. Prior studies in our group showed the successful coordination of DMAP to the related [(^{Dep}nacnac)Mg][Co(η^4-cod)$_2$] (**J**) to give the donor-separated ion pair [(^{Dep}nacnac)Mg(DMAP)$_3$][Co(η^4-cod)$_2$].[2d]

Combination of $Mg[Co(\eta^4\text{-cod})_2]_2$ (**1**; 40,2 mg, 69.8 µmol, 1.0 equiv.) and DMAP (51.2 mg, 0.42 mmol, 6.0 equiv.) in toluene (10 mL) in a centrifuge Schlenk flask, and stirring at ambient temperature for 1 h led to the immediate formation of a fine orange powder. The stirring bar was removed from the reaction and the suspension was centrifuged at 1850 rpm for four minutes (Hettich Rotanta 460 centrifuge). The supernatant was decanted from the orange solid, the residue was dispensed in toluene (5.0 mL), and the suspension was centrifuged again and decanted. The residual solid was dried under reduced pressure to afford $[Mg(DMAP)_6][Co(\eta^4\text{-cod})_2]_2$ (**2**) as a pale orange solid in 89% yield (81.7 mg). NMR spectroscopic data was obtained in DMF-d_7 (Figure S7 and Figure S8), as the DMAP adduct **2** was found insoluble in common solvents (including toluene and THF) and not stable in dichloromethane-d_2, MeCN-d_3 and pyridine-d_5. This prevented further purification after the initial isolation. Attempts to crystallize **2** from mixtures of DMF/toluene were not successful. Therefore, no satisfactory elemental analysis could be obtained for **2**.

The NMR spectroscopic analysis indicates the formation of **2** as a solvent-separated ion pair with an independent $[Mg(DMAP)_6]^{2+}$ and two $[Co(\eta^4\text{-cod})_2]^-$ units. The ^{1}H NMR spectrum of **2** merely shows two signals for the cod ligands located at 1.91 and 2.28 ppm (Figure S7). Likewise, the $^{13}C\{^1H\}$ NMR spectrum of **2** shows only two resonances for the cod ligands at 34.8 and 69.7 ppm, which emerge from the (eight) initially inequivalent signals for the cod ligands (in **1**; Figure S8). The NMR data of **2** is very similar to that of the alkali metal cobaltates $[M^I(thf)_n][Co(\eta^4\text{-cod})_2]$ (M^I = Li, Na, K; **C**-**E**) and of the donor-separated (nacnac)Mg cobaltates, $[(nacnac)Mg(donor)_n][Co(\eta^4\text{-cod})_2]$ (donor = THF or DMAP).[1a,b,e],[2d]

^{1}H NMR (400.13 MHz, 298 K, DMF-d_7; filtered sample) δ = 8.16 (bs, 12H, $(CH_3)_2N$–$C_5\mathit{H}_4N$–DMAP), 6.62 (d, $^3J_{HH}$ = 4.3 Hz, 12H, $(CH_3)_2N$–$C_5\mathit{H}_4N$–DMAP), 3.00 (bs, 36H, $(C\mathit{H}_3)_2N$–C_5H_4N–DMAP), 2.40-2.09 (m, 32H, $C_8\mathit{H}_{12}$–aliphatic and/or olefinic), 2.03-1.76 (m, 16H, $C_8\mathit{H}_{12}$–olefinic and/or aliphatic).

$^{13}C\{^1H\}$ NMR (100.61 MHz, 298 K, DMF-d_7; filtered sample) δ = 155.4 (s, $(CH_3)_2N$–C_5H_4N–DMAP), 150.7 (s, $(CH_3)_2N$–C_5H_4N–DMAP), 107.8 (s, $(CH_3)_2N$–C_5H_4N–DMAP), 69.7 (s, C_8H_{12}–olefinic), 39.4 (s, $\mathit{C}H_3)_2N$–C_5H_4N–DMAP) 34.8 (s, C_8H_{12}–aliphatic).

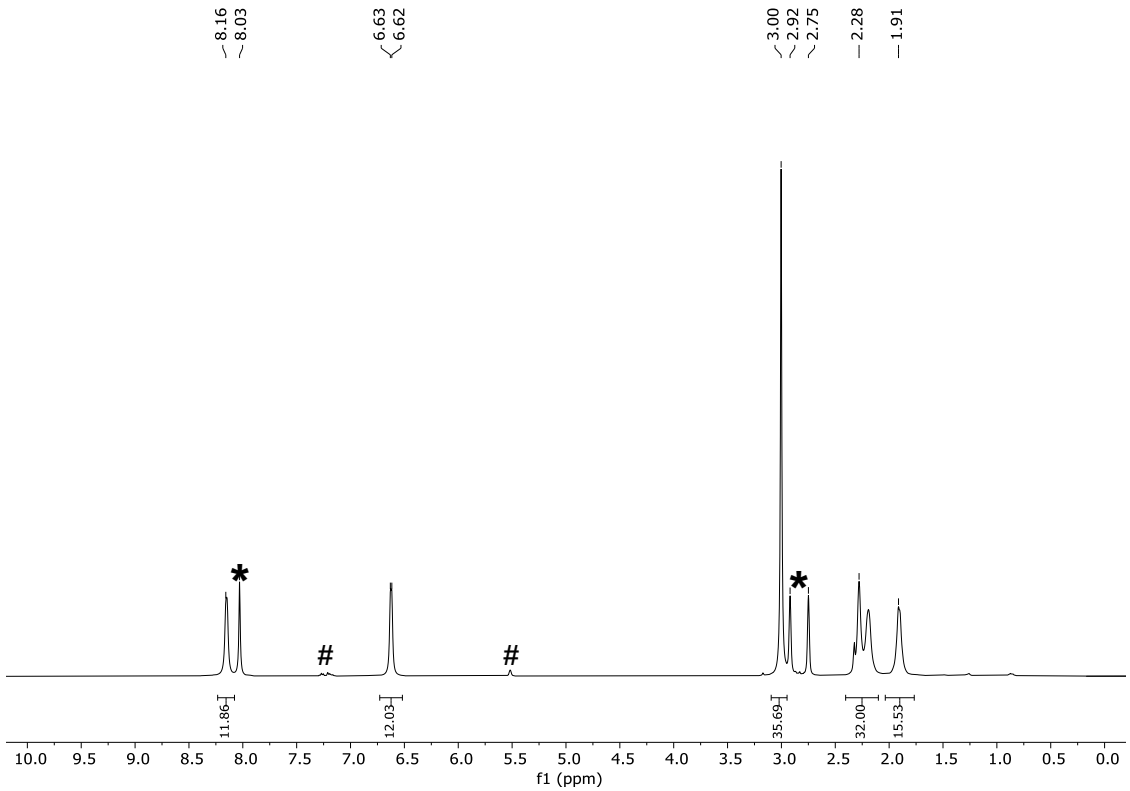

Figure S7. ^{1}H NMR spectrum (400.13 MHz, 298 K, DMF-d$_7$) of [Mg(DMAP)$_6$][Co(η^4-cod)$_2$]$_2$ (**2**). #: unidentified impurities. *: DMF-d$_7$.

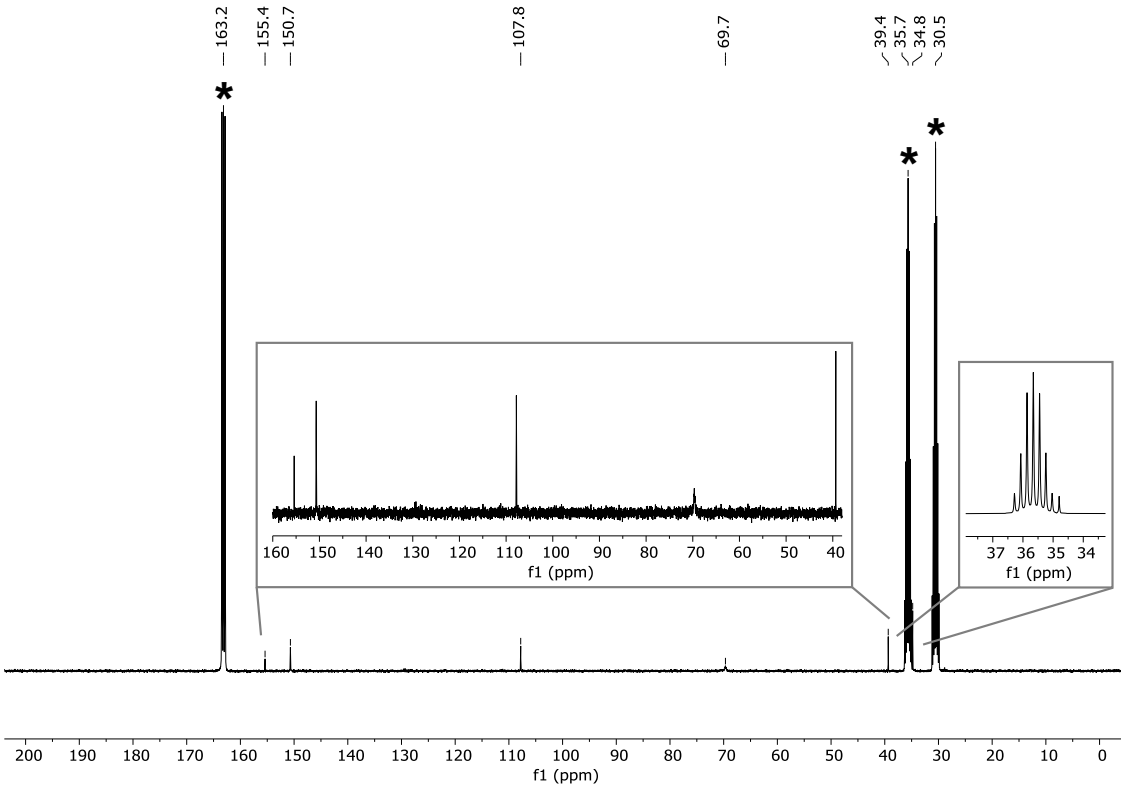

Figure S8. ^{13}C{^{1}H} NMR spectrum (100.61 MHz, 298 K, DMF-d$_7$) of [Mg(DMAP)$_6$][Co(η^4-cod)$_2$]$_2$ (**2**). *: DMF-d$_7$.

3.4.7 Reaction of $Mg[Co(\eta^4\text{-cod})_2]_2$ (1) with Styrene and Dibenzo[*a*,*e*]cyclooctene

3.4.7.1 Reaction with Styrene

The reaction monitoring by ^{1}H NMR spectroscopy was carried out in a J. Young NMR tube. A solution of $Mg[Co(\eta^4\text{-cod})_2]_2$ (**1**) (10.4 mg, 18.1 µmol, 1.0 equiv.) and styrene (8.32 µL, 72.4 µmol, 4.0 equiv.) in toluene-d_8 (0.6 mL) was filtered into an NMR tube. After rotating the sample for 1 d, a ^{1}H NMR spectrum was recorded (Figure S9). No ligand substitution was observed as seen by the absence of free 1,5-cyclooctadiene (between 5.5 and 6.0 ppm) and otherwise identical signals for **1**. The reaction mixture was then heated at 50 °C for 1 d, which led to the formation of minor amounts of free 1,5-cyclooctadiene and isomerized 1,3-cyclooctadiene (label X; Figure S9), and the appearance of a new signal at –2.05 ppm (likely to be a doublet). An upfield-shifted resonance for an η^2-styrene ligand has been identified in the related complexes $[K(18\text{-crown-6})][Co(\eta^4\text{-cod})(\eta^2\text{-styrene})_2]$ (at –0.63 ppm)[3b] and $[(^{Dep}nacnac)Mg(thf)_{3.5}][Co(\eta^4\text{-cod})(\eta^2\text{-styrene})_2]$ (at –1.92 ppm),[1e] indicating that styrene coordination to **1** should be also feasible (for example as $Mg[Co(\eta^4\text{-cod})(\eta^2\text{-styrene})_2]_2$). However, extending the reaction time at higher temperatures (60 °C and 70 °C) did not further promote the reaction. Instead, an increased decomposition of **1** was observed.

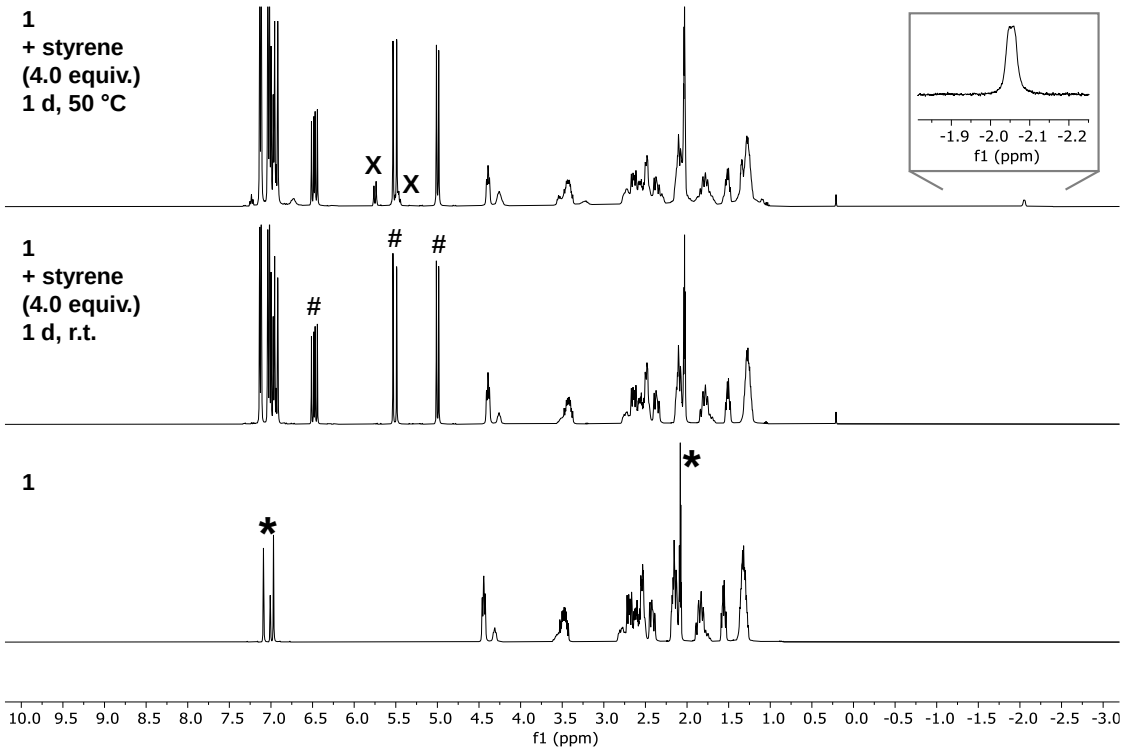

Figure S9. ^{1}H NMR spectroscopic monitoring (toluene-d_8) of the reaction of $Mg[Co(\eta^4\text{-cod})_2]_2$ (**1**) with styrene (4.0 equiv.). Bottom: Isolated sample of **1** before addition. Middle: After addition of styrene (4.0 equiv.) after 1 d at ambient temperature. Top: After 1 d at 50 °C. *: toluene-d_8. #: uncoordinated styrene. X: free (isomerized) 1,3-cyclooctadiene and 1,5-cyclooctadiene.

3.4.7.2 Reaction with Dibenzo[*a*,*e*]cyclooctene (dct)

The reaction monitoring by ^{1}H NMR spectroscopy was carried out in a J. Young NMR tube. A solution of Mg[Co(η^4-cod)$_2$]$_2$ (**1**) (11.4 mg, 19.8 µmol, 1.0 equiv.) and dibenzo[*a*,*e*]cyclooctene (16.2 mg, 79.3 µmol, 4.0 equiv.) in toluene-d$_8$ (0.6 mL) was filtered into an NMR tube. After rotating the sample for 1 d, a ^{1}H NMR spectrum was recorded (Figure S10). No ligand exchange reaction was observed as seen by the absence of free 1,5-cyclooctadiene and otherwise unchanged **1**. The reaction mixture was then heated at 50 °C/2 h and 60 °C/3 h, which led to the formation of minor amounts of free 1,5-cyclooctadiene (label X; Figure S10), but did not result in dct coordination. The observation of free 1,5-cod is likely due to the instability of cobaltate **1** during prolonged heating. This suggests that **1** does not react with dct to give the targeted Mg[Co(η^4-dct)$_2$]$_2$, as observed for the related complexes [K(thf)$_2$][Co(η^4-dct)$_2$][3b] and [(^{Dep}nacnac)Mg(thf)$_{1.7}$][Co(η^4-dct)$_2$].[1e] Steric repulsion of the dct ligands in a geometry analogous to that of **1** can be a factor preventing the formation of a dct-complex of **1**.

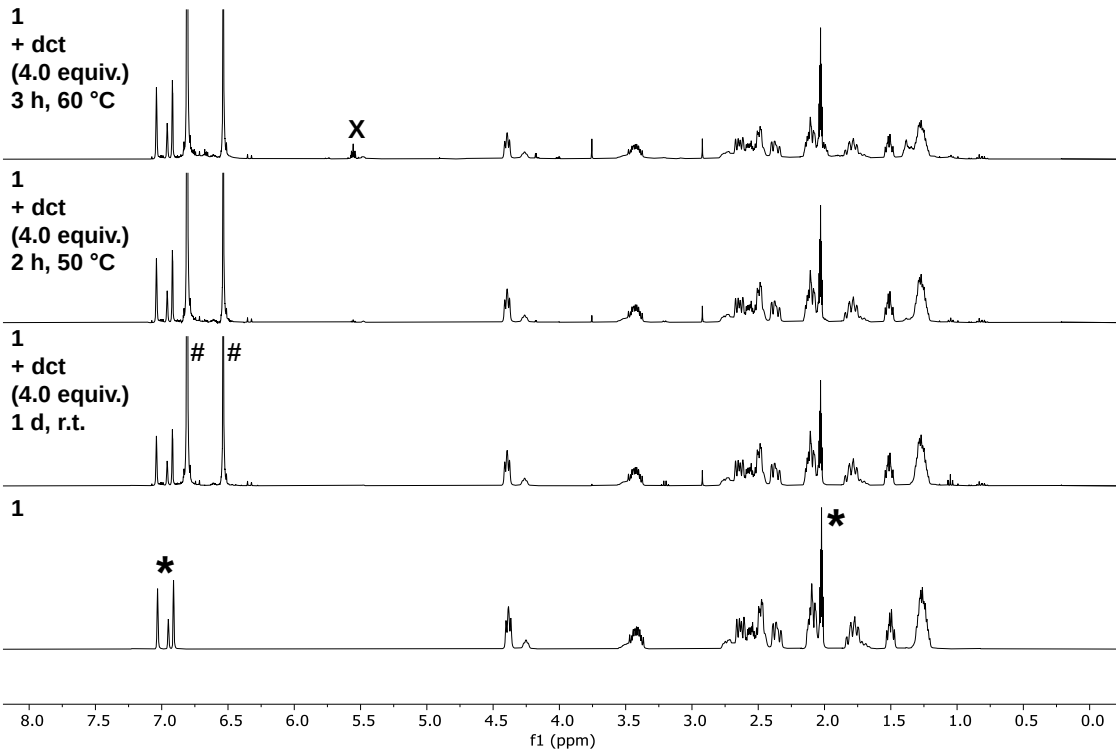

Figure S10. ^{1}H NMR spectroscopic monitoring (toluene-d$_8$) of the reaction of Mg[Co(η^4-cod)$_2$]$_2$ (**1**) with dibenzo[*a*,*e*]cyclooctene (4.0 equiv.). In ascending order: Isolated sample of cobaltate **1** before addition; after addition of dct (4.0 equiv.) after 1 d at ambient temperature; after 2 h at 50 °C; after 3 h at 60 °C. *: toluene-d$_8$. #: uncoordinated dct. X: free (isomerized) 1,5-cyclooctadiene.

3.4.7.3 General Comment

When assessing the unreactive nature of Mg[Co(η^4-cod)$_2$]$_2$ (**1**) toward ligand substitution, it has to be considered that the reactions with **1** were conducted in toluene (due to its insolubility in THF), while the so far reported ligand substitution reactions primarily rely on the use of THF as solvent (see above).[1e],[3b],[6] The choice of solvent may significantly

influence the reactivity of **1** and related cobaltate salts by affecting coordination and stabilization of the countercation during ligand substitution.

3.4.8 NMR Monitoring of the Hydrogenation of α-Methylstyrene

Reaction monitoring by ^{1}H NMR spectroscopy was carried out in a NORELL® intermediate pressure valved NMR tube (S-5-600-MW-IPV-7).[18] The pre-catalyst Mg[Co(η^4-cod)$_2$]$_2$ (**1**; 2 µmol, 2 mol%) was dissolved in toluene-d$_8$ (0.5 mL), α-methylstyrene (13.0 µL, 0.1 mmol, 1.0 equiv.) was added and the solution was transferred to the NMR tube. The first ^{1}H NMR spectrum was recorded (Figure S11). Subsequently, the atmosphere was exchanged with H_2 by three consecutive freeze pump thaw cycles and set to 2 bar of H_2 pressure. Subsequent spectra were recorded after irregular intervals until the substrate was fully consumed or until no further consumption was observed. Prior to the first and between each measurement, the NMR sample was removed from the spectrometer and reversed a few times. After 14 min, the partial hydrogenation of α-methylstyrene (6% according to ^{1}H NMR spectroscopy by relative peak integrals) was observed, which is indicated by the appearance of two new signals at 2.69 ppm and 1.14 ppm (label X; Figure S11).

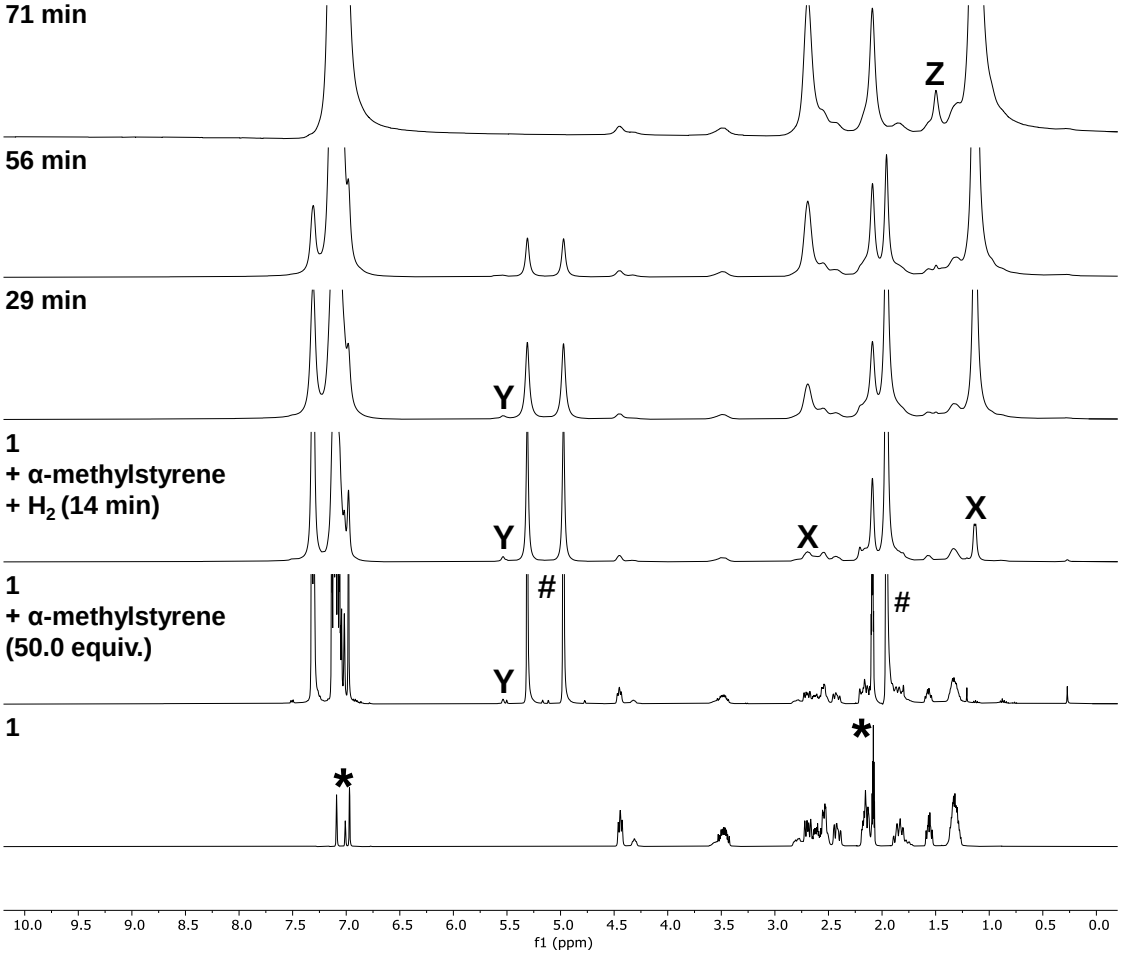

Figure S11. ^{1}H NMR spectroscopic monitoring (toluene-d$_8$) of the hydrogenation of α-methylstyrene with 2 mol% Mg[Co(η^4-cod)$_2$] (**1**). Bottom: Isolated sample of cobaltate **1**. In ascending order: After addition of α-methylstyrene (50.0 equiv.) at ambient temperature and after pressurizing with 2 bar H_2. *: toluene-d$_8$. #: α-methylstyrene. X: cumene. Y: free (isomerized) 1,5-cyclooctadiene. Z: cyclooctane.

After 29 min, cumene has formed in 37%, and after 56 min, the formation of 74% cumene was observed. Complete conversion of α-methylstyrene was achieved after 71 min.

While the signals in the ^{1}H NMR spectrum of **1** and α-methylstyrene are well-resolved prior to H_2 addition, minor line broadening can be observed in the first ^{1}H NMR spectrum after the addition of H_2 (14 min). While broadened, the characteristic signals of **1** are still detected, which indicates that (the majority of) the complex is not transformed in the early stage of the reaction. In addition, the neighboring signals between 5.47 and 5.59 ppm show the formation of free 1,5-cyclooctadiene or hydrogenation products thereof.

The spectroscopic changes are accompanied by the formation of a small amount of suspended solids in the reaction solution, which likely stems from the partial decomposition of **1** in the presence of H_2. Visual inspection over the course of the hydrogenation reaction did not show a notable increase in particle formation, which suggests that the decomposition of **1** primarily occurs upon first contact with H_2. As the reaction proceeds (29 and 56 min), stronger line broadening is observed, which results in the loss of fine structure (e.g., of the doublet at 1.14 ppm), but is overall moderate, as individual signals can still be clearly assigned (cp. with ref. [1e] for pronounced line broadening in related systems). At the end of the hydrogenation (71 min), no more signals for free 1,5-cod (or 1,3-cyclooctadiene or cyclooctene) are observed in the olefinic region, which indicates full conversion to cyclooctane (Figure S11). Furthermore, signals corresponding to **1** are observed after complete conversion of α-methylstyrene, suggesting that **1** stays (in part) intact during the reaction sequence. No upfield shifted signals indicating the formation of a hydride species were detected.

While our previous NMR spectroscopic investigations with the related alkali metal and (nacnac)Mg cobaltates (i.e., complexes **A** and **H**) allowed for a clear distinction between (inactive) Co nanoparticles and an active homotopic catalyst species,[1e] the hydrogenation of α-methylstyrene with **1** features characteristics of both reaction systems. When considering the earlier discussed mercury poisoning experiments (section 3.4.4), which showed that the hydrogenation of α-methylstyrene with **1** is not inhibited by Hg, the continuous product formation in the presence of particles indicates that the hydrogenation of α-methylstyrene may be catalyzed by a molecular species. However, further experiments are needed to definitively determine the homotopic vs. heterotopic nature of the catalyst.

3.4.9 NMR Spectra of $Mg[Co(\eta^4\text{-cod})_2]_2$ (1)

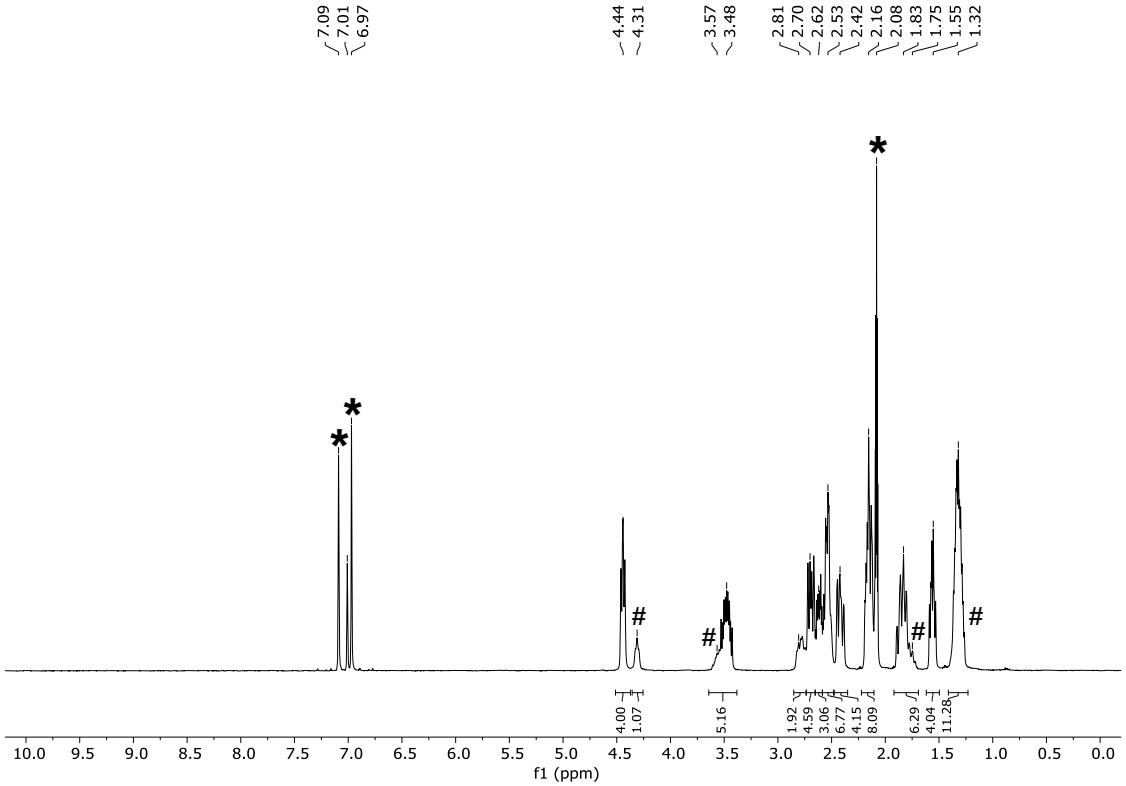

Figure S12. ^{1}H NMR spectrum (400.13 MHz, 298 K, toluene-d_8) of $Mg[Co(\eta^4\text{-cod})_2]_2$ (**1**). Unmarked resonances are the major isomer A. #: minor isomer B. *: toluene-d_8.

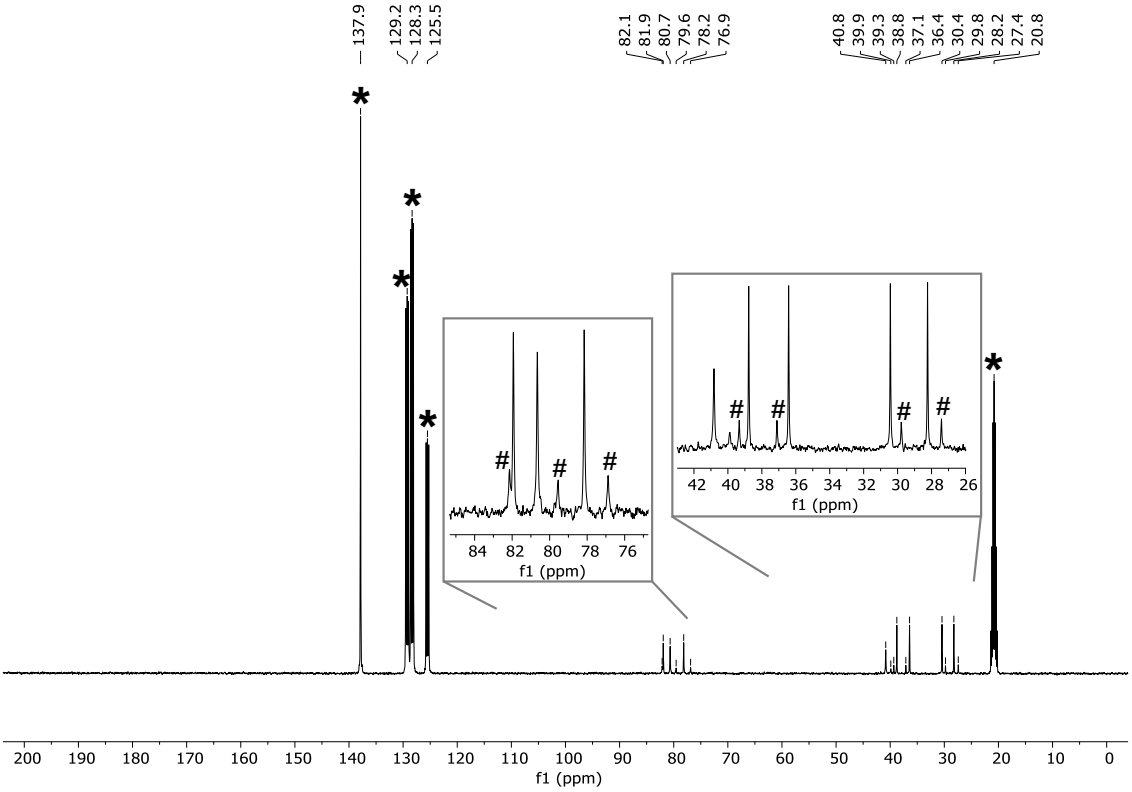

Figure S13. $^{13}C\{^1H\}$ NMR spectrum (100.61 MHz, 298 K, toluene-d_8) of $Mg[Co(\eta^4\text{-cod})_2]_2$ (**1**). Unmarked resonances are the major isomer A. #: minor isomer B. *: toluene-d_8.

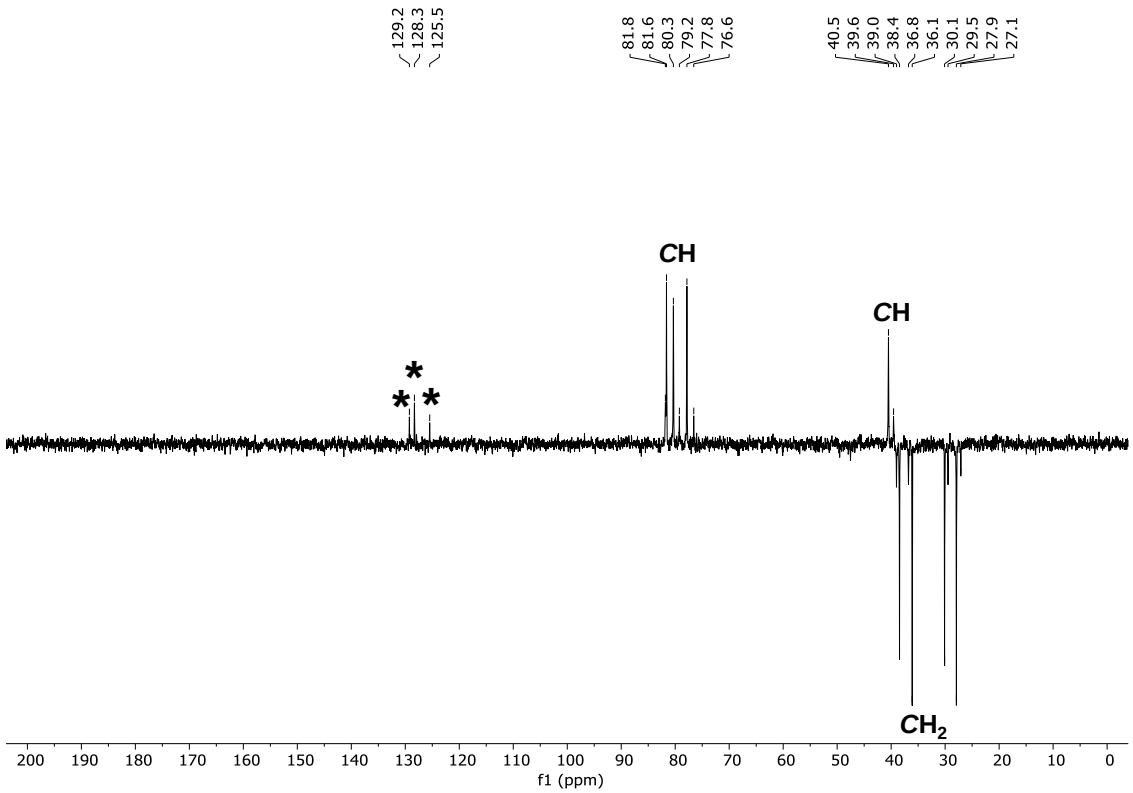

Figure S14. DEPT-135 ^{13}C NMR spectrum (100.61 MHz, 298 K, toluene-d_8) of $Mg[Co(\eta^4\text{-cod})_2]_2$ (**1**). Positive resonances are CH groups and negative resonances are CH_2 groups. *: toluene-d_8.

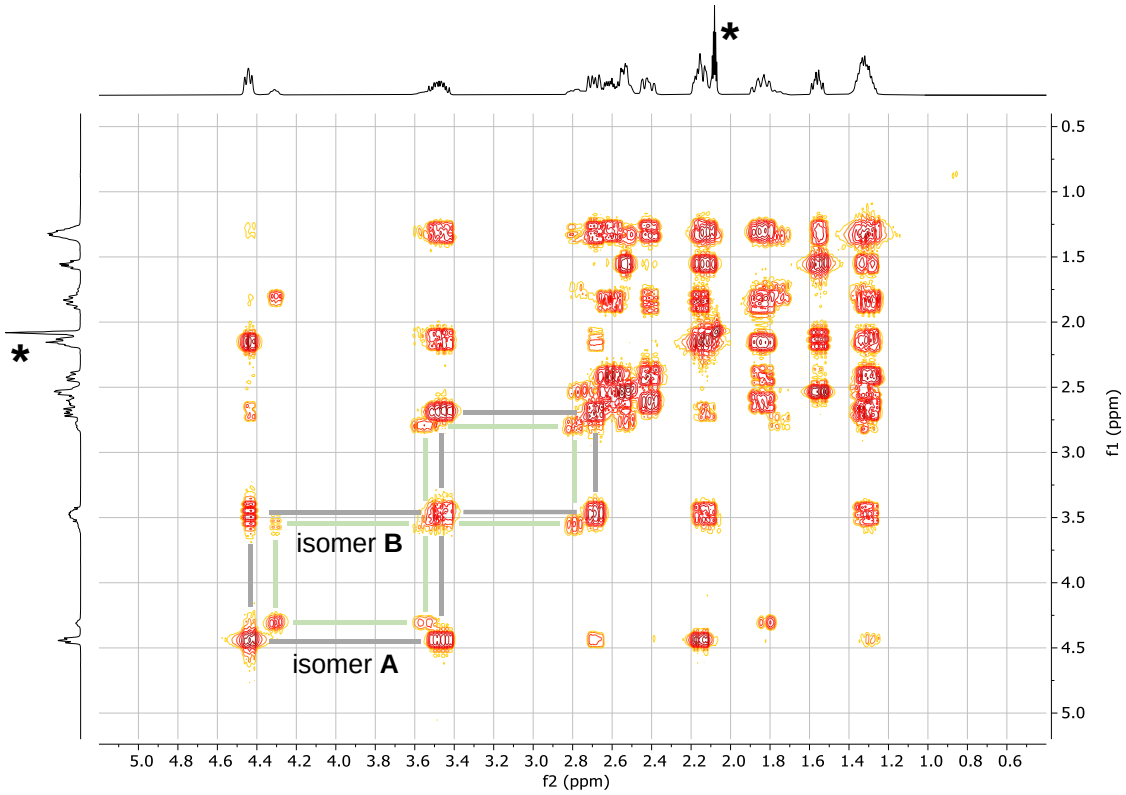

Figure S15. $^1H/^1H$ COSY NMR spectrum (400.13/400.13 MHz, 298 K, toluene-d_8) of $Mg[Co(\eta^4\text{-cod})_2]_2$ (**1**). Selected cross peaks are highlighted to show the interactions of isomer A and isomer B. *: toluene-d_8.

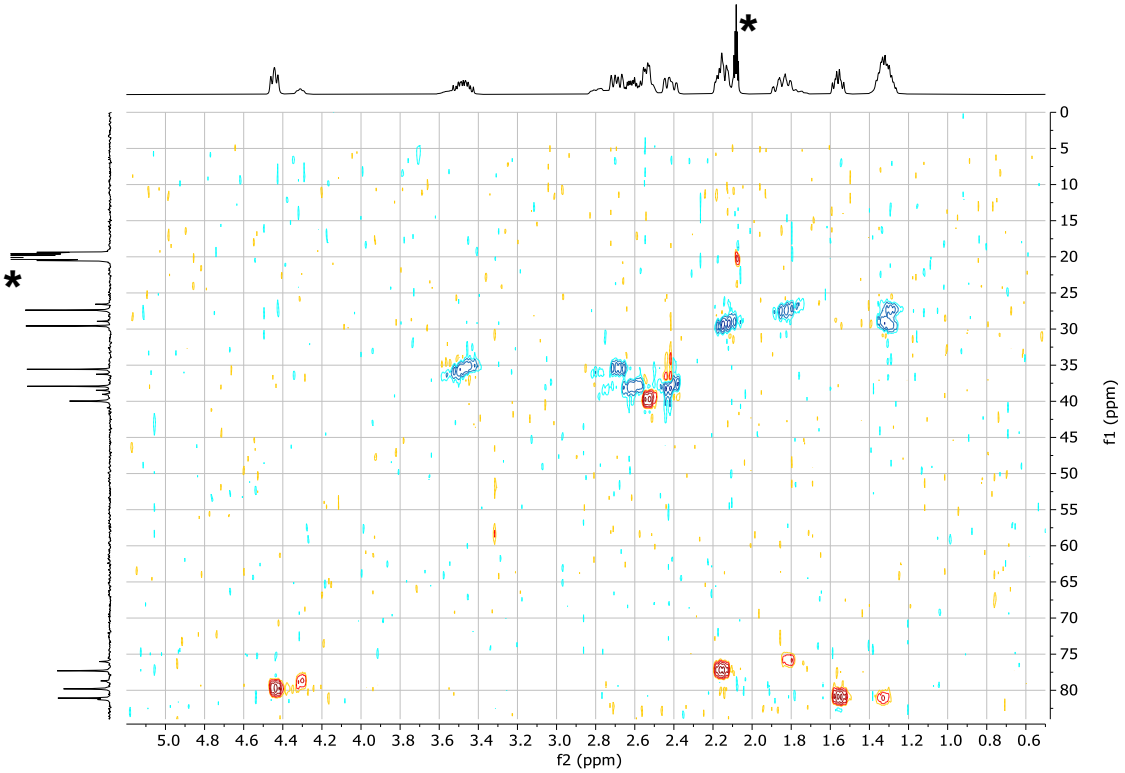

Figure S16. $^{1}H/^{13}C$ HSQC NMR spectrum (400.13/100.61 MHz, 298 K, toluene-d_8) of $Mg[Co(\eta^4\text{-cod})_2]_2$ (**1**). *: toluene-d_8.

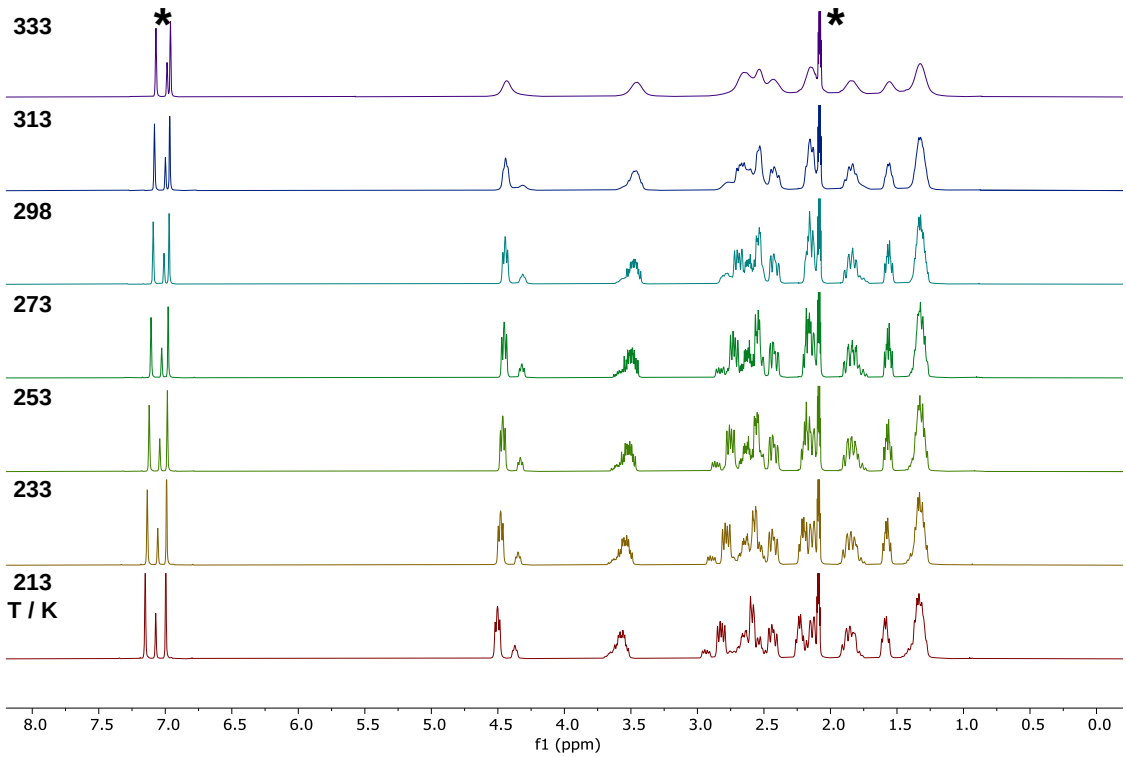

Figure S17. Variable-temperature ^{1}H NMR spectrum (400.13 MHz, 213-333 K, toluene-d_8) of $Mg[Co(\eta^4\text{-cod})_2]_2$ (**1**). *: toluene-d_8.

3.4.10 Single Crystal X-ray Diffraction Data

The single-crystal X-ray diffraction data were recorded on a Rigaku Synergy DW diffractometer with Cu-K_α radiation (λ= 1.54184 Å). Crystals were selected under mineral oil, mounted on micromount loops and quench-cooled using an Oxford Cryosystems open flow N_2 cooling device. Either semi-empirical multi-scan absorption correction[19] or analytical ones[20] were applied to the data. The structures were solved with SHELXT[21] solution program using dual methods and by using Olex2 as the graphical interface.[22] The models were refined with ShelXL[21] using full matrix least squares minimization on F^2.[23] The hydrogen atoms were located in idealized positions and refined isotropically with a riding model. The disorder in **Zn[Co(η⁴-btd)₂]₂** (btd = 1,3-butadiene) was treated with soft displacement parameter and geometrical restraints.

Table S5. Crystallographic data and structure refinement for compounds $Mg[Co(\eta^4\text{-}cod)_2]_2$ (**1**) and **Zn[Co(η⁴-btd)₂]₂**.

Compound	Mg[Co(η⁴-cod)₂]₂ (1)	Zn[Co(η⁴-btd)₂]₂
Empirical formula	$C_{32}H_{48}Co_2Mg$	$C_8H_{12}CoZn_{0.5}$
Formula weight	574.87	199.79
Temperature/K	123(1)	100(1)
Crystal system	monoclinic	monoclinic
Space group	$P2_1/c$	$C2/c$
a/Å	10.48249(5)	19.4505(2)
b/Å	20.11765(9)	7.45850(10)
c/Å	12.99703(6)	10.77860(10)
α/°	90	90
β/°	104.8377(5)	100.2250(10)
γ/°	90	90
Volume/Å³	2649.46(2)	1538.83(3)
Z	4	8
ρ_{calc}g/cm³	1.441	1.725
μ/mm⁻¹	10.163	18.337
F(000)	1224	816
Crystal size/mm³	0.21 × 0.15 × 0.12	0.156 × 0.105 × 0.049
Radiation	Cu Kα (λ = 1.54184)	Cu Kα (λ = 1.54184)
2Θ range for data collection/°	8.298 to 150.46	9.24 to 150.344
Index ranges	-13 ≤ h ≤ 13, -25 ≤ k ≤ 25, -13 ≤ l ≤ 15	-24 ≤ h ≤ 22, -9 ≤ k ≤ 9, -13 ≤ l ≤ 13
Reflections collected	110692	15410
Independent reflections	5420 [R_{int} = 0.0597, R_{sigma} = 0.0183]	1568 [R_{int} = 0.0201, R_{sigma} = 0.0086]
Data/restraints/parameters	5420/0/324	1568/198/155
Goodness-of-fit on F^2	1.056	1.124
Final R indexes [I>=2σ (I)]	R_1 = 0.0333, wR_2 = 0.0926	R_1 = 0.0205, wR_2 = 0.0540
Final R indexes [all data]	R_1 = 0.0348, wR_2 = 0.0938	R_1 = 0.0218, wR_2 = 0.0546
Largest diff. peak/hole / e Å⁻³	0.50/-0.42	0.22/-0.80

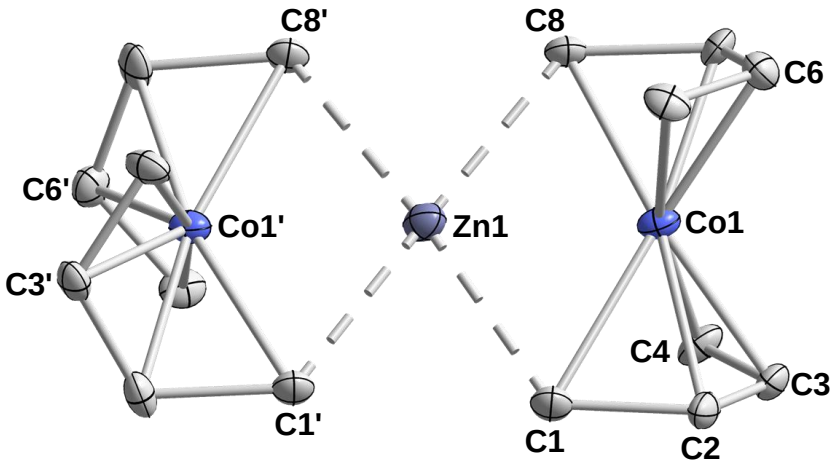

Figure S18. Molecular structure of **Zn[Co(η⁴-btd)₂]₂** (btd = 1,3-butadiene) in the solid state. Part 0+1 are displayed. Ellipsoids are set at the 40% probability level. Hydrogen atoms were omitted for clarity. Selected bond lengths [Å] and angles [°]: Zn1–Co1: 2.304(2), Zn1–C1: 2.295(3), Zn1–C8: 2.303(3), C1–Co1: 2.156(3), C8–Co1: 2.102(3), C1–C2: 1.502(1), C2–C3: 1.376(2), C3–C4: 1.392(1), Co1'–Zn1–Co1: 178.6(2), C1–Zn1–C8: 110.0(1), [Co(η⁴-btd)₂]-to-[Co(η⁴-btd)₂] tilt (plane[C3-Co1-C6]-to-plane[C3'-Co1'-C6']): 86.0(5)°. Zn[Co(η⁴-btd)₂]₂ was synthesized in 51% yield following an adapted literature procedure by Jonas by reacting [K(thf)$_{0.5}$][Co(η²-ethylene)₄] with anhydrous $ZnCl_2$ in the presence of 1,3-butadiene (2.0 M in THF) in THF.[1c] The NMR spectroscopic analysis is in agreement with the reported data. The complex has not been described in the solid state and was therefore characterized by SC-XRD analysis as part of this project.

3.4.11 Quantum Chemical Calculations

All calculations were carried out with the ORCA 5.03 and 5.0.4 quantum chemistry package.[24] Geometry optimizations were performed at the r²SCAN-3c[25] level of theory in the gas phase. Stationary points were confirmed as local minima (no imaginary frequencies) by frequency analysis. Single point energy calculations were performed on the fully optimized geometries (r²SCAN-3c) and the electron densities calculated at the ωB97X-D4/def2-TZVPPD[26] level of theory. Further molecular properties were analyzed using natural bond orbital (NBO 7.0) analyses,[27] IBO analyses[28] (IboView) and NCI analyses[29] (multiwfn 3.8[30]) for non-covalent interactions. Shown isosurfaces were plotted with VMD 1.9.3.[31] Table S6 compares the experimental geometry of Mg[Co(η⁴-cod)₂]₂ (**1**) in the solid state with the computed geometry, obtained at the r²SCAN-3c level of theory.

Table S6. Comparison of structural parameters of Mg[Co(η⁴-cod)₂]₂ (**1**): experimental vs. computational data.

Bond distance [Å] or angle [°]	X-ray structure	Computed structure	Atom numbers
Co^1–Mg^1 / Mg^1–Co^2	2.631(6) / 2.615(6)	2.639 / 2.636	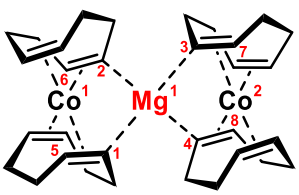
Co^1–Co^2	5.246(2)	5.275	
Mg^1–C^1 / Mg^1–C^2	2.411(2) / 2.362(2)	2.389 / 2.396	
Co^1–Mg^3–Co^2	179.36(4)	179.70	
plane[C1-Co1-C2]-to-plane[C3-Co2-C4] tilt	50.42(6)	43.89	

3.4.11.1 Calculation of the $^{13}C\{^1H\}$ NMR chemical shifts of $Mg[Co(\eta^4\text{-cod})_2]_2$ (1)

The $^{13}C\{^1H\}$ NMR chemical shifts were calculated using the GIAO[32] formalism based on the optimized geometry of **1** (and tetramethylsilane (TMS)) at the r^{2}SCAN-3c level of theory using the CPCM(Toluene) solvation model.[33] For this, the TPSS[34] or PBE0[35] functionals and the pcSseg-2[36] or def2-TZVPP[25c-g] basis sets together with an auxiliary basis set based on the AutoAux keyword and the CPCM(Toluene) solvation model were used. The calculated absolute shifts have been referenced to the absolute shift of TMS (obtained at the identical level of theory). Table S7 summarizes the calculated $^{13}C\{^1H\}$ NMR chemical shifts of **1** at the different levels of theory. All calculations show the distribution of the resonances in a region with three signals at approximately 80.0-100.0 ppm and a region with five signals at approximately 30.0-50.0 ppm, consistent with the experimentally obtained $^{13}C\{^1H\}$ NMR spectrum of **1** (Figure S13). The best computational description is achieved at the PBE0/def2-TZVPP level of theory, which reproduces the $^{13}C\{^1H\}$ NMR chemical shifts of **1** with a deviation of approximately 5 ppm. The $^{13}C\{^1H\}$ NMR chemical shift of the inward-facing, sp^2-hybridized carbon atoms (such as C4 in Table S7) is calculated at 44.9 ppm, upfield-shifted by ca. 40 ppm compared to the other olefinic resonances, which is in agreement with the experimental data (Figure S13 and Figure S14).

Table S7. Calculated $^{13}C\{^1H\}$ NMR chemical shifts of $Mg[Co(\eta^4\text{-cod})_2]_2$ (**1**) using different levels of theory.

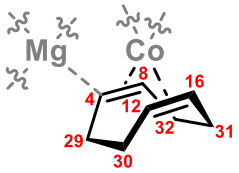		**TPSS/ pcSseg-2**	**TPSS/ def2-TZVPP**	**PBE0/ def2-TZVPP**
		Calculated chemical shift [ppm]		
Exp.[a] [ppm]	TMS	187.3	185.5	188.4
40.8	C4	48.8	47.1	44.9
81.9/80.7/78.2	C8	96.9	95.4	89.4
30.4/28.2	C32	35.5	37.7	31.9
38.8/37.1	C31	44.7	46.9	42.4
81.9/80.7/78.2	C16	88.4	85.4	88.5
81.9/80.7/78.2	C12	87.5	85.3	82.4
30.4/28.2	C30	33.4	35.7	29.7
38.8/37.1	C29	47.4	49.4	44.0

[a] The chemical shifts of the major isomer A of **1** are depicted.

3.4.11.2 NBO Analysis of $Mg[Co(\eta^4\text{-cod})]_2$ (1)

The main findings from NBO analysis of **1** are depicted in Table S8. No Lewis or non-Lewis shared orbitals between the magnesium and cobalt centres are found, and the second order perturbation theory analysis shows that the donor–acceptor interaction between an electron

lone pair and of Co and a vacant or Rydberg orbital on Mg is negligibly small (<1 kcal mol^{-1}).

Table S8. NBO data for Mg[Co(η^4-cod)$_2$]$_2$ (**1**).

NPA charges		**Wiberg bond indices**	
Co1 / Co2	0.26 / 0.25	Co1–Mg1 / Mg1–Co2	0.029 / 0.030
Mg1	1.74	Mg1–C4 / Mg1–C3	0.057 / 0.057
C4 / C8	–0.54 / –0.20	/	/
C12 / C16	–0.30 / –0.25	/	/

Second order perturbation theory analysis

Donor (L) NBO	Acceptor (NL) NBO	E (2) kcal/mol
BD (2) C4–C8	LV (1) Mg1	3.98
BD (2) C3–C7	LV (1) Mg1	4.02
BD (2) C1–C5	LV (1) Mg1	4.24
BD (2) C2–C6	LV (1) Mg1	4.15

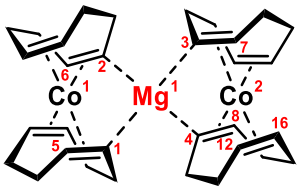

3.4.11.3 IBO Analysis of Mg[Co(η^4-cod)$_2$]$_2$ (1)

IBO analysis shows four localized molecular orbitals that have a contribution from magnesium (Figure S19).

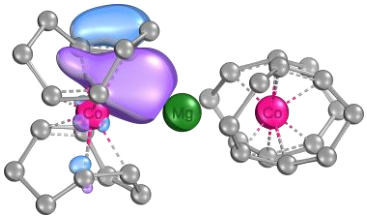

Orb. 140 C4 1.298 C8 0.225 Co2 0.180 Mg1 0.110 (other: 0.187)

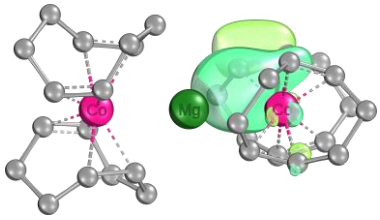

Orb. 141 C2 1.296 C6 0.230 Co2 0.180 Mg1 0.108 (other: 0.186)

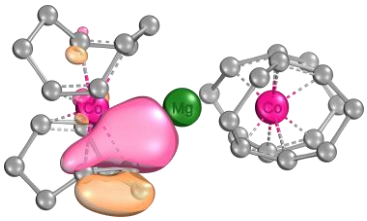

Orb. 142 C3 1.297 C7 0.225 Co2 0.180 Mg1 0.110 (other: 0.188)

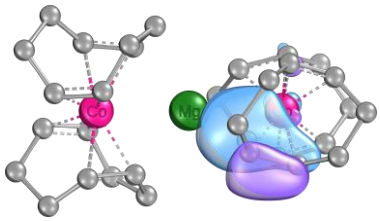

Orb. 143 C1 1.297 C5 0.226 Co2 0.179 Mg1 0.111 (other: 0.188)

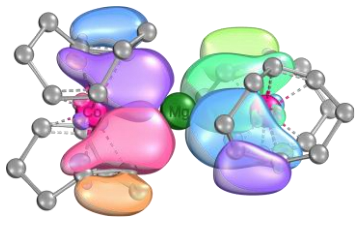

Simultaneous visualization of the **four bonding interactions stabilizing** the **Mg^{2+}** countercation

Figure S19. IBOs of Mg[Co(η^4-cod)$_2$]$_2$ (**1**) showing the bonding interactions between the Mg^{2+} countercation and the two cobaltate anions.

These orbitals are (majorly) shared between the inward-facing double bond of each cod ligand, Co and Mg, and are largely located at the inward-facing C atom (0.65). Co (0.09) and Mg (0.05-0.06) contribute to a much lower extent. The bonding situation can be described as a σ-type interaction between (one node of the π-orbital of) the alkene double bond and the Mg and Co atoms. Next to this, no bond-like localized orbitals involving Mg and Co are found.

3.4.11.4 AIM Analysis of Mg[Co(η⁴-cod)₂]₂ (1)

The descriptors for the bond critical points (3, −1; BCPs **A**-**D**) between Mg^{2+} and the four inward-facing, sp^2-hybridized C atoms of the cod ligands of Mg[Co(η⁴-cod)₂]₂ (**1**) are displayed in Table S9.[37] The classification based on the values of $\rho(r_b)$, $\nabla^2\rho(r_b)$, $G(r_b)$, $V(r_b)$, and $H(r_b)$ is discussed in the following. The $|V(r_b)|/G(r_b)$ ratio is found close to 1 for all BCPs (1.096-1.105), with $V(r_b)\cong G(r_b)$, which can be used as a classification criterion for a closed shell donor-acceptor interaction (please note that the interactions were initially used to describe transition metal interactions).[38] Moreover, the BCPs are in the range $1 < V(r_b)\cong G(r_b) < 2$, which indicates an intermediate bond character between Mg and C, with the interaction not being purely ionic but having some covalent character (typical covalent interactions $|V(r_b)|/G(r_b) > 2$ and typical ionic interactions $|V(r_b)|/G(r_b) < 1$).[7b],[39] The low electron density $\rho(r_b)$, the positive Laplacian of electron density ($\nabla^2\rho(r_b) > 0$), and the negative energy density ($H(r_b) < 0$) at the BCPs support a closed shell bonding interaction with donor-acceptor character.

Table S9. AIM parameters at the bond critical points (3, −1) between Mg^{2+} and the four inward-facing, sp^2-hybridized C atoms of the cod ligands of Mg[Co(η⁴-cod)₂]₂ (**1**).[a]

Bond critical point	**A** (173, Mg1−C1)	**B** (172, Mg1−C2)	**C** (140, Mg1−C3)	**D** (149, Mg1−C4)
$\rho(r_b)$	0.0300	0.0297	0.0299	0.0301
$\nabla^2\rho(r_b)$	0.0862	0.0838	0.0846	0.0870
$G(r_b)$	0.0239	0.0234	0.0236	0.0241
$V(r_b)$	−0.0265	−0.0259	−0.0260	−0.0264
$\lvert V(r_b)\rvert/G(r_b)$	1.098	1.105	1.103	1.096
$G(r_b)/\rho(r_b)$	0.797	0.787	0.790	0.801
$H(r_b)$	−0.0024	−0.0025	−0.0024	−0.0023

[a] Electron density ($\rho(r_b)$ in au), Laplacian of electron density ($\nabla^2\rho(r_b)$ in au), Lagrangian kinetic energy density ($G(r_b)$ in au), potential energy density ($V(r_b)$ in au), ratio $|V(r_b)|/G(r_b)$, ratio $G(r_b)/\rho(r_b)$ in au, electron energy density ($H(r_b)$ in au).

3.4.11.5 NCI Analysis of Mg[Co(η⁴-cod)₂]₂ (1)

The non-covalent interaction analysis of Mg[Co(η⁴-cod)₂]₂ (**1**) is shown in Figure S20. The high-quality integration grid of the software multiwfn was used for the NCI plot calculation. A full representation of the rendered structure of **1** with the NCI surface (3D), a cutout of the interaction between Mg and the four sp^2-hybridized C atoms (3D), as well as the full NCI plot

(2D) are depicted. The NCI analysis shows a strong, attractive interaction between the magnesium countercation and the four inward-facing, sp^2-hybridized carbon atoms of the cod ligands (Figure S20b,c). Using a cutoff, the interaction can be located at $sign(\lambda_2)\rho \approx -0.03$, which is in the range of strong attractive interactions, such as hydrogen bonding interactions (Figure S20d). In line with the other computational calculations (NBO, IBO, AIM), a stabilizing interaction between the Mg^{2+} cation and the sp^2-hybridized C_π atoms of the cod ligands can be identified. Furthermore, a mix of weak attractive and repulsive interactions can be found between the cod ligands of the two $[Co(\eta^4\text{-cod})_2]^-$ units, which is best described by Van der Waals interactions.

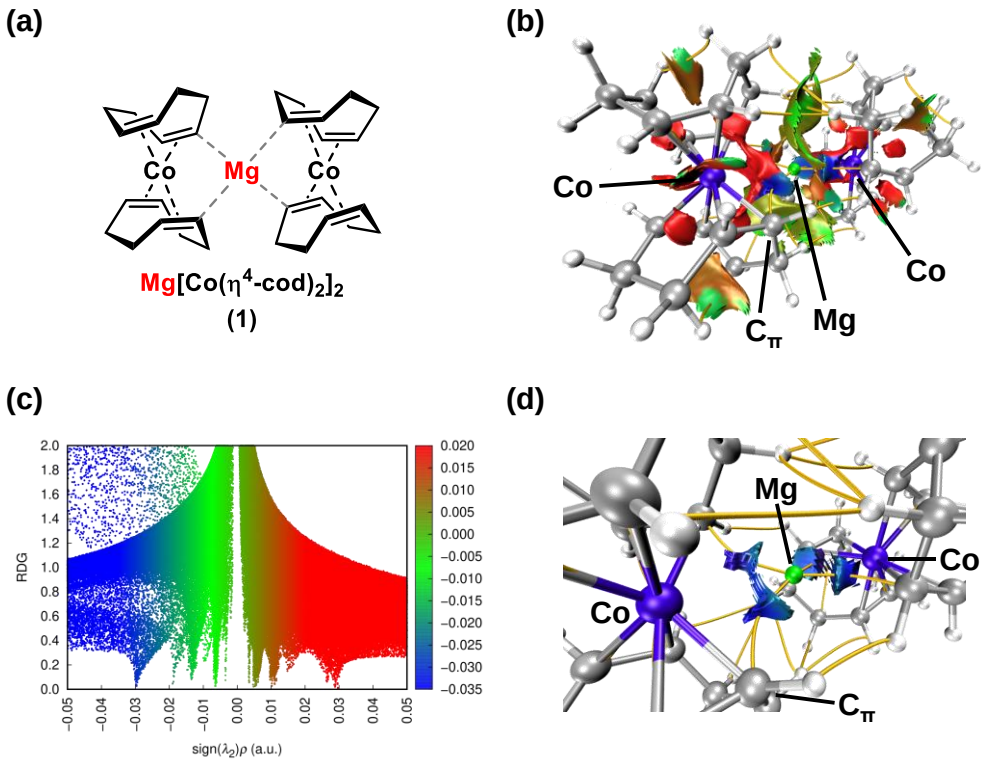

Figure S20. (a) Structure of $Mg[Co(\eta^4\text{-cod})_2]_2$ (**1**). (b) NCI Surface visualization with bond paths (3D, isovalue = 0.4) of **1**. (c) NCI plot (2D) of **1**. (d) Cutout (at $sign(\lambda_2)\rho < -0.02$) of the NCI surface visualization with bond paths (3D) of **1** showing the [C=C]···Mg^{2+} interaction. Diagrams show plots of RDG := reduced density gradient over $sign(\lambda_2)\rho$:= density with sign of the second derivative Hessian matrix. The $sign(\lambda_2)\rho > 0$ (red) are read as strong repulsive interactions, $sign(\lambda_2)\rho \approx 0$ (green) as weak interactions and $sign(\lambda_2)\rho < 0$ (blue) as strong attractive interactions.

3.4.11.6 Cartesian Coordinates of $Mg[Co(\eta^4\text{-cod})_2]_2$ (1)

H = -4212.83797085 Eh
S = -0.08905093 Eh
G = -4212.92702178 Eh
Co 3.95772 16.15939 3.88815
Co 0.59530 12.13600 3.31480
Mg 2.27042 14.15097 3.60126
C 1.36824 13.13879 1.63721
H 2.43673 13.14584 1.39906
C 0.76615 11.87956 1.32653
H 1.47940 11.08211 1.12051
C 1.18864 12.77125 5.23158
H 0.95293 13.76930 5.61459
C 2.24338 16.00898 5.10241
H 2.08153 15.17636 5.79451

C 4.30225 14.67204 2.44360
H 3.61840 14.49923 1.60666
C 3.22206 16.92715 5.59624
H 3.79892 16.55240 6.44115
C 5.08157 15.85406 2.24753
H 4.72750 16.49262 1.43872
C -0.80320 14.41486 1.86236
H -1.06776 15.42158 2.20826
H -1.52563 14.17823 1.07385
C 6.58835 15.92663 2.44692
H 7.03210 16.52165 1.64041
H 7.03458 14.92983 2.35931
C 5.80598 16.26994 4.79927
H 5.78652 16.95541 5.64642
C 0.63004 14.42899 1.28584
C 2.87029 10.91075 4.92484
H 3.94738 10.87675 4.72078
H 2.66509 10.03546 5.55054
C 2.73008 17.39223 2.79664
H 2.77012 17.09442 1.74753
C 5.23631 14.99017 4.99038
H 4.78970 14.80641 5.96901
C 2.53086 12.20753 5.69248
H 2.52549 12.03360 6.78083
H 3.33508 12.94688 5.53982
C 2.11520 10.78600 3.60232
H 2.76221 10.79150 2.72344
C 3.84053 18.12534 3.27408
H 4.62712 18.35845 2.55670
C 0.88820 10.09770 3.46236
H 0.70091 9.60314 2.50957
C 0.02752 10.50181 5.77656
H -0.89535 10.33629 6.34432
H 0.84490 10.35830 6.49211
C -1.41952 12.10648 2.87008
H -1.99466 11.67834 3.69077
C 0.03672 11.92397 5.23617
H -0.90326 12.44900 5.40421
C 3.03693 18.43716 5.62310
H 3.42040 18.83304 6.57054
H 1.97158 18.69246 5.60494
C 4.96889 13.41278 2.99483
H 5.63071 12.95779 2.23986
H 4.21437 12.63409 3.19957
C -0.53844 11.72800 0.55871
H -0.44710 10.90008 -0.15373
H -0.73004 12.62051 -0.04726
C -0.96759 13.43728 3.02417
H -1.20940 13.91676 3.97438
C 6.90520 16.56066 3.80576
H 7.88675 16.23286 4.18857
H 6.97197 17.64881 3.68625
C -1.68996 11.45942 1.53347
H -2.65843 11.78744 1.11886
H -1.77694 10.37813 1.69516
C 5.74069 13.72854 4.29387
H 5.65503 12.88341 4.98796
H 6.81121 13.82432 4.08381
C 3.78096 19.07589 4.44522
H 3.33123 20.04083 4.15538
H 4.81059 19.29778 4.75093
C 0.97031 16.54868 4.45324
H 0.30889 17.00147 5.20965
H 0.37316 15.72248 4.03014
C 1.31131 17.55894 3.33610
H 0.60256 17.44188 2.50716
H 1.16982 18.58367 3.69659
C 0.11965 9.50327 4.61805
H 0.55945 8.54417 4.94067
H -0.89248 9.27274 4.26418
H 0.61670 14.58607 0.19499
H 1.17483 15.30456 1.67898

3.5 References

[1] a) K. Jonas, R. Mynott, C. Krüger, J. C. Sekutowski, Y.-H. Tsay, *Angew. Chem.* **1976**, *88*, 808; b) K. Jonas (Studiengesellschaft Kohle mbH), US4169845 A, **1977**; c) D. Habermann, Organocobaltverbindungen aus (η-Cyclopentadienyl)cobalt-Komplexen durch reduktive C_5H_5-Ablösung, PhD Dissertation, Ruhr-Universität Bochum, **1980**; d) W. W. Brennessel, V. G. Young, Jr., J. E. Ellis, *Angew. Chem. Int. Ed.* **2002**, *41*, 1211; e) M. Gawron, F. Gilch, D. Schmidhuber, J. A. Kelly, T. M. Horsley Downie, A. Jacobi Von Wangelin, J. Rehbein and R. Wolf, *Angew. Chem. Int. Ed.* **2024**, *63*, e202315381.

[2] a) R. Wolf, A. W. Ehlers, J. C. Slootweg, M. Lutz, D. Gudat, M. Hunger, A. L. Spek, K. Lammertsma, *Angew. Chem. Int. Ed.* **2008**, *47*, 4584; b) C. G. P. Ziegler, F. Hennersdorf, J. J. Weigand, R. Wolf, *Z. Anorg. Allg. Chem.* **2020**, *646*, 552; c) G. Hierlmeier, P. Coburger, D. J. Scott, T. M. Maier, S. Pelties, R. Wolf, D. M. Pividori, K. Meyer, N. P. van Leest, B. de Bruin, *Chem. Eur. J.* **2021**, *27*, 14936; d) J. A. Kelly, J. Gramüller, R. M. Gschwind and R. Wolf, *Dalton Trans.* **2021**, *50*, 13985.

[3] a) D. Gartner, A. Welther, B. R. Rad, R. Wolf, A. Jacobi von Wangelin, *Angew. Chem. Int. Ed.* **2014**, *53*, 3722; b) P. Büschelberger, D. Gärtner, E. Reyes-Rodriguez, F. Kreyenschmidt, K. Koszinowski, A. Jacobi von Wangelin and R. Wolf, *Chem. Eur. J.* **2017**, *23*, 3139.

[4] B. N. Baumann, H. Lange, F. Seeberger, P. Büschelberger, R. Wolf, M. Hapke, *Mol. Catal.* **2023**, *550*, 113482.

[5] P. Büschelberger, E. Reyes-Rodriguez, C. Schöttle, J. Treptow, C. Feldmann, A. Jacobi von Wangelin, R. Wolf, *Catal. Sci. Technol.* **2018**, *8*, 2648.

[6] W. W. Brennessel, J. E. Ellis, *Inorg. Chem.* **2012**, *51*, 9076.

[7] a) S. Pelties, T. Maier, D. Herrmann, B. de Bruin, C. Rebreyend, S. Gärtner, I. G. Shenderovich, R. Wolf, *Chem. Eur. J.* **2017**, *23*, 6094; b) T. M. Maier, S. Sandl, I. G. Shenderovich, A. Jacobi von Wangelin, J. J. Weigand, R. Wolf, *Chem. Eur. J.* **2019**, *25*, 238; S. Sandl, T. M. Maier, N. P. van Leest, S. Kröncke, U. Chakraborty, S. Demeshko, K. Koszinowski, B. de Bruin, F. Meyer, M. Bodensteiner, C. Herrmann, R. Wolf, A. Jacobi von Wangelin, *ACS Catal.* **2019**, *9*, 7596; c) C. M. Hoidn, T. M. Maier, K. Trabitsch, J. J. Weigand, R. Wolf, *Angew. Chem. Int. Ed.* **2019**, *58*, 18931; d) S. Hauer, T. M. Horsley Downie, G. Balázs, K. Schwedtmann, J. J. Weigand, R. Wolf, *Angew. Chem. Int. Ed.* **2024**, *63*, e202317170.

[8] a) K. Jonas, G. Koepe and C. Krüger, *Angew. Chem. Int. Ed.* **1986**, *25*, 923; b) M. P. Blake, N. Kaltsoyannis and P. Mountford, *J. Am. Chem. Soc.* **2015**, *137*, 12352; c) R. Green, A. C. Walker, M. P. Blake and P. Mountford, *Polyhedron* **2016**, *116*, 64.

[9] a) G. M. Sheldrick, R. N. F. Simpson, *Chem. Commun. (London)* **1967**, 1015a; b) G. M. Sheldrick, R. N. F. Simpson, *J. Chem. Soc. (A)* **1968**, 1005.

[10] To the best of our knowledge, the only structurally related complex is $Zn[Co(\eta^4\text{-btd})_2]_2$ (btd = 1,3-butadiene), which was already reported in 1980 (ref. [1c]) but only subjected to a small reactivity study with nucleophiles. The solid state structure of $Zn[Co(\eta^4\text{-btd})_2]_2$ is shown in section 3.4.10 (Figure S18), as it was not characterized by SC-XRD analysis in the original report.

[11] a) J. A. Widegren, R. G. Finke, *J. Mol. Catal. A* **2003**, *198*, 317; b) C. A. Jaska, I. Manners, *J. Am. Chem. Soc.* **2004**, *126*, 9776; c) R. H. Crabtree, *Chem. Rev.* **2012**, *112*, 1536; d) D. Gartner, S. Sandl, A. Jacobi von Wangelin, *Catal. Sci. Technol.* **2020**, *10*, 3502.

[12] Syringe filter ROTILABO® Mini-Tip (PTFE), pore size 0.2 µm, 15 mm diameter; available under: https://www.carlroth.com/de/de/spritzenvorsatzfilter/spritzenfilter-rotilabo-mini-tip-polytetrafluorethylen-%28ptfe%29/p/pp45.1, **2025**.

[13] a) A. Jerschow, N. Müller, *J. Magn. Reason., Ser. A* **1996**, *123*, 222; b) A. Jerschow, N. Müller, *J. Magn. Reson.* **1997**, *125*, 372.

[14] E. O. Stejskal, J. E. Tanner, *J. Chem. Phys.* **1965**, *42*, 288.

[15] A. Macchioni, G. Ciancaleoni, C. Zuccaccia, D. Zuccaccia, *Chem. Soc. Rev.* **2008**, *37*, 479.

[16] H. C. Chen, S. H. Chen, *J. Phys. Chem.* **1984**, *88*, 5118.

[17] a) D. Ben-Amotz, K. G. Willis, *J. Phys. Chem.* **1993**, *97*, 7736; b) D. Zuccaccia, A. Macchioni, *Organometallics* **2005**, *24*, 3476.

[18] NORELL® Valved NMR tubes are available under: https://secure.nmrtubes.com/nmr-epr-tubes/valved-for-intermediate-pressure, **2025**.

[19] a) Sheldrick, G. M. SADABS, Bruker AXS, Madison, USA **2007**; b) CrysAlisPro, Scale3 Abspack, Rigaku Oxford Diffraction, **2019**.

[20] R. C. Clark, J. S. Reid, *Acta Crystallogr. A* **1995**, *51*, 887.

[21] G. M. Sheldrick, *Acta Crystallogr. C* **2015**, *71*, 3.

[22] O. V. Dolomanov, L. J. Bourhis, R. J. Gildea, J. A. K. Howard, H. Puschmann, *J. Appl. Crystallogr.* **2009**, *42*, 339.

[23] G. M. Sheldrick, *Acta Crystallogr. A* **2008**, *64*, 112.

[24] a) Neese, F., The ORCA program system. *WIREs Comput. Mol. Sci.* **2012**, 2: 73, https://doi.org/10.1002/wcms.81; b) Neese, F. Software update: The ORCA program system—Version 5.0. WIREs *Comput. Mol. Sci.* **2022**; 12:e1606. https://doi.org/10.1002/wcms.1606.

[25] S. Grimme, A. Hansen, S. Ehlert, J.-M. Mewes, *J. Chem. Phys.* **2021**, *154*, 064103.

[26] a) A. Schäfer, H. Horn, R. Ahlrichs, *J. Chem. Phys.* **1992**, *97*, 2571; b) A. Schäfer, C. Huber, R. Ahlrichs, *J. Chem. Phys.* **1994**, *100*, 5829; c) F. Weigend, R. Ahlrichs, *Phys. Chem. Chem. Phys.* **2005**, *7*, 3297; d) F. Weigend, *Phys. Chem. Chem. Phys.* **2006**, *8*, 1057; e) J.-D. Chai and M. Head-Gordon, *J. Chem. Phys.* **2008**, *128*, 084106; f) J.-D. Chai, M. Head-Gordon, *Phys. Chem. Chem. Phys.* **2008**, *10*, 6615; g) A. Hellweg, D. Rappoport, *Phys. Chem. Chem. Phys.* **2015**, *17*, 1010.

[27] NBO 7.0. E. D. Glendening, J. K. Badenhoop, A. E. Reed, J. E. Carpenter, J. A. Bohmann, C. M. Morales, P. Karafiloglou, C. R. Landis, and F. Weinhold, Theoretical Chemistry Institute, University of Wisconsin, Madison, WI (**2018**).

[28] a) G. Knizia, *J. Chem. Theory Comput.* **2013**, *9*, 4834; b) G. Knizia, J. E. M. N. Klein, *Angew. Chem. Int. Ed.* **2015**, *54*, 5518.

[29] a) E. R. Johnson, S. Keinan, P. Mori-Sánchez, J. Contreras-García, A. J. Cohen, W. Yang, *J. Am. Chem. Soc.* **2010**, *132*, 6498; b) J. Contreras-García, E. R. Johnson, S. Keinan, R. Chaudret, J.-P. Piquemal, D. N. Beratan, W. Yang, *J. Chem. Theory Comput.* **2011**, *7*, 625; c) R. A. Boto, F. Peccati, R. Laplaza, C. Quan, A. Carbone, J.-P. Piquemal, Y. Maday, J. Contreras-Garcia, *J. Chem. Theory Comput.* **2020**, *16*, 4150.

[30] T. Lu, F. Chen, *J. Comput. Chem.* **2011**, *33*, 580.

[31] W. Humphrey, A. Dalke, K. Schulten, *J. Mol. Graph.* **1996**, *14*, 33.

[32] a) F. London, *J. Phys. Radium* **1937**, *8*, 397; b) R. McWeeny, *Phys. Rev.* **1962**, *126*, 1028; c) R. Ditchfield, *Molec. Phys.* **1974**, *27*, 789; d) K. Wolinski, J. F. Hinton, P. Pulay, *J. Am. Chem. Soc.* **1990**, *112*, 8251; e) J. R. Cheeseman, G. W. Trucks, T. A. Keith, M. J. Frisch, *J. Chem. Phys.* **1996**, *104*, 5497; f) G. L. Stoychev, A. A. Auer, R. Izsák, F. Neese, *J. Chem. Theory Comput.* **2018**, 14, 619.

[33] A. V. Marenich, C. J. Cramer, D. G. Truhlar, *J. Phys. Chem. B* **2009**, *113*, 6378.

[34] a) J. Tao, J. P. Perdew, V. N. Staroverov, G. E. Scuseria, *Phys. Rev. Lett.* **2003**, *91*, 146401; b) V. N. Staroverov, G. E. Scuseria, J. Tao, J. P. Perdew, *J. Chem. Phys.* **2003**, *119*, 12129; c) V. N. Staroverov, G. E. Scuseria, J. Tao, J. P. Perdew, *J. Chem. Phys.* **2004**, *121*, 11507.

[35] a) J. P. Perdew, K. Burke, M. Ernzerhof, *Phys. Rev. Lett.* **1996**, *77*, 3865; b) J. P. Perdew, K. Burke, M. Ernzerhof, *Phys. Rev. Lett.* **1997**, *78*, 1396; c) C. Adamo, V. Barone, *J. Chem. Phys.* **1999**, *110*, 6158.

[36] F. Jensen, *J. Chem. Theory Comput.* **2014**, *11*, 132.

[37] B. Silvi, R.J. Gillespie, C. Gatti, "Electron Density Analysis" in *Comprehensive Inorganic Chemistry II*, Elsevier, **2013**, pp. 187–226.

[38] P. Macchi, D. M. Proserpio, A. Sironi, *J. Am. Chem. Soc.* **1998**, *120*, 13429.

[39] R. Gericke, M. A. Bennett, S. H. Privér and S. K. Bhargava, *Inorg. Chem.* **2023**, *62*, 8846.

Chapter 4 Synthesis, Characterization and Reactivity of Phosphine-Stabilized Cobalt Hydrides[a]

Abstract: The hydrogenation of magnesium cobaltate complexes [(^{Ar}nacnac)Mg][Co(η^4-cod)$_2$] (Ar = 2,6-diethylphenyl [Dep], 2,4,6-mesityl [Mes]; cod = 1,5-cyclooctadiene) in the presence of 1,2-bis(dicyclohexylphosphino)ethane (dcpe) affords phosphine-stabilized cobalt hydrides, [(^{Ar}nacnac)Mg][CoH$_4$(dcpe)] (Ar = Dep, **1**; Ar = Mes, **2**). The bimetallic complexes feature three bridging hydride ligands between the Mg and Co atoms, as characterized in the solid state by single crystal X-ray diffraction and shown to be retained in solution by NMR spectroscopy. Computational analysis indicates that the bonding between the cation and anion is dominated by metal-hydride interactions, with negligible metal-metal bonding. The catalytic activity of **1** was tested in the hydrogenation of alkenes. Reactions of **1** and **2** with white phosphorus (P$_4$) furnished *cyclo*-P$_4$ complexes through release of H$_2$.

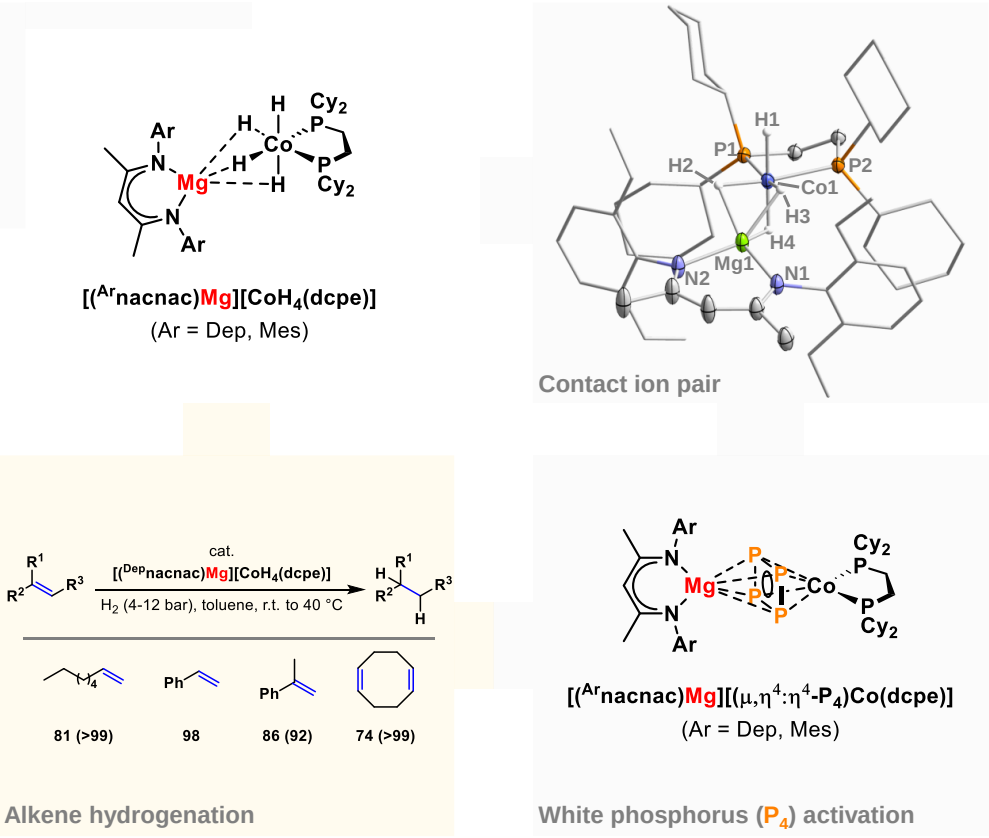

[a] Martin Gawron performed all reactions, characterizations and computational calculations reported in this chapter. Johannes Eder recorded and interpreted the DOSY NMR experiments under the supervision of Ruth M. Gschwind. Robert Wolf supervised and directed the project. Martin Gawron prepared the manuscript, which was edited by Gábor Balázs and Robert Wolf.

4.1 Introduction

Transition metal hydride complexes are crucial intermediates in a wide range of organic transformations including hydrofunctionalization, dehydrogenation and isomerization reactions. While they are typically formed during the course of a catalytic reaction involving the transfer of a hydrogen atom, metal hydride complexes can be isolated from reactions of suitable precursor complexes with dihydrogen (H_2) or a hydride source. Hieber and co-workers synthesized the first transition metal hydride complex $H_2Fe(CO)_4$ in 1931 by the reaction of $Fe(CO)_5$ with barium hydroxide.[1] The structure of $H_2Fe(CO)_4$ remained controversial until the 1950s, when spectroscopic studies unambiguously identified a distorted octahedral geometry of the iron complex with two discrete Fe–H bonds.[2]

Today – nearly 100 years later – first-row transition metal hydrides are well-established compounds that find use in many catalytic reactions essential to both organic synthesis and chemical industry.[3] Among these, the iron group metal hydrides have emerged as promising candidates as they combine lower cost, higher abundance and similar reactivity when compared to their noble metal congeners. The metal hydride motif (M–H) is supported by tailored ligand systems that are typically heteroatom-based with mono- to tridentate binding modes. These include β-diketiminate (commonly referred to as nacnac), phosphine and pincer-based ligands that are ideally suited due to their facile synthesis, diverse modifications and ability to engage in metal-ligand cooperation. Representative examples are displayed in Figure 1. The cobalt hydride complex **A**, stabilized by a bulky nacnac ligand, activates dinitrogen under ambient conditions.[4] In a similar vein, the diphosphine complex **B** hydrogenates CO_2 with a turnover frequency of 3400 h^{-1} at just 1 atm of total pressure.[5] Iron hydride complex **C**, bearing a PNP pincer ligand, efficiently catalyzes both the dimerization and hydroboration of terminal alkynes.[6]

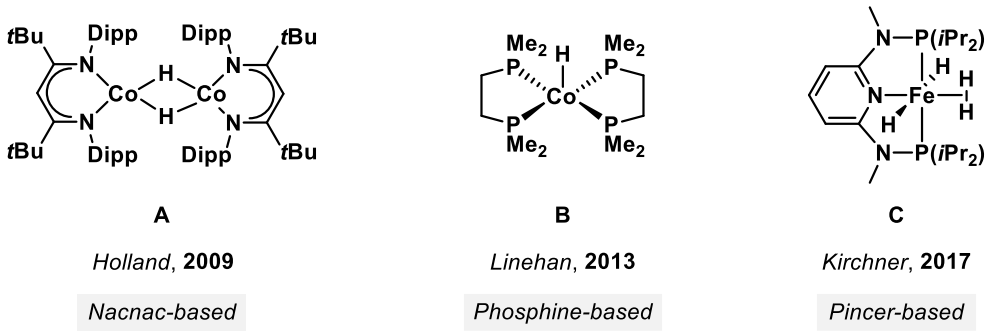

A

Holland, **2009**

Nacnac-based

B

Linehan, **2013**

Phosphine-based

C

Kirchner, **2017**

Pincer-based

Figure 1. Single-site transition metal hydrides of the iron group based on common ligand frameworks. Dipp = 2,6-diisopropylphenyl.

In recent years, there has been growing interest in heterobimetallic metal hydride complexes (Figure 2). The presence of a second metal introduces new properties, offering an alternative strategy to classical complex modification by stereoelectronic ligand tuning.[7] Internal polarization, multisite bond activation, and spatial preorganization are distinct features of such bimetallic systems. Commonly, combinations of transition metals with group 2, 12, or

13 elements are employed which are frequently stabilized by suitable ancillary ligands. This is reflected in the bimetallic structures shown in Figure 2, which feature nacnac-stabilized metals primarily based on Mg and Zn (e.g., **E**,[8] **F**,[9] **H**[10] and **J**-**L**).[11]-[13] In addition, Al-based heterobimetallic complexes with alkoxide, amide or Cp ligands have been reported (e.g., **D**[14] and **G**).[15] Group 1 metal complexes are significantly rarer.[4],[16] Such s-block transition metalates are usually prepared by reduction of a transition metal precursor with a metal hydride reagent or by hydrogenation of a metalate complex. One such example is the sodium ferrate **I**, which was synthesized by reaction of a neutral iron complex with $NaBHEt_3$.[16d] The bimetallic hydride effectively catalyzes the selective isomerization of primary alkenes with high stereo- and regioselectivity at ambient temperature. Additional examples of bimetallic reactivity include the cooperative C–H bond activation of pyridines by the Al/Fe complex **J**[11] and the hydrogenation of different unsaturated substrates using the Mg/Ni complex **K**.[12] In both cases, the reactivity arises from the synergistic interaction between the transition metal and the electropositive main group metal.

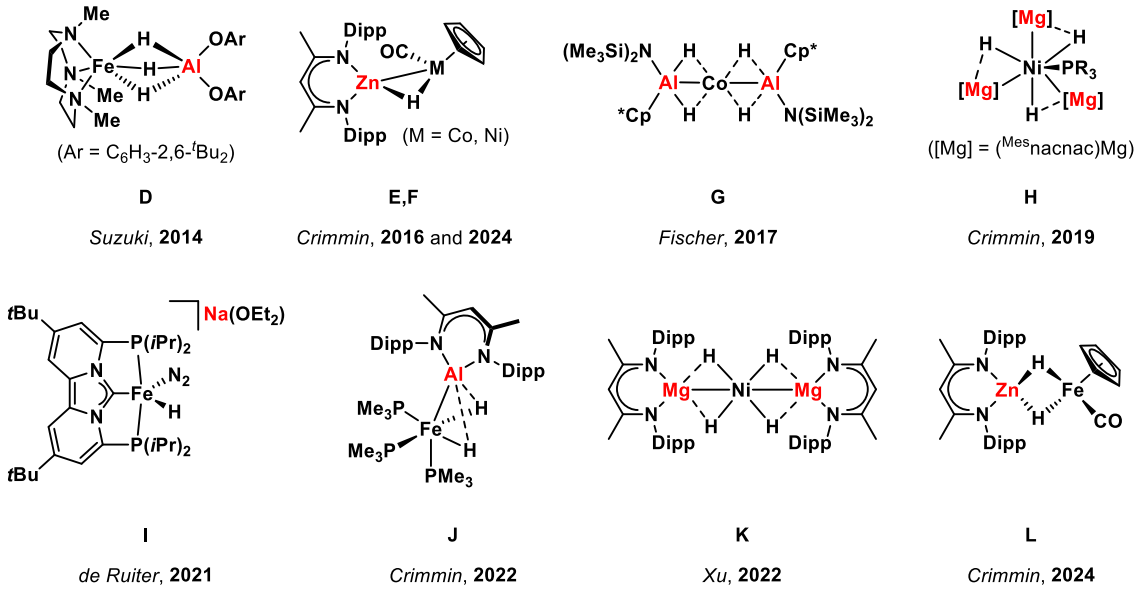

Figure 2. Selected examples of heterobimetallic hydride complexes of the iron group. Mes = 2,4,6-trimethylphenyl.

Previous work from our group documented a cation effect in the hydrogenation of alkenes with anionic cobaltate(–I) pre-catalysts [Cation][$Co(\eta^4\text{-cod})_2$] (cod = 1,5-cyclooctadiene; Figure 3a).[17] The use of different alkali metal ($M(thf)_n$; M = K, Na, Li) and (nacnac)Mg cations showed that the catalytic activity of these complexes increased strongly following the trend: $K^+ < Na^+ < Li^+ <$ (nacnac)Mg^+. The quantum chemical analysis of the turnover-limiting migratory insertion step suggested a favorable, energy-lowering effect of the counterion coordination to the cobalt hydrido intermediates (as depicted for (nacnac)Mg^+ in Figure 3a). Unfortunately, the isolation of hydride complexes or intermediates from the homoleptic alkene cobaltates was not possible, which prevented us from further validating the theoretical findings.

When investigating the catalytic alkene hydrogenation with heteroleptic (^{Dipp}BIAN)$CoBr_2$ (BIAN = bis(imino)acenaphthene) and $LiBHEt_3$, we isolated the anionic hydrido cobaltate $[Li(thf)_3(Et_2O)][\{(^{Dipp}BIAN)Co\}_2(\mu\text{-}H)_3]$ (**M**),[18] which is the only hydrido complex characterized so far in the reductive cobaltate catalysis (Figure 3b).[17]-[19] The lithium salt **M** showed moderate reactivity in the hydrogenation of 1,5-cyclooctadiene and was suggested to be a catalytically relevant off-cycle intermediate of the (BIAN)Co-catalyzed hydrogenation reaction. Other anionic cobalt hydrides are hardly known. However, D. Habermann (Jonas group, MPI for Coal Research, Mühlheim/Ruhr) reported the synthesis of alkali metal hydrido cobaltates $[M(thf)_n][CoH_4(dcpe)]$ (M = K, **N**; Li, **O**; dcpe = 1,2-bis(dicyclohexyl-phosphino)ethane) by the two-step reaction of an ethylene cobaltate precursor with diphosphine and H_2 (Figure 3c).[20] The complexes **N** and **O** were characterized by IR and NMR spectroscopy. Complex **O** catalyzed the hydrogenation of ethylene (98% ethane).

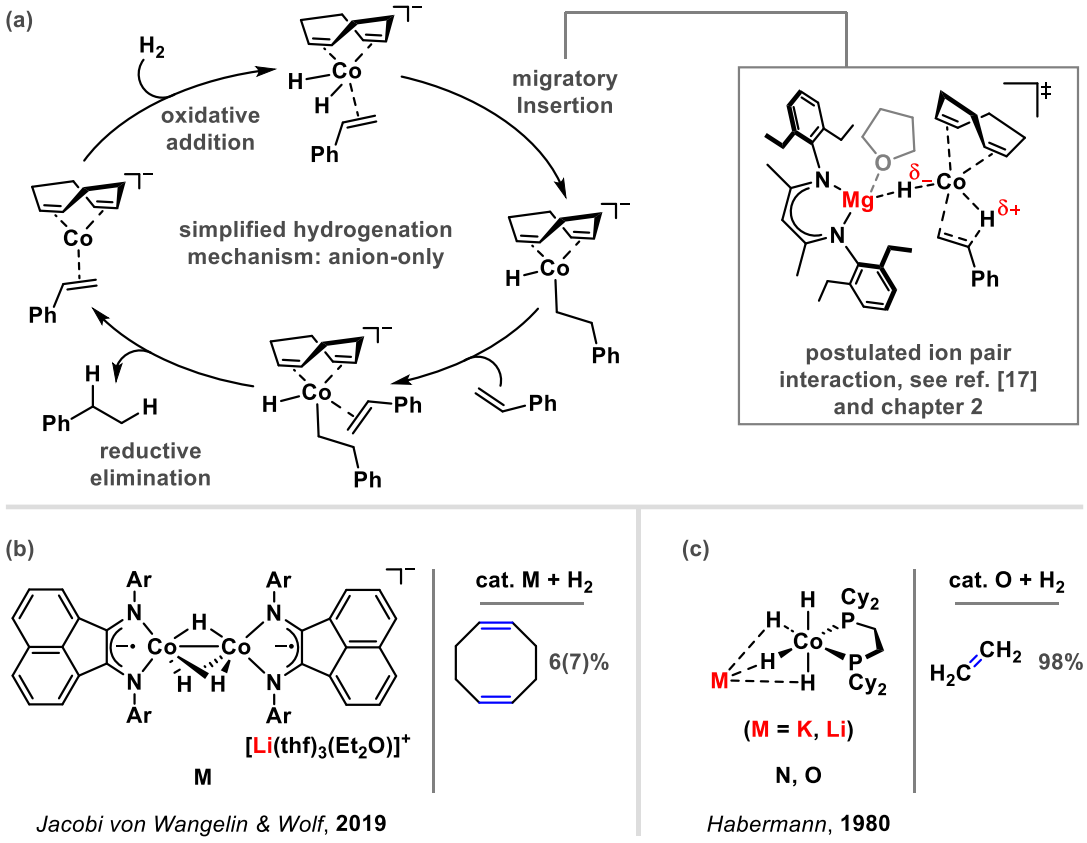

Figure 3. (a) Simplified anion-only mechanism for the hydrogenation of styrene with $[Co(\eta^4\text{-}cod)_2]^-$ and countercation interaction in the migratory insertion step. (b) First isolated anionic hydrido cobaltate **M** and hydrogenation of 1,5-cyclooctadiene. (c) Phosphine-stabilized alkali metal hydrido cobaltates **N**, **O** and hydrogenation of ethylene.

Inspired by the structural similarity of **N** and **O** to the hydride intermediates proposed in our study (Figure 3a),[17] we decided to investigate the synthesis of related complexes. Here, we describe further phosphine-stabilized cobalt hydrides, $[(^{Ar}nacnac)Mg][CoH_4(dcpe)]$ (Ar = 2,6-diethylphenyl [Dep], **1**; Ar = Mes, **2**), which were prepared by reaction of H_2 with $[(^{Ar}nacnac)Mg][Co(\eta^4\text{-}cod)_2]$ (Ar = Dep, Mes), in the presence of dcpe. We analyze the solid-state molecular structures of **1** and **2**, their behavior in solution using multinuclear

NMR spectroscopy, and the bonding situation of **1** by quantum chemical methods. Furthermore, initial results on the catalytic properties of **1** in alkene hydrogenation and the potential of **1** and **2** for small molecule activation are reported.

4.2 Results and Discussion

4.2.1 Synthesis and Characterization of [(^{Ar}nacnac)Mg][CoH_4(dcpe)] (Ar = Dep, 1; Ar = Mes, 2)

The complexes [(^{Ar}nacnac)Mg][CoH_4(dcpe)] (Ar = Dep, **1**; Ar = Mes, **2**) were obtained by the reaction of [(^{Ar}nacnac)Mg][Co(η^4-cod)$_2$] (Ar = Dep, Mes) with H_2 in the presence of 1,2-bis(dicyclohexylphosphino)ethane (Scheme 1). The reaction proceeds at 60 °C for 2 d (complex **2**) or 3 d (complex **1**) yielding an off-white microcrystalline solid. Recrystallization afforded colorless crystals of **1** and **2** in 30% and 21% yield, respectively. Notably, the cod ligand in [(^{Dep}nacnac)Mg][Co(η^4-cod)$_2$] is not substituted in the absence of H_2. This indicates that the hydrogenation of 1,5-cyclooctadiene is essential to drive the reaction.

The chiral magnesium salt [($^{(-)\text{-}(S)\text{-}Naph}$nacnac)Mg][$CoH_4$(dcpe)] (**3**) was synthesized by an analogous procedure, but its isolation has so far not been achieved (section 4.4.3).

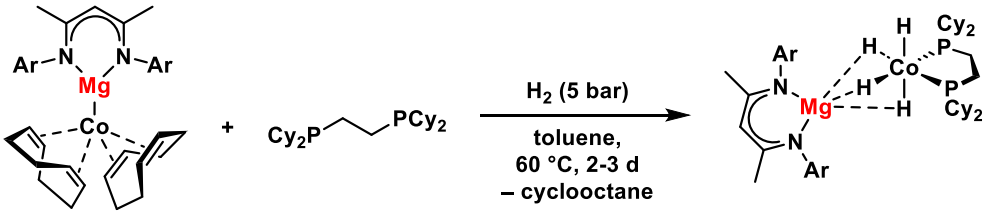

Scheme 1. Synthesis of [(^{Ar}nacnac)Mg][CoH_4(dcpe)] (Ar = Dep, **1**; Ar = Mes, **2**) by hydrogenation of [(^{Ar}nacnac)Mg][Co(η^4-cod)$_2$] (Ar = Dep, Mes) in the presence of dcpe.

Single crystal X-ray diffraction analysis of **1** and **2** revealed similar contact ion pair structures with three bridging hydride ligands between the [(^{Ar}nacnac)Mg]$^+$ cation and the [CoH_4(dcpe)]$^-$ anion (Figure 4). The Co atom is octahedrally coordinated by one dcpe ligand and four hydride ligands, which places the metal center in a formal +3 oxidation state. The structures of **1** and **2** feature similar Co–Mg distances of 2.394(7) and 2.429(6) Å, respectively. The Co–H bond distances vary from 1.36(3) to 1.58(3) Å, and the Mg–H distances from 1.88(3) to 2.05(3) Å. Other reported magnesium-transition metal hydrides reveal similar bond metrics (e.g., for (^{Dipp}nacnac)$Mg_2Ni(\mu\text{-}H)_4$ (**K**): Ni–Mg 2.486(1) Å, Ni–H 1.46-1.50 Å, and Mg–H 2.01-2.05 Å).[10],[12],[21],[22]

Recrystallization of an isolated sample of **1** from cold *n*-pentane/THF gave the THF adduct [(^{Dep}nacnac)Mg(thf)][CoH_4(dcpe)] (**4**). This complex features one THF molecule coordinating to the [(^{Dep}nacnac)Mg]$^+$ cation but is otherwise analogous to the solid-state structure of **1** (Figure S40). In contrast to the precursor complexes [(^{Ar}nacnac)Mg][Co(η^4-cod)$_2$] and related alkene cobaltates,[17],[19b],[23] which crystallize from THF as solvent-separated ion pairs, complex **4** crystallizes from THF as a contact ion pair, retaining its bridging hydride

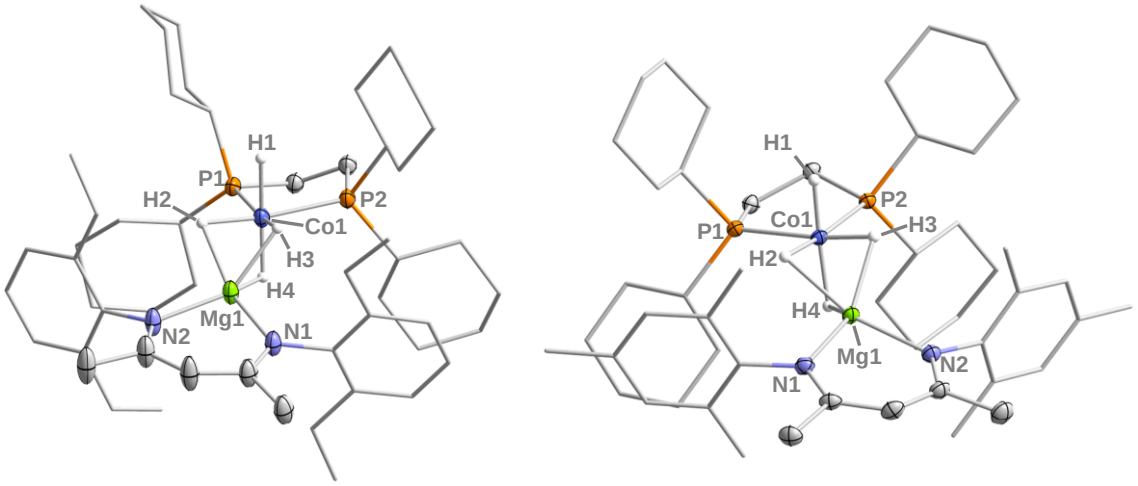

Figure 4. Solid-state molecular structures of **1** (left) and **2** (right). Thermal ellipsoids are drawn at 40% probability level. H atoms are omitted for clarity except for the hydrides (H1-H4) between Co1 and Mg1. Selected bond lengths [Å] and angles [°]: **1**: Mg1–Co1 2.429(6) Å, Co1–H1 1.52(3) Å, Co1–H2 1.51(2) Å, Co1–H3 1.50(3) Å, Co1–H4 1.458(2) Å, Mg1–H2 2.02(2) Å, Mg1–H3 1.88(3) Å, Mg1–H4 2.05(3) Å, Co1–P1 2.144(5) Å, Co1–P2 2.145(5) Å, Mg1–N1 2.060(2) Å, Mg1–N2 2.054(2) Å, H1–Co1–H4 172.2(2), H2–Co1–H3 83.1(2), H2–Mg1–H3 61.6(1), P1–Co1–P2 89.44(2), N1–Mg1–N2 92.33(7). **2**: Mg1–Co1 2.394(7) Å, Co1–H1 1.36(3) Å, Co1–H2 1.50(3) Å, Co1–H3 1.46(3) Å, Co1–H4 1.58(3) Å, Mg1–H2 1.97(3) Å, Mg1–H3 1.94(3) Å, Mg1–H4 1.97(3) Å, Co1–P1 2.141(7) Å, Co1–P2 2.133(6) Å, Mg1–N1 2.039(2) Å, Mg1–N2 2.034(2) Å, H1–Co1–H4 173.2(2), H2–Co1–H3 88.0(2), H2–Mg1–H3 63.4(1), P1–Co1–P2 91.10(2), N1–Mg1–N2 92.70(8).

structural motif. The NMR spectroscopic analysis of **1** and **2** in toluene-d_8 is in line with the molecular structure determined by X-ray crystallography (section 4.4.8). At ambient temperature, the ^{1}H NMR spectrum of **1** confirms the presence of four hydride ligands at a chemical shift of –14.84 ppm,[10],[12] along with the expected signals for the dcpe and nacnac units (Figure 5, top). The hydride resonance appears as a triplet ($^2J_{PH}$ = 10.3 Hz) due to the coupling with the P atoms of the dcpe ligand. Based on the solid-state structure of **1**, three inequivalent hydride resonances would be expected; the observation of only one signal indicates a rapid exchange process that renders all hydride ligands equivalent on the NMR timescale.

When the NMR sample is cooled to –80 °C, the hydride resonance splits into two partly overlapping resonances at –14.5 ppm and –14.9 ppm in an approximate 1:1 ratio (Figure 5, bottom; see also Figure S23 for a variable-temperature (VT) ^{1}H NMR spectrum of **1** in THF-d_8). This is due to the chemically inequivalent axial (H1 and H4) and equatorial (H2 and H3) hydrogen atoms at Co. Both signals are significantly broadened with line-widths of 137 Hz (–14.5 ppm) and 100 Hz (–14.9 ppm) at –80 °C compared to a line-width of 30 Hz (–14.84 ppm) at ambient temperature. In the ^{31}P{^{1}H} NMR spectrum, the dcpe ligand gives rise to one broad singlet (line-width = 121 Hz) at 117.5 ppm, which does not split in the ^{31}P NMR spectrum (Figure S18 and Figure S19). The ^{1}H and ^{31}P{^{1}H} NMR spectra of **2** are largely identical to those of **1**, showing very similar signals for the [CoH_4(dcpe)]$^-$ unit (Figure S24 and Figure S25).

In the ATR-IR spectra of **1** and **2**, three Co–H stretches at $\tilde{\nu}_{Co-H}$ = 1936, 1778, and 1748 cm^{-1} (for **1**) and at $\tilde{\nu}_{Co-H}$ = 1920, 1784, and 1735 cm^{-1} (for **2**) were detected (Figure S36 and Figure S38), which compare well with the calculated values for **1** ($\tilde{\nu}_{Co-H}$ = 2007, 1870, and 1808 cm^{-1}; Figure S37).

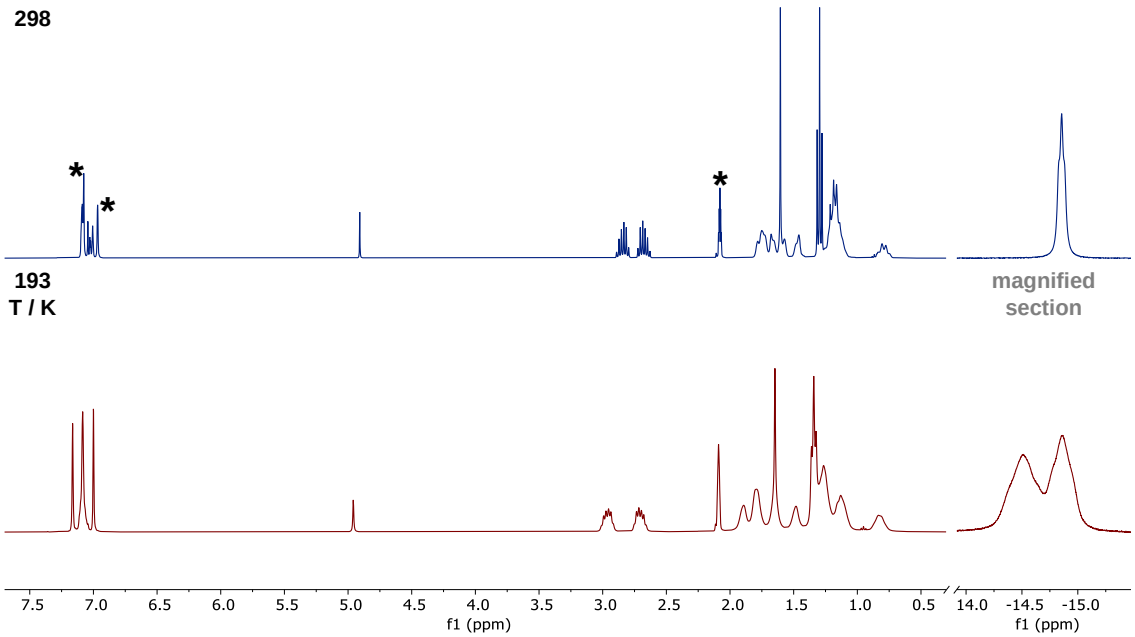

Figure 5. ^{1}H NMR spectrum (400.13 MHz, toluene-d$_8$) of [(^{Dep}nacnac)Mg][CoH$_4$(dcpe)] (**1**) at ambient temperature (298 K) and at –80 °C (193 K); the hydride signals are separately magnified. *: toluene-d$_8$.

To investigate whether **1** remains as a contact ion pair in solution or dissociates into a solvent-separated ion pair, we carried out DOSY NMR experiments in toluene-d$_8$ and THF-d$_8$ (section 4.4.6). For all relevant ^{1}H NMR signals of **1**, very similar diffusion coefficients ($D \approx$ 6.8 x 10^{-10} m^2 s^{-1} in toluene-d$_8$ and $D \approx$ 7.5 x 10^{-10} m^2 s^{-1} in THF-d$_8$) were obtained which correspond to hydrodynamic volumes of $V_H \approx$ 1179 Å^3 in toluene-d$_8$ and $V_H \approx$ 1176 Å^3 in THF-d$_8$. These findings support the presence of a contact ion pair in both solvents.

Quantum chemical calculations were performed to investigate the electronic structure and bonding within the bridging hydride motif of **1** (see section 4.4.11 for details). The charges derived from natural population analysis (NPA) are positive for Mg (+1.73) and negative for Co (–0.45) and the four hydride ligands (H1: –0.10, H2: –0.25, H3: –0.26, and H4: –0.41; Figure 6a and Table S7). The negative NPA charge on cobalt reflects the strong σ-donating and weak π-accepting nature of the hydride and dcpe ligands. According to natural bond order (NBO) analysis, the bonding between the (nacnac)Mg and Co(dcpe) units is dominated by metal-hydride interactions, rather than direct metal-metal bonding (section 4.4.11.1). The Wiberg bond indices (WBIs) for the Co–H bonds range from 0.32 to 0.44, while those for Mg–H are very low (≤ 0.09), indicating mainly ionic Mg–H interactions. The Mg–Co interaction shows a small WBI of 0.04, indicating negligible orbital overlap.

Second order perturbation theory analysis further establishes significant donor-acceptor

interactions between Mg and the bridging hydrides (21.0-33.6 kcal mol^{-1}; H2-H4), while any donor-acceptor interactions between the cobalt and magnesium atoms are negligible (<1 kcal mol^{-1}; Table S7). A topological analysis by quantum theory of atoms in molecules (QTAIM) identified bond critical points (BCPs) between the Co and H atoms but no BCPs between the Mg and the three bridging H atoms (Figure 6b and Table S8). This is consistent with a description of **1** as an intimate ion pair comprising an anionic [CoH_4(dcpe)]$^-$ unit with four covalent Co–H bonds, stabilized by non-covalent interactions of the [(^{Dep}nacnac)Mg]$^+$ cation with the three bridging hydride ligands. A complementary non-covalent interaction (NCI) analysis of **1** confirms the attractive [Co–H]···Mg^{2+} interactions (Figure S42).

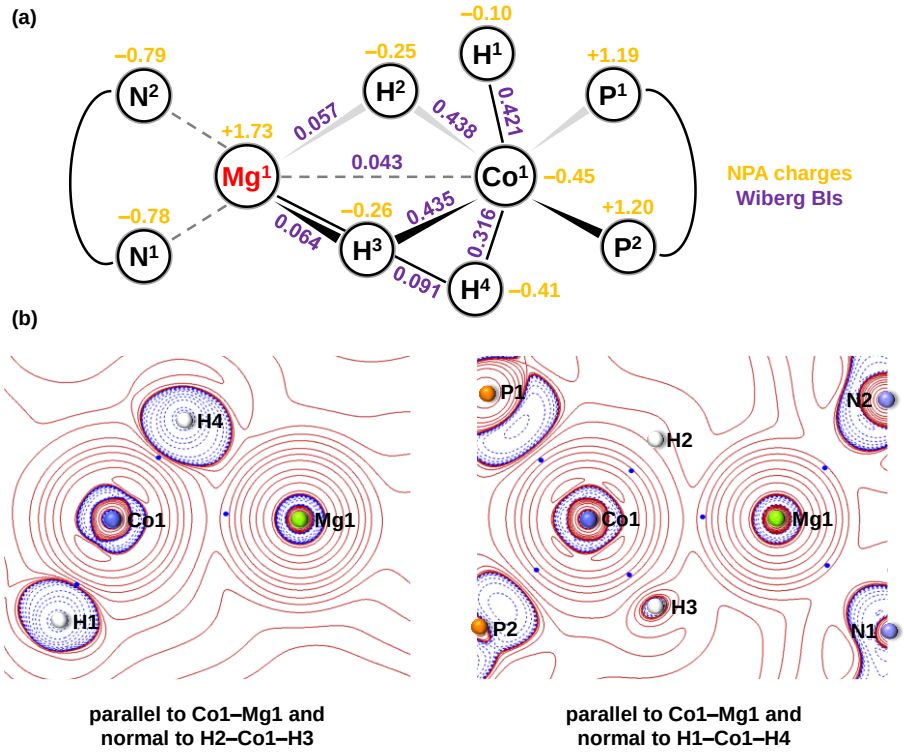

Figure 6. (a) NBO analysis including NPA charges and Wiberg bond indices of **1**. (b) Plot of the Laplacian of the electron density of **1** parallel to the Co1–Mg1 axis and normal to either the H2–Co1–H3 plane or the H1–Co1–H4 plane displaying two of the four bond critical points between Co and H (blue dots: bond critical points).

4.2.2 Hydrogenation Reactions with [(^{Dep}nacnac)Mg][CoH_4(dcpe)] (1)

Complex **1** is a phosphine-stabilized analog of [(^{Dep}nacnac)Mg)][Co(η^4-cod)$_2$], which is highly active in the catalytic hydrogenation of tri- and tetra-substituted alkenes.[17] To test the capability of **1** for H_2 activation, we first investigated hydrogen-deuterium exchange using D_2 (see sections 4.4.5.1 for details). Exposure of a benzene solution of **1** to D_2 (5 bar) at ambient temperature for 7 d resulted in 83% deuterium incorporation in the hydride positions, based on the integration of the residual hydride signal relative to a CH_2 signal of the Dep substituent (Scheme 2a and Figure S3). The reduced intensity of the hydride resonance of **1** in the ^{1}H NMR spectrum was accompanied by the formation of a deuteride resonance in the ^{2}H NMR spectrum indicating the formation of mixed H/D derivatives of **1**;

inter alia [(Depnacnac)Mg][CoD4(dcpe)] (**1-D**). Notably, heating a solution of **1** in toluene-d8 at 60 °C for 8 d also produced mixed H/D derivatives, with an overall deuterium incorporation of 71% (Scheme 2b and Figure S4). In the absence of D_2, this deuteration is attributed to C–D bond activation of toluene-d8 by **1**. No H/D exchange is observed at ambient temperature.

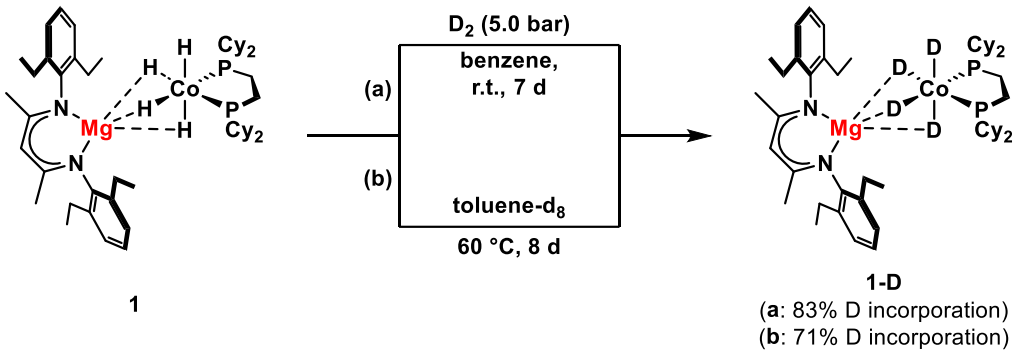

Scheme 2. H/D exchange of [(Depnacnac)Mg][Co(H4)(dcpe)] (**1**) with D_2 (a) and toluene-d8 (b).

Prompted by the observed reactivity of **1** toward D_2 and toluene-d8, we next evaluated its properties in the hydrogenation of styrene (see section 4.4.5.3 for details). In an initial NMR tube experiment, the alkene substrate was fully converted to ethylbenzene using 5 mol% of **1** under mild conditions (5 bar H_2, r.t., 22 h; Figure S6). Well-resolved NMR spectra with sharp signals were observed throughout the reaction, which indicates the absence of Co nanoparticles.[17],[24] New cobalt complexes were not observed spectroscopically and only the signals of **1** were observed during and after the hydrogenation reaction in the ^{1}H and ^{31}P{^{1}H} NMR spectra. This suggests that **1** is the reservoir for the active catalyst, which remains undetected.

The hydrogenation of other mono- to tri-substituted alkenes using pre-catalyst **1** was subsequently studied (Table 1 and section 4.4.4 for details). To achieve hydrogenation of the more demanding alkenes, a slightly increased temperature of 40 °C and higher pressures of H_2 (up to 12 bar) were required. Under these conditions and using a low catalyst loading, 1-octene and α-methylstyrene were hydrogenated to the alkane in 81% and 86%, respectively, and 1,5-cyclooctadiene gave a mixture of cyclooctane and cyclooctene, resulting in the hydrogenation of 53% of the C=C bonds present in cod (Table 1, entries 3-5). In contrast, tri-substituted alkenes such as α-methylstilbene (13%) and 1,1,2-triphenylethylene (3%) gave only low yields (Table 1, entry 4), suggesting that steric bulk of the substrates impedes hydrogenation. Increasing the catalyst loading (to 4 mol%) did not improve the hydrogenation of these alkenes (Table 1, entry 5). Interestingly, the toluene solvent was partially hydrogenated at H_2 pressures of 8 and 12 bar,[25] placing it in competition with the C=C bond of sterically demanding vinylarenes (Figure S2).

Mercury poisoning did not inhibit the hydrogenation of α-methylstyrene, suggesting that Co nanoparticles are not responsible for the catalytic activity (Table S1, entries 12-15). This is consistent with the findings from the ^{1}H NMR spectroscopic monitoring study (see above).

Table 1. Hydrogenation of alkenes with [(^{Dep}nacnac)Mg][CoH_4(dcpe)] (**1**).[a]

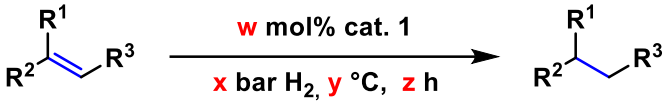

		Yield (Conv.) [%]				
Entry	**Conditions**	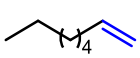	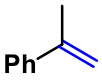	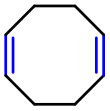	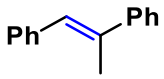	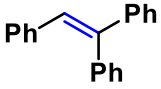
1	2 mol% cat., 2 bar H_2, 30 °C, 3 h	-	1 (3)	-	-	-
2	2 mol% cat., 2 bar H_2, 40 °C, 20 h	71 (>99)[b]	38 (41)	-	-	-
3	2 mol% cat., 4 bar H_2, 40 °C, 20 h	81 (92)[b]	70 (80)	14[c]+37[d] (>99)[e]	8 (23)	-
4	2 mol% cat., 8 bar H_2, 40 °C, 20 h	-	86 (92)	29[c]+32[d] (>99)[e]	13 (32)	3 (5)
5	2 mol% cat., 12 bar H_2, 40 °C, 20 h	-	72 (85)	32[c]+42[d] (>99)[e]	7 (27)[f]	1 (26)[f]

[a] Standard conditions: 0.2 mmol substrate (0.4 mol/L toluene). Yields and conversions were determined by quantitative GC-FID analysis vs. internal *n*-pentadecane. Conversions are given in parentheses if <90%. [b] Isomerization to internal double bonds. [c] Formation of cyclooctane. [d] Formation of cyclooctene. [e] Formation of notable amounts of bicyclo[3.3.0]octane as assigned by GC-MS analysis. [f] 4 mol% **1** instead of 2 mol%.

Based on the facile hydrogenation of terminal alkenes with **1**, we next investigated its reactivity with styrene in the absence of H_2 (see section 4.4.5.2 for details). Assuming a molecular hydrogenation mechanism involving alkene intermediates, **1** was expected to form a styrene complex. To our surprise, addition of excess styrene to **1** in toluene-d_8 at ambient temperature led to only minor consumption of **1** overnight.

Heating to 60 °C was required to drive the reaction to completeness, as indicated by the disappearance of the hydride signal of **1** and the partial hydrogenation of styrene in the ^{1}H NMR spectrum (Scheme 3, top and Figure S5). A downfield shift of the characteristic γ-H atom of the β-diketiminate ligand in the ^{1}H NMR spectrum and the formation of two broad singlets in a 1:1 ratio at 95.1 and 77.5 ppm in the ^{31}P{^{1}H} NMR spectrum indicate the formation of a styrene cobaltate, possibly [(^{Dep}nacnac)Mg][Co(η^2-styrene)$_n$(dcpe)] (n = 1 or 2). The inequivalence of the phosphorus atoms of the dcpe ligand suggests the formation of an intimate ion pair, in which the cobaltate anion directly interacts with the magnesium cation. The related complex [Li(thf)$_3$][Co(η^2-ethylene)$_2$(dcpe)] shows a resonance for the phosphorus atoms of the dcpe ligand at 88.5 ppm in the ^{31}P NMR spectrum, further supporting the assignment of a cobalt-alkene complex.[20] All attempts to isolate and crystallographically characterize the proposed complex were not successful.

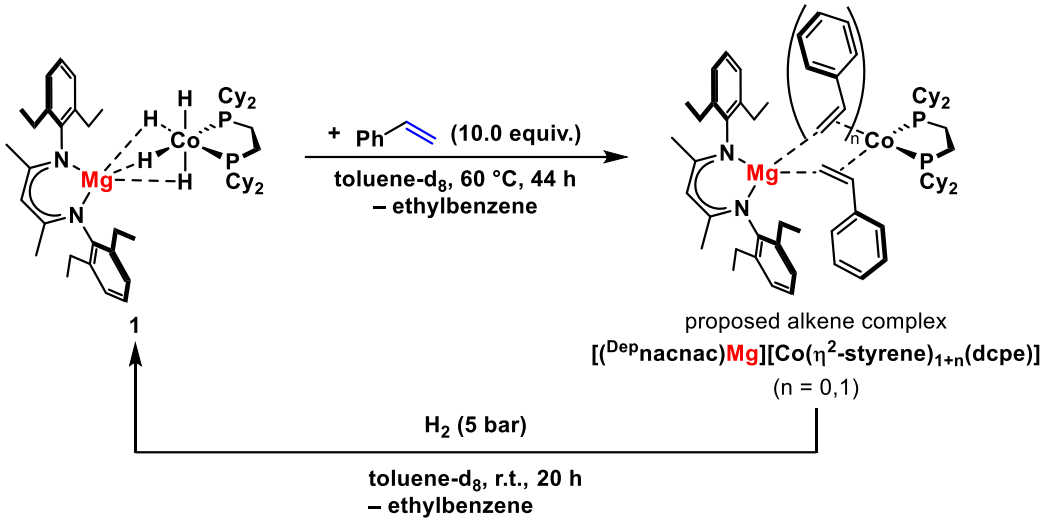

Scheme 3. Stepwise hydrogenation of styrene using **1** in toluene-d_8 through a proposed intermediary styrene cobaltate and recovery of **1** upon exposure to H_2.

To further validate the structural assignment, we anticipated that exposure of the alkene species to H_2 would regenerate the hydride complex **1** (Scheme 3, bottom and Figure 7; see section 4.4.5.4 for details). Accordingly, **1** was treated with 10.0 equivalents of styrene at 60 °C in toluene-d_8, and the reaction progress was monitored by ^{1}H and ^{31}P{^{1}H} NMR spectroscopy. The formation of the proposed styrene complex [(^{Dep}nacnac)Mg]-[Co(η^2-styrene)$_n$(dcpe)] (n = 1 or 2) was observed (label ◇; Figure 7, middle), which was then subjected to an atmosphere of H_2 (5 bar). This resulted in complete consumption of the intermediary alkene species and regeneration of cobalt hydride **1** (Figure 7, top). Simultaneously, the remaining styrene substrate was fully hydrogenated to ethylbenzene (Figure 7, top).

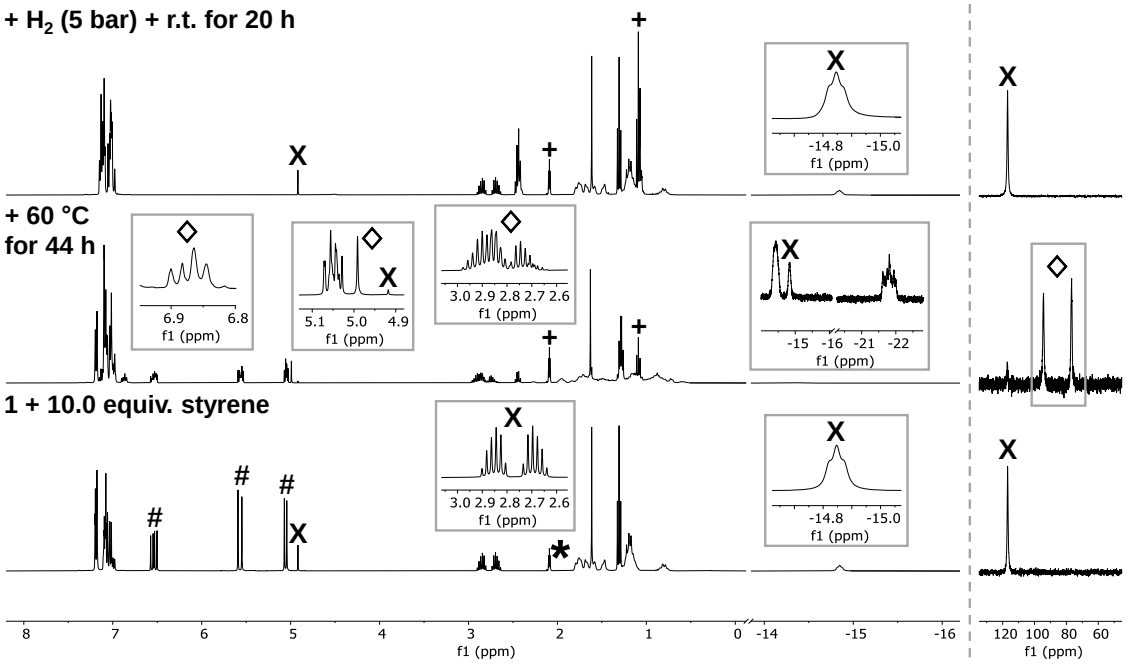

Figure 7. ^{1}H (left) and $^{31}P\{^{1}H\}$ (right) NMR spectra (400.13/161.98 MHz, 298 K, toluene-d_8) of the stepwise styrene hydrogenation using **1** through a proposed intermediary alkene complex and recovery of **1** upon exposure to H_2. *: toluene-d_8. #: styrene. +: ethylbenzene. X: **1**. ◇: proposed alkene complex.

These results support the reversible formation of an alkene-bound intermediate in the catalytic cycle. The ability to regenerate **1** under H_2 atmosphere suggests the prevalence of alkene intermediates in the catalytic cycle.

When performing the same recovery experiment in THF-d_8, decomposition of **1** was observed (Figure S8). The initial treatment of **1** with styrene likely forms an alkene intermediate. However, a significant loss of phosphorus signal intensity in the $^{31}P\{^{1}H\}$ NMR spectrum and negligible recovery of the hydride signal in the ^{1}H NMR spectrum upon H_2 exposure suggest that **1** cannot be regenerated from this species. In line with the literature data, the presence of characteristic ^{1}H NMR signals after the reaction of **1** with styrene indicates the formation of the alkoxide-bridged Mg dimer $[(^{Dep}nacnac)Mg(O^{n}Bu)]_2$.[17] This dimer is likely formed by the ring-opening of THF, which suggests that the proposed alkene intermediate does not contain a (nacnac)Mg motif. Thus, THF is not suitable for use with pre-catalyst **1**.

4.2.3 Synthesis and Characterization of $[(^{Ar}nacnac)Mg][(\mu,\eta^4{:}\eta^4\text{-}P_4)Co(dcpe)]$ (Ar = Dep, 5; Ar = Mes, 6)

After investigating the reactivity of **1** in alkene substitution and hydrogenation reactions, we next explored the reactivity of **1** and **2** toward white phosphorus (P_4). Encouragingly, a solution of $[(^{Ar}nacnac)Mg][CoH_4(dcpe)]$ (Ar = Dep, **1**; Ar = Mes, **2**) in toluene reacts cleanly with 1.1 equivalents of P_4 to form *cyclo*-P_4 complexes $[(^{Ar}nacnac)Mg][(\mu,\eta^4{:}\eta^4\text{-}P_4)Co(dcpe)]$ (Ar = Dep, **5**; Ar = Mes, **6**) (Scheme 4).[26] The immediate evolution of H_2 was observed upon addition of P_4. Crystallization from cold toluene/*n*-pentane (for **5**) and benzene/*n*-hexane (for **6**) yielded the complexes in 24% and 23% yield, respectively.

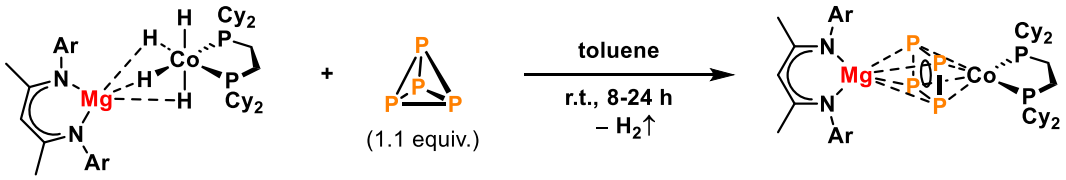

(Ar = Dep, **1**; Ar = Mes, **2**) (Ar = Dep, **5**; Ar = Mes, **6**)

Scheme 4. Synthesis of $[(^{Ar}nacnac)Mg][(\mu,\eta^4{:}\eta^4\text{-}P_4)Co(dcpe)]$ (Ar = Dep, **5**; Ar = Mes, **6**) by reaction of $[(^{Ar}nacnac)Mg][CoH_4(dcpe)]$ (Ar = Dep, **1**; Ar = Mes, **2**) with white phosphorus (P_4).

SC-XRD analysis on **5** and **6** revealed contacted ion pairs that contain a $\mu,\eta^4{:}\eta^4$-coordinated *cyclo*-P_4 ligand sandwiched between the β-diketiminate magnesium and the cobalt diphosphine units (Figure 8). The *cyclo*-P_4 ring is positioned significantly closer to the Co center than to the Mg center (Co–P 2.259(1)-2.289(1) Å, Mg–P 2.684(2)-2.743(2) Å for **5**). The cyclo-P_4 ligand is slightly rectangular with P–P bond distances of 2.184(1) to 2.258(1) Å (mean: 2.23(4) Å) for **5** and 2.178(6) to 2.280(6) Å (mean: 2.22(5) Å) for **6**. These bond lengths are longer than expected for the *cyclo*-P_4^{2-} anion (2.147 ± 0.002 Å)[27] and are closer

to the expected value for a P–P single bond (2.22 Å based on the sum of the covalent atomic radii; compare to the calculated value of 2.04 Å for a P=P double bond).[28]

Related anionic *cyclo*-P_4 cobalt complexes stabilized by α-diimine ligands feature shorter P–P bond lengths (2.132(4) to 2.173(5) Å[29] and 2.1539(9) to 2.1772(1) Å).[30] A bridging *cyclo*-P_4^{2-} ligand in a homodinuclear β-diketiminate cobaltate anion features P–P distances of 2.154(1) to 2.225(1) Å, while its neutral congener formally obtained by single-electron oxidation features a more rectangular P_4 unit (P–P 2.130(1) to 2.298(1) Å).[31] The P–P distances in **5** and **6** (2.178(6) to 2.280(6) Å) are comparable to those in the homodinuclear cobalt β-diketiminate complexes,[31] which we tentatively attribute to interactions with the Lewis acidic magnesium cation. However, further investigations are required to fully uncover the reasons for the relatively long P–P bonds in **5** and **6**.

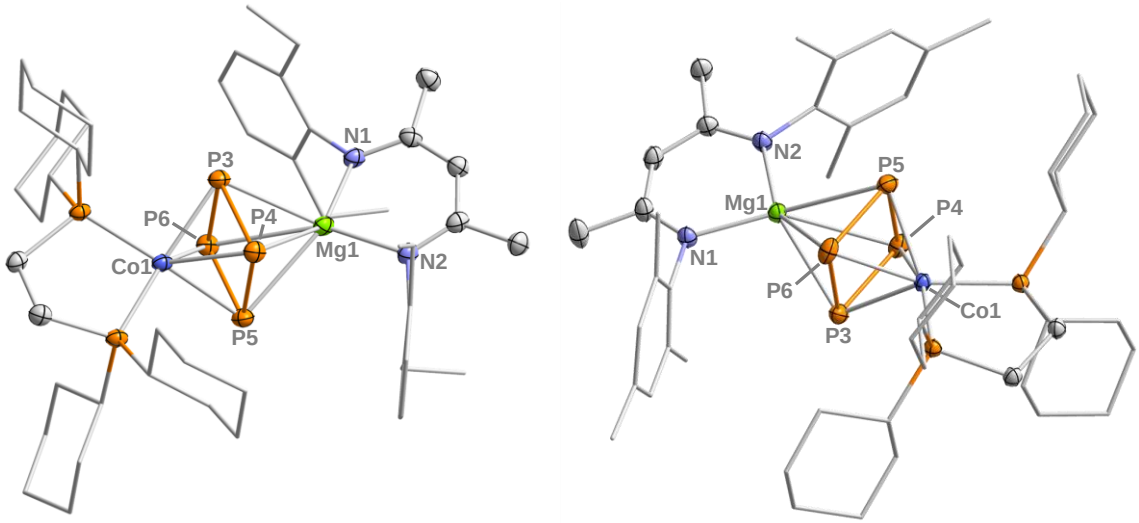

Figure 8. Solid-state molecular structure of **5** (left) and **6** (right). Thermal ellipsoids are drawn at 40% probability level. H atoms are omitted for clarity. Selected bond lengths [Å] and angles [°]: **5**: Co1–P1 2.146(1) Å, Co1–P2 2.149(1) Å, Co1–P3 2.259(1) Å, Co1–P4 2.270(1) Å, Co1–P5 2.288(1) Å, Co1–P6 2.289(1) Å, Mg1–P3 2.684(2) Å, Mg1–P4 2.704(2) Å, Mg1–P5 2.743(2) Å, Mg1–P6 2.725(2) Å, P3–P4 2.191(1) Å, P4–P5 2.258(1) Å, P5–P6 2.184(1) Å, P6–P3 2.257(1) Å, Mg1–N1 2.036(3) Å, Mg1–N2 2.030(3) Å, P3–P4–P5 89.68(5), P4–P5–P6 90.29(5), P3–Co1–P4 57.85(4), P3–Co1–P5 87.24(4), P3–Mg1–P4 47.98(3), P3–Mg1–P5 70.63(4), N1–Mg1–N2 93.69(1). **6**: Co1–P1 2.154(4) Å, Co1–P2 2.155(4) Å, Co1–P3 2.261(5) Å, Co1–P4 2.287(4) Å, Co1–P5 2.295(5) Å, Co1–P6 2.267(5) Å, Mg1–P3 2.636(6) Å, Mg1–P4 2.785(6) Å, Mg1–P5 2.818(7) Å, Mg1–P6 2.691(6) Å, P3–P4 2.184(6) Å, P4–P5 2.233(6) Å, P5–P6 2.178(6) Å, P6–P3 2.280(6) Å, Mg1–N1 2.034(1) Å, Mg1–N2 2.026(1) Å, P3–P4–P5 90.33(2), P4–P5–P6 90.91(2), P3–Co1–P4 57.41(2), P3–Co1–P5 86.88(2), P3–Mg1–P4 47.43(1), P3–Mg1–P5 70.01(2), N1–Mg1–N2 94.10(5).

The $^{31}P\{^1H\}$ NMR spectra of **5** and **6** in toluene-d_8 feature a broad singlet for the phosphorus atoms of the dcpe ligand at 103.5 ppm and 103.9 ppm, respectively, and a triplet resonance for the *cyclo*-P_4 unit at 88.1 ppm ($^2J_{PP}$ = 10.9 Hz) and 87.1 ppm ($^2J_{PP}$ = 8.9 Hz), respectively (Figure S29 and Figure S33). In comparison, the previously reported *cyclo*-P_4 iron complex [($^{Ph}PP_2^{Cy}$)Fe(η^4-P_4)] ($^{Ph}PP_2^{Cy}$ = PhP($CH_2CH_2PCy_2$)) containing a tridentate phosphine ligand shows a broad $^{31}P\{^1H\}$ NMR singlet at 53.2 ppm due to dynamic behavior at ambient temperature.[32]

The facile synthesis of complexes **5** and **6** and the possibility to generate them *in situ* (with

H_2 as the only by-product), prompted us to investigate their reactivity toward selected reagents (Scheme 5). These studies were conducted using derivative **5** due to its better availability. Initially, the reaction of **5** with three equivalents of 4-dimethylaminopyridine (DMAP) was attempted to test whether it forms a donor-separated ion pair (section 4.4.7.1). $^{31}P\{^1H\}$ NMR spectroscopic monitoring indicated the clean conversion to a new species, which was identified as $[(^{Dep}nacnac)Mg(DMAP)_3][(\eta^4\text{-}P_4)Co(dcpe)]$ (**7**) by preliminary SC-XRD analysis. Notably, the *cyclo*-P_4 ligand is now terminally bound to Co, which is evident in an upfield shift of its $^{31}P\{^1H\}$ NMR resonance to 61.0 ppm, closely matching that of $[(^{Ph}PP_2^{Cy})Fe(\eta^4\text{-}P_4)]$ (53.2 ppm).[32]

Next, the reactivity of **5** with Cy_2PCl and Ph_3SnCl was investigated (sections 4.4.7.2 and 4.4.7.3). While the first reaction yielded the *cyclo*-pentaphosphido complex $[(\eta^4\text{-}P_5Cy_2)Co(dcpe)]$ (**8**) by elimination of "$(^{Dep}nacnac)MgCl$" (Figure S14),[29],[33] the second reaction gave an unselective product mixture as shown by multiple signals in the $^{31}P\{^1H\}$ NMR spectrum of the reaction solution (Figure S15). Future work will focus on the isolation and detailed characterization of **7** and **8**.

Lastly, the reaction of **5** with *N*,*N*′-diisopropylcarbodiimide was investigated (section 4.4.7.4). Heterocumulenes have been shown to insert into P–P bonds[34] and bind to the magnesium center in heterobimetallic complexes via an amidinate-type coordination.[22],[35] Analysis of the ^{31}P NMR spectrum of the reaction solution after 1 d revealed the selective formation of a polyphosphorus species with four inequivalent phosphorus atoms (Figure S16).

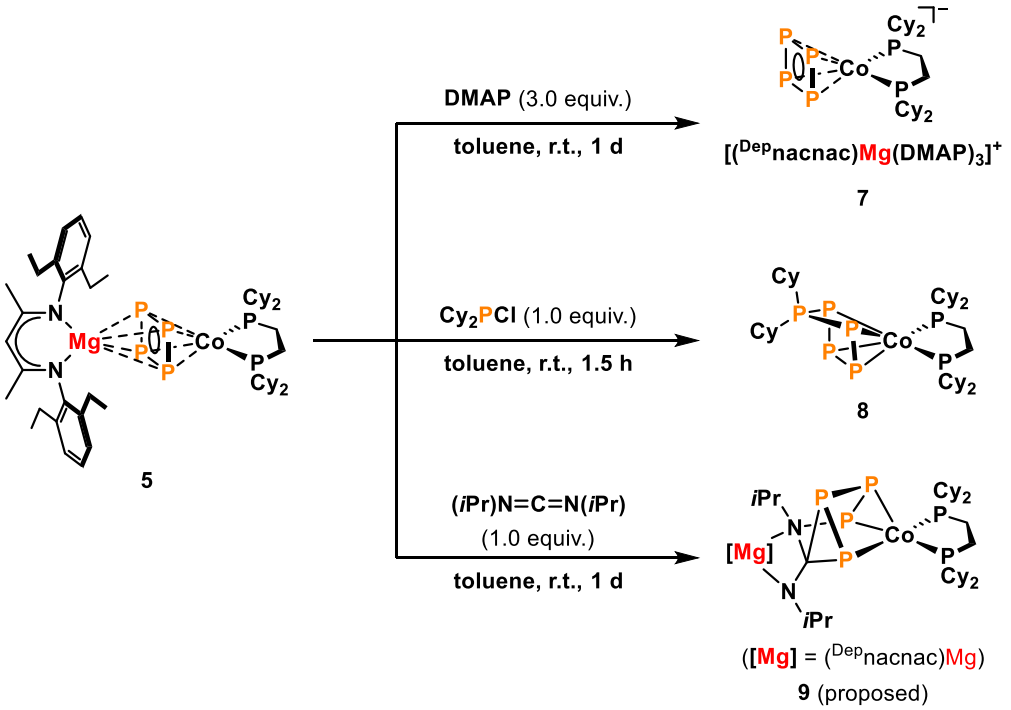

Scheme 5. Preliminary reactivity study of $[(^{Dep}nacnac)Mg][(\mu,\eta^4\text{:}\eta^4\text{-}P_4)Co(dcpe)]$ (**4**) with DMAP, Cy_2PCl, and *N*,*N*′-diisopropylcarbodiimide.

The observed AEMX spin system closely resembles that of the previously reported [(Ar*BIAN)Co(Me_3SiNC)(P_4CO^tBu)] (Ar* = 2,6-dibenzhydryl-4-isopropylphenyl, BIAN = 1,2-bis(imino)acenaphthene).[30] Based on the similar $^{31}P\{^1H\}$ NMR data, an analogous structural model for **9** is proposed, where the amidinate carbon atom bridges a terminal and an internal P atom and interacts with the second terminal P atom via nitrogen (Scheme 5). Unfortunately, crystallographic characterization of this complex has not yet been achieved. This preliminary reactivity study shows promising reactivity of the *cyclo*-P_4 complex **5**. Future work will focus on the isolation and characterization of the formed complexes **7** and **8** and the proposed bimetallic complex **9**.

4.3 Conclusion

The incorporation of a stabilizing diphosphine ligand enabled the facile synthesis of β-diketiminate magnesium tetrahydrido cobaltates. Inspired by a report by D. Habermann,[20] we synthesized the hydride complexes [(^{Ar}nacnac)Mg][CoH_4(dcpe)] (Ar = Dep, **1**; Ar = Mes, **2**) via the hydrogenation of [(^{Ar}nacnac)Mg][Co(η^4-cod)$_2$] (Ar = Dep, Mes) in the presence of 1,2-bis(dicyclohexylphosphino)ethane. Crystallographic and NMR spectroscopic studies revealed an intimate ion pair character of **1** in both non-coordinating (toluene) and coordinating (THF) solvents. Quantum chemical analysis of the bridging hydride structural motif further demonstrated that strong metal-hydride interactions are dominant, while negligible metal-metal bonding is observed. Complex **1** is a pre-catalyst for alkene hydrogenation reactions and serves as a reservoir for the reversible formation of the catalytically active species. This was demonstrated by the reversible formation of a styrene complex from **1**. These results support the direct involvement of the Mg countercation in the hydrogenation reaction, which was previously proposed only *in silico* for [(^{Dep}nacnac)Mg][Co(η^4-cod)$_2$].[17] Finally, complexes **1** and **2** cleanly reacted with white phosphorus (P_4) to give the *cyclo*-P_4 complexes [(^{Ar}nacnac)Mg][(μ,η^4:η^4-P_4)Co(dcpe)] (Ar = Dep, **5**; Ar = Mes, **6**). Compounds **5** and **6** were structurally characterized and exhibited promising reactivity toward electrophilic molecules.

4.4 Supporting Information

4.4.1 General Information

All reactions and product manipulations were carried out in flame-dried glassware under an inert atmosphere of argon/nitrogen using standard Schlenk-line or glovebox techniques (maintained at <0.1 ppm H_2O and <0.1 ppm O_2). [(^{Ar}nacnac)Mg][Co(η^4-cod)$_2$] (Ar = Dep, Mes)[23] and [($^{(-)\text{-}(S)\text{-}Naph}$nacnac)Mg][Co($\eta^4$-cod)$_2$][36] were prepared according to procedures previously reported in the chemical literature.

Solvents were dried and degassed with an *MBraun SPS800* solvent purification system. All dry solvents were stored under argon over activated 3 Å molecular sieves in gas-tight ampules. Commercially available olefins were purified by distillation (Kugelrohr) and in case of liquids degassed and dried over molecular sieves (3 Å).

NMR spectra were recorded on Bruker Avance 400 and Avance Neo 500 spectrometers at 298 K unless otherwise noted and internally referenced to residual solvent resonances (^{1}H NMR: THF-d$_8$: 1.72 ppm, toluene-d$_8$: 2.09 ppm, C_6D_6: 7.16 ppm, ^{13}C{^{1}H} NMR: THF-d$_8$: 25.3 ppm, toluene-d$_8$: 137.8 ppm, C_6D_6: 128.1 ppm). Chemical shifts δ are given in ppm referring to external standards of tetramethylsilane (^{1}H, ^{13}C{^{1}H} spectra), 85% phosphorus acid (^{31}P and ^{31}P{^{1}H} spectra). ^{1}H and ^{13}C NMR signals were assigned based on 2D NMR spectra (^{1}H/^{1}H-COSY, ^{1}H/^{13}C-HSQC, ^{1}H/^{13}C-HMQC). Spin-spin splitting is denoted as follows: s = singlet, d = doublet, t = triplet, qt = quartet, m = multiplet, b = broad, pt = pseudo triplet.

FT-IR spectra were recorded with a Bruker ALPHA spectrometer equipped with a diamond ATR unit.

Hydrogenation reactions were carried out in a 300 mL high pressure reactor (*Parr™*) in 4 mL glass vials. The reaction vessels were loaded under argon, purged with hydrogen, sealed and the internal pressure was adjusted. Hydrogen (99.9992%) was purchased from *Linde*. Deuterium (99.8%) was purchased from *Sigma-Aldrich*.

Yields of the catalytic studies were determined using gas chromatography with FID detector (GC-FID) by *Shimadzu GC2025*. H_2 was used as carrier gas. A *Restek Rxi*® (30 m x 0.25 mm x 0.25 µm) column was used. The standard heating procedure was: 50 °C (2 min), 25 °C/min → 280 °C (5 min). Calibration with internal standard *n*-pentadecane and analytically pure samples. Non-commercial calibration samples were prepared by hydrogenation with Pd/C (10% Pd basis). Gas chromatography with mass-selective detector (GC-MS) was conducted with an *Agilent 7820A GC* system with *mass detector 5977B*. H_2 as carrier gas and a *HP-5MS* (30 m x 0.25 mm x 0.25 µm) column were used. The standard heating procedure was: 50 °C → 300 °C.

4.4.2 Synthesis of Compounds

[(^{Dep}nacnac)Mg][CoH$_4$(dcpe)] (1)

[(^{Dep}nacnac)Mg][Co(η^4-cod)$_2$] (301.2 mg, 0.456 mmol, 1.0 equiv.) and dcpe (192.7 mg, 0.456 mmol, 1.0 equiv.) were dissolved in toluene (10 mL) in a J. Young Schlenk flask. The yellow greenish solution was subjected to three freeze-pump-thaw cycles, after which H_2 (4 bar overpressure) was added to the thawed solution at ambient temperature. Heating to 60 °C while stirring for 3 days gave a purple solution. The residual overpressure was carefully released, and all volatiles were removed *in vacuo*. The residue was dispensed in *n*-pentane (5.0 mL), stirred briefly, and the solvent was again evaporated to dryness to remove traces of toluene. To the residue was added *n*-pentane (5.0 mL), the suspension was sonicated and then stirred at −30 °C for 30 min. The purple supernatant was removed by filtration with a filter cannula, and the gray solid was treated twice more with *n*-pentane (3.0 and 2.0 mL) in an analogous manner. The resulting solid was dried *in vacuo* to give [(^{Dep}nacnac)Mg][CoH$_4$(dcpe)] (**1**) as an off-white powder in 59% crude yield. The solid was dissolved in toluene/*n*-pentane (2:3 *v*/*v*; 5.0 mL). Filtration and subsequent storage at −30 °C for 7 days gave colorless crystals of **1**, which were isolated by decanting the mother liquor. The crystals were washed with cold *n*-pentane (−35 °C; 2.0 mL) and dried under reduced pressure.

Crystallization of an isolated sample of **1** from cold *n*-pentane/THF (−35 °C; ca. 1:0.1) gave the THF adduct [(^{Dep}nacnac)Mg(thf)][CoH$_4$(dcpe)] (**4**), which was characterized by SC-XRD analysis (Figure S40).

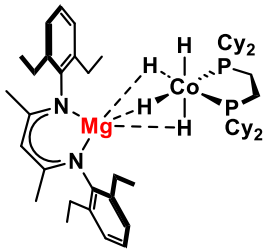

$C_{51}H_{85}CoMgN_2P_2$, MW = 871.44 g/mol

Yield: 118.7 mg, 30%

^{1}H NMR (400.13 MHz, 298 K, toluene-d$_8$) δ = 7.12-7.09 (m, 4H, C*H*$_{aryl}$-Dep; overlap with solvent signal), 7.06-7.03 (m, 2H, C*H*$_{aryl}$-Dep), 4.92 (s, 1H, CH$_3$C(N)C*H*=), 2.92-2.78 (m, 4H, C*H*$_2$CH$_3$-Dep), 2.75-2.61 (m, 4H, C*H*$_2$CH$_3$-Dep), 1.83-1.71 (m, 8H, C$_6$*H*$_{11}$-Cyclohexyl), 1.70-1.64 (m, 4H, C$_6$*H*$_{11}$-Cyclohexyl), 1.62 (s, 6H, C*H*$_3$C(*N*)CH=), 1.64-1.54 (m, 4H, C$_6$*H*$_{11}$-Cyclohexyl; overlap with signal at 1.62 ppm), 1.54-1.40 (m, 4H, C$_6$*H*$_{11}$-Cyclohexyl), 1.31 (t, $^3J_{HH}$ = 7.6 Hz, 12H, CH$_2$C*H*$_3$-Dep), 1.27-1.06 (m, 24H, C$_6$*H*$_{11}$-Cyclohexyl), 0.88-0.71 (m, 4H, C$_6$*H*$_{11}$-Cyclohexyl), −14.84 (t, $^2J_{PH}$ = 10.2 Hz, 4H, [Mg][Co*H*$_4$]-Hydride) ppm.

^{13}C{^{1}H} NMR (100.61 MHz, 298 K, toluene-d$_8$) δ = 168.5 (s, CH$_3$*C*(N)−), 148.7 (s, *C*$_{aryl}$-Dep), 137.7 (s, *C*$_{aryl}$-Dep), 126.3 (s, *C*H$_{aryl}$-Dep), 124.8 (s, *C*H$_{aryl}$-Dep), 95.6 (s,

$CH_3C(N)CH$=), 37.1 (pt, $^nJ_{CP}$ = 10.7 Hz, *C*H of dcpe ipso to P), 28.9 (s, dcpe), 28.3 (pt, $^nJ_{CP}$ = 4.5 Hz, dcpe), 28.1 (pt, $^nJ_{CP}$ = 5.7 Hz, dcpe), 27.4 (s, dcpe), 25.7 (s, CH_2CH_3-Dep), 24.3 (s, $CH_3C(N)$), 24.3 (pt, $^nJ_{CP}$ = 19.7 Hz, dcpe), 14.4 (s, CH_2CH_3-Dep) ppm. One aliphatic carbon resonance for the dcpe ligand cannot be detected or overlaps with another signal.
$^{31}P\{^1H\}$ NMR (161.98 MHz, 298 K, toluene-d_8): 117.5 (bs, Cy_2PCH_2–) ppm.

IR (solidstate) $\bar{\nu}$ = 2920s, 2849m, 1936w (Co–H), 1178w (Co–H), 1775w (Co–H), 1536m, 1522s, 1438s, 1392s, 1371s, 1263m, 1178m, 1105w, 1026w, 850m, 740m, 665m, 533m, 461m, 428m, 407m cm^{-1}.

Elemental Analysis calcd. C 70.29, H 9.83, N 3.21; found C 70.90, H 9.78, N 3.17

[(^{Mes}nacnac)Mg][CoH_4(dcpe)] (2)

[(^{Mes}nacnac)Mg][Co(η^4-cod)$_2$] (261.4 mg, 0.413 mmol, 1.0 equiv.) and dcpe (174.5 mg, 0.413 mmol, 1.0 equiv.) were dissolved in toluene (30 mL) in a J. Young Schlenk flask. The yellow greenish solution was subjected to three freeze-pump-thaw cycles, after which H_2 (4 bar overpressure) was added to the thawed solution at ambient temperature. Heating to 60 °C while stirring for 40 h gave a purple solution. The residual overpressure was carefully released, and all volatiles were removed *in vacuo*. The residue was dispensed in *n*-pentane (5.0 mL), stirred briefly, and the solvent was again evaporated to dryness to remove traces of toluene. To the residue was added *n*-pentane (5.0 mL), the suspension was sonicated and then stirred at –30 °C for 30 min. The purple supernatant was removed by filtration with a filter cannula, and the gray solid was treated once more with *n*-pentane (5.0 mL) in an analogous manner. The resulting solid was dried *in vacuo* to give [(^{Mes}nacnac)Mg][CoH_4(dcpe)] (**2**) as an off-white powder in 53% crude yield. The solid was dissolved in toluene/*n*-pentane (3:4 *v*/*v*; 14.0 mL). Filtration and subsequent storage at –30 °C for 14 days gave colorless crystals of **2**, which were isolated by decanting the mother liquor. The crystals were washed with cold *n*-pentane (–35 °C; 2.0 mL) and dried under reduced pressure.

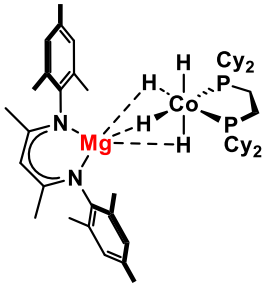

$C_{49}H_{81}CoMgN_2P_2$, MW = 843.39 g/mol

Yield: 72.9 mg, 21%

^1H NMR (400.13 MHz, 298 K, toluene-d_8) δ = 6.85 (s, 4H, CH_{aryl}-Mes), 4.91 (s, 1H, $CH_3C(N)CH$=), 2.29 (s, 12H, *o*-CH_3-Mes), 2.24 (s, 6H, *p*-CH_3-Mes), 1.87-1.73 (m, 8H,

C_6H_{11}-Cyclohexyl), 1.72-1.65 (m, 4H, C_6H_{11}-Cyclohexyl), 1.54-1.40 (m, 4H, C_6H_{11}-Cyclohexyl), 1.63 (s, 6H, $CH_3C(N)CH$=), 1.65-1.56 (m, 4H, C_6H_{11}-Cyclohexyl; overlap with signal at 1.63 ppm), 1.54-1.43 (m, 4H, C_6H_{11}-Cyclohexyl), 1.33-1.05 (m, 24H, C_6H_{11}-Cyclohexyl), 0.97-0.80 (m, 4H, C_6H_{11}-Cyclohexyl), −14.85 (bs, 4H, [Mg][CoH_4]-Hydride) ppm.

^{13}C{^{1}H} NMR (100.61 MHz, 298 K, toluene-d_8) δ = 168.3 (s, CH_3C(N)−), 147.1 (s, C_{aryl}-Mes), 132.7 (s, C_{aryl}-Mes), 132.2 (s, C_{aryl}-Mes), 129.8 (s, CH_{aryl}-Mes), 95.5 (s, $CH_3C(N)CH$=), 36.9 (pt, $^nJ_{CP}$ = 10.6 Hz, *C*H of dcpe *ipso* to P), 29.1 (s, dcpe), 28.9 (s, dcpe), 28.3 (pt, $^nJ_{CP}$ = 4.6 Hz, dcpe), 28.0 (pt, $^nJ_{CP}$ = 5.7 Hz, dcpe), 27.5 (s, dcpe), 24.2 (pt, $^nJ_{CP}$ = 19.3 Hz, dcpe), 23.8 (s, CH_3C(N)), 21.4 (s, *p*-CH_3-Mes), 19.7 (s, *o*-CH_3-Mes) ppm.

^{31}P{^{1}H} NMR (161.98 MHz, 298 K, toluene-d_8): 118.2 (bs, Cy_2PCH_2−) ppm.

IR (solid state) $\bar{\nu}$ = 2915m, 2844m, 1920w (Co−H), 1784w (Co−H), 1735w (Co−H), 1542m, 1524m, 1445m, 1393s, 1373s, 1262m, 1198m, 1147m, 1002w, 855m, 744m, 653m, 503m, 419s cm^{-1}.

Elemental Analysis calcd. C 69.78, H 9.68, N 3.32; found C 70.05, H 9.79, N 3.15

[(^{Dep}nacnac)Mg][(μ,η^4:η^4-P$_4$)Co(dcpe)] (5)

To a colorless solution of [(^{Dep}nacnac)Mg][CoH_4(dcpe)] (**1**; 99.9 mg, 0.115 mmol, 1.0 equiv.) in toluene (5.0 mL) was added white phosphorus (P_4; 15.6 mg, 0.126 mmol, 1.1 equiv.) at ambient temperature. Immediate H_2 gas evolution and a color change to red was observed. The mixture was stirred at ambient temperature overnight to give a deep reddish-brown solution, which was evaporated to dryness under reduced pressure. The residual solid was redissolved in toluene/*n*-pentane (1:2 *v*/*v*, 6.0 mL). Filtration and subsequent storage at −35 °C for 7 days gave dark red crystals of **5**, which were isolated by decanting the mother liquor. The crystals were washed with cold *n*-pentane (−35 °C; 2.0 mL) and dried under reduced pressure.

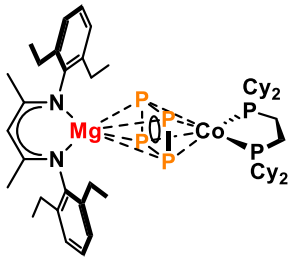

$C_{51}H_{81}CoMgN_2P_6$, MW = 991.30 g/mol

Yield: 27.0 mg, 24%

^{1}H NMR (400.13 MHz, 298 K, toluene-d_8) δ = 7.12-7.09 (m, 4H, CH_{aryl}-Dep; overlap with solvent signal), 7.08-7.03 (m, 2H, CH_{aryl}-Dep), 5.09 (s, 1H, $CH_3C(N)CH$=), 3.26-3.11 (m, 4H, CH_2CH_3-Dep), 2.94-2.78 (m, 4H, CH_2CH_3-Dep), 1.88-1.77 (m, 8H, C_6H_{11}-Cyclohexyl;

overlap with signal at 1.83 ppm), 1.83 (s, 6H, C*H*$_3$C(*N*)CH=), 1.76-1.61 (m, 14H, C$_6$*H*$_{11}$-Cyclohexyl), 1.60-1.53 (m, 6H, C$_6$*H*$_{11}$-Cyclohexyl), 1.52-1.40 (m, 4H, C$_6$*H*$_{11}$-Cyclohexyl), 1.31 (s, 12H, $^3J_{HH}$ =7.6 Hz, CH$_2$C*H*$_3$-Dep), 1.17-0.97 (m, 12H, C$_6$*H*$_{11}$-Cyclohexyl), 0.79-0.62 (m, 4H, C$_6$*H*$_{11}$-Cyclohexyl) ppm.

^{13}C{^{1}H} NMR (100.61 MHz, 298 K, toluene-d$_8$) δ = 169.7 (s, CH$_3$*C*(N)–), 147.9 (s, *C*$_{aryl}$-Dep), 138.3 (s, *C*$_{aryl}$-Dep), 126.0 (s, *C*H$_{aryl}$-Dep), 95.6 (s, CH$_3$C(N)*C*H=), 40.0 (pt, $^nJ_{CP}$ = 11.6 Hz, *C*H of dcpe *ipso* to P), 29.3 (s, dcpe), 29.0 (s, dcpe), 28.0 (pt, $^nJ_{CP}$ = 5.8 Hz, dcpe), 27.9 (pt, $^nJ_{CP}$ = 4.6 Hz, dcpe), 27.1 (s, dcpe), 25.8 (pt, $^nJ_{CP}$ = 9.5 Hz, dcpe), 24.6 (s, *C*H$_3$C(N)), 14.3 (s, CH$_2$C*H*$_3$-Dep) ppm. One aromatic carbon resonance for the 2,6-diethylphenyl substituent cannot be detected or overlaps with another signal.

^{31}P{^{1}H} NMR (161.98 MHz, 298 K, toluene-d$_8$): 103.5 (bs, Cy$_2$*P*CH$_2$–), 88.1 (t, $^2J_{PP}$ = 10.9 Hz, *cyclo*-P$_4$) ppm.

Elemental Analysis calcd. C 61.79, H 8.24, N 2.83; found C 62.61, H 8.51, N 2.68

[(^{Mes}nacnac)Mg][(μ,η^4:η^4-P$_4$)Co(dcpe)] (6)

To a colorless solution of [(^{Mes}nacnac)Mg][CoH$_4$(dcpe)] (**2**; 29.7 mg, 35.2 μmol, 1.0 equiv.) in toluene (2.0 mL) was added white phosphorus (P$_4$; 4.8 mg, 38.7 μmol, 1.1 equiv.) at ambient temperature. Immediate H$_2$ gas evolution and a color change to red was observed. The mixture was stirred at ambient temperature for 8 h to give a deep reddish-brown solution, which was evaporated to dryness under reduced pressure. The residual solid was redissolved in benzene/*n*-hexane (1:2 *v*/*v*, 1.2 mL) mixture. Filtration and subsequent storage at –35 °C for 14 days gave dark red crystals of **6**, which were isolated by decanting the mother liquor. The crystals were washed with cold *n*-pentane (–35 °C; 1.0 mL) and dried under reduced pressure.

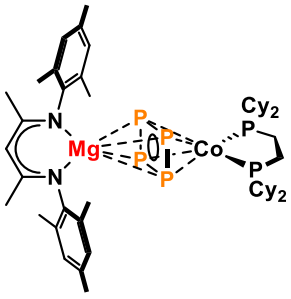

C$_{49}$H$_{77}$CoMgN$_2$P$_6$, MW = 963.25 g/mol

Yield: 7.7 mg, 23%

^{1}H NMR (400.13 MHz, 298 K, toluene-d$_8$) δ = 6.81 (s, 4H, C*H*$_{aryl}$-Mes), 5.07 (s, 1H, CH$_3$C(N)C*H*=), 2.48 (s, 12H, *o*-C*H*$_3$-Mes), 2.09 (s, 6H, *p*-C*H*$_3$-Mes), 1.94-1.82 (m, 8H, C$_6$*H*$_{11}$-Cyclohexyl), 1.80 (s, 6H, C*H*$_3$C(*N*)CH=), 1.76-1.58 (m, 16H, C$_6$*H*$_{11}$-Cyclohexyl), 1.58-1.45 (m, 8H, C$_6$*H*$_{11}$-Cyclohexyl), 1.15-0.97 (m, 12H, C$_6$*H*$_{11}$-Cyclohexyl), 0.82-0.65 (m, 4H, C$_6$*H*$_{11}$-Cyclohexyl) ppm.

$^{13}C\{^1H\}$ NMR (100.61 MHz, 298 K, toluene-d_8) δ = 169.5 (s, CH_3C(N)–), 146.6 (s, C_{aryl}-Mes), 133.3 (s, C_{aryl}-Mes), 132.9 (s, C_{aryl}-Mes), 129.7 (s, CH_{aryl}-Mes), 95.7 (s, $CH_3C(N)CH$=), 40.2 (pt, $^nJ_{CP}$ = 11.3 Hz, *C*H of dcpe *ipso* to P), 29.3 (s, dcpe), 29.0 (s, dcpe), 28.0 (pt, $^nJ_{CP}$ = 5.6 Hz, dcpe), 27.8 (pt, $^nJ_{CP}$ = 4.5 Hz, dcpe), 27.1 (s, dcpe), 25.7 (pt, $^nJ_{CP}$ = 19.6 Hz, dcpe), 24.4 (s, CH_3C(N)), 21.4 (s, *p*-CH_3-Mes), 21.4-20.1 (s, *o*-CH_3-Mes; overlap with solvent signal) ppm.

$^{31}P\{^1H\}$ NMR (161.98 MHz, 298 K, toluene-d_8): 103.9 (bs, Cy_2PCH_2–), 87.1 (t, $^2J_{PP}$ = 8.9 Hz, *cyclo*-P_4) ppm.

Elemental Analysis calcd. C 61.10, H 8.06, N 2.91; found n.d.

4.4.3 Synthesis and Attempted Isolation of [((–)-(*S*)-Naphnacnac)Mg][CoH_4(dcpe)] (3)

The synthesis of the chiral cobalt hydride [((–)-(*S*)-Naphnacnac)Mg][CoH_4(dcpe)] (**3**) was attempted by treating [((–)-(*S*)-Naphnacnac)Mg][Co(η⁴-cod)$_2$] with dcpe and H_2 (Scheme S1).

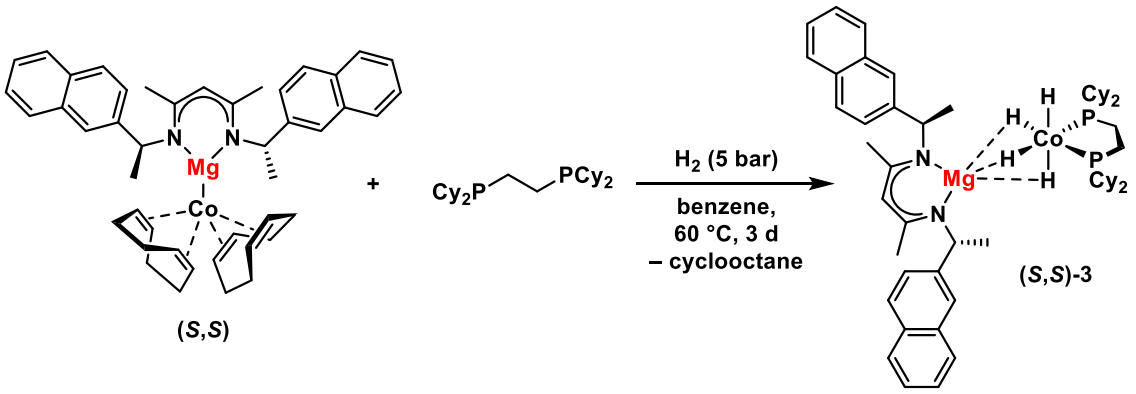

Scheme S1. Attempted synthesis of [((–)-(*S*)-Naphnacnac)Mg][CoH_4(dcpe)] (**3**) by reaction of [((–)-(*S*)-Naphnacnac)Mg][Co(η⁴-cod)$_2$] with dcpe and H_2 (5 bar).

[((–)-(*S*)-Naphnacnac)Mg][Co(η⁴-cod)$_2$] (100.1 mg, 0.142 mmol, 1.0 equiv.) and dcpe (60.0 mg, 0.142 mmol, 1.0 equiv.) were dissolved in benzene (4.0 mL) in a J. Young Schlenk flask. The yellow greenish solution was subjected to three freeze-pump-thaw cycles, after which H_2 (4 bar overpressure) was added to the thawed solution at ambient temperature. Heating to 60 °C while stirring for 3 days gave a purple solution. The residual overpressure was carefully released, and an aliquot was taken for NMR analysis (Figure S1). All volatiles were removed *in vacuo* and the oily residue redissolved in *n*-pentane and the solvent was again evaporated to dryness (repeated 3 x with 2.0 mL each) to give a foam-like voluminous solid. This solid was again redissolved in a minimal amount of *n*-pentane (1.0 mL), filtered, and placed at –35 °C for crystallization. Trace amounts of a crystalline solid formed after 14 days, which could not be analyzed by SC-XRD due to poor crystal quality. Further attempts to obtain high quality single crystals or a suitable amount for isolation were not successful. Although the isolation of **3** was severely hampered by its high solubility even in highly apolar solvents, the selective conversion observed by $^{31}P\{^1H\}$ NMR spectroscopic analysis suggests that an improved crystallization procedure may enable access to **3**.

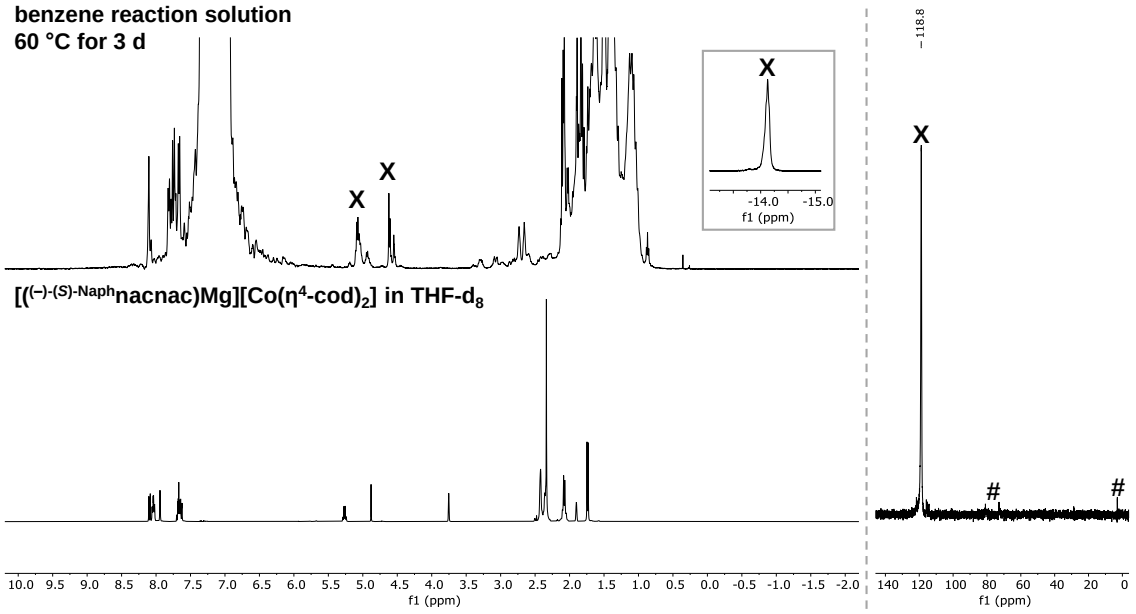

Figure S1. ^{1}H (left) and $^{31}P\{^{1}H\}$ (right) NMR spectra (400.13/161.98 MHz, 298 K, C_6D_6 capillary) of the reaction solution after stirring at 60 °C for 3 d. X: proposed [((–)-(*S*)-Naphnacnac)Mg][CoH_4(dcpe)] (**3**); two conformers are observed. #: minor side products.

4.4.4 Hydrogenation Reactions with [(Depnacnac)Mg][CoH_4(dcpe)] (1)

4.4.4.1 General Procedure

In a glovebox, an oven-dried (160 °C) 4 mL reaction vial was charged with *n*-pentadecane (20 µL, 72.4 µmol) as the internal standard for GC-FID quantification. The liquid substrate (0.2 mmol) was added followed by the pre-catalyst as a stock solution in toluene (0.5 mL), if not stated otherwise. In the case of solid substrates, the solid was first weighed into the vial followed by the addition of the liquids. The reaction vial was transferred to a high-pressure reactor, which was sealed and removed from the glovebox. The reactor was purged with a continuous flow of H_2 (0.5-0.8 bar overpressure for 30 s) and the reaction pressure and temperature were set. After the indicated reaction time, the reaction vessel was depressurized, the vials were retrieved and treated with a saturated aqueous solution of NH_4Cl (1.0 mL) and diluted with ethyl acetate. An aliquot of the organic phase was filtered over a short pad of silica and washed with ethyl acetate (1 x 2.0 mL). The solution was analyzed by GC-FID (and GC-MS for selected experiments).

4.4.4.2 Initial Optimization and Hg Poisoning Experiments

Initial optimization and mercury poisoning reactions were conducted following the general procedure (section 4.4.4.1) and are summarized in Table S1. Solvent screening (toluene, THF, and 1,4-dioxane) for the hydrogenation of α-methylstyrene and 1-octene under mild conditions (2 mol% **1**, 2 bar H_2, 40 °C, 20 h) showed a slight improvement for α-methylstyrene in toluene (Table S1, entries 1-3) and for 1-octene in 1,4-dioxane (Table S1, entries 4-6). Following indications that pre-catalyst **1** may decompose in ethereal solvents such as THF via solvent ring-opening (see section 4.4.5.4 for details), all further hydrogenation reactions were conducted in toluene. A concentration screening for the

hydrogenation of α-methylstyrene indicates that the initial reaction volume was already optimal, with lower yields observed upon significant dilution or concentration (Table S1, entries 7-11). Hg poisoning experiments using excess mercury (50 µL; 1690 mol%; addition at t = 0 min) did not inhibit α-methylstyrene hydrogenation under two different conditions, with the reaction reaching a comparable level of completeness (Table S1, entries 12-14). This indicates that the hydrogenation using **1** is homotopic under the applied conditions.

Table S1. Initial optimization and Hg poisoning experiments.[a]

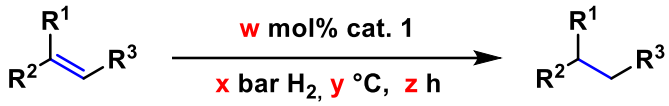

Entry	Substrate	Conditions	Manipulation	Yield (conv.) [%]
1	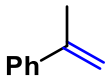	2 mol%, 2 bar H_2, 40 °C, 20 h, solvent	solvent = toluene	38 (41)
2			solvent = THF	30 (41)
3			solvent = 1,4-dioxane	23 (23)
4	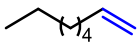	2 mol%, 2 bar H_2, 40 °C, 20 h, solvent	solvent = toluene	69 (>99)[b]
5			solvent = THF	64 (>99)[b]
6			solvent = 1,4-dioxane	81 (>99)[b]
7	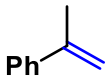	2 mol%, 2 bar H_2, 40 °C, 20 h, xx mL toluene	0.1 mL	25 (39)
8			0.25 mL	33 (43)
9			0.50 mL	38 (41)
10			1.5 mL	32 (32)
11			2.0 mL	26 (31)
12	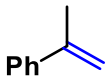	2 mol%, 4 bar H_2, 40 °C, 20 h	none	70 (80)
13			Hg (1690 mol%)[c]	67 (75)
14		2 mol%, 8 bar H_2, 40 °C, 20 h	None	86 (92)
15			Hg (1690 mol%)[c]	92 (>99)

[a] Standard conditions: 0.2 mmol substrate (0.4 mol/L in toluene). [b] Isomerization to internal double bonds. [c] Hg (1690 mol%; 50 µL) was added at t = 0 min.

Hydrogenation experiments at an increased H_2 pressure (8-12 bar) led to increased partial hydrogenation of the toluene solvent to produce methylcyclohexane.[25] An exemplary GC-FID chromatogram for the hydrogenation of α-methylstilbene at 12 bar H_2 (4 mol% **1**, 40 °C, 20 h) is displayed in Figure S2. The formation of methylcyclohexane is observed at t_R = 1.371 min, which suggests that solvent hydrogenation may compete with alkene hydrogenation and therefore limit the targeted reduction.

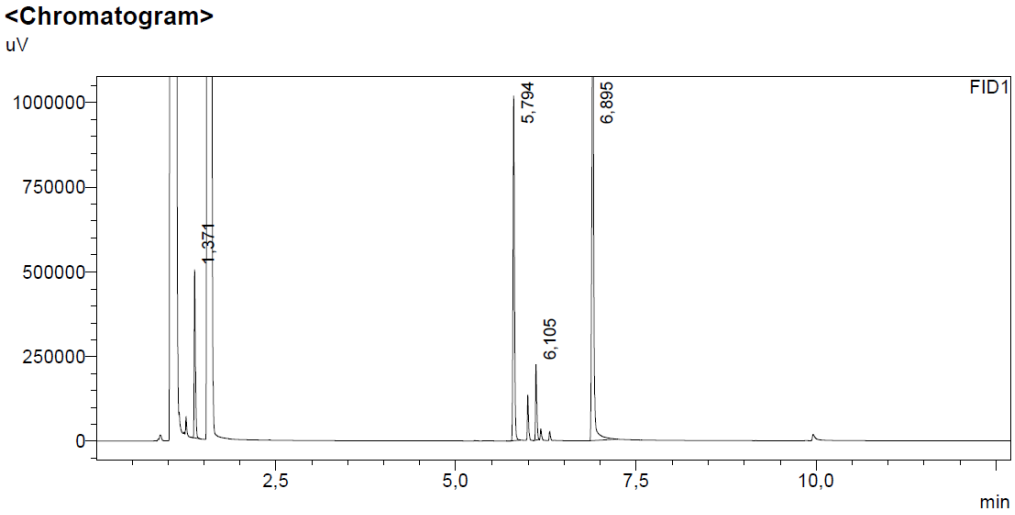

Figure S2. GC-FID chromatogram for the hydrogenation of α-methylstilbene (t_R = 6.895 min) to 1-methyl-1,2-diphenylethane (t_R = 6.105 min) at high pressure (4 mol% **1**, 12 bar H_2, 40 °C, 20 h; *n*-pentadecane at t_R = 5.794 min). The peak at t_R = 1.371 min corresponds to methylcyclohexane.

4.4.5 Supporting Studies on the Reactivity of [(^{Dep}nacnac)Mg][CoH_4(dcpe)] (1)

4.4.5.1 H/D exchange reactions of [(^{Dep}nacnac)Mg][CoH_4(dcpe)] (1)

H/D Exchange with D_2

[(^{Dep}nacnac)Mg][CoH_4(dcpe)] (**1**; 102.6 mg, 0.12 mmol, 1.0 equiv.) was dissolved in benzene (4.0 mL) and the colorless solution was transferred to a J. Young Schlenk flask. Subsequently, the atmosphere was exchanged with D_2 by two consecutive freeze-pump-thaw cycles and set to a D_2 pressure of 5 bar. The clear, darkened solution was stirred at ambient temperature for 7 d, after which the solvent was evaporated under reduced pressure.

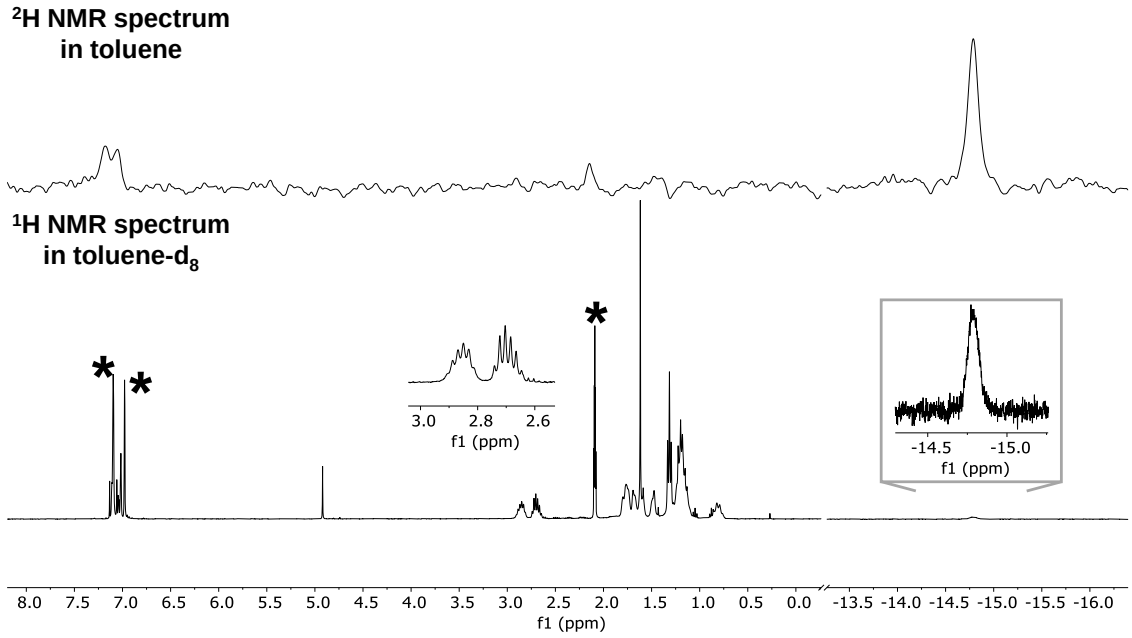

Figure S3. ^{1}H and ^{2}H NMR spectra (400.13/61.42 MHz, 298 K, toluene-d_8 or toluene) of the H/D exchange of **1** by reaction with D_2 (5 bar) at r.t. for 7 d. The hydride signal (−14.79 ppm) was referenced to the resonance of the ethyl group of the β-diketiminate ligand (2.85 ppm; integral 4.00). *: toluene-d_8.

The gray residue was stirred in cold *n*-pentane for 30 min (–30 °C; 2.0 mL), the solid was isolated by filtration and dried *in vacuo* to afford a light-gray powder (50.8 mg; 49%). ^{1}H NMR spectroscopic analysis shows 83% deuterium incorporation into **1**, according to a reduced hydride signal at –14.79 ppm with an integral of 0.68 (vs. initially 4.0); a corresponding ^{2}H NMR resonance at the same shift confirms deuteration (Figure S3).

H/D Exchange with Toluene-d_8

[(^{Dep}nacnac)Mg][CoH_4(dcpe)] (**1**; 10.0 mg, 11.5 µmol, 1.0 equiv.) was dissolved in toluene-d_8 (0.6 mL) and the colorless solution was transferred to a J. Young NMR tube. After initial ^{1}H and ^{31}P{^{1}H} NMR spectra were recorded, the solution was heated at 60 °C for 8 d. Subsequent spectra were recorded after irregular intervals, monitoring a slow H/D exchange with toluene-d_8 (Figure S4 and Table S2). After 8 d, the hydride signal is reduced to an integral of 1.17 (initially 4.0), which corresponds to an incorporation of 71% deuterium into **1**. No apparent changes were observed in the simultaneous ^{31}P{^{1}H} NMR spectroscopic monitoring. No H/D exchange with toluene-d_8 was observed at ambient temperature.

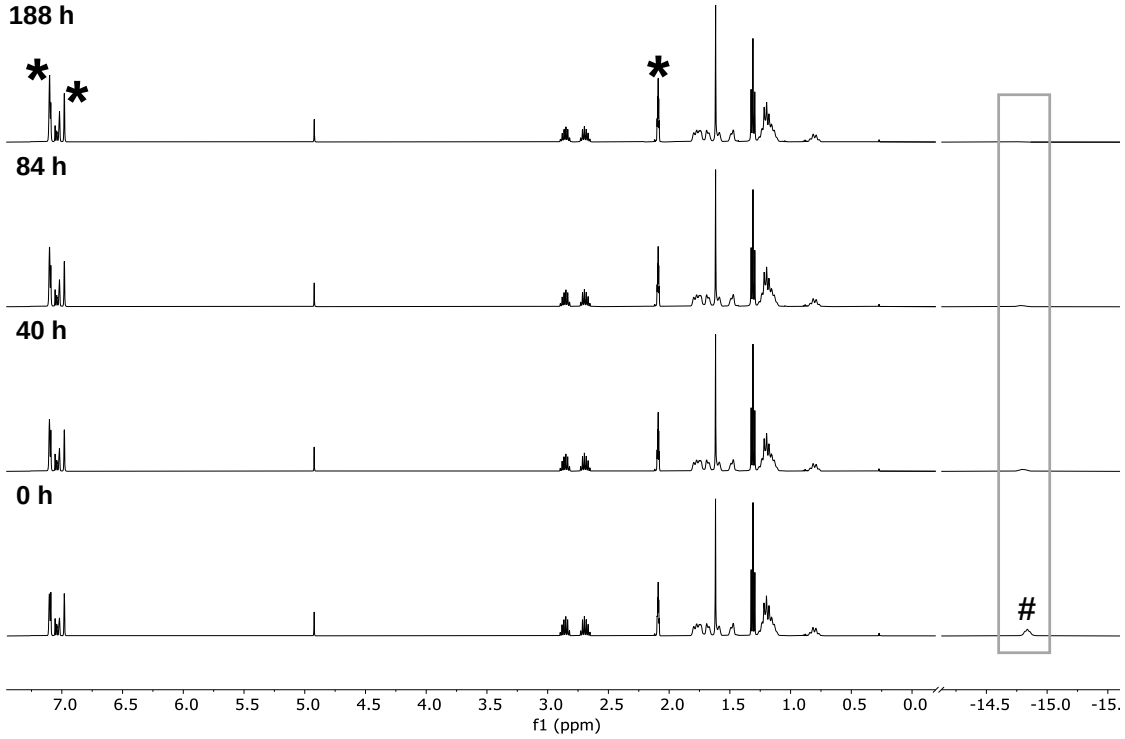

Figure S4. Quantitative ^{1}H NMR spectra (500.13 MHz, 298 K, toluene-d_8; relaxation delay = 30 s) of the H/D exchange of **1** by reaction with toluene-d_8 at 60 °C for 8 d. #: hydride signal of **1**. The hydride signal (–14.83 ppm) was referenced to the resonance of the ethyl group of the β-diketiminate ligand (2.85 ppm; integral 4.00). *: toluene-d_8.

Table S2. H/D exchange of **1** by reaction with toluene-d_8 at 60 °C.

t [h]	0	16	40	60	84	188
Hydride integral	4.00	2.89	2.20	1.82	1.65	1.17

[a] The hydride signal (–14.83 ppm) was referenced to the resonance of the ethyl group of the β-diketiminate ligand (2.85 ppm; integral 4.00) in the quantitative ^{1}H NMR spectrum of **1** (500.13 MHz, 298 K, toluene-d_8; pulse sequence zg30, O1P = –5.0 ppm, relaxation delay = 30 s).

4.4.5.2 Reaction of [(^{Dep}nacnac)Mg][CoH_4(dcpe)] (1) with Styrene

NMR Scale Reaction

[(^{Dep}nacnac)Mg][CoH_4(dcpe)] (**1**; 15.0 mg, 17.2 µmol, 1.0 equiv.) was dissolved in toluene-d_8 (0.6 mL), styrene (19.8 µL, 0.1 mmol, 10.0 equiv.) was added and the solution was transferred to a J. Young NMR tube. The solution was heated at 60 °C for 20 h, resulting in a color change from colorless to orange-to-brown. ^{1}H and ^{31}P{^{1}H} NMR spectra reveal the formation of a new species (label ◇; Figure S5) and near-complete consumption of **1** (label X; Figure S5). Accompanied by the partial hydrogenation of styrene, this suggests the formation of a styrene containing intermediate, such as [(^{Dep}nacnac)Mg]-[Co(η^2-styrene)$_n$(dcpe)] (n = 1, 2).

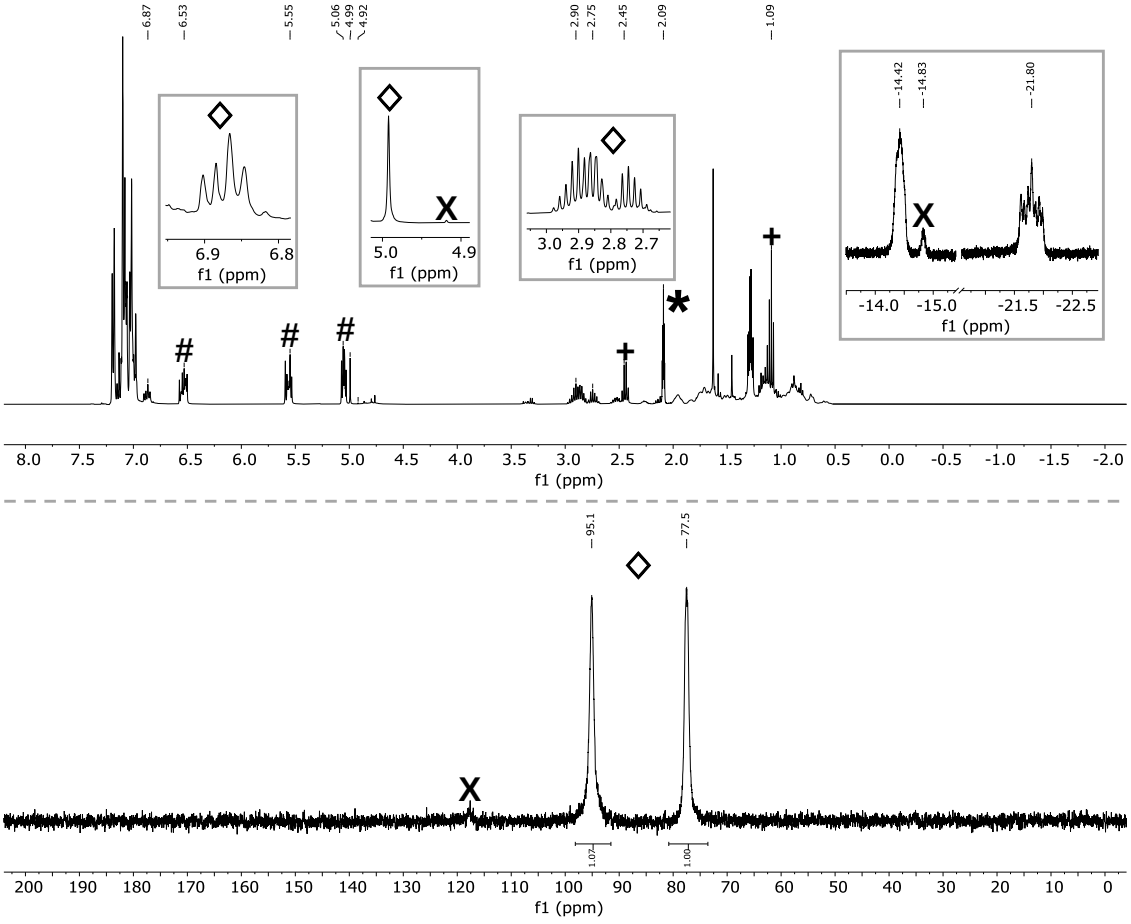

Figure S5. ^{1}H (top) and ^{31}P{^{1}H} (bottom) NMR spectra (400.13/161.98 MHz, 298 K, toluene-d_8) of the reaction of **1** with styrene (10.0 equiv.) at 60 °C for 20 h. *: toluene-d_8. X: **1**. ◇: proposed alkene complex. #: (partially) deuterated styrene. +: partially deuterated ethylbenzene.

Although no signals for coordinated styrene can be clearly assigned in the olefinic region of the ^{1}H NMR spectrum (two newly formed overlaying signals at ca. 6.80 ppm may correspond to coordinated styrene; label ◇), two chemically inequivalent signals for the dcpe ligand in the ^{31}P{^{1}H} NMR spectrum indicate the formation of a contacted ion pair, in which the cobaltate anion directly coordinates to the β-diketiminate magnesium cation. Comparison with a related lithium bis(alkene)cobaltate, [Li(thf)$_3$][Co(η^2-ethylene)$_2$(dcpe)], which shows

a ^{31}P NMR resonance at 88.5 ppm, supports the formation of an alkene complex of **1**.[20] In addition, two minor hydride signals at −14.42 and −21.80 ppm appeared, likely corresponding to a mixed hydrogen-deuterium complex (Figure S5, top). This is supported by observed deuterium incorporation in the styrene substrate after heating at 60 °C (label #; Figure S5). A H/D exchange with toluene-d_8 likely forms a partially deuterated derivative of **1**, which deuterates styrene by an insertion/elimination sequence (see also section 4.4.5.1).

Scale-Up Reaction

[(^{Dep}nacnac)Mg][CoH_4(dcpe)] (**1**; 49.7 mg, 57.0 µmol, 1.0 equiv.) was dissolved in toluene (2.0 mL), styrene (65.6 µL, 0.57 mmol, 10.0 equiv.) was added and the solution was transferred to a Schlenk flask. The solution was heated at 60 °C for 24 h, resulting in a color change from colorless to orange-to-brown. The mixture was evaporated to dryness under reduced pressure and the residue was redissolved in *n*-hexane (1.0 mL). Filtration and subsequent storage at −35 °C for crystallization gave a small amount of a dark microcrystalline precipitate, which did not diffract in SC-XRD analysis. NMR spectroscopic analysis was not conducted due to the limited quantity of this solid.

4.4.5.3 Hydrogenation of Styrene with [(^{Dep}nacnac)Mg][CoH_4(dcpe)] (1)

Reaction monitoring by ^{1}H NMR spectroscopy was carried out in a NORELL® intermediate pressure valved NMR tube (S-5-600-MW-IPV-7).[37] The pre-catalyst [(^{Dep}nacnac)Mg]-[CoH_4(dcpe)] (**1**; 10 µmol, 5 mol%) was dissolved in toluene-d_8 (0.6 mL), styrene (23.0 µL, 0.2 mmol, 1.0 equiv.) was added and the solution was transferred to the NMR tube. The first ^{1}H NMR spectrum was recorded (Figure S6, bottom). Subsequently, the atmosphere was exchanged with H_2 by three consecutive freeze-pump-thaw cycles and set to 5 bar of H_2 pressure. Subsequent spectra were recorded after irregular intervals until the substrate was fully consumed or until no further consumption was observed. Prior to the first and between each measurement, the NMR sample was removed from the spectrometer and rotated at 10 rpm. After 100 min, the partial hydrogenation of styrene (14% according to ^{1}H NMR spectroscopy, by relative peak integrals) was observed, which is indicated by the appearance of two new signals at 2.45 ppm and 1.09 ppm (Figure S6, middle). After 21 h 45 min, the hydrogenation was near-quantitative with 98% cumene formed (Figure S6, top).

The ^{1}H NMR spectra of the styrene hydrogenation remain well-resolved prior to and after H_2 addition, and no line broadening can be observed at any time. The characteristic signals for pre-catalyst **1** are detected during the whole experiment (label X; Figure S6), which suggests that **1** is only partially converted into a catalytically active species. No other cobalt complex was detected during the NMR spectroscopic monitoring. Visual inspection of the reaction solution throughout the hydrogenation reaction did not show any precipitation. The simultaneous monitoring by ^{31}P{^{1}H} NMR spectroscopy gave always a single signal (bs, 116.9 ppm) for the pre-catalyst **1**. These observations are consistent with a homotopic

hydrogenation mechanism involving an active species derived from pre-catalyst **1**, which is suggested to function as a reversible off-cycle intermediate.

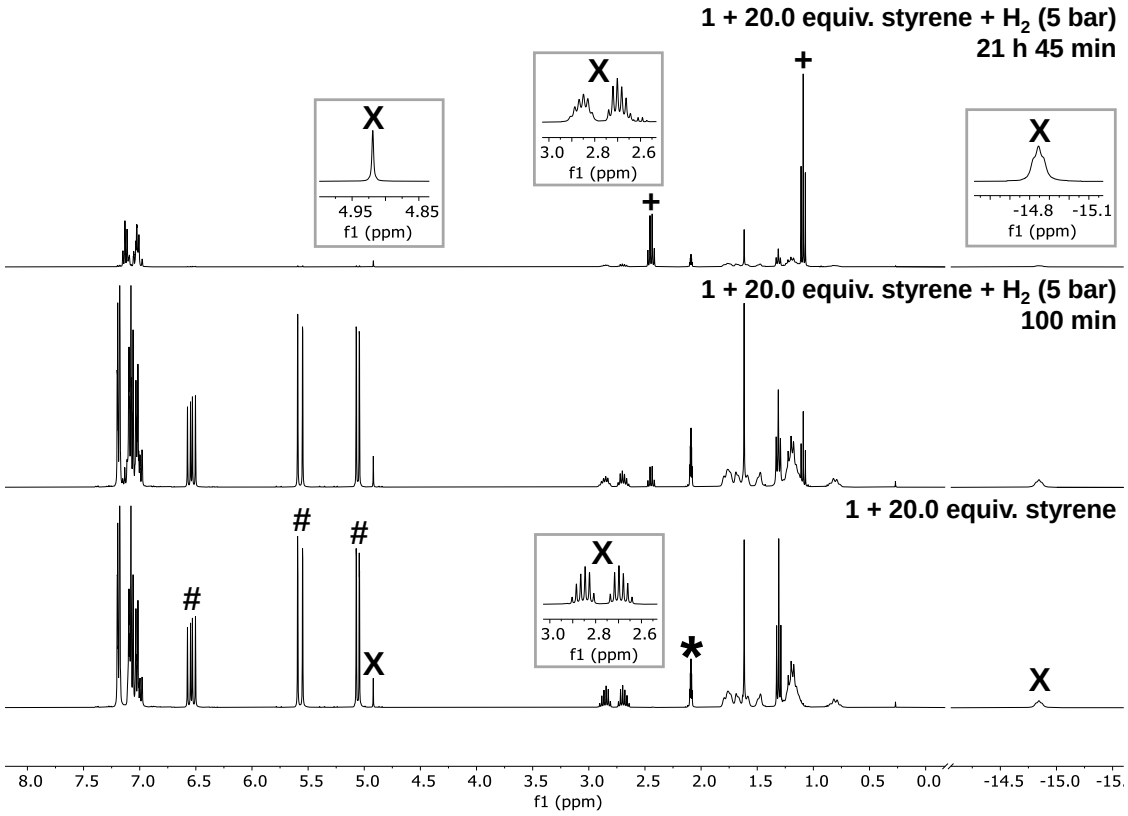

Figure S6. ^{1}H NMR spectroscopic monitoring (400.13 MHz, 298 K, toluene-d_8) of the hydrogenation of styrene with 5 mol% [(^{Dep}nacnac)Mg][CoH_4(dcpe)] (**1**). Bottom: Cobaltate **1** and styrene (20.0 equiv.) prior to H_2 addition. Middle and top: After pressurizing with 5 bar H_2 at ambient temperature. *: toluene-d_8. #: styrene. +: ethylbenzene. X: **1**.

4.4.5.4 Stepwise Hydrogenation of Styrene with [(^{Dep}nacnac)Mg][CoH_4(dcpe)] (1) Through a Proposed Alkene Intermediate

Reaction Monitoring in Toluene-d_8

The stepwise hydrogenation of styrene was carried out in a NORELL® intermediate pressure valved NMR tube (S-5-600-MW-IPV-7).[37] The pre-catalyst [(^{Dep}nacnac)Mg][CoH_4(dcpe)] (**1**; 17.2 µmol, 10 mol%) was dissolved in toluene-d_8 (0.6 mL), styrene (19.8 µL, 0.1 mmol, 1.0 equiv.) was added and the solution was transferred to the NMR tube. After initial ^{1}H and ^{31}P{^{1}H} NMR spectra were recorded (Scheme 3, bottom), the solution was heated at 60 °C for 44 h, resulting in a color change from colorless to orange-to-brown. ^{1}H and ^{31}P{^{1}H} NMR spectra showed almost complete consumption of **1** and the formation of an unidentified intermediate (label ◇; Scheme 3, middle), along with partial hydrogenation of styrene (label +; Scheme 3, middle; see also Figure S34 for full ^{31}P{^{1}H} NMR spectra). Two minor hydride signals at approximately −14.5 and −22.0 ppm appeared, likely corresponding to a mixed hydrogen-deuterium complex (Scheme 3, middle). Furthermore, deuterium incorporation in the styrene substrate after heating at 60 °C is observed (label #; Figure S7, middle). As mentioned earlier in section 4.4.5.2, a H/D exchange with toluene-d_8 likely forms a partially

deuterated variant of **1**, which deuterates styrene by an insertion/elimination sequence. Subsequently, the atmosphere was exchanged with H_2 by three consecutive freeze-pump-thaw cycles and set to a H_2 pressure of 5 bar. The NMR sample was rotated at 10 rpm for 20 h prior to the third measurement, with no color change observed. Complete hydrogenation of styrene was confirmed by the appearance of two new signals at 2.45 ppm and 1.09 ppm in the ^{1}H NMR spectrum (label +; Scheme 3, top). Corresponding signals in the ^{2}H NMR spectrum indicate deuterium incorporation (label +; Figure S7, top). The proposed cobalt complex (label ◇; Scheme 3, middle) is fully consumed, and the cobalt hydride **1** is regenerated (label X; Scheme 3, top). The additional hydride signals (−14.5 and −22.0 ppm) disappear, and the triplet structure of the hydride signal of **1** suggests no deuterium incorporation.

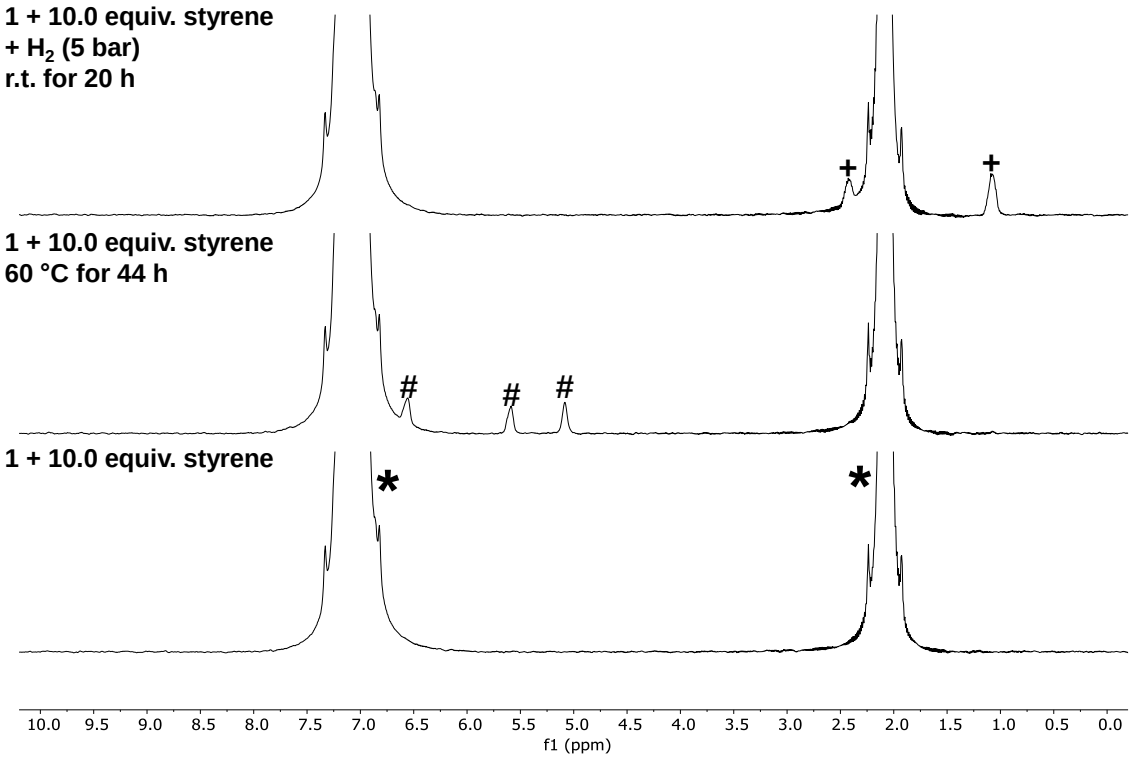

Figure S7. ^{2}H NMR spectra (61.42 MHz, 298 K, toluene-d_8) of the stepwise styrene hydrogenation using **1** through an intermediary alkene complex. *: toluene-d_8. #: partially deuterated styrene. +: partially deuterated ethylbenzene.

Reaction Monitoring in THF-d_8

The stepwise hydrogenation of styrene was carried out in a NORELL® intermediate pressure valved NMR tube (S-5-600-MW-IPV-7).[37] The pre-catalyst [(^{Dep}nacnac)Mg][CoH_4(dcpe)] **1**; 11.5 µmol, 0.25 equiv.) was dissolved in THF-d_8 (0.6 mL), styrene (5.3 µL, 45.9 µmol, 1.0 equiv.) was added and the solution was transferred to the NMR tube (Scheme S2). After initial ^{1}H and ^{31}P{^{1}H} NMR spectra were recorded (Figure S8, bottom), the solution was heated at 40 °C for 24 h, resulting in a color change from colorless to intense red-to-brown.

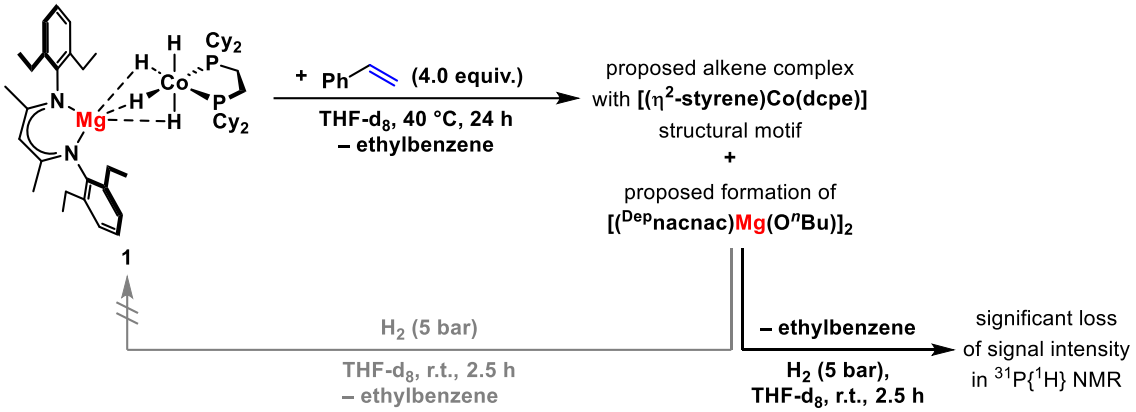

Scheme S2. Stepwise hydrogenation of styrene using **1** in THF-d$_8$ through a proposed intermediary styrene complex leading to decomposition of **1**.

^{1}H and ^{31}P{^{1}H} NMR spectra showed consumption of **1** and the formation of an unidentified intermediate (label ◇; Figure S8, middle), along with partial hydrogenation of styrene (label +; Figure S8, middle; see also Figure S35 for full ^{31}P{^{1}H} NMR spectra). Two new signals in a 2:1 ratio between 4.70 and 4.50 ppm in the ^{1}H NMR spectrum and a broad resonance at approximately 93.0 ppm in the ^{31}P{^{1}H} NMR spectrum indicate the formation of an alkene intermediate (label ◇; Figure S8, middle and Scheme S2).[20] Furthermore, signals at 4.78 ppm and between 2.50 and 2.00 ppm in the ^{1}H NMR spectrum (label $; Figure S8, middle and top) indicate the formation of an alkoxide-bridged β-diketiminate Mg dimer.[17] This suggests that THF undergoes ring opening after treatment of **1** with styrene likely forming [(Depnacnac)Mg(O^{n}Bu)]$_2$) and an unidentified alkene intermediate possibly containing a [(η^2-styrene)Co(dcpe)] structural motif (label ◇; Figure S8, middle and Scheme S2).

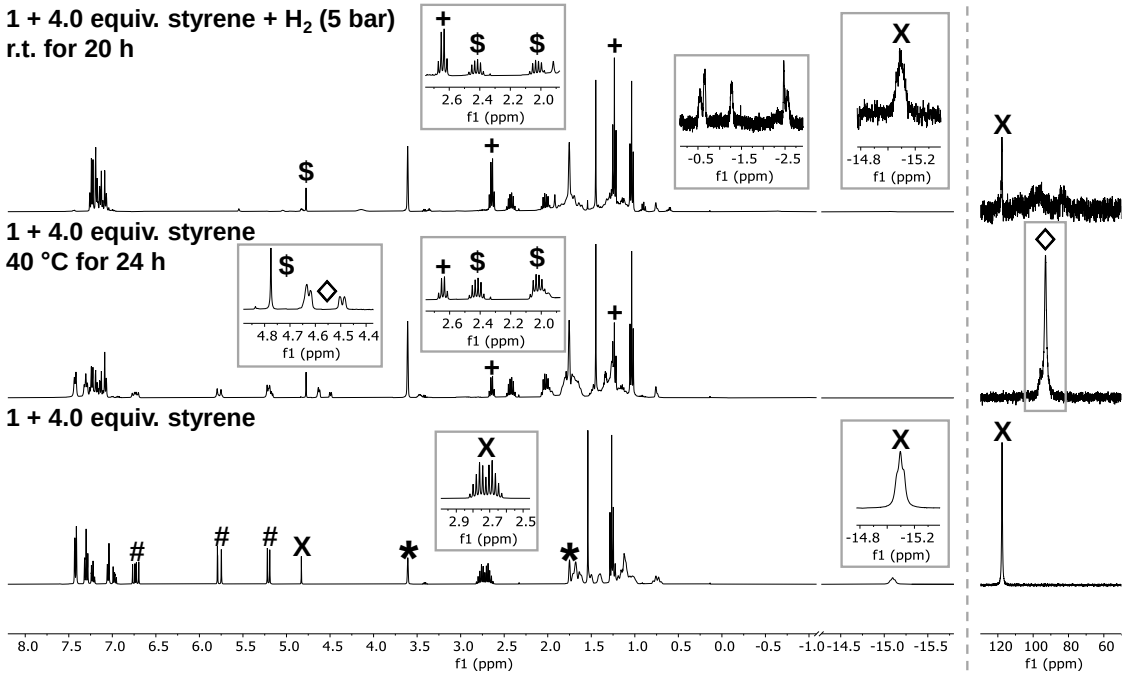

Figure S8. Top: Proposed reaction sequence of the stepwise styrene hydrogenation through a proposed styrene complex using **1** in THF-d$_8$. Bottom: ^{1}H (left) and ^{31}P{^{1}H} (right) NMR spectra

(400.13/161.98 MHz, 298 K, THF-d_8) of the stepwise styrene hydrogenation. *: THF-d_8. #: styrene. +: ethylbenzene. X: **1**. ◇: proposed alkene complex. $: proposed [(^{Dep}nacnac)Mg(O^nBu)]$_2$).

The atmosphere was then exchanged with H_2 (3x freeze-pump-thaw cycles, 5 bar H_2) and the NMR sample was rotated at 10 rpm for 2.5 h prior to the third measurement. Styrene was fully hydrogenated (label +; Figure S8, top) and the alkene intermediate consumed (Figure S8, top), but only trace amounts of the cobalt hydride **1** were regenerated (label X; Figure S8, top). A significant loss of phosphorus signal intensity in the $^{31}P\{^1H\}$ NMR spectrum suggests substantial decomposition of the catalyst species. Therefore, THF is not suitable for use with pre-catalyst **1**.

4.4.6 DOSY NMR Analysis of [(^{Dep}nacnac)Mg][CoH_4(dcpe)] (1)

General Information

Diffusion-ordered NMR spectroscopy (DOSY) experiments were conducted on a Bruker Avance III HD 600 MHz spectrometer, equipped with a TBI 5 mm $^1H/^{19}F$-BB probe. All measurements were performed at 298 K, with the temperature validated using internal NMR calibration standards from Bruker.

The DOSY measurements were performed with convection compensating double stimulated echo (DSTE) pulse sequence developed by Jerschow and Müller.[38] The diffusion time delay was set to 40 ms. Smoothed square (SMSQ10.100) gradient shapes and a linear gradient ramp (32 increments, 5% to 95% of the maximum gradient strength) were used.

The NMR data were processed, analyzed, and plotted using TopSpin 3.2 software. Data evaluation was carried out using a Python script developed by Christian Scholtes, in which the DOSY data were fitted to the Stejskal-Tanner equation.[39]

$$I = I_0 \cdot \exp\left[-\gamma^2 G^2 \delta^2 \left(\Delta - \frac{\delta}{3}\right) D\right]$$

where I is the signal with the gradient, I_0 is the signal intensity without diffusion weighting, γ is the gyromagnetic ratio, G is the strength of the gradient pulse, δ is the duration of the pulse, Δ is the time interval between the two pulses and D the diffusion coefficient.

The calculated diffusion coefficient for TMS (D_{ref}) was applied to the Stokes-Einstein equation,[40]

$$D_i = \frac{k_B T}{F c \pi \eta r_H},$$

to obtain viscosity correction for each individual sample. Here, k_B is the Boltzmann constant, T the temperature, F is the shape factor (set to 1 for a spherical shape), η the viscosity of the sample, r_H the hydrodynamic radius of the analytes, and c a correction factor which was determined by using a semi-empirical modification by Chen.[41]

$$c_{Chen} = \frac{6F}{1 + 0.695 \left(\frac{r_{solv}}{r_{ref}}\right)^{2.234}}$$

The hydrodynamic radii values for TMS (r_{ref} = 2.96 Å) and toluene (r_{solv} = 2.88 Å) were calculated using hard-sphere increments.[42]

By inserting the Chen correction factor to the Stokes-Einstein equation,

$$\eta\,[kg/ms] = \frac{k_B T\,(1 + 0.695 \left(\frac{r_{solv}}{r_{ref}}\right)^{2.234})}{6\pi D_{ref}\, r_{ref}},$$

the correction factor for the viscosity of each respective sample (η) is determined. Finally, by incorporating all correction equations, the hydrodynamic radii can be iteratively calculated by

$$D = \frac{kT\,(1 + 0.695 \left(\frac{r_{solv}}{r_H}\right)^{2.234})}{6\pi\eta r_H}.$$

Using the hydrodynamic radii, the respective Volumes (V_H) were calculated with the assumption of a spherical shape.

Sample Preparation

A 10 mM solution of [(^{Dep}nacnac)Mg][CoH_4(dcpe)] (**1**) was prepared by dissolving the respective sample in THF-d_8 or toluene-d_8. The solution was then filtered, and an aliquot (0.5 mL) was transferred into a J. Young NMR tube. Tetramethylsilane (TMS) was used as a reference and was added by withdrawing 500 µL from the headspace of a degassed TMS sample, just above the surface of the liquid and injected into the NMR tube, which was then sealed immediately afterwards.

Experimental Data

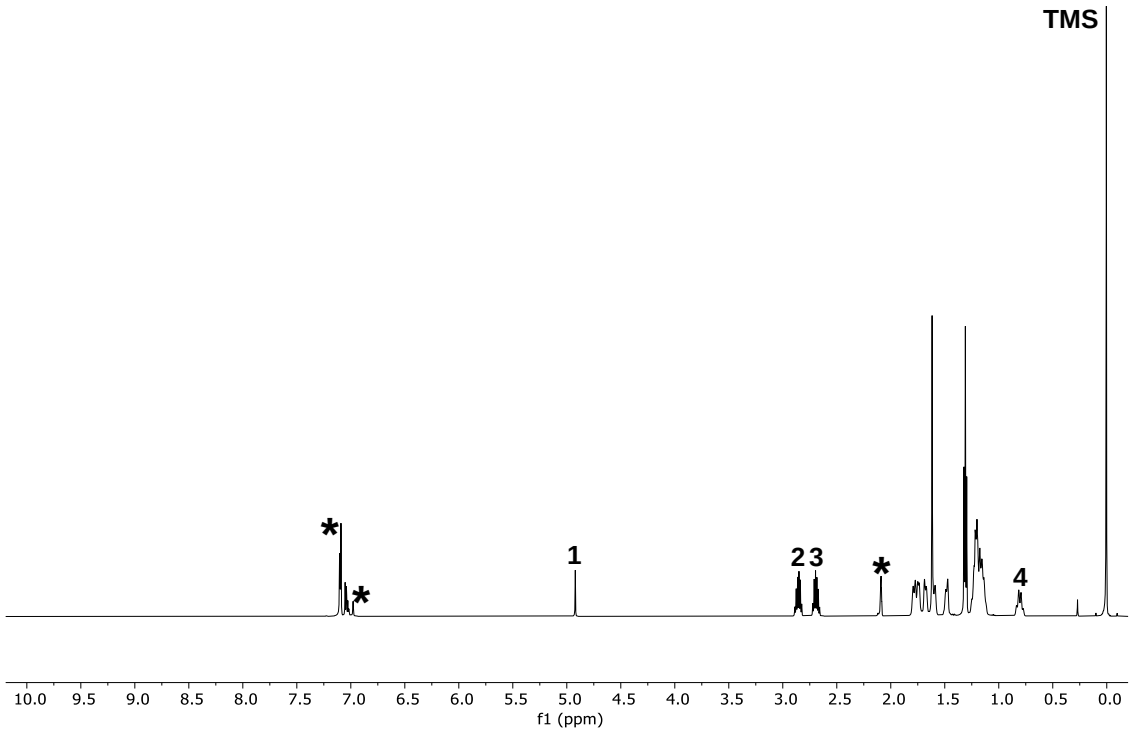

Figure S9. ^{1}H NMR spectrum of [(^{Dep}nacnac)Mg][CoH_4(dcpe)] (**1**) and TMS (600.13 MHz, 298 K, toluene-d_8), showing the signals 1-4 used for the DOSY analysis. *: toluene-d_8.

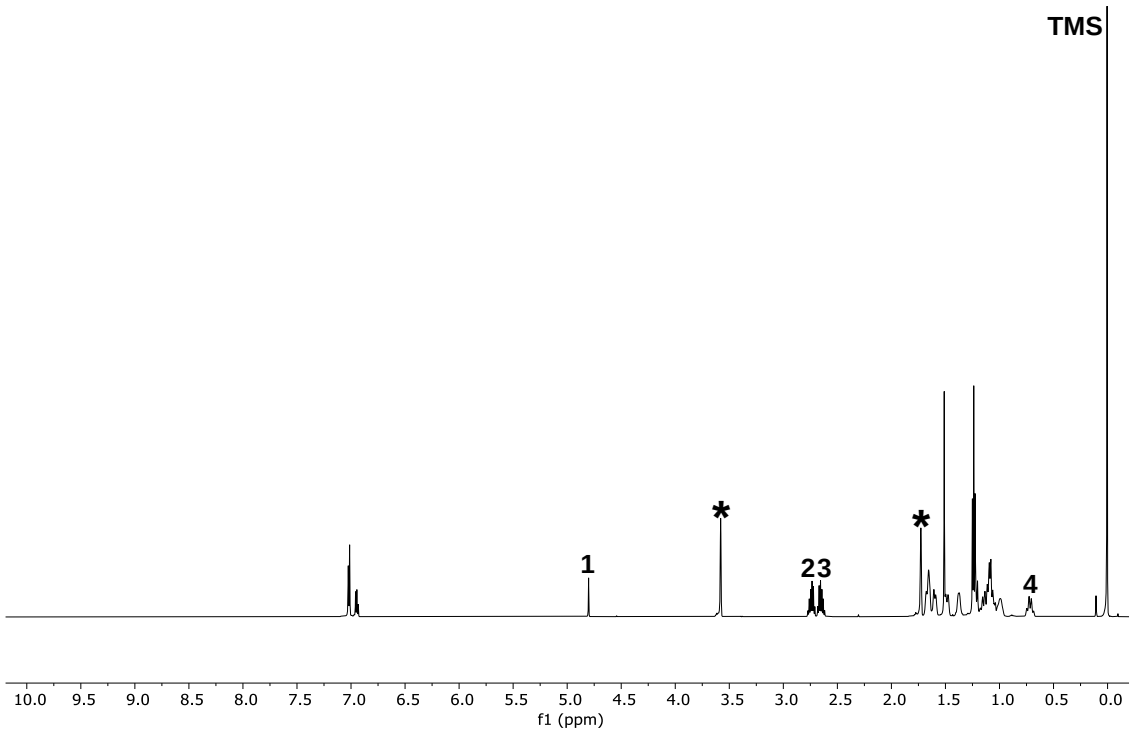

Figure S10. ^{1}H NMR spectrum of [(^{Dep}nacnac)Mg][CoH_4(dcpe)] (**1**) and TMS (600.13 MHz, 298 K, THF-d_8), showing the signals 1-4 used for the DOSY analysis. *: THF-d_8.

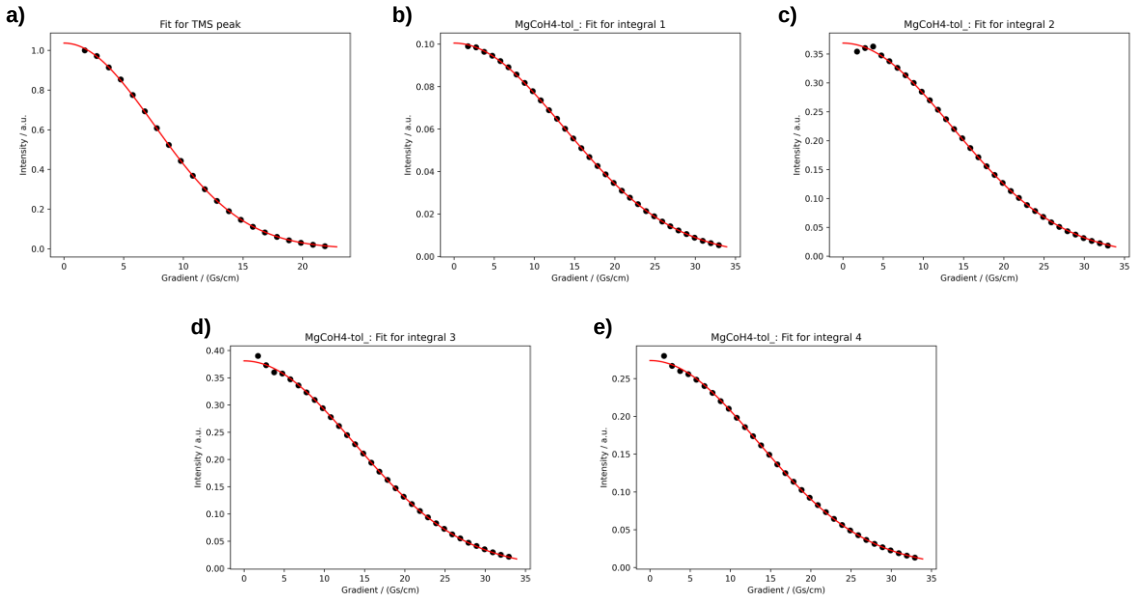

Figure S11. DOSY plots (signal intensity against gradient strength) of TMS and the signals 1-4 of [(^{Dep}nacnac)Mg][CoH_4(dcpe)] (**1**) in toluene-d_8.

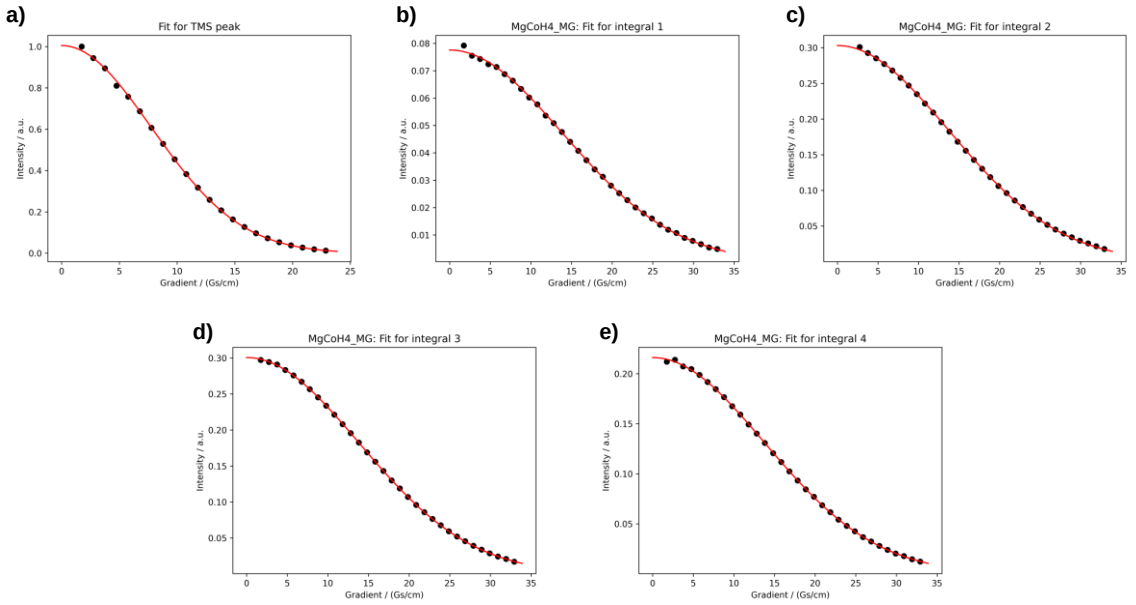

Figure S12. DOSY plots (signal intensity against gradient strength) of TMS and the signals 1-4 of [(^{Dep}nacnac)Mg][CoH_4(dcpe)] (**1**) in THF-d_8.

Table S3. Self-diffusion coefficients of signals 1-4 of [(^{Dep}nacnac)Mg][CoH_4(dcpe)] (**1**) in toluene-d_8 and THF-d_8. Signals 1-3 belong to the [(^{Dep}nacnac)Mg]$^+$ unit and signal 4 belongs to the [CoH_4(dcpe)]$^-$ unit.

Signal	Chemical shift [ppm]	Diffusion coefficient D_i [$m^2 \cdot s^{-1}$]
	Toluene	
/	TMS	2.2e-09 ± 7.45e-12
1	5.03-5.01	6.6973e-10 ± 1e-12
2	3.00-2.92	6.7657e-10 ± 1.22e-12
3	2.83-2.75	6.6749e-10 ± 3.65e-12
4	0.96-0.86	6.8442e-10 ± 1.19e-12
Mean diffusion coefficient D (**1**-**4**) [$m^2 \cdot s^{-1}$]		6.75e-10 ± 1.19e-12
Average radius r_H [Å]		6.554 ± 0.06091
Average volume V_H[a] [Å^3]		1.179e+03 ± 32.88
	THF	
/	TMS	2.37e-09 ± 2.01e-11
1	4.93-4.89	7.3522e-10 ± 3.7e-12
2	2.89-2.80	7.5426e-10 ± 2.26e-12
3	2.80-2.70	7.4774e-10 ± 9.12e-13
4	0.87-0.77	7.5256e-10 ± 1.92e-12
Mean diffusion coefficient D (**1**-**4**) [$m^2 \cdot s^{-1}$]		7.47e-10 ± 1.92e-12
Average radius r_H [Å]		6.548 ± 0.0629
Average volume V_H[a] [Å^3]		1.176e+03 ± 33.89

[a] The average volume V_H was calculated assuming a spherical shape.

4.4.7 Reactivity Study of [(^{Dep}nacnac)Mg][(μ,η^4:η^4-P_4)Co(dcpe)] (5)

[(^{Dep}nacnac)Mg][(μ,η^4:η^4-P_4)Co(dcpe)] (**5**) was either reacted as an isolated solid or a solution of [(^{Dep}nacnac)Mg][CoH_4(dcpe)] (**1**; 1.0 equiv.) and P_4 (1.1 equiv.) in toluene was stirred at ambient temperature for 24 h, after which the *in situ* generated [(^{Dep}nacnac)Mg][(μ,η^4:η^4-P_4)Co(dcpe)] (**5**) was reacted with a selected reagent (Scheme S3).

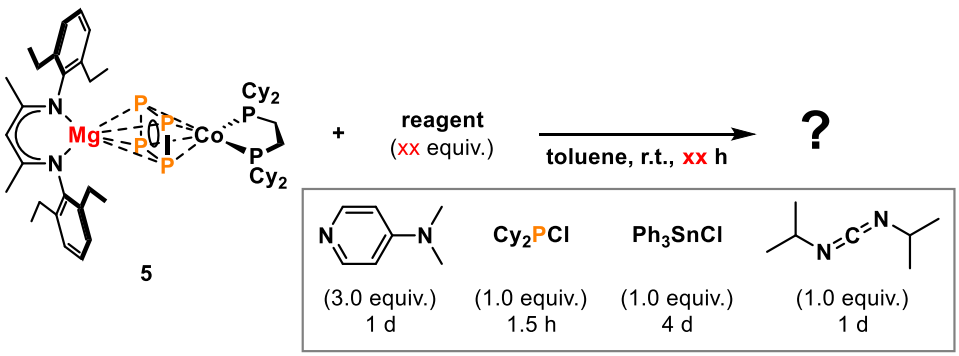

Scheme S3. Reaction of [(^{Dep}nacnac)Mg][(μ,η^4:η^4-P_4)Co(dcpe)] (**5**) with different small molecules.

4.4.7.1 Reaction with 4-(Dimethylamino)pyridine (DMAP)

[(Depnacnac)Mg][(μ,η⁴:η⁴-P₄)Co(dcpe)] (**5**; 10.0 mg, 10.1 μmol, 1.0 equiv.) was reacted with 4-(dimethylamino)pyridine (3.7 mg, 30.3 μmol, 3.0 equiv.) at ambient temperature for 1 d, resulting in a modest color change to dark yellow-to-brown. $^{31}P\{^{1}H\}$ NMR spectroscopic analysis of the reaction solution indicated selective formation of a new species (Figure S13). The mixture was evaporated to dryness, the residue redissolved in toluene/*n*-hexane (1:2 *v*/*v*, 1.5 mL), filtered and cooled to −35 °C for crystallization. Small amounts of orange-to-brown plates formed, which confirmed the formation of [(Depnacnac)Mg(DMAP)₃][(η⁴-P₄)Co(dcpe)] (**7**) in a "What is this?" experiment (Table S5). Unfortunately, poor crystal quality prevented further SC-XRD analysis.

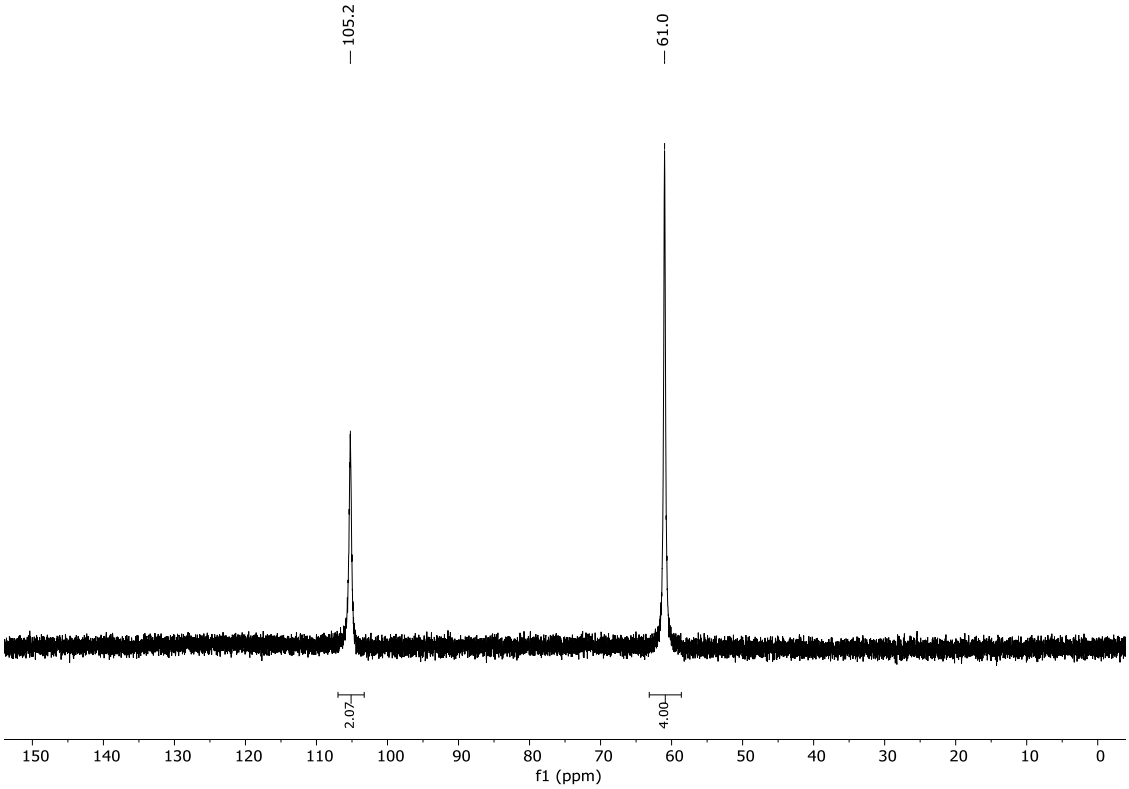

Figure S13. $^{31}P\{^{1}H\}$ NMR spectrum (202.46 MHz, 298 K, toluene-d_8) of the reaction of [(Depnacnac)Mg][(μ,η⁴:η⁴-P₄)Co(dcpe)] (**5**) with DMAP after reacting at ambient temperature for 1 d.

4.4.7.2 Reaction with Cy_2PCl

[(Depnacnac)Mg][(μ,η⁴:η⁴-P₄)Co(dcpe)] (**5**; 57.4 μmol, 1.0 equiv.; from 50.0 mg of **1**) was reacted with dicyclohexylchlorophosphine (12.7 μL, 57.4 μmol, 1.0 equiv.) at ambient temperature for 1.5 h. An immediate color change to deep yellow-to-brown was observed. $^{31}P\{^{1}H\}$ NMR spectroscopic analysis of a reaction aliquot indicated selective formation of [(η⁴-P_5Cy_2)Co(dcpe)] (**8**)[29],[33] by elimination of "(Depnacnac)MgCl" (Figure S14). The mixture was evaporated to dryness, the residue washed with *n*-hexane (2.0 mL), and then redissolved in toluene/*n*-hexane (1:1 *v*/*v*, 4.0 mL). Both solutions were cooled to −35 °C for crystallization. In each case, small amounts of a brownish precipitate were formed but were

accompanied by the formation of colorless crystals of [(Depnacnac)MgCl]$_2$. However, clean isolation of **8** and separation of the product mixture were unsuccessful.

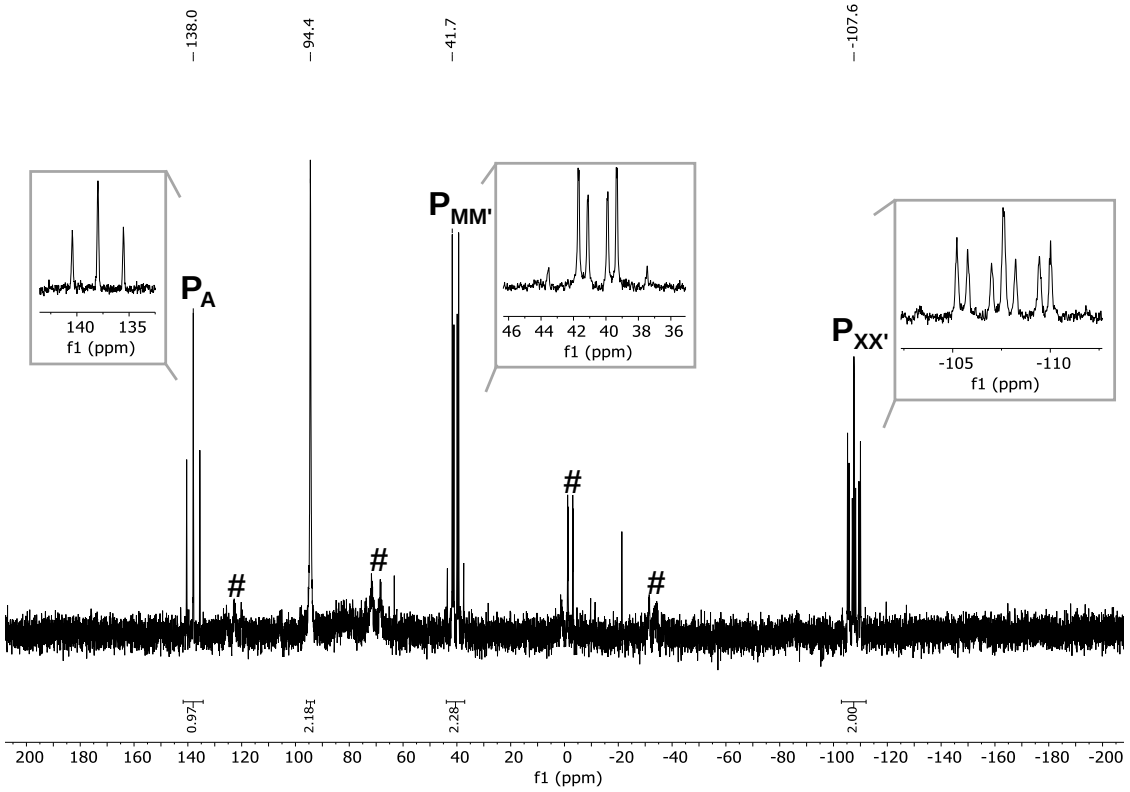

Figure S14. $^{31}P\{^1H\}$ NMR spectrum (161.98 MHz, 298 K, C_6D_6 capillary) of the reaction of [(Depnacnac)Mg][(μ,η^4:η^4-P$_4$)Co(dcpe)] (**5**) with Cy_2PCl after stirring at ambient temperature for 1.5 h. #: unidentified side product.

4.4.7.3 Reaction with Ph_3SnCl

[(Depnacnac)Mg][(μ,η^4:η^4-P$_4$)Co(dcpe)] (**5**; 17.2 μmol, 1.0 equiv.; from 15.0 mg of **1**) was reacted with triphenyltin chloride (6.6 mg, 17.1 μmol, 1.0 equiv.) at ambient temperature for 4 d. A color change to deep yellow-to-brown was observed within 1 h. $^{31}P\{^1H\}$ NMR spectroscopic analysis of the reaction solution indicated unselective reaction of **5** with Ph_3SnCl (Figure S15). The mixture was evaporated to dryness, the residue redissolved in toluene/*n*-pentane (1:1 *v*/*v*, 1.0 mL), filtered and cooled to –35 °C for crystallization. No crystallization was observed. Multiple signals between 250.0 and –50.0 ppm indicate the formation of several reaction products, which likely feature P/Sn cage motifs.[43] The absence of a $^{31}P\{^1H\}$ NMR signal for free dcpe suggests that the "Co(dcpe)" motif of **5** remains intact, although the identification of any reaction product by crystallization was not successful.

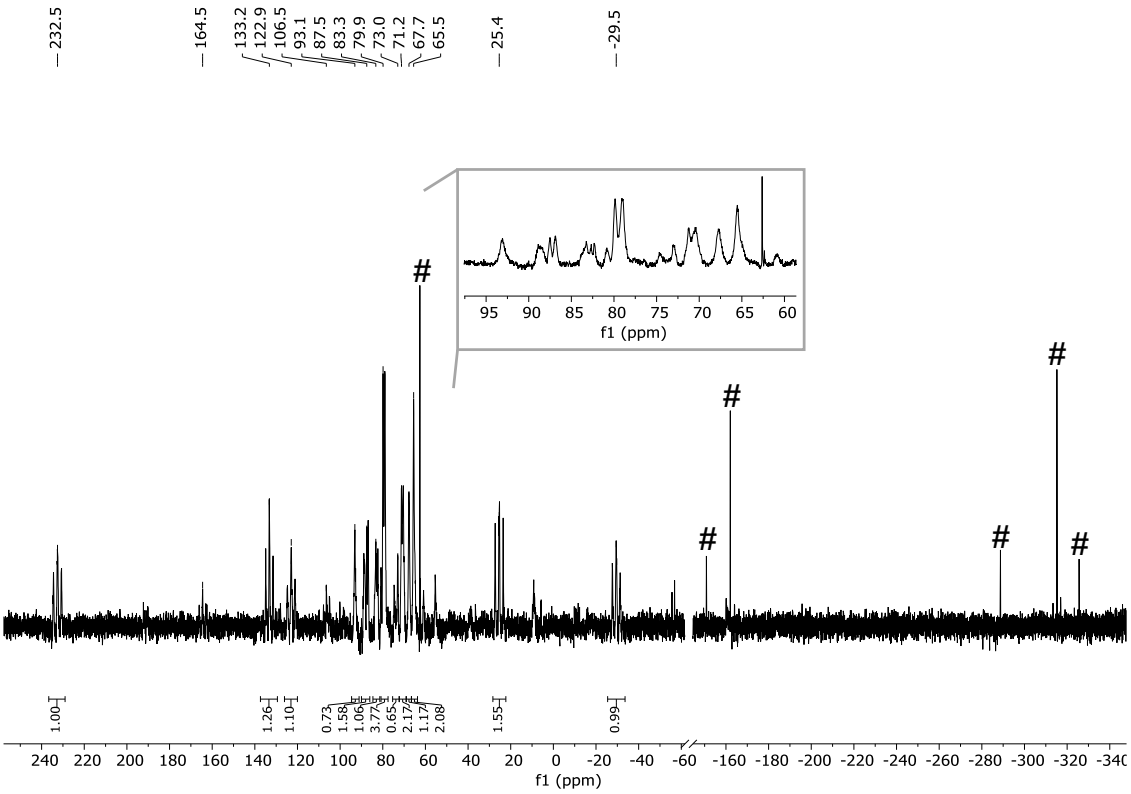

Figure S15. $^{31}P\{^{1}H\}$ NMR spectrum (202.46 MHz, 298 K, C_6D_6 capillary) of the reaction of [(^{Dep}nacnac)Mg][(μ,η⁴:η⁴-P_4)Co(dcpe)] (**5**) with Ph_3SnCl after reacting at ambient temperature for 4 d. #: additional side products.

4.4.7.4 Reaction with *N,N'*-Diisopropylcarbodiimide (DIC)

[(^{Dep}nacnac)Mg][(μ,η⁴:η⁴-P_4)Co(dcpe)] (**5**; 57.4 μmol, 1.0 equiv.; from 50.0 mg of **1**) was reacted with *N,N'*-diisopropylcarbodiimide (8.9 μL, 57.4 μmol, 1.0 equiv.) at ambient temperature for 1 d, with no visible color change. ^{31}P NMR spectroscopic analysis of a reaction aliquot indicated selective conversion to a new species (Figure S16, left).

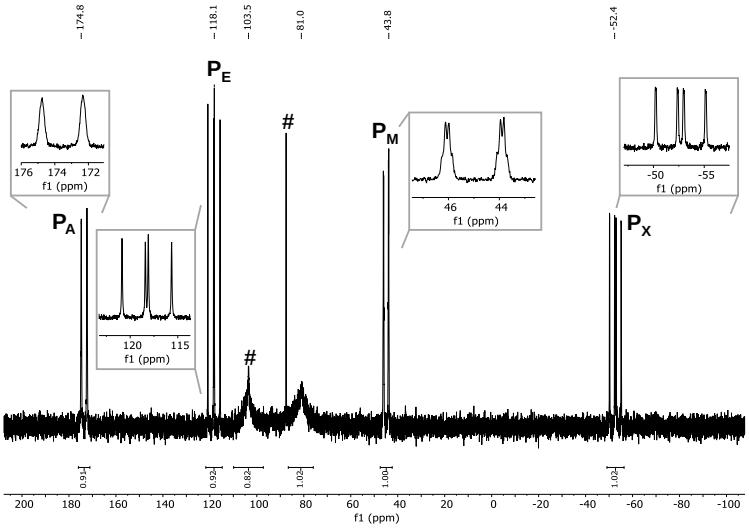

^{31}P NMR shifts and coupling constants

	Δ [ppm]	$^{n}J_{PP}$ [Hz]
P_A	174.8	390
P_E	118.1	447, 390
P_M	43.8	350, 20
P_X	–52.4	447, 350, 12

proposed structure

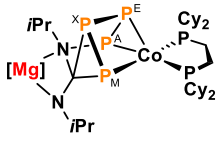

([**Mg**] = (^{Dep}nacnac)Mg)

9 (proposed)

Figure S16. Left: ^{31}P NMR spectrum (161.98 MHz, 298 K, C_6D_6 capillary) of the reaction of [(^{Dep}nacnac)Mg][(μ,η⁴:η⁴-P_4)Co(dcpe)] (**5**) with DIC after stirring at ambient temperature for 2 d. *: unreacted **5**. Right: ^{31}P NMR shifts and coupling constants and proposed product structure.

The mixture was evaporated to dryness, the residue redissolved in *n*-pentane (1.0 mL) and cooled to –35 °C for crystallization. Small amounts of a brownish precipitate formed but were not suitable for SC-XRD analysis. Further attempts to isolate and clearly assign the structure of the reaction product were unsuccessful.

The signal pattern in the ^{31}P NMR spectrum suggests the formation of a coordination complex featuring a phosphorus chain (Figure S16, right). A bimetallic magnesium cobalt complex is likely formed by insertion of the carbodiimide into the *cyclo*-P_4 motif. A structural model **9** is proposed, based on the similarity of the observed AEMX spin system of the P_4 core in the ^{31}P NMR spectrum with reported complexes.[30],[34a],[44]

4.4.8 NMR Spectroscopic Data

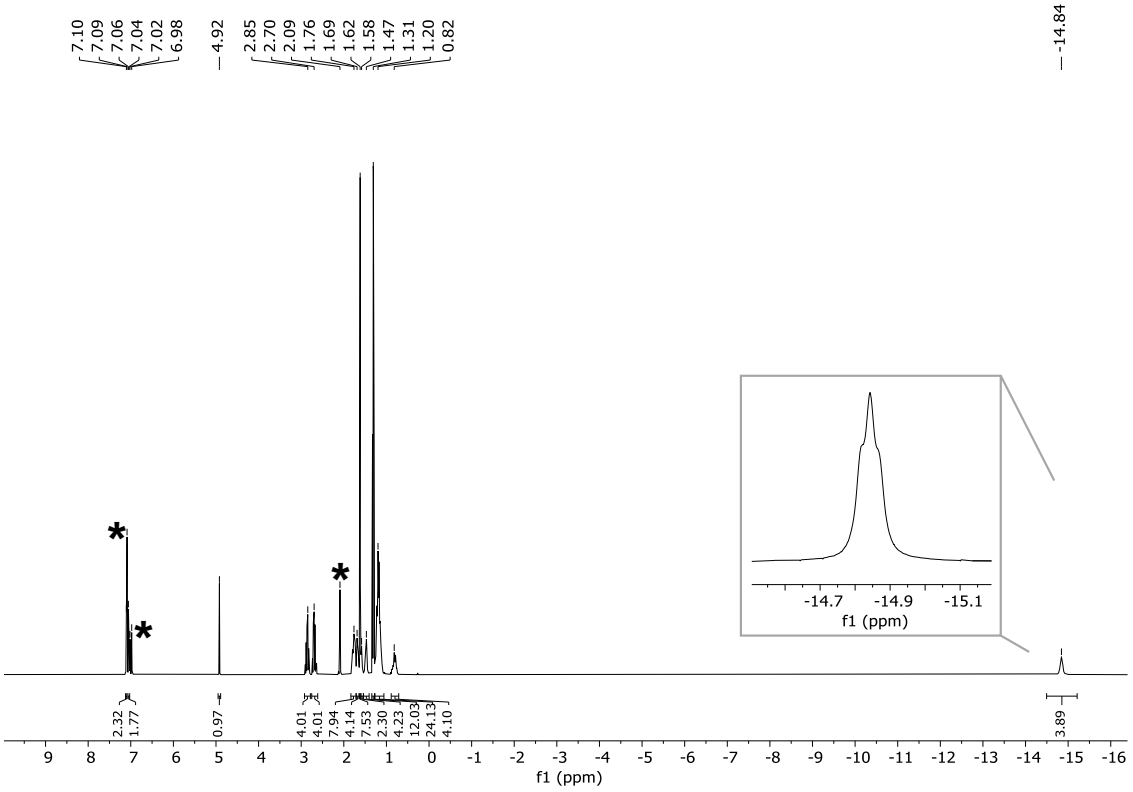

Figure S17. ^{1}H NMR spectrum (400.13 MHz, 298 K, toluene-d_8) of [(^{Dep}nacnac)Mg][CoH_4(dcpe)] (**1**). *: toluene-d_8.

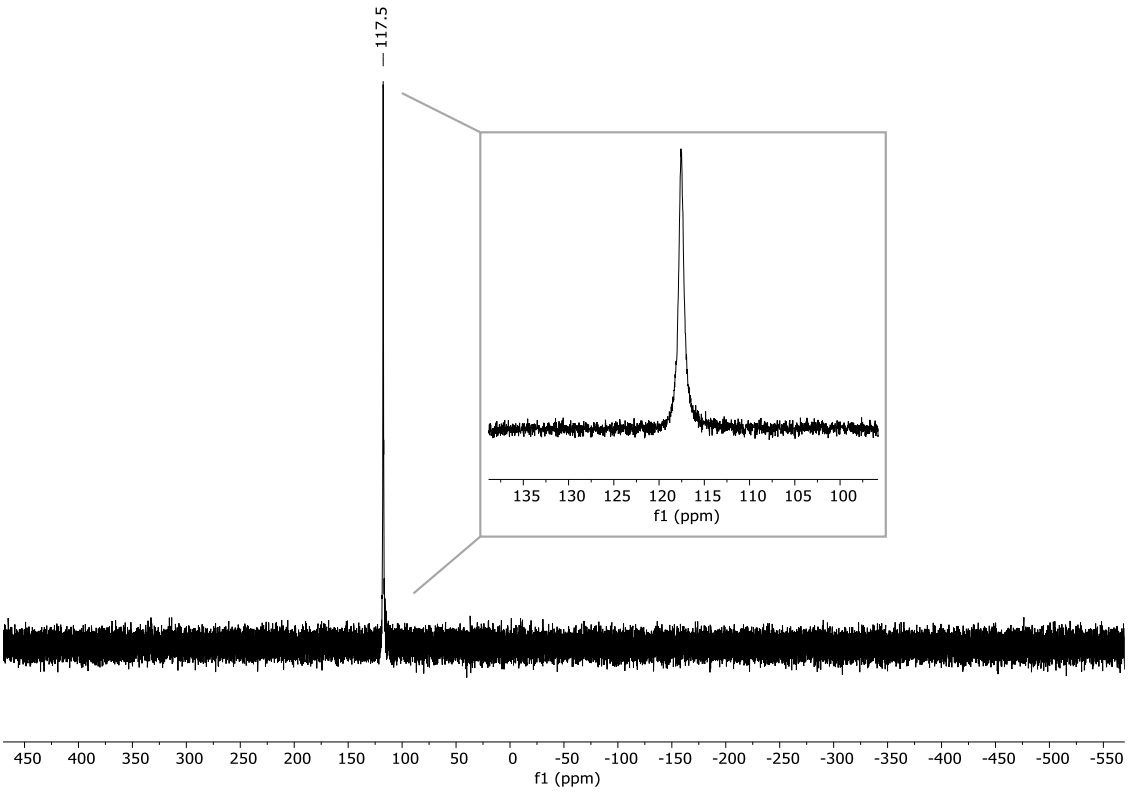

Figure S18. ^{31}P{^{1}H} NMR spectrum (161.98 MHz, 298 K, toluene-d_8) of [(^{Dep}nacnac)Mg][CoH_4(dcpe)] (**1**).

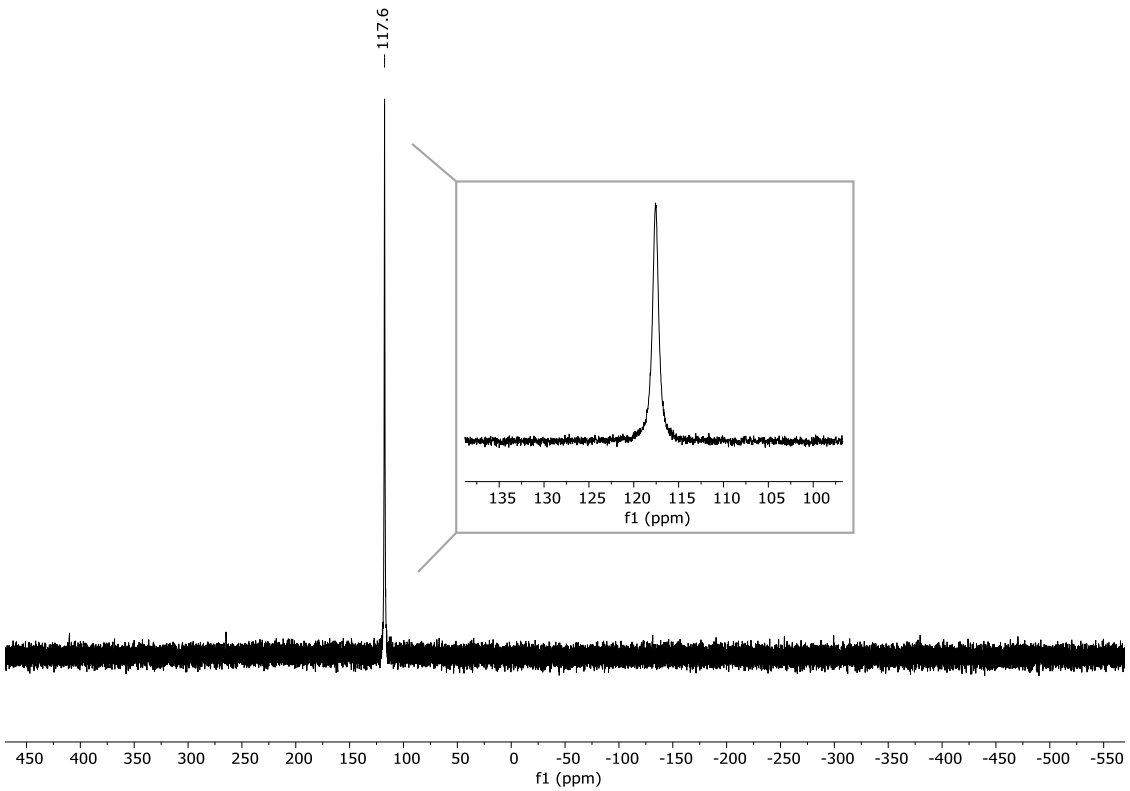

Figure S19. ^{31}P NMR spectrum (161.98 MHz, 298 K, toluene-d_8) of [(^{Dep}nacnac)Mg][CoH_4(dcpe)] (**1**).

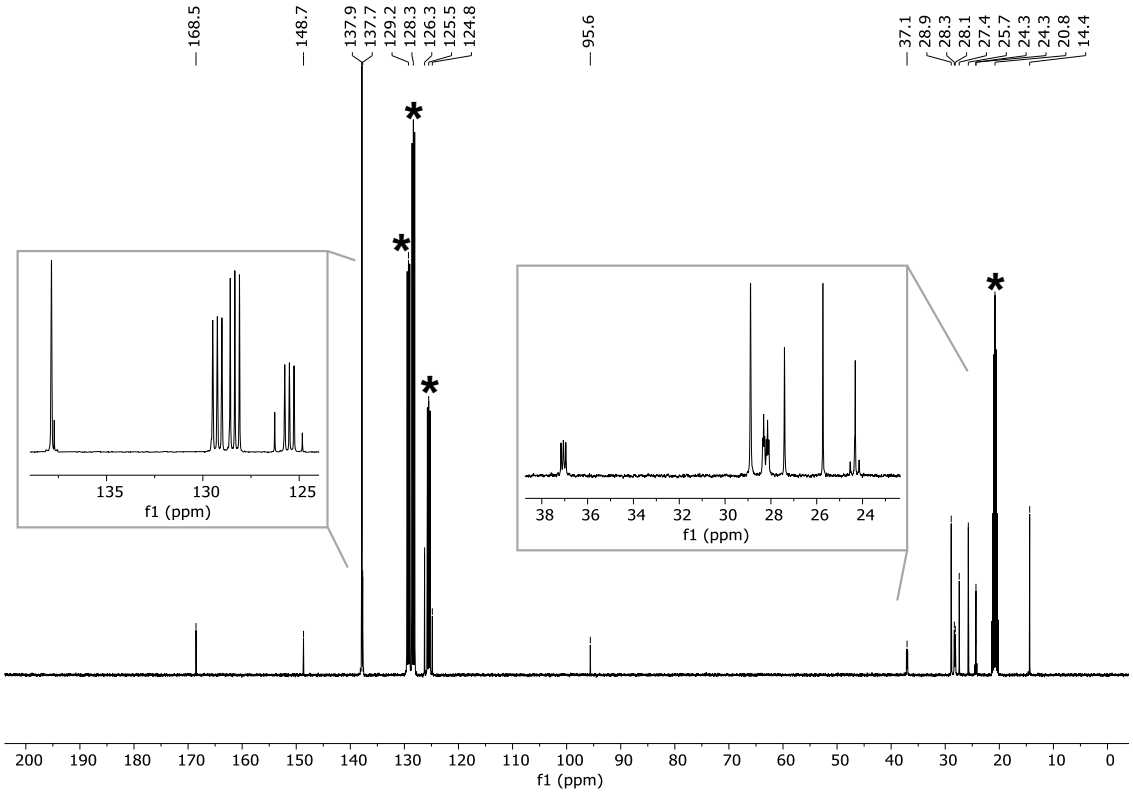

Figure S20. $^{13}C\{^1H\}$ NMR spectrum (100.61 MHz, 298 K, toluene-d_8) of [(^{Dep}nacnac)Mg][CoH_4(dcpe)] (**1**). *: toluene-d_8.

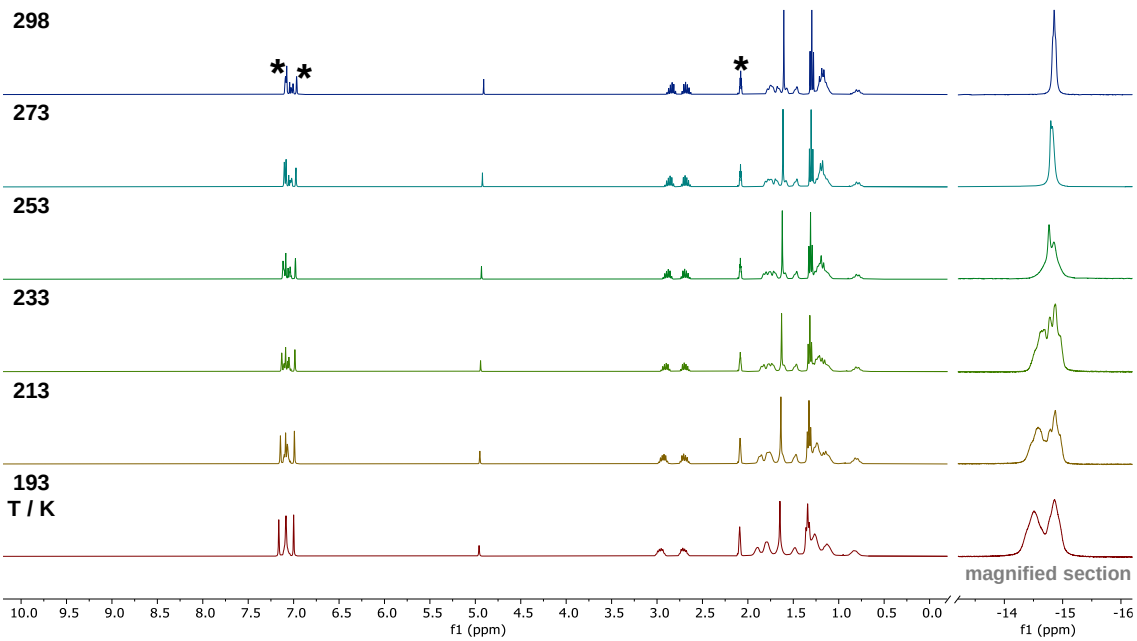

Figure S21. Variable-temperature ^{1}H NMR spectrum (400.13 MHz, 298-193 K, toluene-d$_8$) of [(^{Dep}nacnac)Mg][CoH$_4$(dcpe)] (**1**) showing the hydride shift region as a separately magnified section. *: toluene-d$_8$.

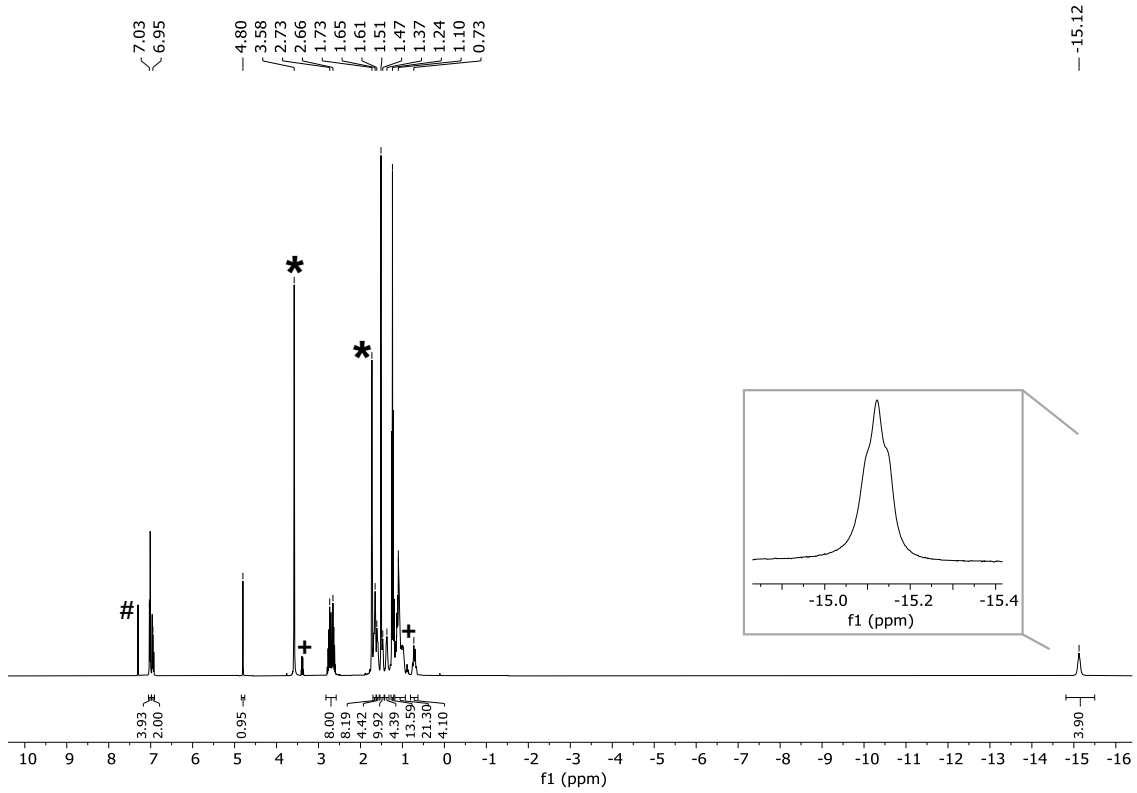

Figure S22. ^{1}H NMR spectrum (400.13 MHz, 298 K, THF-d$_8$) of [(^{Dep}nacnac)Mg][CoH$_4$(dcpe)] (**1**). *: THF-d$_8$. #: benzene. +: Et$_2$O.

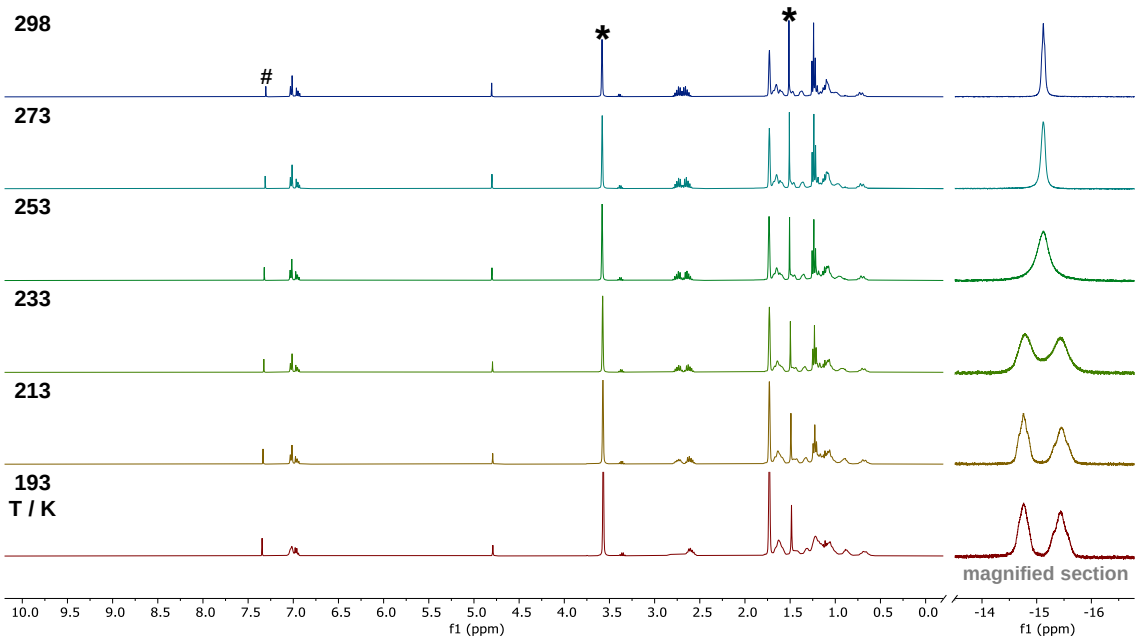

Figure S23. Variable-temperature ^{1}H NMR spectrum (400.13 MHz, 298-193 K, THF-d_8) of [(^{Dep}nacnac)Mg][CoH_4(dcpe)] (**1**) showing the hydride shift region as a separately magnified section. *: THF-d_8. #: benzene.

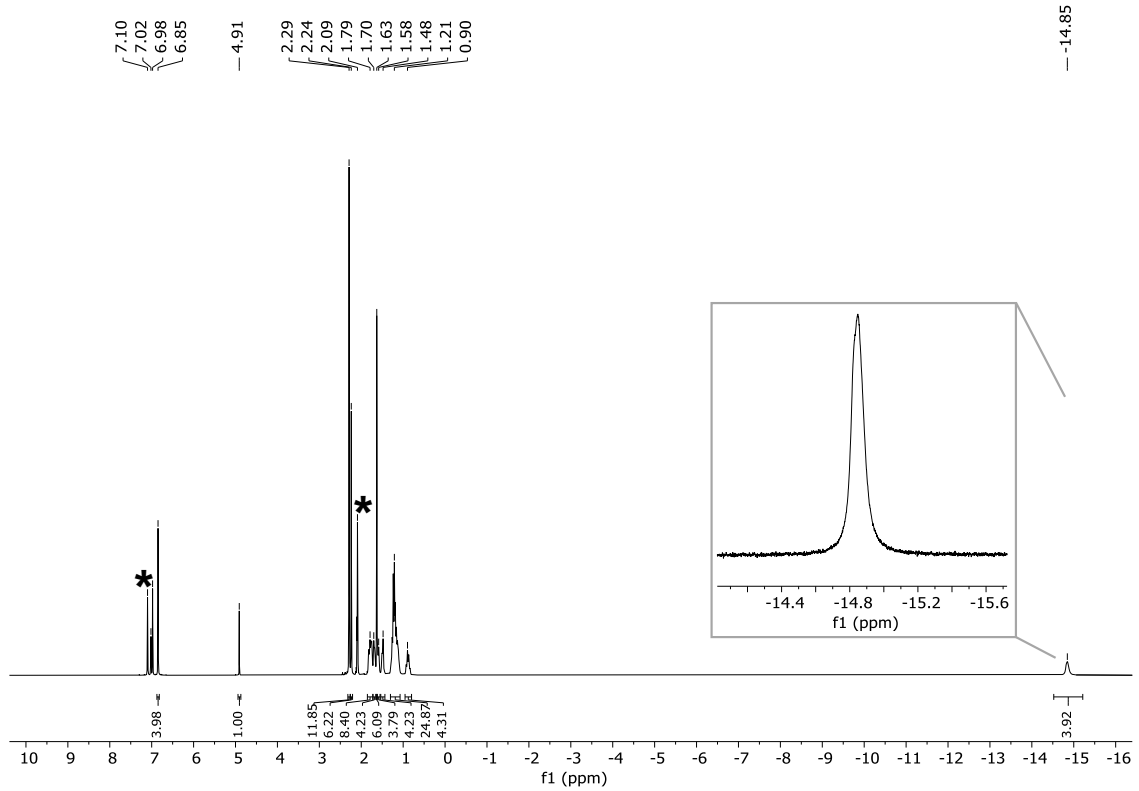

Figure S24. ^{1}H NMR spectrum (400.13 MHz, 298 K, toluene-d_8) of [(^{Mes}nacnac)Mg][CoH_4(dcpe)] (**2**). *: toluene-d_8.

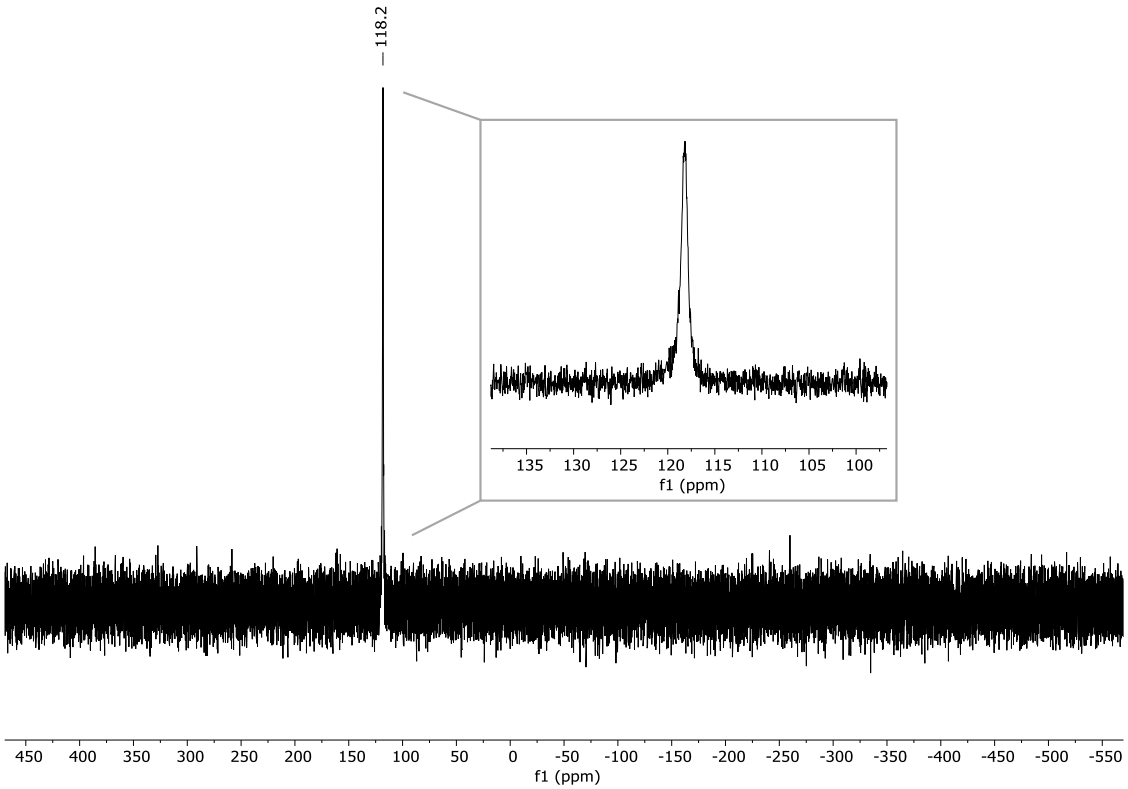

Figure S25. $^{31}P\{^{1}H\}$ NMR spectrum (161.98 MHz, 298 K, toluene-d_8) of [(^{Mes}nacnac)Mg][CoH_4(dcpe)] (**2**).

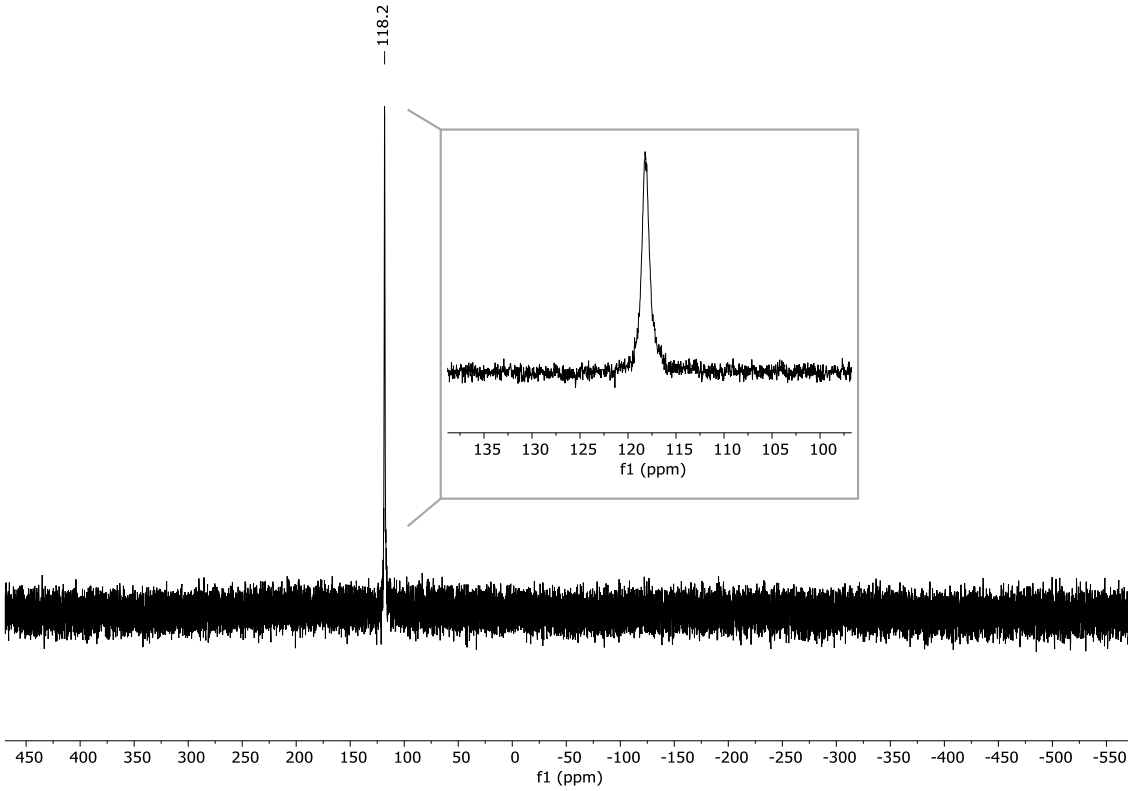

Figure S26. ^{31}P NMR spectrum (161.98 MHz, 298 K, toluene-d_8) of [(^{Mes}nacnac)Mg][CoH_4(dcpe)] (**2**).

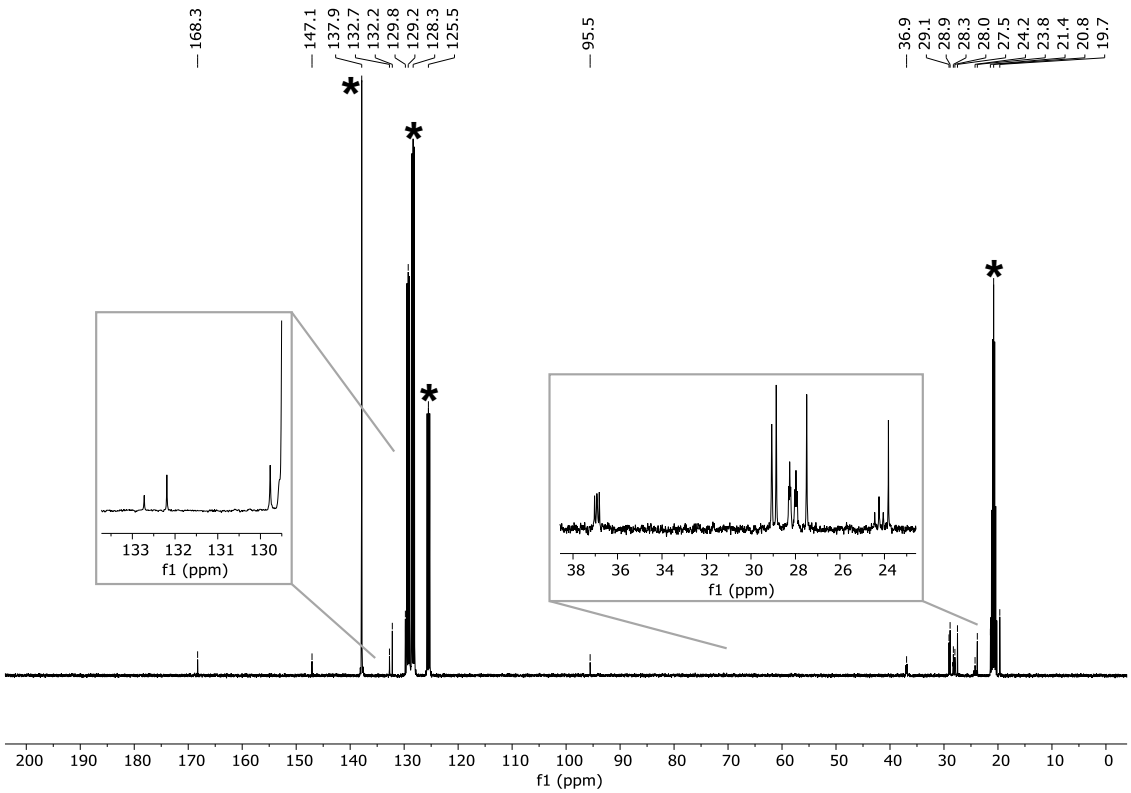

Figure S27. $^{13}C\{^{1}H\}$ NMR spectrum (100.61 MHz, 298 K, toluene-d_8) of [(^{Mes}nacnac)Mg][CoH_4(dcpe)] (**2**). *: toluene-d_8.

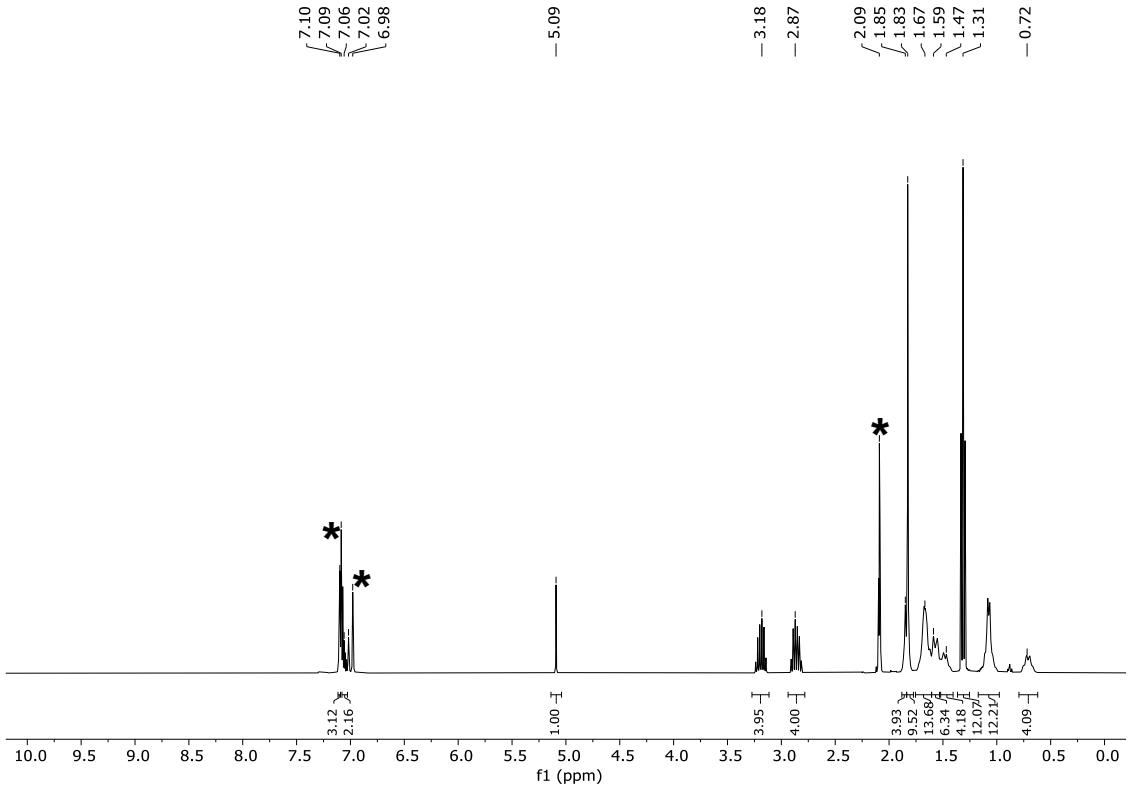

Figure S28. ^{1}H NMR spectrum (400.13 MHz, 298 K, toluene-d_8) of [(^{Dep}nacnac)Mg][(μ,η^4:η^4-P_4)Co(dcpe)] (**5**). *: toluene-d_8.

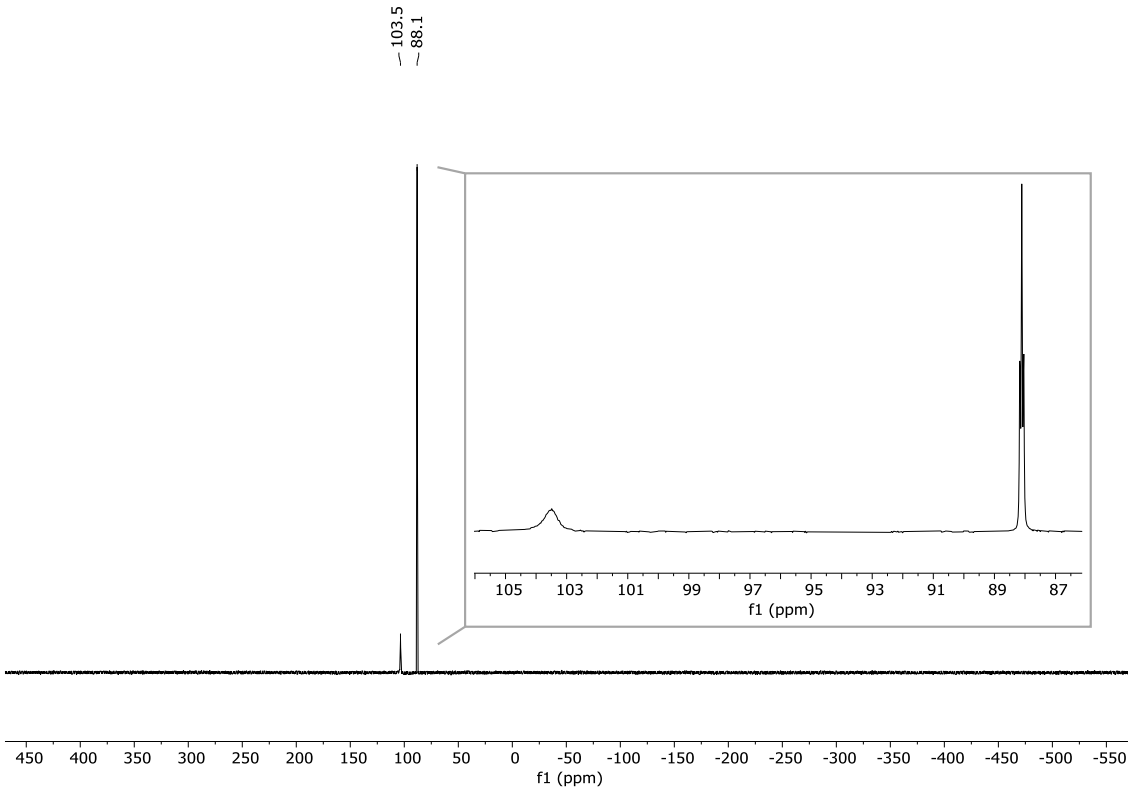

Figure S29. $^{31}P\{^{1}H\}$ NMR spectrum (161.98 MHz, 298 K, toluene-d_8) of [(^{Dep}nacnac)Mg][(μ,η⁴:η⁴-P_4)Co(dcpe)] (**5**).

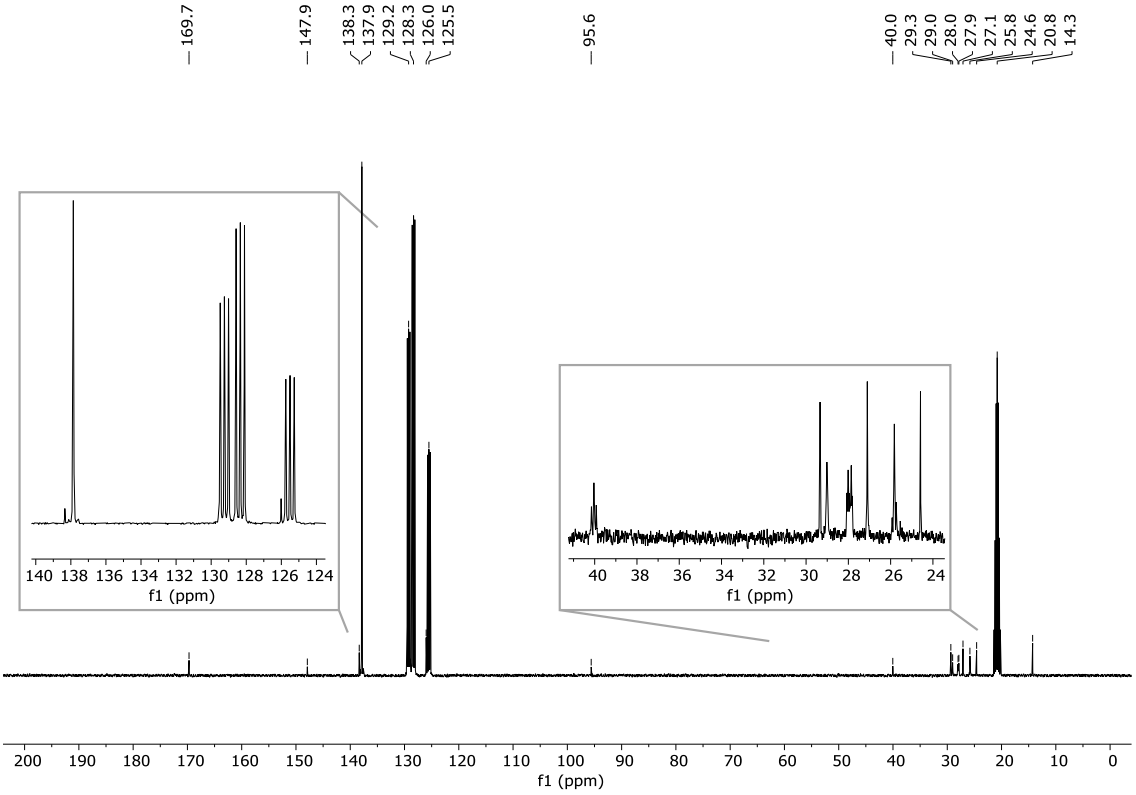

Figure S30. $^{13}C\{^{1}H\}$ NMR spectrum (100.61 MHz, 298 K, toluene-d_8) of [(^{Dep}nacnac)Mg][(μ,η⁴:η⁴-P_4)Co(dcpe)] (**5**). *: toluene-d_8.

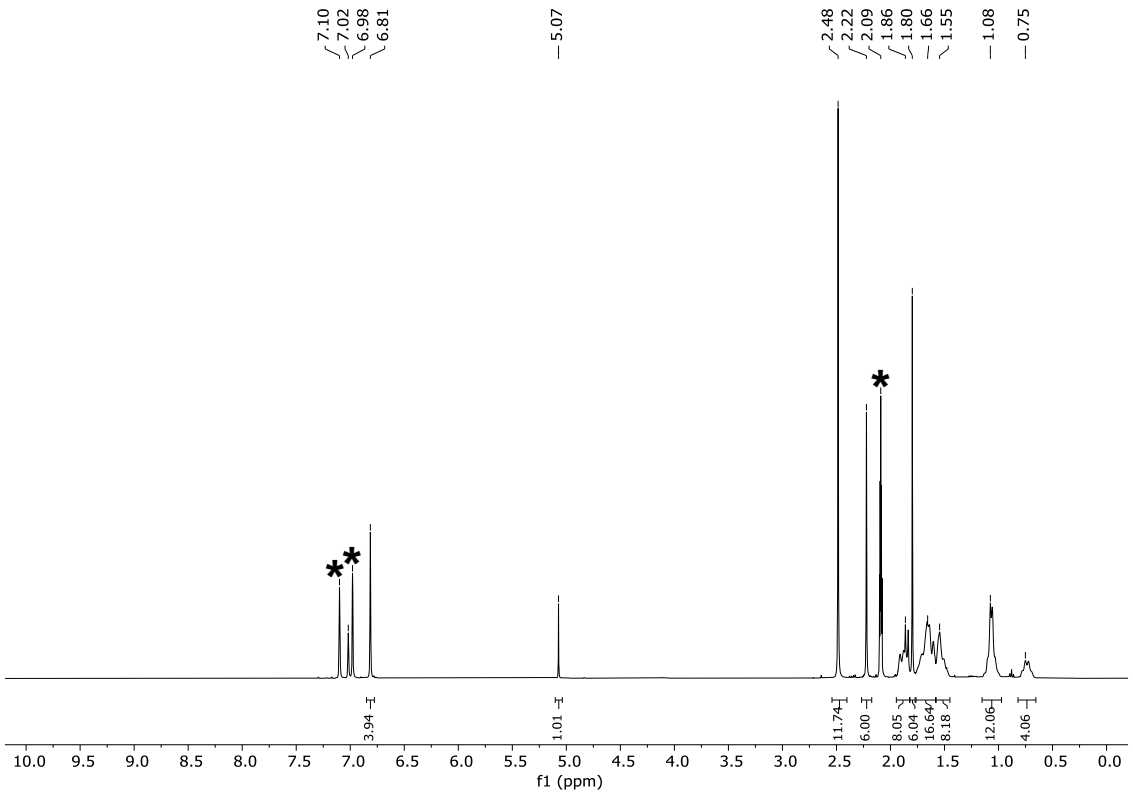

Figure S31. ^{1}H NMR spectrum (400.13 MHz, 298 K, toluene-d$_8$) of [(^{Mes}nacnac)Mg][(μ,η^4:η^4-P$_4$)Co(dcpe)] (**6**). *: toluene-d$_8$.

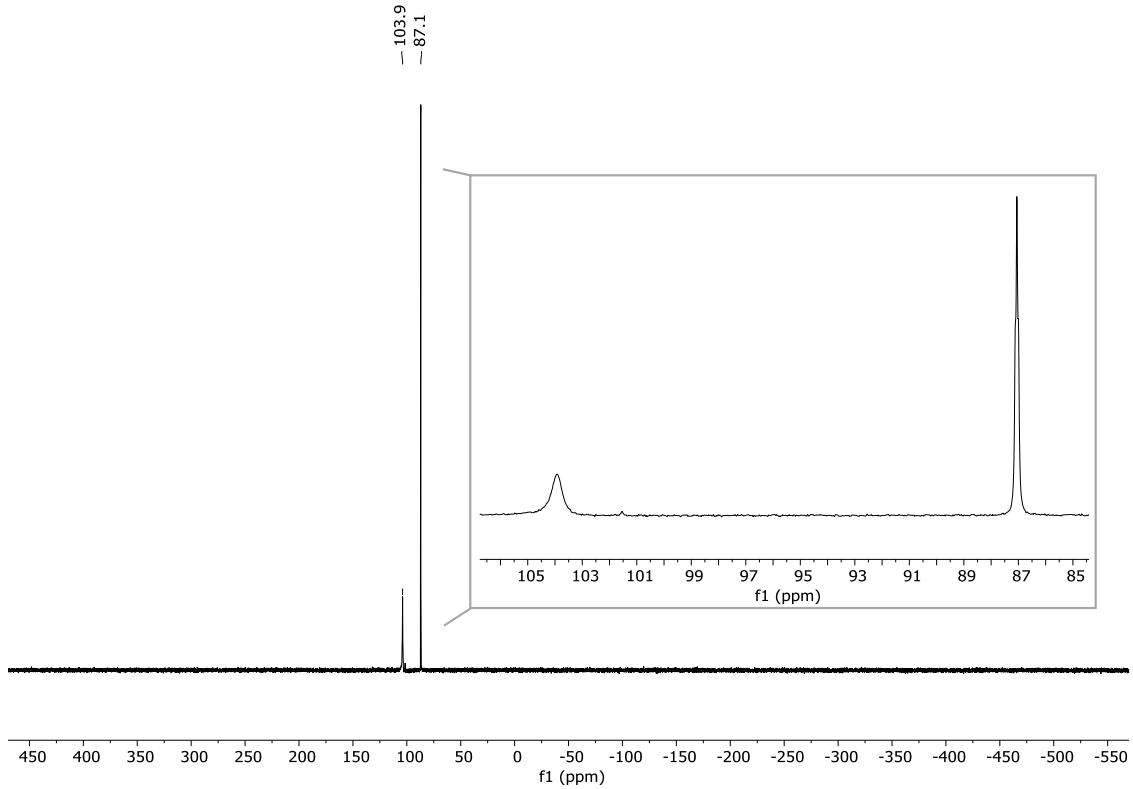

Figure S32. ^{31}P{^{1}H} NMR spectrum (161.98 MHz, 298 K, toluene-d$_8$) of [(^{Mes}nacnac)Mg][(μ,η^4:η^4-P$_4$)Co(dcpe)] (**6**).

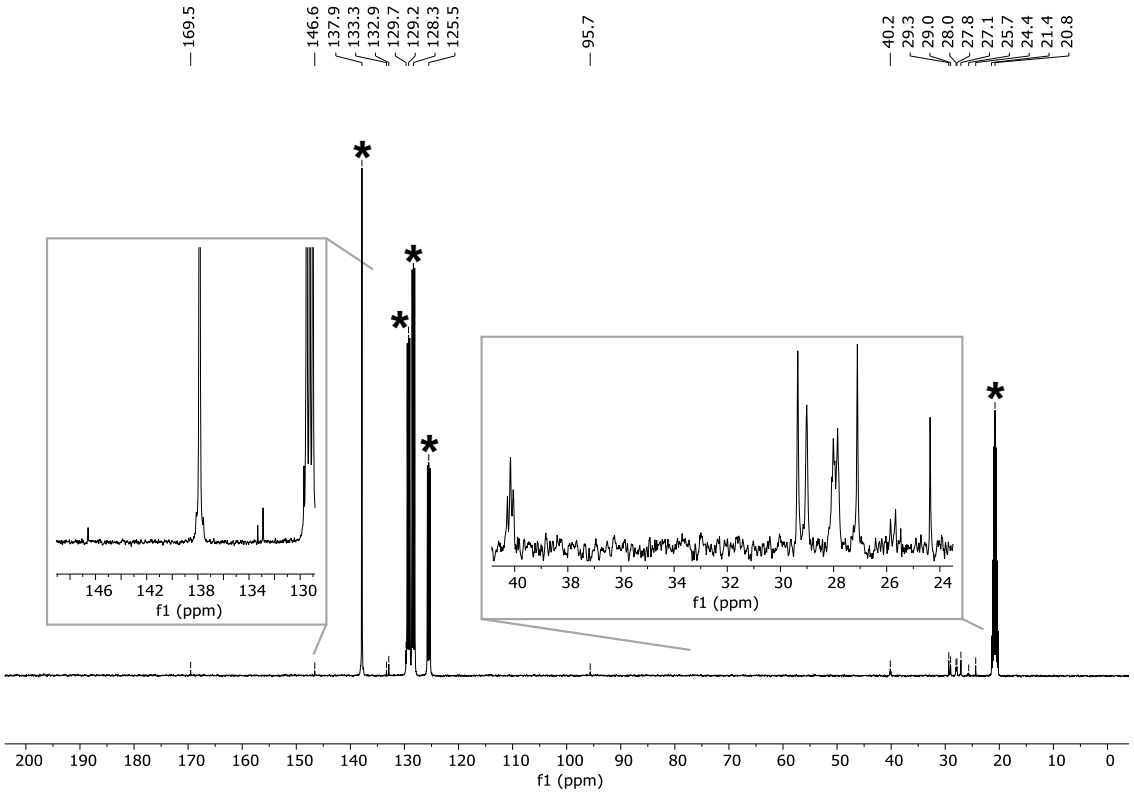

Figure S33. $^{13}C\{^{1}H\}$ NMR spectrum (100.61 MHz, 298 K, toluene-d_8) of [(^{Mes}nacnac)Mg][(μ,η^4:η^4-P_4)Co(dcpe)] (**6**). *: toluene-d_8.

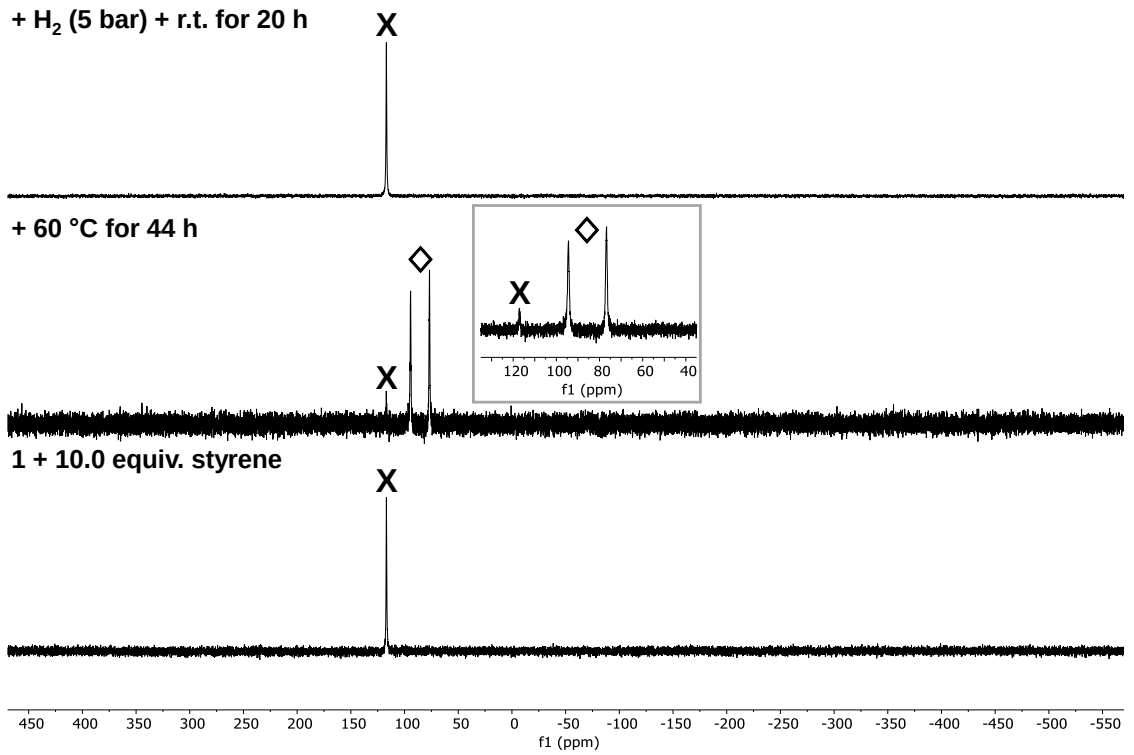

Figure S34. $^{31}P\{^{1}H\}$ NMR spectra (161.98 MHz, 298 K, toluene-d_8) of the reaction of **1** with styrene (10.0 equiv.) and subsequent H_2 exposure in toluene-d_8. X: **1**. ◇: proposed styrene complex.

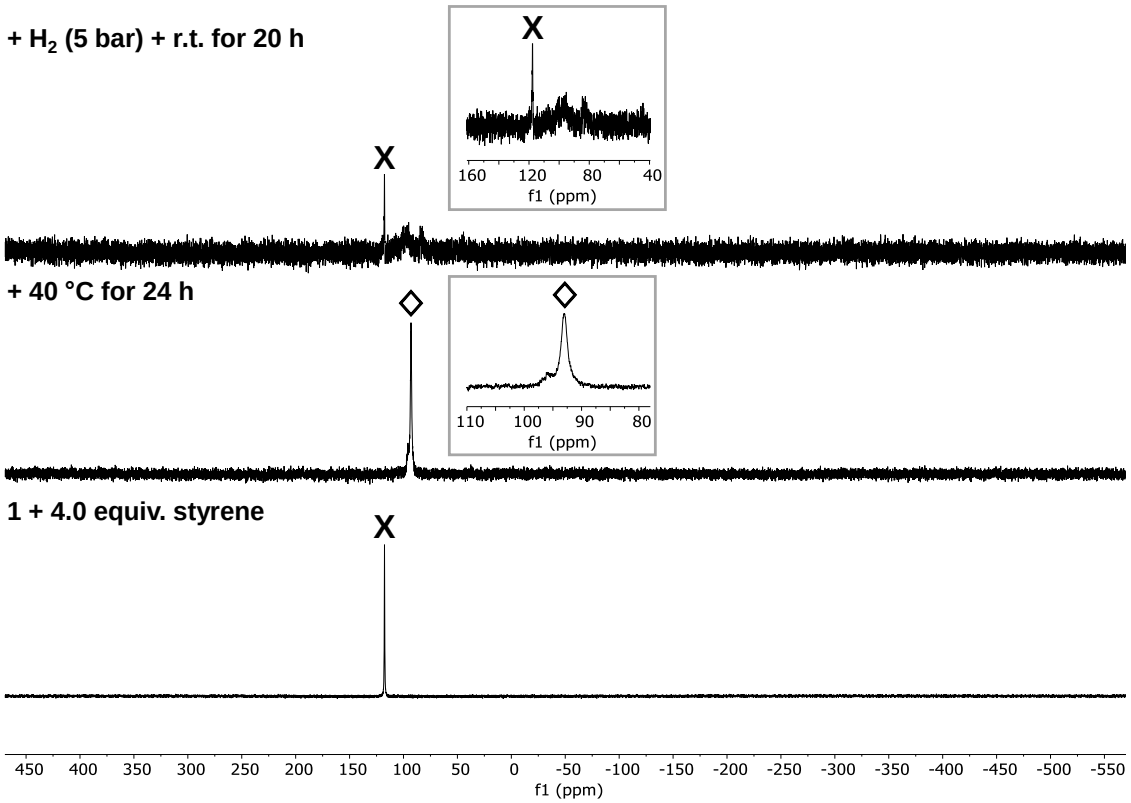

Figure S35. $^{31}P\{^{1}H\}$ NMR spectra (161.98 MHz, 298 K, THF-d_8) of the reaction of **1** with styrene (10.0 equiv.) and subsequent H_2 exposure in THF-d_8. X: **1**. ◇: proposed alkene complex.

4.4.9 IR Spectroscopic Data

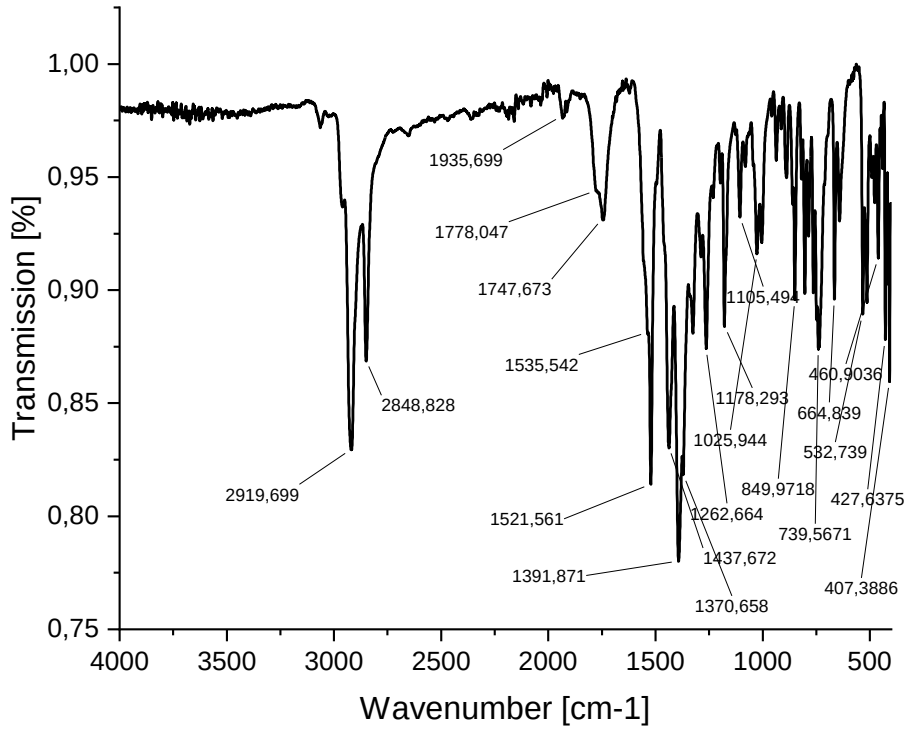

Figure S36. Solid-state ATR-IR spectrum of [(^{Dep}nacnac)Mg][CoH_4(dcpe)] (**1**).

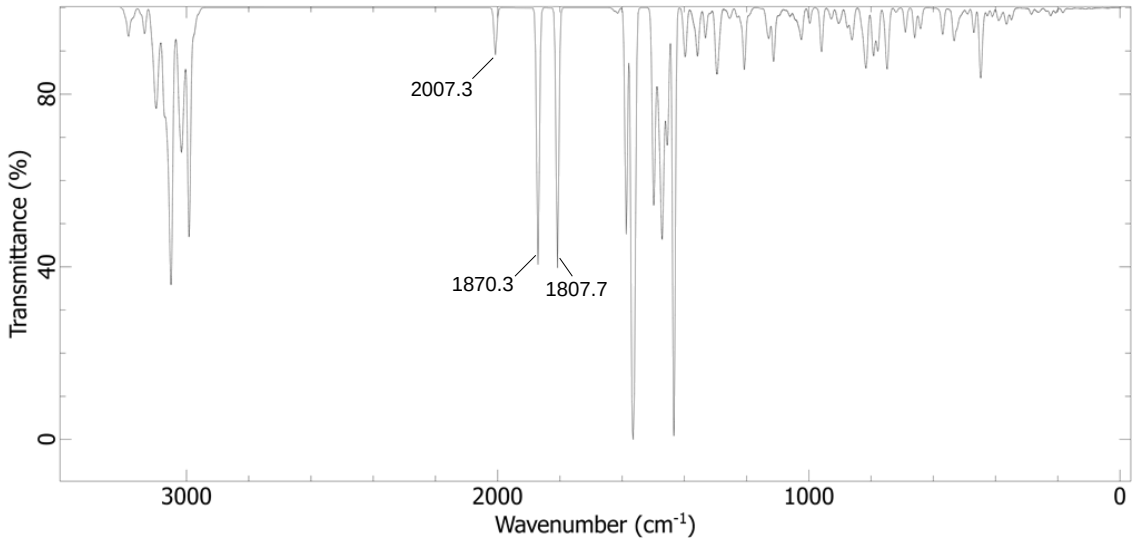

Figure S37. DFT calculated IR spectrum of [(^{Dep}nacnac)Mg][CoH_4(dcpe)] (**1**) at the r^{2}SCAN-3c level of theory. Absorption bands at 2007.3, 1870.3, and 1807.7 cm^{-1} correspond to Co–H vibrations.

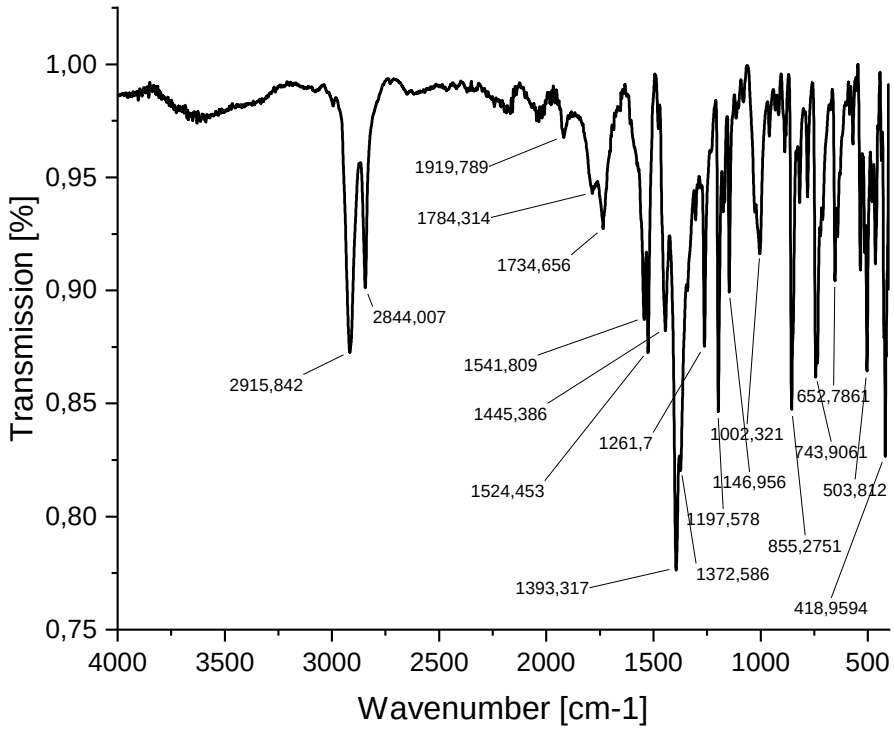

Figure S38. Solid-state ATR-IR spectrum of [(^{Mes}nacnac)Mg][CoH_4(dcpe)] (**2**).

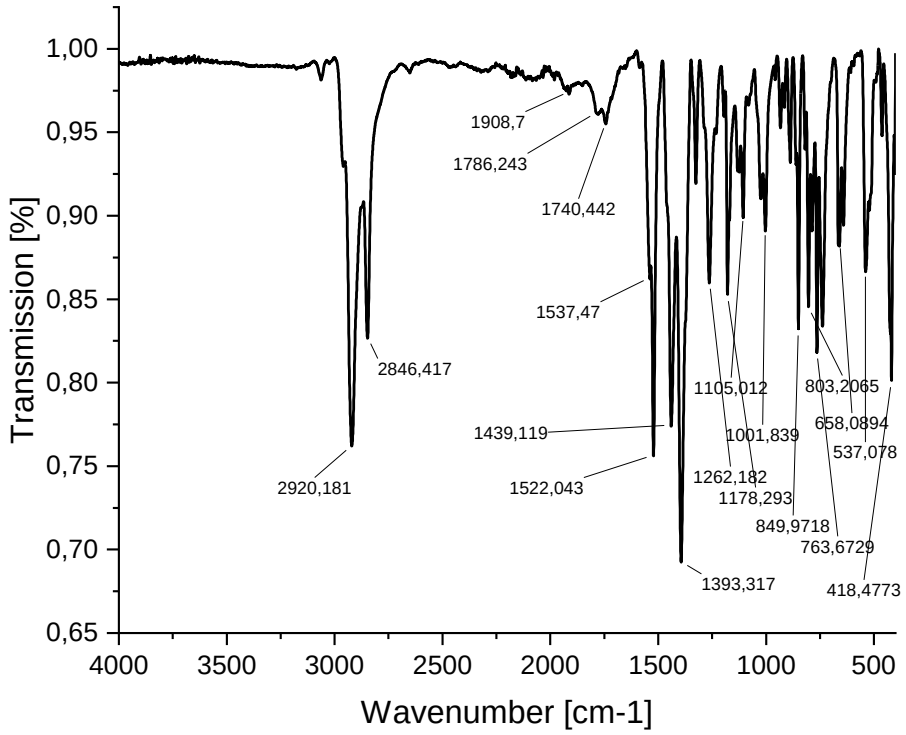

Figure S39. Solid-state ATR-IR spectrum of [(^{Dep}nacnac)Mg][CoD_4(dcpe)] (**1-D**); 83% deuterium incorporation according to ^{1}H NMR analysis.

4.4.10 Single Crystal X-ray Diffraction Data

The single-crystal X-ray diffraction data were recorded on Rigaku Synergy DW or GV1000 Titan^{S2} diffractometers with Cu-K_α radiation (λ= 1.54184 Å). Crystals were selected under mineral oil, mounted on micromount loops and quench-cooled using an Oxford Cryosystems open flow N_2 cooling device. Either semi-empirical multi-scan absorption correction[45] or analytical ones[46] were applied to the data. The structures were solved with SHELXT[47] solution program using dual methods and by using Olex2 as the graphical interface.[48] The models were refined with ShelXL[47] using full matrix least squares minimization on F^2.[49] The hydrogen atoms were located in idealized positions and refined isotropically with a riding model. A distance restraint (DFIX) was used to adequately model the Co1–H4 bond in the solid-state molecular structure of [(^{Dep}nacnac)Mg][CoH_4(dcpe)] (**1**).

Table S4. Crystallographic data and structure refinement for compounds [(^{Ar}nacnac)Mg][CoH_4(dcpe)] (Ar = Dep, **1**; Ar = Mes, **2**) and [(^{Dep}nacnac)Mg(thf)][CoH_4(dcpe)] (**4**).

Compound	**1**	**2**	**4**
Empirical formula	$C_{51}H_{85}CoMgN_2P_2$	$C_{49}H_{81}CoMgN_2P_2$	$C_{110}H_{186}Co_2Mg_2N_4O_2P_4$
Formula weight	871.38	843.33	1886.98
Temperature/K	100(1)	123(1)	123(1)
Crystal system	monoclinic	orthorhombic	triclinic
Space group	$P2_1/c$	$Fdd2$	P-1
a/Å	18.2180(2)	44.1761(2)	12.4693(2)
b/Å	10.83380(10)	34.47260(10)	21.6585(3)
c/Å	25.5588(2)	12.66360(10)	22.9140(4)
α/°	90	90	62.622(2)
β/°	106.6310(10)	90	77.6140(10)
γ/°	90	90	79.4390(10)
Volume/Å^3	4833.52(8)	19284.95(18)	5341.64(17)
Z	4	16	2
ρ_{calc}/cm^3	1.197	1.162	1.173
μ/mm^{-1}	3.787	3.781	3.476
F(000)	1896	7328	2056
Crystal size/mm^3	0.112 × 0.06 × 0.035	0.176 × 0.079 × 0.067	0.281 × 0.173 × 0.128
Radiation	Cu Kα (λ = 1.54184)	Cu Kα (λ = 1.54184)	Cu Kα (λ = 1.54184)
2Θ range for data collection/°	5.062 to 150.554	6.504 to 149.948	7.294 to 133.952
Index ranges	-22 ≤ h ≤ 22, -13 ≤ k ≤ 13, -31 ≤ l ≤ 30	-53 ≤ h ≤ 55, -43 ≤ k ≤ 42, -13 ≤ l ≤ 15	-14 ≤ h ≤ 14, -25 ≤ k ≤ 25, -27 ≤ l ≤ 27
Reflections collected	84427	75777	101126
Independent reflections	9915 [R_{int} = 0.0343, R_{sigma} = 0.0217]	8440 [R_{int} = 0.0251, R_{sigma} = 0.0145]	18922 [R_{int} = 0.0703, R_{sigma} = 0.0402]
Data/restraints/parameters	9915/1/536	8440/1/520	18922/0/1161
Goodness-of-fit on F^2	1.093	1.03	1.022
Final R indexes [I>=2σ (I)]	R_1 = 0.0396, wR_2 = 0.1071	R_1 = 0.0231, wR_2 = 0.0595	R_1 = 0.0480, wR_2 = 0.1243
Final R indexes [all data]	R_1 = 0.0436, wR_2 = 0.1098	R_1 = 0.0240, wR_2 = 0.0601	R_1 = 0.0535, wR_2 = 0.1294
Largest diff. peak/hole / e Å^{-3}	1.04/-0.34	0.24/-0.18	0.71/-0.41
Flack parameter	/	-0.0249(11)	/

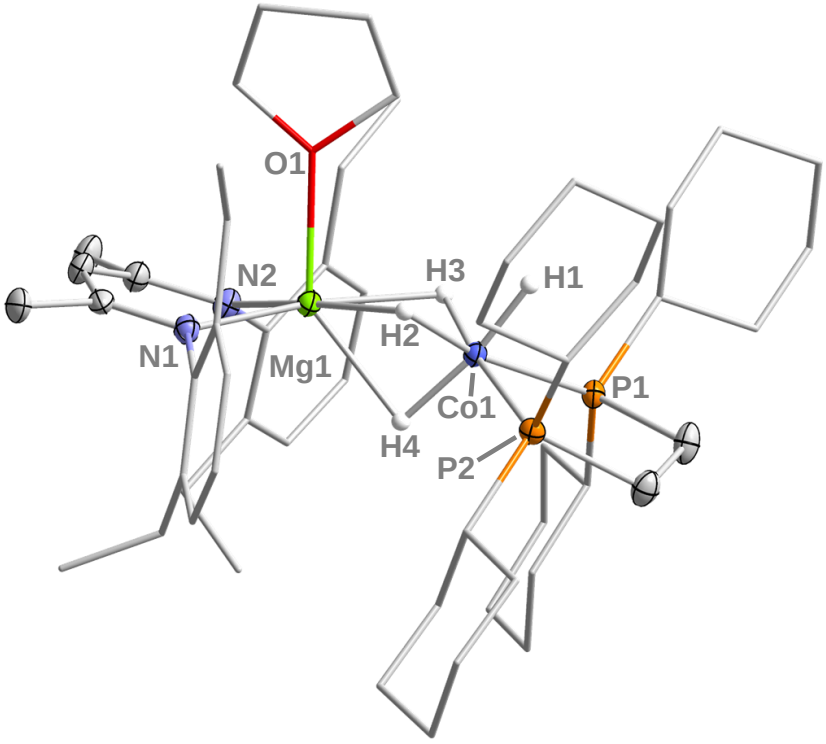

Figure S40. Solid-state molecular structure of [(^{Dep}nacnac)Mg(thf)][CoH_4(dcpe)] (**4**). Thermal ellipsoids are drawn at 40% probability level. H atoms are omitted for clarity except for the hydrides (H1-H4) between Co1 and Mg1. The asymmetric unit of **4** contains two molecules, one of which is displayed. Selected bond lengths [Å] and angles [°]: Mg1–Co1 2.490(6) Å, Co1–H1 1.303(3) Å, Co1–H2 1.463(2) Å, Co1–H3 1.448(2) Å, Co1–H4 1.472(4) Å, Mg1–O1 2.168(3) Å, Mg1–H2 1.890(5) Å, Mg1–H3 2.011(4) Å, Mg1–H4 2.107(4) Å, Co1–P1 2.137(6) Å, Co1–P2 2.136(6) Å, Mg1–N1 2.094(2) Å, Mg1–N2 2.086(2) Å, H1–Co1–H4 170.30(3), H2–Co1–H3 89.95(1), H2–Mg1–H3 63.58(2), P1–Co1–P2 90.69(2), N1–Mg1–N2 89.41(8).

Table S5. Crystallographic data and structure refinement for compounds [(^{Ar}nacnac)Mg]-[(μ,η^4:η^4-P_4)Co(dcpe)] (Ar = Dep, **5**; Ar = Mes, **6**) and [(^{Dep}nacnac)Mg(DMAP)$_3$][(η^4-P_4)Co(dcpe)] (**7**).

Compound	**5**	**6**	**7** (WIT experiment)
Empirical formula	$C_{51}H_{81}CoMgN_2P_6$	$C_{58}H_{86}CoMgN_2P_6$	$C_{72}H_{111}CoMgN_8P_6\cdot(C_7H_8)$
Formula weight	991.23	1080.34	1449.87
Temperature/K	123(1)	123(1)	123(1)
Crystal system	monoclinic	triclinic	triclinic
Space group	$P2_1/c$	P-1	P-1
a/Å	13.94350(10)	11.75190(10)	10.89904(11)
b/Å	14.12540(10)	13.71020(10)	13.64478(16)
c/Å	26.6583(2)	19.1055(2)	28.5968(3)
α/°	90	83.7010(10)	90.4419(9)
β/°	98.2800(10)	81.7700(10)	98.2194(9)
γ/°	90	77.3350(10)	110.3030(10)
Volume/Å^3	5195.82(7)	2962.67(5)	3940.04(8)
Z	4	2	2
ρ_{calc}g/cm^3	1.267	1.211	/
μ/mm^{-1}	4.717	4.179	/
F(000)	2120	1154	/
Crystal size/mm^3	0.121 × 0.1 × 0.031	0.116 × 0.049 × 0.035	/
Radiation	Cu Kα (λ = 1.54184)	Cu Kα (λ = 1.54184)	Cu Kα (λ = 1.54184)
2Θ range for data collection/°	6.702 to 150.184	4.688 to 148.604	/
Index ranges	-17 ≤ h ≤ 16, -16 ≤ k ≤ 17, -32 ≤ l ≤ 33	-14 ≤ h ≤ 14, -17 ≤ k ≤ 16, -23 ≤ l ≤ 23	/
Reflections collected	64096	52180	/
Independent reflections	10569 [R_{int} = 0.0417, R_{sigma} = 0.0274]	11922 [R_{int} = 0.0336, R_{sigma} = 0.0249]	/
Data/restraints/parameters	10569/0/560	11922/0/540	/
Goodness-of-fit on F^2	1.094	1.096	/
Final R indexes [I>=2σ (I)]	R_1 = 0.0546, wR_2 = 0.1399	R_1 = 0.0321, wR_2 = 0.0882	/
Final R indexes [all data]	R_1 = 0.0596, wR_2 = 0.1421	R_1 = 0.0342, wR_2 = 0.0894	/
Largest diff. peak/hole / e Å^{-3}	0.67/-0.43	0.32/-0.23	/
Flack parameter	/	/	/

4.4.11 Computational Studies

All calculations were carried out with the ORCA 5.03 and 5.0.4 quantum chemistry package.[50] Geometry optimizations were performed at the r²SCAN-3c[51] level of theory in the gas phase. Stationary points were confirmed as local minima (no imaginary frequencies) by frequency analysis. Single point energy calculations were performed on the fully optimized geometries (r²SCAN-3c) and the electron densities calculated at the ωB97X-D4/def2-TZVP[52] level of theory. Further molecular properties were analyzed using natural bond orbital (NBO 7.0) analyses,[52] IBO analyses (IboView[54] and NCI analyses[55] (multiwfn 3.8[56]) for non-covalent interactions. Shown iso-surfaces were plotted with VMD 1.9.3.[57] Calculated IR Spectra were rendered using the software Avogadro.[58] Table S6 compares the experimental geometry of [(Depnacnac)Mg][CoH₄(dcpe)] (**1**) in the solid state with the computed geometry, obtained at the r²SCAN-3c level of theory.

Table S6. Comparison of structural parameters of [(Depnacnac)Mg][CoH₄(dcpe)] (**1**): experimental vs. computational data.

Bond distance [Å] or angle [°]	X-ray Structure	Computed structure	Atom numbers (from DFT)
$Co^1–H^{1[a]}$	1.517(1)	1.480	
$Co^1–H^2/H^3/H^4$	1.511(1)/1.503(2)/ 1.458(1)	1.517/1.525/1.584	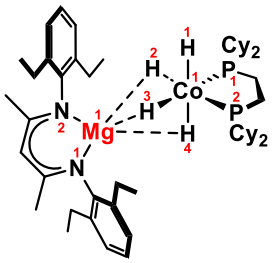
$Mg^1–H^2/H^3/H^4$	2.021(2)/1.876(1)/ 2.055(3)	2.054/2.010/1.965	
$Co^1–P^1/P^2$	2.144(3)/2.145(2)	2.148/2.145	
$H^1–Co^1–H^4$	83.14(1)	90.5	
$H^2–Mg^4–H^3$	61.67(6)	64.2	
$Mg^1–N^1/N^2$	2.060(2)/2.053(2)	2.053/2.055	

4.4.11.1 NBO Analysis of [(Depnacnac)Mg][CoH₄(dcpe)] (1)

The main findings from NBO analysis of **1** are depicted in Table S7. No Lewis or non-Lewis shared orbitals between the magnesium and cobalt centres are found, and the second order perturbation theory analysis shows that the donor–acceptor interaction between an electron lone pair of Co and a vacant or Rydberg orbital of Mg is negligibly small (<1 kcal mol⁻¹). Significant donor–acceptor interactions are found between the bridging H atoms (H2-H4) and Mg (21.0-33.6 kcal mol⁻¹).

Table S7. NBO data for [(Depnacnac)Mg][CoH_4(dcpe)] (**1**).

NPA Charges		Wiberg bond indices	
Co^1	–0.45	Co^1–Mg^1	0.043
Mg^1	1.73	Co^1–H^1 / H^2 / H^3 / H^4	0.421 / 0.438 / 0.435 / 0.316
P^1 / P^2	1.19 / 1.20	Mg^1–H^2 / H^3 / H^4	0.057 / 0.064 / 0.091
H^1 / H^2 / H^3 / H^4	–0.10 / –0.25 / –0.26 / –0.41	Mg^1–N^1 / N^2	0.0725 / 0.0733
[(Depnacnac)Mg]	0.84	Co^1–P^1 / P^2	0.3547 / 0.3527
[CoH_4(dcpe)]	–0.84	/	/

Second order perturbation theory analysis

Donor (L) NBO	Acceptor (NL) NBO	E (2) kcal/mol
LP (1) H2	LV (1) Mg1	21.03
LP (1) H3	LV (1) Mg1	26.80
LP (1) H4	LV (1) Mg1	33.61
BD (1) Co1–H1	LV (1) Mg1	0.36

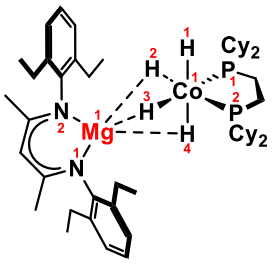

4.4.11.2 IBO Analysis of [(Depnacnac)Mg][CoH_4(dcpe)] (1)

The IBO analysis of [(Depnacnac)Mg][CoH_4(dcpe)] (**1**) shows four intrinsic bond orbitals for the Co–H bonds, three of which have a contribution from magnesium (Figure S41). The IBOs are largely located between the respective H atom (1.214-1.464) and Co atom (0.305-0.696) with minor contributions from Mg (0.071-0.107) in case of the three bridging H atoms (H2-H4).

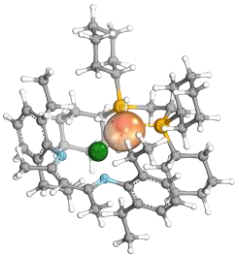

Orb. 222 H3 1.326 Co1 0.536 Mg1 0.084 (+ other: 0.054)

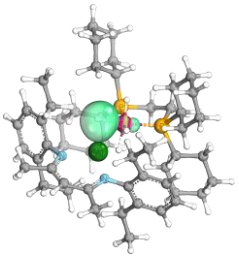

Orb. 223 H2 1.316 Co1 0.557 Mg1 0.071 (+ other: 0.056)

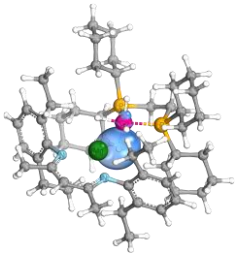

Orb. 224 H4 1.464 Co1 0.305 Mg1 0.107 (+ other: 0.125)

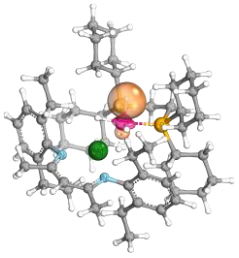

Orb. 225 H1 1.214 Co1 0.696 (+ other: 0.091)

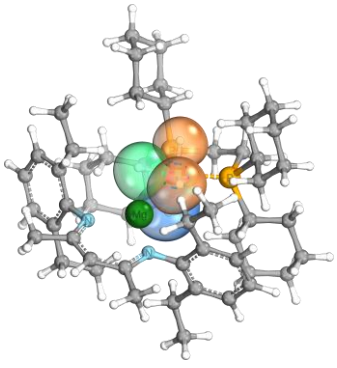

Orb. 222-225 simultaneous visualization of the Co–H(–Mg) bonding interactions

Figure S41. IBOs of [(Depnacnac)Mg][CoH_4(dcpe)] (**1**) showing the bonding interactions within the bridging hydride structural motif.

The bonding situation is best described as a σ-type interaction between Co and H (cobalt hydride bond), with the intrinsic bond orbitals for the bridging hydrides (H2-H4) showing slight extension toward Mg. No bond-like localized orbitals involving Mg and Co are found.

4.4.11.3 AIM Analysis of [(^{Dep}nacnac)Mg][CoH$_4$(dcpe)] (1)

The descriptors for the bond critical points (3, −1; BCPs) of the bridging hydride structural motif (Mg-μ-H$_3$–Co) of [(^{Dep}nacnac)Mg][CoH$_4$(dcpe)] (**1**) are displayed in Table S8.[59] The classification based on the values of $\rho(r_b)$, $\nabla^2\rho(r_b)$, $G(r_b)$, $V(r_b)$, and $H(r_b)$ is discussed in the following. The $|V(r_b)|/G(r_b)$ ratio is found close to 1 (1.102) for the BCP **A** between Co1 and Mg1, with $V(r_b)\cong G(r_b)$, which can be used as a classification criterion for a closed shell donor-acceptor interaction (please note that the interactions were initially used to describe transition metal interactions).[59],[60] The BCP is in the range $1 < V(r_b)\cong G(r_b) < 2$ and is close to 1, which indicates a largely ionic bond character between Mg and Co with some covalent contribution (typical covalent interactions $|V(r_b)|/G(r_b) > 2$ and typical ionic interactions $|V(r_b)|/G(r_b) < 1$).[60],[61] The low electron density $\rho(r_b)$, the positive Laplacian of electron density ($\nabla^2\rho(r_b) > 0$), and the negative energy density ($H(r_b) < 0$) at the BCP **A** support a predominantly electrostatic interaction with only minor covalent character. The BCPs **B**-**E** between Co1 and H1-H4 are in the range $1 < V(r_b)\cong G(r_b) < 2$, and with values of 1.463-1.787 significantly closer to 2. The Co–H bonds are best described as closed-shell interactions exhibiting strong electron-sharing character. The higher electron density $\rho(r_b)$ at the BCPs implies greater shared electron density and the more negative $H(r_b)$ values reflect stronger covalent contributions. Notably, the terminal hydride H1 (BCP **B**) shows the highest covalent character ($\rho(r_b) = 0.1341$, $|V(r_b)|/G(r_b) = 1.787$), whereas the bridging hydrides H2-H4 (BCPs **C**-**E**) display lower covalency ($\rho(r_b) \leq 0.1205$, $|V(r_b)|/G(r_b) \leq 1.621$), which likely stems from additional electron sharing with Mg.

Table S8. AIM parameters at the bond critical points (3, −1) of the bridging hydride structural motif of [(^{Dep}nacnac)Mg][CoH$_4$(dcpe)] (**1**).[a]

Bond critical point	**A** (20, Co1–Mg1)	**B** (30, Co1–H1)	**C** (29, Co1–H2)	**D** (24, Co1–H3)	**E** (17, Co1–H4)
$\rho(r_b)$	0.0352	0.1341	0.1205	0.1178	0.1004
$\nabla^2\rho(r_b)$	0.1242	0.0877	0.1599	0.1659	0.2101
$G(r_b)$	0.0346	0.1031	0.1055	0.1041	0.0979
$V(r_b)$	−0.0381	−0.1842	−0.1710	−0.1668	−0.1432
$\lvert V(r_b)\rvert/G(r_b)$	1.102	1.787	1.621	1.602	1.463
$G(r_b)/\rho(r_b)$	0.983	0.769	0.875	0.884	0.974
$H(r_b)$	−0.0035	−0.0812	−0.0655	−0.0627	−0.0453

[a] Electron density ($\rho(r_b)$ in au), Laplacian of electron density ($\nabla^2\rho(r_b)$ in au), Lagrangian kinetic energy density ($G(r_b)$ in au), potential energy density ($V(r_b)$ in au), ratio $|V(r_b)|/G(r_b)$, ratio $G(r_b)/\rho(r_b)$ in au, electron energy density ($H(r_b)$ in au).

4.4.11.4 NCI Analysis of [(^{Dep}nacnac)Mg][CoH_4(dcpe)] (1)

The non-covalent interaction analysis of [(^{Dep}nacnac)Mg][CoH_4(dcpe)] (**1**) is shown in Figure S42. The high quality integration grid of the software multiwfn was used for the NCI plot calculation. A full representation of the rendered structure of **1** with the NCI surface (3D), a cutout of the interaction between Mg^{2+} and the hydride ligands at Co (3D), as well as the full NCI plot (2D) are depicted. The NCI analysis shows a strong, attractive interaction between the magnesium countercation and three of the four hydride ligands bound to Co (Figure S42B and C). Using a cutoff, the interaction can be located at sign(λ_2)$\rho \approx -0.03$ to -0.04, which is in the range of strong attractive interactions, such as hydrogen bonding interactions (Figure S42D). In addition, a mix of weak attractive and repulsive interactions can be found between the hydrocarbon substituents of the [(^{Dep}nacnac)Mg]$^+$ cation and the [CoH_4(dcpe)]$^-$ anion of **1**, which is best described by Van der Waals interactions.

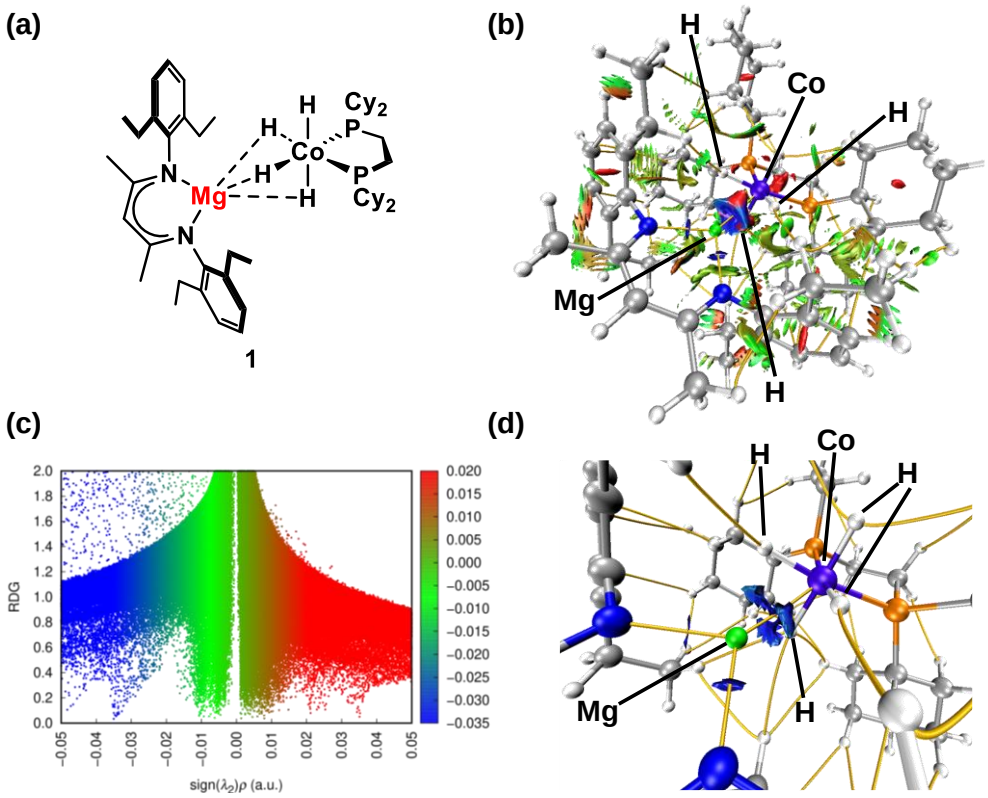

Figure S42. (a) Structure of [(^{Dep}nacnac)Mg][CoH_4(dcpe)] (**1**). (b) NCI Surface visualization with bond paths (3D, isovalue = 0.4) of **1**. (c) NCI plot (2D) of **1**. (d) Cutout (at sign(λ_2)$\rho < -0.02$) of the NCI surface visualization with bond paths (3D) of **1** showing the [Co–H]···Mg^{2+} interaction. Diagrams show plots of RDG := reduced density gradient over sign(λ_2)ρ := density with sign of the second derivative Hessian matrix. The sign(λ_2)$\rho > 0$ (red) are read as strong repulsive interactions, sign(λ_2)$\rho \approx 0$ (green) as weak interactions and sign(λ_2)$\rho < 0$ (blue) as strong attractive interactions.

4.4.11.5 Cartesian Coordinates of [(^{Dep}nacnac)Mg][CoH_4(dcpe)] (1)

[(^{Dep}nacnac)Mg][CoH_4(dcpe)] (**1**)

H = -4367.95929582 Eh

G = -4368.10653671 Eh

Co 11.28074 7.23977 9.20907

P 13.32754 7.67693 9.69052

P 10.83939 6.91925 11.28342

Mg 10.29394 6.13119 7.31719

N 8.60353 4.98465 7.10575

N 10.64078 6.09872 5.29211
C 13.76319 9.50640 9.66277
H 13.15357 9.88714 10.50185
C 12.32245 7.45849 12.29981
H 12.17259 8.51928 12.53198
H 12.36270 6.92655 13.25842
C 11.92953 6.48889 4.82669
C 13.61464 7.27668 11.50245
H 13.94336 6.23352 11.54806
H 14.42649 7.88591 11.91836
C 9.47274 7.90428 12.09772
H 9.60335 7.76693 13.18445
C 12.25234 7.85525 4.71155
C 15.23075 9.85069 9.95591
H 15.58160 9.34586 10.86418
H 15.86743 9.49681 9.13364
C 10.48704 5.17319 11.87347
H 9.64864 4.84627 11.23623
C 7.99159 4.50857 8.30085
C 12.86697 5.49059 4.50202
C 14.12709 5.87986 4.04513
H 14.85109 5.11526 3.77089
C 9.73584 3.56439 13.67220
H 9.45227 3.47545 14.72869
H 8.86011 3.26334 13.07877
C 15.41593 11.36591 10.10323
H 14.84940 11.71463 10.97928
H 16.47155 11.59636 10.29547
C 14.80975 6.82541 8.92612
H 15.67225 7.10349 9.55633
C 11.67725 4.25042 11.57378
H 11.97102 4.35792 10.52375
H 12.53756 4.55661 12.18907
C 15.09604 7.27199 7.48765
H 14.24747 6.99498 6.84733
H 15.19179 8.35949 7.42204
C 10.06988 5.02500 13.34341
H 10.88908 5.36041 13.99704
H 9.20273 5.65241 13.57508
C 16.29077 5.09621 7.02396
H 17.23267 4.64064 6.69247
H 15.51321 4.77136 6.31969
C 13.52724 8.19993 4.26185
H 13.79656 9.24601 4.15690
C 11.34148 2.79287 11.89567
H 10.52539 2.46635 11.23614
H 12.20483 2.15061 11.67883
C 16.37915 6.61946 6.96405
H 16.56352 6.94703 5.93383
H 17.23212 6.96454 7.56837
C 9.55776 9.40786 11.79849
H 10.54499 9.80974 12.05819
H 9.43988 9.55580 10.71796
C 14.45767 7.22286 3.92462
H 15.43896 7.51226 3.55952
C 14.66704 5.29734 8.95877
H 13.80298 5.01762 8.34328
H 14.45204 4.93873 9.97251
C 8.08360 7.39018 11.69991
H 7.95994 7.54399 10.61919
H 7.98497 6.31256 11.86706
C 6.96823 5.27188 8.89484
C 10.90473 2.63254 13.35202
H 10.62921 1.59062 13.55884
H 11.75179 2.87274 14.01208
C 15.93422 4.61535 8.43159
H 16.77098 4.83463 9.11154
H 15.79973 3.52572 8.43943
C 7.07413 9.64621 12.20646
H 6.30701 10.17965 12.78171
H 6.86951 9.84088 11.14315
C 8.46716 10.17647 12.55254

H 8.63250 10.08002 13.63609
H 8.53656 11.24590 12.31649
C 6.98772 8.14124 12.46108
H 5.99904 7.75847 12.17643
H 7.09793 7.94610 13.53859
C 13.27452 10.24218 8.40558
H 12.22200 9.99959 8.23054
H 13.82881 9.89078 7.52450
C 6.79673 3.80511 5.93074
H 7.04225 2.80883 6.31830
H 6.40142 3.69726 4.91980
H 6.01203 4.20040 6.58355
C 11.20509 8.89384 5.03973
H 10.29449 8.66991 4.46665
H 10.91858 8.77262 6.09433
C 8.03239 4.67760 5.94401
C 8.43895 3.30831 8.88046
C 12.52437 4.02390 4.62320
H 13.17430 3.45650 3.94600
H 11.49474 3.84545 4.29528
C 6.37982 4.79552 10.06575
H 5.58537 5.36334 10.54027
C 9.74551 5.71171 4.38352
C 13.46818 11.75362 8.55259
H 13.13456 12.26361 7.63968
H 12.82766 12.11881 9.36940
C 6.55065 6.57306 8.24870
H 6.35309 6.40074 7.18295
H 7.41708 7.25212 8.26257
C 14.92469 12.10624 8.85815
H 15.03946 13.18955 8.98970
H 15.55324 11.82318 8.00046
C 8.52562 5.08758 4.69256
H 7.91319 4.81877 3.84048
C 12.68084 3.47122 6.04535
H 12.33589 2.43287 6.09864
H 12.09736 4.05411 6.76597
H 13.72451 3.50073 6.37092
C 10.04531 5.91219 2.91356
H 10.43465 6.91854 2.72867
H 9.15023 5.75568 2.30940
H 10.81847 5.21499 2.57084
C 11.61073 10.34435 4.80318
H 11.87073 10.52940 3.75495
H 12.46872 10.62761 5.42232
H 10.78331 11.01084 5.06495
C 6.79683 3.59904 10.63786
H 6.32004 3.23728 11.54466
C 7.81990 2.86506 10.05083
H 8.13249 1.92960 10.50480
C 9.57910 2.54776 8.24241
H 9.52217 2.66588 7.15429
H 10.52273 3.03770 8.53387
C 5.34671 7.27104 8.87083
H 5.11431 8.18373 8.31368
H 5.53282 7.56048 9.90982
H 4.45655 6.63238 8.85211
C 9.65567 1.06098 8.58259
H 10.45402 0.58504 8.00463
H 8.71466 0.55322 8.34370
H 9.87385 0.88411 9.64015
H 11.57703 7.66631 7.78398
H 9.78484 7.24169 8.91353
H 10.98219 8.67602 9.40190
H 11.45595 5.70877 8.84433 8

4.5 References

[1] W. Hieber, F. Leutert, *Naturwissenschaften* **1931**, *19*, 360.

[2] J. E. Ellis, *Organometallics* **2003**, *22*, 3322.

[3] a) P. J. Chirik, *Acc. Chem. Res.* **2015**, *48*, 1687; b) N. A. Eberhardt, H. Guan, *Chem. Rev.* **2016**, *116*, 8373; c) L. Alig, M. Fritz, S. Schneider, *Chem. Rev.* **2019**, *119*, 2681; d) W. Ai, R. Zhong, X. Liu, Q. Liu, *Chem. Rev.* **2019**, *119*, 2876.

[4] K. Ding, W. W. Brennessel, P. L. Holland, *J. Am. Chem. Soc.* **2009**, *131*, 10804.

[5] M. S. Jeletic, M. T. Mock, A. M. Appel, J. C. Linehan, *J. Am. Chem. Soc.* **2013**, *135*, 11533.

[6] N. Gorgas, L. G. Alves, B. Stöger, A. M. Martins, L. F. Veiros, K. Kirchner, *J. Am. Chem. Soc.* **2017**, *139*, 8130.

[7] a) J. Campos, *Nat. Rev. Chem.* **2020**, *4*, 696; b) M. Navarro, J. J. Moreno, M. Pérez-Jiménez, J. Campos, *Chem. Commun.* **2022**, *58*, 11220.

[8] O. Ekkert, A. J. P. White, M. R. Crimmin, *Angew. Chem. Int. Ed.* **2016**, *55*, 16031.

[9] M. Perez-Jimenez, B. L. Geoghegan, A. Collauto, M. M. Rößler, M. R. Crimmin, *Angew. Chem. Int. Ed.* **2024**, *63*, e202411828.

[10] M. Garçon, C. Bakewell, G. A. Sackman, A. J. P. White, R. I. Cooper, A. J. Edwards, M. R. Crimmin, *Nature* **2019**, *574*, 390.

[11] N. Gorgas, A. J. P. White, M. R. Crimmin, *J. Am. Chem. Soc.* **2022**, *144*, 8770.

[12] Y. Cai, S. Jiang, T. Rajeshkumar, L. Maron, X. Xu, *J. Am. Chem. Soc.* **2022**, *144*, 16647.

[13] M. Perez-Jimenez, M. R. Crimmin, *Chem. Sci.* **2024**, *15*, 1424.

[14] M. Oishi, T. Endo, M. Oshima, H. Suzuki, *Inorg. Chem.* **2014**, *53*, 5100.

[15] J. Weßing, C. Göbel, B. Weber, C. Gemel, R. A. Fischer, *Inorg. Chem.* **2017**, *56*, 3517.

[16] a) T. A. Bazhenova, L. M. Kachapina, A. E. Shilov, M. Yu. Antipin, Yu. T. Struchkov, *J. Organomet. Chem.* **1992**, *428*, 107; b) K. P. Chiang, C. C. Scarborough, M. Horitani, N. S. Lees, K. Ding, T. R. Dugan, W. W. Brennessel, E. Bill, B. M. Hoffman, P. L. Holland, *Angew. Chem. Int. Ed.* **2012**, *51*, 3658; c) D.-H. Manz, P.-C. Duan, S. Dechert, S. Demeshko, R. Oswald, M. John, R. A. Mata, F. Meyer, *J. Am. Chem. Soc.* **2017**, *139*, 16720; d) S. Garhwal, A. Kaushansky, N. Fridman, G. De Ruiter, *Chem Catal.* **2021**, *1*, 631.

[17] M. Gawron, F. Gilch, D. Schmidhuber, J. A. Kelly, T. M. Horsley Downie, A. Jacobi Von Wangelin, J. Rehbein, R. Wolf, *Angew. Chem. Int. Ed.* **2024**, *63*, e202315381.

[18] S. Sandl, T. M. Maier, N. P. Van Leest, S. Kröncke, U. Chakraborty, S. Demeshko, K. Koszinowski, B. De Bruin, F. Meyer, M. Bodensteiner, C. Herrmann, R. Wolf, A. Jacobi Von Wangelin, *ACS Catal.* **2019**, *9*, 7596.

[19] a) D. Gärtner, A. Welther, B. R. Rad, R. Wolf, A. Jacobi von Wangelin, *Angew. Chem. Int. Ed.* **2014**, *53*, 3722; b) P. Büschelberger, D. Gärtner, E. Reyes-Rodriguez, F. Kreyenschmidt, K. Koszinowski, A. Jacobi von Wangelin, R. Wolf, *Chem. Eur. J.* **2017**,

23, 3139; c) T. M. Maier, S. Sandl, I. G. Shenderovich, A. Jacobi von Wangelin, J. J. Weigand, R. Wolf, *Chem. Eur. J.* **2019**, *25*, 238.

[20] D. Habermann, Organocobaltverbindungen aus (η-Cyclopentadienyl)cobalt-Komplexen durch reduktive C_5H_5-Ablösung, PhD Dissertation, Ruhr-Universität Bochum, **1980**.

[21] L. Fohlmeister, S. Liu, C. Schulten, B. Moubaraki, A. Stasch, J. D. Cashion, K. S. Murray, L. Gagliardi, C. Jones, *Angew. Chem. Int. Ed.* **2012**, *51*, 8294.

[22] J. Huang, X. Zheng, I. Del Rosal, B. Zhao, L. Maron, X. Xu, *Inorg. Chem.* **2020**, *59*, 13473.

[23] J. A. Kelly, J. Gramüller, R. M. Gschwind, R. Wolf, *Dalton Trans.* **2021**, *50*, 13985.

[24] D. Gärtner, S. Sandl, A. Jacobi Von Wangelin, *Catal. Sci. Technol.* **2020**, *10*, 3502.

[25] See for previous reports on arene hydrogenation by transition metal phosphine and phosphite complexes: a) E. L. Muetterties, F. J. Hirsekorn, *J. Am. Chem. Soc.* **1974**, *96*, 4063; b) M. C. Rakowski, F. J. Hirsekorn, L. S. Stuhl, E. L. Muetterties, *Inorg. Chem.* **1976**, *15*, 2379; c) L. S. Stuhl, M. Rakowski DuBois, F. J. Hirsekorn, J. R. Bleeke, A. E. Stevens, E. L. Muetterties, *J. Am. Chem. Soc.* **1978**, *100*, 2405; d) K. Jonas, *Angew. Chem. Int. Ed.* **1985**, *24*, 295; e) M. D. Fryzuk, J. B. Ng, S. J. Rettig, J. C. Huffman, K. Jonas, *Inorg. Chem.* **1991**, *30*, 2437.

[26] Selected examples of the reaction of transition metal hydride complexes with P_4: a) J. C. Green, M. L. H. Green, G. E. Morris, J. Chem. Soc. *Chem. Commun.* **1974**, 212; b) E. Cannillo, A. Coda, K. Prout, J.-C. Daran, *Acta Crystallogr. B* **1977**, *33*, 2608; c) N. Etkin, M. T. Benson, S. Courtenay, M. J. McGlinchey, A. D. Bain, D. W. Stephan, *Organometallics* **1997**, *16*, 3504; d) M. Peruzzini, J. A. Ramirez, F. Vizza, *Angew. Chem. Int. Ed.* **1998**, *37*, 2255; e) P. J. Chirik, J. A. Pool, E. Lobkovsky, *Angew. Chem. Int. Ed.* **2002**, *41*, 3463; f) P. Barbaro, A. Ienco, C. Mealli, M. Peruzzini, O. J. Scherer, G. Schmitt, F. Vizza, G. Wolmershäuser, *Chem. Eur. J.* **2003**, *9*, 5195; g) M. D. Walter, J. Grunenberg, P. S. White, *Chem. Sci.* **2011**, *2*, 2120.

[27] The P–P bond lengths in $Cs_2P_4{\cdot}2NH_3$ containing the only weakly interacting P_4^{2-} anion are 2.146(1) and 2.1484(9) Å: F. Kraus, J. C. Aschenbrenner, N. Korber, *Angew. Chem. Int. Ed.* **2003**, *42*, 4030. See also for a detailed discussion on the *cyclo*-P_4^{2-} anion in molybdenum complexes: K. A. Mandla, M. L. Neville, C. E. Moore, A. L. Rheingold, J. S. Figueroa, *Angew. Chem. Int. Ed.* **2019**, *58*, 15329.

[28] a) P. Pyykkö, M. Atsumi, *Chem. Eur. J.* **2009**, *15*, 186; b) P. Pyykkö, M. Atsumi, *Chem. Eur. J.* **2009**, *15*, 12770.

[29] C. M. Hoidn, T. M. Maier, K. Trabitsch, J. J. Weigand, R. Wolf, *Angew. Chem. Int. Ed.* **2019**, *58*, 18931.

[30] S. Hauer, T. M. Horsley Downie, G. Balázs, K. Schwedtmann, J. J. Weigand, R. Wolf, *Angew. Chem. Int. Ed.* **2024**, *63*, e202317170.

[31] S. Yao, N. Lindenmaier, Y. Xiong, S. Inoue, T. Szilvási, M. Adelhardt, J. Sutter, K. Meyer, M. Driess, *Angew. Chem. Int. Ed.* **2015**, *54*, 1250.

[32] A. Cavaillé, N. Saffon-Merceron, N. Nebra, M. Fustier-Boutignon, N. Mézailles, *Angew. Chem. Int. Ed.* **2018**, *57*, 1874.

[33] a) C. G. P. Ziegler, T. M. Maier, S. Pelties, C. Taube, F. Hennersdorf, A. W. Ehlers, J. J. Weigand, R. Wolf, *Chem. Sci.* **2019**, *10*, 1302; b) K. Trabitsch, S. Hauer, K. Schwedtmann, P. Royla, J. J. Weigand, R. Wolf, *Inorg. Chem. Front.* **2025**, *12*, 2013.

[34] a) S. Pelties, A. W. Ehlers, R. Wolf, *Chem. Commun.* **2016**, *52*, 6601; b) S. Hauer, G. Balázs, F. Gliese, F. Meurer, T. M. Horsley Downie, C. Hennig, J. J. Weigand, R. Wolf, *Inorg. Chem.* **2024**, *63*, 20141.

[35] M. P. Blake, N. Kaltsoyannis, P. Mountford, *Chem. Commun.* **2013**, *49*, 3315.

[36] F. Gilch, Ion-Pairing Effects in Hydrogenation Catalysis, Master's Thesis, Universität Regensburg, **2021**.

[37] NORELL® Valved NMR tubes are available under: https://secure.nmrtubes.com/nmr-epr-tubes/valved-for-intermediate-pressure, **2025**.

[38] a) A. Jerschow, N. Müller, *J. Magn. Reson., Ser. A* **1996**, *123*, 222; b) A. Jerschow, N. Müller, *J. Magn. Reson.* **1997**, *125*, 372.

[39] E. O. Stejskal, J. E. Tanner, *J. Chem. Phys.* **1965**, *42*, 288.

[40] A. Macchioni, G. Ciancaleoni, C. Zuccaccia, D. Zuccaccia, *Chem. Soc. Rev.* **2008**, *37*, 479.

[41] H. C. Chen, S. H. Chen, *J. Phys. Chem.* **1984**, *88*, 5118.

[42] a) D. Ben-Amotz, K. G. Willis, *J. Phys. Chem.* **1993**, *97*, 7736; b) D. Zuccaccia, A. Macchioni, *Organometallics* **2005**, *24*, 3476.

[43] C. M. Hoidn, C. Rödl, M. L. McCrea-Hendrick, T. Block, R. Pöttgen, A. W. Ehlers, P. P. Power, R. Wolf, *J. Am. Chem. Soc.* **2018**, *140*, 13195.

[44] M. Scheer, U. Becker, E. Matern, *Chem. Ber.* **1996**, *129*, 721.

[45] a) Sheldrick, G. M. SADABS, Bruker AXS, Madison, USA **2007**; b) CrysAlisPro, Scale3 Abspack, Rigaku Oxford Diffraction, **2019**.

[46] R. C. Clark, J. S. Reid, *Acta Crystallogr. A* **1995**, *51*, 887.

[47] G. M. Sheldrick, *Acta Crystallogr. C* **2015**, *71*, 3.

[48] O. V. Dolomanov, L. J. Bourhis, R. J. Gildea, J. A. K. Howard, H. Puschmann, *J. Appl. Crystallogr.* **2009**, *42*, 339.

[49] G. M. Sheldrick, *Acta Crystallogr. A* **2008**, *64*, 112.

[50] a) Neese, F., The ORCA program system. *WIREs Comput. Mol. Sci.* **2012**, 2: 73, https://doi.org/10.1002/wcms.81; b) Neese, F. Software update: The ORCA program system—Version 5.0. WIREs *Comput. Mol. Sci.* **2022**; 12:e1606. https://doi.org/10.1002/wcms.1606.

[51] S. Grimme, A. Hansen, S. Ehlert, J.-M. Mewes, *J. Chem. Phys.* **2021**, *154*, 064103.

[52] a) A. Schäfer, H. Horn, R. Ahlrichs, *J. Chem. Phys.* **1992**, *97*, 2571; b) A. Schäfer, C. Huber, R. Ahlrichs, *J. Chem. Phys.* **1994**, *100*, 5829; c) F. Weigend, R. Ahlrichs, *Phys. Chem. Chem. Phys.* **2005**, *7*, 3297; d) F. Weigend, *Phys. Chem. Chem. Phys.* **2006**, *8*, 1057; e) J.-D. Chai and M. Head-Gordon, *J. Chem. Phys.* **2008**, *128*, 084106; f) J.-D. Chai, M. Head-Gordon, *Phys. Chem. Chem. Phys.* **2008**, *10*, 6615.

[53] NBO 7.0. E. D. Glendening, J. K. Badenhoop, A. E. Reed, J. E. Carpenter, J. A. Bohmann, C. M. Morales, P. Karafiloglou, C. R. Landis, and F. Weinhold, Theoretical Chemistry Institute, University of Wisconsin, Madison, WI (**2018**).

[54] a) G. Knizia, *J. Chem. Theory Comput.* **2013**, *9*, 4834; b) G. Knizia, J. E. M. N. Klein, *Angew. Chem. Int. Ed.* **2015**, *54*, 5518.

[55] a) E. R. Johnson, S. Keinan, P. Mori-Sánchez, J. Contreras-García, A. J. Cohen, W. Yang, *J. Am. Chem. Soc.* **2010**, *132*, 6498; b) J. Contreras-García, E. R. Johnson, S. Keinan, R. Chaudret, J.-P. Piquemal, D. N. Beratan, W. Yang, *J. Chem. Theory Comput.* **2011**, *7*, 625; c) R. A. Boto, F. Peccati, R. Laplaza, C. Quan, A. Carbone, J.-P. Piquemal, Y. Maday, J. Contreras-Garcia, *J. Chem. Theory Comput.* **2020**, *16*, 4150.

[56] T. Lu, F. Chen, *J. Comput. Chem.* **2011**, *33*, 580.

[57] W. Humphrey, A. Dalke, K. Schulten, *J. Mol. Graph.* **1996**, *14*, 33.

[58] M. D. Hanwell, D. E. Curtis, D. C. Lonie, T. Vandermeersch, E. Zurek, G. R. Hutchison, *J. Cheminform.* **2012**, *4*, DOI 10.1186/1758-2946-4-17.

[59] B. Silvi, R.J. Gillespie, C. Gatti, "Electron Density Analysis" in *Comprehensive Inorganic Chemistry II*, Elsevier, **2013**, pp. 187–226.

[60] a) P. Macchi, D. M. Proserpio, A. Sironi, *J. Am. Chem. Soc.* **1998**, *120*, 13429; b) R. Gericke, M. A. Bennett, S. H. Privér and S. K. Bhargava, *Inorg. Chem.* **2023**, *62*, 8846.

[61] C. Gatti, *Z. Kristallogr. Cryst. Mater.* **2005**, *220*, 399.

Chapter 5 Photocatalytic Functionalization of White Phosphorus with Aryl Bromides and Chlorides[a,b]

Abstract: We report the implementation of a consecutive photoinduced electron transfer (conPET) strategy for the functionalization of white phosphorus (P_4) with inexpensive and widely available aryl bromides and chlorides. By employing a well-known acridinium based photocatalyst under near-UV irradiation, this protocol gives direct access to valuable triarylphosphines and tetraarylphosphonium salts. The reaction mechanism is elucidated by NMR spectroscopic studies and model reactions.

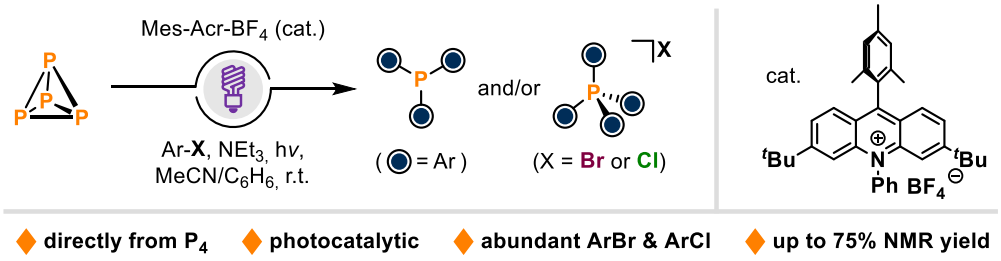

[a] Reproduced with changes from M. Gawron, J. Rückel, R. Wolf, *Chem. Commun.* **2024**, *60*, 9777–9780 with permission from the Royal Society of Chemistry.

[b] Martin Gawron performed most of the experimental work. The functionalization reactions starting from $NaPH_2$ (Table S19-Table S24) and parts of the photocatalyst screening starting from P_4 (Table S4) were conducted by Jannes Rückel. Robert Wolf supervised and directed the project. Martin Gawron wrote the manuscript draft, which was edited by all authors.

5.1 Introduction

Arylphosphines (Ar_3P) and tetraarylphosphonium salts ($[Ar_4P]^+$) are widely used chemicals with myriad applications as synthetic reagents, catalyst ligands, extractants, and phase transfer catalysts (among many other applications).[1]-[5] Their conventional synthesis starts from white phosphorus (P_4), which is the main resource for the vast majority of organophosphorus compounds.[6] This multi-step process relies on the chlorination of P_4 with Cl_2 gas and proceeds via chlorinated intermediates (such as PCl_3), which are further converted to the desired monophosphorus species.[7]

It is desirable to replace the traditional chlorination route to organophosphorus compounds with more direct, single step procedures that minimize waste generation and the use of hazardous chemicals.[8] In recent years, photo- and electrochemistry, main group chemistry and transition metal coordination chemistry have led to some remarkable breakthroughs.[9]-[13] Nevertheless, the efficient and catalytic functionalization of P_4 has remained challenging due to the difficulties associated with the selective cleavage of six P–P bonds and the simultaneous forging of up to 16 P–C bonds.

We have developed a photocatalytic protocol for the arylation of P_4 with aryl iodides (Figure 1), allowing for the formation of Ar_3P and $[Ar_4P]I$ in a single reaction step.[9] This method is limited to a few photocatalysts, the most successful one being $[Ir(dtbbpy)(ppy)_2]PF_6$. Unfortunately, the iridium-based photocatalyst and the aryl iodide substrates are both expensive and limited in supply (Figure 1a). Considering that aryl chlorides and bromides make up the vast majority of commercially available (and affordable) aryl halides,[14] their use would make the photocatalytic P_4 arylation much more attractive and relevant. However, this has been very challenging due to their strong carbon–halogen bonds and negative redox potentials (Figure 1b).[15],[16] Here, we describe the photocatalytic arylation of P_4 with aryl bromides and chlorides. By using a potent acridinium-based photocatalyst,[17] this method affords valuable triarylphosphines and tetraarylphosphonium salts in a single reaction step from P_4 (Figure 1c). To our knowledge, this is the first example of the successful use of aryl bromides and chlorides in the catalytic functionalization of P_4.

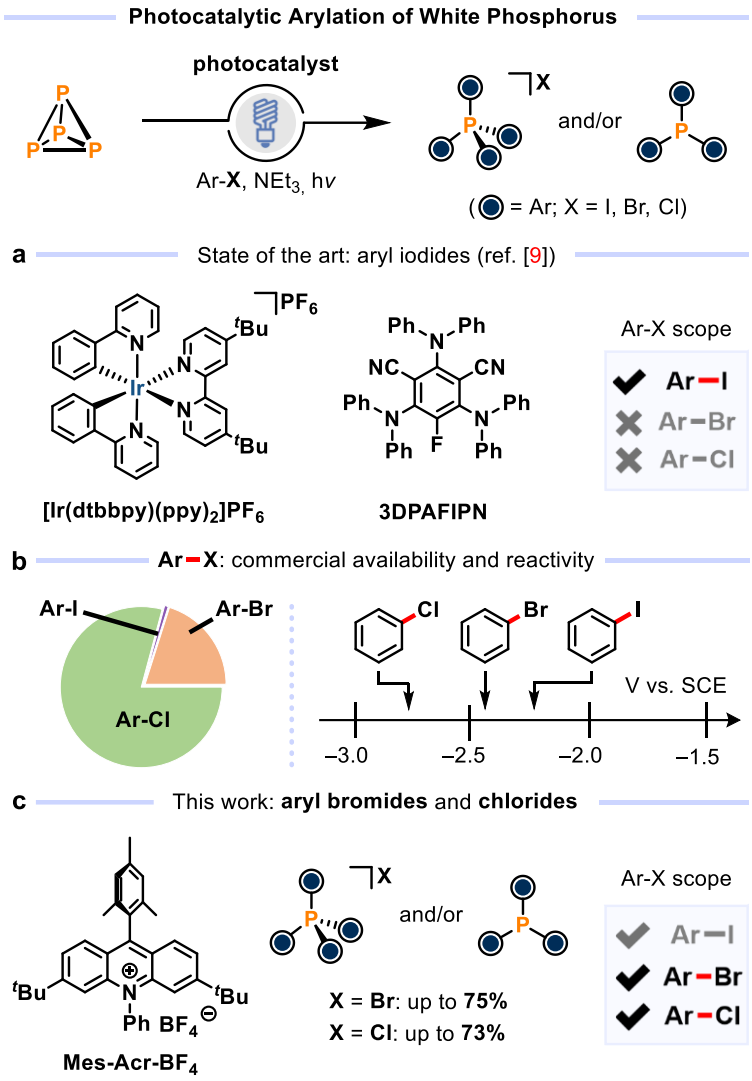

Figure 1. General reaction scheme for the photocatalytic arylation of P_4. (a) Established catalysts and substrates. (b) Commercial availability of ArX (X = I, Br, Cl) and reduction potentials of PhX (in DMF, data taken from ref. [16]). (c) The reaction concept presented in this work employing aryl bromides and chlorides.

5.2 Results and Discussion

Recently, Nicewicz and co-workers reported the implementation of a consecutive photoinduced electron transfer (conPET) strategy, which facilitated the efficient photoreduction of otherwise recalcitrant aryl bromides and chlorides using the photocatalyst Mes-Acr-BF_4 (9-mesityl-3,6-di-tert-butyl-10-phenylacridinium tetrafluoroborate).[17] Considering our previous work on the arylation of P_4 with aryl iodides, we reasoned that this conPET strategy could be used in a similar manner to functionalize P_4. An initial experiment employing near-UV irradiation (390 nm) of P_4, 4-bromoanisole (E_{red} = −2.90 V vs. SCE in MeCN),[17] NEt_3 and Mes-Acr-BF_4 in acetonitrile/benzene yielded the phosphonium salt [(4-OMe-C_6H_4)$_4$P]Br (47% yield determined by NMR spectroscopy) and the tertiary phosphine (4-OMe-C_6H_4)$_3$P (9% yield; Table S1). Control experiments showed that the photocatalyst, irradiation and the sacrificial reductant NEt_3 are essential components for a successful reaction (Table S1).

After optimization (Table S2-Table S9), we investigated the scope of the photocatalytic arylation reaction (Figure 2). Various substituted aryl bromides and chlorides successfully engaged in the P–C coupling, including substrates bearing both electron-donating (e.g., Me, OMe, SMe) and electron-withdrawing groups (e.g., CN, CO_2Me, CF_3). Aryl bromides were employed in 20–44 h reaction times, while the use of aryl chlorides required longer reaction times (44–68 h). Generally, the tetraarylphosphonium salt was the major product but was accompanied by notable quantities of triarylphosphine when unsubstituted and *para*- or *meta*-substituted aryl halides were used. *ortho*-Substituted aryl halides exclusively gave the tertiary phosphine (e.g., tris(*o*-tolyl)phosphine obtained from 2-bromotoluene, Figure 2). For bromoarenes, combined spectroscopic yields of Ar_3P and $[Ar_4P]Br$ up to 75% were observed (see 3-bromotoluene, Figure 2). Similarly, the use of aryl chlorides enabled product formation in up to 73% combined spectroscopic yields (see electron-rich chloroarenes such as 3-chloroanisole, Figure 2). This method is more suitable for electron-rich haloarenes than for electron-poor haloarenes.

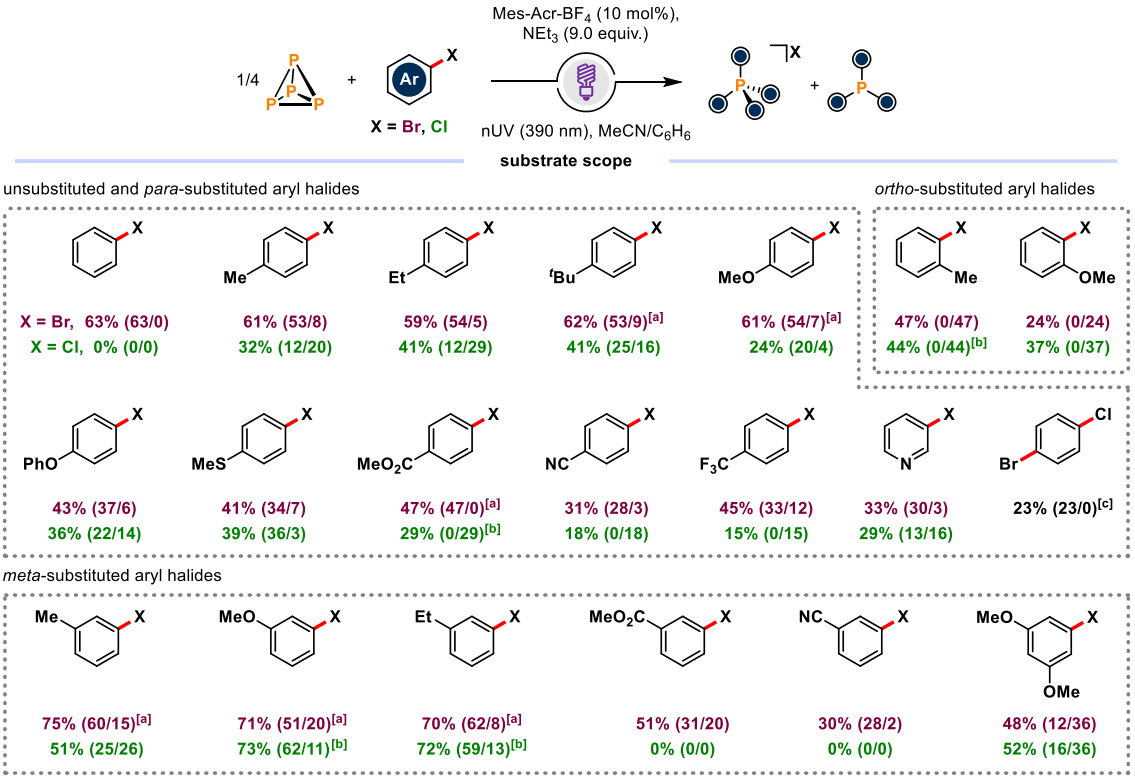

Figure 2. Substrate scope for the photocatalytic arylation of P_4 with aryl halides (X = Br, Cl). Yields ($[Ar_4P]X/Ar_3P$) were determined by recording quantitative $^{31}P\{^1H\}$ NMR spectra with Ph_3PO added as an internal standard. Standard conditions: 0.01 mmol P_4 (0.25 equiv.; as a stock solution in 65.3 µL benzene), 4.0 µmol Mes-Acr-BF_4 (10 mol% based on the P atom), 0.44 mmol ArX (11.0 equiv. based on the P atom), 0.36 mmol NEt_3 (9.0 equiv. based on the P-atom) in 0.1 mL MeCN, reaction time = 20 h (for X = Br) and 44 h (for X = Cl) unless noted otherwise. The samples were prepared under N_2 atmosphere in a sealed tube and irradiated with near-UV LEDs (390 nm, 40 W). [a] Reaction time = 44 h. [b] Reaction time = 68 h. [c] $[Ph_4P]X$ (X = Br or Cl) was formed exclusively.

Thus, aryl chlorides with electron withdrawing groups generally gave modest yields (0–29%) of the arylated phosphines and phosphonium salts. Tetraphenylphosphonium bromide and

tris(*o*-tolyl)phosphine were synthesized as representative products on a preparative scale and were isolated by crystallization from CH_2Cl_2/Et_2O in 39% yield (for $[Ph_4P]Br$) or by sublimation in 28% yield (for $(o\text{-tol})_3P$; see section 5.4.5 for a detailed description of the isolation procedures).

Following the successful reaction development, we conducted ^{31}P NMR spectroscopic studies and model reactions to gain insight into the reaction mechanism. Our mechanistic proposal is displayed in Figure 3. Analogous to the conPET mechanism proposed by Nicewicz, the P_4 arylation proceeds by an initial photoexcitation of the acridinium salt with near-UV light (step i). This photocatalyst is then reduced by NEt_3, generating the acridine radical Mes-Acr• (step ii). Consecutive photoexcitation of this radical gives Mes-Acr•* (step iii), which is an extremely strong reductant with an estimated excited state reduction potential of E_{red} = −3.36 V vs. SCE (for comparison, the reduction potentials of 4-bromoanisole and 4-chloroanisole are $E_{red} \leq -2.90$ V vs. SCE).[17] The aryl radicals generated through this conPET process (step iv) are readily trapped by P_4 or P_4-derived intermediates (step v). Analogous to our previous observations with aryl iodides, the arylation of P_4 proceeds via the sequential formation of $ArPH_2$, Ar_2PH, Ar_3P and finally $[Ar_4P]^+$ (steps vi-viii).[9]

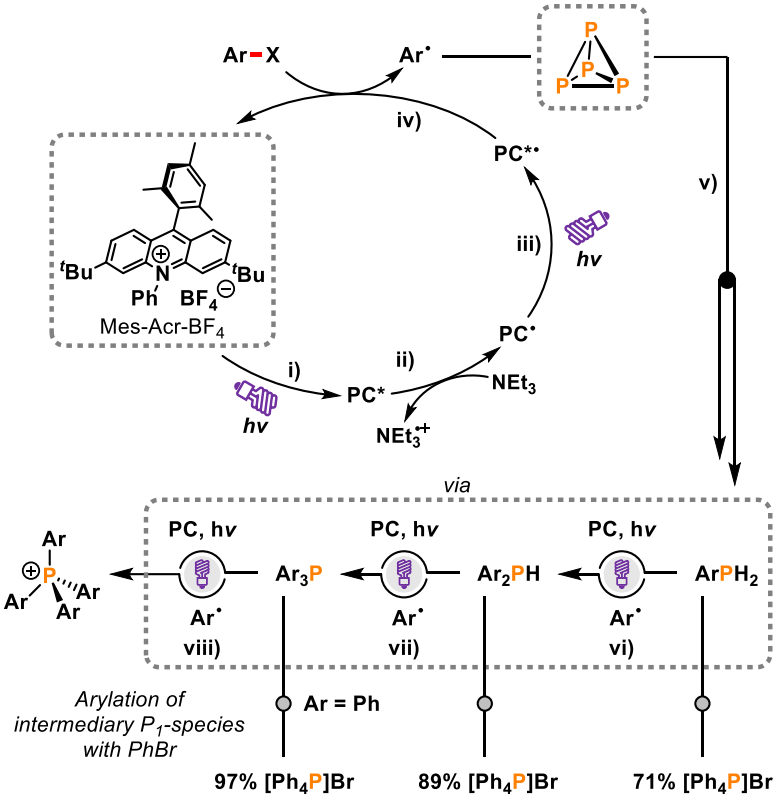

Figure 3. Proposed mechanism for the photocatalytic arylation of P_4 involving aryl radical generation through conPET (steps i-iv) and sequential radical reaction via P–P bond cleavage toward Ar_3P and $[Ar_4P]^+$ (steps v-viii). Direct phenylation of Ph_nPH_{3-n} (n = 1, 2, 3) with PhBr.

This was confirmed by the $^{31}P\{^1H\}$ NMR spectroscopic monitoring of the P_4 arylation with PhBr under standard conditions (Table S10 and Figure S65). P_4 was completely consumed after 30 min, while traces of Ph_3P, $PhPH_2$, Ph_2PH and Ph_4P_2 were detected after 1 h (Figure

S66). The formation of Ph_3P and $[Ph_4P]Br$ proceeds slowly, reaching a combined NMR yield of 58% after 6 h. Subsequently, Ph_3P is further converted into $[Ph_4P]Br$, which is the exclusive product detected by $^{31}P\{^1H\}$ NMR spectroscopy after 20 h (63% NMR yield). In agreement with this, catalytic arylations of $PhPH_2$, Ph_2PH, Ph_3P and Ph_4P_2 with PhBr yielded $[Ph_4P]Br$ in similar or superior yields in comparison with the P_4 reaction (e.g., 97% $[Ph_4P]Br$ from Ph_3P; Figure 3 and S7, see section 5.4.7 for details).

Further $^{31}P\{^1H\}$ NMR spectroscopic analysis of the phenylation of P_4 identified several intermediates and side products, such as $Ph_2P(NEt_2)$ and the divinyldiphosphine $[PhP(CHCH_2)]_2$ (Figure 4 and Figure S68). These observations indicate that the reaction mechanism is similar to that proposed for the P_4 arylation reaction using aryl iodides, for which similar P-containing species were detected.[9] While polyphosphorus intermediates $[P_n]$ (n > 2) could not be observed in our monitoring study with P_4, the $^{31}P\{^1H\}$ NMR spectroscopic analysis of the phenylation of the cyclopentaphosphine Ph_5P_5 showed that smaller cyclophosphines such as Ph_3P_3 and Ph_4P_4 can be detected at an early stage (Figure S70).[18] This suggests that related oligophosphines are conceivable reaction intermediates.

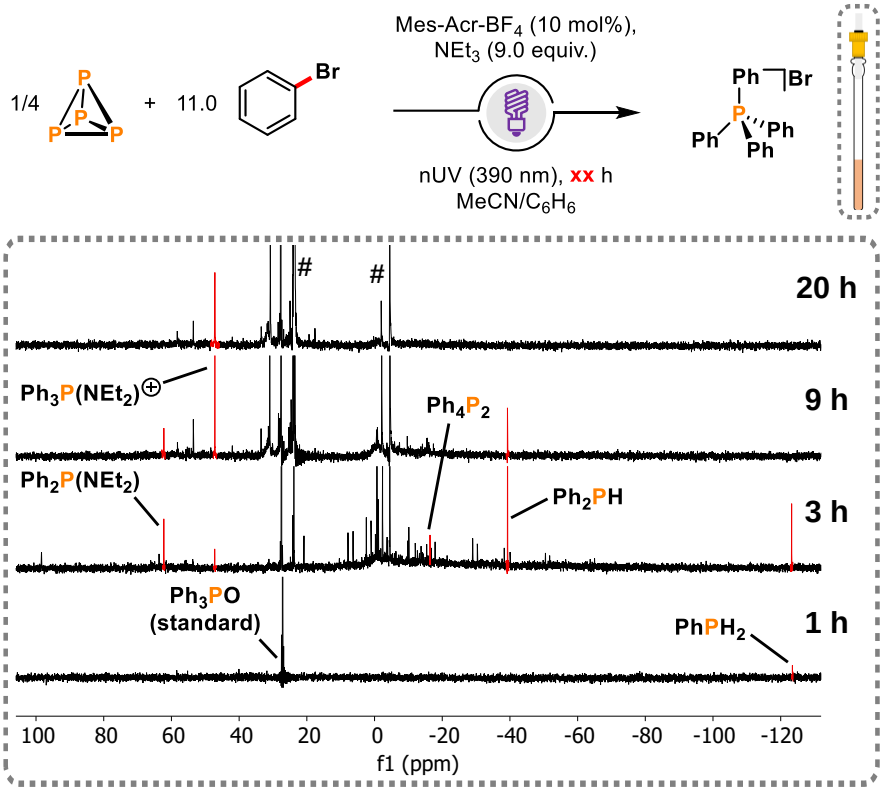

Figure 4. Identification of selected reaction intermediates and side-products (red) in the phenylation of P_4 with PhBr by $^{31}P\{^1H\}$ NMR spectroscopy (NS 512). The reaction was conducted in a J. Young NMR tube. #: Ph_3P and $[Ph_4P]Br$.

Note that PH_3 was not observed, suggesting that it does not significantly contribute to the mechanism (see section 5.4.6.2). In accordance with this, the use of $NaPH_2$ (as a surrogate for PH_3) resulted in inferior yields for several electron-rich and electron-deficient aryl bromides (e.g., $[Ph_4P]Br$ was obtained in only 19% yield from PhBr; Table S24).

This stands in contrast to the arylation of $NaPH_2$ with aryl iodides, which was feasible in good yields.[9] Finally, we observed that the reaction product $[Ph_4P]Br$ is unstable under the applied reaction conditions. Exposing an isolated sample of $[Ph_4P]Br$ to near-UV irradiation (390 nm) in the presence of Mes-Acr-BF_4 and NEt_3 (9 equiv. per P atom) resulted in the formation of Ph_3P (52% NMR yield) and 41% $[Ph_4P]Br$, recovered after 20 h (Table S18). Further investigations confirmed that the intermediates $PhPH_2$, Ph_2PH, Ph_3P and Ph_4P_2 also decompose partially under the reaction conditions, forming preceding P–H-functionalized phosphines (e.g., Ph_2PH → $PhPH_2$; Table S15) when irradiated with 390 nm LED light in the presence of Mes-Acr-BF_4 and NEt_3. These results emphasize the possibility of an unproductive de-arylation reaction limiting the catalytic efficiency.

5.3 Conclusion

In conclusion, we have developed an efficient photocatalytic protocol for the arylation of P_4 with aryl bromides and chlorides, affording triarylphosphines and tetraarylphosphonium salts in up to 75% combined yield of Ar_3P and $[Ar_4P]X$ (X = Br, Cl). This protocol overcomes a major methodological limitation in the direct functionalization of P_4, thereby highlighting the significant potential of photoredox catalysis in the field. The isolation of selected products illustrates the practicality of the reported approach, which relies on a conPET mechanism enabled by the highly reducing photocatalyst Mes-Acr-BF_4. Given the increasing utility of photoredox methods in organic synthesis, this strategy is likely to be further developed in the future.

5.4 Supporting Information

5.4.1 General Information

All reactions and manipulations were performed under an N_2 atmosphere (< 0.1 ppm O_2, H_2O) using an MBraun Glovebox. All glassware was oven-dried (160 °C) overnight prior to use. Benzene was dried over Na and stored over molecular sieves (3 Å). Acetonitrile, dimethyl sulfoxide and dimethylformamide were distilled from CaH_2 and stored over molecular sieves (3 Å). Benzene was distilled from Na/benzophenone and stored over molecular sieves (3 Å). Acetone was stirred over $CaSO_4$ (3 h) and distilled after dynamically drying over molecular sieves (3 Å). THF and toluene were purified using a MBraun SPS-800 system and stored over molecular sieves (3 Å). C_6D_6 was stored over molecular sieves (3 Å). All other chemicals were purchased from major suppliers; liquids were purified by Kugelrohr distillation and freeze-pump-thaw degassed three times prior to use; white phosphorus (P_4) was purified by sublimation; all other chemicals were used as received.

Caution. P_4 is toxic and highly pyrophoric and should be handled, manipulated and quenched with corresponding caution.

Qualitative NMR spectra were recorded at room temperature on Bruker Avance III HD 400 (400 MHz) spectrometers and were processed using MestReNova v14.0.0. Chemical shifts δ, are reported in parts per million (ppm); ^{1}H and ^{13}C shifts are reported relative to $SiMe_4$ and were calibrated to residual solvent peaks, while ^{31}P shifts were referenced externally to 85% H_3PO_4 (aq.).

NMR samples were prepared in the glovebox using NMR tubes fitted with screw caps. Optimization reactions (see section 5.4.3), photocatalytic phenylation reactions of $PhPH_2$, Ph_2PH, Ph_4P_2 and Ph_3P (see section 5.4.7), and photocatalytic arylation reactions of $NaPH_2$ (see section 5.4.8) were analyzed by $^{31}P\{^{1}H\}$ NMR spectroscopy using only a single scan (DS = 0, D1 = 2 s). The accuracy of this method was confirmed by preparing solutions of $(o\text{-tol})_3P$ or $[Ph_4P]Cl$ of defined concentrations with each 0.05 mmol Ph_3PO in $MeCN/C_6H_6$ (1.5 mL, 0.5 mL, respectively), and comparing the measured and expected relative integrals of the corresponding signals (Figure S1).

Quantitative measurements for the substrate screening were conducted on Bruker Avance HD III 400 (400 MHz) spectrometers. Yields were determined by 1D $^{31}P\{^{1}H\}$ NMR spectroscopy. In order to meet quantitative conditions, special attention was paid to the following aspects:

- Pulse lengths were calibrated. The O1P of the spectrum was set close to the frequencies of interest to enable maximum excitation.
- T_1 relaxation times were determined for all peaks of interest and a D1 of ≥ 5 × T_1 was used to ensure full relaxation between scans.

- The NS was adjusted so that the signal to noise ratio (S/N-ratio) was higher than 100/1. In order to reduce measurement time and to increase the S/N-ratio compared to a standard 1D experiment using only a 90° pulse (zg experiment), the zgig pulse program (inverse gated decoupled) was used, applying proton decoupling during the acquisition time. Since the zgig pulse program uses decoupling, it had to be ensured that any signal enhancement due to nuclear Overhauser effect (NOE) is negligible. Therefore, zg and zgig experiments were conducted and the integrals of the signals of interest were compared. For all reaction mixtures investigated, the integrals corresponding to both the internal standard (Ph_3PO) and the product stayed constant.
- After acquisition, the spectra were processed and integrated, and the yields were determined by referencing the integral of the product to that of the standard Ph_3PO.
- The quantitative NMR spectra of the substrate screening are shown in section 5.4.4.

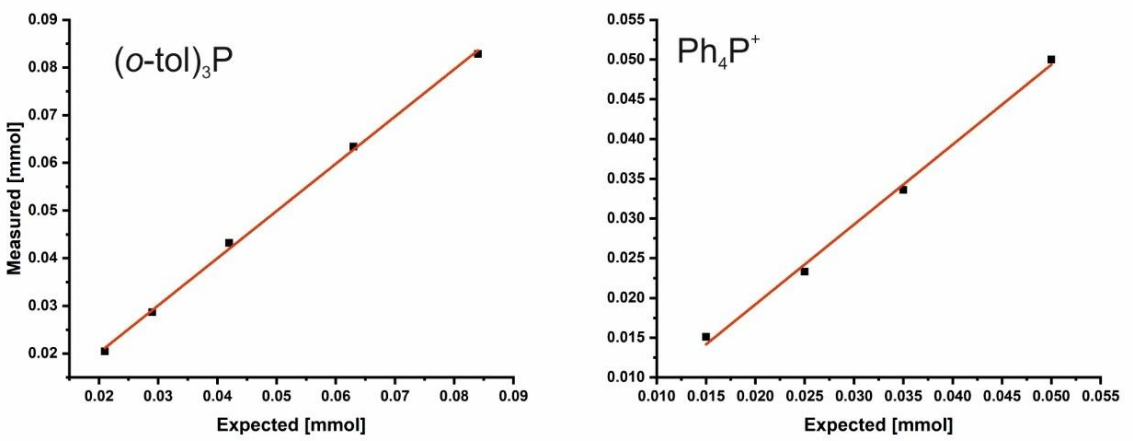

Figure S1. Plots showing the consistency between measured (by integration against 0.05 mmol Ph_3PO using a $^{31}P\{^1H\}$ NMR experiment (zgig) with a single scan) and expected (based on mass added) molar quantities of (*o*-tol)$_3$P (left) or [Ph_4P]Cl (right) in MeCN/C_6H_6 (3:1) solutions.

5.4.2 General Protocol for Photocatalytic Functionalization of P_4 (0.04 mmol Scale)

To a 10 mL stoppered tube equipped with a stirring bar were added the appropriate aryl bromide or aryl chloride (0.44 mmol, 11.0 equiv. based on the phosphorus atom), NEt_3 (50.2 µL, 0.36 mmol, 9.0 equiv. based on the phosphorus atom), 9-mesityl-3,6-di-*tert*-butyl-10-phenylacridinium tetrafluoroborate (Mes-Acr-BF_4; 2.3 mg, 4.0 µmol, 10 mol% based on the phosphorus atom) and P_4 (1.2 mg, 0.01 mmol, 0.25 equiv., as a stock solution in 65.5 µL benzene). The mixture was dissolved in acetonitrile (0.1 mL). The tube was sealed, placed in a custom-made flask holder (Figure S2, left), and irradiated with nUV light (390 nm, 40 W, Kessil PR160L in a PR160 Rig with Fan Kit, Figure S2, right) for 20 h (for ArBr) or 44 h (for ArCl) (unless stated otherwise). Ph_3PO (0.02 mmol, stock solution in benzene) was subsequently added to act as an internal standard. The resulting mixture was subjected to NMR analysis.

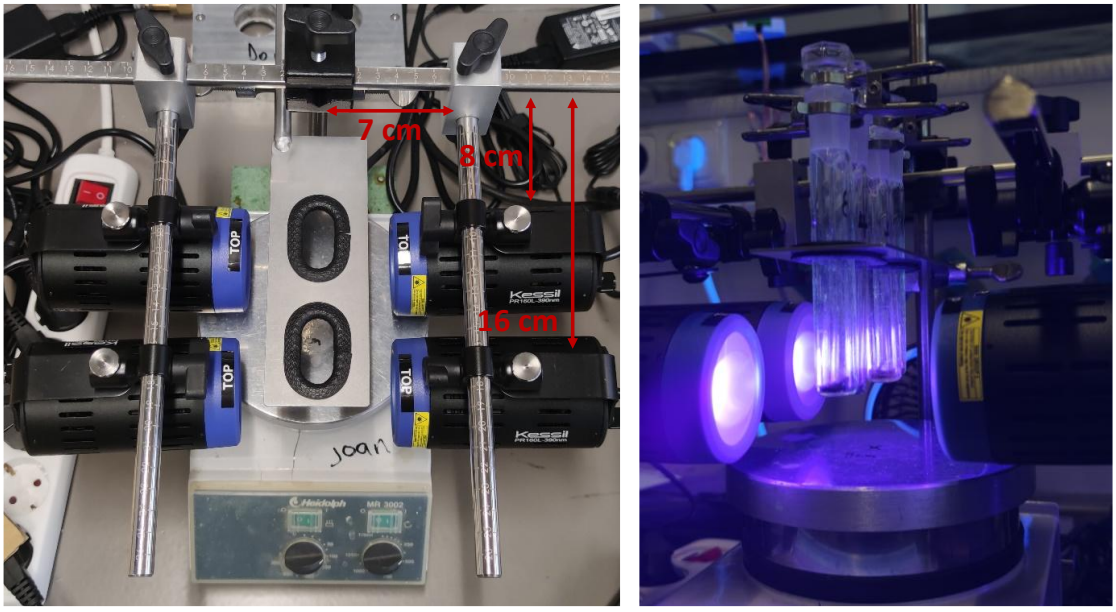

Figure S2. Setup used for photocatalytic reactions at 0.04 mmol scale.

5.4.3 Optimization of Reaction Conditions

Table S1. Photocatalytic functionalization of P_4 to $[Ar_4P]Br$ and Ar_3P: screening of control experiments.[a]

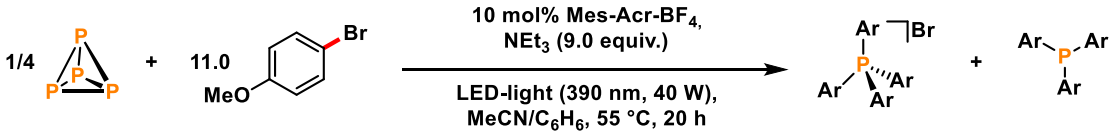

Entry	Conditions	Full conv. of P_4?	Form. of $[Ar_4P]Br$ / %	Form. of Ar_3P / %
1	Standard[a]	✓	47	9
2	No photocatalyst	✗	0	0
3	No light[b]	✗	0	0
4	No NEt_3	✓	0	0
5	No 4-Bromoanisole[c]	✓	0	0
6	4-Fluoroanisole instead of 4-Bromoanisole	✓	0	0
7	4-Iodoanisole instead of 4-Bromoanisole	✓	19	0
8	4-Chloroanisole instead of 4-Bromoanisole	✓	4	14
9	P_{red} instead of P_4[d]	/	0	0

[a] For the general protocol, see section 5.4.2. Ar = 4-OMe–C_6H_4–. [b] The reaction flask was heated to 55 °C. [c] No PH_3 formation was observed. [d] The reaction was conducted in MeCN (0.1 mL) and without benzene.

Table S2. Photocatalytic functionalization of P_4 to $[Ar_4P]Br$ and Ar_3P: screening of LEDs at different wavelengths and electrical power.[a]

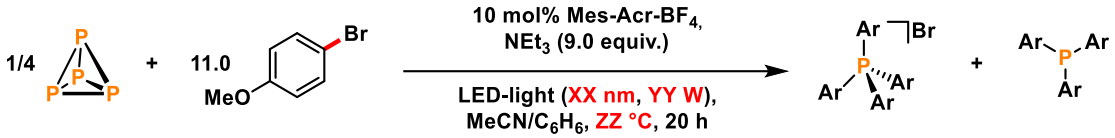

Entry	LED wavelength[b]	LED power[d]	Full conv. of P_4?	Form. of $[Ar_4P]Br$ / %	Form. of Ar_3P / %
1	390 nm	40 W	✓	47	9
2	390 nm	30 W	✓	43	9
3	390 nm	20 W	✓	38	7
4	390 nm	10 W	✓	23	10
5	370 nm	40 W	✓	37	10
6	370 nm[c]	40 W	✓	42	12
7	427 nm	40 W	✓	7	8
8	456 nm	40 W	✓	0	0

[a] For the general protocol, see section 5.4.2. Different LEDs were used. Ar = 4-OMe–C_6H_4–. [b] Kessil PR160L LED. [c] PR160L-370 nm Gen 2 LED. [d] The temperature varies with the electrical power. For: 40 W → T = ≈55 °C, 30 W → T = ≈45 °C, 20 W → T = ≈40 °C, 10 W → T = ≈35 °C.

Table S3. Photocatalytic functionalization of P_4 to $[Ar_4P]Br$ and Ar_3P: screening of solvents.[a]

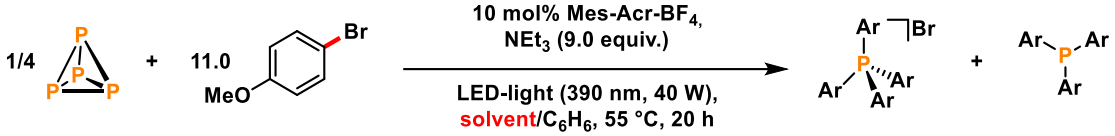

Entry	Solvent	Full conv. of P_4?	Form. of $[Ar_4P]Br$ / %	Form. of Ar_3P / %
1	Acetonitrile	✓	47	9
2	DMF	✓	4	6
3	DMSO	✓	16	6
4	Benzene	✓	19	6
5	Acetone	✓	31	5
6	THF	✓	12	8
7	4-Bromoanisole[b]	✓	18	6

[a] For the general protocol, see section 5.4.2. Ar = 4-OMe–C_6H_4–. The general protocol (section 5.4.2) was modified to use the solvent system indicated (identical solvent volume). [b] Added additionally as solvent (0.1 mL).

Table S4. Photocatalytic functionalization of P_4 to $[Ar_4P]Br$ and Ar_3P: screening of photocatalysts.[a]

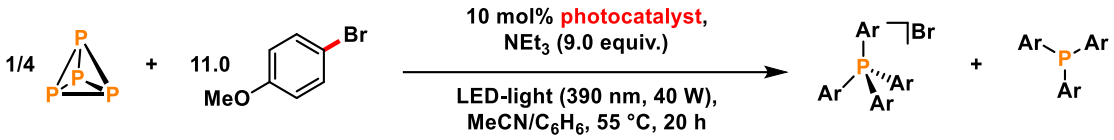

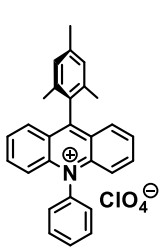

H-Mes-Acr-ClO_4

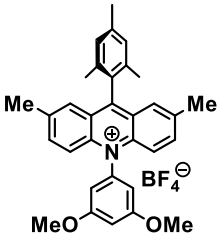

Me-Mes-Acr-BF_4

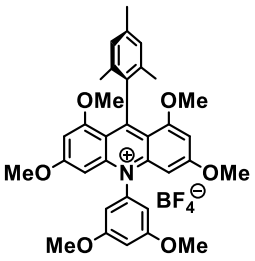

$(MeO)_2$-Mes-Acr-BF_4

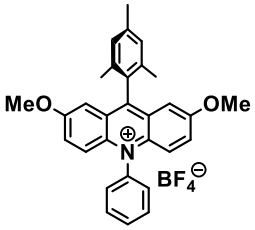

MeO-Mes-Acr-BF_4

Entry	Photocatalyst	LED wavelength[b]	Full conv. of P_4?	Form. of $[Ar_4P]Br$ / %	Form. of Ar_3P / %
1	H-Mes-Acr-ClO_4	390 nm	✓	9	8
2	Me-Mes-Acr-BF_4	390 nm	✓	34	7
3	$(MeO)_2$-Mes-Acr-BF_4	390 nm	✓	0	5
4	MeO-Mes-Acr-BF_4	390 nm	✓	32	15
5	MeO-Mes-Acr-BF_4	370 nm	✓	27	16
6	MeO-Mes-Acr-BF_4	427 nm	✓	6	9
7	MeO-Mes-Acr-BF_4	456 nm	✓	0	0

[a] For the general protocol, see section 5.4.2. Ar = 4-OMe–C_6H_4–. The general protocol (section 5.4.2) was modified to use the photocatalyst indicated. [b] All reactions were carried out at 40 W electrical power.

Table S5. Photocatalytic functionalization of P_4 to $[Ar_4P]Br$ and Ar_3P: concentration screening.[a]

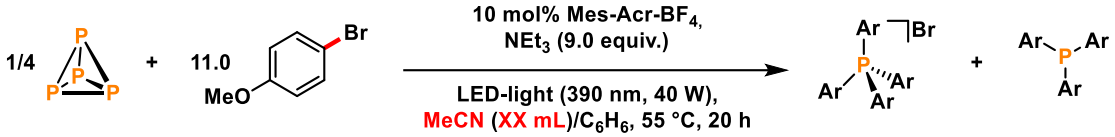

Entry	Solvent volume	Full conv. of P_4?	Form. of $[Ar_4P]Br$ / %	Form. of Ar_3P / %
1	0.05 mL	✓	47	7
2	0.1 mL	✓	47	9
3	0.25 mL	✓	34	12
4	0.5 mL	✓	30	15
5	1.0 mL	✓	24	17
6	2.0 mL	✓	9	14

[a] For the general protocol, see section 5.4.2. Ar = 4-OMe–C_6H_4–. The general protocol (section 5.4.2) was modified to use the indicated amount of MeCN.

Table S6. Photocatalytic functionalization of P_4 to $[Ar_4P]Br$ and Ar_3P: screening of catalyst loading.[a]

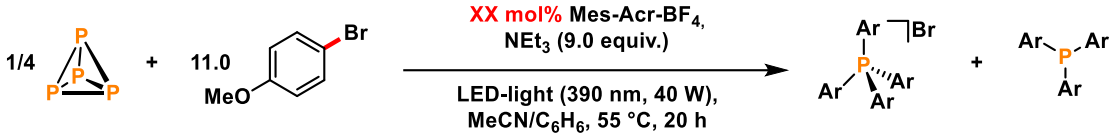

Entry	Catalyst loading	Full conv. of P_4?	Form. of $[Ar_4P]Br$ / %	Form. of Ar_3P / %
1	1.0 mol%	✓	7	7
2	5.0 mol%	✓	32	10
3	7.5 mol%	✓	36	13
4	10 mol%	✓	47	9
5	20 mol%	✓	43	8
6	2 x 10 mol%[b]	✓	48	0
7	50 mol%	✓	40	0

[a] For the general protocol, see section 5.4.2. Ar = 4-OMe–C_6H_4–. The general protocol (section 5.4.2) was modified to use the indicated amount of the photocatalyst Mes-Acr-BF_4. [b] Addition of the second photocatalyst portion (2.3 mg, 10 mol%, 4.0 µmol; in 0.1 mL MeCN) after 20 h irradiation time and then additional 20 h irradiation.

Table S7. Photocatalytic functionalization of P_4 to $[Ar_4P]Br$ and Ar_3P: screening of reductants.[a]

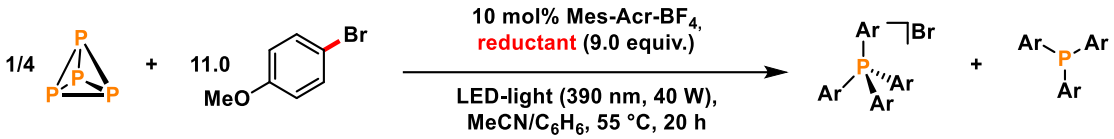

Entry	Reductant	Full conv. of P_4?	Form. of $[Ar_4P]Br$ / %	Form. of Ar_3P / %
1	NEt_3	✓	47	9
2	DIPEA	✓	31	9
3	N^nBu_3	✓	29	10
4	Hantzsch ester[b]	✓	0	0
5	DABCO	✓	0	0
6	HN^iPr_2[c]	✓	12	3
7	$NMe_2{}^nPr$	✓	23	12
8	$NaHCO_2$[b]	✓	/	/

[a] For the general protocol, see section 5.4.2. Ar = 4-OMe–C_6H_4–. The general protocol (section 5.4.2) was modified to use the indicated reducing agent (identical stoichiometry). [b] 0.5 mL MeCN. [c] Additional unidentified signals between 5.0 and 32.0 ppm observed.

Table S8. Photocatalytic functionalization of P_4 to $[Ar_4P]Br$ and Ar_3P: screening of reductant and substrate stoichiometry.[a]

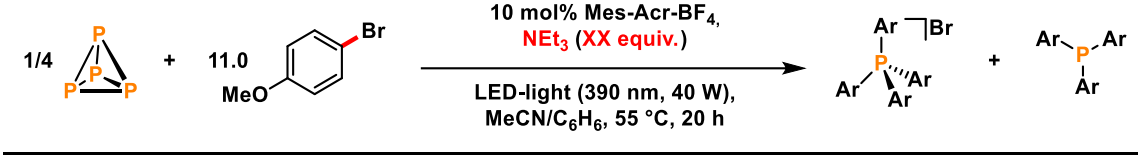

Entry	Stoichiometry[b] NEt_3:4-Bromoanisole	Full conv. of P_4?	Form. of $[Ar_4P]Br$ / %	Form. of Ar_3P / %
1	4:44	✓	/	/
2	18:44	✓	26	8
3	24:44	✓	38	9
4	30:44	✓	41	9
5	36:44	✓	45	9
6	42:44	✓	35	9
7	56:44	✓	31	11
8	72:44	✓	25	15
9	36:20	✓	19	12
10	36:32	✓	30	15
11	36:44	✓	47	9
12	36:60	✓	42	7
13	36:80	✓	40	8

[a] For the general protocol, see section 5.4.2. Ar = 4-OMe–C_6H_4–. [b] Listed equivalents are defined per P_4 molecule.

Table S9. Photocatalytic functionalization of P_4 to $[Ar_4P]Br$ and Ar_3P: re-charge experiments.[a]

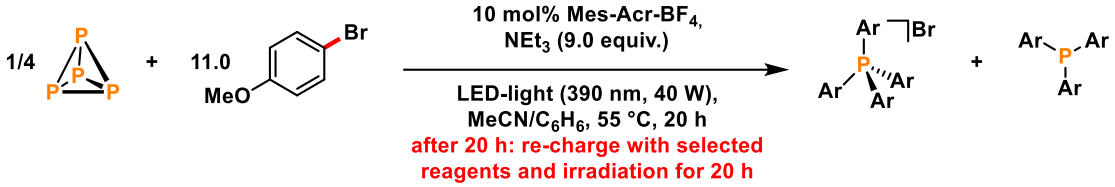

Entry	Re-charge	Full conv. of P_4?	Form. of $[Ar_4P]Br$ / %	Form. of Ar_3P / %
1	No re-charge but irradiation	✓	52	6
2	P_4 + ArBr + NEt_3 + Mes-Acr-BF_4	✓	38	11
3	ArBr + NEt_3 + Mes-Acr-BF_4	✓	58	0
4	ArBr + NEt_3[b]	✓	58	7

[a] For the general protocol, see section 5.4.2. Ar = 4-OMe–C_6H_4–. After the reaction was completed following the general protocol, the reaction tube was transferred to a glovebox, re-charged with the indicated reagents and irradiated for an additional 20 h. The reagents were added in equivalent amounts as described in the general protocol; P_4 (1.2 mg, 0.01 mmol, as a stock solution in 65.5 µL benzene); ArBr (55.1 µL, 11.0 equiv., 0.44 mmol); NEt_3 (50.2 µL, 9.0 equiv., 0.36 mmol); Mes-Acr-BF_4 (2.3 mg, 10 mol%, 4.0 µmol; in 0.1 mL MeCN). [b] MeCN (0.1 mL) and benzene (65.5 µL) were added.

Table S10. Photocatalytic functionalization of P_4 to $[Ph_4P]Br$ and Ph_3P: kinetic investigations.[a]

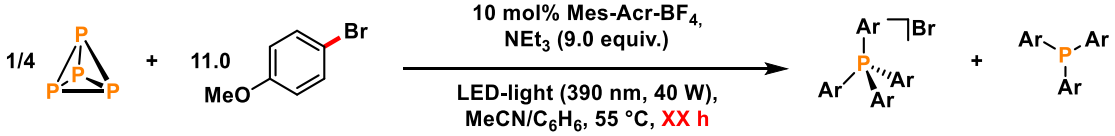

Entry	Time	Full conv. of P_4?	Form. of $[Ph_4P]Br$ / %	Form. of Ph_3P / %	Form.[b] of Ph_2PH / %	Form.[b] of $PhPH_2$ / %	Form.[b] of Ph_4P_2 / %
1	10 min	✗	0	0	✗	✓	✗
2	30 min	✓	0	1	✓	✓	✓
3	1 h	✓	6	9	✓	✓	✓
4	2 h[c]	✓	21	15	✓	✗	✓
5	4 h[c]	✓	38	13	✓	✗	✗
6	6 h[c]	✓	50	8	✗	✗	✗
7	14 h[c]	✓	53	6	✗	✗	✗
8	20 h[c]	✓	63	0	✗	✗	✗
9	44 h	✓	64	0	✗	✗	✗

[a] For the general protocol, see section 5.4.2. [b] The formation of Ph_2PH, $PhPH_2$ and Ph_4P_2 was assessed in the $^{31}P\{^1H\}$ NMR spectrum (NS 512). [c] The formation of $[Ph_3P(NEt_2)]Br$ can be observed in the $^{31}P\{^1H\}$ NMR spectrum (NS 512).[9]

5.4.4 Characterization of Photocatalytic Arylation Reactions at 0.04 mmol Scale

The conversions were determined by quantitative $^{31}P\{^{1}H\}$ (zgig) NMR experiments (161.98 MHz, 298 K, C_6D_6 capillary) from the reaction solution as described in section 5.4.2 (Ph_3PO [0.02 mmol] was used as internal standard, see section 5.4.1 for further information). The $^{31}P\{^{1}H\}$ NMR spectroscopic data for aryl bromides is provided after 20 h reaction time, with additional data available for selected substrates after 44 h reaction time (Table S11). The $^{31}P\{^{1}H\}$ NMR spectroscopic data for aryl chlorides is provided after 44 h reaction time, with additional data available for selected substrates after 68 h reaction time (Table S11). The spectroscopic data was assigned to the stated products based on the chemical shifts reported in the literature.[9]

5.4.4.1 $^{31}P\{^{1}H\}$ NMR Spectroscopic Data for Aryl Bromides After 20 h and Aryl Chlorides After 44 h Reaction Time

Aryl bromides – 20 h reaction time:

Tetraphenylphosphonium bromide

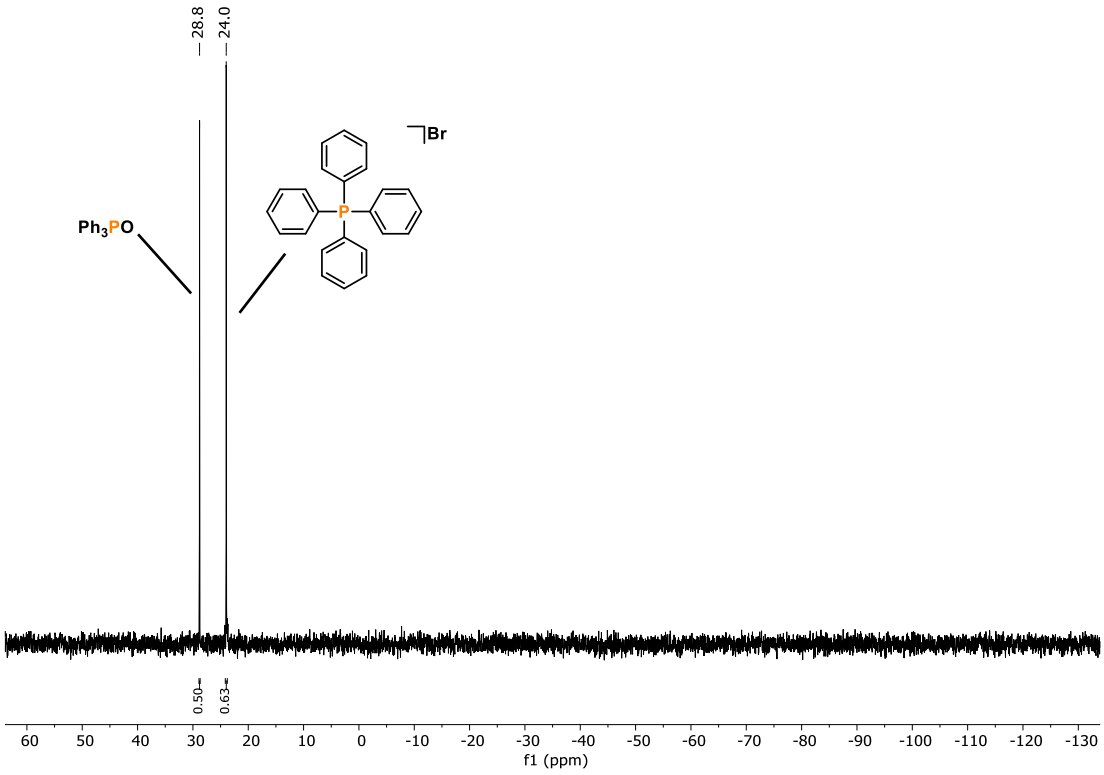

Figure S3. Quantitative single scan $^{31}P\{^{1}H\}$ (zgig) NMR spectrum for the photocatalytic functionalization of P_4 using bromobenzene.

Tetrakis(4-methoxyphenyl)phosphonium bromide and tris(4-methoxyphenyl)phosphine

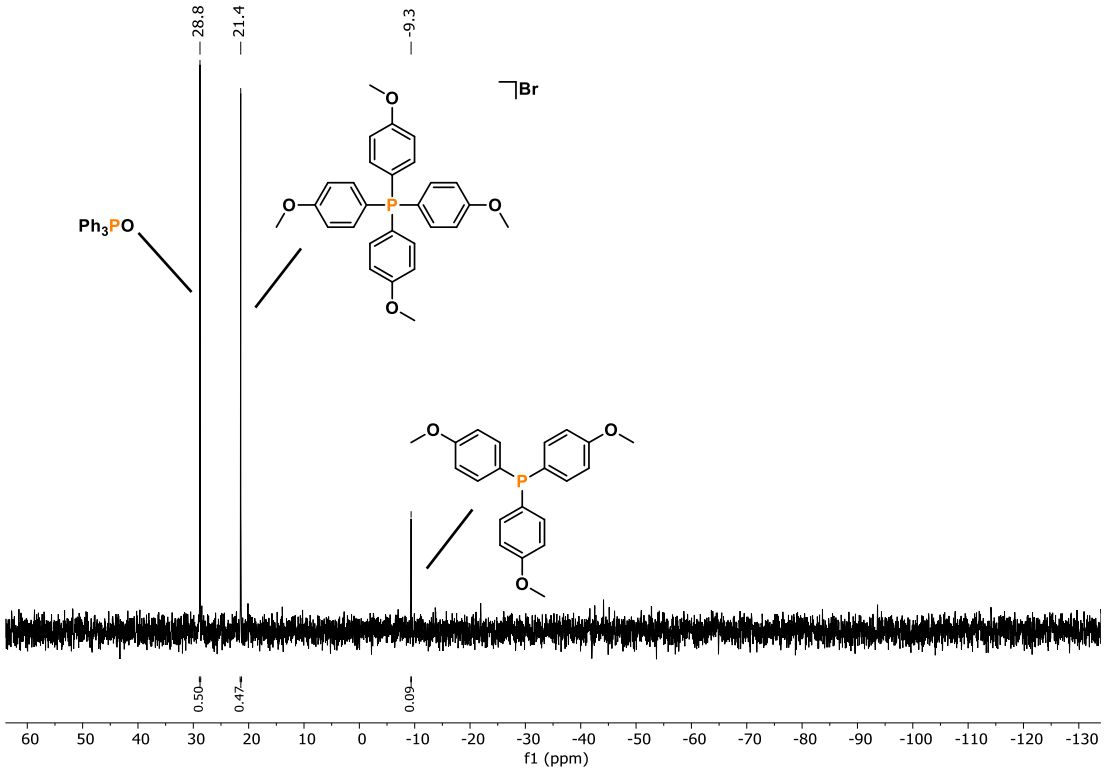

Figure S4. Quantitative single scan $^{31}P\{^{1}H\}$ (zgig) NMR spectrum for the photocatalytic functionalization of P_4 using 4-bromoanisole.

Tetrakis(3-methoxyphenyl)phosphonium bromide and tris(3-methoxyphenyl)phosphine

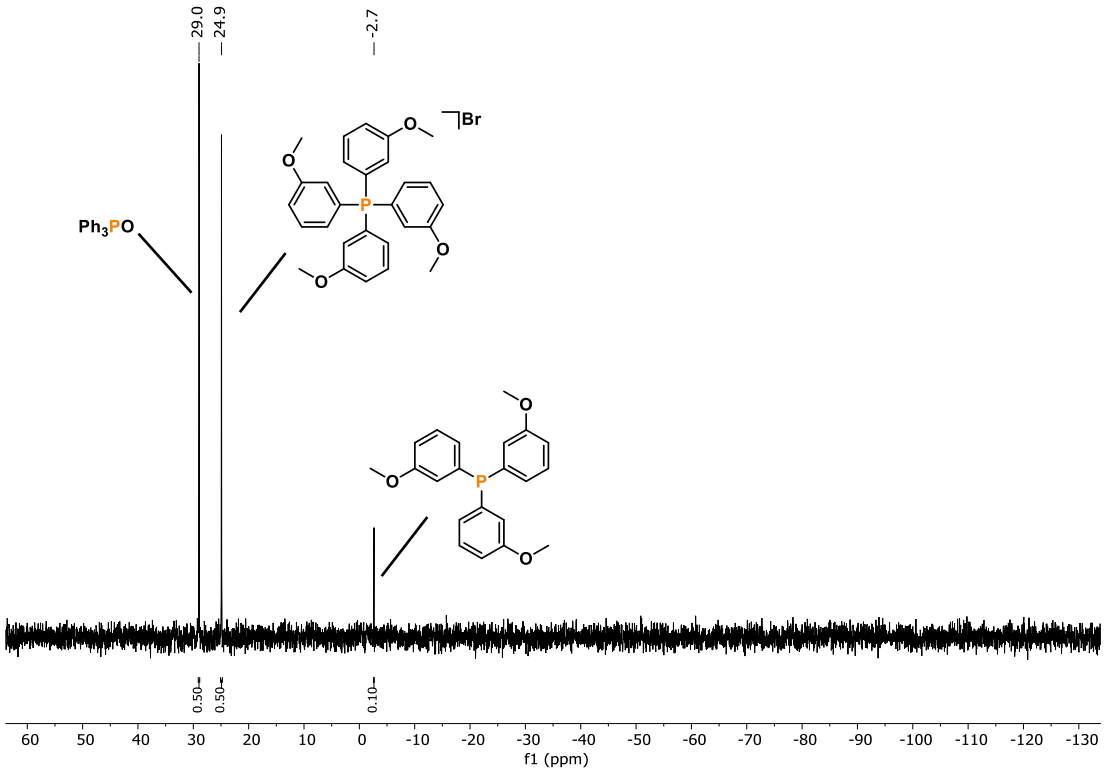

Figure S5. Quantitative single scan $^{31}P\{^{1}H\}$ (zgig) NMR spectrum for the photocatalytic functionalization of P_4 using 3-bromoanisole.

Tris(2-methoxyphenyl)phosphine

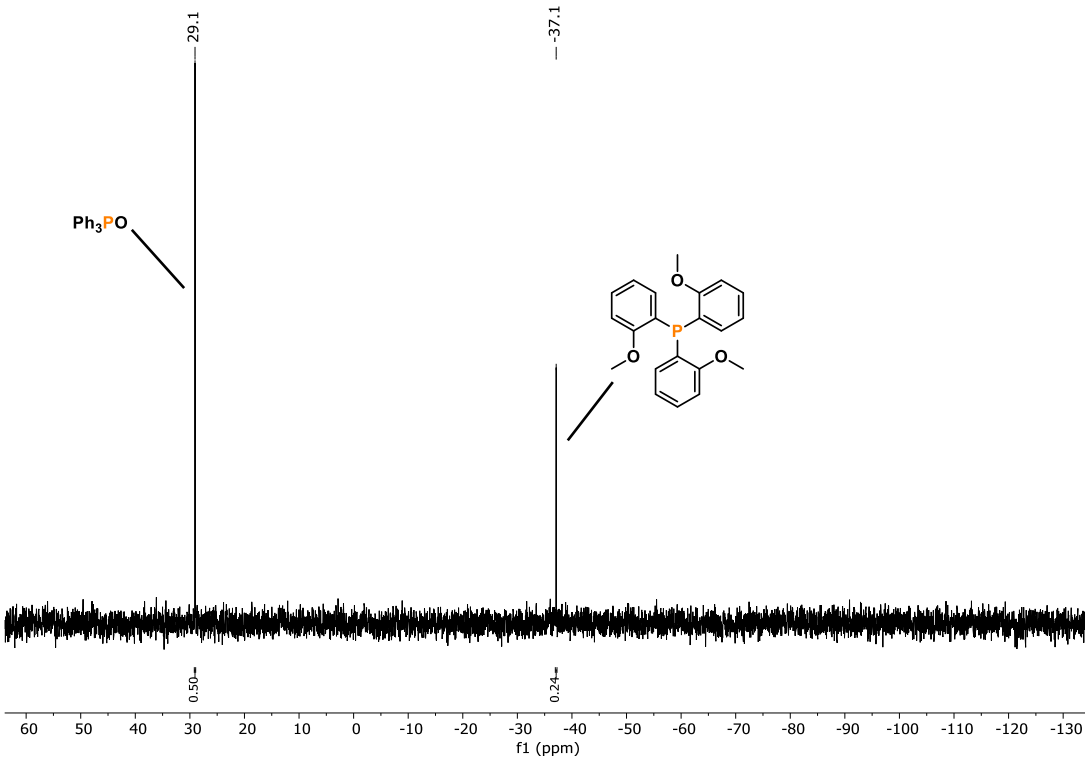

Figure S6. Quantitative single scan $^{31}P\{^{1}H\}$ (zgig) NMR spectrum for the photocatalytic functionalization of P_4 using 2-bromoanisole.

Tetrakis(3,5-dimethoxyphenyl)phosphonium bromide and tris(3,5-dimethoxyphenyl)-phosphine[19]

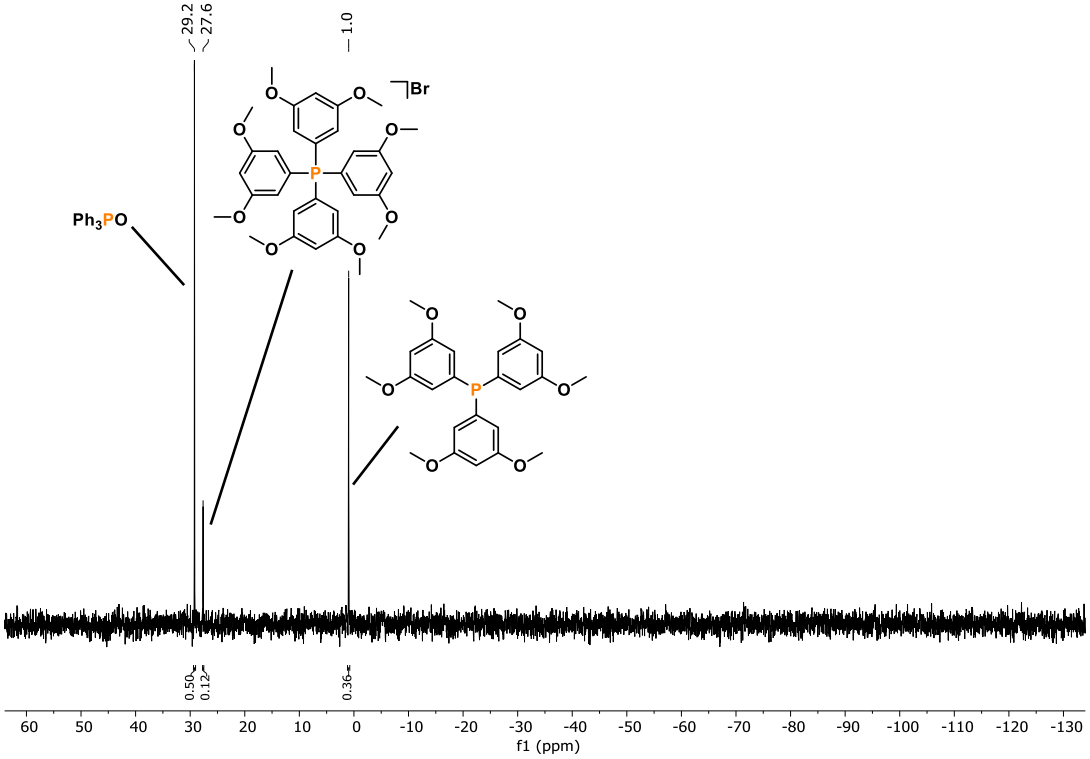

Figure S7. Quantitative single scan $^{31}P\{^{1}H\}$ (zgig) NMR spectrum for the photocatalytic functionalization of P_4 using 1-bromo-3,5-dimethoxybenzene.

Tetra(*p*-tolyl)phosphonium bromide and tris(*p*-tolyl)phosphine

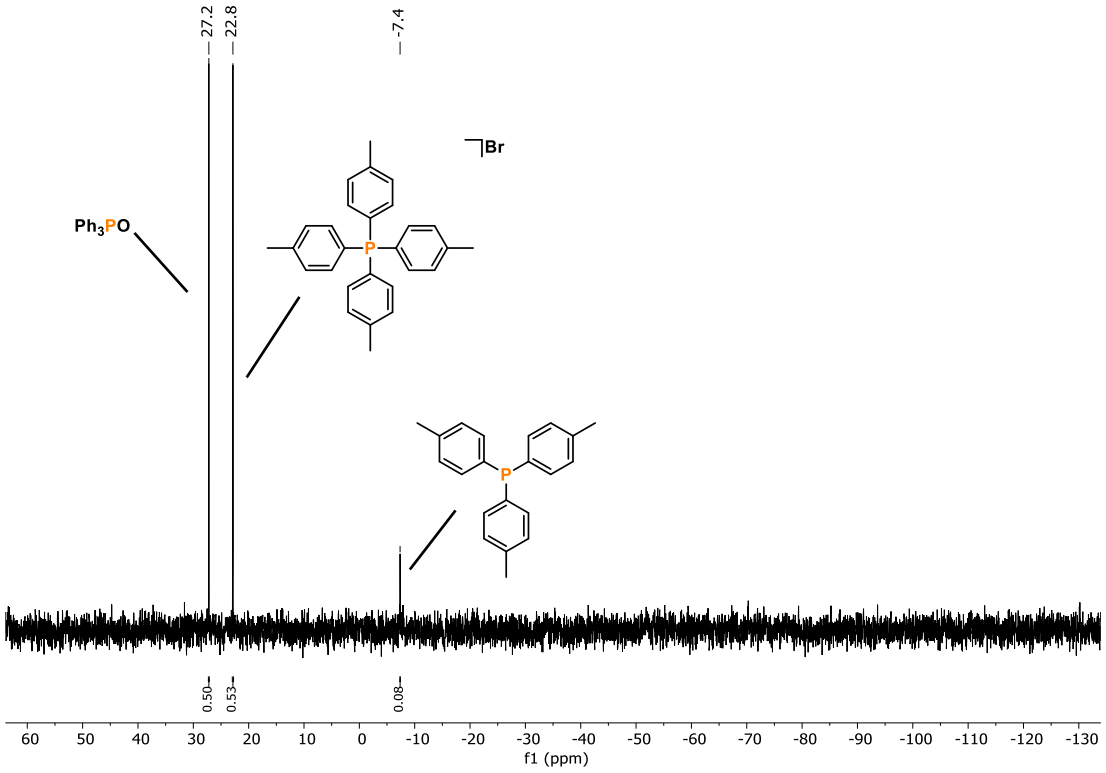

Figure S8. Quantitative single scan $^{31}P\{^{1}H\}$ (zgig) NMR spectrum for the photocatalytic functionalization of P_4 using 4-bromotoluene.

Tetra(*m*-tolyl)phosphonium bromide and tris(*m*-tolyl)phosphine

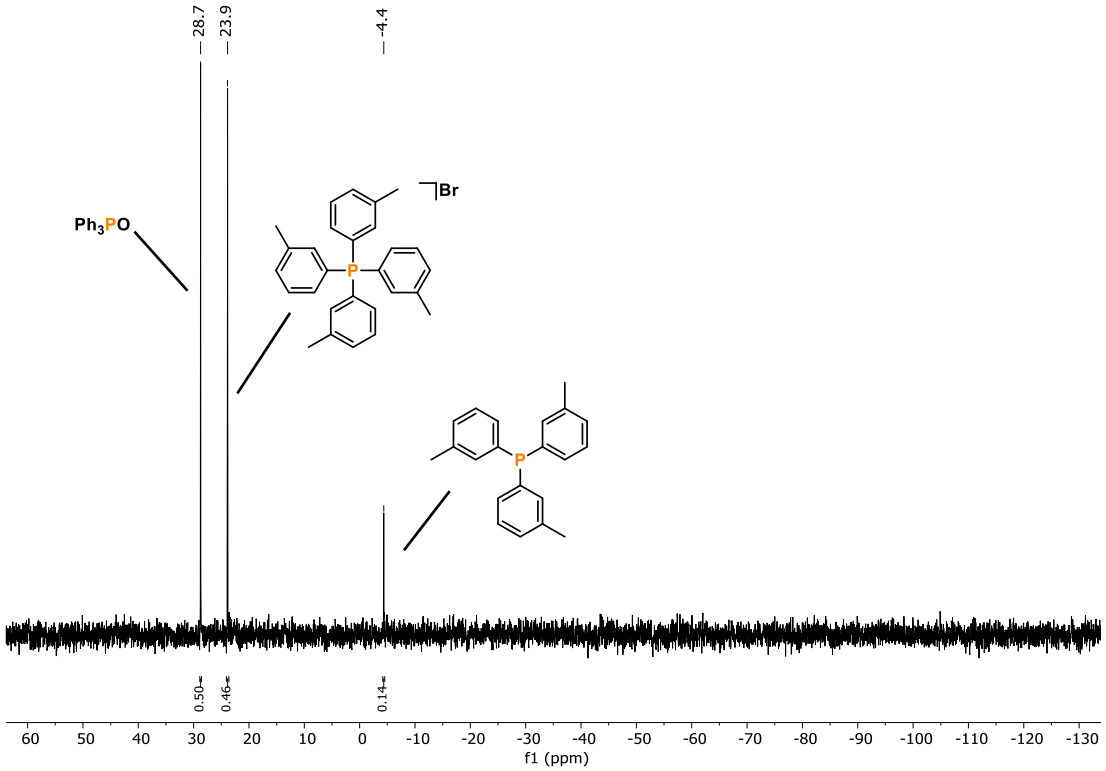

Figure S9. Quantitative single scan $^{31}P\{^{1}H\}$ (zgig) NMR spectrum for the photocatalytic functionalization of P_4 using 3-bromotoluene.

Tris(*o*-tolyl)phosphine

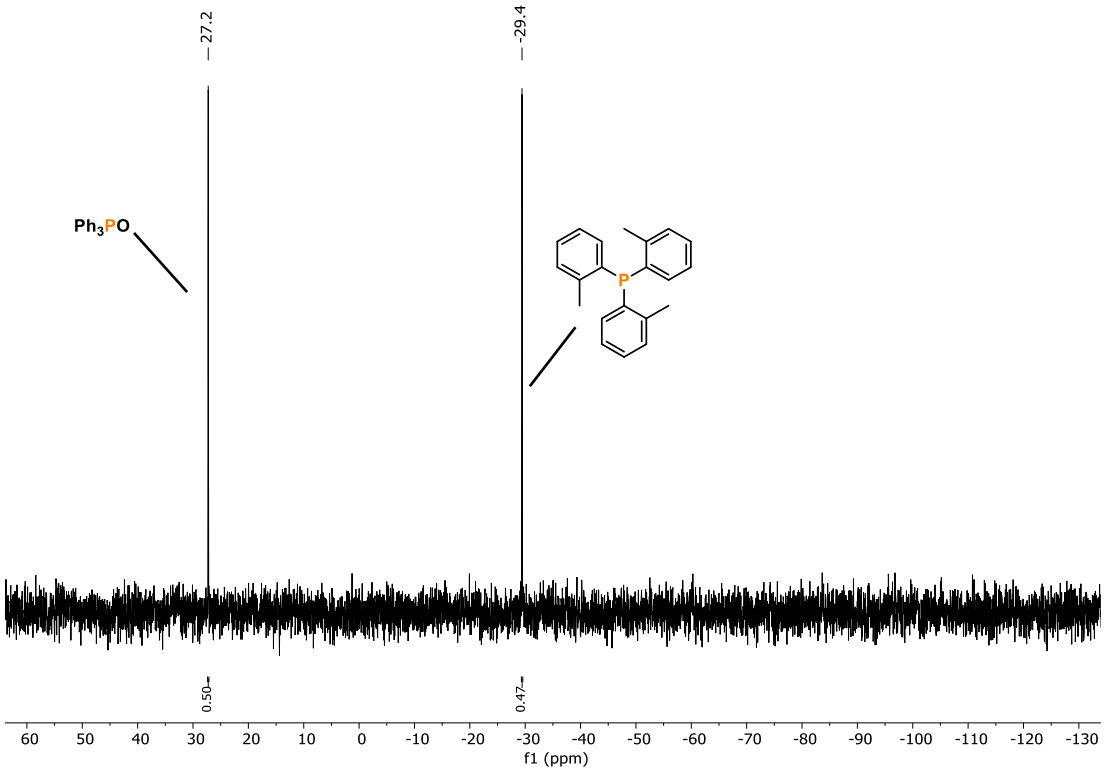

Figure S10. Quantitative single scan $^{31}P\{^{1}H\}$ (zgig) NMR spectrum for the photocatalytic functionalization of P_4 using 2-bromotoluene.

Tetrakis(4-ethylphenyl)phosphonium bromide and tris(4-ethylphenyl)phosphine

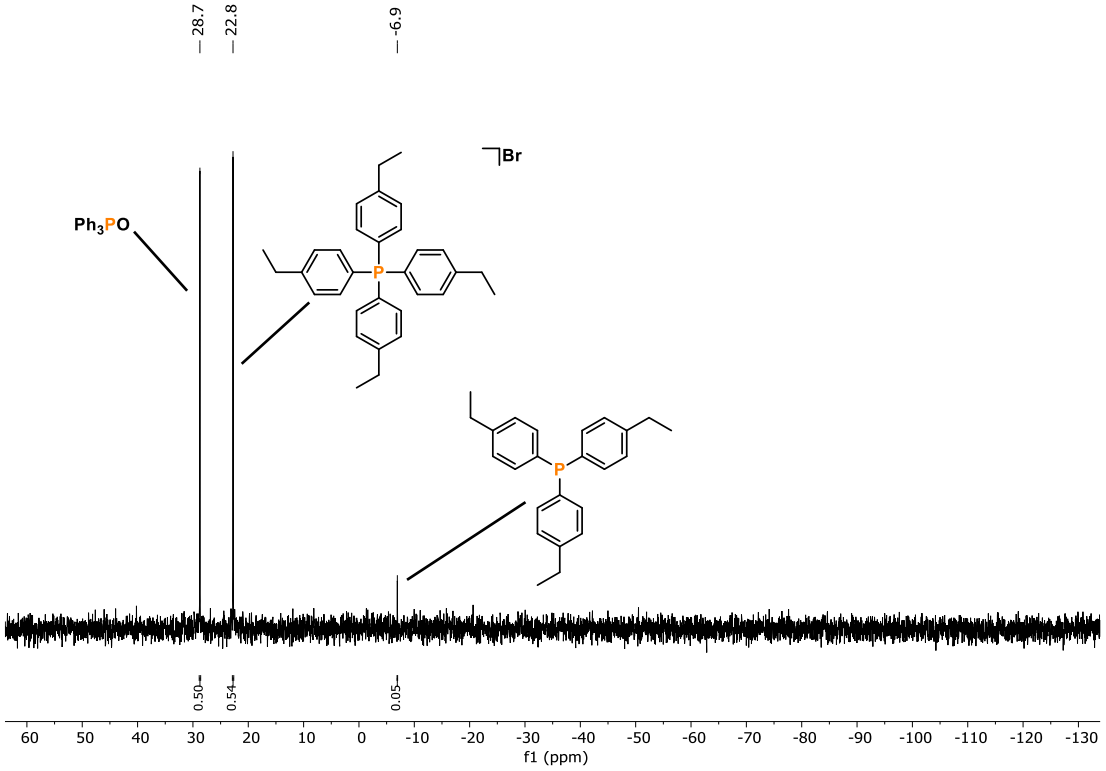

Figure S11. Quantitative single scan $^{31}P\{^{1}H\}$ (zgig) NMR spectrum for the photocatalytic functionalization of P_4 using 1-bromo-4-ethylbenzene.

Tetrakis(3-ethylphenyl)phosphonium bromide and tris(3-ethylphenyl)phosphine[20]

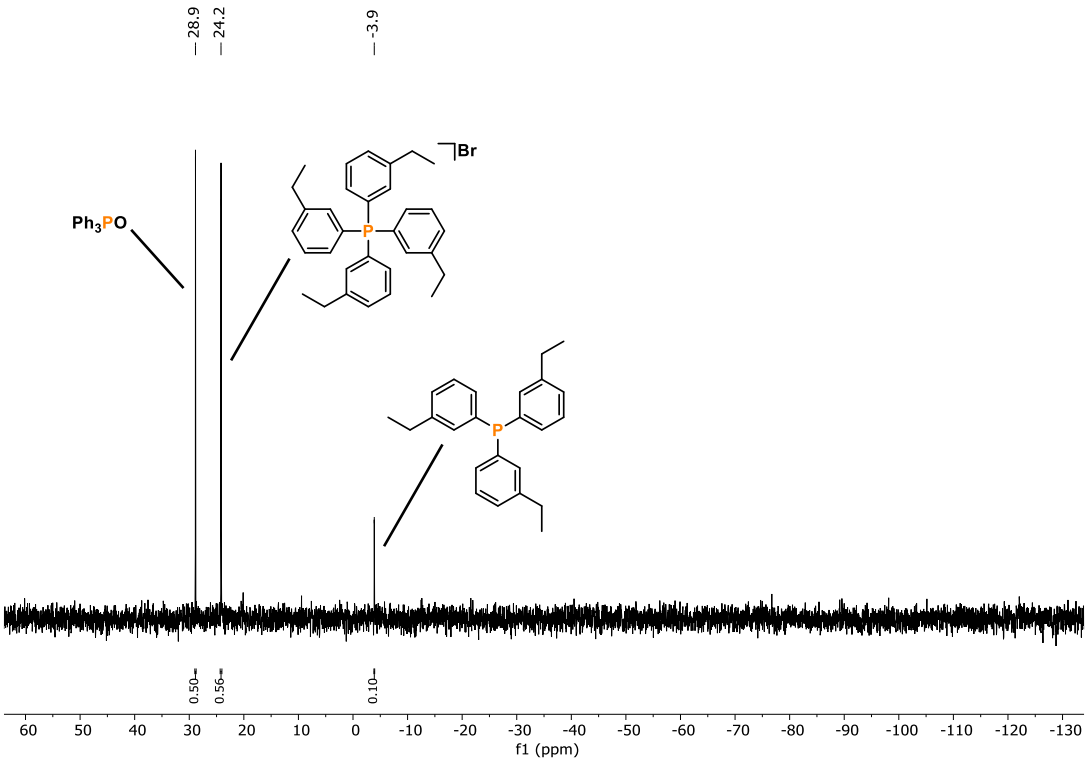

Figure S12. Quantitative single scan $^{31}P\{^{1}H\}$ (zgig) NMR spectrum for the photocatalytic functionalization of P_4 using 1-bromo-3-ethylbenzene.

Tetrakis[(4-methylthio)phenyl]phosphonium bromide and tris[(4-methylthio)phenyl]-phosphine[21]

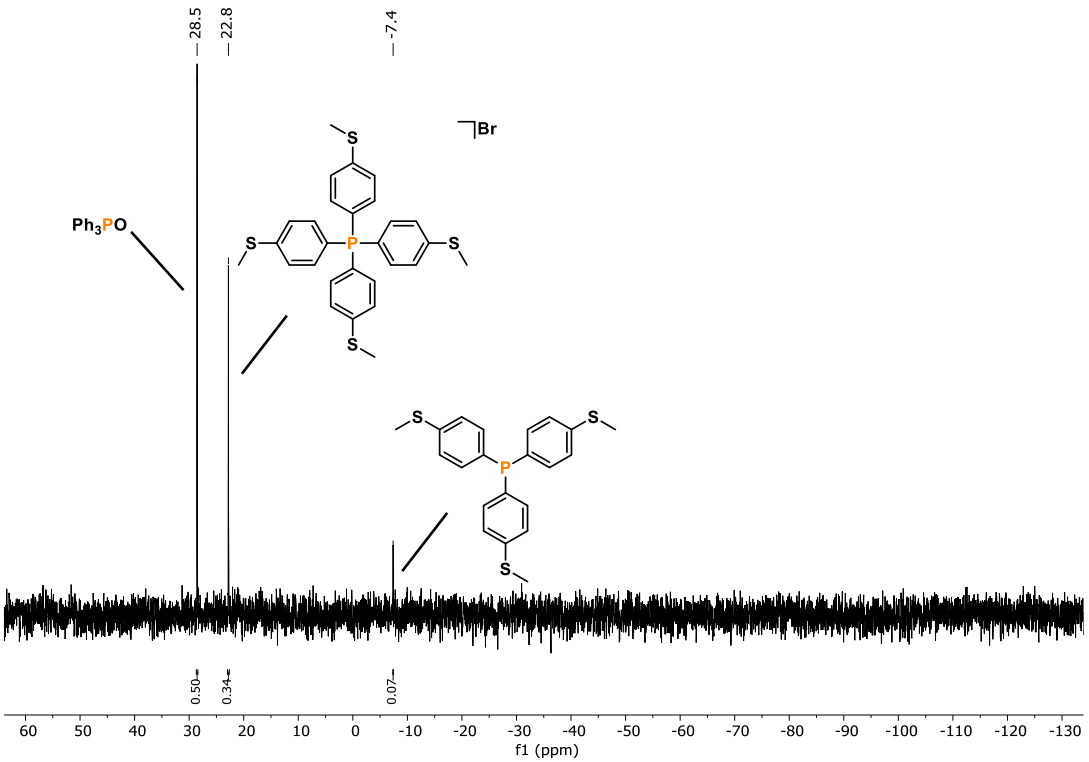

Figure S13. Quantitative single scan $^{31}P\{^{1}H\}$ (zgig) NMR spectrum for the photocatalytic functionalization of P_4 using 4-bromothioanisole.

Tetrakis(4-phenoxyphenyl)phosphonium bromide and tris(4-phenoxyphenyl)phosphine[22]

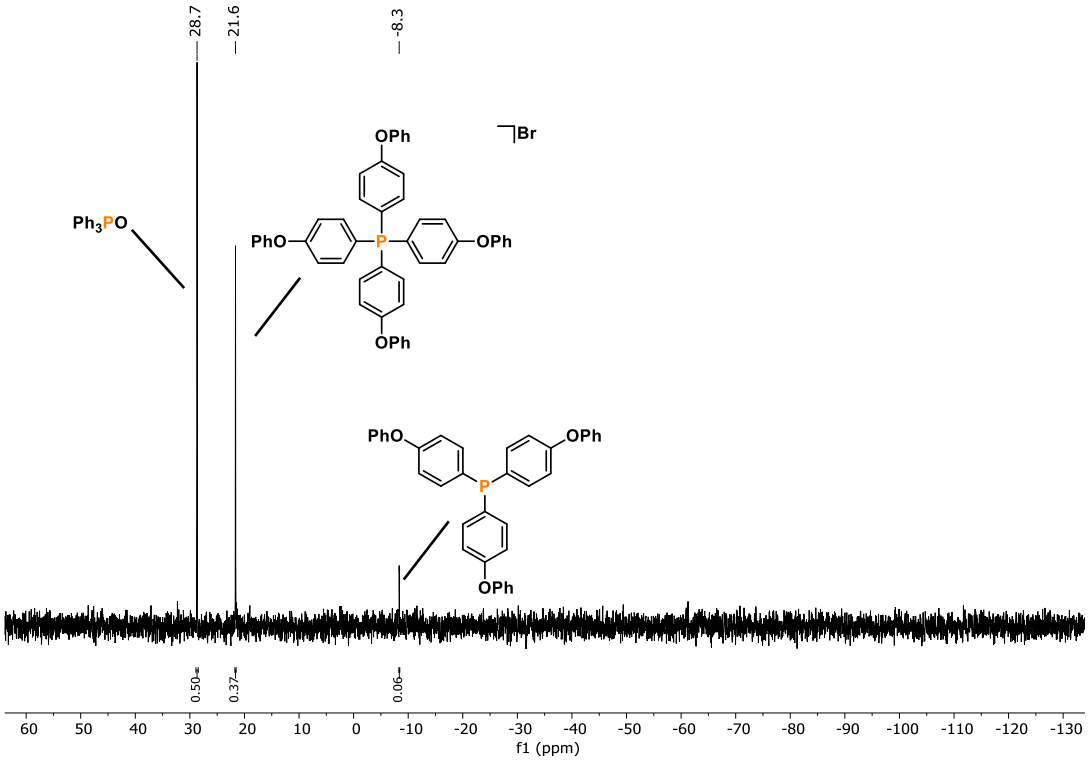

Figure S14. Quantitative single scan $^{31}P\{^{1}H\}$ (zgig) NMR spectrum for the photocatalytic functionalization of P_4 using 1-bromo-4-phenoxybenzene.

Tetrakis[(4-*tert*-butyl)phenyl]phosphonium bromide and tris[(4-*tert*-butyl)phenyl]-phosphine

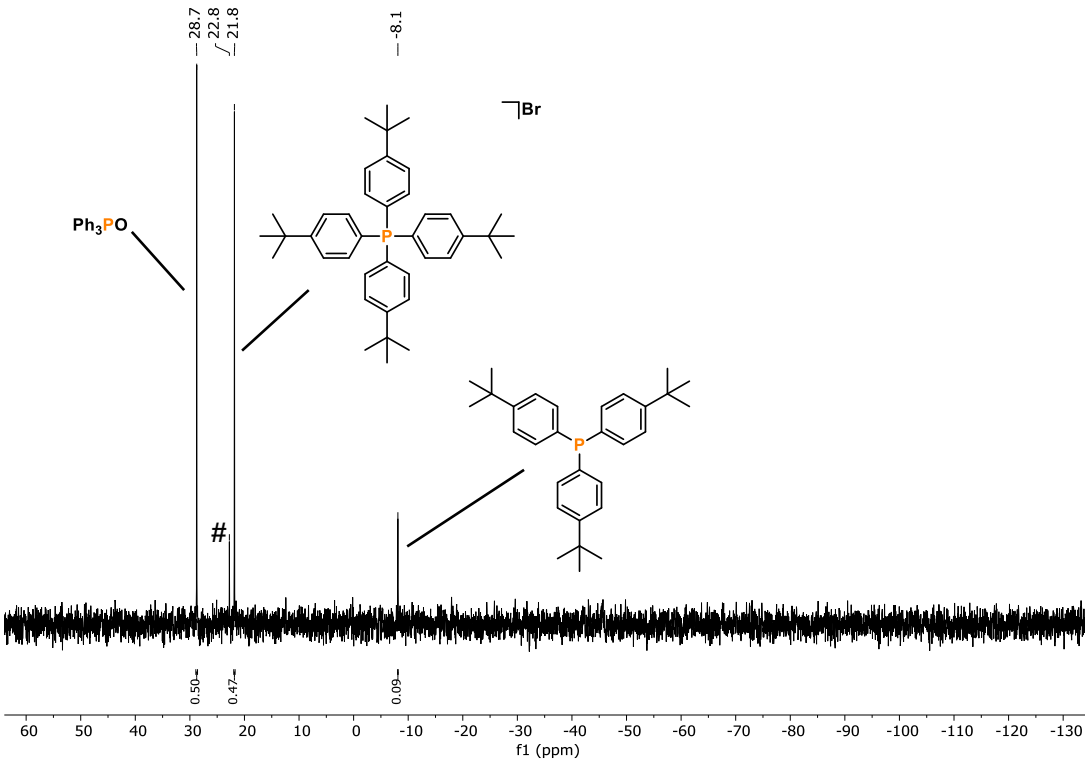

Figure S15. Quantitative single scan $^{31}P\{^{1}H\}$ (zgig) NMR spectrum for the photocatalytic functionalization of P_4 using 1-bromo-4-*tert*-butylbenzene. #: unidentified signal.

Tetrakis(4-methyl benzoate)phosphonium bromide

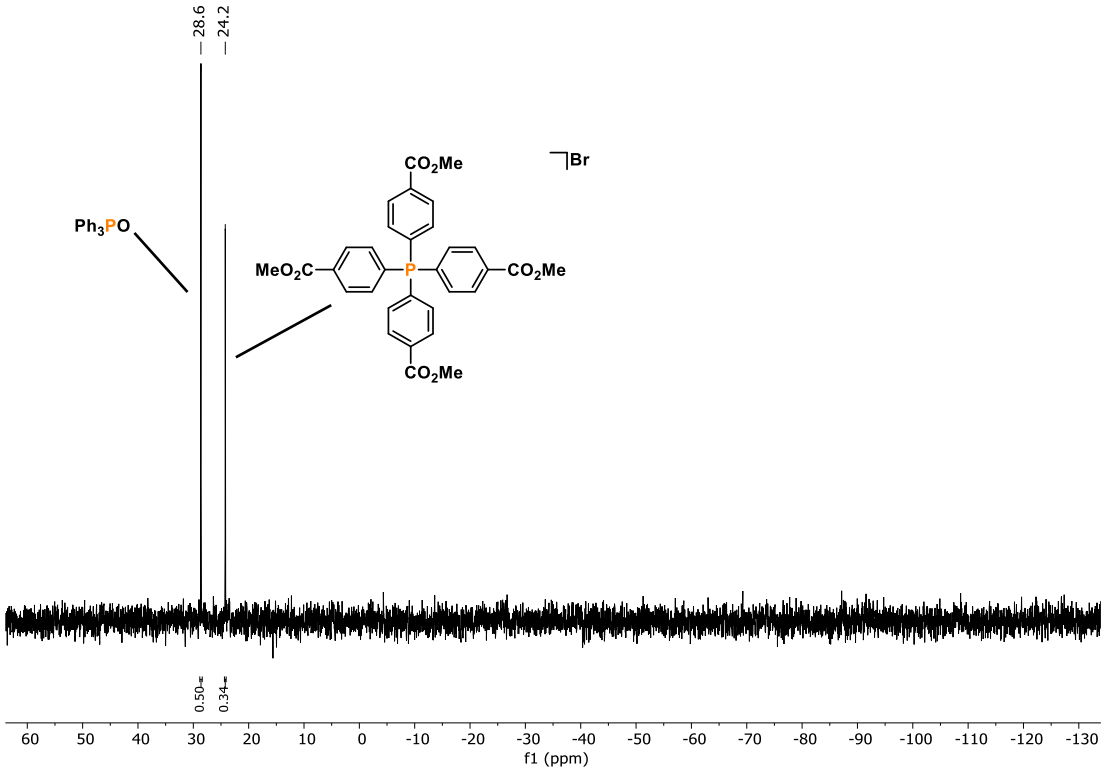

Figure S16. Quantitative single scan $^{31}P\{^{1}H\}$ (zgig) NMR spectrum for the photocatalytic functionalization of P_4 using methyl 4-bromobenzoate.

Tetrakis(3-methyl benzoate)phosphonium bromide and tris(3-methyl benzoate)phosphine

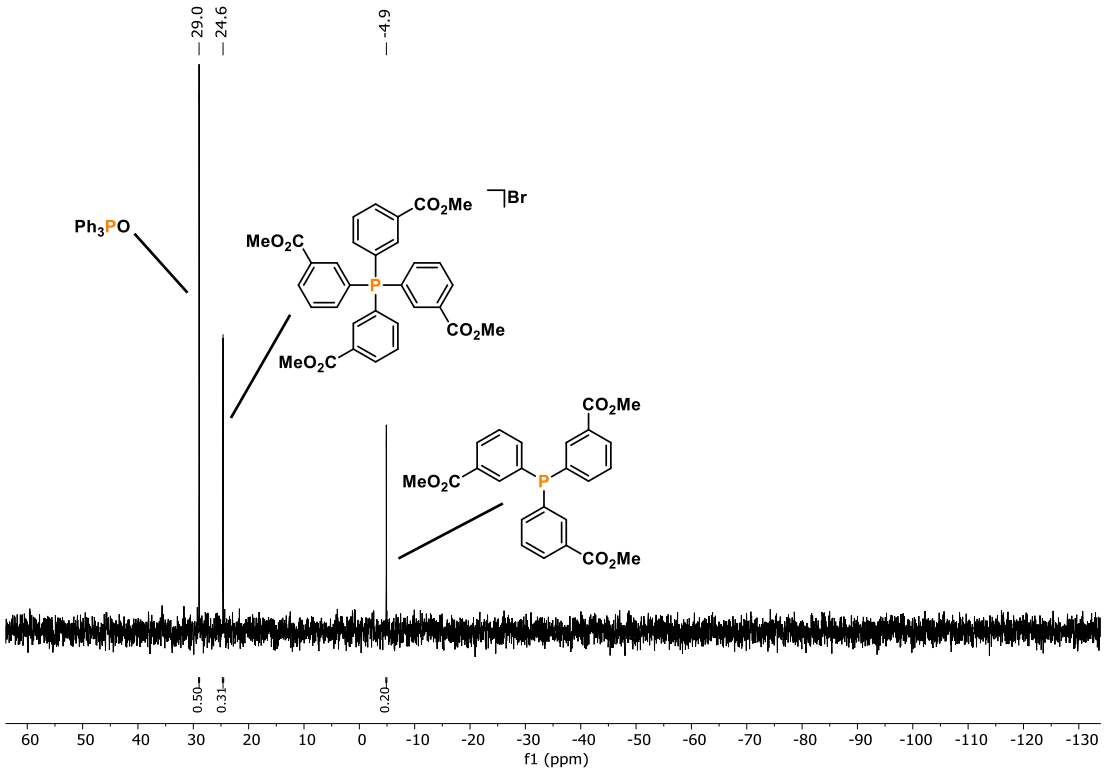

Figure S17. Quantitative single scan $^{31}P\{^{1}H\}$ (zgig) NMR spectrum for the photocatalytic functionalization of P_4 using methyl 3-bromobenzoate.

Tetrakis[(4-cyano)phenyl]phosphonium bromide and tris[(4-cyano)phenyl]phosphine[23]

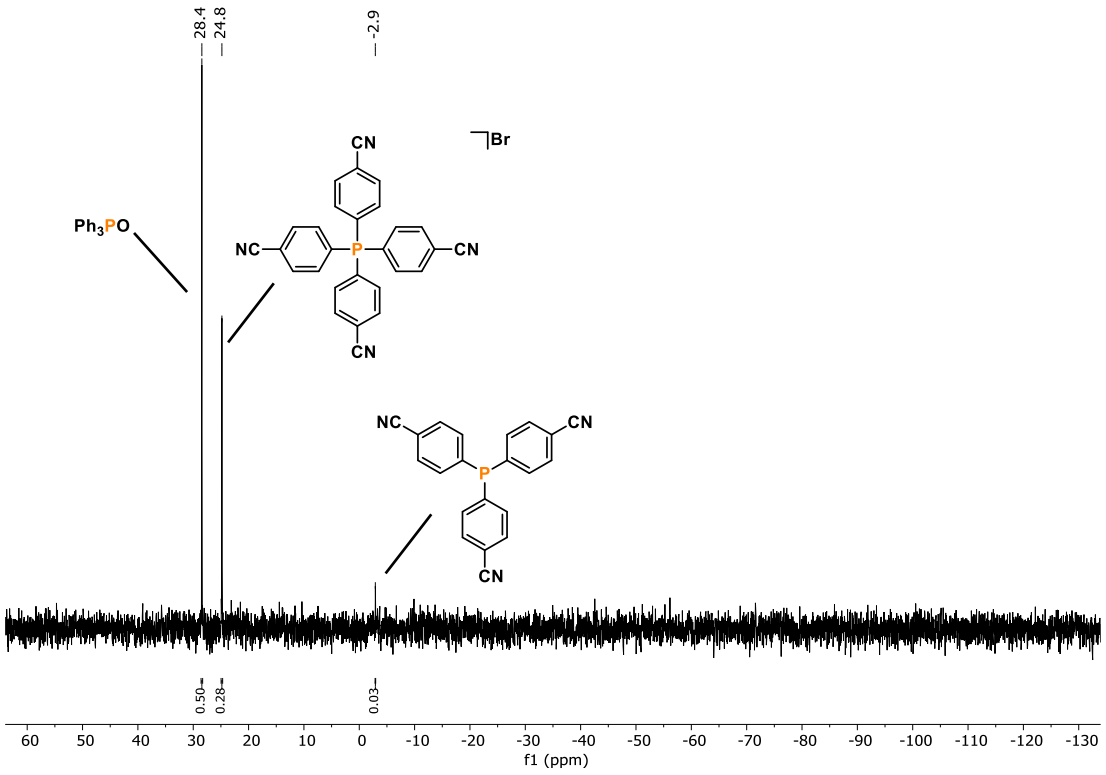

Figure S18. Quantitative single scan $^{31}P\{^{1}H\}$ (zgig) NMR spectrum for the photocatalytic functionalization of P_4 using 4-bromobenzonitrile.

Tetrakis[(3-cyano)phenyl]phosphonium bromide and tris[(3-cyano)phenyl]phosphine[24]

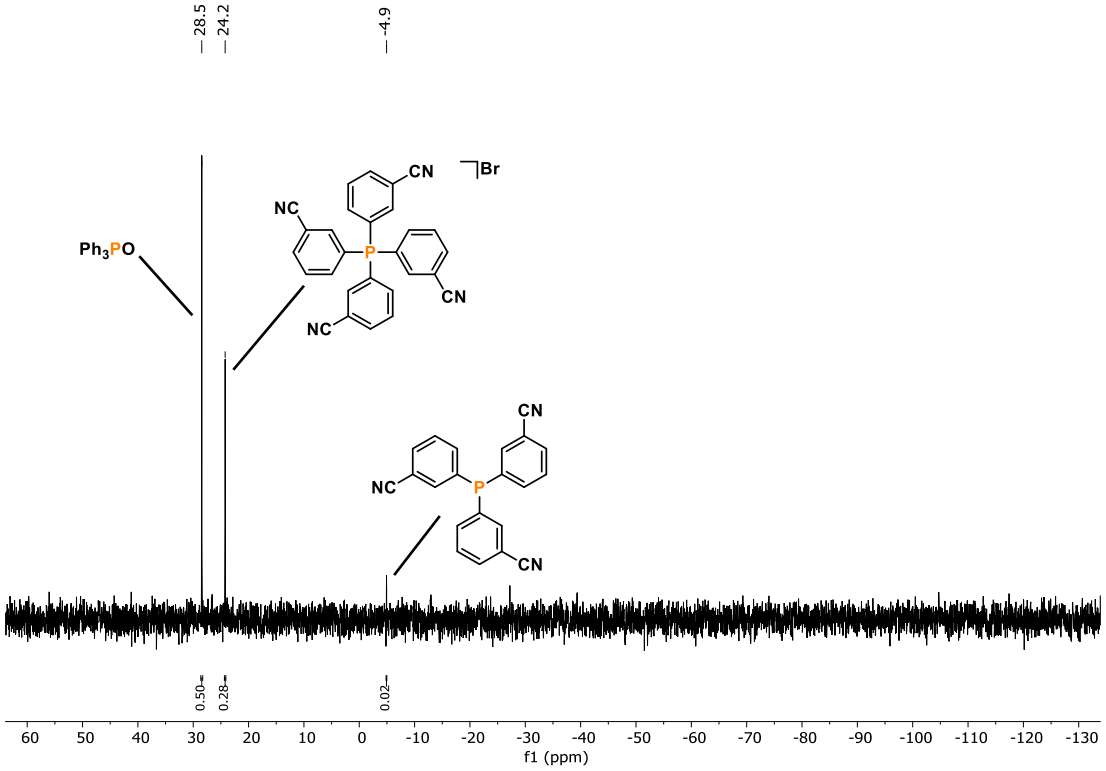

Figure S19. Quantitative single scan $^{31}P\{^{1}H\}$ (zgig) NMR spectrum for the photocatalytic functionalization of P_4 using 3-bromobenzonitrile.

Tetrakis[(4-trifluoromethyl)phenyl]phosphonium bromide and tris[(4-trifluoromethyl)-phenyl]phosphine

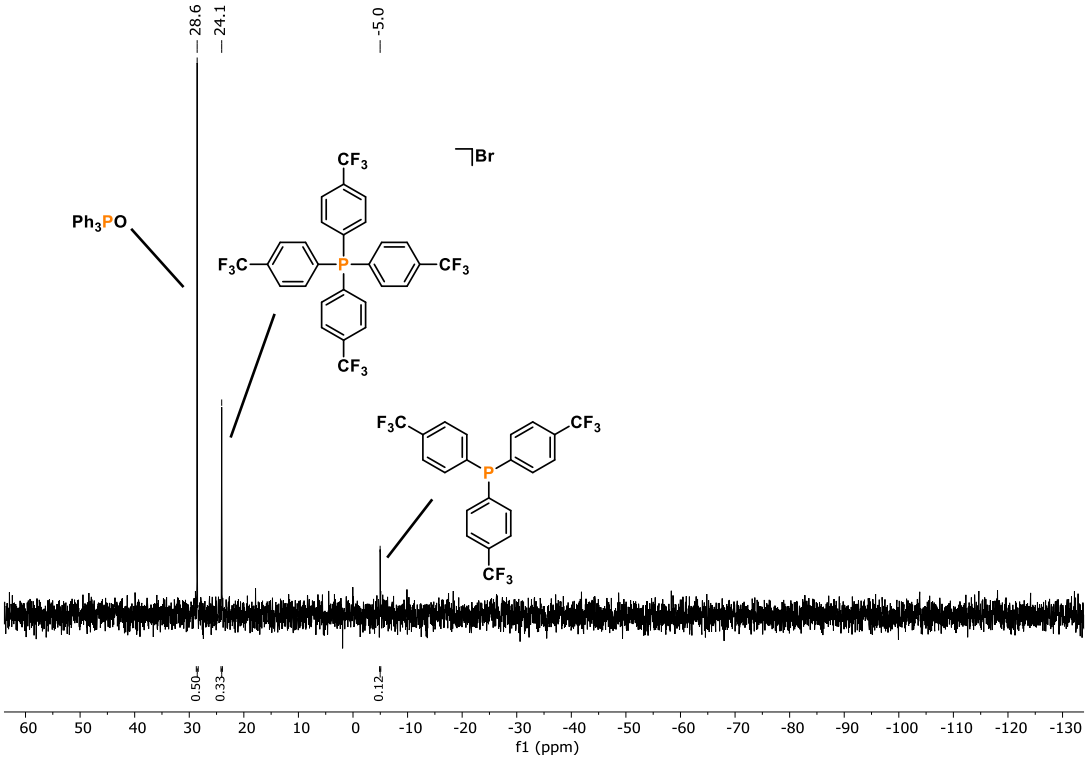

Figure S20. Quantitative single scan $^{31}P\{^{1}H\}$ (zgig) NMR spectrum for the photocatalytic functionalization of P_4 using 4-bromobenzotrifluoride.

Tetrakis(pyridine-3-yl)phosphonium bromide and tris(pyridine-3-yl)phosphine

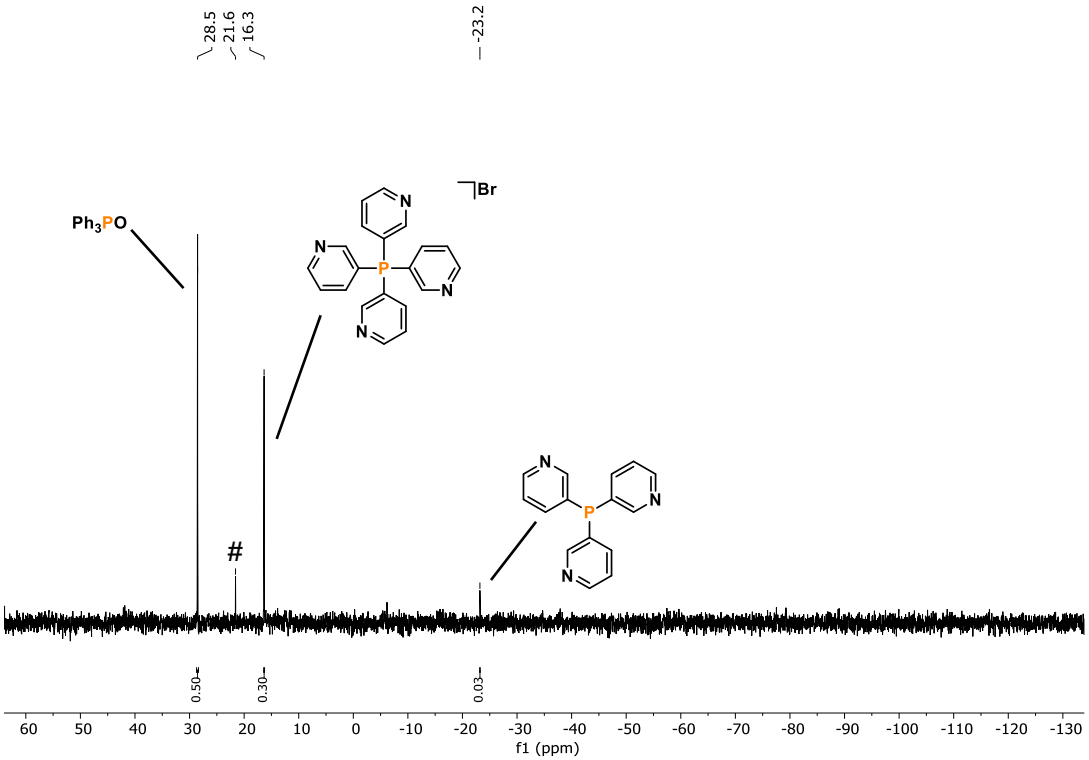

Figure S21. Quantitative single scan $^{31}P\{^{1}H\}$ (zgig) NMR spectrum for the photocatalytic functionalization of P_4 using 3-bromopyridine. #: unidentified signal.

Aryl chlorides – 44 h reaction time:

Tetraphenylphosphonium chloride and triphenylphosphine

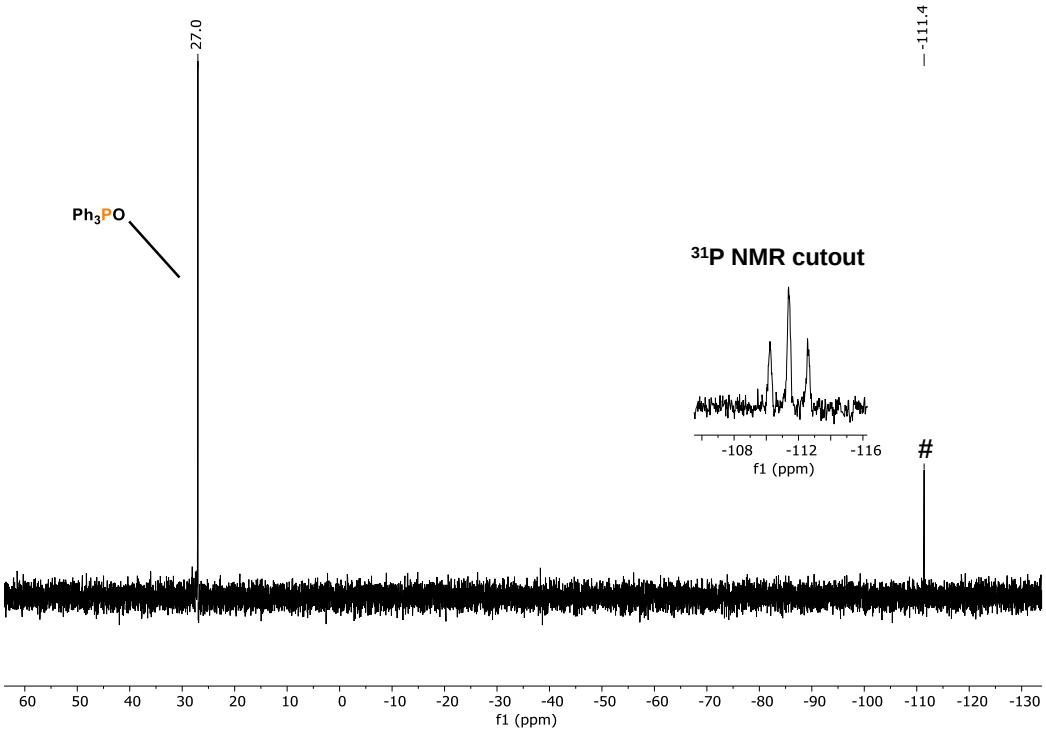

Figure S22. Quantitative single scan $^{31}P\{^{1}H\}$ (zgig) NMR spectrum for the photocatalytic functionalization of P_4 using chlorobenzene. #: formation of $HPPh_2$ (assigned by ^{31}P NMR analysis, $^{1}J_{PH}$ = 188.9 Hz; shift of signal likely due to coordinative interactions).

Tetra(4-methoxyphenyl)phosphonium chloride and tris(4-methoxyphenyl)phosphine

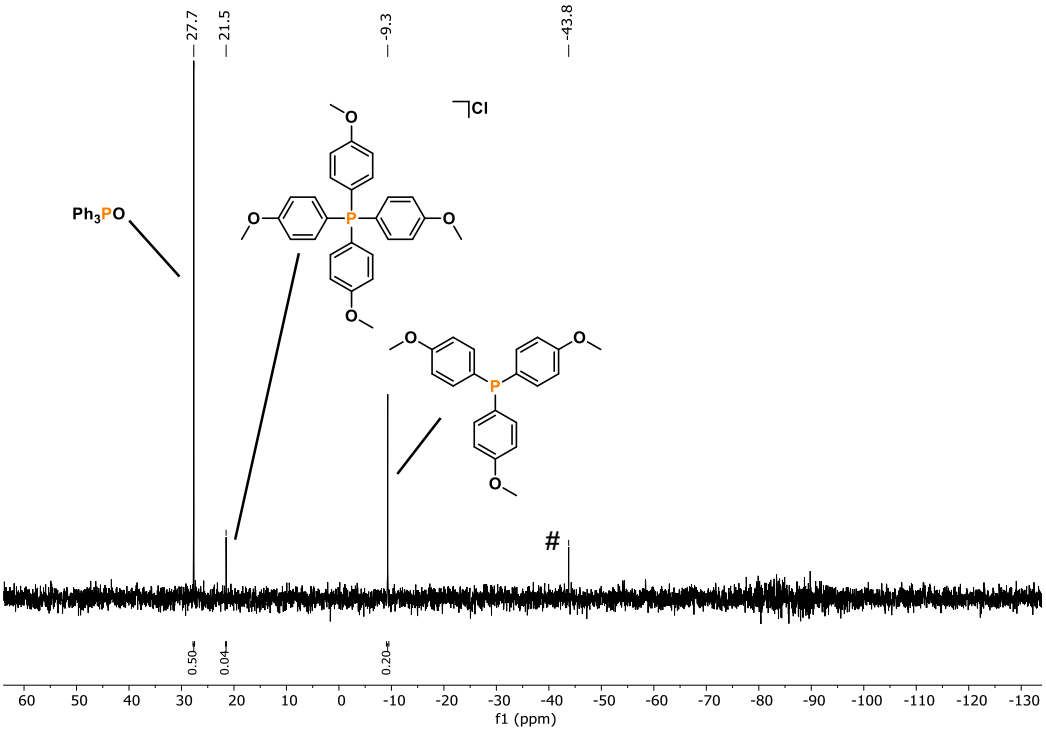

Figure S23. Quantitative single scan $^{31}P\{^{1}H\}$ (zgig) NMR spectrum for the photocatalytic functionalization of P_4 using 4-chloroanisole. #: di(*p*-methoxyphenyl)phosphine.

Tetra(3-methoxyphenyl)phosphonium chloride and tris(3-methoxyphenyl)phosphine

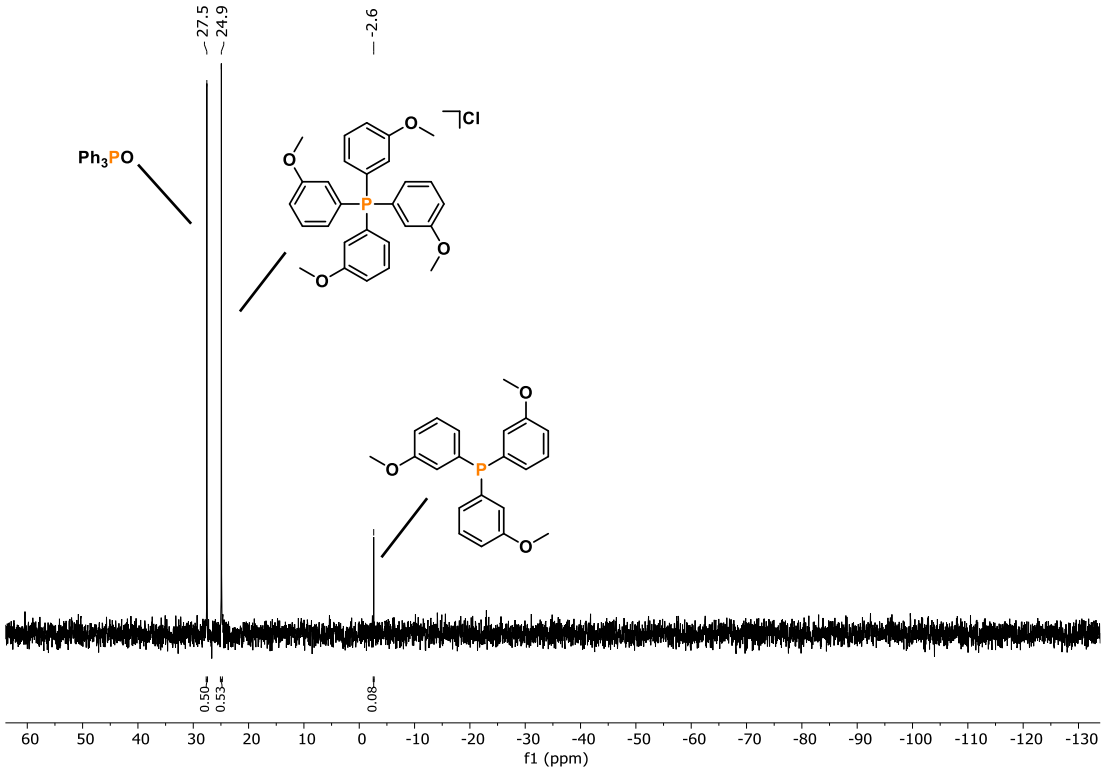

Figure S24. Quantitative single scan $^{31}P\{^{1}H\}$ (zgig) NMR spectrum for the photocatalytic functionalization of P_4 using 3-chloroanisole.

Tris(2-methoxyphenyl)phosphine

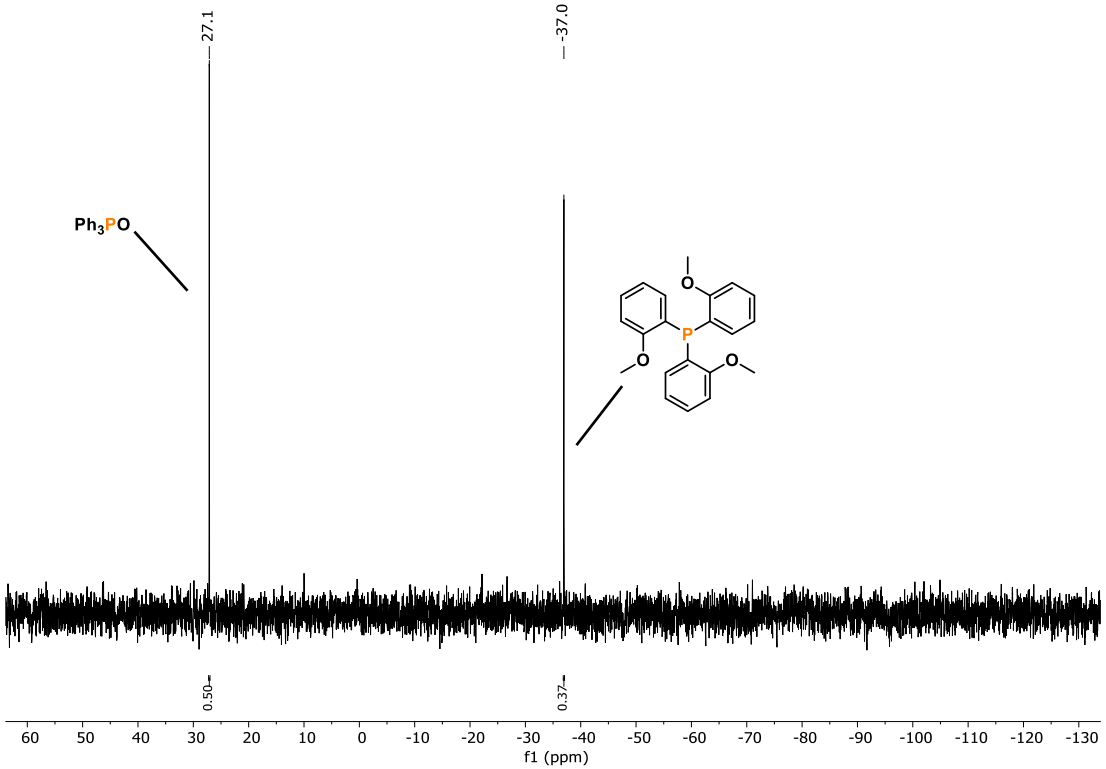

Figure S25. Quantitative single scan $^{31}P\{^{1}H\}$ (zgig) NMR spectrum for the photocatalytic functionalization of P_4 using 2-chloroanisole.

Tetra(*p*-tolyl)phosphonium chloride and tris(*p*-tolyl)phosphine

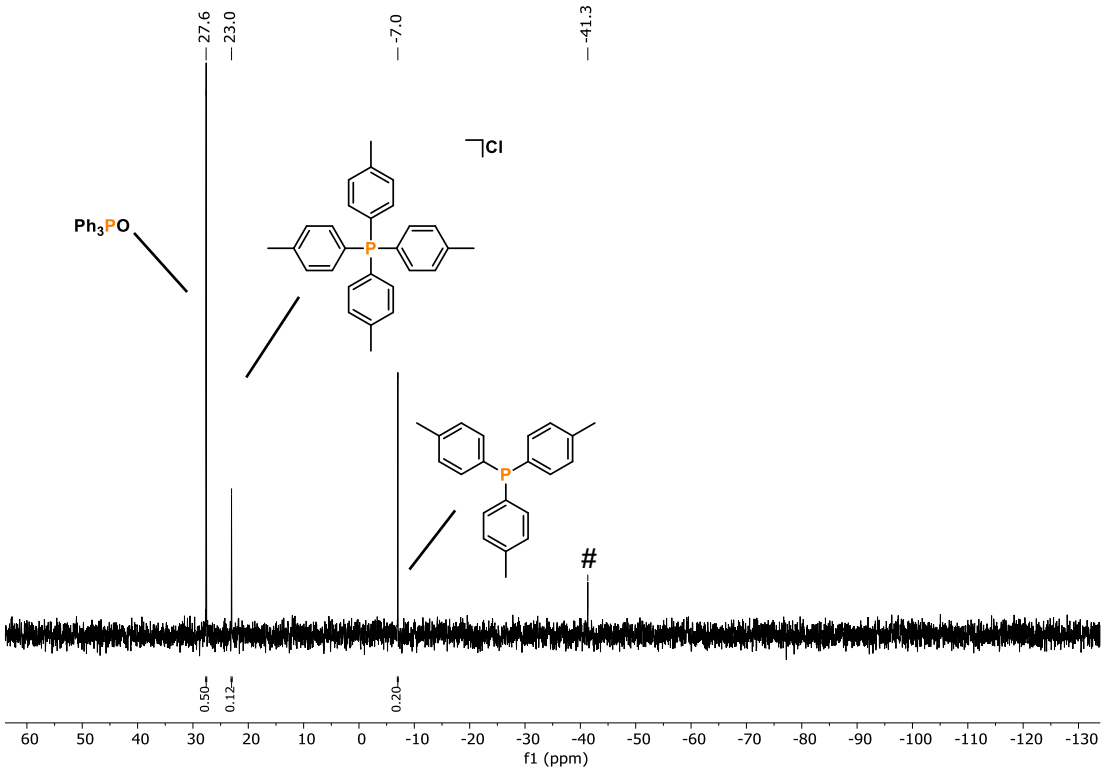

Figure S26. Quantitative single scan $^{31}P\{^{1}H\}$ (zgig) NMR spectrum for the photocatalytic functionalization of P_4 using 4-chlorotoluene. #: di(*p*-tolyl)phosphine.

Tetra(*m*-tolyl)phosphonium chloride and tris(*m*-tolyl)phosphine

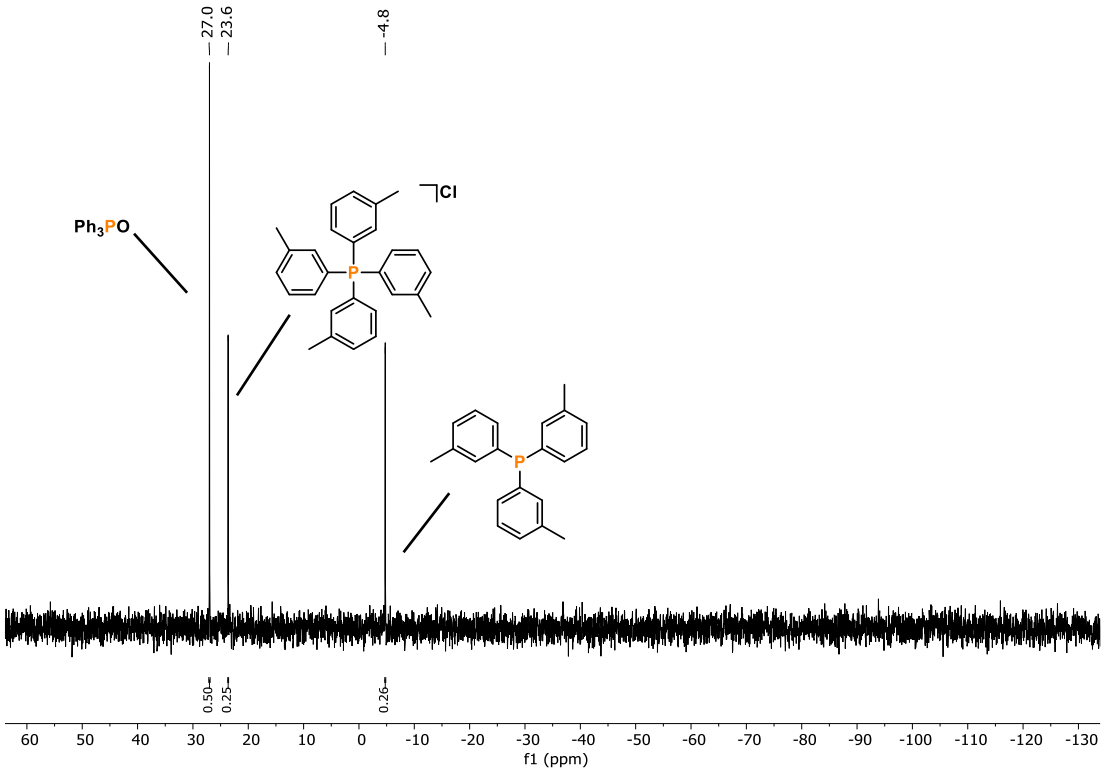

Figure S27. Quantitative single scan $^{31}P\{^{1}H\}$ (zgig) NMR spectrum for the photocatalytic functionalization of P_4 using 3-chlorotoluene.

Tris(*o*-tolyl)phosphine

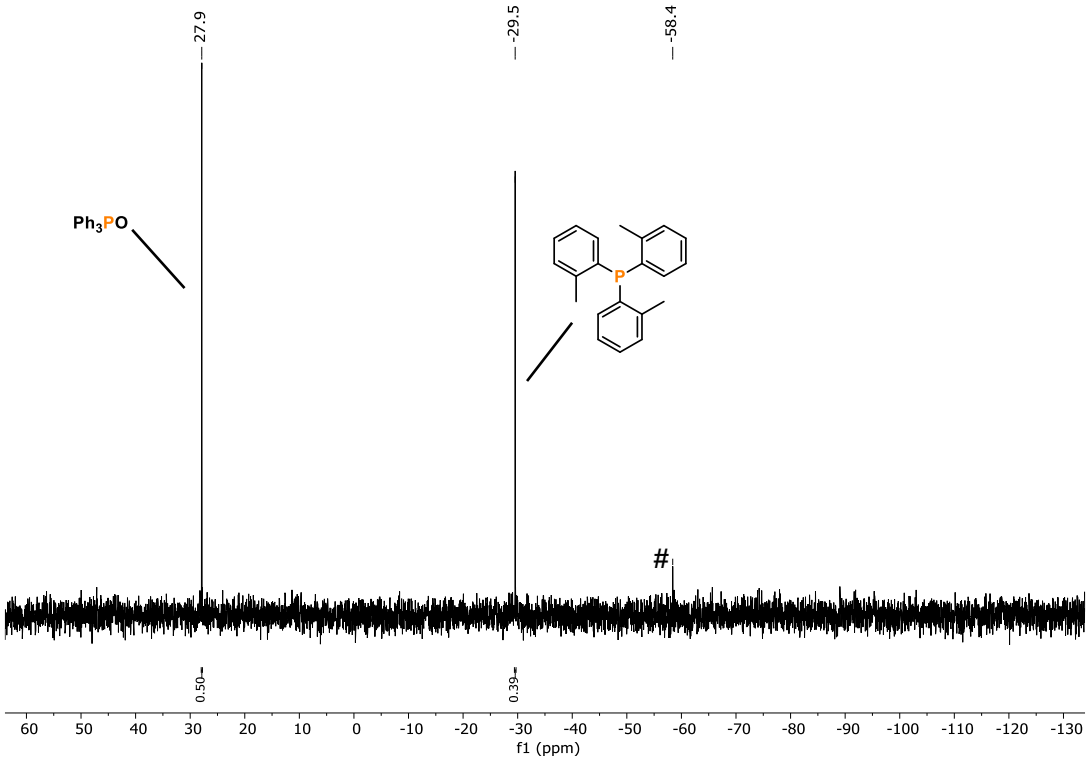

Figure S28. Quantitative single scan $^{31}P\{^{1}H\}$ (zgig) NMR spectrum for the photocatalytic functionalization of P_4 using 2-chlorotoluene. #: di(*o*-tolyl)phosphine.

Tetrakis[(4-methylthio)phenyl]phosphonium chloride and tris[(4-methylthio)phenyl]-phosphine[21]

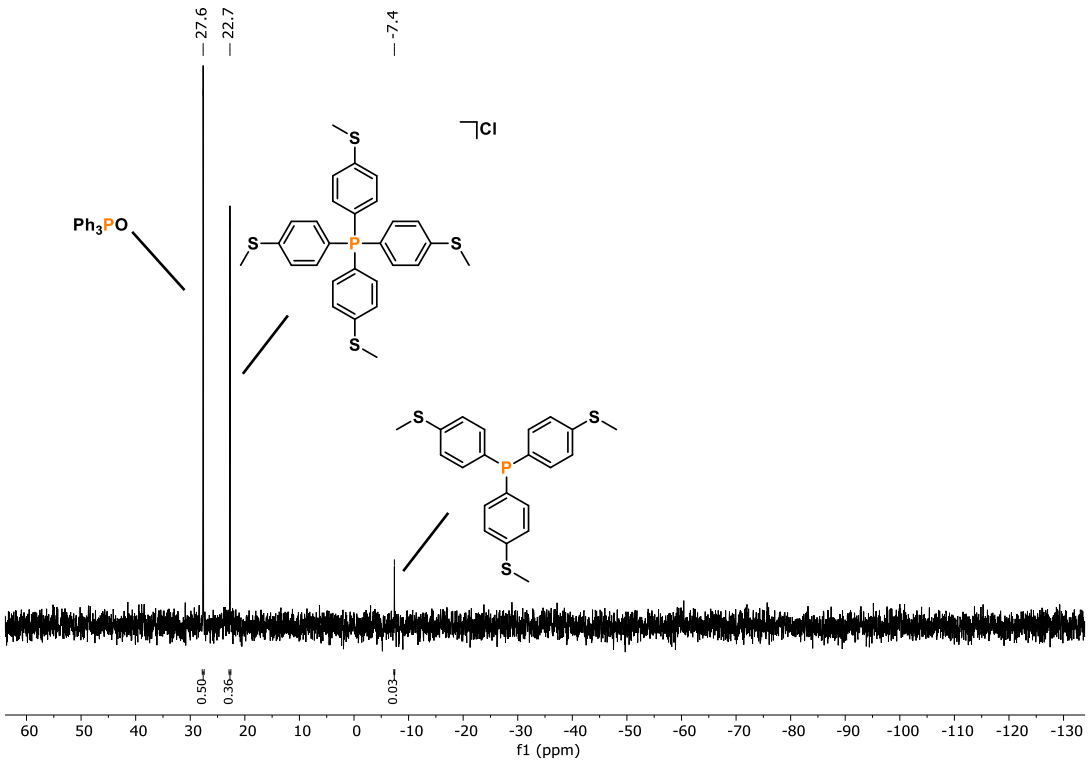

Figure S29. Quantitative single scan $^{31}P\{^{1}H\}$ (zgig) NMR spectrum for the photocatalytic functionalization of P_4 using 4-chlorothioanisole**.**

Tetrakis(4-phenoxyphenyl)phosphonium chloride and tris(4-phenoxyphenyl)phosphine[22]

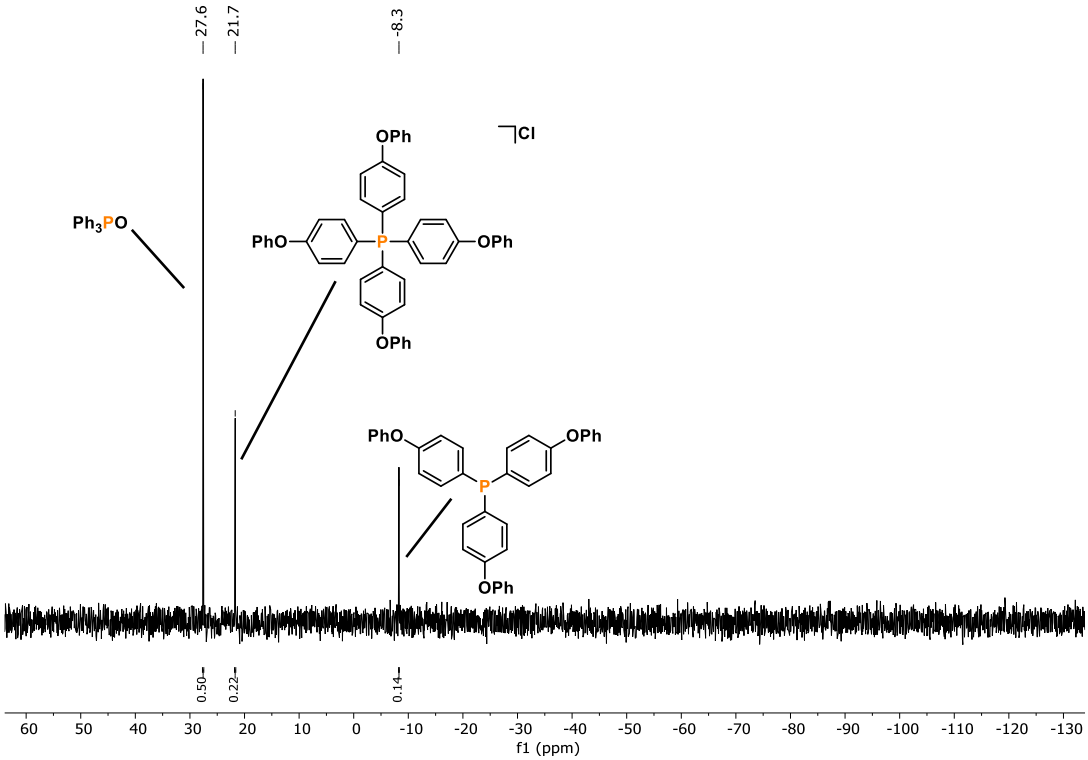

Figure S30. Quantitative single scan $^{31}P\{^{1}H\}$ (zgig) NMR spectrum for the photocatalytic functionalization of P_4 using 1-chloro-4-phenoxybenzene.

Tetrakis(3,5-dimethoxyphenyl)phosphonium chloride and tris(3,5-dimethoxyphenyl)-phosphine[19]

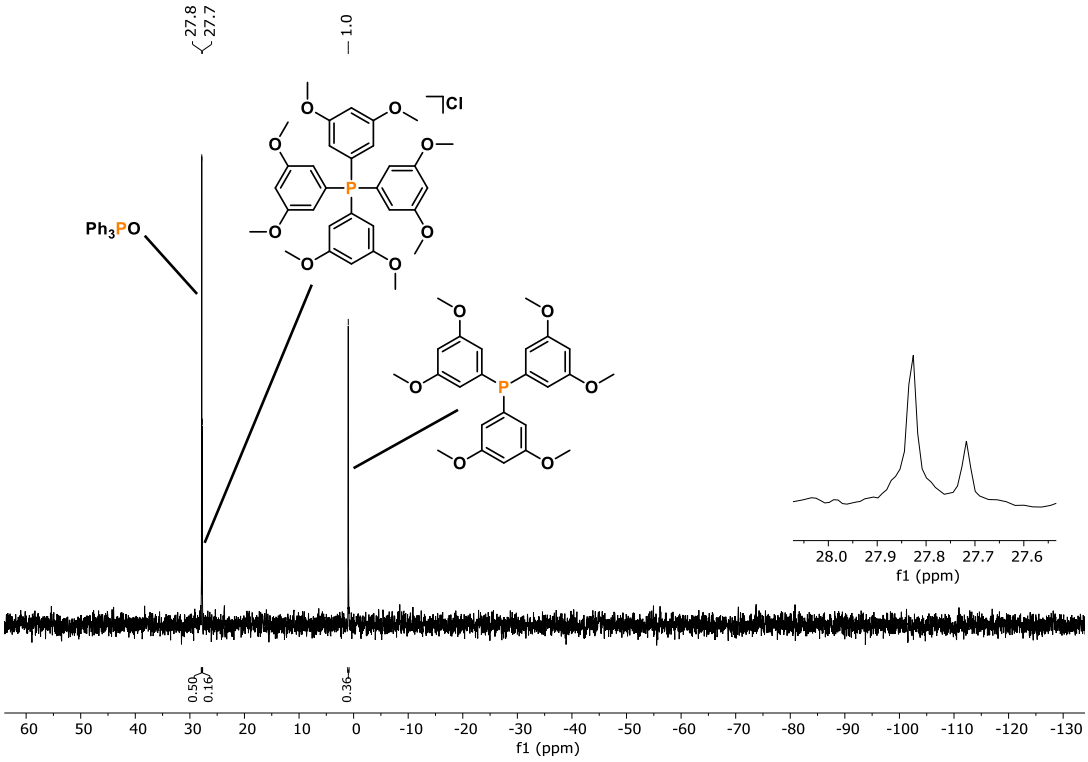

Figure S31. Quantitative single scan $^{31}P\{^{1}H\}$ (zgig) NMR spectrum for the photocatalytic functionalization of P_4 using 1-chloro-3,5-dimethoxybenzene.

Tetrakis[(4-*tert*-butyl)phenyl]phosphonium chloride and tris[(4-*tert*-butyl)phenyl]-phosphine

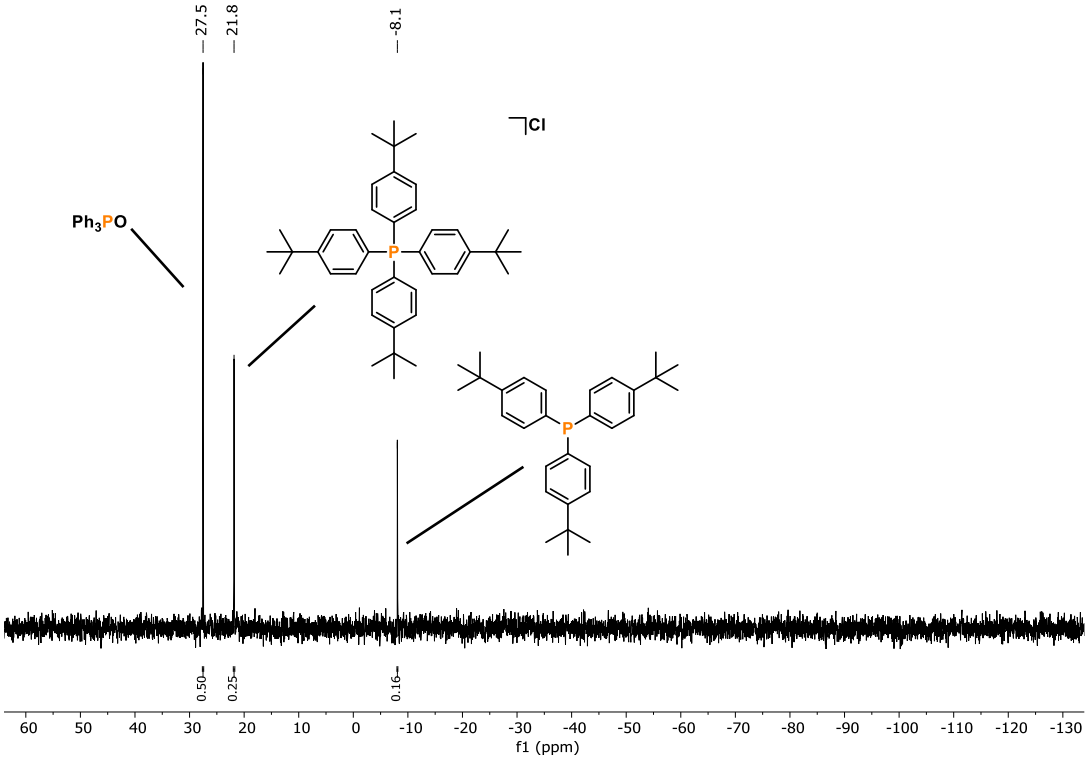

Figure S32. Quantitative single scan $^{31}P\{^{1}H\}$ (zgig) NMR spectrum for the photocatalytic functionalization of P_4 using 1-chloro-4-*tert*-butylbenzene.

Tetrakis(4-ethylphenyl)phosphonium chloride and tris(4-ethylphenyl)phosphine

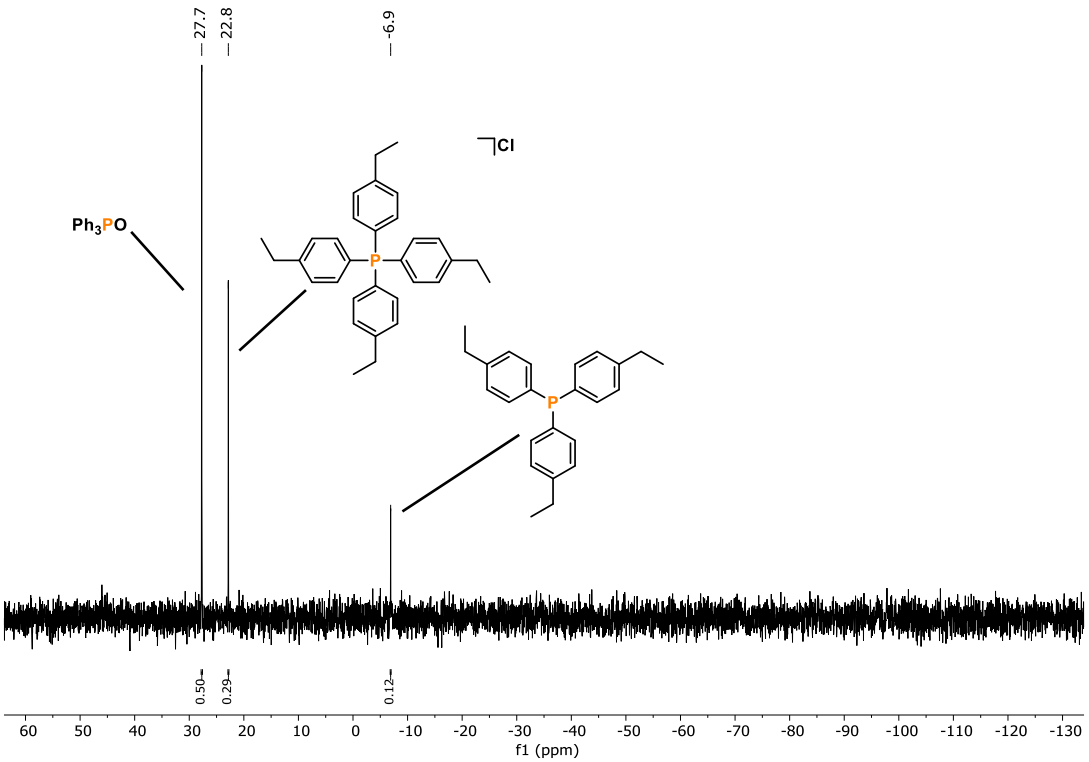

Figure S33. Quantitative single scan $^{31}P\{^{1}H\}$ (zgig) NMR spectrum for the photocatalytic functionalization of P_4 using 1-chloro-4-ethylbenzene.

Tetrakis(3-ethylphenyl)phosphonium chloride and tris(3-ethylphenyl)phosphine[20]

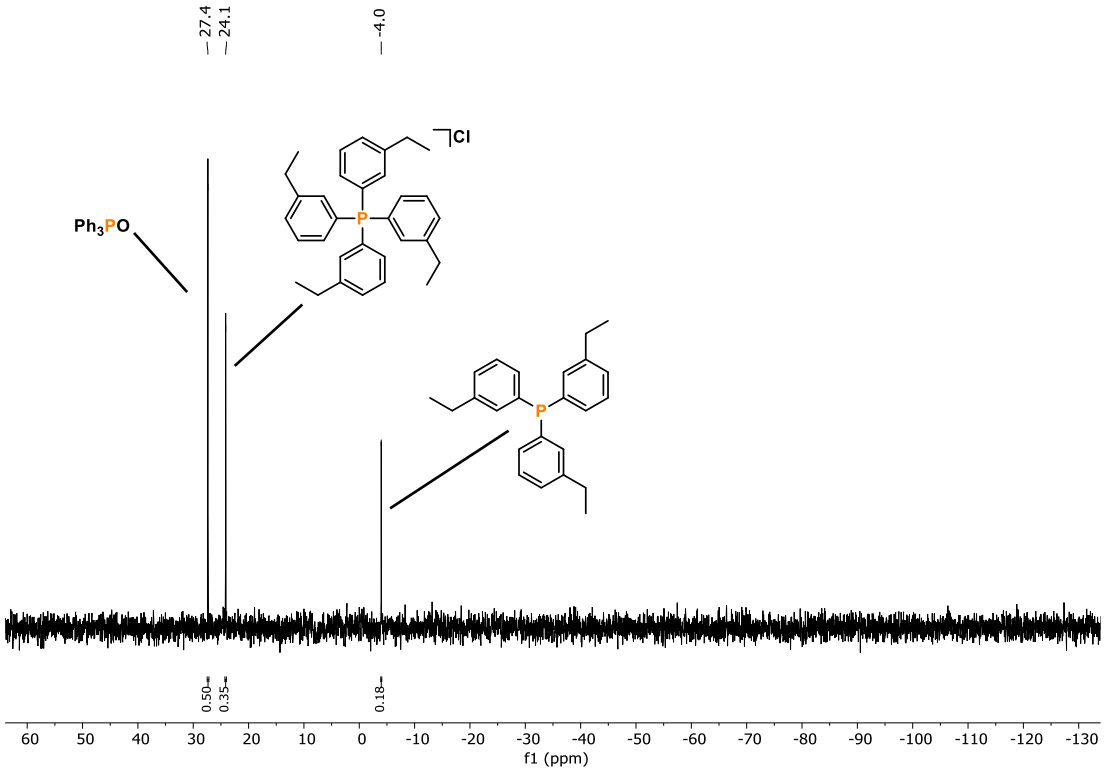

Figure S34. Quantitative single scan $^{31}P\{^{1}H\}$ (zgig) NMR spectrum for the photocatalytic functionalization of P_4 using 1-chloro-3-ethylbenzene.

Tris[(4-cyano)phenyl]phosphine

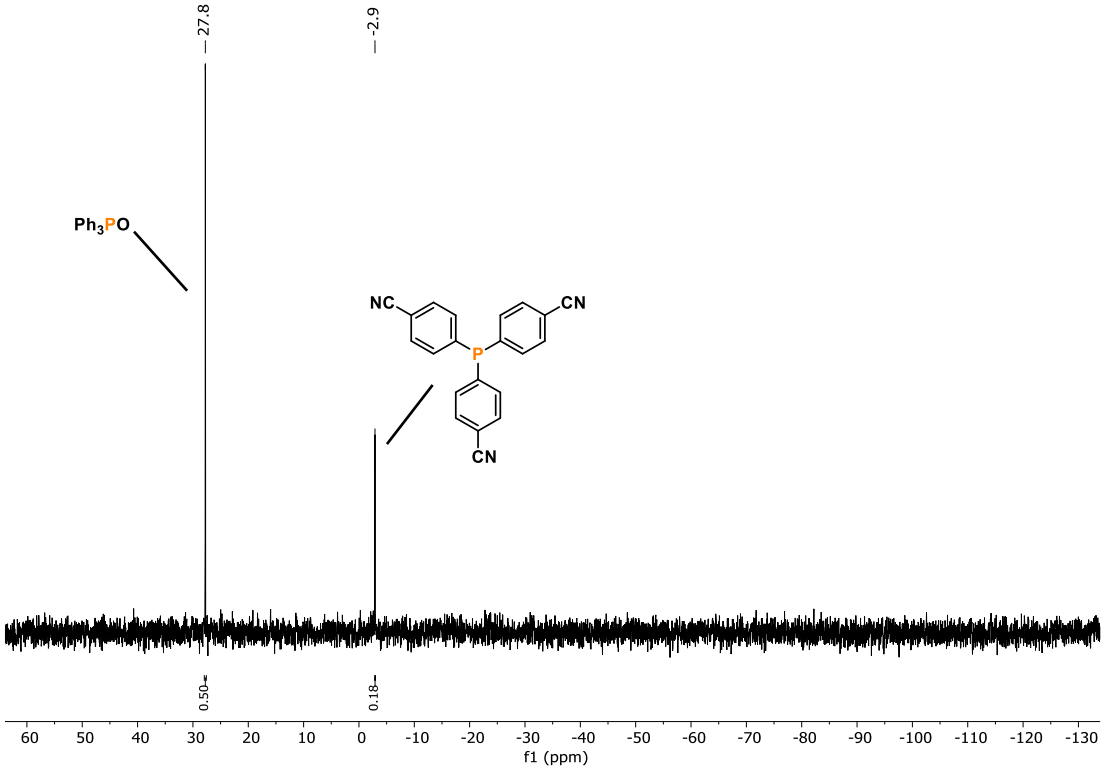

Figure S35. Quantitative single scan $^{31}P\{^{1}H\}$ (zgig) NMR spectrum for the photocatalytic functionalization of P_4 using 4-chlorobenzonitrile.

Tetrakis[(3-cyano)phenyl]phosphonium chloride and tris[(3-cyano)phenyl]phosphine[24]

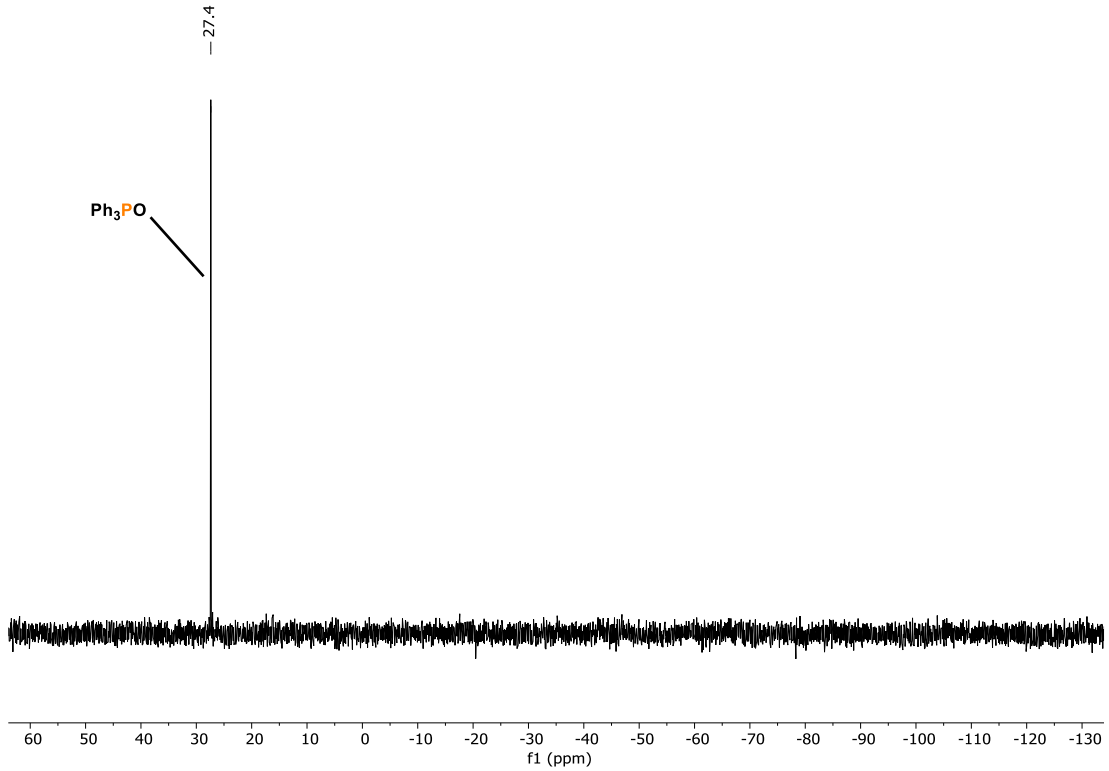

Figure S36. Quantitative single scan $^{31}P\{^{1}H\}$ (zgig) NMR spectrum for the photocatalytic functionalization of P_4 using 3-chlorobenzonitrile.

Tris(4-methyl benzoate)phosphine

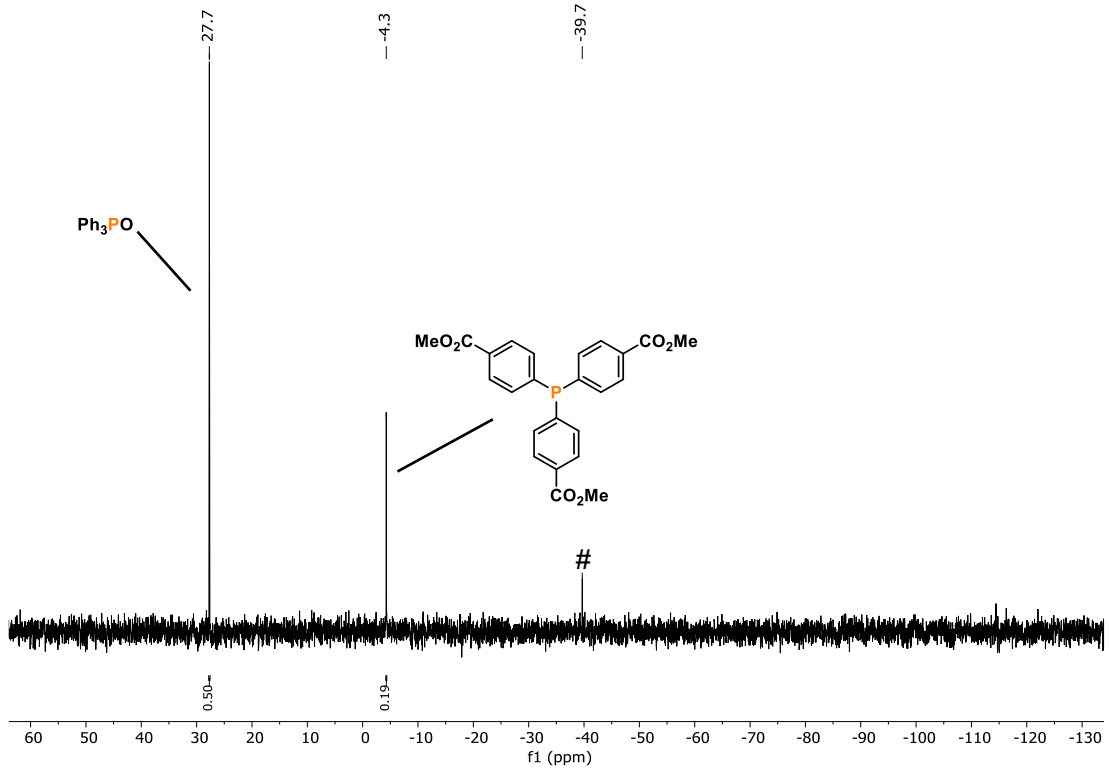

Figure S37. Quantitative single scan $^{31}P\{^{1}H\}$ (zgig) NMR spectrum for the photocatalytic functionalization of P_4 using methyl 4-chlorobenzoate. #: Ar_2PH. Ar = 4-methylcarboxyphenyl.

Tetrakis(3-methyl benzoate)phosphonium chloride and tris(3-methyl benzoate)phosphine

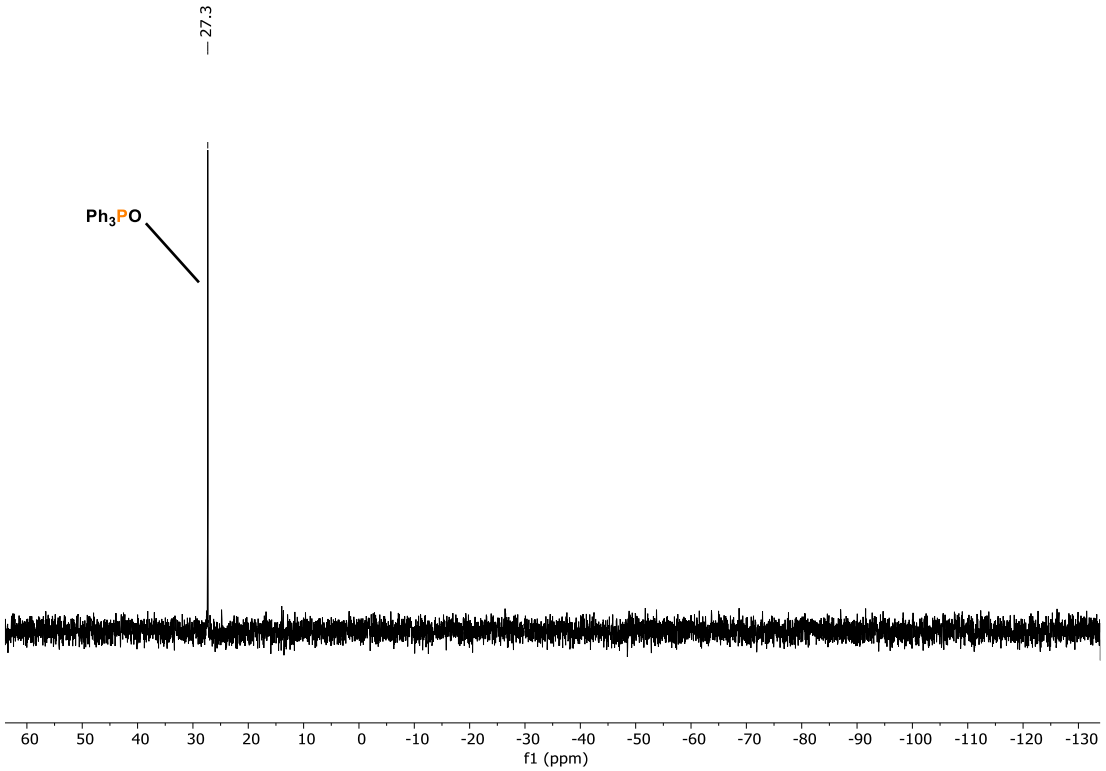

Figure S38. Quantitative single scan $^{31}P\{^{1}H\}$ (zgig) NMR spectrum for the photocatalytic functionalization of P_4 using methyl 3-chlorobenzoate.

Tris[(4-trifluoromethyl)-phenyl]phosphine

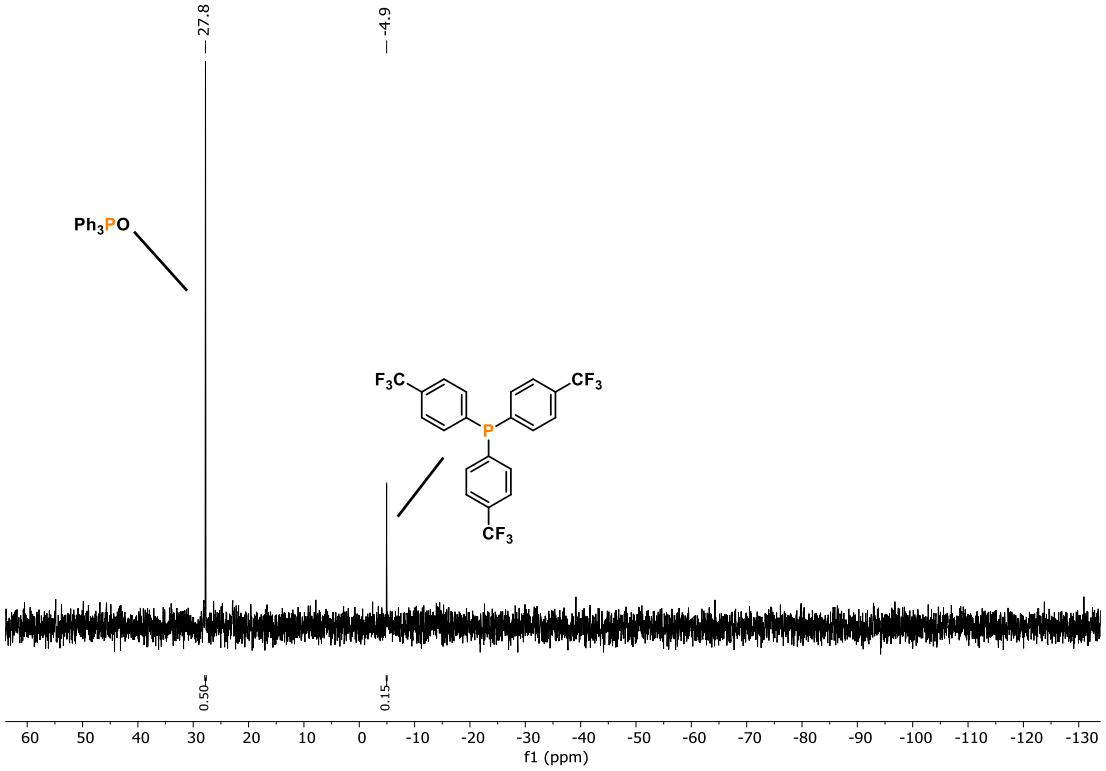

Figure S39. Quantitative single scan $^{31}P\{^{1}H\}$ (zgig) NMR spectrum for the photocatalytic functionalization of P_4 using 4-chlorobenzotrifluoride.

Tetraphenylphosphonium halide (X = Br, Cl) from 1-bromo-4-chlorobenzene

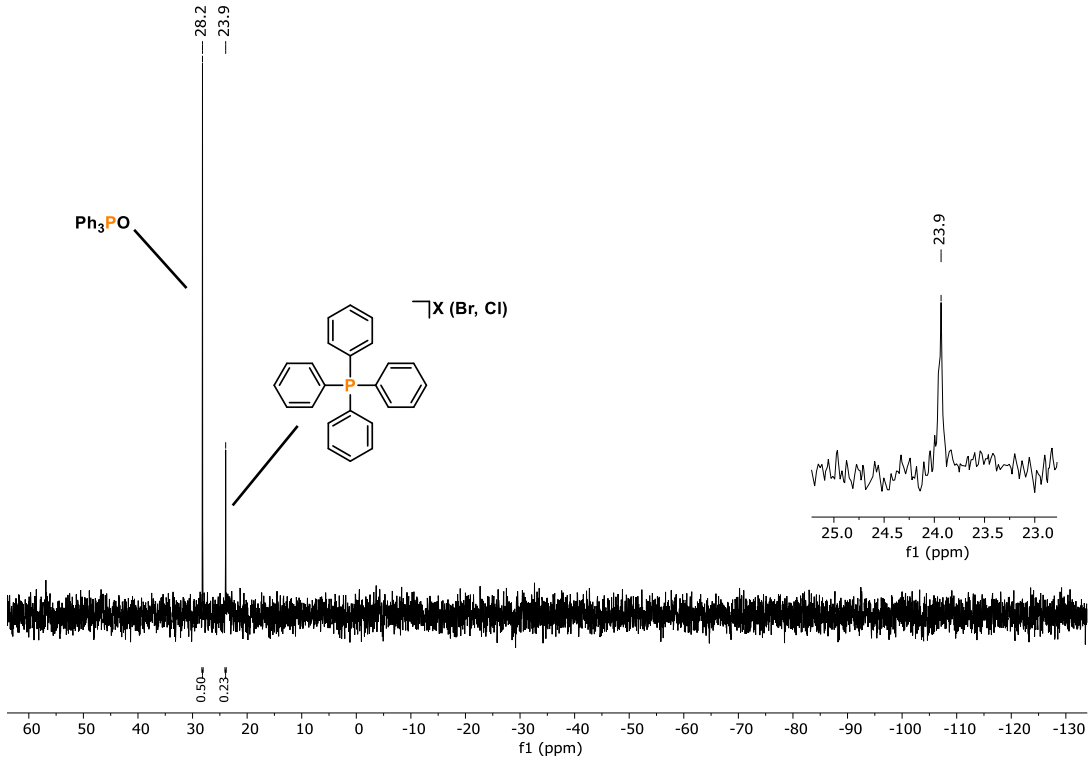

Figure S40. Quantitative single scan $^{31}P\{^{1}H\}$ (zgig) NMR spectrum for the photocatalytic functionalization of P_4 using 1-bromo-4-chlorobenzene. The cutout shows the exclusive formation of $[Ph_4P]X$ (X = Br, Cl).

Tetrakis(pyridine-3-yl)phosphonium chloride and tris(pyridine-3-yl)phosphine

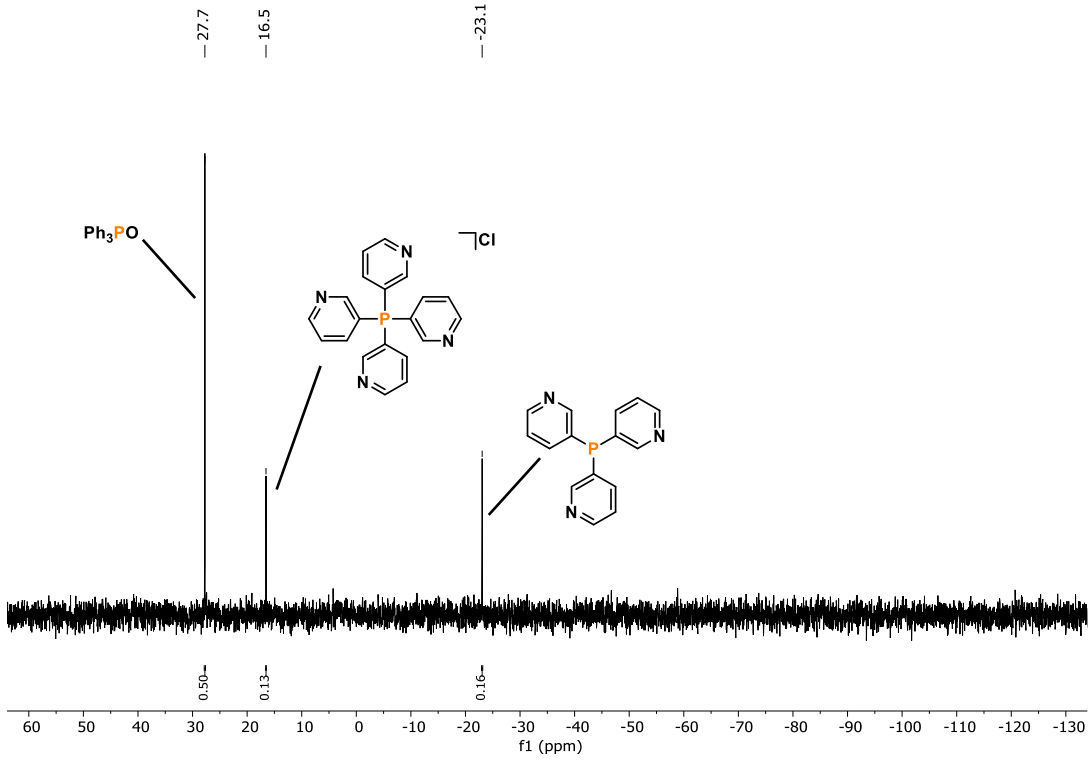

Figure S41. Quantitative single scan $^{31}P\{^{1}H\}$ (zgig) NMR spectrum for the photocatalytic functionalization of P_4 using 3-chloropyridine.

5.4.4.2 $^{31}P\{^{1}H\}$ NMR Spectroscopic Data for Aryl Bromides After 44 h and Aryl Chlorides After 68 h Reaction Time

Table S11. Photocatalytic functionalization of P_4 to $[Ar_4P]X$ (X = Br, Cl) and Ar_3P: extended reaction times.[a]

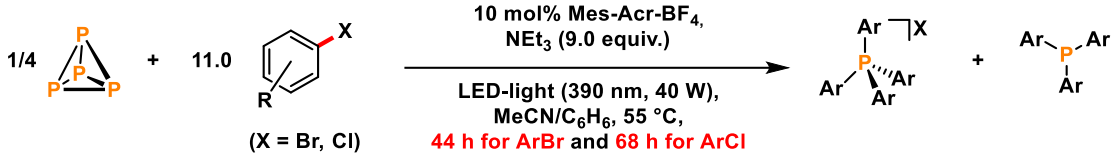

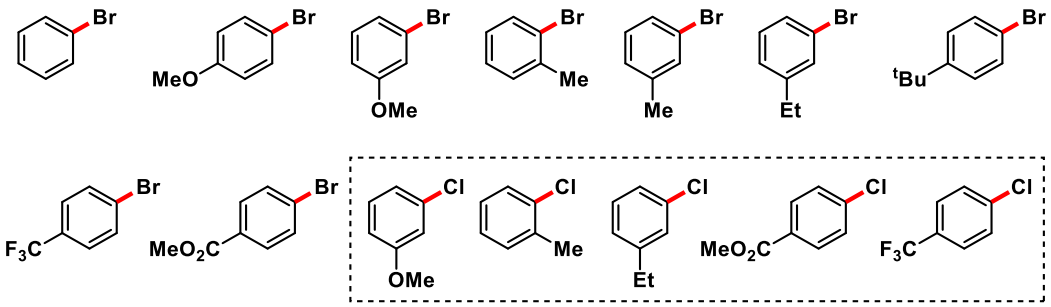

Entry	Substrate		Full conv. of P_4?	Form. of $[Ar_4P]X$ / %	Form. of Ar_3P / %
	X	R			
1	Br	R = H	✓	64	0
2	Br	R = 4-OMe	✓	54	7
3	Br	R = 3-OMe	✓	51	20
4	Br	R = 2-Me	✓	0	50
5	Br	R = 3-Me	✓	60	15
6	Br	R = 3-Et	✓	62	8
7	Br	R = 4-^{t}Bu	✓	53	9
8	Br	R = 4-CF_3	✓	32	12
9	Br	R = 4-CO_2Me	✓	47	0
10	Cl	R = 3-OMe	✓	62	11
11	Cl	R = 2-Me	✓	0	44
12	Cl	R = 3-Et	✓	59	13
13	Cl	R = 4-CO_2Me	✓	0	29
14	Cl	R = 4-CF_3	✓	0	16

[a] For the general protocol, see section 5.4.2. The reaction time was extended to 44 h for aryl bromides and to 68 h for aryl chlorides.

The screening of different aryl bromides and chlorides for extended reaction times (for X = Br: 44 h and X = Cl: 68 h) shows that the product formation ([Ar_4P]X/Ar_3P) can be noticeably improved (e.g., combined 71% [Ar_4P]Br/Ar_3P starting from 3-bromoansiole or combined 73% [Ar_4P]Cl/Ar_3P starting from 3-chloroanisole instead of 60% [Ar_4P]Br/Ar_3P or 61% [Ar_4P]Cl/Ar_3P, respectively; see Table S11). Yet, prolonged reaction times were not found to be beneficial for all haloarenes, as indicated by the similar NMR yields for bromobenzene (63% vs. 64%) or 2-chlorotoluene (39% vs. 44%). A general correlation between extended reaction times and improved yields was not observed.

Aryl bromides – 44 h reaction time:

Tetraphenylphosphonium bromide

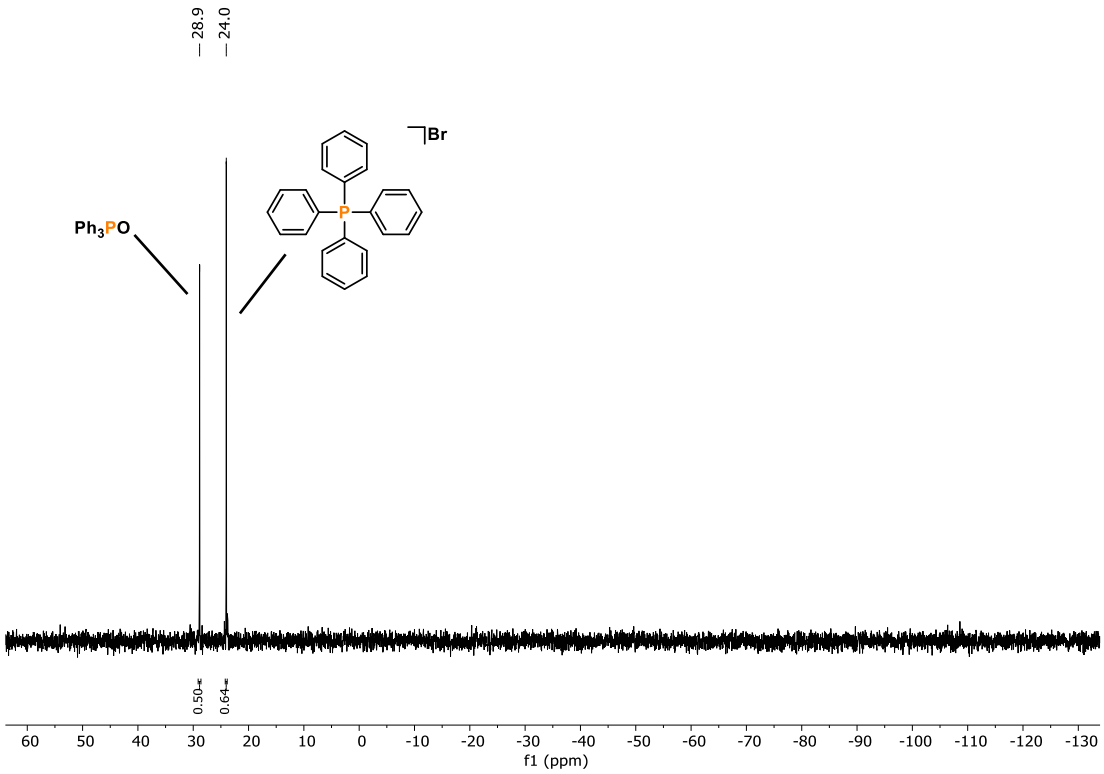

Figure S42. Quantitative single scan $^{31}P\{^1H\}$ (zgig) NMR spectrum for the photocatalytic functionalization of P_4 using bromobenzene after 44 h reaction time.

Tetrakis(4-methoxyphenyl)phosphonium bromide and tris(4-methoxyphenyl)phosphine

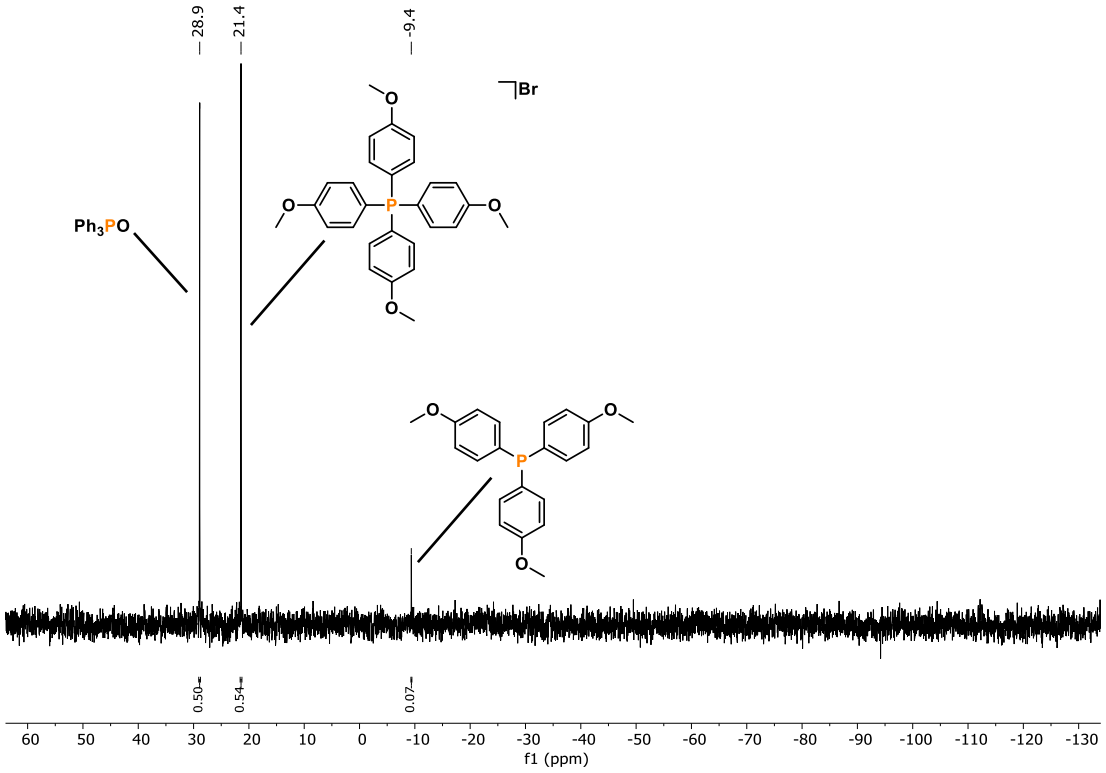

Figure S43. Quantitative single scan $^{31}P\{^{1}H\}$ (zgig) NMR spectrum for the photocatalytic functionalization of P_4 using 4-bromoanisole after 44 h reaction time.

Tetrakis(3-methoxyphenyl)phosphonium bromide and tris(4-methoxyphenyl)phosphine

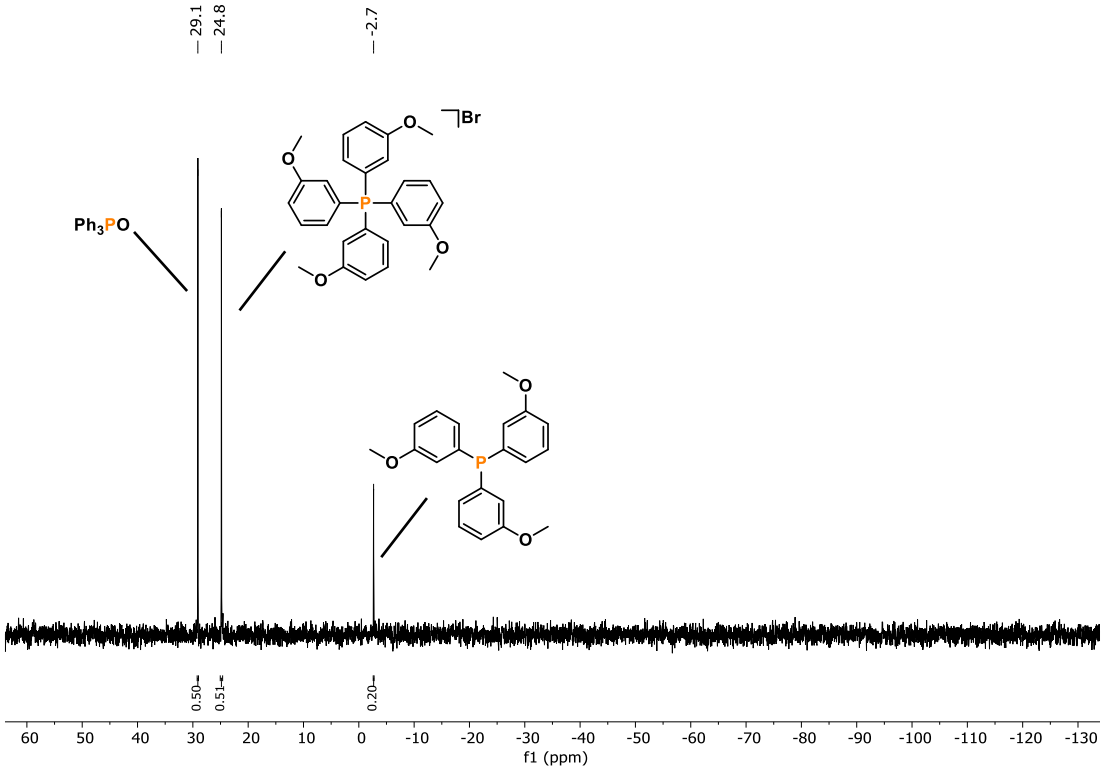

Figure S44. Quantitative single scan $^{31}P\{^{1}H\}$ (zgig) NMR spectrum for the photocatalytic functionalization of P_4 using 3-bromoanisole after 44 h reaction time.

Tris(*o*-tolyl)phosphine

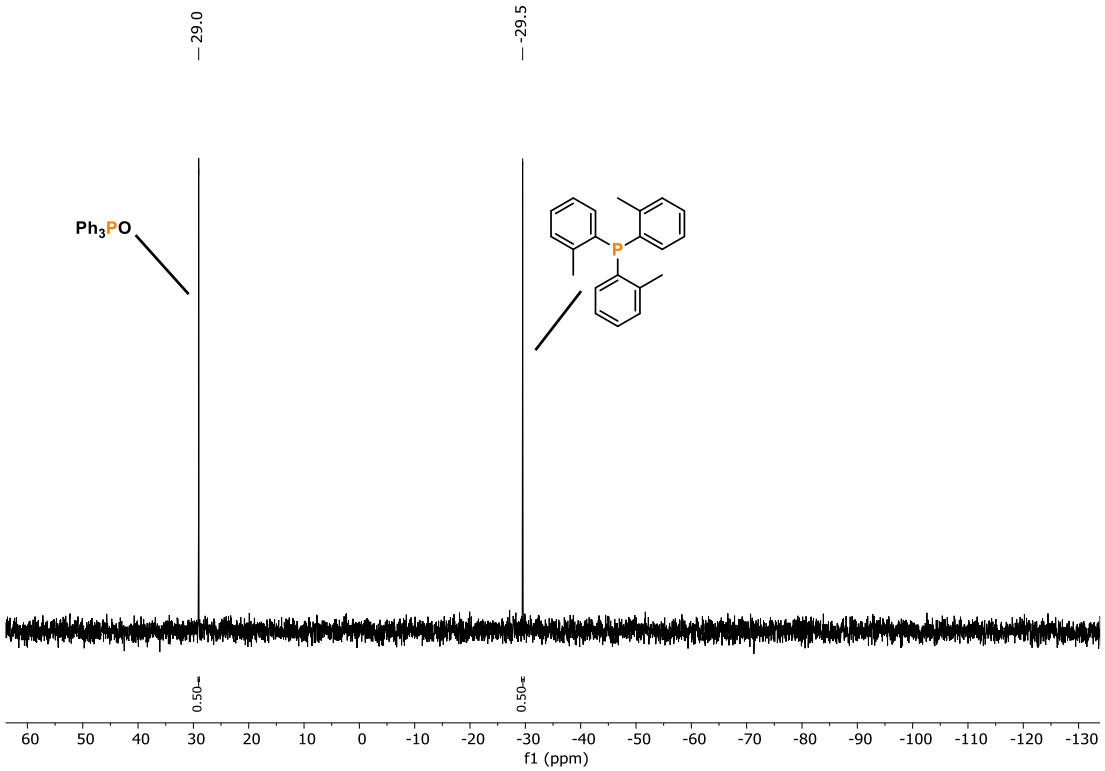

Figure S45. Quantitative single scan $^{31}P\{^{1}H\}$ (zgig) NMR spectrum for the photocatalytic functionalization of P_4 using 2-bromotoluene after 44 h reaction time.

Tetra(*m*-tolyl)phosphonium bromide and tris(*m*-tolyl)phosphine

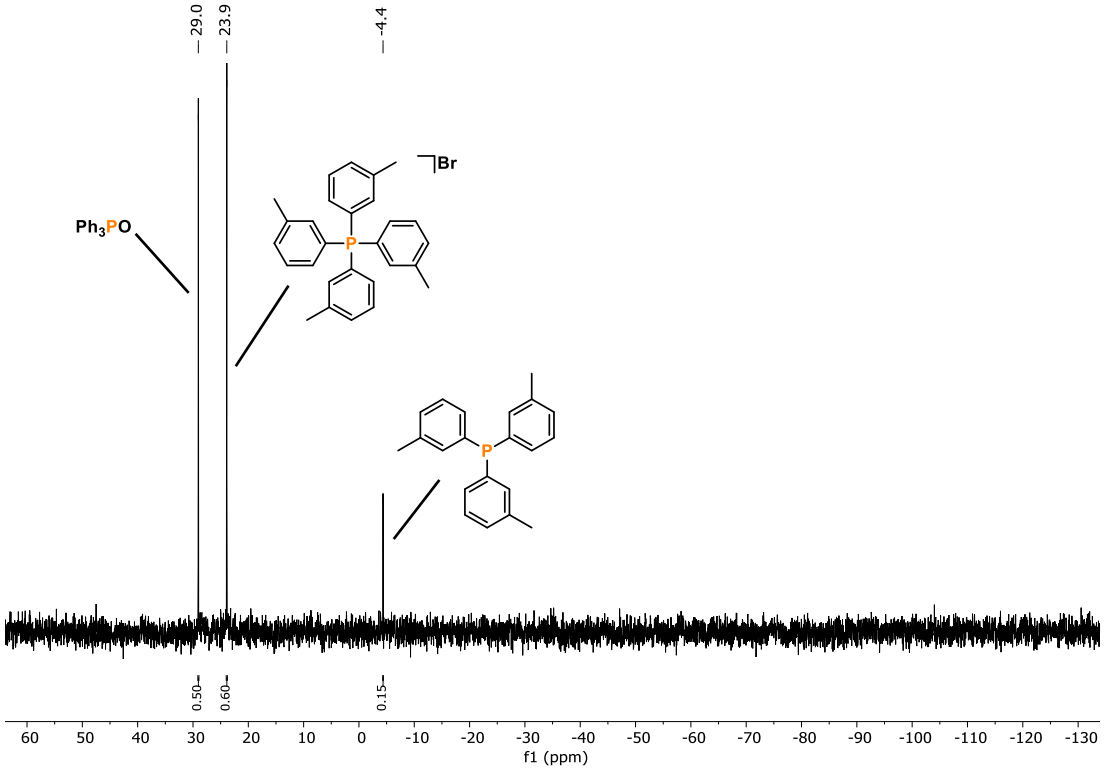

Figure S46. Quantitative single scan $^{31}P\{^{1}H\}$ (zgig) NMR spectrum for the photocatalytic functionalization of P_4 using 3-bromotoluene after 44 h reaction time.

Tetrakis(3-ethylphenyl)phosphonium bromide and tris(3-ethylphenyl)phosphine[20]

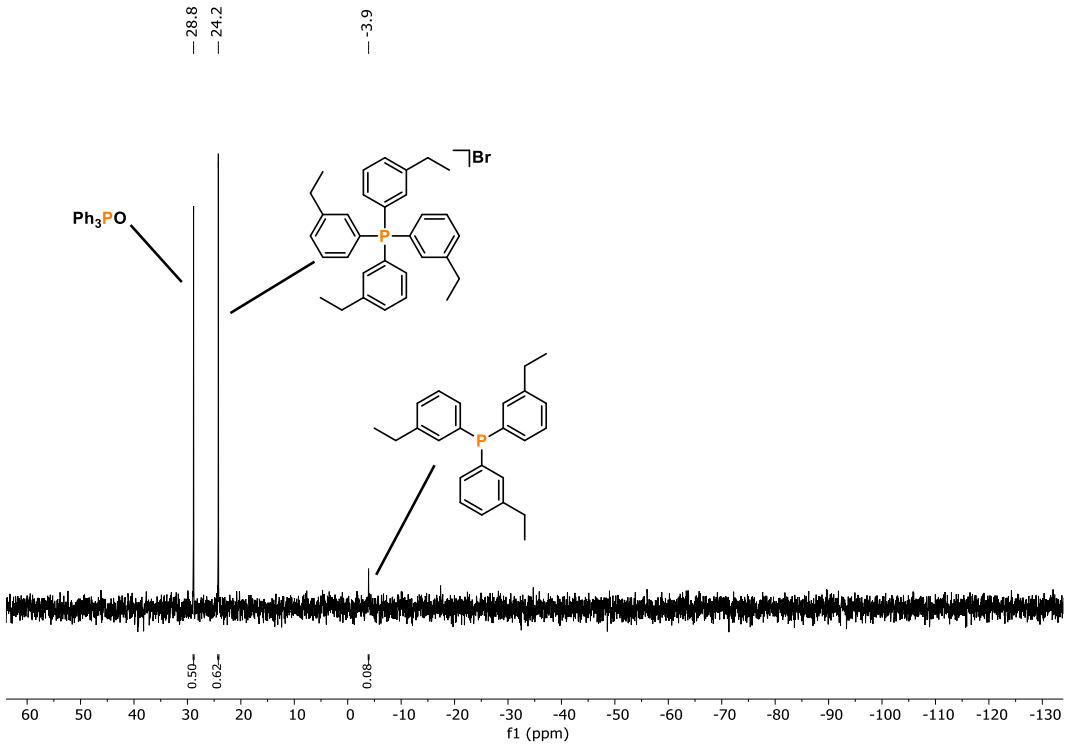

Figure S47. Quantitative single scan $^{31}P\{^{1}H\}$ (zgig) NMR spectrum for the photocatalytic functionalization of P_4 using 1-bromo-3-ethylbenzene after 44 h reaction time.

Tetrakis[(4-*tert*-butyl)phenyl]phosphonium bromide and tris[(4-*tert*-butyl)phenyl]-phosphine

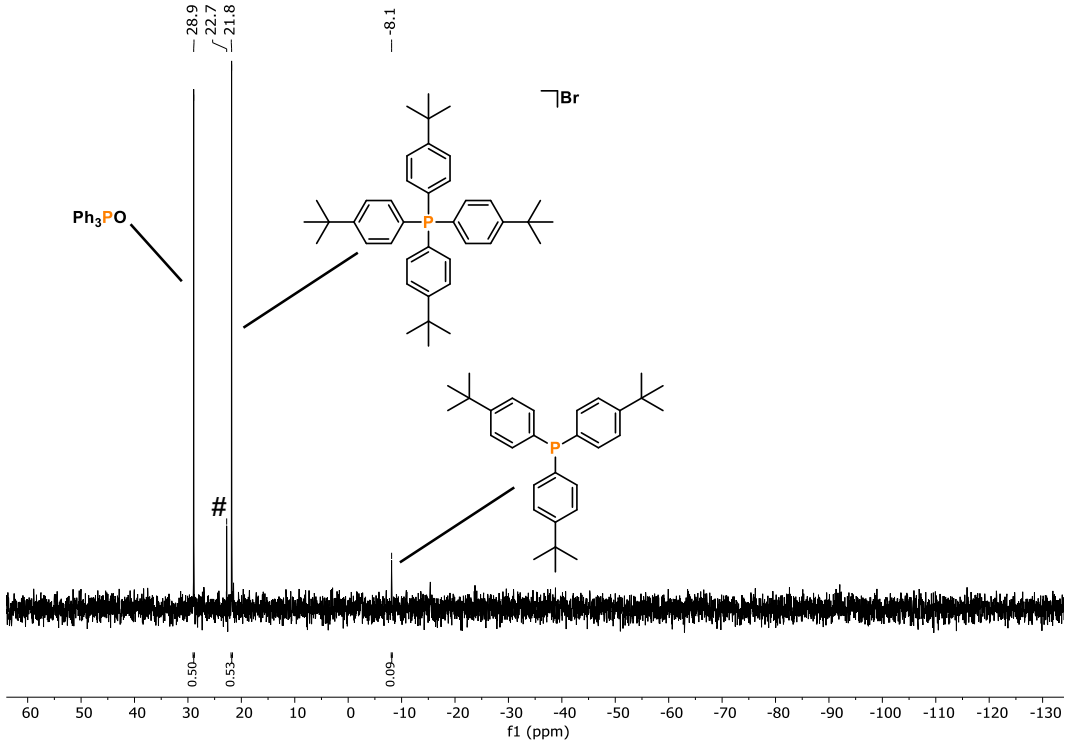

Figure S48. Quantitative single scan $^{31}P\{^{1}H\}$ (zgig) NMR spectrum for the photocatalytic functionalization of P_4 using 4-bromo-*tert*-butylbenzene after 44 h reaction time. #: unidentified signal.

Tetrakis[(4-trifluoromethyl)phenyl]phosphonium bromide and tris[(4-trifluoromethyl)-phenylphosphine

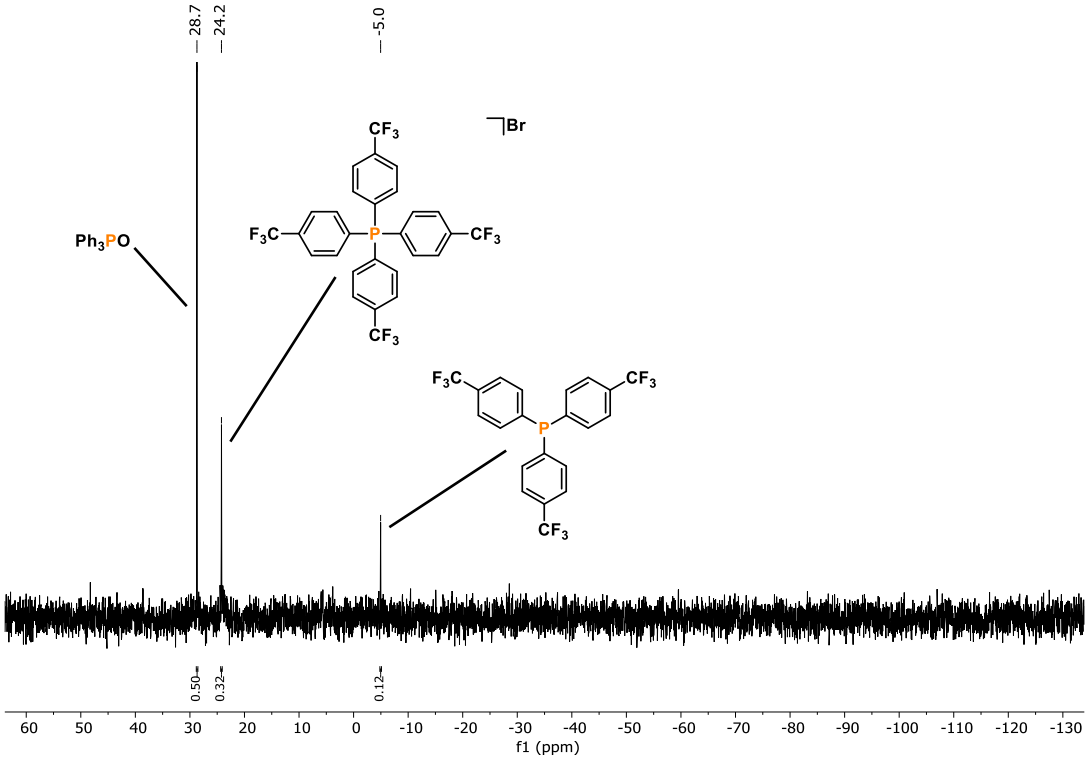

Figure S49. Quantitative single scan $^{31}P\{^{1}H\}$ (zgig) NMR spectrum for the photocatalytic functionalization of P_4 using 4-bromobenzotrifluoride after 44 h reaction time.

Tetrakis(4-methyl benzoate)phosphonium bromide and tris(4-methyl benzoate)phosphine

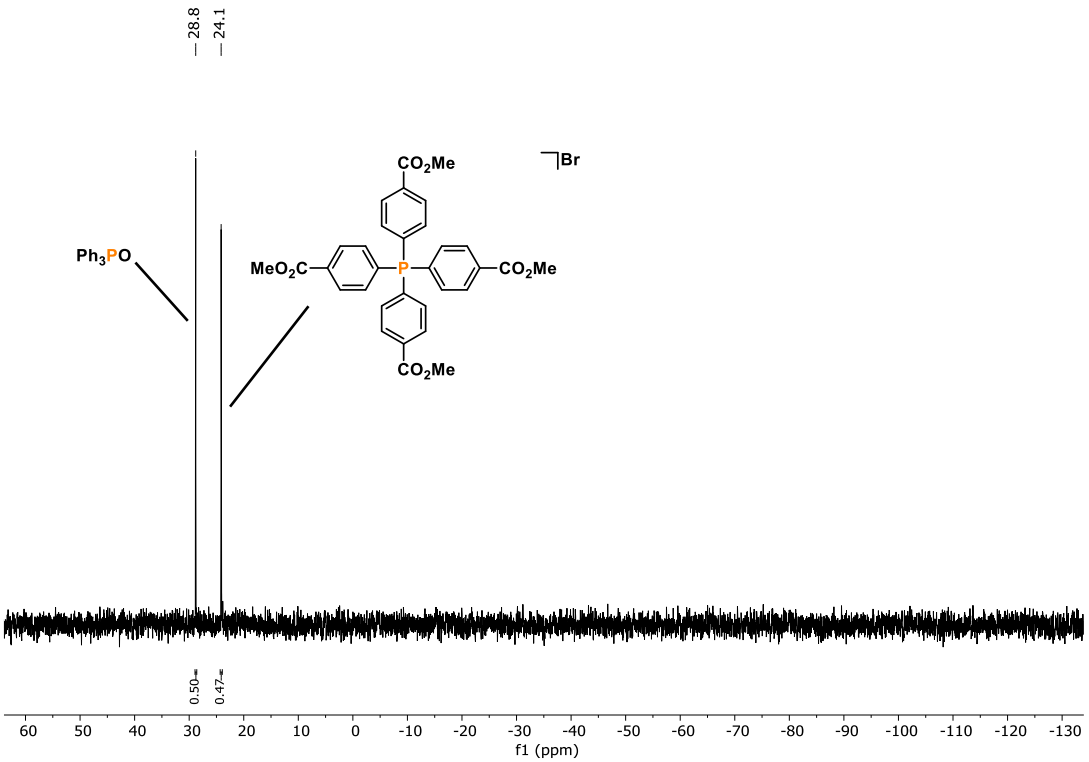

Figure S50. Quantitative single scan $^{31}P\{^{1}H\}$ (zgig) NMR spectrum for the photocatalytic functionalization of P_4 using methyl 4-bromobenzoate after 44 h reaction time.

Aryl chlorides – 68 h reaction time:

Tetrakis(3-methoxyphenyl)phosphonium chloride and tris(3-methoxyphenyl)-phosphine

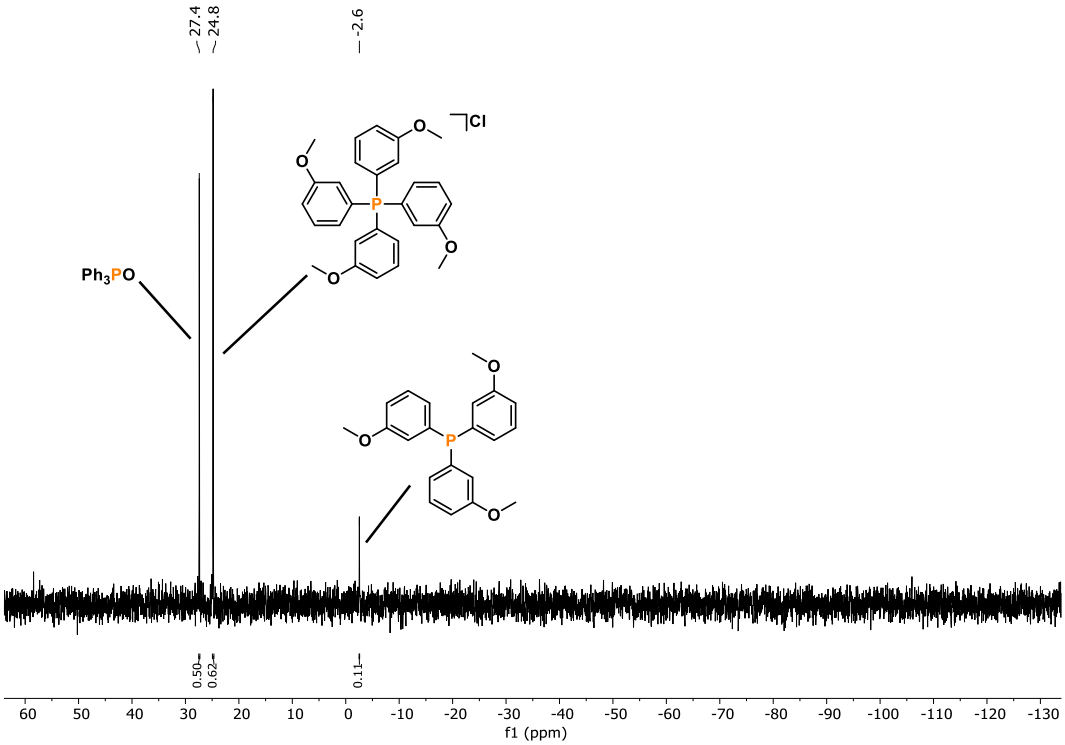

Figure S51. Quantitative single scan $^{31}P\{^{1}H\}$ (zgig) NMR spectrum for the photocatalytic functionalization of P_4 using 3-chloroanisole after 68 h reaction time.

Tris(*o*-tolyl)phosphine

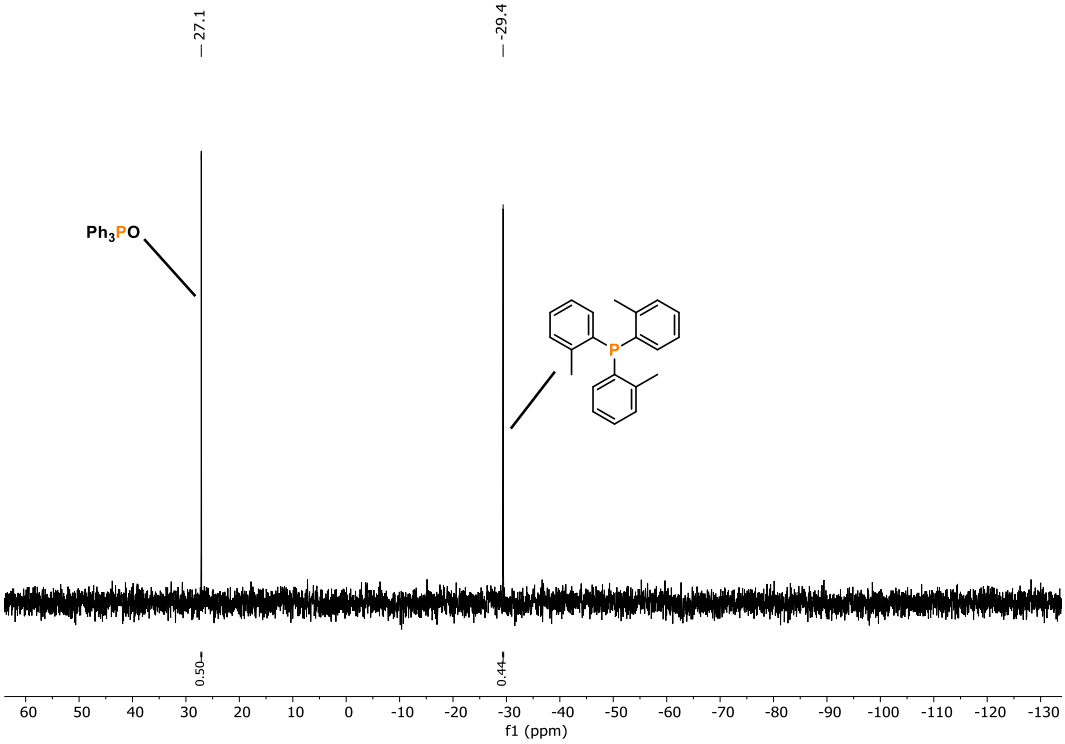

Figure S52. Quantitative single scan $^{31}P\{^{1}H\}$ (zgig) NMR spectrum for the photocatalytic functionalization of P_4 using 2-chlorotoluene after 68 h reaction time.

Tetrakis(3-ethylphenyl)phosphonium chloride and tris(3-ethylphenyl)phosphine[20]

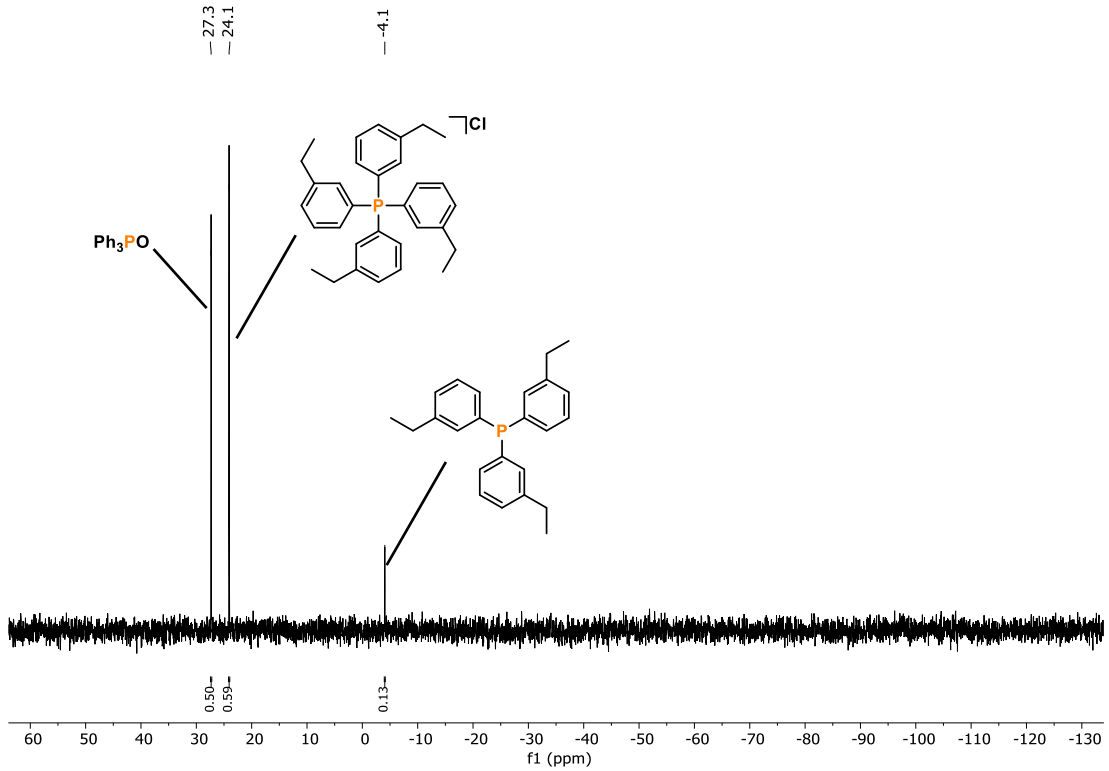

Figure S53. Quantitative single scan $^{31}P\{^{1}H\}$ (zgig) NMR spectrum for the photocatalytic functionalization of P_4 using 1-chloro-3-ethylbenzene after 68 h reaction time.

Tris[(4-trifluoromethyl)phenyl]phosphine

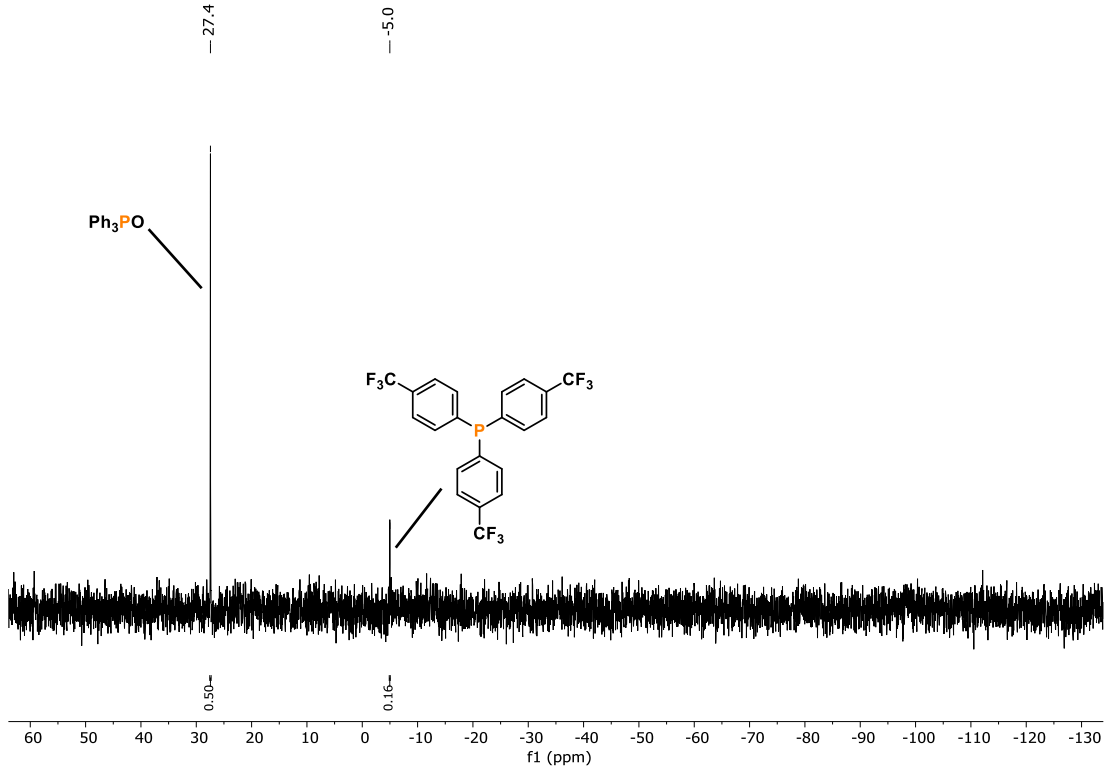

Figure S54. Quantitative single scan $^{31}P\{^{1}H\}$ (zgig) NMR spectrum for the photocatalytic functionalization of P_4 using 4-chlorobenzotrifluoride after 68 h reaction time.

Tris(4-methyl benzoate)phosphine

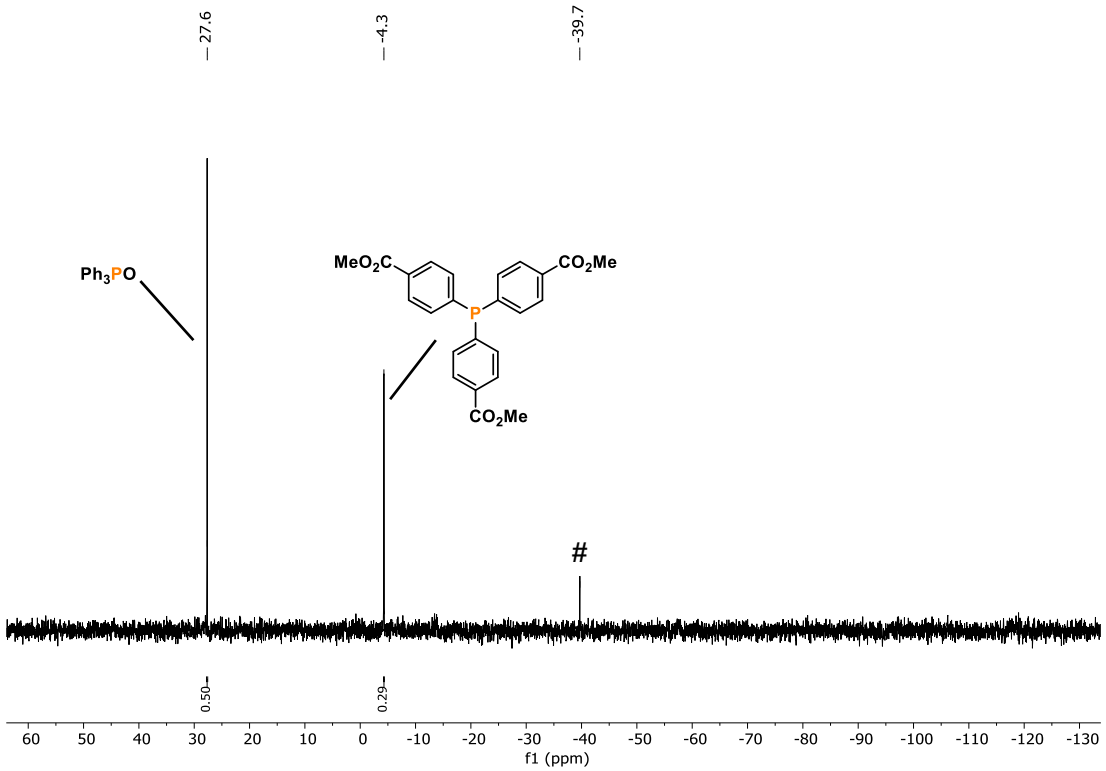

Figure S55. Quantitative single scan $^{31}P\{^{1}H\}$ (zgig) NMR spectrum for the photocatalytic functionalization of P_4 using methyl 4-chlorobenzoate after 68 h reaction time. #: Ar_2PH. Ar = 4-methylcarboxyphenyl.

5.4.4.3 Reaction Data for Additional and Unsuccessful Substrates (X = Br, Cl)

Table S12. Photocatalytic functionalization of P_4 to $[Ar_4P]X$ (X = Br, Cl) and Ar_3P: additional and unsuccessful substrates.[a]

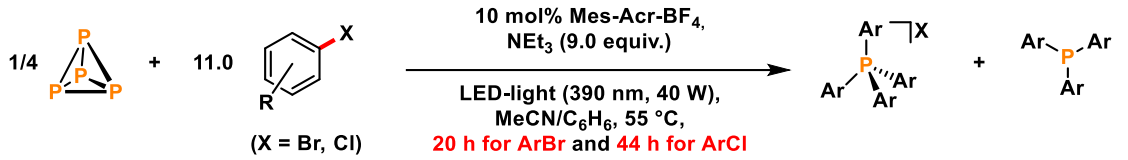

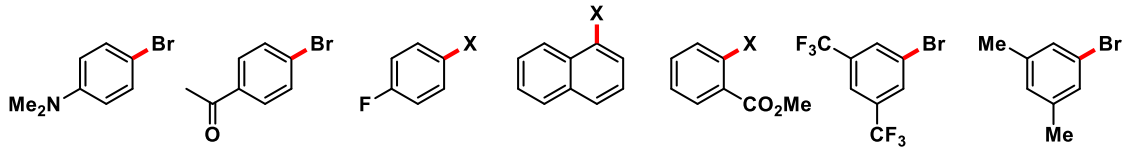

Entry	Substrate		Full conv. of P_4?	Form. of $[Ar_4P]X$ / %	Form. of Ar_3P / %
	X	R			
1	Br	R = 4-NMe_2	✓	0	0
2	Br	R = 4-C(O)Me	✓	0	0
3	Br	R = 4-F	✓	25[b]	10
4	Cl	R = 4-F	✓	0	10
5	Br	R = 1-Napht.	✓	0	24
6	Cl	R = 1-Napht.	✓	0	7
7	Br	R = 2-CO_2Me	✓	0	0
8	Cl	R = 2-CO_2Me	✓	0	4
9	Br	3,5-$(CF_3)_2$	✓	0	9
10	Br	3,5-Me_2	✓	14	28

[a] For the general protocol, see section 5.4.2. [b] Additional unidentified signal with a similar chemical shift as the phosphonium salt signal.

5.4.5 Synthesis of $[Ph_4P]Br$ and (*o*-tol)$_3$P on a Preparative Scale

5.4.5.1 Tetraphenylphosphonium Bromide, $[Ph_4P]Br$:

To a 100 mL stoppered Schlenk tube equipped with a stirring bar were added bromobenzene (926.7 µL, 8.8 mmol, 11.0 equiv. based on the phosphorus atom), NEt_3 (1004 µL, 7.2 mmol, 9.0 equiv. based on the phosphorus atom), 9-mesityl-3,6-di-*tert*-butyl-10-phenylacridinium tetrafluoroborate (Mes-Acr-BF_4; 45.9 mg, 0.08 mmol, 10 mol% based on the phosphorus atom) and P_4 (24.8 mg, 0.2 mmol, 0.25 equiv., as a stock solution in 1306 µL benzene). The mixture was dissolved in acetonitrile (2.0 mL). The tube was sealed, fixed with a clamp (Figure S56), and irradiated with nUV light (390 nm, 40 W, Kessil PR160L in a PR160 Rig with Fan Kit) for 48 h. Ph_3PO (0.4 mmol, 111.2 mg; added as solid) was subsequently added to act as an internal standard.

The resulting mixture was subjected to quantitative $^{31}P\{^{1}H\}$ NMR analysis, which showed formation of 66% tetraphenylphosphonium bromide and 2% triphenylphosphine (Figure S57).

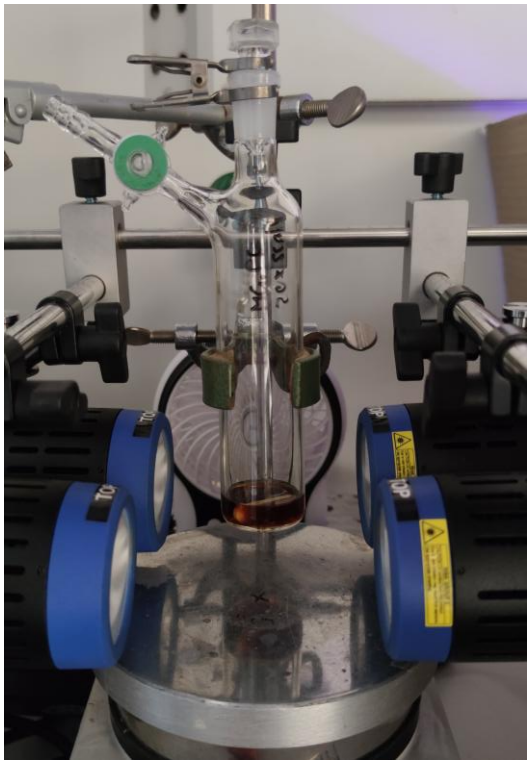

Figure S56. Setup used for photocatalytic reactions at 0.8 mmol scale of P_4.

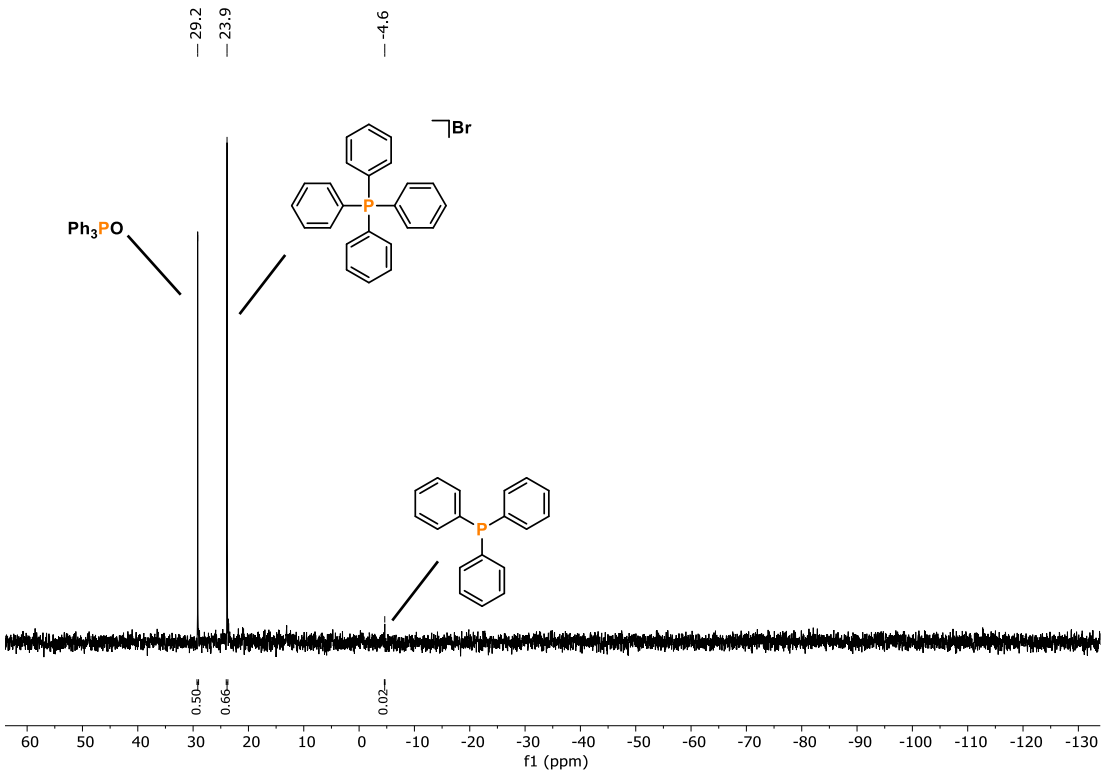

Figure S57. Quantitative single scan $^{31}P\{^{1}H\}$ (zgig) NMR spectrum for the 20-fold scale-up photocatalytic functionalization of P_4 using bromobenzene.

Work-up (without addition of internal standard Ph_3PO):

The suspension was evaporated to dryness in vacuo at 100 °C, and the resulting orange wax-like residue was dispensed in Et_2O (2 x 20 mL), manually scratched, sonicated for 30 min, and filtered to give a pale yellow solid. The solid was dried again *in vacuo*, dissolved in CH_2Cl_2 (10 mL) and extracted with aqueous HBr (3 x 20 mL; 1 mL HBr 47%wt in 50 mL H_2O, pH = 1) to remove NEt_3·HBr. The combined aqueous phases were re-extracted with CH_2Cl_2 (1 x 10 mL). The combined organic phase was added to H_2O (300 mL). The emulsion was concentrated to ca. 200 mL using a rotary evaporator at 50 °C, after which the separation of an orange wax-like precipitate was observed (precipitation of an orange waxy solid at glass wall was already observed during the extraction step). The concentrated solution was filtered (Sartorius, filter paper grade 1289), and the clear pale-yellow filtrate was evaporated to dryness. The residue was dissolved in CH_2Cl_2 (10 mL) and the resulting pale-yellow solution was added dropwise to a solution of Et_2O (100 mL) while stirring. An off-white solid precipitated, which was isolated by filtration and dried under reduced pressure. The obtained solid was dissolved in CH_2Cl_2 (30 mL) and charcoal (3.0 g) was added to the solution. The suspension was stirred for 30 min at ambient temperature and filtered (sartorius, filter paper grade 1289) to obtain a clear, pale-yellow filtrate. The solvent was removed *in vacuo*. Recrystallization of the solid residue from CH_2Cl_2/Et_2O (1:3, 5:15 mL) yielded an off-white, NMR-spectroscopically clean solid, which was dried at 100 °C under reduced pressure for 1 day (130.1 mg, 39%). The NMR spectroscopic data are consistent with the data reported in the literature.[25]

^{1}H NMR (400.13 MHz, $CDCl_3$, 298 K): δ = 7.95-7.86 (m, 1H), 7.83-7.73 (m, 2H), 7.68-7.57 (m, 2H).
^{13}C{^{1}H} NMR (100.61 MHz, $CDCl_3$, 298 K): δ = 136.0 (d, *J* = 3.1 Hz), 134.6 (d, *J* = 10.2 Hz), 131.0 (d, *J* = 12.9 Hz), 117.6 (d, *J* = 89.4 Hz).
^{31}P{^{1}H} NMR (161.98 MHz, $CDCl_3$, 298 K): δ = 23.8 (s).

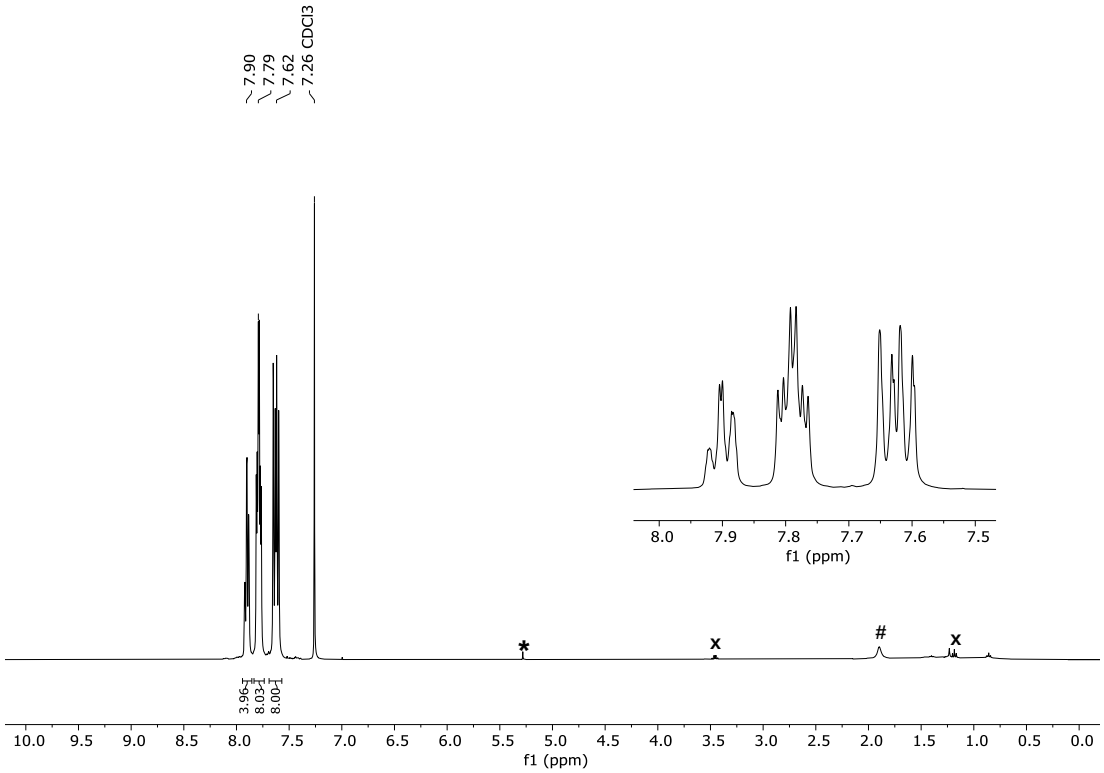

Figure S58. ^{1}H NMR spectrum (400.13 MHz, $CDCl_3$, 298 K) of tetraphenylphosphonium bromide prepared from P_4 on a 0.8 mmol scale. *: residual CH_2Cl_2. x: residual Et_2O. #: residual water from $CDCl_3$.

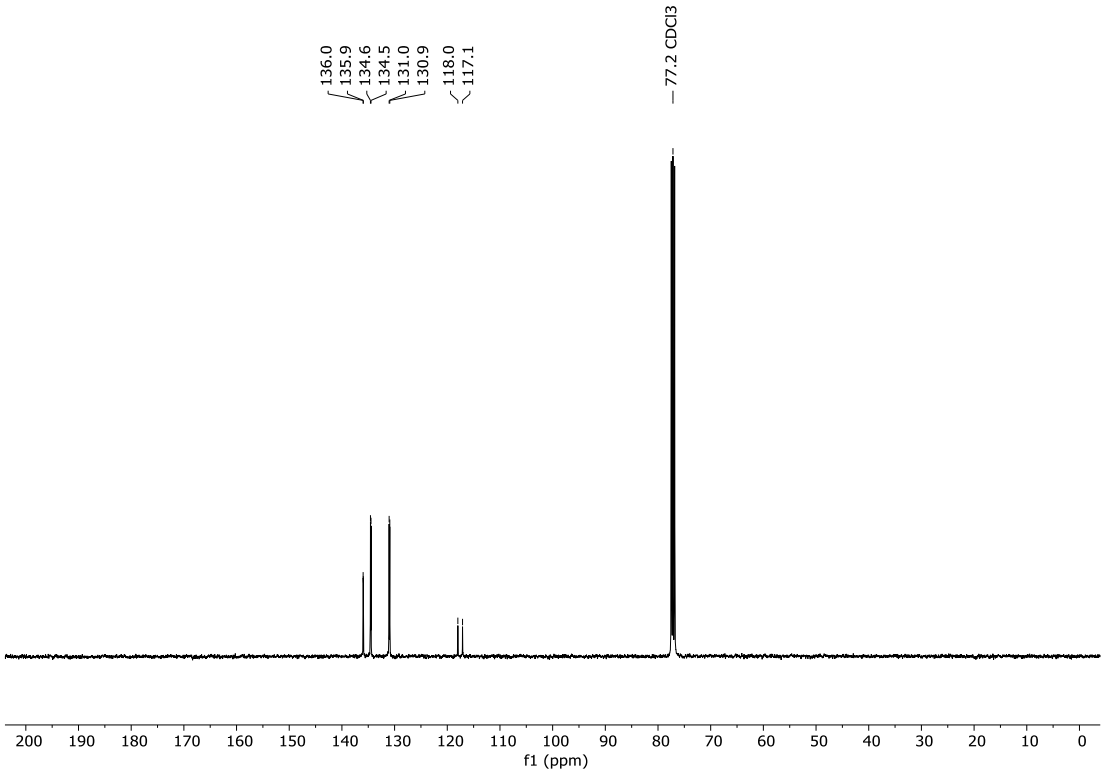

Figure S59. $^{13}C\{^{1}H\}$ NMR spectrum (100.61 MHz, $CDCl_3$, 298 K) of tetraphenylphosphonium bromide prepared from P_4 on a 0.8 mmol scale.

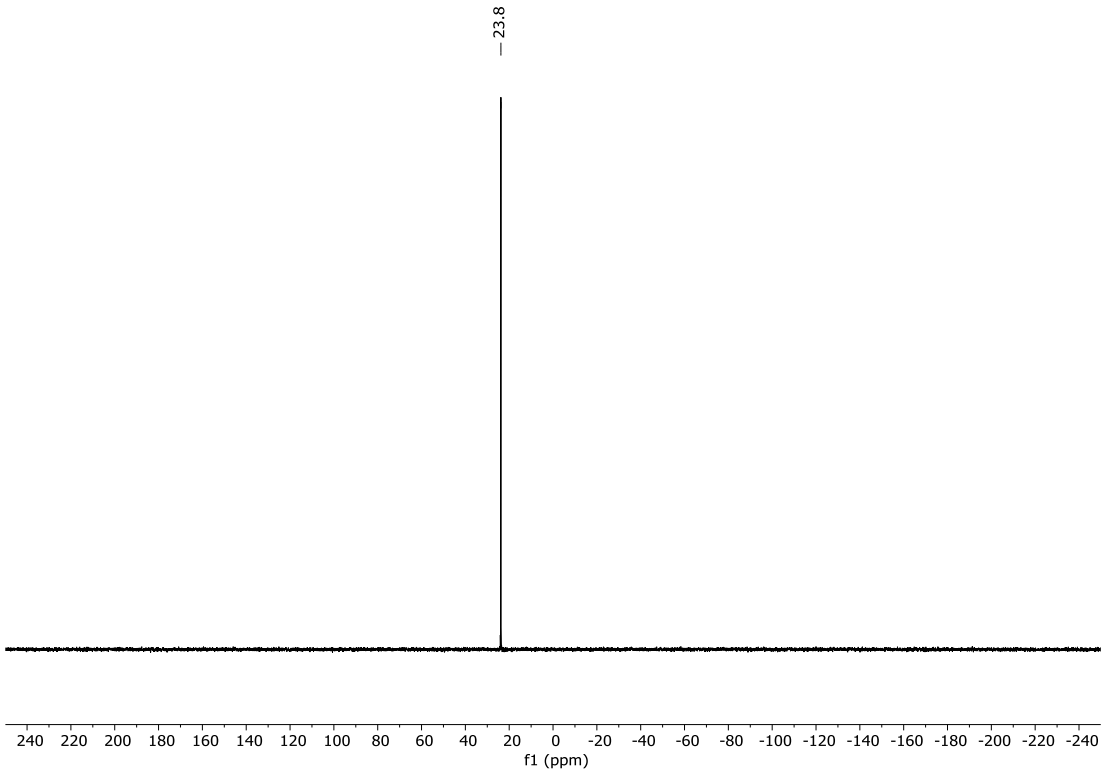

Figure S60. $^{31}P\{^{1}H\}$ NMR spectrum (161.98 MHz, $CDCl_3$, 298 K) of tetraphenylphosphonium bromide prepared from P_4 on a 0.8 mmol scale.

5.4.5.2 Tris(*o*-tolyl)phosphine, (*o*-tol)$_3$P:

To a 100 mL stoppered Schlenk tube equipped with a stirring bar were added 2-bromotoluene (1058 µL, 8.8 mmol, 11.0 equiv. based on the phosphorus atom), NEt_3 (1004 µL, 7.2 mmol, 9.0 equiv. based on the phosphorus atom), 9-mesityl-3,6-di-*tert*-butyl-10-phenylacridinium tetrafluoroborate (Mes-Acr-BF_4; 45.9 mg, 0.08 mmol, 10 mol% based on the phosphorus atom) and P_4 (24.8 mg, 0.2 mmol, 0.25 equiv., as a stock solution in 1306 µL benzene). The mixture was dissolved in acetonitrile (2.0 mL). The tube was sealed, fixed with a clamp (Figure S56), and irradiated with nUV light (390 nm, 40 W, Kessil PR160L in a PR160 Rig with Fan Kit) for 48 h. Ph_3PO (0.4 mmol, 111.2 mg; added as solid) was subsequently added to act as an internal standard. The resulting mixture was subjected to quantitative $^{31}P\{^{1}H\}$ NMR analysis and showed formation of 42% tris(*o*-tolyl)phosphine and minor formation of di(*o*-tolyl)phosphine (Figure S61).

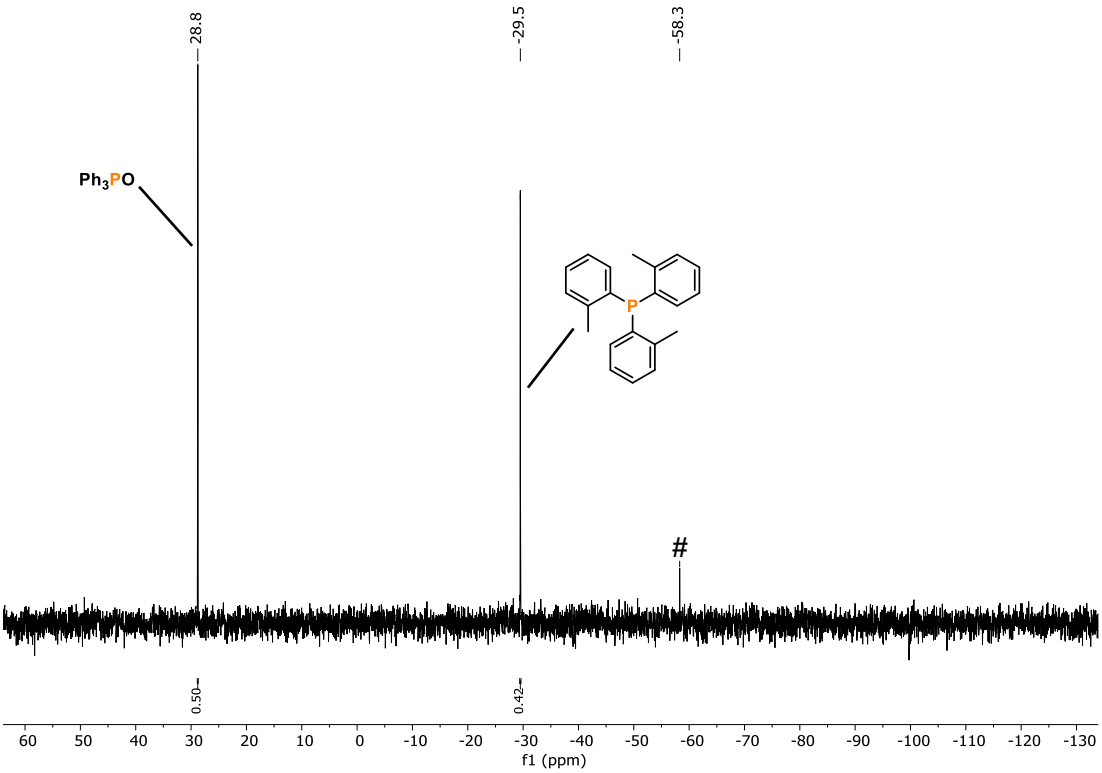

Figure S61. Quantitative single scan $^{31}P\{^{1}H\}$ (zgig) NMR spectrum for the 20-fold scale-up photocatalytic functionalization of P_4 using 2-bromotoluene. #: di(*o*-tolyl)phosphine.

Work-up (without addition of internal standard Ph_3PO):

The suspension was evaporated to dryness in vacuo at 100 °C, and the resulting orange wax-like residue was treated with n-hexane (30 mL). The mixture was stirred for 2 h, and the clear, pale-yellow supernatant filtered into a sublimation flask. The solvent was removed in vacuo and the residual orange wax-like solid was sublimed twice (ca. 1.0 x 10^{-2} mbar to ca. 6.0 x 10^{-3} mbar, 100 °C) to give an off-white solid (67 mg, 28%). The NMR spectroscopic data are consistent with the data reported in the literature.[26]

^{1}H NMR (400.13 MHz, $CDCl_3$, 298 K): δ = 7.29-7.20 (m, 6H), 7.10-7.03 (m, 3H), 6.76-6.67 (m, 3H), 2.39 (s, 9H).

$^{13}C\{^{1}H\}$ NMR (100.61 MHz, $CDCl_3$, 298 K): δ = 142.9 (d, *J* = 26.1 Hz), 134.7 (d, *J* = 11.0 Hz), 133.2 (s), 130.2 (d, *J* = 4.8 Hz), 128.8 (s), 126.3 (s), 21.3 (d, *J* = 21.4 Hz).

$^{31}P\{^{1}H\}$ NMR (161.98 MHz, $CDCl_3$, 298 K): δ = −28.9 (s).

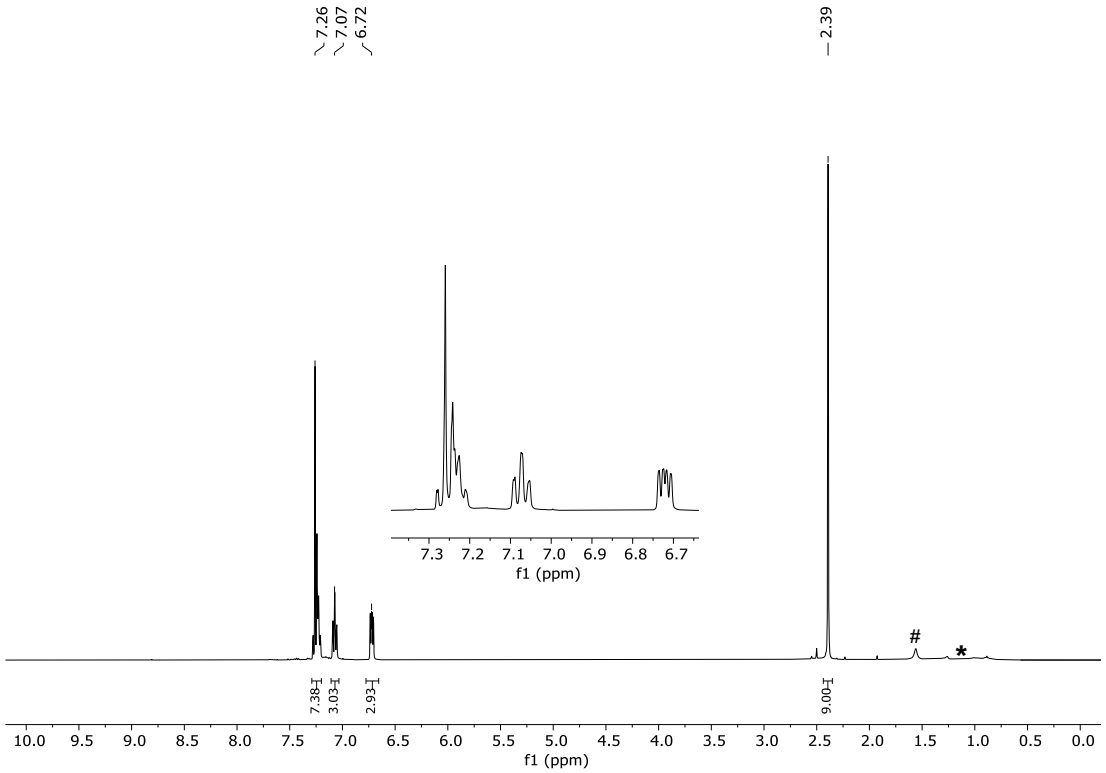

Figure S62. ^{1}H NMR spectrum (400.13 MHz, $CDCl_3$, 298 K) of tris(*o*-tolyl)phosphine prepared from P_4 on a 0.8 mmol scale. #: residual water from $CDCl_3$. *: residual *n*-hexane.

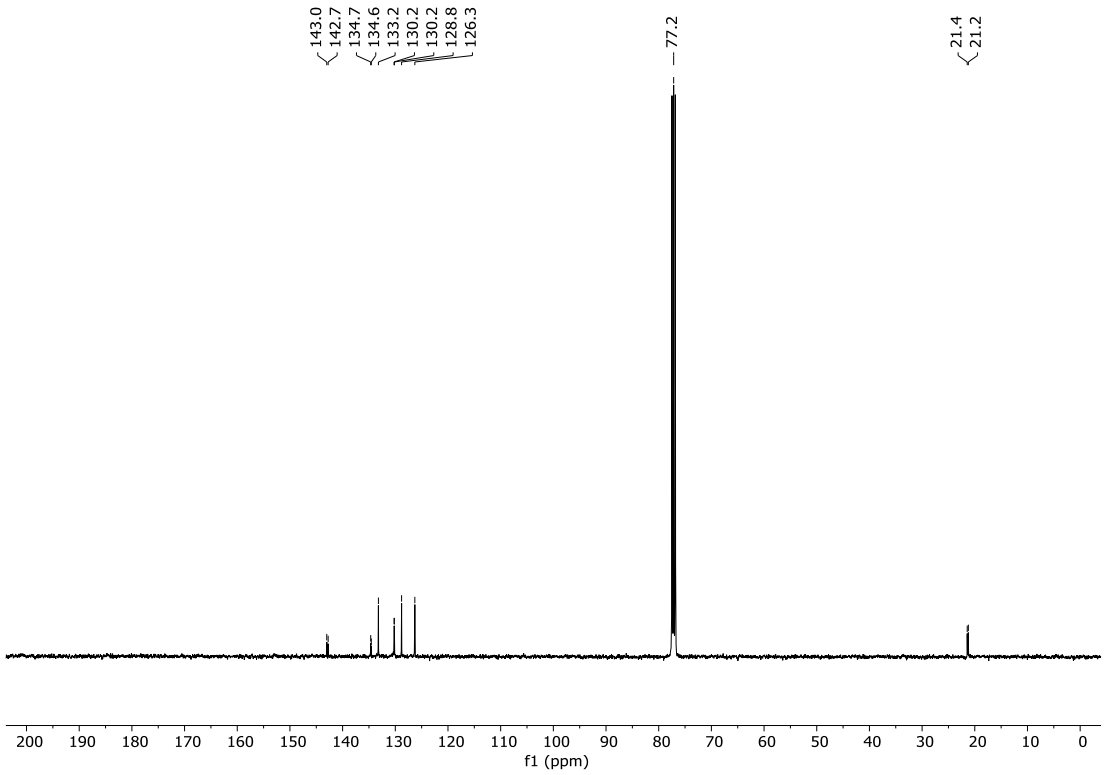

Figure S63. $^{13}C\{^{1}H\}$ NMR spectrum (100.61 MHz, $CDCl_3$, 298 K) of tris(*o*-tolyl)phosphine prepared from P_4 on a 0.8 mmol scale.

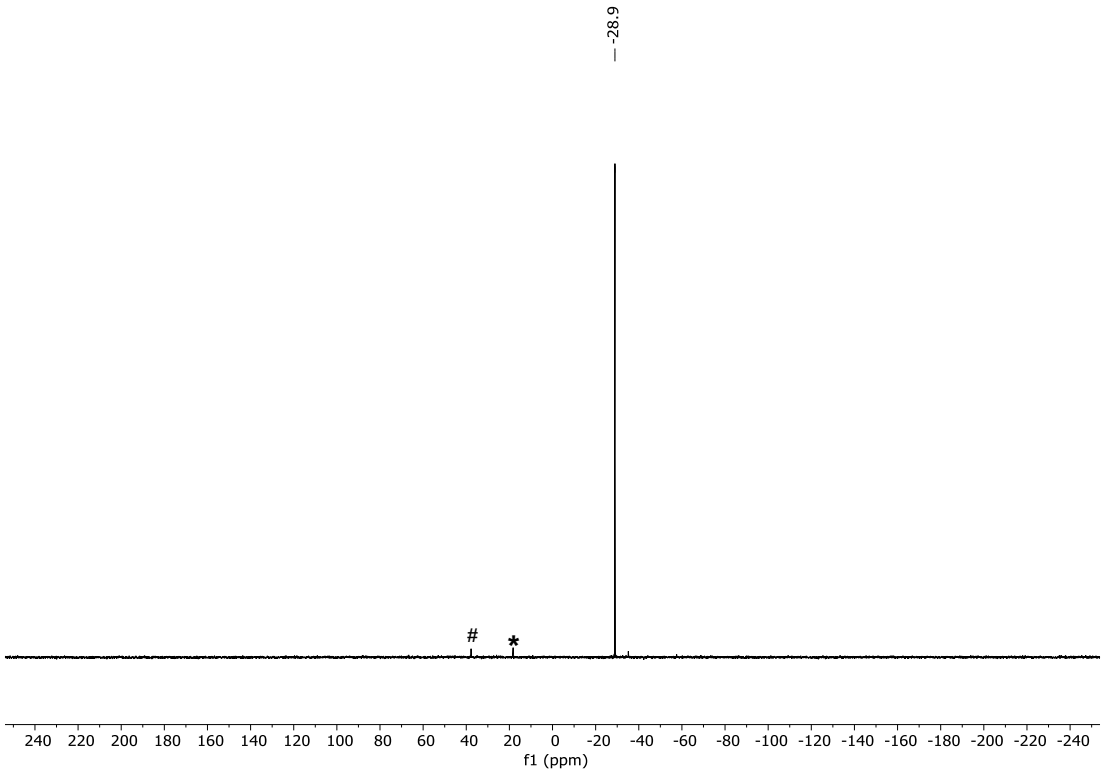

Figure S64. $^{31}P\{^{1}H\}$ NMR spectrum (161.98 MHz, $CDCl_3$, 298 K) of tris(*o*-tolyl)phosphine prepared from P_4 on a 0.8 mmol scale. #: tris(*o*-tolyl)phosphine oxide. *: bis(*o*-tolyl)phosphine oxide.

5.4.6 NMR Spectroscopic Investigations

5.4.6.1 Reaction Monitoring and Intermediate Identification

The reaction mixture was prepared according to the general protocol (see section 5.4.2) using bromobenzene as the substrate. The individual reactions were stopped after the indicated reaction time (see Table S10), internal standard (Ph_3PO; 0.02 mmol, stock solution in benzene) was added, and the mixture subjected to quantitative $^{31}P\{^{1}H\}$ NMR analysis. The NMR spectroscopic reaction monitoring is depicted in Figure S65. In the $^{31}P\{^{1}H\}$ NMR spectrum (NS 512) after 1 h reaction time, the formation of mono- and diphosphorus intermediates can be observed (Figure S66).

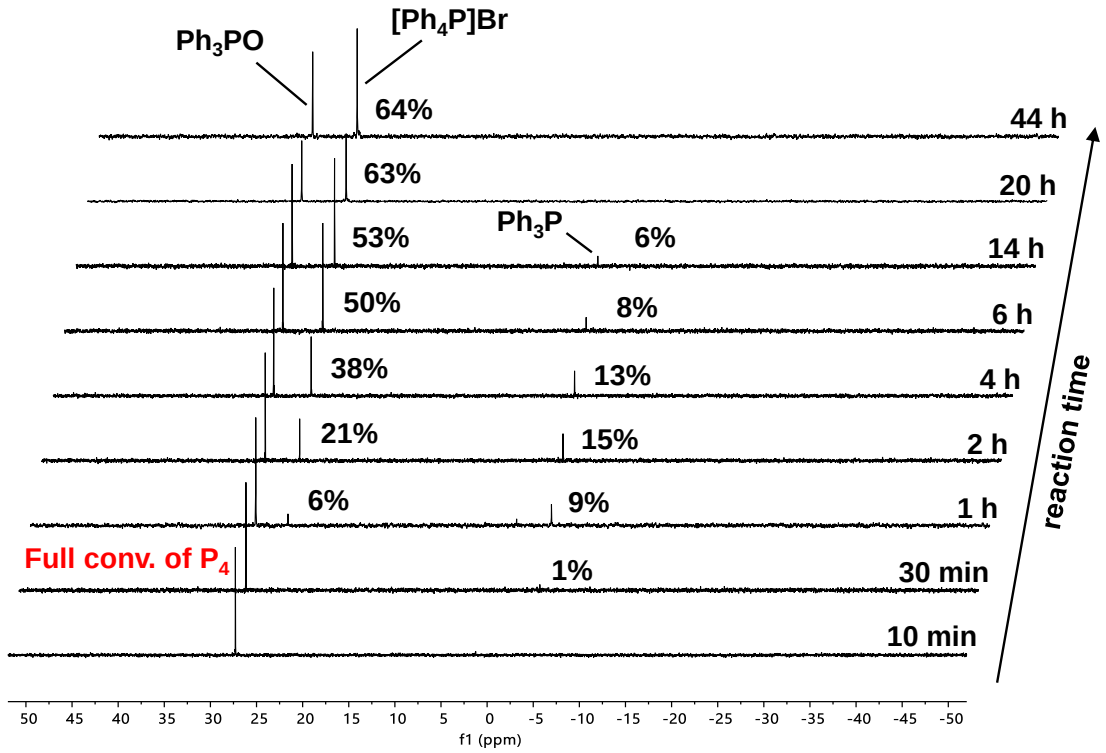

Figure S65. $^{31}P\{^{1}H\}$ NMR spectroscopic reaction monitoring (t ≤ 44 h) of the photocatalytic phenylation of P_4 using standard conditions (see section 5.4.2).

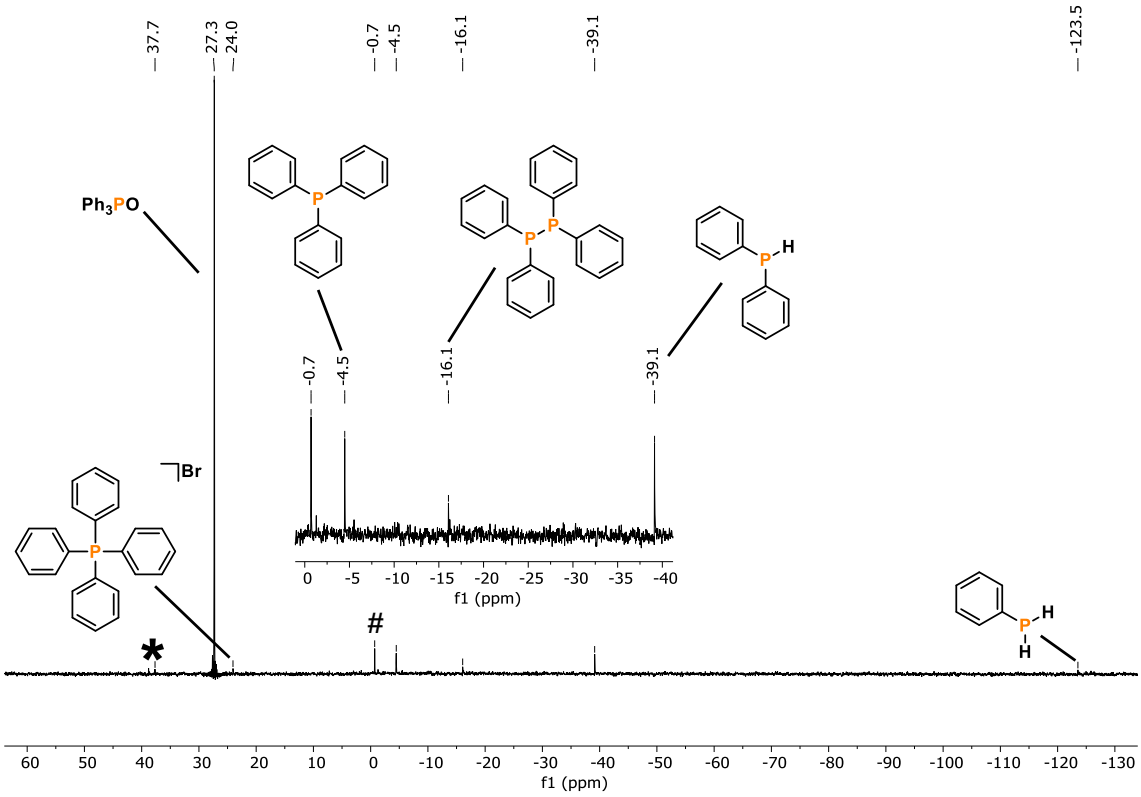

Figure S66. $^{31}P\{^{1}H\}$ NMR spectroscopic reaction monitoring (t ≤ 44 h) of the photocatalytic phenylation of P_4 using standard conditions (see section 5.4.2). $^{31}P\{^{1}H\}$ NMR spectrum (NS 512) after 1 h reaction time. #: unidentified signal. *: Formation of $[Ph_2P(NEt_2)(CH{=}CHCH{=}CHNEt_2)]Br$ (37.7 ppm).[9]

5.4.6.2 Assessment of PH_3 Formation and Identification of Additional Reaction Intermediates

A) The reaction mixture was prepared according to the general protocol (see section 5.4.2), but in absence of aryl substrate and on a threefold scale up. The reaction mixture was transferred into a J. Young NMR tube and irradiated with nUV light (390 nm, 40 W, Kessil PR160L in a PR160 Rig with Fan Kit, Figure S2, right) for 20 h. After that, the mixture was subjected to $^{31}P\{^{1}H\}$ NMR analysis. In the $^{31}P\{^{1}H\}$ NMR spectrum (NS 20480), a major signal for residual P_4 at −523.1 ppm can be observed. Next to this, a series of unidentified signals residing between 4.0 and −8.0 ppm can be observed. The formation of PH_3 only appears in a negligible amount as indicated by the quartet signal at −241.4 ppm, which can only be observed with adequate resolution after 20480 scans. Thus, in the absence of aryl substrate, P–H bond formation ultimately resulting in PH_3 does not seem to be a significant process.

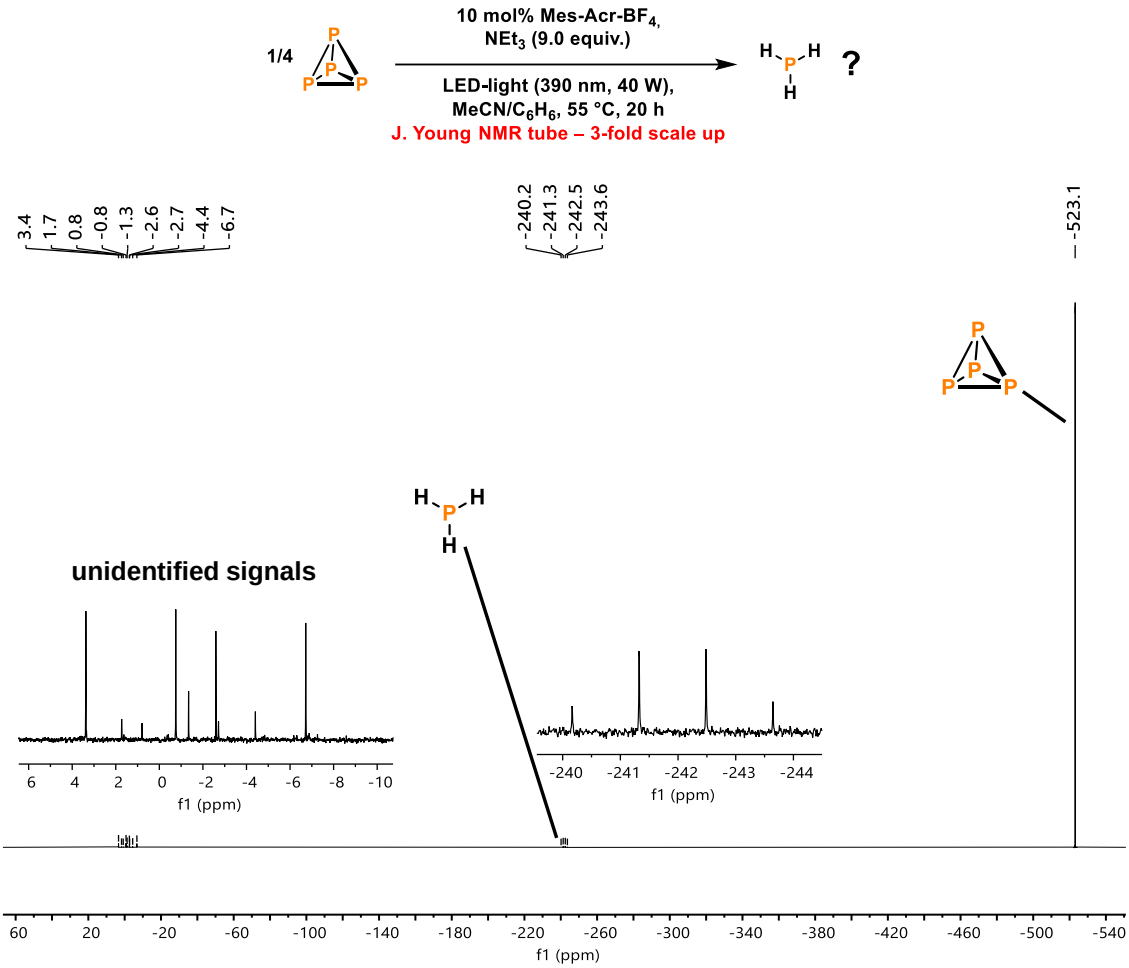

Figure S67. ^{31}P NMR spectrum (161.98 MHz, C_6D_6, 298 K, NS 20480) of the attempted PH_3 formation using photocatalytic conditions in the absence of substrate.

B) The reaction mixture was prepared according to the general protocol (see section 5.4.2), with bromobenzene as the aryl substrate and on a threefold scale-up. The reaction mixture was transferred into a J. Young NMR tube and irradiated with nUV light (390 nm, 40 W, Kessil PR160L in a PR160 Rig with Fan Kit, Figure S2, right) for 20 h (formation of 53%

[Ph_4P]Br and 3% Ph_3P). The mixture was subjected to $^{31}P\{^1H\}$ NMR analysis after 20 min, 1 h, 3 h, 9 h and 20 h. The progress of product formation was assessed with a standard capillary bearing Ph_3PO (0.02 mmol in MeCN-d_3). The NMR spectroscopic reaction monitoring is depicted in Figure S68. During the monitoring, no formation of PH_3 was observed at any time (Figure S68, see absence of signal between –236 and –250 ppm). In addition, while not all P_4 was consumed after 3 h irradiation, the formation of $PhPH_2$ and Ph_2PH next to other monophosphorus intermediates (Figure S68, see a-f) could be observed.[9] This is a strong indication, that the breakdown of P_4 does not primarily result in the formation of PH_3 but likely proceeds through other intermediates, e.g., linear or cyclic polyphosphorus species, "P_nR_x" with n = 2-4, which could not be identified (apart from the diphosphine Ph_4P_2 and the divinyldiphosphine [$PhP(CHCH_2)]_2$). Accordingly, the arylation of $NaPH_2$ as a PH_3-surrogate did not furnish comparable results to the P_4 system based on the use of Mes-Acr-BF_4 as a photocatalyst (see below, S8). The aminophosphine intermediates and side products, which are primarily observed at 3 h and 9 h reaction time do not appear in significant quantities; however, the sum of all species can account for a substantial portion of the overall arylation reaction and thus may present an additional factor limiting the (quantitative) formation of Ar_3P and [Ar_4P]X (X = Br, Cl).

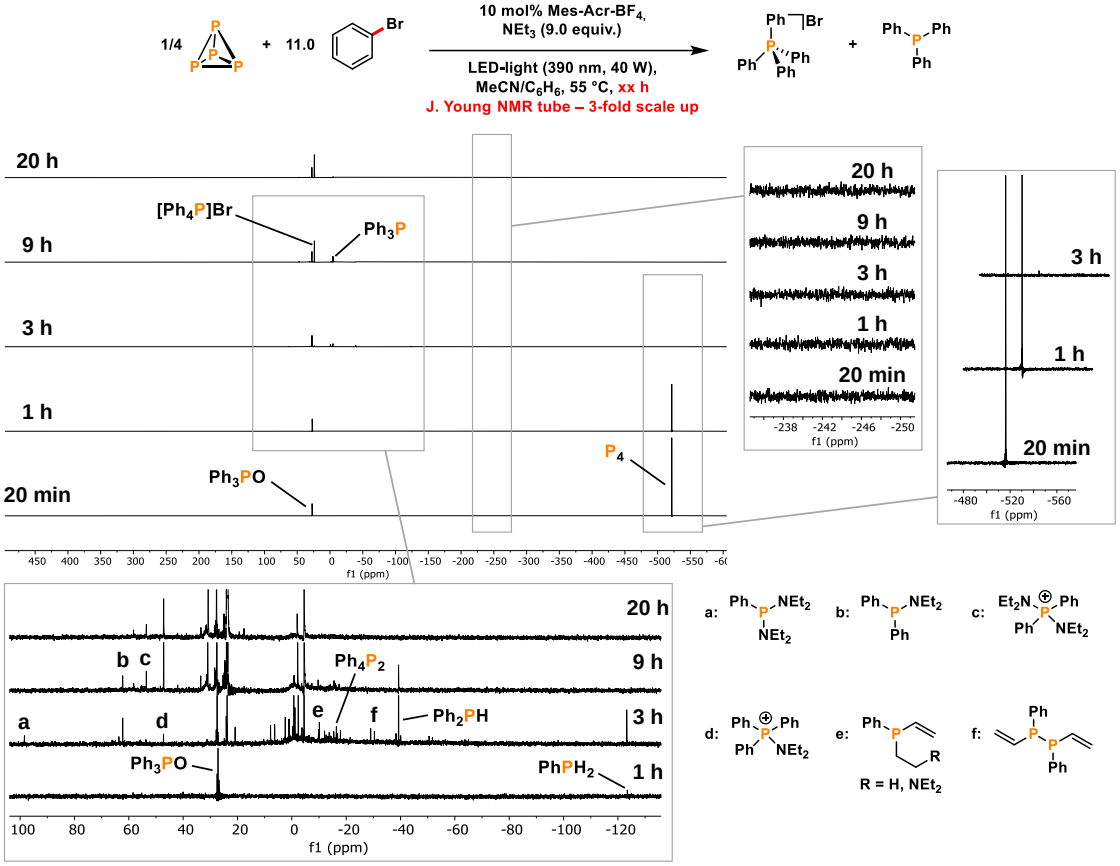

Figure S68. $^{31}P\{^1H\}$ NMR reaction monitoring (161.98 MHz, C_6D_6, 298 K, NS 512) of the phenylation of P_4 in a J. Young NMR tube and identification of additional reaction intermediates and side products in agreement with the literature.[9] No observation of PH_3 formation throughout the whole reaction monitoring.

C) The reaction mixture was prepared according to the general protocol (see section 5.4.2), with bromobenzene as the aryl substrate and Ph_5P_5 as P-atom source (instead of P_4) on a threefold scale-up (0.12 mmol P-atom). The reaction mixture was transferred into a J. Young NMR tube and irradiated with nUV light (390 nm, 40 W, Kessil PR160L in a PR160 Rig with Fan Kit, Figure S2, right) for 20 h (formation of 62% $[Ph_4P]Br$, Figure S69).

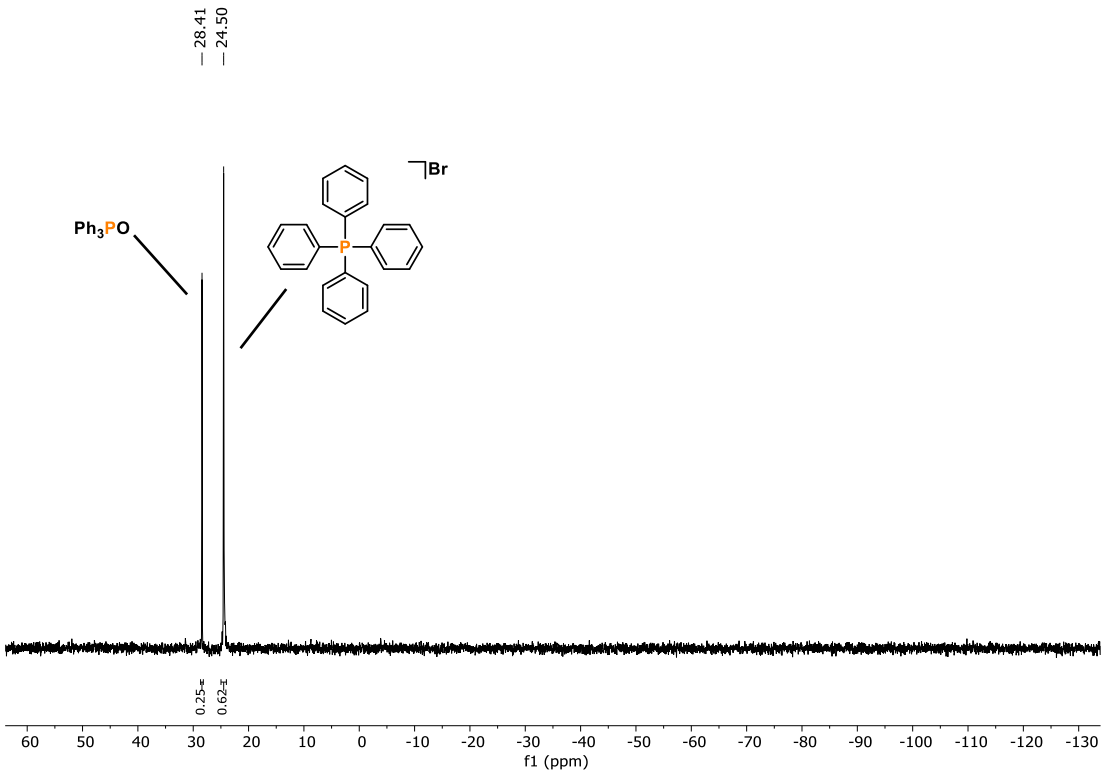

Figure S69. Quantitative single scan $^{31}P\{^1H\}$ (zgig) NMR spectrum for the photocatalytic functionalization of Ph_5P_5 using bromobenzene in a J. Young NMR tube after 20 h reaction time.

In addition, the mixture was subjected to $^{31}P\{^1H\}$ NMR analysis after 20 min, 1 h and 3 h. The progress of product formation was assessed with a standard capillary bearing Ph_3PO (0.03 mmol in MeCN-d_3). The NMR spectroscopic reaction monitoring is depicted in Figure S70. The phenylation of Ph_5P_5 with PhBr showed that the smaller cyclophosphine Ph_3P_3 is formed after irradiation for 20 min and can still be observed after irradiation for 1 h.[18] The cyclophosphane Ph_4P_4 is already present as a minor impurity in the starting material Ph_5P_5 but notably accumulates during initial irradiation for 20 min, after which it is almost completely consumed after 1 h reaction time. During this period, Ph_5P_5 is fully consumed, which is in alignment with the rapid consumption of P_4 in the NMR monitoring study (Figure S65 and Figure S68). After irradiation for 1 h (20 min), the P_1-intermediates $PhPH_2$ and Ph_2PH can be observed and are subsequently converted to Ph_3P and $[Ph_4P]Br$, which are the dominant reaction products after irradiation for 3 h. This indicates that the photocatalytic phenylation starting from a cyclopolyphosphine follows an analogous stepwise sequence as observed for P_4. Moreover, smaller cyclophosphines (or linear polyphosphorus species) should be accessible starting from P_4 and are eventually converted into P_1-species – however,

their concentrations might be very low and their consumption fast, which prevents observation by ^{31}P NMR spectroscopy.

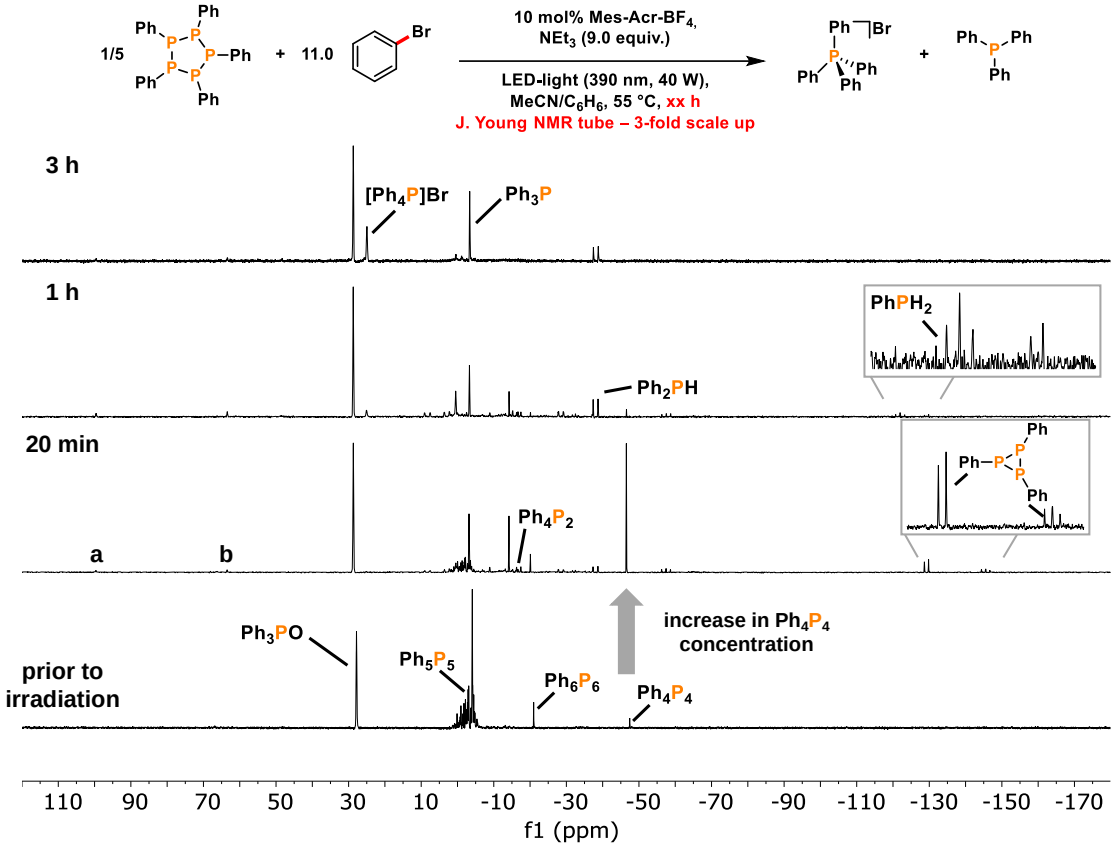

Figure S70. ^{31}P NMR reaction monitoring (161.98 MHz, MeCN-d_3, 298 K, NS 512 or NS 1024) of the phenylation of Ph_5P_5 in a J. Young NMR tube. Identification of cyclic polyphosphorus intermediates and side products in agreement with the literature.[9],[18] a: $PhP(NEt_2)_2$. b: $Ph_2P(NEt_2)$.

5.4.6.3 Stability of P_4 Under Irradiation

A solution of P_4 (0.02 mmol) was irradiated either in a mixture of MeCN/C_6H_6 (3/2 *v*/*v*, 525.2 µL) or in a standard reaction mixture in the absence of photocatalyst (0.1 mL of MeCN was added instead; twofold scale up). Both initially clear, colorless solutions turn turbid after 20 h (only P_4: orange precipitation; with reagents: brown precipitation). $^{31}P\{^1H\}$ NMR spectroscopic analysis using the same pulse sequence (zgpg30, NS 256) as for the calibration shows only a resonance for residual P_4 (and internal standard Ph_3PO; Table S13 and Figure S71). 68% of the white phosphorus signal remained when only P_4 was irradiated and 74% of the P_4 signal intensity remained in the standard reaction mixture in the absence of photocatalyst. While P_4 partially decomposes when irradiated with nUV light, the formation of polyphosphorus species "P_nR_x" (with n = 2-4) or any other degradation product was not observed. Instead, it is likely that P_4 polymerizes to high(er)-molecular weight polyphosphorus species.

Table S13. Stability study of P_4 under irradiation with nUV light.

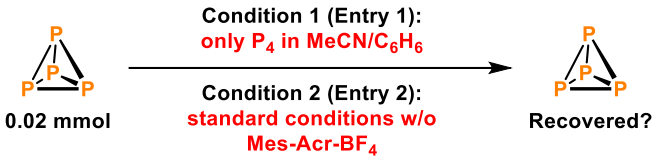

Entry		Full conv. of P_4?		Remaining P_4 signal intensity	
	1		✗		68%
	2		✗		74%

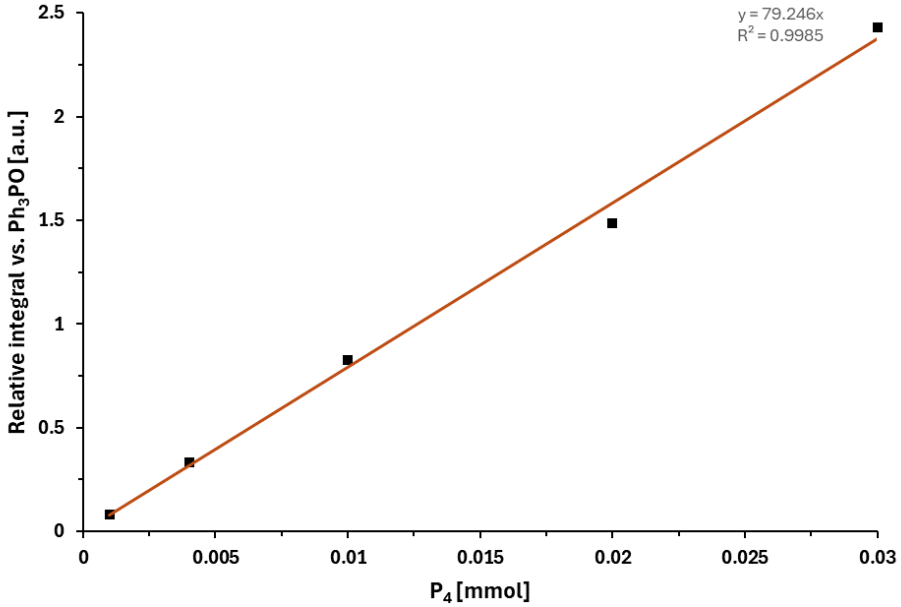

Figure S71. Plot showing the relative integral of a solution of P_4 vs. internal standard Ph_3PO (0.04 mmol) against the expected (based on mass added) molar quantities of P_4 (0.001 to 0.03 mmol) in a $MeCN/C_6H_6$ (3:2) solution using a $^{31}P\{^1H\}$ NMR experiment (zgpg30, NS 256).

5.4.7 Photocatalytic Phenylation of $PhPH_2$, Ph_2PH, Ph_4P_2 and Ph_3P and Stability Study with $[Ph_4P]Br$

To a 10 mL stoppered tube equipped with a stirring bar was added bromobenzene (0.0 to 0.44 mmol, 0.0 to 11.0 equiv. based on the phosphorus atom), NEt_3 (0.0 to 0.36 mmol, 0.0 to 9.0 equiv. based on the phosphorus atom), 9-mesityl-3,6-di-*tert*-butyl-10-phenylacridinium tetrafluoroborate (Mes-Acr-BF_4; 2.3 mg, 4.0 µmol, 10 mol% based on the phosphorus atom) and the P-atom source ($Ph_{3-n}PH_n$ [n = 0-2], 0.04 mmol, 1.0 equiv. or Ph_4P_2, 0.02 mmol, 7.4 mg, 0.5 equiv. or $[Ph_4P]Br$, 16.8 mg, 0.04 mmol, 1.0 equiv.). The mixture was dissolved in acetonitrile/benzene (0.1 + 0.0655 mL). The tube was sealed, placed in a custom-made flask holder (Figure S2, left), and irradiated with nUV light (390 nm, 40 W, Kessil PR160L in a PR160 Rig with Fan Kit, Figure S2, right) for 20 h (unless stated otherwise). Ph_3PO (0.02 mmol, stock solution in benzene) was subsequently added to act as an internal standard. The resulting mixture was subjected to NMR analysis.

Table S14. Photochemical functionalization of Ph_3P to $[Ph_4P]Br$.[a]

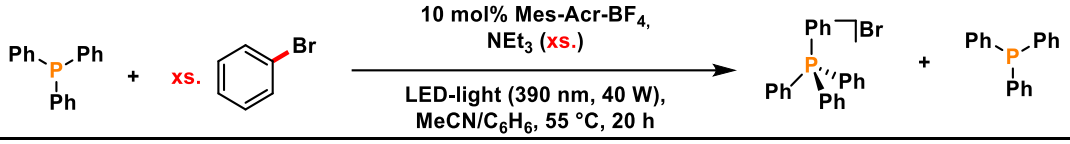

Entry	Conditions[b] NEt_3:PhBr	Form. of $[Ph_4P]Br$ / %	Form. of Ph_3P / %	Intermediates	Consumption of Ph_3P / %
1	9:11	86	0	/	>99
2	3:5	97	0	/	>99
3	2:3	89	0	/	>99
4	9:0	0	0	Ph_2PH, $PhPH_2$[c]	70

[a] The general protocol for reactions at 0.04 mmol scale (section 5.4.2) was modified by replacing P_4 with Ph_3P (10.5 mg, 0.04 mmol). [b] Listed equivalents are defined per P atom. [c] A minor signal for $PhPH_2$ can be observed in the $^{31}P\{^1H\}$ NMR spectrum (NS 64).

Table S15. Photochemical functionalization of Ph_2PH to $[Ph_4P]Br$.[a]

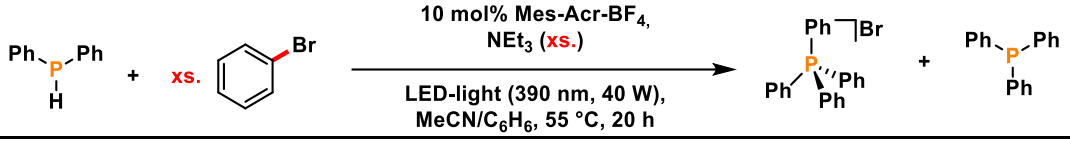

Entry	Conditions[b] NEt_3:PhBr	Form. of $[Ph_4P]Br$ / %	Form. of Ph_3P / %	Intermediates	Consumption of Ph_2PH / %
1	9:11	89	0[c]	/	>99
2	3:5	85	0[c]	/	>99
3	2:3	39	40	/	>99[d]
4	9:0	0	0	$PhPH_2$	68[e]

[a] The general protocol for reactions at 0.04 mmol scale (section 5.4.2) was modified by replacing P_4 with Ph_2PH (6.96 µL, 0.04 mmol). [b] Listed equivalents are defined per P atom. [c] A minor signal for Ph_3P can be observed in the $^{31}P\{^1H\}$ NMR spectrum (NS 64). [d] A minor signal for Ph_3P can be observed in the $^{31}P\{^1H\}$ NMR spectrum (NS 64). [e] Non-calibrated value assessed by integration of the signal in the single scan $^{31}P\{^1H\}$ NMR spectrum.

Table S16. Photochemical functionalization of $PhPH_2$ to $[Ph_4P]Br$.[a]

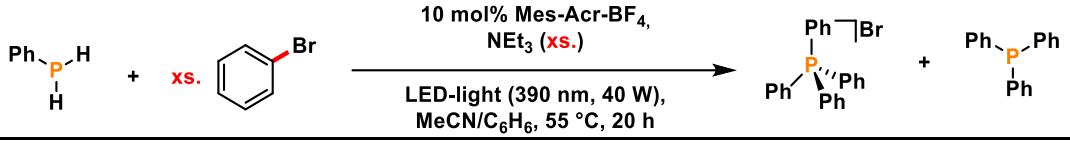

Entry	Conditions[b] NEt_3:PhBr	Form. of $[Ph_4P]Br$ / %	Form. of Ph_3P / %	Intermediates	Consumption of $PhPH_2$ / %
1	9:11	71	0	Ph_3P[c]	>99
2	6:8	64	6	/	>99
3	3:5	21	35	Ph_4P_2, Ph_2PH[d]	>99
4	9:0	0	0	/	37[e]

[a] The general protocol for reactions at 0.04 mmol scale (section 5.4.2) was modified by replacing P_4 with $PhPH_2$ (4.40 µL, 0.04 mmol). [b] Listed equivalents are defined per P atom. [c] A minor signal for Ph_3P can be observed in the $^{31}P\{^1H\}$ NMR spectrum (NS 64). [d] A minor signal for Ph_2PH can be observed in the $^{31}P\{^1H\}$ NMR spectrum (NS 64). [e] Non-calibrated value assessed by integration of the signal in the single scan $^{31}P\{^1H\}$ NMR spectrum.

Table S17. Photochemical functionalization of Ph_4P_2 to $[Ph_4P]Br$.[a]

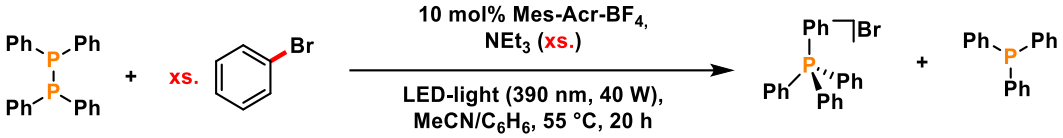

Entry	Conditions[b] NEt_3:PhBr	Form. of $[Ph_4P]Br$ / %	Form. of Ph_3P / %	Intermediates	Consumption of Ph_4P_2 / %
1	9:11	91	0	/	>99
2	3:5	82	0[c]	/	>99
3	2:3	72	19	/	>99
4	9:0	0	0	Ph_2PH, $PhPH_2$	>99

[a] The general protocol for reactions at 0.04 mmol scale (section 5.4.2) was modified by replacing P_4 with Ph_4P_2 (7.4 mg, 0.02 mmol). [b] Listed equivalents are defined per P atom. [c] A minor signal for Ph_3P can be observed in the $^{31}P\{^1H\}$ NMR spectrum (NS 64).

Table S18. Stability test of tetraphenylphosphonium bromide $[Ph_4P]Br$ toward photocatalytic conditions.[a]

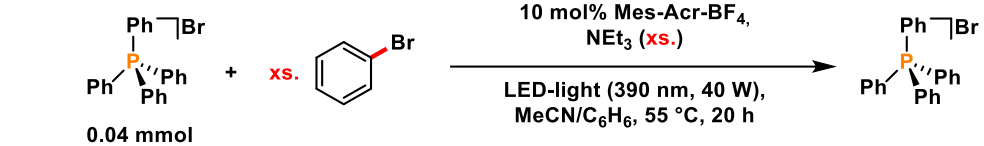

Entry	Conditions[b] NEt_3:PhBr	Recovered $[Ph_4P]Br$/ %	Formation of Ph_3P / %
1	9:11	81	/[c]
2	3:5	78	/[c]
3	9:0	41	52
4	0:0	97	/

[a] The general protocol for reactions at 0.04 mmol scale (section 5.4.2) was modified by replacing P_4 with $[Ph_4P]Br$ (16.8 mg, 0.04 mmol; 100% spectroscopic yield) for a stability check of the phosphonium salt under the photocatalytic reaction conditions. The phosphonium salt was fully dissolved in the reaction mixture. [b] Listed equivalents are defined per P atom. [c] No formation of Ph_3P or other phosphorus species was observed.

5.4.8 Photocatalytic Arylation of $NaPH_2$

To a 10 mL stoppered tube equipped with a stirring bar were added the appropriate aryl bromide (0.44 mmol, 11.0 equiv. based on the phosphorus atom), NEt_3 (50.2 µL, 0.36 mmol, 9.0 equiv. based on the phosphorus atom), 9-mesityl-3,6-di-*tert*-butyl-10-phenylacridinium tetrafluoroborate (Mes-Acr-BF_4; 2.3 mg, 4.0 µmol, 10 mol% based on the phosphorus atom) and $NaPH_2$ (0.04 mmol, 2.2 mg, 1.0 equiv.). The mixture was dissolved in acetonitrile (0.1 mL). The tube was sealed, placed in a custom-made flask holder (Figure S2, left), and irradiated with nUV light (390 nm, 40 W, Kessil PR160L in a PR160 Rig with Fan Kit, Figure S2, right) for 20 h (unless stated otherwise). Ph_3PO (0.02 mmol, stock solution in benzene) was subsequently added to act as an internal standard. The resulting mixture was subjected to NMR analysis.

Table S19. Photocatalytic functionalization of $NaPH_2$ to $[Ar_4P]Br$ and Ar_3P: screening of control experiments.[a]

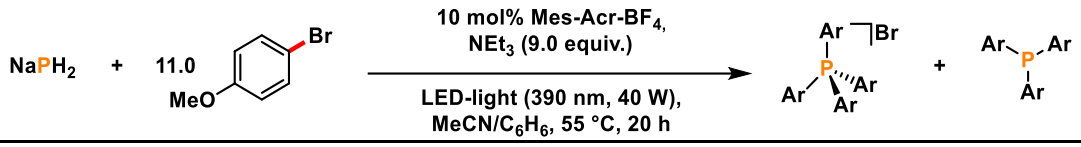

Entry	Conditions	Full conv. of $NaPH_2$?	Form. of $[Ar_4P]Br$ / %	Form. of Ar_3P / %
1	Standard	✓	32	4
2	No photocatalyst	✓	0	2
3	No light[b]	✓	0	0
4	No NEt_3	✓	0	4

[a] The general protocol for reactions at 0.04 mmol scale (section 5.4.2) was modified by replacing P_4 with $NaPH_2$ (2.2 mg, 0.04 mmol). Ar = 4-OMe–C_6H_4–. [b] The reaction flask was heated to 55 °C.

Table S20. Photocatalytic functionalization of $NaPH_2$ to $[Ar_4P]Br$ and Ar_3P: screening of solvents.[a]

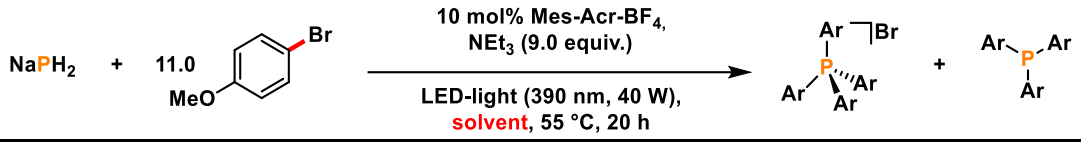

Entry	Solvent	Full conv. of $NaPH_2$?	Form. of $[Ar_4P]Br$ / %	Form. of Ar_3P / %
1	Acetonitrile	✓	32	4
2	DMF	✓	5	6
3	DMSO	✓	13	0
4	Benzene	✓	8	0
5	Acetone	✓	14	0
6	THF	✓	6	2

[a] The general protocol for reactions at 0.04 mmol scale (section 5.4.2) was modified by replacing P_4 with $NaPH_2$ (2.2 mg, 0.04 mmol). Ar = 4-OMe–C_6H_4–. The general protocol (section 5.4.2) was modified to use the solvent system indicated (identical solvent volume).

Table S21. Photocatalytic functionalization of $NaPH_2$ to $[Ar_4P]Br$ and Ar_3P: concentration screening.[a]

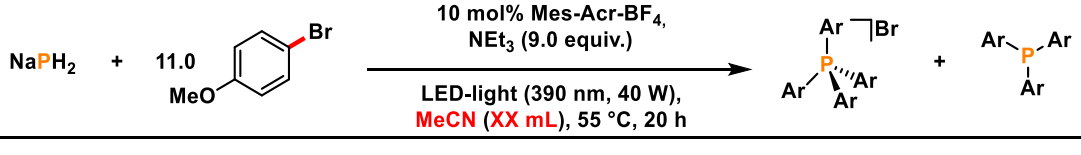

Entry	Solvent volume	Full conv. of $NaPH_2$?	Form. of $[Ar_4P]Br$ / %	Form. of Ar_3P / %
1	0.1 mL	✓	32	4
2	0.5 mL	✓	10	6
3	1.0 mL	✓	0	6
4	2.0 mL	✓	1	0

[a] The general protocol for reactions at 0.04 mmol scale (section 5.4.2) was modified by replacing P_4 with $NaPH_2$ (2.2 mg, 0.04 mmol). Ar = 4-OMe–C_6H_4–. The general protocol (section 5.4.2) was modified to use the indicated amount of MeCN

Table S22. Photocatalytic functionalization of $NaPH_2$ to $[Ar_4P]Br$ and Ar_3P: screening of reductants.[a]

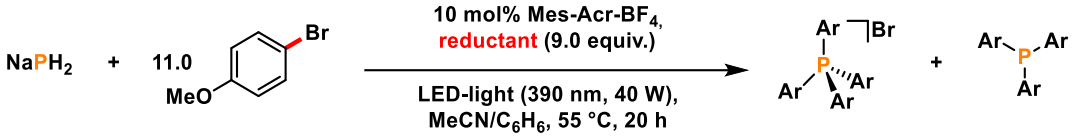

Entry	Reductant	Full conv. of $NaPH_2$?	Form. of $[Ar_4P]Br$ / %	Form. of Ar_3P / %
1	NEt_3	✓	32	4
2	DIPEA	✓	24	5
3	N^nBu_3	✓	29	8
4	$NMe_2{}^nPr$	✓	9	5

[a] The general protocol for reactions at 0.04 mmol scale (section 5.4.2) was modified by replacing P_4 with $NaPH_2$ (2.2 mg, 0.04 mmol). Ar = 4-OMe–C_6H_4–. The general protocol (section 5.4.2) was modified to use the indicated reducing agent (identical stoichiometry).

Table S23. Photocatalytic functionalization of $NaPH_2$ to $[Ar_4P]Br$ and Ar_3P: screening of reductant and substrate stoichiometry.[a]

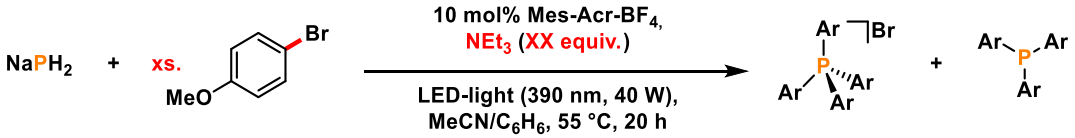

Entry	Stoichiometry NEt_3:4-Bromoanisole	Full conv. of $NaPH_2$?	Form. of $[Ar_4P]Br$ / %	Form. of Ar_3P / %
1	9:5	✓	11	6
2	9:7	✓	20	3
3	9:9	✓	30	5
4	9:11	✓	32	4
5	9:13	✓	21	3
6	9:15	✓	22	4
7	9:17	✓	27	3
8	3:11	✓	26	2
9	5:11	✓	30	2
10	7:11	✓	33	5
11	11:11	✓	20	5
12	13:11	✓	12	10
13	15:11	✓	7	6

[a] The general protocol for reactions at 0.04 mmol scale (section 5.4.2) was modified by replacing P_4 with $NaPH_2$ (2.2 mg, 0.04 mmol). Ar = 4-OMe–C_6H_4–.

Table S24. Photocatalytic functionalization of $NaPH_2$ to $[Ar_4P]Br$ and Ar_3P: screening of substrates.[a]

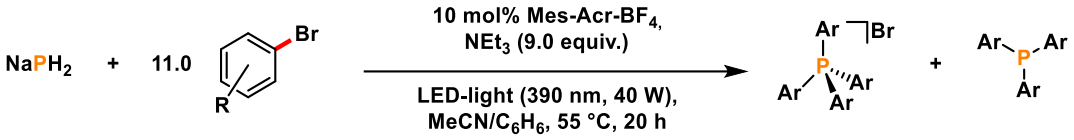

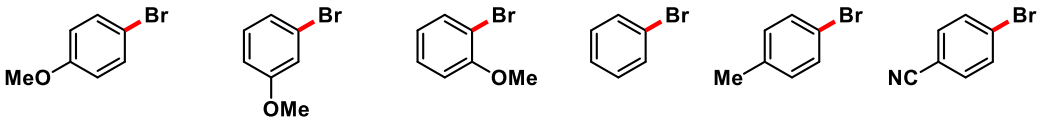

Entry	Substrate	Full conv. of $NaPH_2$?	Form. of $[Ar_4P]Br$ / %	Form. of Ar_3P / %
1	R = 4-OMe	✓	32	4
2	R = 3-OMe	✓	21	4
3	R = 2-OMe	✓	12	0
4	R = H	✓	19	0
5	R = 4-Me	✓	19	7
6	R = 4-CN	✓	7	0

[a] The general protocol for reactions at 0.04 mmol scale (section 5.4.2) was modified by replacing P_4 with $NaPH_2$ (2.2 mg, 0.04 mmol). The general protocol (section 5.4.2) was modified to use the indicated substrate (identical stoichiometry).

5.5 References

[1] a) G. Wittig, U. Schöllkopf, *Chem. Ber.* **1954**, *87*, 1318; b) G. Wittig, W. Haag, *Chem. Ber.* **1955**, *88*, 1654.

[2] a) L. H. Pignolet, Homogeneous Catalysis with Metal Phosphine Complexes, Springer, New York, **1983**; b) P. C. J. Kamer, P. W. N. M. van Leeuwen, J. N. H. Reek, *Acc. Chem. Res.* **2001**, *34*, 895; c) K. Wu, A. G. Doyle, *Nat. Chem.* **2017**, *9*, 779; d) A. L. Clevenger, R. M. Stolley, J. Aderibigbe, J. Louie, *Chem. Rev.* **2020**, *120*, 6124.

[3] a) M. S. El-Shahawi, S. S. M. Hassan, A. M. Othman, M. A. Zyada, M. A. El-Sonbati, *Anal. Chim. Acta* **2005**, *534*, 319; b) J. Castillo, M. T. Coll, A. Fortuny, P. Navarro Donoso, R. Sepúlveda, A. M. Sastre, *Hydrometallurgy* **2014**, *141*, 89.

[4] a) B. T. Ramanjaneyulu, M. Pareek, V. Reddy, R. Vijaya Anand, *Helv. Chim. Acta* **2014**, *97*, 431; b) Z. Deng, J.-H. Lin, J.-C. Xiao, *Nat. Commun.* **2016**, *7*, 10337.

[5] a) S. Kondo, T. Mori, H. Kunisada, Y. Yuki, Makromol. Chem., *Rapid Commun.* **1990**, *11*, 309; b) C. M. Starks, C. L. Liotta, M. E. Halpern, Phase-Transfer Catalysis, Springer, Netherlands, 1994; c) T. Werner, *Adv. Synth. Catal.* **2009**, *351*, 1469.

[6] a) "Phosphorus Compounds, Organic": J. Svara, N. Weferling, T. Hofmann, Ullmann's Encyclopedia of Industrial Chemistry, Wiley, Weinheim, **2006**; b) "Phosphorus Compounds, Inorganic": G. Bettermann, W. Krause, G. Riess and T. Hofmann, Ullmann's Encyclopedia of Industrial Chemistry, Wiley, Weinheim, **2006**.

[7] D. E. C. Corbridge, Phosphorus 2000. Chemistry, Biochemistry & Technology, Elsevier, Amsterdam, 2000.

[8] a) D. J. Scott, *Angew. Chem. Int. Ed.* **2022**, *61*, e202205019; b) Y. Liu, X. Chen, B. Yu, *Chem. Eur. J.* **2023**, *29*, e202302142.

[9] a) U. Lennert, P. B. Arockiam, V. Streitferdt, D. J. Scott, C. Rödl, R. M. Gschwind, R. Wolf, *Nat. Catal.* **2019**, *2*, 1101; b) P. B. Arockiam, U. Lennert, C. Graf, R. Rothfelder, D. J. Scott, T. G. Fischer, K. Zeitler, R. Wolf, *Chem. Eur. J.* **2020**, *26*, 16374; c) R. Rothfelder, V. Streitferdt, U. Lennert, J. Cammarata, D. J. Scott, K. Zeitler, R. M. Gschwind, R. Wolf, *Angew. Chem. Int. Ed.* **2021**, *60*, 24650.

[10] a) G. Lu, J. Chen, X. Huangfu, X. Li, M. Fang, G. Tang, Y. Zhao, *Org. Chem. Front.* **2019**, *6*, 190; b) M. Till, V. Streitferdt, D. J. Scott, M. Mende, R. M. Gschwind, R. Wolf, *Chem. Commun.* **2022**, *58*, 1100; c) F. Chen, M. Bai, Y. Zhang, W. Liu, X. Huangfu, Y. Liu, G. Tang, Y. Zhao, *Angew. Chem. Int. Ed.* **2022**, *61*, e202210334. d) X. Huangfu, W. Liu, H. Xu, Z. Wang, J. Wei, W.-X. Zhang, *Inorg. Chem.* **2023**, *62*, 12009; e) Z. Cai, Y. Zhang, Y. Cao, Y. Liu, G. Tang, Y. Zhao, *ACS Catal.* **2023**, *13*, 8330; f) Y. Chen, W. Liu, X. Huangfu, J. Wei, J. Yu, W.-X. Zhang, *Chem. Eur. J.* **2023**, e202302289.

[11] a) D. G. Yakhvarov, E. V. Gorbachuk, O. G. Sinyashin, *Eur. J. Inorg. Chem.* **2013**, *2013*, 4709; b) Y. Mei, Z. Yan, L. L. Liu, *J. Am. Chem. Soc.* **2022**, *144*, 1517.

[12] a) S. K. Ghosh, C. C. Cummins, J. A. Gladysz, *Org. Chem. Front.* **2018**, *5*, 3421; b) Y. Wang, T. Szilvási, S. Yao, M. Driess, *Nat. Chem.* **2020**, *12*, 801; c) D. J. Scott, J.

Cammarata, M. Schimpf, R. Wolf, *Nat. Chem.* **2021**, *13*, 458; d) M. Donath, K. Schwedtmann, T. Schneider, F. Hennersdorf, A. Bauzá, A. Frontera, J. J. Weigand, *Nat. Chem.* **2022**, *14*, 384.

[13] a) B. M. Cossairt, C. C. Cummins, *New J. Chem.* **2010**, *34*, 1533; b) S. Reichl, E. Mädl, F. Riedlberger, M. Piesch, G. Balázs, M. Seidl, M. Scheer, *Nat. Commun.* **2021**, *12*, 5774.

[14] Commercial availability of aryl halides: ArI (2200), ArBr (61,000), ArCl (240,000); as assessed by a substructure search (screening compounds) on the eMolecules database, accessed May 02, 2024; see also: Y. Zabolotna, D. M. Volochnyuk, S. V. Ryabukhin, D. Horvath, K. S. Gavrilenko, G. Marcou, Y. S. Moroz, O. Oksiuta, A. Varnek, *J. Chem. Inf. Model.* **2021**, *62*, 2171.

[15] a) M. Cybularczyk-Cecotka, J. Szczepanik, M. Giedyk, *Nat. Catal.* **2020**, *3*, 872; b) S. Wu, J. Kaur, T. A. Karl, X. Tian, J. P. Barham, *Angew. Chem. Int. Ed.* **2022**, *61*, e202107811; c) L.-L. Liao, L. Song, S.-S. Yan, J.-H. Ye, D.-G. Yu, *Trends Chem.* **2022**, *4*, 512.

[16] L. Pause, M. Robert and J. M. Savéant, *J. Am. Chem. Soc.* **1999**, *121*, 7158.

[17] X I. A. MacKenzie, L. Wang, N. P. R. Onuska, O.F. Williams, K. Begam, A. M. Moran, B. D. Dunietz, A. Nicewicz, *Nature* **2020**, *580*, 76.

[18] a) K. Schwedtmann, R. Schoemaker, F. Hennersdorf, A. Bauzá, A. Frontera, R. Weiss, J. J. Weigand, *Dalton Trans.* **2016**, *45*, 11384; b) A. N. Barrett, C. R. Woof, C. A. Goult, D. Gasperini, M. F. Mahon, R. L. Webster, *Inorg. Chem.* **2021**, *60*, 16826.

[19] a) For the phosphonium salt $[Ar_4P]Br$ (Ar = 3,5-Dimethoxyphenyl): S. H. Dempsey, S. R. Kass, *J. Org. Chem.* **2022**, *87*, 15466; b) For the phosphine Ar_3P (Ar = 3,5-Dimethoxyphenyl): D. Sinou, D. Maillard, A. Aghmiz, A. M. Masdeui-Bultó, *Adv. Synth. Catal.* **2003**, *345*, 603.

[20] The assignment of the phosphonium salt $[Ar_4P]X$ and the phosphine Ar_3P (Ar = 3-Ethylphenyl; X = Br, Cl) appears to be unreported; its formation was based on the characteristic chemical shift.

[21] The phosphonium salt $[Ar_4P]X$ (X = Br, Cl; Ar = 4-Methylthiophenyl) appears to be unreported; its formation was based on the characteristic chemical shift. The assignment of the phosphine Ar_3P was based on the following literature reference: F. Ragaini, L. Lunardi, D. Tomasoni, V. Guglielmi, *J. Organomet. Chem.* **2004**, *689*, 3621.

[22] The phosphonium salt $[Ar_4P]X$ (X = Br, Cl; Ar = 4-Phenoxyphenyl) appears to be unreported; its formation was based on the characteristic chemical shift. The assignment of the phosphine Ar_3P was based on the following literature reference: C. Rieg, D. Dittmann, Z. Li, R. Lawitzki, K. Gugeler, S. Maier, G. Schmitz, J. Kästner, D. P. Estes, M. Dyballa, *Chem. Eur. J.* **2021**, *27*, 17012.

[23] The assignment of the phosphonium salt $[Ar_4P]Br$ (Ar = 4-Cyanophenyl) appears to be unreported; its formation was based on the characteristic chemical shift.

[24] The phosphonium salt $[Ar_4P]Br$ (Ar = 3-Cyanophenyl) appears to be unreported; its formation was based on the characteristic chemical shift. The assignment of the phosphine Ar_3P was based on the following literature reference: V. Ravindar, H. Hemling, H. Schumann, J. Blum, *Synth. Commun.* **1992**, *22*, 841.

[25] D. Marcoux and A. B. Charrette, *J. Org. Chem.* **2008**, *73*, 590.

[26] M. Kuroboshi, H. Tanaka, H. Kawakubo, T. Yano, K. Kobayashi, S. Kamenoue, T. Akagi, *Synthesis* **2011**, *24*, 4091.

Chapter 6 Summary and Conclusion

Chapter 1. Synergistic Effects in Bimetallic s-Block and d-Block Metal Compounds: Small Molecule Activation and Catalysis

Bimetallic s-block and d-block metal compounds represent a growing class of catalysts with distinct modes of reactivity. These systems exploit the combined effects of a transition metal – typically serving as the catalytic center – and an s-block metal cation, which tunes the reactivity through non-covalent interactions, electronic effects and auxiliary substrate coordination.

The introductory chapter reviews recent advances in fundamental chemical transformations promoted by s- and d-block heterobimetallic complexes (Figure 1). Following a brief classification of their properties and cooperative reactivity modes, the applications of these complexes in small molecule activation and catalysis are outlined. Examples cover a wide range of transformations where bimetallic effects are not only beneficial but often essential. Hydrogenation, bond activation (e.g., C–H), isomerization, and polymerization reactions demonstrate clear dependence on the cooperative role of both metals. Structural and mechanistic studies support cooperative activation modes, such as multisite substrate binding or parallel activation at separate metal centers. Intimate ion pairing is essential in many systems, facilitating close proximity and communication between the metal centers. Strikingly, cation-dependent reactivity may significantly influence catalytic behavior.

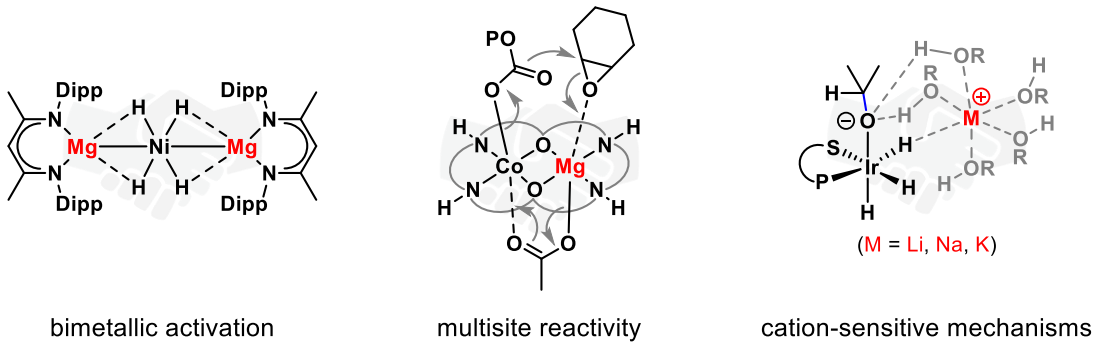

Figure 1. Selected examples of cooperative reactivity in s-block and d-block bimetallic compounds.

Chapter 2. Counterion Effect in Cobaltate-Catalyzed Alkene Hydrogenation

Low-valent metalates are increasingly employed in homogeneous catalysis; however, the crucial influence of the counterion on their reactivity is often neglected. In chapter 2, a systematic investigation of alkene hydrogenation using a series of cobaltate complexes is reported. The pre-catalysts of the general structure [Cation][Co(η^4-cod)$_2$] (where Cation = K(thf)$_{0.25}$ (**2-1**), Na(thf)$_{1.5}$ (**2-2**), Li(thf)$_2$ (**2-3**), (^{Dep}nacnac)Mg (**2-4**), and N(^{n}Bu)$_4$ (**2-5**); cod = 1,5-cyclooctadiene, ^{Dep}nacnac = {2,6-Et$_2$C$_6$H$_3$NC(CH$_3$)}$_2$CH) were employed in comparative hydrogenation reactions of unfunctionalized alkenes in THF (Figure 2).

With increasing steric demand, the lithium salt **2-3** and magnesium salt **2-4** significantly outperform the other catalysts, resulting in the reactivity trend: K^+ (**2-1**) < Na^+ (**2-2**) < Li^+ (**2-3**) < (^{Dep}nacnac)Mg^+ (**2-4**). The lack of reactivity observed for the tetra-*n*-butyl-ammonium cobaltate **2-5** further indicates that a metal containing cation is essential for hydrogenation activity. Consistent with the catalytic investigations, reaction progress analyses and pre-catalyst hydrogenation experiments revealed differing reaction rates for the cobaltate salts **2-1** to **2-5**. The most active pre-catalyst [(^{Dep}nacnac)Mg][Co(η^4-cod)$_2$] (**2-4**) efficiently hydrogenated tri- and tetra-substituted alkenes under mild conditions. Poisoning studies and NMR spectroscopic monitoring experiments support the homotopic nature of the reaction mechanism.

Combined molecular dynamics (MD) simulations and density functional theory (DFT) calculations of the styrene hydrogenation reaction suggest that the s-block metal cation coordinates to the hydride ligand ([Co–H]···M^+) during the turnover-limiting migratory insertion step. Compared to the anion-only model system, this interaction has a beneficial, energy-lowering effect, with the lowest activation barriers calculated for M = Li (**2-3**) and M = (^{Dep}nacnac)Mg (**2-4**). Non-covalent interaction (NCI) analysis of the migratory insertion transition states for **2-1** to **2-4** reveal progressively stronger attractive interactions of the metal cations with one of the hydrido ligands, following the trend: K^+ (**2-1**) < Na^+ (**2-2**) < Li^+ (**2-3**) < (^{Dep}nacnac)Mg^+ (**2-4**). This induces a stronger Co–H bond polarization, which is proposed to improve the catalytic activity.

This study shows that countercation coordination can significantly modulate the reactivity of metalate anions in hydrogenation and possibly other hydride-mediated reactions. More broadly, it highlights the critical influence of countercation identity on reactivity, emphasizing the importance of detailed studies on ion pairing interactions in future work.

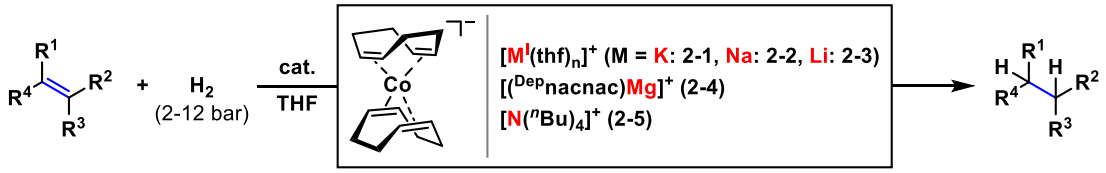

	K (2-1)	Na (2-2)	Li (2-3)	Mg (2-4)	N(^{n}Bu)$_4$ (2-5)
$(CH_2)_4$	63	98	>99	>99	1 (23)
Ph	8 (15)	76 (82)	>99	>99	1 (7)
Ph	4 (6)	20 (20)	72 (77)	>99	/

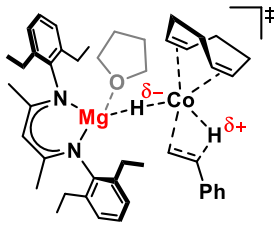

Figure 2. Alkene hydrogenation using s-block metal cobaltates **2-1** to **2-5**. Comparative reactivity study showing the countercation effect and proposed [Co–H]···M^+ interaction in the migratory insertion transition state of styrene hydrogenation.

Chapter 3. A Highly Reduced Magnesium Dicobalt Complex for the Hydrogenation of Tri- and Tetra-Substituted Alkenes

The exceptional reactivity of [(^{Dep}nacnac)Mg][Co(η^4-cod)$_2$] in alkene hydrogenation (chapter 2) raised the question of whether the β-diketiminate ligand in the [(^{Dep}nacnac)Mg]$^+$ countercation influences catalytic activity. While preliminary studies suggested no direct involvement of the β-diketiminate ligand, a definitive answer to this question required a ligand-free magnesium cobaltate complex.

This chapter reports the synthesis and characterization of an unsupported magnesium dicobalt complex Mg[Co(η^4-cod)$_2$]$_2$ (**3-1**) through the reaction of [K(thf)$_{0.33}$][Co(η^4-cod)$_2$] with 0.5 equivalents of MgCl$_2$. The solid-state molecular structure of **3-1** features a trinuclear contact ion pair, in which a Mg^{2+} cation is sandwiched by two [Co(η^4-cod)$_2$]$^-$ units. The two [Co(η^4-cod)$_2$]$^-$ anions are rotated towards each other at 50.42(6)° along the Co–Mg–Co axis, which is effectively linear with an angle of 179.36(4)° (Co1–Mg1–Co2). NMR spectroscopic studies, including DOSY NMR investigations, suggest that the ion triple remains intact in toluene solution, while further coordination experiments show that the intimate ion pair structure cannot be broken by Lewis donors such as THF. Quantum chemical studies indicate the presence of an ionic magnesium-cobalt interaction and weak dative bonds between the 1,5-cyclooctadiene ligands and Mg^{2+}, which were experimentally verified by ^{13}C{^{1}H} NMR chemical shift analysis.

Complex **3-1** efficiently catalyzes the hydrogenation of sterically challenging tri- and tetra-substituted alkenes, outperforming the related alkali metal salts and the magnesium β-diketiminate salt (see chapter 2). These results highlight a pronounced counterion effect, inherent to the Mg^{2+} cation and independent of the supporting β-diketiminate ligand.

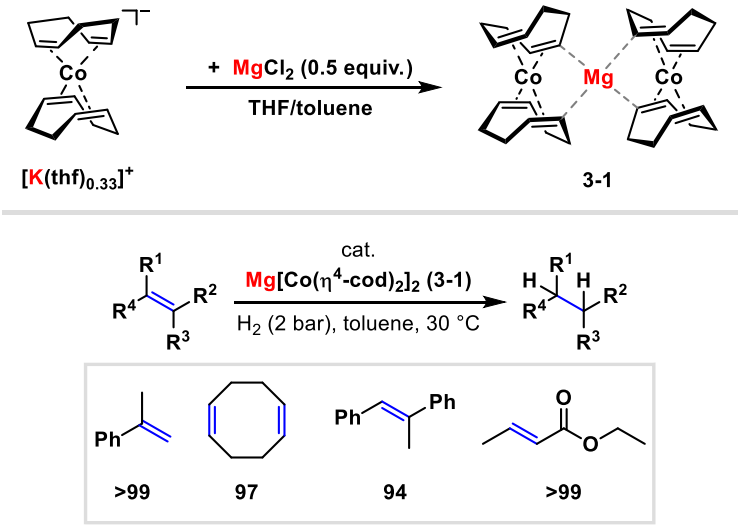

Figure 3. Synthesis of Mg[Co(η^4-cod)$_2$]$_2$ (**3-1**) from [K(thf)$_{0.33}$][Co(η^4-cod)$_2$] and hydrogenation catalysis using **3-1**.

Chapter 4. Synthesis, Characterization and Reactivity of Phosphine-Stabilized Cobalt Hydrides

Bimetallic cobalt hydride intermediates with direct cation-hydride interactions were proposed in the hydrogenation reactions using alkali and alkaline earth metal cobaltates as pre-catalysts (chapter 2). While the intimate ion pair structures were computationally modeled and the influence of the s-block metal cation linked to the observed reactivity, the isolation of any bimetallic hydride species was unsuccessful.

Chapter 4 reports on the stabilization of β-diketiminate magnesium tetrahydride cobaltates by diphosphines. The complexes [(^{Ar}nacnac)Mg][CoH_4(dcpe)] (Ar = 2,6-diethylphenyl [Dep], **4-1**; Ar = 2,4,6-mesityl [Mes], **4-2**) were obtained by hydrogenating [(^{Ar}nacnac)Mg][Co(η^4-cod)$_2$] (Ar = Dep, Mes) in the presence of 1,2-bis(dicyclohexylphosphino)ethane (dcpe). Structural and spectroscopic analysis of the hydride **4-1** reveals an intimate ion pair character in non-coordinating and coordinating solvents (toluene vs. THF). Computational studies suggest strong magnesium-hydride and cobalt-hydride interactions, with no metal-metal bonding observed. Complex **4-1** is a suitable pre-catalyst for alkene hydrogenation reactions. Notably, an experimental monitoring of the catalytic cycle shows that **4-1** can be converted into an alkene complex by reaction with styrene, which is fully recovered upon exposure to H_2. These results suggest the function of **4-1** as a reversible reservoir for the active catalyst and support the direct involvement of the countercation in the hydrogenation reaction, which was initially proposed only *in silico* for the related alkene pre-catalysts (Figure 2, chapter 2). Moreover, complexes **4-1** and **4-2** readily react with white phosphorus (P_4) to form *cyclo*-P_4 complexes [(^{Ar}nacnac)Mg][(μ,η^4:η^4-P_4)Co(dcpe)] (Ar = Dep, **4-5**; Ar = Mes, **4-6**), which were structurally characterized and display promising reactivity toward small molecules in a preliminary study.

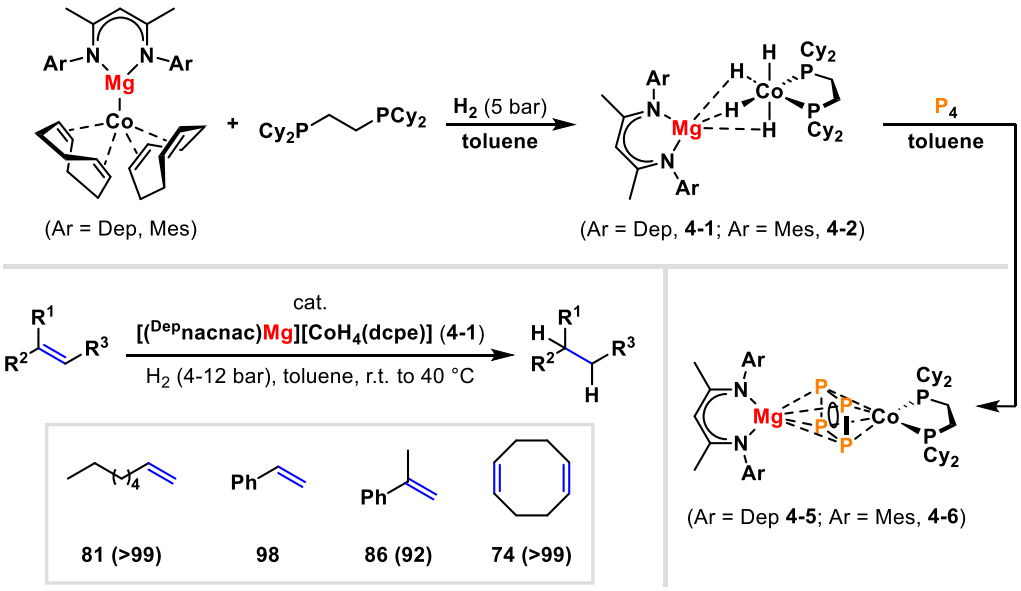

Figure 4. Synthesis of [(^{Ar}nacnac)Mg][CoH_4(dcpe)] (Ar = Dep, **4-1**; Ar = Mes, **4-2**) from [(^{Ar}nacnac)Mg][Co(η^4-cod)$_2$]. Hydrogenation catalysis using **4-1**, and reaction of **4-1** and **4-2** with P_4 to *cyclo*-P_4 complexes [(^{Ar}nacnac)Mg][(μ,η^4:η^4-P_4)Co(dcpe)] (Ar = Dep, **4-5**; Ar = Mes, **4-6**).

Chapter 5. Photocatalytic Functionalization of White Phosphorus with Aryl Bromides and Chlorides

In a distinct project, chapter 5 describes the direct synthesis of arylated phosphines and phosphonium salts from P_4 using an efficient photocatalytic approach. By employing the organic photocatalyst Mes-Acr-BF_4 (9-mesityl-3,6-di-*tert*-butyl-10-phenylacridinium tetrafluoroborate) and NEt_3 under near-UV light irradiation, this method enables the direct arylation of P_4 with inexpensive and readily available aryl bromides and chlorides, affording triarylphosphines and tetraarylphosphonium salts in up to 75% combined yield of Ar_3P and $[Ar_4P]X$ (X = Br, Cl) (Figure 5). This method represents a significant advancement over previous photocatalytic protocols, which were limited to aryl iodides and/or relied on a precious metal photocatalyst.

Mechanistic studies, including ^{31}P NMR spectroscopic monitoring and model reactions, support a stepwise arylation of P_4 via the sequential formation of polyphosphorus and monophosphorus intermediates. While it remains difficult to identify early reaction intermediates (i.e., P_n-species with n > 2), the formation of $PhPH_2$, Ph_2PH, and Ph_4P_2 is confirmed by $^{31}P\{^1H\}$ NMR spectroscopic monitoring of the phenylation of P_4. In addition, the phenylation of the cyclopentaphosphine Ph_5P_5 showed that smaller cyclophosphines such as Ph_4P_4 and Ph_3P_3 can be detected at an early stage, suggesting that related oligophosphines are conceivable reaction intermediates. Further studies on product stability showed that both the phosphonium salts (e.g., $[Ph_4P]Br$) and earlier reaction intermediates (e.g., Ph_3P, Ph_2PH, $PhPH_2$, and Ph_4P_2) are unstable under the photocatalytic conditions employed. These findings suggest the possibility of an unproductive de-arylation reaction, limiting the catalytic efficiency.

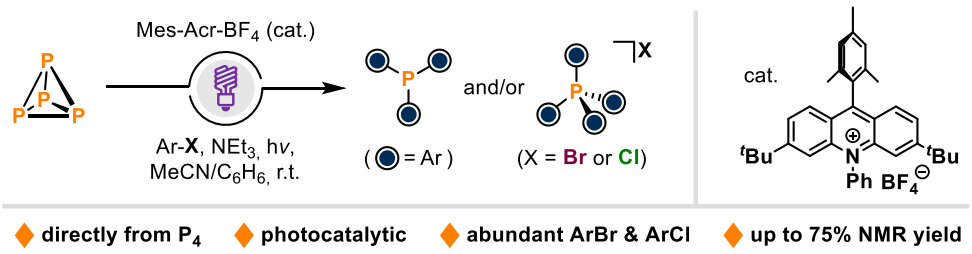

Figure 5. Photocatalytic synthesis of arylated phosphines (Ar_3P) and phosphonium salts ($[Ar_4P]X$; X = Br, Cl) directly from P_4, employing cheap and abundant aryl bromides and chlorides.

Conclusion

In summary, this doctoral thesis highlights the potential of countercation-sensitive mechanisms in reductive catalysis with cobaltate anions. Hydrogenations of unfunctionalized alkenes employing a series of cobaltate pre-catalysts (**2-1** to **2-5** and **3-1**) containing the same anion but different organic and s-block metal cations demonstrated a marked effect of the counterion on the catalytic performance. Computational investigations attributed these reactivity changes to the formation of intimate ion pair structures, in which direct interactions between the cobalt hydride and the s-block metal cation play a pivotal role. Targeted synthesis enabled the isolation of bimetallic cobalt hydride complexes (**4-1** and **4-2**) featuring direct s-block metal-cobalt hydride interactions. Bimetallic hydride **4-1** was demonstrated to act as a potent pre-catalyst in alkene hydrogenation, and mechanistic experiments suggest its function as a reversible reservoir for the active catalytic species.
These results establish a foundation for countercation-sensitive hydrogenation catalysis employing anionic metalate pre-catalysts. The identity of the countercation and ion pairing effects can crucially influence the reactivity. Based on these insights, it should become possible to deliberately tune the reactivity of metalates by modulation of their countercations.

The final part of this thesis covered a distinct project on the photocatalytic functionalization of white phosphorus (P_4) using inexpensive and abundant aryl bromides and chlorides. This work expands the limited set of catalytic methods currently available for the functionalization of P_4. Although still at an early stage, the methodology provides a promising foundation for the future development of practical methods for the efficient functionalization of P_4.

Chapter 7 Acknowledgements

Abschließend möchte ich Danke sagen, denn diese Arbeit wäre ohne die Hilfe zahlreicher Personen nicht möglich.

Zuerst und ganz besonders möchte ich mich bei Prof. Dr. Robert Wolf für die Betreuung in den letzten Jahren bedanken. Für deine Unterstützung in jeglichen Belangen, die wissenschaftliche Freiheit und das mir entgegengebrachte Vertrauen bin ich sehr dankbar.
Für die Anfertigung des Zweitgutachtens spreche ich Prof. Dr. Axel Jacobi von Wangelin meinen ausdrücklichen Dank aus. Ebenso danke ich Prof. Dr. Ruth M. Gschwind für die Übernahme der Rolle der Drittprüferin und Prof. Dr. Patrick Nürnberger für seine Bereitschaft, den Vorsitz der Prüfungskommission zu übernehmen.
Vielen Dank an Gábor Balázs, für die vielen Gespräche, dein stets offenes Ohr und das Korrekturlesen dieser Arbeit.

Weiter möchte ich mich bei den Mitarbeitern der zentralen Analytik und Werkstätten bedanken, insbesondere bei Birgit Hischa, Sabine Stempfhuber, Florian Meurer und Dr. Michael Bodensteiner (Röntgenstrukturanalyse), Tuan-Anh Nguyen, Sebastian Bock, Fritz Kastner, Annette Schramm, Georgine Stühler, und Dr. Ilya Shenderovich (NMR-Abteilung), Barbara Baumann und Helmut Schüller (Elementaranalyse), Carl-Heinz Hierl, Helena Ackermann, Romy Knop, Markus Lindner (Glasbläserei), Peter Fuchs und Andreas Gruber (Elektronikwerkstatt) und Andreas Graf und Thomas Meyer (Feinmechanik).

Vielen Dank an meine Kooperationspartner für die gute Zusammenarbeit und wertvollen Beiträge. Danke an Prof. Dr. Axel Jacobi von Wangelin (Universität Hamburg) sowie Daniel Schmidhuber und Prof. Dr. Julia Rehbein (Universität Regensburg). Großer Dank an meine Bacheloranden und Forschungspraktikanten Alexis Stamatopoulos, Florian Sixt, Jannes Rückel und Xaver Weichselgartner für eure Unterstützung im Labor.

Ich möchte mich auch bei allen früheren und aktuellen Arbeitskreismitgliedern bedanken – für die tolle Stimmung, das vertrauensvolle Miteinander und all die schönen gemeinsamen Momente, an die ich mich gerne zurückerinnern werde.

Ein großes Danke an meine direkten Laborkollegen Jose Cammarata, Felix Seeberger, Jannes Rückel, Michael Mende, und Marion Till für unzählige lustige Gespräche, hitzige Diskussionen, spontane Tanzstunden im Labor, tiefgehende Videoanalysen, und so vieles mehr. Es war immer schön ins Labor zu kommen.

Insbesondere Danke an Jose, Felix und John Kelly für die Unterstützung im Labor, die vielen gemeinsamen Abende, die Reisen und Ausflüge, die (absurden) Debatten, und vor allem für eure Freundschaft.

Meinen Eltern, Andreas und Olga, und meinem Bruder Eduard danke ich von Herzen. Für eure bedingungslose Unterstützung, euren festen Glauben an mich und eure Hilfe in kleinen wie großen Dingen. Danke, dass ich mich immer auf euch verlassen konnte.

Zuletzt möchte ich mich bei meiner Partnerin Matea bedanken. Danke, dass du mir in diesem wichtigen Lebensabschnitt Rückhalt geboten hast, mich immer wieder ermutigt und dich von Herzen über selbst meine kleinsten Erfolge mitgefreut hast. Hvala ti što si radost koju često trebam, ali ponekad zaboravim pronaći.

Chapter 8 Curriculum Vitae

Education

June.2021 to present	**PhD, Chemistry** under the Supervision of Prof. Dr. Robert Wolf at the University of Regensburg, Germany
Oct.2018 to Dec.2020	**M.Sc. Advanced Synthesis and Catalysis** of the Elite Network of Bavaria at the University of Regensburg, Germany Final Grade: 1.0
Oct.2015 to Sept.2018	**B.Sc. Chemistry** at the University of Regensburg, Germany Final Grade: 1.3
Sept.2007 to June.2015	**Higher Education Entrance Qualification (Abitur)** at the Gymnasium Waldkraiburg, Germany Final Grade: 1.1

Training and Work Experience

Sept.2023 to Dec.2023	**Research Internship (PhD)** under the Supervision of Prof. Dr. Yasuhiro Ohki at the Institute for Chemical Research, University of Kyoto, Japan
Dec.2020 to March.2021	**Industry Internship** in Research and Development at Novaled GmbH in Dresden, Germany
Juli.2019 to Sept.2019	**Research Internship (M.Sc.)** under the Supervision of Prof. Dr. Stephen P. Thomas at the University of Edinburgh, Scotland
June.2019 to Juli.2019	**Scientific Assistant** under the Supervision of PD Dr. Jonathan Bauer at the University of Regensburg, Germany

Honors and Awards

Aug.2021 to Juli.2023	**Kekulé-Fellowship** of the "Fonds der Chemischen Industrie"
Juli.2022	**M.Sc. Graduation Award** for Excellent Score from the "Universitätsstiftung Dr. Alfons Paulus"
June.2019	**B.Sc. Graduation Award** for Excellent Score from the "Universitätsstiftung Dr. Alfons Paulus"
Apr.2019 to March.2020	**Deutschlandstipendium-Scholarship**
June.2015	**GDCh-Abitur Award** in Chemistry

Conference Contributions

Sept.2024	**Poster Presentation** at the "GDCh Conference on Inorganic Chemistry" in Munich, Germany
Sept.2024	**Poster Presentation** at the "23rd Lecture Conference ORCHEM 2024" in Regensburg, Germany
July.2024	**Poster Presentation** at the "29th PhotoIUPAC – IUPAC Symposium on Photochemistry" in València, Spain
March.2023	**Poster Presentation** at the "19th European Workshop on Phosphorus Chemistry (EWPC)" in Donostia-San Sebastián, Spain
March.2023	**Oral Talk** at the "AG Phosphorchemie" in Dresden, Germany
Sept.2022	**Oral Talk** at the "17. Koordinationschemie-Treffen (KCT)" in Jena, Germany
Juli.2022	**Poster Presentation** at the "29th International Conference on Organometallic Chemistry (ICOMC)" in Prague, Czech Republic
Oct.2019	**Oral Talk** at the "6th Croatian Chemistry Student Symposium" in Zagreb, Croatia

Chapter 9 List of Publications

[1] J. Rückel, T. Pavlovska, M. Gawron, R. Cibulka, R. Wolf, "Deazaflavin-Catalyzed Arylation of White Phosphorus with Aryl Bromides and Chlorides", submitted to *Adv. Synth. Catal.* on **14/04/2025**.

[2] M. Gawron, J. Rückel, R. Wolf, "Photocatalytic functionalization of white phosphorus with aryl bromides and chlorides", *Chem. Commun.* **2024**, *60*, 9777–9780.

[3] M. Gawron, F. Gilch, D. Schmidhuber, J. A. Kelly, T. M. Horsley Downie, A. Jacobi von Wangelin, J. Rehbein, R. Wolf, "Counterion Effect in Cobaltate-Catalyzed Alkene Hydrogenation", *Angew. Chem. Int. Ed.* **2024**, *63*, e202315381.

[4] T. M. Maier, M. Gawron, P. Coburger, M. Bodensteiner, R. Wolf, N. P. van Leest, B. de Bruin, S. Demeshko, F. Meyer, "Low-Valence Anionic α-Diimine Iron Complexes: Synthesis, Characterization, and Catalytic Hydroboration Studies", *Inorg. Chem.* **2020**, *59*, 16035–16052.

Eidesstaattliche Erklärung

Ich erkläre hiermit an Eides statt, dass ich die vorliegende Arbeit ohne unzulässige Hilfe Dritter und ohne Benutzung anderer als der angegebenen Hilfsmittel angefertigt habe; die aus anderen Quellen direkt oder indirekt übernommenen Daten und Konzepte sind unter Angabe des Literaturzitats gekennzeichnet. Die Arbeit wurde bisher weder im In- noch im Ausland in gleicher oder ähnlicher Form einer anderen Prüfungsbehörde vorgelegt.

Martin Gawron